

Crystal Chemistry of Boron-Bearing Mullite-Type Compounds

Inauguraldissertation
der Philosophisch-naturwissenschaftlichen Fakultät
der Universität Bern

vorgelegt von

Martin Fisch
von Egnach TG

Leiter der Arbeit:
Prof. Dr. T. Armbruster
Institut für Geologie

Von der Philosophisch-naturwissenschaftlichen Fakultät angenommen.

Original document saved on the web server of the University Library of Bern



This work is licensed under a
Creative Commons Attribution-Non-Commercial-No derivative works 2.5 Switzerland
licence. To see the licence go to <http://creativecommons.org/licenses/by-nc-nd/2.5/ch/> or
write to Creative Commons, 171 Second Street, Suite 300, San Francisco, California 94105,
USA.

Copyright Notice

This document is licensed under the Creative Commons Attribution-Non-Commercial-No derivative works 2.5 Switzerland. <http://creativecommons.org/licenses/by-nc-nd/2.5/ch/>

You are free:



to copy, distribute, display, and perform the work

Under the following conditions:



Attribution. You must give the original author credit.



Non-Commercial. You may not use this work for commercial purposes.



No derivative works. You may not alter, transform, or build upon this work..

For any reuse or distribution, you must take clear to others the license terms of this work.

Any of these conditions can be waived if you get permission from the copyright holder.

Nothing in this license impairs or restricts the author's moral rights according to Swiss law.

The detailed license agreement can be found at:

<http://creativecommons.org/licenses/by-nc-nd/2.5/ch/legalcode.de>

Crystal Chemistry of Boron-Bearing Mullite-Type Compounds

Inauguraldissertation
der Philosophisch-naturwissenschaftlichen Fakultät
der Universität Bern

vorgelegt von
Martin Fisch
von Egnach TG

Leiter der Arbeit:
Prof. Dr. T. Armbruster
Institut für Geologie

Von der Philosophisch-naturwissenschaftlichen Fakultät angenommen.

Bern, 13. April 2011

Der Dekan
Prof. Dr. S. Decurtins

Contents

1	Summary	1
2	Introduction	3
2.1	Mullite	3
2.2	Boron-Mullites	9
2.3	Element Boron	19
2.4	Crystal Chemistry of Boron-Bearing Minerals	25
2.5	Analytical Techniques for Boron Analysis	27
3	Boron Mullite Synthesis Experiments	29
3.1	Al ₂ O ₃ -B ₂ O ₃ Compounds with Mullite-Type Structure	30
3.2	Al ₂ O ₃ -B ₂ O ₃ -SiO ₂ Compounds with Mullite-Type Structure	42
3.3	Discussion	44
4	Crystal-Chemistry of Mullite-Type Aluminoborates Al₁₈B₄O₃₃ and Al₅BO₉: A stoichiometry puzzle	47
4.1	Abstract	48
4.2	Introduction	48
4.3	Historical Background	50
4.4	Experimental	51
4.5	Results	57
4.6	Discussion	64
5	Thermal Expansion of Aluminoborates	69
5.1	Abstract	70
5.2	Introduction	70
5.3	Sample Description	70
5.4	X-ray Diffraction Methods	71
5.5	Results and Discussion	73
5.6	Discussion	80
6	Thermal Stability of Jeremejevite	83
6.1	Introduction	83
6.2	Experimental	83

6.3	Results	84
6.4	Discussion	84
7	Stability at High Pressure, Elastic Behavior and Pressure-Induced Structural Evolution of "Al₅BO₉", a Mullite-Type Ceramic Material	89
7.1	Abstract	90
7.2	Introduction	90
7.3	Experimental Methods	93
7.4	Elastic Behavior	95
7.5	Structural Evolution with Pressure	97
7.6	Discussion and Conclusions	103
8	Solid Solution Experiments	107
8.1	Introduction	107
8.2	Experimental	109
8.3	Results	110
8.4	Discussion	112
	References	131
A	Supplementary Data	147
A.1	Supplementary Data for Chapter 4	147
A.2	Supplementary Data for Chapter 5	171
A.3	Supplementary Data for Chapter 7	194
B	Powder X-ray Diffraction Tips & Tricks	209
B.1	Configuring a Measurement Program for the X'Pert Pro Diffractometer	210
B.2	Configuring the X'Pert Pro MPD Diffractometer	214
B.3	Theory on Rietveld Refinements	220
B.4	High-Temperature Measurements Using the Anton-Paar HTK 1200 Furnace	226
B.5	Rietveld Refinements with Topas Academic v. 4.1	231
C	Acknowledgments	259
D	Publications	261
E	Declaration	263
F	Curriculum Vitae	265

1 Summary

Compounds with mullite-type crystal structures are characterized by unique thermal properties making them important raw materials for industrial applications. Within a constrained stability field in the system $\text{Al}_2\text{O}_3\text{-B}_2\text{O}_3\text{-SiO}_2$, mullite-type boron compounds exist. Boron-bearing aluminosilicates with mullite-type structures are rare in nature and restricted to specific formation conditions, whereas mullite-type aluminoborates have not been observed in nature. With regard on industrial applications, $\text{Al}_{18}\text{B}_4\text{O}_{33}$ is the most cited boron-mullite.

Difficulties in precise quantitative boron analyses may be the reason that this compound is reported with two slightly different compositions: $\text{Al}_{18}\text{B}_4\text{O}_{33}$ ($=\text{Al}_{4.91}\text{B}_{1.09}\text{O}_9$, $9\text{Al}_2\text{O}_3:2\text{B}_2\text{O}_3$) and Al_5BO_9 ($5\text{Al}_2\text{O}_3:\text{B}_2\text{O}_3$). The crystal structure of this compound is in agreement with the Al_5BO_9 stoichiometry and the discrepancy to the boron-rich composition was explained by a small amount of boron substituting aluminum.

In this study, single-crystal and powder samples were synthesized by flux, solid-state and sol-gel methods from various Al- and B-containing starting materials representing both stoichiometries. Position and coordination of boron in the crystal structures of the samples was precisely determined by single-crystal and powder X-ray diffraction (XRD), as well as by ^{11}B and ^{27}Al solid-state MAS nuclear magnetic resonance (NMR), Fourier-transformed infrared (FTIR) and Raman spectroscopy. Results indicated that none of the products crystallized as $\text{Al}_{18}\text{B}_4\text{O}_{33}$ but rather as $\text{Al}_{5-x}\text{B}_{1+x}\text{O}_9$ with $x \approx 0.03(2)$, which is close to Al_5BO_9 . This result was subsequently confirmed from quantitative B_2O_3 analyses by laser-ablation inductively coupled plasma mass spectrometry.

Compounds with boron in the crystal structure are known for low thermal expansion due to rigid behavior of the boron polyhedra. From in-situ measured high-temperature X-ray diffraction data, thermal expansion parameters α were obtained for synthetic Al_5BO_9 , $\text{Al}_4\text{B}_2\text{O}_9$ and natural grandidierite ($(\text{Fe,Mg})\text{Al}_3\text{BSiO}_9$). Despite its different structure type, F-rich jeremejevite ($\text{Al}_6\text{B}_5\text{O}_{15}(\text{F,OH})_3$) was included because it contains the same cations as the aluminoborates.

Results showed that anisotropic thermal expansion of the compounds is governed by changes of M-O-M angles and anomalous anisotropic behavior of Al- and Mg-polyhedra, whereas angular changes and expansion of boron polyhedra are not significant. Expansion of Al_5BO_9 is lowest parallel to the chains of Al-octahedra.

During high-temperature data collection of jeremejevite ($\text{Al}_6\text{B}_5\text{O}_{15}\text{F}_3$), the sample decomposed above ca. 800°C , yielding a phase identified as mullite-type $\text{Al}_4\text{B}_2\text{O}_9$. At ca. 1050°C , $\text{Al}_4\text{B}_2\text{O}_9$ transforms to Al_5BO_9 .

Elastic behavior and pressure-induced structural evolution of Al_5BO_9 was analyzed by in-situ high-pressure single-crystal X-ray diffraction up to 7.4 GPa at hydrostatic conditions. With increasing pressure, the unit cell volume decreases due to changes of M-O-M angles. The lowest compressibility has been found along the chains of octahedra.

Solid solutions in the "B-mullite" stability field have been suspected, however, only few systematic data are available. Thus, sol-gel derived samples between compositions of aluminoborates Al_5BO_9 and $\text{Al}_4\text{B}_2\text{O}_9$ and the aluminosilicate sillimanite (Al_2SiO_5) were synthesized at 950°C and 1250°. Decreasing lattice parameters of mullite-like phases (space group $Pbam$) may indicate boron incorporation in the 950°C samples. Samples with less than 20 mol-% SiO_2 and more than 20 mol-% B_2O_3 contain four-fold coordinated boron, as identified from FTIR spectra. A mullite-type phase in space group $Cmc2_1$ was detected in the 1250° samples. Refining this phase with variable amounts of Al_5BO_9 - and sillimanite-modules may indicate a trend to more Si towards sillimanite composition. However, excess phases and sluggish reaction rates are an unambiguous indicator for non-equilibrium conditions. These preliminary results may thus be regarded as lead for further studies.

2 Introduction

2.1 Mullite

Mullite as mineral occurs rarely in nature where it forms as prismatic needles from contact metamorphosed (high temperature, low pressure) clay-sandstones (Tröger, 1971) or in argillaceous inclusions in Tertiary eruptive rocks (Figure 2.1). Mullite is often associated with corundum, sillimanite, kyanite, magnetite, spinel, pseudobrookite, sanidine and cordierite (Anthony et al., 2003).

Mullite as crystalline compound was used in synthetic materials long before it was found as a mineral in nature, although the material was not known and recognized as mullite.

Around 620 AD, the Chinese were among the first who used fired clay for the production of porcelanic wares (Schneider 2005a and refs. therein). In their advanced furnaces they were able to reach temperatures as high as 1250°C to 1400°C (Kerr et al. 2004), at which mullite is formed from the raw materials.

In the late Middle Age in Europe, ceramic crucibles known as "Hessian porcelain wares" (Figure 2.2) were prominent for their superior quality. Their outstanding properties and quality were ascribed to the secret production process known as the "mystery of the Hessian wares" (Marcos et al. 2006). Hessian wares were made from a mixture of kaolinitic clay and quartz sand, which was subsequently heated at – for that time – unusually high temperatures. The processing of the raw materials at high temperatures led to the formation of mullite which acted as reinforcer of the ceramic materials (Figure 2.9).

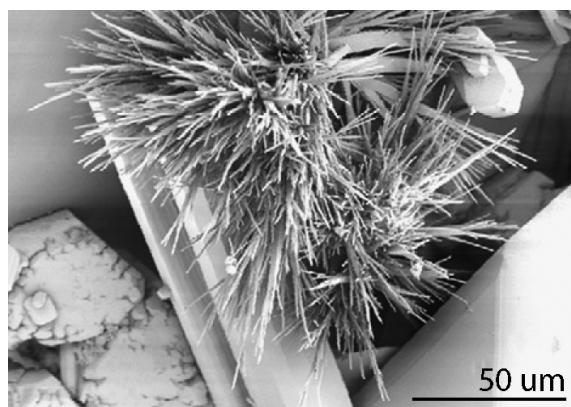


Figure 2.1: SEM photograph of mullite fibers found in volcanic rocks (Eifel Mountain, Germany, from Schneider et al. 2008).

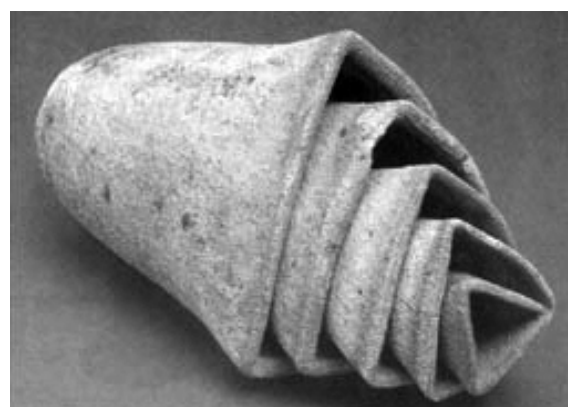


Figure 2.2: Ceramic crucibles known as "Hessian porcelain wares" (from Marcos et al. 2006).

From 1850 to the early 20th century, scientists observed agicular, fibrous crystals occurring in synthetic compounds produced at high temperature in the system $\text{Al}_2\text{O}_3\text{-SiO}_2$. Based on their habit, the crystals were identified as sillimanite (Fischer and Schneider 2005, Schneider 2005a and refs. therein) and its polymorph andalusite (Deville and Caron 1865).

Shepherd et al. (1909) concluded that in the system "Alumina-Silica" ($\text{Al}_2\text{O}_3\text{-SiO}_2$), crystals identified as "sillimanite" together with corundum and cristobalite were the only phases stable at high temperature, and that the Al_2SiO_5 polymorphs andalusite and kyanite transformed to sillimanite when heated above 1300°C.

Bowen et al. (1924a) recognized that this synthetic compound was in fact not sillimanite ($\text{Al}_2\text{O}_3\text{:SiO}_2$) but a crystalline material of which they confirmed the chemical composition of $3\text{Al}_2\text{O}_3\text{:2SiO}_2$. While investigating rock samples originating from the Scottish Hebridean Island of Mull, Bowen et al. (1924a) found the same material as naturally occurring mineral: "Found in fused argillaceous inclusions in Tertiary eruptive rocks of the Western Isles of Mull, Scotland. Occurs as abundant prisms associated with rare plates of corundum. It is also abundantly developed in many artificial melts and in porcelains, being the material usually called sillimanite. Its similarity to sillimanite is very great." Based on the on the locality at which it was first found, Bowen and Greig (1924b) and Bowen et al. (1924c) proposed the name "mullite" for this alumosilicate mineral.

When stating: "The discovery of mullite is a striking example of the application of physical-chemical methods to mineralogy. The mineral was first noted in artificial preparations and later sought for in argillaceous rocks that had been subjected to a high heat," Bowen et al. (1924a) could not be aware that within the same century, the material first known from synthetic products and only later found in nature would again become a thoroughly investigated and very prominent synthetic crystalline compound.

Nowadays, due to its rare occurrence in nature and the large volume of mullite used in industry, synthetic mullite plays an important role. Mullite can be produced by heat treatment from kaolinite ($\text{Al}_2\text{Si}_2\text{O}_5(\text{OH})_4$) and related materials like aluminous sheet silicates (e.g. muscovite $\text{KAl}_3\text{Si}_3\text{O}_{10}(\text{OH},\text{F})_2$), from the polymorphs sillimanite, kyanite and andalusite (Al_2SiO_5) and from staurolite ($(\text{Fe}^{2+},\text{Mg})_2\text{Al}_9(\text{Si},\text{Al})_4\text{O}_{20}(\text{O},\text{OH})_4$) and topaz ($\text{Al}_2\text{SiO}_4(\text{F},\text{OH})_2$) at temperatures between 1000°C and ca. 1700°C. In all cases, the formed mullite is accompanied by excess SiO_2 , unless an aluminum source is added (Komarneni et al. 2005). Using the mentioned raw materials is an easy large-scale production route for mullite ceramics, however, most mullites produced from those raw materials are not chemically pure. Synthesis of chemically pure mullite is possible by reaction sintering (solid-state reaction mullites or sinter mullites) of materials like (purified) quartz, cristobalite and fused silica with corundum ($\alpha\text{-Al}_2\text{O}_3$), $\gamma\text{-Al}_2\text{O}_3$ and aluminum hydroxides like gibbsite ($\text{Al}(\text{OH})_3$), diaspore and boehmite (both $\text{AlO}(\text{OH})$). "Sinter mullites" often have compositions close to $3\text{Al}_2\text{O}_3\text{:2SiO}_2$ (Komar-

neni et al. 2005). By controlled cooling of fused Al_2O_3 and SiO_2 (e.g. quartz sand) in electric arc furnaces, "fused mullite" is produced (Schneider 2004). Large mullite single crystals have been successfully produced with float zone and the Czochralski method. Both fused mullite and mullite single-crystals are known with compositions close to $2\text{Al}_2\text{O}_3:\text{SiO}_2$ (Komarneni et al. 2005). So called "chemical mullite" (Schneider et al. 2008) is produced from precursors derived from a wide range of different sol-gel routes, which allow the production of chemically very pure mullites with Al_2O_3 contents up to 90 wt.-% (Schneider 2004). Depending on the production process, controlled incorporation of other cations than Al and Si into mullite and factors like growth rate, speed and crystal size and shape can be controlled for various specialized applications (Schneider 2004, Komarneni et al. 2005, Schneider et al. 2008).

2.1.1 Mullite Crystal Structure

Sensu stricto, "mullite" is the name of the natural mineral mullite with a composition of $3\text{Al}_2\text{O}_3:2\text{SiO}_2$ (Bowen et al. 1924a, Bowen and Greig 1924b, Bowen et al. 1924c). It has been shown by Fischer et al. (1994; 1996) and Fischer and Schneider (2005) that mullite crystallizes as solid solution with variable $\text{Al}_2\text{O}_3:\text{SiO}_2$ ratio, which can be explained with the formula of $\text{Al}_2(\text{Al}_{2+2x}\text{Si}_{2-2x})\text{O}_{10-x}$ within a compositional range between $0.18 \leq x \leq 0.88$. For $x = 0$, the composition is equal to sillimanite, for $x = 1$ it equals Al_2O_3 . A linear relationship between the crystallographic a -axis and the molar Al_2O_3 content is known (Fischer et al. 1994; 1996).

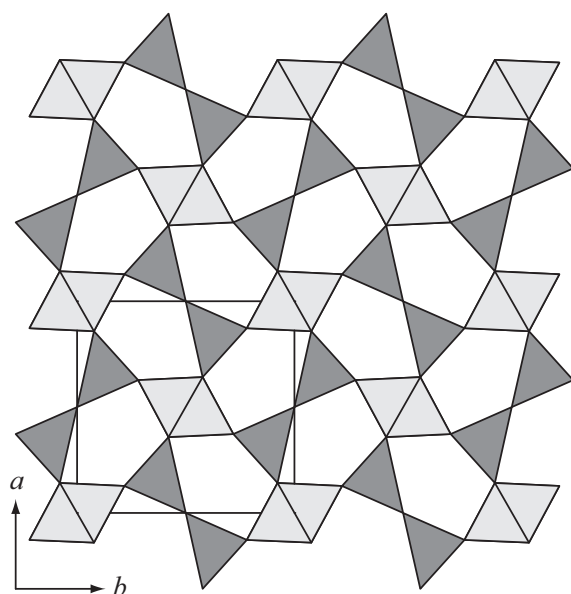


Figure 2.3: Idealized "mullite" structure visualized as sillimanite structure projected along the c -axis without any vacancies. (Al,Si) ordering in sillimanite is not shown. The chains of AlO_6 octahedra (light gray) expand along $[001]$. The bowtie of (Al,Si)-tetrahedra is shown in dark gray.

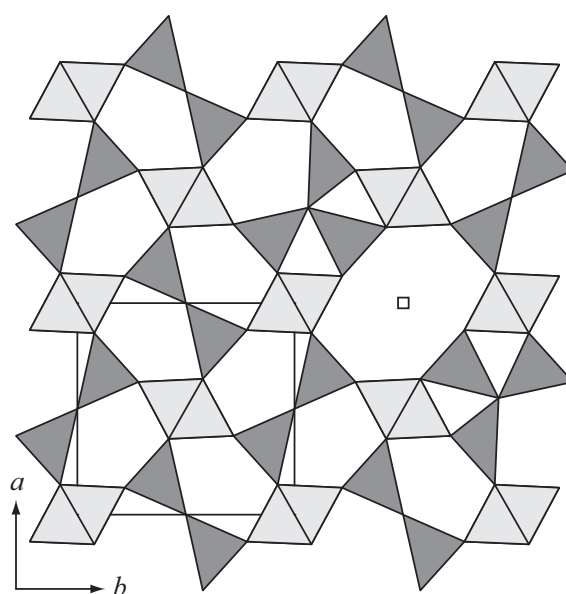


Figure 2.4: Idealized "mullite" structure visualized as oxygen deficient sillimanite structure projected along $[001]$. A local vacancy is shown (\square) where the $(\text{Al,Si})_2\text{O}_7$ bowtie is broken and tetrahedra flip to nearby oxygen sites.

The average structure of mullite in space group $Pbam$ with lattice parameters of about $a \approx 7.57 \text{ \AA}$, $b \approx 7.68 \text{ \AA}$, $c \approx 2.88 \text{ \AA}$, $V \approx 167.44 \text{ \AA}^3$ (Angel and Prewitt 1986) can be explained by the ordered structure of sillimanite: Chains of edge-connected AlO_6 octahedra expand along the c -axis (Figure 2.3). Compared to sillimanite, the c -axis is halved. At the height of $z = \frac{1}{2}$ (which corresponds to $z = \frac{1}{4}$ and $\frac{3}{4}$ in sillimanite due to the doubled c -axis) adjacent octahedral chains are interlinked by (Al,Si)-tetrahedra. Two corner linked (Al,Si)-tetrahedra form bowties, which expand as a double chain along $[001]$ (Figure 2.3). In contrast to sillimanite, Al and Si distribution is not strictly ordered, however, local ordering has been observed (Angel and Prewitt 1986, Angel et al. 1991, Brunauer et al. 2001a, Fischer and Schneider 2005, Rahman and Freimann 2005). Mullite has a higher Al content than sillimanite, hence, some Si^{4+} is replaced by Al^{3+} . As this exchange is not charge neutral, it can be formalized as: $\text{Si}^{4+} \rightarrow \text{Al}^{3+} + \frac{1}{2} \square_{\text{oxygen}}^{2-}$, or $2\text{Si}^{4+} \rightarrow 2\text{Al}^{3+} + \square_{\text{oxygen}}^{2-}$.

Angel and Prewitt (1986) and refs. therein showed that the oxygen vacancy is localized at the oxygen site interconnecting the $(\text{Al,Si})_2\text{O}_7$ bowtie. As a consequence of the missing ligand, the central positions of the two tetrahedra building the former bowtie (which are now only three-fold coordinated) flip to nearby oxygen sites, leaving a local void in the structure (Figure 2.4). As shown before, the number of oxygen vacancies depend on the mullite composition (Figure 2.5) and at a certain amount of Al_2O_3 , charge balance in mullite consisting only of Al_2O_3 and SiO_2 of must be compensated by oxygen vacancies at other sites.

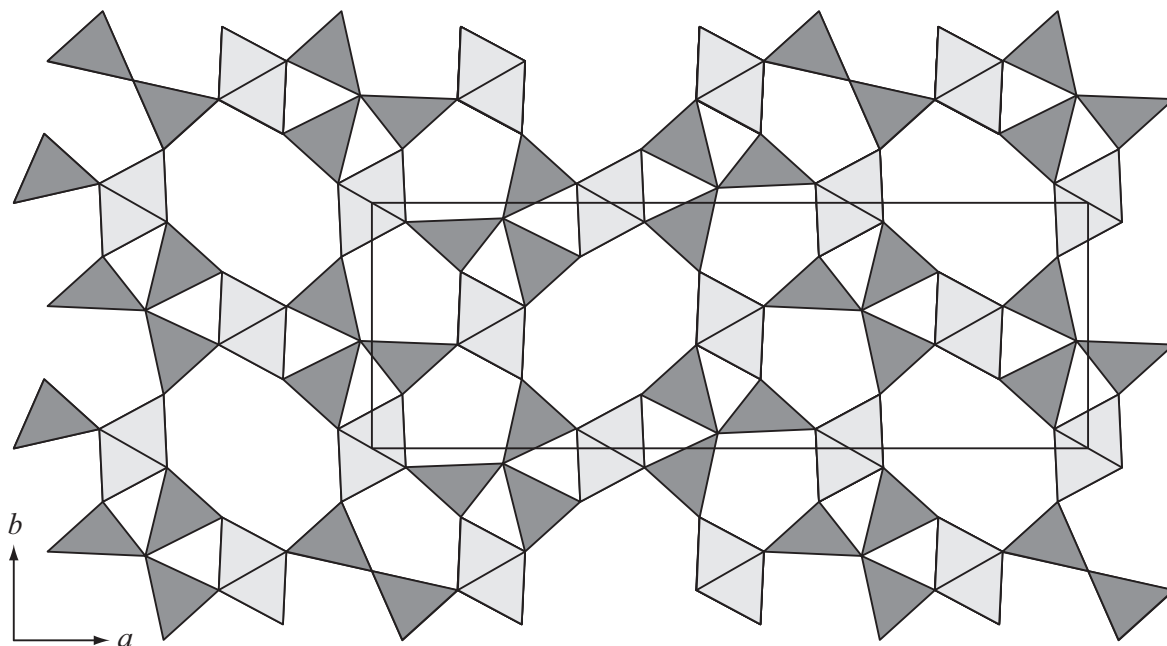


Figure 2.5: Hypothetically ordered structure of a $4\text{Al}_2\text{O}_3:1\text{SiO}_2$ -mullite. The supercell with a three-fold a -axis is indicated with the black frame (modified after Fischer and Schneider 2005).

2.1.2 Definition of Mullite-Type Structures

As more and more synthetic compounds with mullite-like properties were found, a classification was needed. To provide a consistent classification of the relations of different mullite-like structures, the term "mullite-type" was introduced by Fischer and Schneider (2005). The classification is based on mullite characteristic features (see below) and the relation between different mullite-types is based on their relation to the aristotype space group $P4/mbm$. Hence, "mullite-type" does not classify compounds directly on their exact structure and chemistry but rather comprises an expandable family of structures with common (i.e. mullite-like) structural features. Most noticeable are the parallel chains of edge-connected octahedra, which are interlinked with ordered or disordered arrangements polyhedra of different coordination. Fischer and Schneider (2005) defined the following four characteristics which structures must comply in order to belong to the mullite-type family:

1. A mullite-type structure crystallizes in a space group, which can be traced back to the tetragonal space group $P4/mbm$ by group-subgroup relations. The group-subgroup relations are used to classify mullite-type compounds in different groups and are extensively described in Fischer and Schneider (2005);
2. Chains of edge-connected MO_6 octahedra are "linear representing single Einer-chains in their highest topological symmetry in space group $P4/mbm$ ". This means that MO_6 chains expand linearly (i.e. as stringed together octahedra) in one direction (Figure 2.6);
3. In an edge-connected chain of MO_6 octahedra, two oxygen apexes do not contribute to the chain linkages. An axis through these apex atoms must point towards an edge of an octahedron in an adjacent chain. This edge is parallel to the expansion direction of the chain (Figure 2.7). In a hypothetical structure consisting of the MO_6 -chains only in space group $P4/mbm$, this angle ω is 90° . In mullite-type crystal structures, it can vary from 30° to 90° . The lower limit of 30° is based on experimental data from investigations on mullite-type crystal structures;
4. Viewed along the chains of MO_6 octahedra, the structure should resemble the orthogonal metric of space group $P4/mbm$ as close as possible. The angle γ' (Figure 2.7) is the angle between basis vectors of the unit cell projected onto the plane perpendicular to the expansion direction of the AlO_6 chains. The tolerance of γ' is $90^\circ \pm 5^\circ$. A mullite-type structure can also crystallize in an e.g. monoclinic crystal system as long as the angle of the basis vectors in a plane perpendicular to the direction of the chains is $90^\circ \pm 5^\circ$. The deviation of 5° from 90° is based on experimental data from known structures and may be increased when new structures with mullite-like physical properties are discovered.

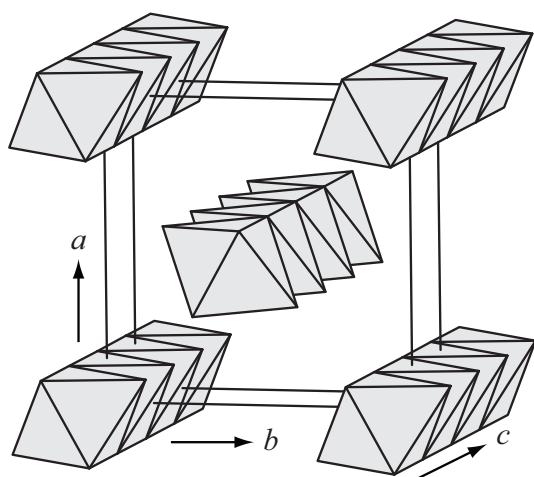


Figure 2.6: Chains of edge-connected AlO_6 octahedra expanding unfolded and linear in one direction. In the simplified structure shown here (data from Angel and Prewitt 1986), the translational distance between octahedra is equal to the length of the c -axis.

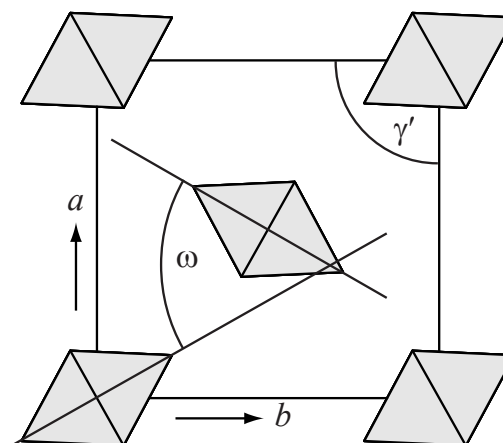


Figure 2.7: Simplified crystal structure of mullite (data from Angel and Prewitt 1986), projected along the c -axis. The angle ω between adjacent chains of octahedra and the angle γ' between the basis vectors projected onto the plane perpendicular to the chain direction are displayed (modified after Fischer and Schneider 2008a).

2.1.3 Applications of Mullite

Mullite is widely used in ceramics industry due to outstanding properties like its very high melting point of about 1890°C , its low thermal expansion coefficient, which is the reason for good thermal shock and spalling resistance, its good insulating properties due to the low thermal conductivity, the high creep resistance, its high shear modulus, a high electrical resistance and a low gas permeability (Komarneni et al. 2005). Schneider et al. (2008) divided mullite application in three groups:

Monolithic mullite ceramics. This group includes traditional ceramics (i.e. tableware and porcelain) and industrial ceramic products like refractory materials and engineering ceramics (Schneider et al. 2008). Engineering materials comprise mechanical guides, brake linings, filters, supporting substrates for catalysts, corrosion resistant crucibles, casings for thermocouples and heat exchangers, substrates for electronic devices with high-temperature stability and high electrical resistance but also mechanical parts like conveyor belts (Figure 2.8) in high-temperature furnaces and reinforced parts in engines and turbines. Refractory materials include chamotte stones and mullite based bricks in various types of industrial furnaces. Transparent mullite glass-ceramics have been successfully applied as high-temperature stable windows (Okada and Schneider 2005, Schneider 2004).

Mullite coatings. They are used to protect surfaces of materials against corrosion and oxidation due to environmental factors like gases, acids and bases, heat etc. The thin (few

μm) coatings can be applied onto substrates by chemical and physical vapor-deposition and plasma- and flame spray methods (Basu and Sarin 2005).

Mullite matrix composites. Composites of a mullite matrix, which is reinforced with fibers or whiskers of mullite or of different composition (e.g. SiC, Al_2O_3) in order to improve durability and mechanical strength, especially at high temperature (Figure 2.9) are called "mullite matrix composites". The mechanism may be compared to the use of asbestos fibers in cement materials. Mullite matrix composites are a field of ongoing research, however, potential applications may include propeller blades of gas turbines and heat shields in aerospace industry (Schneider 2005b) as well as military applications (MIL-HDBK-17-5 2002). Mullite fibers can also be used as reinforcer of glasses and glass ceramics (Travitzky 1998).

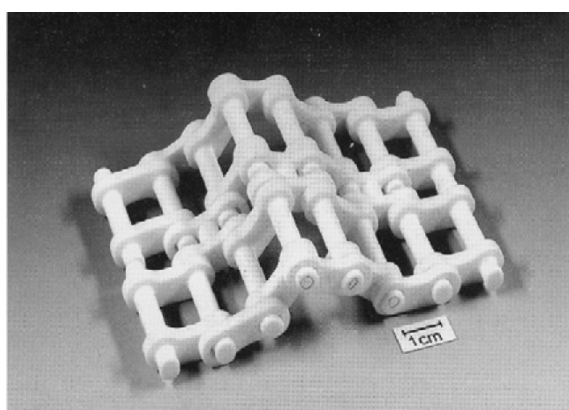


Figure 2.8: Conveyor belt made from sintered mullite. Such parts are used to feed high-temperature furnaces (from Schneider et al. 2008).

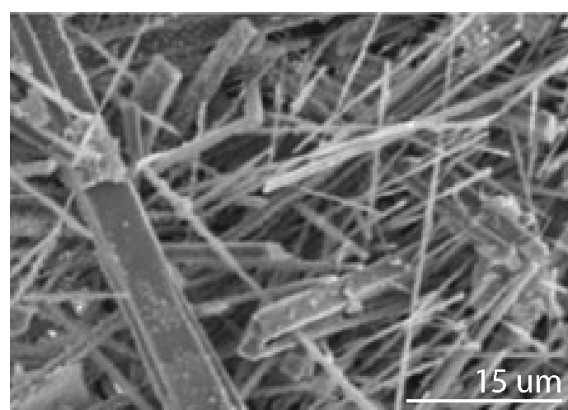


Figure 2.9: Mullite fibers in a cross-section from a Hessian crucible. The performance of the Hessian crucibles is ascribed to the fibers, which act as reinforcer in the ceramic matrix (from Marcos et al. 2006).

2.2 Boron-Mullites

From analyses of crystalline by-products obtained while investigating glasses in the system $\text{Al}_2\text{O}_3\text{-B}_2\text{O}_3\text{-SiO}_2$, Dietzel and Scholze (1955) suggested a solid solution between 3:2 mullite and a silicon-free aluminoborate compound identified as $\text{Al}_{18}\text{B}_4\text{O}_{33}$ ($9\text{Al}_2\text{O}_3:2\text{B}_2\text{O}_3$) (Baumann and Moore 1942). This assumption was based on a hypothetical, although not charge neutral exchange of $\text{B}^{3+} \rightarrow \text{Si}^{4+}$ and due to the similar physical properties of mullite and $\text{Al}_{18}\text{B}_4\text{O}_{33}$ (Scholze 1956, Benner and Baumann 1938, Baumann and Moore 1942).

A phase which showed the same X-ray diffraction pattern as $\text{Al}_{18}\text{B}_4\text{O}_{33}$ was observed by Werding and Schreyer (1984) while investigating compounds in the system $\text{MgO-Al}_2\text{O}_3\text{-B}_2\text{O}_3\text{-SiO}_2\text{-H}_2\text{O}$. They conclude: "According to Scholze this phase exhibits solid solution with mullite, consequently, it has been referred to as "B-mullite" here." Based on their own experiments in the system $\text{Al}_2\text{O}_3\text{-B}_2\text{O}_3\text{-SiO}_2\text{-H}_2\text{O}$, from results of Mazza et al. (1992) who

produced crystalline compounds with mullite-like X-ray diffraction lines and variable boron content, and from small amounts of boron found in sillimanite (Grew and Hinthorne 1983), Werding and Schreyer (1996) introduced the term "boron-mullite".

The compositional field of the boron-mullites is constraint by 3:2 mullite ($3\text{Al}_2\text{O}_3:2\text{SiO}_2$) and 2:1 mullite ($2\text{Al}_2\text{O}_3:1\text{SiO}_2$) and the silicon free aluminoborates Al_5BO_9 ($5\text{Al}_2\text{O}_3:1\text{B}_2\text{O}_3$) with mullite-type structure and AlBO_3 ($\text{Al}_2\text{O}_3:\text{B}_2\text{O}_3$) with calcite-type structure (Capponi et al. 1972, Bither 1973, Vegas et al. 1977), as shown in Figure 2.10.

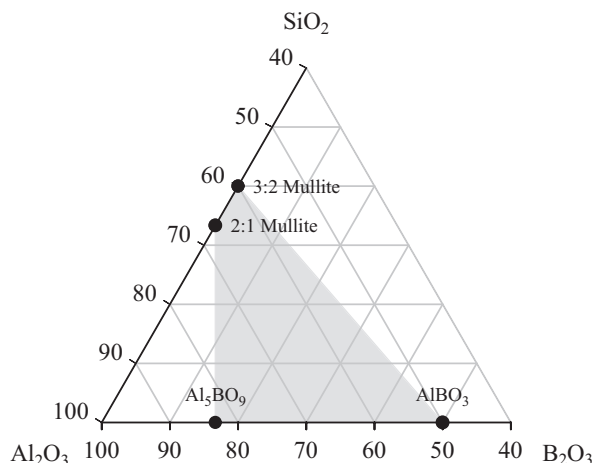


Figure 2.10: Plot showing the boron-mullite stability field in the system $\text{Al}_2\text{O}_3\text{-B}_2\text{O}_3\text{-SiO}_2$ as defined by Werding and Schreyer (1996). Units are mol-%.

Not all compounds within the boron-mullite field necessarily crystallize with mullite-type structures (e.g. AlBO_3 with calcite-type structure). On the other hand, e.g. grandidierite $(\text{Mg,Fe})\text{Al}_3\text{BSiO}_9$ (Stephenson and Moore 1968), is not included in the boron-mullite field despite its mullite-type crystal structure. As also a natural aluminum borosilicate named "boromullite" exists (Buick et al. 2008), a precise interpretation of the term "boron-mullite" is difficult.

Consequently, Fischer and Schneider (2008a) introduced the term "mullite-type boron compound", which includes any boron-containing compound with mullite-type structure. "Boron-mullite" and "B-mullite" are reserved for chemically pure aluminoborates and aluminum borosilicates with mullite-type structures. In this context, a mullite-type boron compound must fulfill the same structural requirements as those set up for mullite-type structures (Section 2.1.2) and the mullite classification scheme of Fischer and Schneider (2005) is also applied to mullite-type boron compounds.

2.2.1 Phases in the Boron Mullite Compositional Field

Phases with a chemical composition within or close to the boron-mullite compositional field (Werding and Schreyer 1996) are shown in Figure 2.11. Due to the few known aluminoborate

structures, the high-pressure phase Al_3BO_6 (Capponi et al. 1972) with norbergite structure (White et al. 1965), hydrothermally synthesized AlBO_3 with calcite structure (Capponi et al. 1972, Bither 1973, Vegas et al. 1977), the microporous framework structures PKU-5 ($\text{Al}_4\text{B}_6\text{O}_{15}$, Jing et al. 2004) and PKU-6 ($\text{HAl}_2\text{B}_3\text{O}_8$, Yang et al. 2007) and hexagonal jeremejevite (hydrothermally formed in granitic pegmatites, Foord et al. 1981) are also included. Al_3BO_6 and AlBO_3 have been found as co-products of jeremejevite syntheses (Stachowiak and Schreyer 1998, Reynaud 1977). A detailed description of the structure of jeremejevite and its thermal evolution is given in Section 5.5.4 in Chapter 5.

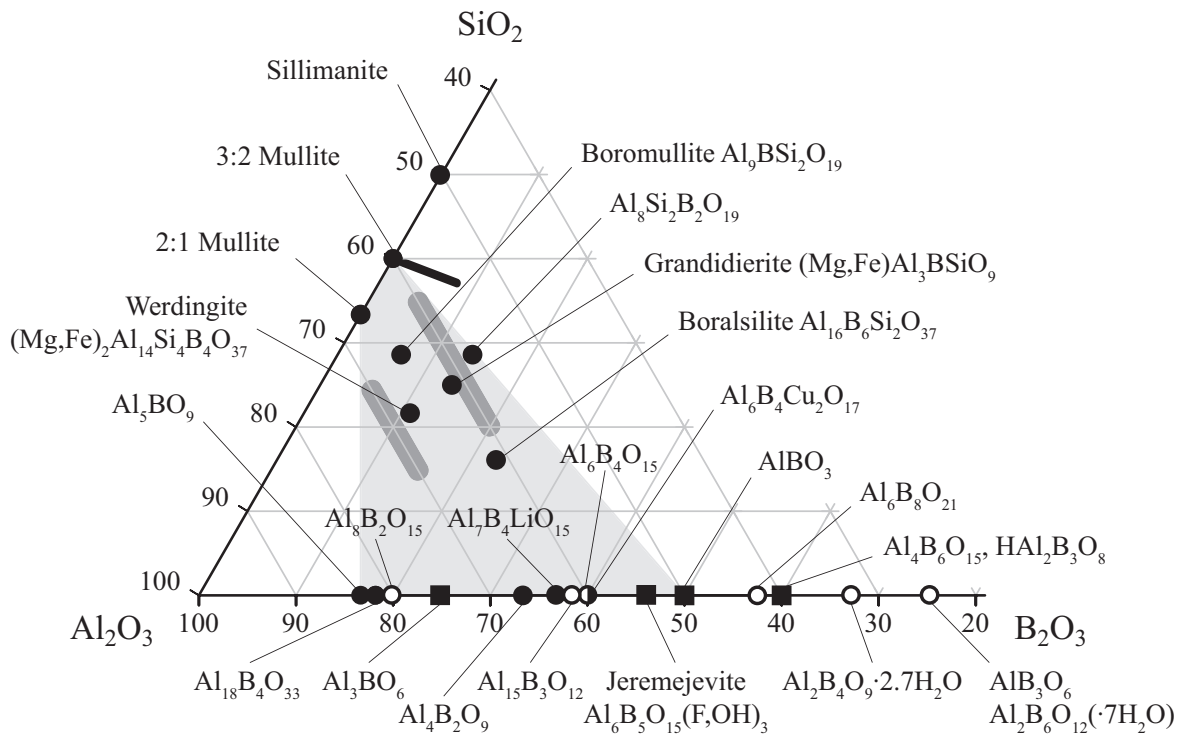


Figure 2.11: Plot showing phases with chemical compositions in or close to the boron-mullite stability field (light-gray) defined by Werding and Schreyer (1996). Except on the Al_2O_3 - B_2O_3 line, only phases with mullite-type crystal structures are shown. For werdingite, grandidierite, jeremejevite, $\text{Al}_7\text{B}_4\text{LiO}_{15}$, $\text{Al}_6\text{B}_4\text{Cu}_2\text{O}_{17}$ and $\text{HAl}_2\text{B}_3\text{O}_8$, the system has to be extended according to the chemistry of the phases and the compositional projection onto the Al_2O_3 - B_2O_3 - SiO_2 system is shown. Phases indicated with filled black circles crystallize with mullite-type structure (Fischer and Schneider 2008a), whereas black squares indicate phases with different crystal structures. The crystal structure of phases indicated with unfilled circles has not been solved so far, however, they are found as secondary phases in synthesis experiments of jeremejevite or of phases with mullite-type structures. Incorporation of boron into mullites as proposed by Griesser et al. (2008) is indicated with the two dark-gray fields, whereas boron-doped mullites according to Zhang et al. (2010) are indicated with the black line. Units are mol-%.

Several aluminoborate structures are still not solved and their composition is only guessed from questionable chemical analyses. During hydrothermal synthesis experiments starting from $\text{Al}(\text{OH})_3$ and H_3BO_3 , Lehmann and Teske (1973) found $\text{Al}_6\text{B}_4\text{O}_{15}$, $\text{Al}_2\text{B}_4\text{O}_9 \cdot 2.7\text{H}_2\text{O}$

and $\text{Al}_2\text{B}_6\text{O}_{12}\cdot 7\text{H}_2\text{O}$. Reynaud (1977) reports $\text{Al}_8\text{B}_2\text{O}_{15}$, synthesized from AlF_3 , borax and H_3BO_3 at 1400°C , and $\text{Al}_6\text{B}_8\text{O}_{21}$, found during a hydrothermal synthesis experiment as a co-phase of jeremejevite. From some of the phases, powder X-ray patterns exist, however, none of the phases has been indexed, nor are any structure solutions available so far. $\text{Al}_6\text{B}_8\text{O}_{21}$ was subsequently confirmed by Stachowiak and Schreyer (1998) in jeremejevite synthesis experiments. The existence of AlB_3O_6 is rather unclear, however, it is mentioned as AlB_3O_6 in an US patent on glasses (Rogers 1950), by Stachowiak and Schreyer (1998) and as $\text{Al}_2\text{B}_6\text{O}_{12}$ and $\text{Al}_2\text{B}_6\text{O}_{12}\cdot 7\text{H}_2\text{O}$ by Lehmann and Teske (1973). During a series of experiments on the stability of the mineral werdingite, Werding and Schreyer (1992) obtained $\text{Al}_8\text{Si}_2\text{B}_2\text{O}_{19}$ (Niven et al. 1991). This phase could be indexed with orthorhombic lattice parameters similar to those of Al_5BO_9 (Sokolova et al. 1978). No further evidence than a reference in Stachowiak and Schreyer (1998) provides any proof for the existence of $\text{Al}_5\text{B}_3\text{O}_{12}$.

In this section, phases crystallizing with mullite-type crystal structures are listed according to the classification concept of Fischer and Schneider (2005). The concept has been extended by Fischer and Schneider (2008a) and unit cell settings of the structures of boron-bearing mullite-type compounds are standardized to the one of mullite for better comparison. Nonetheless, structures in this chapter are reported in their standard space group setting.

$\text{Al}_6\text{B}_4\text{Cu}_2\text{O}_{17}$ group. This group includes the borates $\text{Al}_6\text{B}_4\text{Cu}_2\text{O}_{17}$ (Kaduk et al. 1999) and $\text{Al}_7\text{B}_4\text{LiO}_{17}$ (Åhman et al. 1997), which both crystallize in tetragonal space group $I4/m$ ($a = b \approx 10.5 \text{ \AA}$, $c \approx 5.6 \text{ \AA}$). The structure of $\text{Al}_6\text{B}_4\text{Cu}_2\text{O}_{17}$ consists of chains AlO_6 octahedra expanding parallel to the c -axis. Neighboring chains are interconnected by BO_3 triangles and clusters of $(\text{Al,Cu})\text{O}_5$ bipyramids, which are connected at an oxygen atom that is statistically distributed around the four-fold axis. Åhman et al. (1997) already noticed analogies of $\text{Al}_7\text{B}_4\text{LiO}_{17}$ to mullite, sillimanite and andalusite due to the AlO_6 -chains expanding along the c -axis. The crystal structure of $\text{Al}_7\text{B}_4\text{LiO}_{17}$ is similar to the one of $\text{Al}_6\text{B}_4\text{Cu}_2\text{O}_{17}$, however, empty channels in $\text{Al}_6\text{B}_4\text{Cu}_2\text{O}_{17}$ are filled with statistically distributed Li (Figure 2.12). Both structures have recently been reinvestigated and confirmed (Plachinda and Belokoneva 2008).

Grandidierite group. Grandidierite $((\text{Mg,Fe})\text{Al}_3\text{BSiO}_9)$ was first discovered in Madagascar and is named after the French naturalist and explorer Alfred Grandidier. The type locality is Andrahomana on the south coast of Madagascar where it has been found as anhedral elongated crystals up to ca. 8 cm length. It is a bluish-greenish to blackish prismatic mineral that is known from 40 localities worldwide (a comprehensive list of localities is given in Grew 1996). It occurs as rare accessory mineral in aluminous boron-rich rocks of continental or oceanic crust where it is formed during metamorphism at pressures lower than 10 kbar (e.g. pegmatites, aplites, gneisses, xenoliths, pelitic hornfels and calc-silicatic rocks). Its temperature stability at atmospheric pressure is between 550°C and ca. 1200°C and it can thus also exist in sanidinite facies rocks, e.g. volcanic xenoliths (Schreyer and Werding 1997). Typical mineral assemblages are quartz, K-feldspar, plagioclase, biotite, garnet, spinel, corundum,

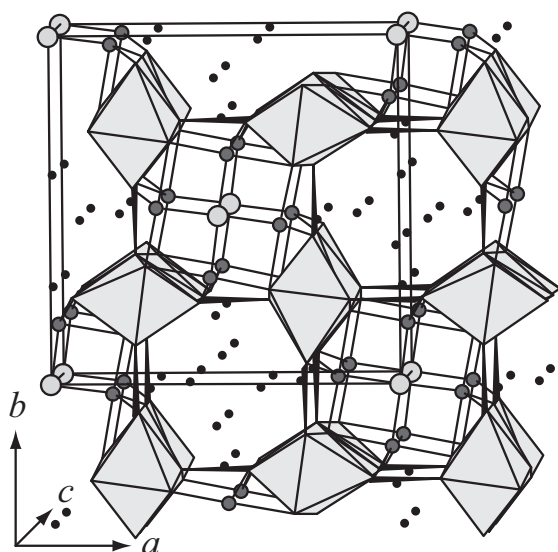


Figure 2.12: $\text{Al}_7\text{B}_4\text{LiO}_{17}$ structure in space group $I4/m$. Al atoms are gray, AlO_6 octahedra light gray and BO_3 units black. Only one oxygen atom around the four fold axis is shown (light gray sphere). Li atoms (black), are statistically distributed at the available positions. In the $\text{Al}_6\text{B}_4\text{Cu}_2\text{O}_{17}$ structure, the gray sphere is occupied by (Al,Cu) and the channel with Li atoms is empty.

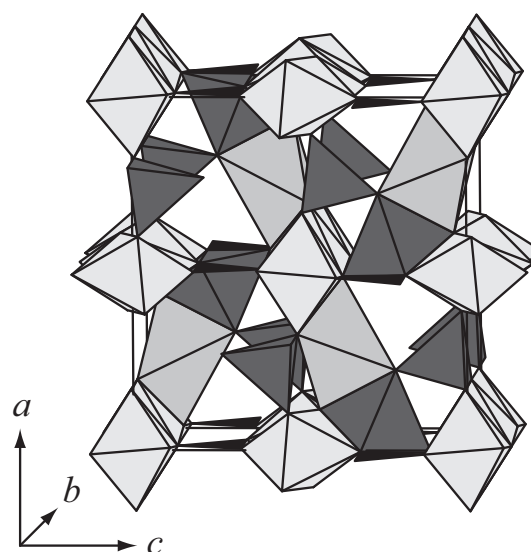


Figure 2.13: The crystal structure of grandierite in space group $Pnma$. Al-octahedra are light gray, BO_3 units are black. SiO_4 tetrahedra and AlO_5 polyhedra are dark gray, $(\text{Fe,Mg})\text{O}_5$ polyhedra are light gray.

sillimanite, andalusite, cordierite, tourmaline, kornerupine, sapphirine, serendibite and sinhalite (Anthony et al. 2003). In pelitic rocks, its occurrence seems to be restricted to rocks, in which muscovite and other phases typical for aluminous amphibolite-facies rocks are missing (Grew 1996).

Grandierite $(\text{Mg,Fe})\text{Al}_3\text{BSiO}_9$, is the Mg-rich member of the grandierite-ominelite series (Dzikowski et al. 2007, Hiroi et al. 2001) and is of particular interest because it contains both Al and (Mg,Fe) in five-fold coordination (MacKenzie and Meinhold 1997, Dzikowski et al. 2007, Farges 2001). The grandierite crystal structure (space group $Pnma$, $a \approx 10.96 \text{ \AA}$, $b \approx 5.76 \text{ \AA}$, $c \approx 10.33 \text{ \AA}$) contains two different chains of edge-connected AlO_6 octahedra parallel to the b -axis. One chain is rather straight whereas the other is folded. Adjacent Al-octahedra are directly connected by corner-linked chains of BO_3 , AlO_5 , SiO_4 and MgO_5 polyhedra (Figure 2.13). Thermal evolution of the structure of grandierite is discussed in Section 5.5.3 in Chapter 5.

Mullite group. Mazza et al. (1992) investigated boron incorporation into mullites and proposed a solid solution between compounds produced from starting materials with $\text{Al}_{6-x}\text{B}_x\text{O}_9$ ($1 \leq x \leq 3$) composition. Average crystal structures were solved in space group $Pbam$ with pseudotetragonal lattice parameters $a \approx b \approx 7.62 \text{ \AA}$ and $c \approx 2.8 \text{ \AA}$. With infrared investiga-

tions, BO_3 incorporation into $\text{Al}_{6-x}\text{B}_x\text{O}_9$ with $x = 1$ was proposed. The structure of $\text{Al}_{6-x}\text{B}_x\text{O}_9$ with $x = 2$ is similar to the one with $x = 1$, however, one Al site is replaced by a BO_4 site. The occurrence of a BO_4 site in this structure was confirmed by ^{11}B MAS NMR spectroscopy by MacKenzie et al. (2007). When heated to temperatures between 900°C to 1000°C , the compounds yield Al_5BO_9 (Chapter 4) and $\text{Al}_4\text{B}_2\text{O}_9$ (Fischer et al. 2008b). Average structures of both phases according to Mazza et al. (1992) are shown in Figures 2.14 and 2.15.

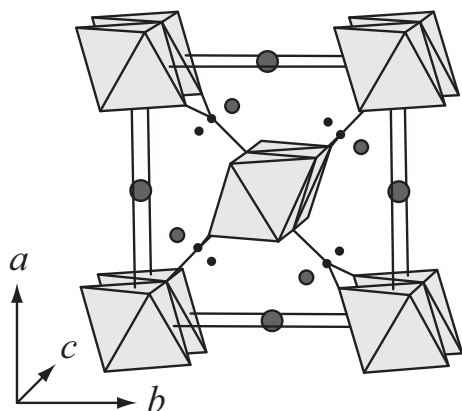


Figure 2.14: Representation of the average structure of $\text{Al}_4\text{B}_2\text{O}_9$ according to Mazza et al. (1992) in space group $Pbam$. Al-octahedra are light gray, boron atoms are represented as black spheres. The small gray sphere represents Al, the larger gray one represents O.

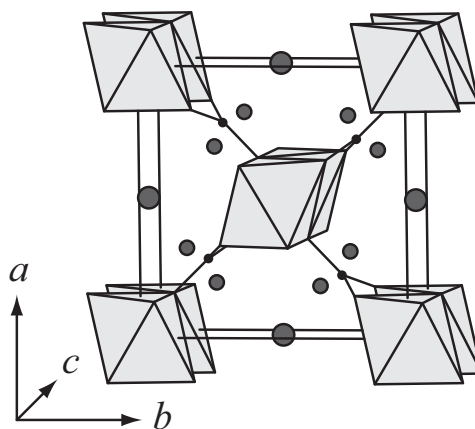


Figure 2.15: Representation of the average structure of Al_5BO_9 according to Mazza et al. (1992) in space group $Pbam$. Al-octahedra are light gray, boron atoms are represented as black spheres. The small gray sphere represents Al, the larger gray one represents O. In contrast to $\text{Al}_4\text{B}_2\text{O}_9$, the additional B site is replaced by Al.

A "mullite-like" phase with $\text{Al}_{8+x}\text{P}_{1-x}\text{B}_{1+x}\text{O}_{16+x/2}$ with $0 \leq x \leq 0.6 \pm 0.1$ is described in Mazza et al. (2001). Orthorhombic lattice parameters similar to those of mullite are presented, however, no space group is indicated. As the compounds are described as "mullite-like" containing four-fold coordinated boron, it can be assumed that structure solutions were done in space group $Pbam$, as in Mazza et al. (1992).

Boron incorporation into the mullite structure was also investigated by Griesser et al. (2008). They proposed a limited solid solution due to decreasing lattice parameters with increasing boron content (Figure 2.11). The final products of Griesser et al. (2008) were investigated by powder X-ray diffraction and FTIR, hence, exact mechanism of boron incorporation into the structure is not completely resolved.

In a recent study on boron-doped mullites (Zhang et al. 2010) with B_2O_3 contents of up to 6.14 wt.-% (Figure 2.11), results of Griesser et al. (2008) were confirmed. Moreover, increasing boron content led to a reduction of crystallization-temperature.

Sillimanite group. Grew and Hinthorne (1983) found B- and Mg-containing sillimanite in boron-rich volcanic and sedimentary rocks subjected to granulite-facies metamorphic condi-

tions. However, high temperatures alone do not guarantee high B contents in sillimanite even when large boron quantities are available. A B \rightarrow Si substitution is suspected and seems to be coupled with Mg \rightarrow Al substitution (Grew 1996). For comparison, the structure of B-free sillimanite according to Winter and Ghose (1979) in space group $Pbnm$ with $a \approx 7.49$ Å, $b \approx 7.68$ Å, $c \approx 5.78$ Å is shown in Figure 2.16.

Fischer and Schneider (2008a) also included $PbMBO_4$ with $M = Al^{3+}, Ga^{3+}, Fe^{3+}, Cr^{3+}, Mn^{3+}$ (Park et al. 2003) compounds in this group because of the same symmetry as sillimanite (in space group $Pbam$). In contrast to sillimanite, AlO_6 chains are alternatingly linked with BO_3 triangles or Pb atoms bonded to the chains. At least $PbAlBO_4$ is not high-temperature stable and the mullite-type structure is lost at $775^\circ C$. In Figure 2.17 the structure of $PbAlBO_4$ is shown in space group $Pnma$ with $a \approx 6.92$ Å, $b \approx 5.71$ Å, $c \approx 8.02$ Å.

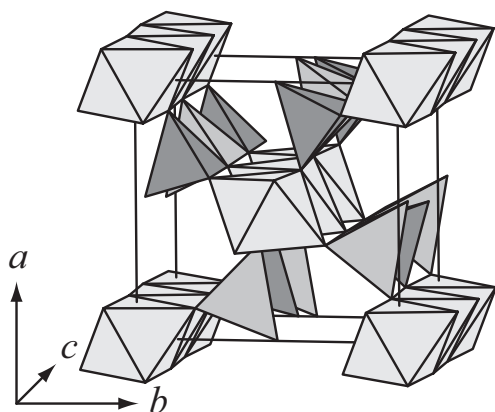


Figure 2.16: Structural representation of sillimanite (in $Pbnm$, Winter and Ghose 1979). Al-octahedra are light gray, chains of alternating AlO_4 and SiO_4 tetrahedra are gray and dark gray, respectively.

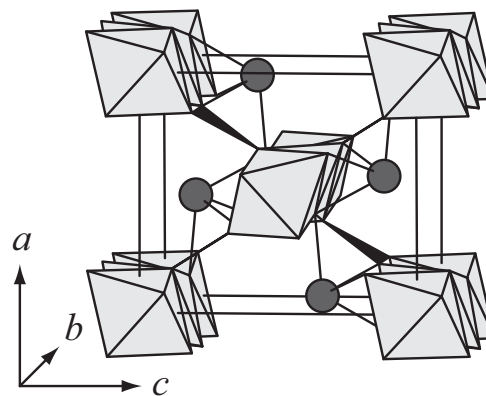


Figure 2.17: Crystal structure drawing of $PbAlBO_4$ according to Park et al. (2003) in space group $Pnma$. Al-octahedra are represented in light gray, whereas BO_3 triangles are drawn in black. Asymmetrically bonded lead atoms (four bonds to octahedra) are plotted as gray spheres.

Weringite group. Weringite $((Mg,Fe)_2Al_{14}Si_4B_4O_{37})$ is a (Mg,Fe)-Al-borosilicate found in granulite-facies metamorphosed metasediments and gneisses (Anthony et al. 2003) in Namaqualand (type locality), South Africa. It is stable at pressures up to ca. 10 kbar and temperatures between ca. $700^\circ C$ and $1200^\circ C$. It occurs together kornrupine, grandidierite, zircon, and rutile (Anthony et al. 2003) in hercynite-sillimanite-rich layers in a supercrustal gneissic sequence (Moore et al. 1990, Grew 1996). The Mg-endmember was successfully synthesized by Wering and Schreyer (1992). Weringite has an idealized chemical composition of $(Mg,Fe)_2Al_{14}Si_4B_4O_{37}$ (Moore et al. 1990) and crystallizes in triclinic space group $P\bar{1}$ with $a \approx 7.97$ Å, $b \approx 8.16$ Å, $c \approx 11.36$ Å, $\alpha \approx 110.36^\circ$, $\beta \approx 110.88^\circ$ and $\gamma \approx 84.67^\circ$ (Figure 2.18). Two non equivalent AlO_6 chains are interlinked with either AlO_4 and BO_3 groups (only BO_3 shown in the structural drawing), with $(Al,Fe)O_4$ and SiO_4 tetrahedra and with AlO_5 and

(Al,Mg)O₅ polyhedra (Niven et al. 1991).

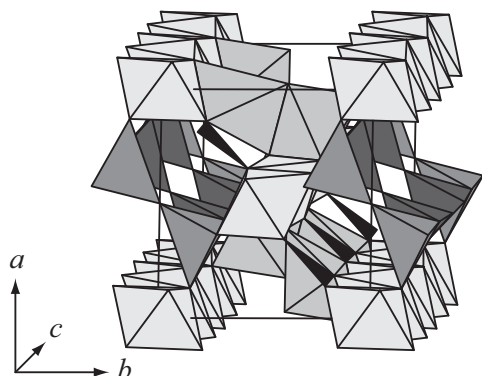


Figure 2.18: The triclinic crystal structure of werdingite in space group $P\bar{1}$. Al-octahedra are plotted light gray, BO₃ units in black. (Al,Fe)O₄ and SiO₄ tetrahedra are dark gray, AlO₅ and (Mg,Fe)O₅ polyhedra are gray.

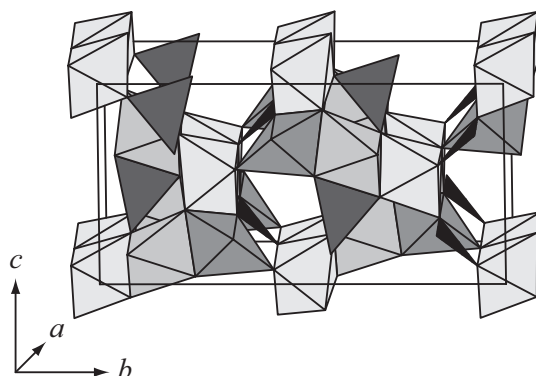


Figure 2.19: Structural drawing of Al₅BO₉ in space group $Cmc2_1$ (Sokolova et al. 1978). Al-octahedra (light gray) are interconnected with BO₃ triangles (black), AlO₄ tetrahedra (dark gray) and two different AlO₅ polyhedra. For better visualization of the mullite-type structure, the unit cell is shifted by 0, 0.1164, 0.5.

A₉B₂ (Al₁₈B₄O₃₃) group. Al₁₈B₄O₃₃ was first mentioned by Baumann and Moore (1942) who determined that the compound previously cited as 3 Al₂O₃:B₂O₃ (Mallard 1887, Benner and Baumann 1938) has a composition of 9 Al₂O₃:2 B₂O₃. Subsequent structural investigations were in agreement with Al₅BO₉ composition (Sokolova et al. 1978). The boron discrepancy was explained with substitution of 9% B^(IV) → Al^(IV) (Ihara et al. 1980) and it has been shown that up to 10% of octahedral Al can be replaced by Cr³⁺ (Garsche et al. 1991). The compound is still frequently cited as Al₁₈B₄O₃₃. Recently, Fisch et al. (2011) showed that the Al₁₈B₄O₃₃ composition is rather unlikely and that the compound should be cited as Al_{5-x}B_{1+x}O₉ with $x \approx 0.03$ (Chapter 4). The structure is shown in Figure 2.19 (space group $Cmc2_1$, $a \approx 5.67$ Å, $b \approx 15.01$ Å, $c \approx 7.68$ Å). Isolated edge-sharing AlO₆ octahedra run parallel to the a -axis. Proximate octahedral chains are connected by pairs of edge-sharing AlO₅ polyhedra and AlO₄ linked with BO₃ triangles. One side of an AlO₅ polyhedra pair is connected to octahedra and linked to BO₃ triangles, whereas the other side links to octahedra and AlO₄ tetrahedra. The structure is described in more detail in Chapter 4 and thermal evolution of the compound is discussed in Section 5.5.1 in Chapter 5.

Boromullite Al₉BSi₂O₁₉ was reported in granulite-facies metapelitic rocks from Mount Stafford, Australia (type locality), where it is formed during anatexis (Grew et al. 2008). At its type locality, it occurs together with tourmaline, werdingite, grandidierite, sillimanite, cordierite, K-feldspar and rarely, biotite, hercynite, ilmenite and quartz (Buick et al. 2008). It crystallizes in the same space group as Al₁₈B₄O₃₃ ($Cmc2_1$) and has similar lattice parameters. Structurally, boromullite corresponds to a 1:1 polysome composed of Al₅BO₉ and Al₂SiO₅

modules (Figure 2.20). The Al_2SiO_5 module contains all Si and has the topology of sillimanite with a doubled b -axis (resulting in a composition of $\text{Al}_4\text{Si}_2\text{O}_{10}$) whereas the Al_5BO_9 module agrees with the structural model of Sokolova et al. (1978).

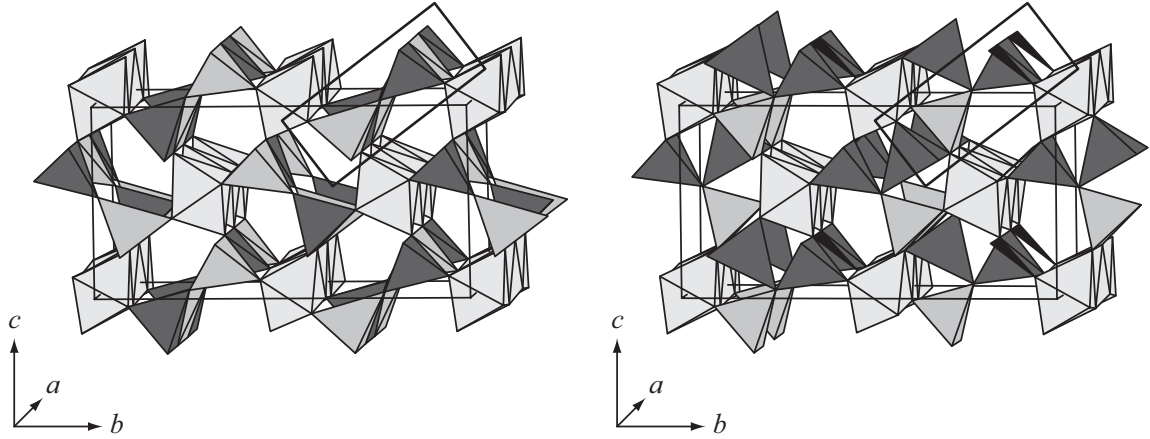


Figure 2.20: Structural representation of the sillimanite (left) and Al_5BO_9 (right) modules of boromullite. Al-octahedra are represented in light gray. The important structural difference between the two modules with respect to the 1:1 polysome boromullite is marked with the black square. For better comparison to the Al_5BO_9 structure, the unit cell is shifted by 0.25443, 0.12121, 0.65357.

Boralsilite ($\text{Al}_{16}\text{B}_6\text{Si}_2\text{O}_{37}$) and $\text{Al}_4\text{B}_2\text{O}_9$ group. The mineral boralsilite ($\text{Al}_{16}\text{B}_6\text{Si}_2\text{O}_{37}$) was found as the first anhydrous Al-B-silicate relatively widespread in granulite-facies granitic pegmatites in metapelitic rocks at Larsemann Hills, East Antarctica (type locality). It crystallizes as bundles of prisms in assemblages with quartz, K-feldspar, tourmaline, plagioclase, werdingite, dumortierite, grandierite and sillimanite (Grew et al. 1998). The crystal structure has been solved by Peacor et al. (1999) in space group $C2/m$ with $a \approx 14.77 \text{ \AA}$, $b \approx 5.57 \text{ \AA}$, $c \approx 15.08 \text{ \AA}$, $\beta \approx 91.96^\circ$. Three different AlO_6 chains prolong parallel to the b -axis. They are interconnected by three different polyhedral arrangements. One consists of an Si_2O_7 bowtie, the second of AlO_5 polyhedra, AlO_4 tetrahedra and BO_3 triangles, and the third is built up from AlO_5 polyhedra and BO_4 tetrahedra (Figure 2.21).

Several ambiguous structure solutions for mullite-type $\text{Al}_4\text{B}_2\text{O}_9$ exist but Scholze (1956) was the first who indexed it with orthorhombic lattice parameters $a = 14.8(2) \text{ \AA}$, $b = 15.1(2) \text{ \AA}$ and $c = 5.6(1) \text{ \AA}$. After recognizing the similarity of the $\text{Al}_4\text{B}_2\text{O}_9$ structure to the one of boralsilite, Fischer et al. (2008b) provided a promising, although not completely solved structure in space group $C2/m$ ($a \approx 14.81 \text{ \AA}$, $b \approx 5.54 \text{ \AA}$, $c \approx 15.05 \text{ \AA}$, $\beta \approx 90.91^\circ$) based on powder XRD, ^{11}B and ^{27}Al MAS-NMR data: Three types of edge-connected chains of AlO_6 octahedra extend parallel to the b -axis, interlinked by three different polyhedral configurations (Figure 2.22). One of them is a complex arrangement of distorted AlO_5 , AlO_4 polyhedra and BO_3 triangles. The second one comprises AlO_{4+1} and BO_4 tetrahedra which are disordered

with AlO_4 tetrahedra and BO_3 triangles due to a partially occupied oxygen site. The third type contains BO_3 and/or BO_4 units and replaces the Si_2O_7 bowtie in boralsilite. Its exact configuration has not been resolved yet. Thermal evolution of $\text{Al}_4\text{B}_2\text{O}_9$ is discussed in Section 5.5.2 in Chapter 5.

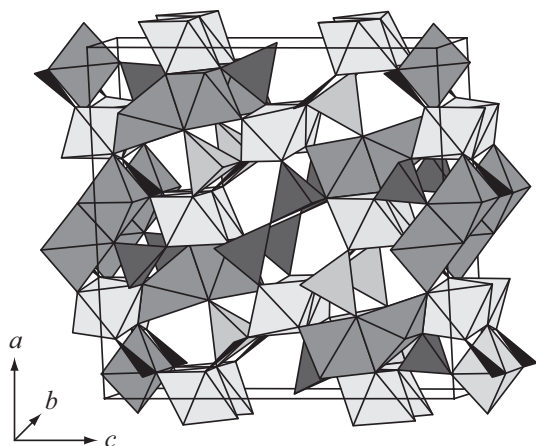


Figure 2.21: Crystal structure of boralsilite (in $C2/m$). AlO_6 chains are drawn in light gray. The chains are interconnected with AlO_5 and AlO_4 polyhedra, BO_3 triangles and Si_2O_7 bowties (dark gray).

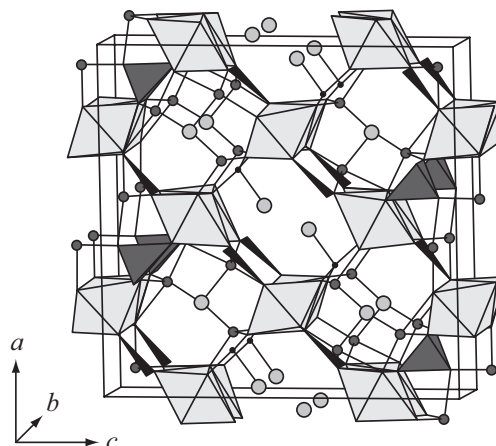


Figure 2.22: $\text{Al}_4\text{B}_2\text{O}_9$ structure according to Fischer and Schneider (2008a) in space group $C2/m$. AlO_6 octahedra (light gray) are interconnected with Al-polyhedra (Al is represented with the small sphere) and BO_4 tetrahedra (dark gray). The Si_2O_7 bowtie of boralsilite is replaced by BO_3 units (black) and further two O sites and two B sites of which the exact configuration has not been solved yet (modified after Fischer and Schneider 2008a).

2.2.2 Applications of Boron Mullites

With regard to industrial application, the compounds $\text{Al}_{18}\text{B}_4\text{O}_{33}$ and $\text{Al}_4\text{B}_2\text{O}_9$ are most cited. Due to mullite-like properties and the low-cost production (ca. $\frac{1}{20}$ to $\frac{1}{10}$ of the cost of SiC, Kim et al. 2004 and Song et al. 2007), easy fabrication in large quantities (Wada et al. 1991, Ray 1992, Sokolov and Gasparyan 2004, Zhang et al. 2006, Peng et al. 2006, Elssfah et al. 2007, Xinyong et al. 2007, Wang et al. 2008, Zhou et al. 2009, Chen et al. 2009), high strength (Ray 1992, Xinyong et al. 2007, Gatta et al. 2010) and low thermal expansion and conductivity (Wada et al. 1993; 1994), $\text{Al}_{18}\text{B}_4\text{O}_{33}$ and $\text{Al}_4\text{B}_2\text{O}_9$ are used as reinforcer in ceramic and ceramic/metal matrix composites and in glass ceramics (Peng et al. 2006, Wang et al. 2008, Fan et al. 2009, Feng et al. 2009, Lee et al. 2010, Geng et al. 2010). $\text{Al}_{18}\text{B}_4\text{O}_{33}$ has been proposed as reinforcer in fire insulations in ships due to its low weight, as construction components in nuclear reactors because of its neutron absorbing capabilities and in refractory linings due to the high resistance against borosilicate melts (Garsche et al. 1991 and refs. therein). Recently, nanotubes have been reported (Ma et al. 2002, Li and

Chang 2006) and $\text{Al}_{18}\text{B}_4\text{O}_{33}$ fibers have been coated with boron nitride, Bi_2O_3 and ZnAl_2O_4 to enhance strength between matrix and aluminoborate nanowires or whiskers (Zhang et al. 2005, Song et al. 2007, Fei et al. 2010, Liu et al. 2010a;b, Yue et al. 2010).

2.3 Element Boron

The metalloid boron is the fifth element of the periodic table and belongs to group 13 (boron group) with an electronic configuration of a full K shell ($1s^2$) and three electrons in the L shell ($2s^2 2p^1$) resulting in a trivalent boron ion B^{3+} . It has two stable isotopes, ^{11}B and ^{10}B , with a ratio of about 80:20 (Palmer and Swihart 1996). Boron does not occur in nature as pure element. Except from a few rare fluorine-minerals (e.g. avogadrite ($(\text{K,Cs})\text{BF}_4$), barberiite (NH_4BF_4), ferrucite (NaBF_4), Anovitz and Grew 1996) and one nitride (cubic BN, although its genesis is unclear, Dobrzhinetskaya et al. 2008), boron is always associated with oxygen in nature (Kistler and Helvacı 2006).

The name "boron" originates from "baurach", which is the Arabian word for borax (Smith 1985) and the Persian word for white (Oganov 2010). Boron-containing minerals are known since Babylonian times when they were used as flux for gold-welding. In the Middle Ages, borax (tincal) was brought from Asia and used as welding and enameling agents. At the beginning of the 18th century, boric acid (H_3BO_3) was produced from borax, and in 1778, sassolite (natural boric acid) was discovered in fumaroles at Sasso, Italy (Anovitz and Grew 1996).

Elemental boron was recognized in 1808 from the reaction of boric acid with potassium independently by Joseph Louis Gay-Lussac and Louis Jacques Thénard, naming it bore, and by Sir Humphry Davy, who called it boracium in analogy to other metals he found. Subsequently, he discovered that the new element was not a metal, hence, Davy changed the name from boratium to boron, combining the names of borax and carbon (Anovitz and Grew 1996).

In 1864, large borax deposits were discovered in California, Nevada and Oregon, starting the highly profitable "borax era" in the USA. Until the 1980's, California was the main global supplier of boron-bearing compounds (Smith and Medrano 1996). Today, more than 80% of the world's boron demand is supplied by the USA (California), Turkey and South America (Chile, Argentina, Bolivia and Peru) (Garrett 1998, Smith 2002).

Major materials sold and processed are boric acid (H_3BO_3) and borax penta- and decahydrate ($\text{Na}_2\text{B}_4\text{O}_5(\text{OH})_4 \cdot 5\text{H}_2\text{O}$, $\text{Na}_2\text{B}_4\text{O}_5(\text{OH})_4 \cdot 8\text{H}_2\text{O}$) (Carpenter and Kistler 2006). Of further importance are colemanite ($\text{Ca}_2\text{B}_6\text{O}_{11} \cdot 5\text{H}_2\text{O}$), ulexite ($\text{NaCaB}_5\text{O}_6(\text{OH})_6 \cdot 5\text{H}_2\text{O}$) and kernite ($\text{Na}_2\text{B}_4\text{O}_6(\text{OH})_2 \cdot 3\text{H}_2\text{O}$).

2.3.1 Geological Occurrence and Enrichment of Boron

Boron occurs widespread in upper crustal rocks, found in sedimentary, volcanic, plutonic and metamorphic environments. It is an enriched upper crustal element (ca. 15 ppm) and abundant in the lower crust (ca. 2 ppm), relative to the primitive mantle, which contains ca. 0.6 ppm B (Smith and Medrano 1996). The B concentration of the primitive mantle is similar to the one in C1 chondrites (ca. 0.7 ppm, Leeman and Sisson 1996). Due to hydrothermal alteration, fractional crystallization, interaction with oceanic sediments (which contain up to 100 ppm B, Vils et al. 2008) and serpentinization (interaction with seawater, Bonatti et al. 1984), estimation of the boron content of unaltered oceanic crust is difficult.

Wherever boron is observed, its distribution is very uneven. Contents in granites can reach 40 ppm, 180 ppm in oceanic sediment and up to 270 ppm in altered oceanic crust (Grew et al. 2011 and refs. therein).

Boron is soluble and mobile in aqueous solutions which transport and disperse it. Such aqueous solutions comprise e.g. salt and borax lakes (up to ca. 9000 ppm), brines (up to ca. 2200 ppm), hot springs and fumaroles (up to ca. 2000 ppm), seawater (ca. 4.5 ppm), sedimentary waters (up to ca. 2 ppm) and fresh water (up to ca. 0.01 ppm) at the Earth's surface. At depth, boron is distributed by hydrothermal fluids (Henry and Dutrow 1996 and refs. therein).

Despite its relative enrichment in the crust, boron has to get further enriched by geochemical processes (magmatic or transport in aqueous fluids) in order to allow formation of boron-bearing minerals. If the amount of available boron during crystallization is too low for formation of boron minerals (e.g. tourmaline), traces of boron will replace major elements in minerals (e.g. trace boron incorporation into feldspars, Deegan et al. 2010). With increasing boron content, partial or full substitution of B \rightarrow Al have been observed in e.g. boron-bearing feldspars (Stamatakis 1989, Higgins and Shaw 1984), boron-feldspars (reedmergenite, NaBSi₃O₈, Appleman and Clark 1965) and borosilicates.

Local areas, where B is concentrated in minerals and thus may form various kinds of boron deposits, can be categorized in three different processes (Watanabe 1975): (1) Endogenic processes include crystallization of boron minerals in melts and solutions, rock-alteration (metasomatism) due to magmatic and hydrothermal activity and metamorphic mobilization and concentration of boron; (2) Accumulation of boron due to volcanic activities (fumaroles, volcanoes); (3) Exogenic processes such as mechanical accumulation and chemical precipitation.

Endogenic processes. Melting of upper earth crust alone does not provide enough B to a melt in order to form a high content of boron minerals. Most B is brought to the melt by remelting of low metamorphosed metasediments, in which B is already present in e.g. tourmaline and sheet silicates. As long as boron is contained in the melt, it acts as flux for silicate melting, lowers the viscosity of the melt and allows it to persist to lower temperatures

(Dingwell et al. 1996). Boron behaves as incompatible element in igneous systems and is concentrated in the melt by crystal fractionation. It tends to be enriched in felsic and silicic differentiates of magmatism (granites including alkaline to aluminous types and its textural variants pegmatites, porphyries and rhyolites). After formation of rock forming silicates, boron is accumulated in the residual solution until a crystal-melt equilibrium is reached or it is dissolved and expelled from the melt in an aqueous phase (London et al. 1996). As boron is a highly soluble element, boron content of igneous melts is directly related to the fluid content of the melt, and boron will escape the melt when the first fluids are released. Concentrated boron in the residual melt and/or boron concentrated in an escaping fluid reacts with wallrock forming metasomatic minerals (mostly tourmaline, axinite $(\text{Ca}_2(\text{Fe}^{2+}, \text{Mg}, \text{Mn}^{2+})\text{Al}_2\text{BSi}_4\text{O}_{15}(\text{OH}))$ and other boron-bearing silicates). Amount and type of metasomatic minerals depends on the type of wallrock. In contact with carbonate formations (skarns), boron mineralization is common and a few commercial deposits have formed (Garrett 1998). Danburite $(\text{CaB}_2(\text{SiO}_4)_2)$ and datolite $(\text{CaBSiO}_4(\text{OH}))$ are typical skarn borate minerals (Smith 2002).

As soon as boron is transported in fluids, the distinction between igneous and metamorphic conditions is rather difficult. In connection with metamorphic processes, boron (e.g. from boron bearing phyllosilicates in sediments) is mobilized and subsequently fixed by crystallization (Watanabe 1975).

During low-grade hydrothermal overprint ($T < 350^\circ\text{C}$), boron and other fluid-mobile elements can be leached before any textural change of the host-rock is observed.

During contact metamorphism, intrusion of fluids or magma can act as effective transfer media for boron, resulting in depletion of boron in the intrusive rock. Depending on the type of surrounding rock and the interaction with the B-rich fluid, tourmaline or skarn deposits containing other borosilicates are formed.

Subduction of either continental or oceanic crust leads to devolatilization, recrystallization and redistribution of elements within mineral assemblages. Boron mobility depends on fluid availability, P-T-stability of boron-bearing phases and the relative partitioning between these phases (Leeman and Sisson 1996).

Tourmaline-group minerals are the main metamorphic borosilicates because they are commonly present in felsic metamorphic rocks (Grew 1996). Boron content is, however, not dominated by B in tourmaline, but by ab- and adsorbed boron in clays and sheet silicates (especially muscovite, $\text{KAl}_3\text{Si}_3\text{O}_{10}(\text{OH}, \text{F})_2$) due to their high occurrence (Leeman and Sisson 1996). Other borosilicates are only present if the host rock is highly enriched in boron or due to special bulk composition.

Volcanic activities. Boron is often encountered in fumarolic vapor, in thermal springs and in hydrothermal fluids. The occurrence of these products may be related to magmatic activity. It is important to note that boron is very unevenly distributed in volcanic products. High-temperature volcanic gases can contain up to ca. 35 ppm of B, whereas the boron content of

e.g. hot springs seems to depend vastly on the country rock type (Christ and Harder 1974, Garrett 1998). Nonetheless, surface water of geothermal springs, containing boron leached from country rock, is an important continental boron source. In contrast, volcanic activities seem to play a minor role as boron source in marine deposits (Grew et al. 2011).

Sassolite (H_3BO_3) is a prominent boron mineral occurring at active volcanic sites. At Sasso (Tuscany), fumaroles mainly consisting of steam, CO_2 , and only ca. 0.01% of H_3BO_3 are responsible for the formation of sassolite deposits (type locality) (Garrett 1998, Anthony et al. 2003). Other fumaroles are known in active areas such as Vulcano (Lipari islands), where emitted H_3BO_3 reacted with surrounding rocks to form H-, Na- and Ca-borates. After the 1851 eruption, sassolite was found at Mount Vesuvius. In Japan, sassolite encrustations are found in fumaroles of the Shows-Shinzan and Asama volcanoes (Watanabe 1975).

Exogenic processes. Exogenic processes leading to boron accumulation can be a result of enrichment due to mechanical accumulation (e.g. weathering resistant tourmaline is concentrated in sediments) or chemical precipitation processes. Chemical precipitation processes can be further divided into boron concentration due to evaporation on land and evaporation of seawater (Watanabe 1975).

The principal source of terrestrial evaporite zones are long-lasting boron-rich springs. They are often related to faulted basins at active collision zones (Smith and Medrano 1996), where fluids from volcanic and hydrothermal processes have been enriched with boron due to previous metamorphism of boron-rich sediments. However, this cannot be applied as a general rule because e.g. large United States boron deposits are far away from large-scale fault zones and the reason of their occurrence is not completely known. Nevertheless, all deposits lie on local rift zones perpendicular to large-scale fault zones and appear to have been formed by geothermal springs in areas with active volcanoes (Garrett 1998). Another possibility to form boron rich waters (surface waters) is due to weathering of silicates. Whereas tourmaline is relatively weathering resistant, boron enriched materials, such as B-bearing feldspars and micas are decomposed and B is going into solution and is subsequently transported. Transport distance is related to the country rock type and weathering conditions. Boron in solution is further rapidly ab- and adsorbed if e.g. Fe- and Al-hydroxides and phyllosilicates are present (Christ and Harder 1974).

Once available, boron-rich waters are concentrated in closed basins in arid regions with high evaporation rate leading to precipitation of boron minerals (mainly borax and ulexite, possibly also colemanite, Grew et al. 2011). Due to the high mobility of boron in fluids, continental evaporite boron deposits do not survive longer geological times unless they become protected, e.g. by a layer of clay (Smith 2002). If a boron deposit is not shielded from meteoric water and groundwater, soluble boron is leached from the surface and transported into deeper sediments where new boron containing minerals form.

After initial deposition, most sedimentary deposits were altered at higher temperature

and/or pressure, often surrounded by solutions with compositions differing from the sediment composition (Smith 2002). After deposition and subsequent burial, minerals are subjected to thermal diagenesis, often combined with transformation to a lower hydration state (Smith and Medrano 1996). This process has been observed e.g. in the deposit at Boron, Kramer district, CA, where initially deposited borax transformed to kernite + 6 H₂O. Reaction diagenesis occurs, when primary or already thermally altered borate sediments interact with solutions of different chemical composition. After thermal diagenesis, the deposit at Boron was altered by reaction diagenesis due to a contact of Ca-bearing ground water. Borax transformed to ulexite, which subsequently transformed to colemanite. As a result, cross-cutting veins of ulexite and colemanite have been observed at the deposit at Boron (Smith and Medrano 1996).

Continuous evaporation of seawater can also lead to formation of boron deposits. The rather low amount of B in seawater is concentrated and boron is mainly bound (ab- and adsorbed) by clay minerals (Watanabe 1975). In connection with salt domes, boron may be concentrated on the surface of the dome. The only large marine deposit is the Inder formation in Russia (Garrett 1998). It was most likely formed by intruding high-borate geothermal springs and its borate minerals are localized in overlying gypsum layers.

2.3.2 Commercially Relevant Boron Deposits

The only two large boron deposits prospected so far, located in California (Mojave Desert) and in Turkey (provinces of Eskişehir, Kütahya and Balıkesir), are of sedimentary origin. More than 80% of the world's boron demand are covered by these two deposits, however, many small deposits exist in other countries, e.g. Russia, China, Tibet, South America (Garrett 1998, Smith 2002). Principal sedimentary borate ore minerals are borax, kernite and ulexite in the United States and borax, ulexite and colemanite in Turkey. The same minerals as well as hydroboracite (CaMgB₆O₈(OH)₆·3H₂O) are found in South American deposits. Calcium borosilicates danburite and datolite, found in skarn-type metamorphic rocks in Russia and the metamorphic magnesium borate szaibelyite (MgBO₂(OH)) found in China are less important.

Processing of the boron minerals is usually done on-site by relatively simple procedures. After mining, the boron ore is sorted, ground, and subsequently leached. A hot (ca. 90°C) inorganic acid (e.g. sulfuric acid) reacts with borax, kernite, colemanite, ulexite and hydroboracite to form boric acid, which is then added to new raw material. The process is repeated until the desired purity-grade is reached (Garrett 1998). Boric oxide (B₂O₃) can be produced from boric acid by heat treatment (Smith 1985).

2.3.3 Applications of Boron

Boron. In its pure elemental form, boron is an important dopant for germanium and silicon in semiconductor industry and often used in pyrotechnic applications (flares, ignitors,

explosives and delay compositions) (Baudis and Fichte 1985). In nuclear reactors, boron (often as enriched ^{10}B) acts as neutron moderator and is used in emergency shutdown systems (Schwetz 1985).

Boron oxide and boric acid. Both compounds are intensively used in ceramic and glass industry for the production of borosilicate glasses, insulation and textile fibreglasses and as fluxing agents in porcelain enamels and ceramic glazes (Smith 1985). Minor uses of H_3BO_3 are as flux in welding and soldering, as disinfectant, fungicide and insecticide (wood protection, cockroach control), water softener (Anovitz and Grew 1996), as additive in nuclear reactor cooling water (Smith 1985).

Borates. B_2O_3 and H_3BO_3 are used as fluxing agents in welding and smelting (K-, Na-, Ca-borates), as water softener in washing powders (borax, Hammond 1985), as neutron absorbers in nuclear reactors (Na-, Ca-borates), lubricants (K-borates). Barium borates are used as fire retardants and lithium borates are used in glass production (Smith 1985).

Boron carbide and boron nitride. Synthetic boron carbide and nitride compounds are very hard materials, comparable to SiC, WC and diamond. Boron carbide (composition close to B_4C , Balakrishnarajan et al. 2007) is used as abrasive material (for polishing and grinding hard materials as WC and ceramics) and in resistant engineering components (e.g. nozzles for sand-blasting equipment). Due to its lower production cost, ^{10}B -enriched B_4C has almost completely replaced elemental boron from nuclear reactors (Schwetz 1985).

Boron nitride is the second hardest material after diamond and is applied in similar applications as those of diamond (grinding, drilling, etc.). Sintered BN parts are used as cutting tools for hardened steels and in rock-drills. Because of its high chemical resistance, BN is a preferential material for strong lab ware (Schwetz 1985).

Iron-boron alloys. Small amounts of boron (max. 30 ppm) increase hardness of C-, Mg-, Cr-, Mo-hardened steels. It further improves the cutting properties of high-speed steels. Boron-bearing alloys are called ferroboration, if the boron content is higher than ca. 10–20 wt.-%. Boron is also used in the production of metallic glasses (Baudis and Fichte 1985).

Other applications. Metal borides are used for electrolytic production of aluminum (TiB_2) and as Cu deoxidizer (CaB_6). Other applications are lab ware (crucibles, boats) and high electronic emission applications (e.g. LaB_6 as electrodes in electron microscopes) (Schwetz 1985).

Organic boron compounds comprise boron halides, B-F compounds and boranes (Brotherton and Guibert 1985). Boron halides are used in organic synthesis (BF_3), for the production of boron fibers (BCl_3), and for polymerization of alkenes (BBr_3). Fluoroboric acid HBF_4 is used for the production of fluoroborate salts and as etching agent for silicon and glass. Molten

alkali and ammonium fluoroborates are used as fluxing agents in soldering and NH_4BF_4 combined with nitro compounds is explosive. Boranes (H-B compounds) are highly reactive, often used as reducers in organic chemistry and in organic synthesis. Trimethylborate $((\text{CH}_3\text{O})_3\text{B})$ is the most important boric acid ester because of its use in the production of diborane. It is further used as antioxidant in fuels (Garrett 1998).

2.3.4 Crystal Structure of Boron

Elemental boron forms a structurally unique class of materials. The common structural unit is a B_{12} icosahedron, in which each boron atom has five neighbors (Nelmes et al. 1993). Elemental boron crystallizes in four different crystal structures.

α - B_{12} boron (space group $R\bar{3}m$, $a \approx 4.9 \text{ \AA}$, $c \approx 12.58 \text{ \AA}$) is stable at ambient conditions and has a B_{12} icosahedral configuration at each corner of the unit cell. The icosahedra are rather regular with B-B distances in the range of 1.75 \AA to 1.81 \AA (Will and Kiefer 2001).

β - B_{106} boron crystallizes at ambient conditions in the same space group as α -boron and is stable up to ca. 2500K (Oganov et al. 2009), however, all B icosahedra are rotated relative to the one in the center. Combined with vacancies, this results in a supercell with almost doubled lattice parameters than those of α -boron (Widom and Mihalkovič 2008).

γ - B_{28} has been produced by Oganov et al. (2009) at temperatures between 1800K and 2000K and at pressures higher than 19 GPa. It crystallizes in space group $Pn\bar{3}m$ ($a \approx 5.05 \text{ \AA}$, $b \approx 5.61 \text{ \AA}$, $c \approx 6.98 \text{ \AA}$) and consists of B_{12} icosahedra and B_2 pairs. The structure can be compared to a NaCl structure in which icosahedra and B_2 pairs play the role of "anion" and "cation", respectively (Oganov et al. 2009).

Tetragonal boron T-192 has been reported by Vlasse et al. (1979) at high temperatures and intermediate pressures. Possible space groups are $P4_1$ or $P4_3$ and the unit cell content consists of $\text{B}_{21} \cdot 2\text{B}_{12} \cdot \text{B}_{2.5}$. Due to partially filled interstitial sites, the unit-cell content varies from 190 to 192 atoms (Oganov et al. 2009).

2.4 Crystal Chemistry of Boron-Bearing Minerals

Boron polyhedra in crystal structures are isolated or share vertices with each other or with other tetrahedra (Anovitz and Grew 1996). The possible polyhedral arrangements of boron polyhedra have been systematized by Burns et al. (1995), Grice et al. (1995) and Hawthorne et al. (1996).

Generally, the structures of borate minerals are based on $\text{B}(\text{O},\text{OH})_3$ and $\text{B}(\text{O},\text{OH})_4$ polyhedra (Figures 2.23 and 2.24). $\text{B}(\text{O},\text{OH})_3$ groups have an average bond valence of z/ρ (where z is the cation charge and ρ is the coordination number) of 1 valence unit, whereas a $\text{B}(\text{O},\text{OH})_4$ polyhedron has 0.75 valence units. It is therefore possible that borate groups occurring as discrete oxyanions (e.g. BO_3^{3-}) polymerize forming finite clusters, chains, sheets or frameworks. At ambient conditions, only corner-linked B-polyhedra have been observed so far (Filatov and

Bubnova 2000), however, edge-connected BO_x groups are known from structures synthesized at high pressure and high temperature (Filatov and Bubnova 2008). The clusters are referred to as "fundamental building blocks" (Burns et al. 1995). Due to different bond valence sums, it is energetically not favorable to build large clusters consisting solely of $\text{B}(\text{O},\text{OH})_4$ tetrahedra.

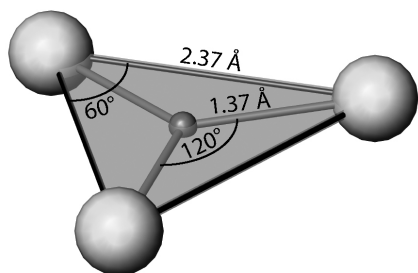


Figure 2.23: Structural drawing of an ideal BO_3^{3-} equilateral triangle. Bond lengths and angles are indicated.

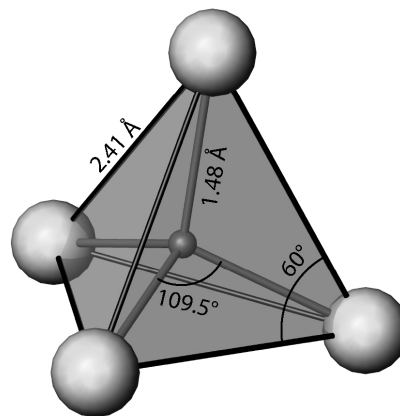


Figure 2.24: Structural drawing of an ideal BO_4^{5-} tetrahedron. Bond lengths and angles are indicated.

It is interesting to point out that an isotope fractionation of ^{11}B and ^{10}B occurs between trigonal and tetrahedral coordinated boron species. The heavier ^{11}B is preferentially three-fold coordinated, whereas the ^{10}B isotope is concentrated in four-fold coordinated sites. The isotope fractionation factor ($[\text{B}^{11}/\text{B}^{10}]_{\text{trigonal}}/[\text{B}^{11}/\text{B}^{10}]_{\text{tetragonal}}$) is ca. 1.03 at room temperature and decreases with temperature (Palmer and Swihart 1996, Kakihana et al. 1977).

From refined crystal structures containing $\text{B}(\text{O},\text{OH})_3$ and/or $\text{B}(\text{O},\text{OH})_4$ groups, Hawthorne et al. (1996) investigated central-ligand bond lengths and angles. The average center-ligand distance in $\text{B}(\text{O},\text{OH})_3$ triangles is 1.370 Å, with a rms deviation of 0.017 Å. A Gaussian distributed minimum of 1.322 and maximum of 1.428 Å has been observed with a variation range of 0.106 Å. In $\text{B}(\text{O},\text{OH})_4$, the mean distance is 1.476 Å with a rms deviation of 0.025 Å. The Gaussian distributed minimum and maximum observed distances in $\text{B}(\text{O},\text{OH})_4$ are 1.397 Å and 1.512 Å, respectively with a variation of 0.115 Å. For an ideally coordinated $\text{B}(\text{O},\text{OH})_3$ group, coordination would represent an equilateral triangle with $(\text{O},\text{OH})\text{-B}(\text{O},\text{OH})$ angles of 120° and $(\text{O},\text{OH})\text{-(O},\text{OH})\text{-(O},\text{OH})$ angles of 60° . $\text{B}(\text{O},\text{OH})\text{-B}$ angles in an ideally coordinated $\text{B}(\text{O},\text{OH})_4$ polyhedron are 109.47° . Actual angles depend on the linkage of BO_x groups with neighboring polyhedra.

Isolated BO_3 and BO_4 polyhedra have practically no thermal expansion when heated and behave similar to AlO_4 and SiO_4 tetrahedra (Filatov and Bubnova 2000; 2008, Hazen and Prewitt 1977, Tucker et al. 2000). Crystal structures containing BO_x groups can be regarded as special because not only isolated BO_x groups but also polymerized groups of BO_x polyhedra remain rigid at high temperature. However, with rising temperature, single BO_x groups or

rigid polymerized BO_x group clusters act as structural hinges in order to allow structural changes. Thermal invariability of the BO_x groups or clusters is the main reason for highly anisotropic and sometimes even negative thermal expansion of BO_x containing crystals. At high-pressure conditions, borates become denser due to decreasing bond lengths, increased coordination number and BO_4 polymerization via O-O edges (Filatov and Bubnova 2008).

2.5 Analytical Techniques for Boron Analysis

Boron was recognized as mineral constituent in the late 18th century. More or less reliable wet-chemical analyses were possible only about 100 years later, however, they remained a challenge until today (e.g. due to boron loss at higher temperatures). Easy and fast quantitative analysis of boron is still difficult because B is not detected with most X-ray fluorescence methods and also electron microprobes require special analyzer crystals (Anovitz and Grew 1996).

Electron microprobes can be equipped with thin-window detectors for energy-dispersive spectrometry (EDS) and layered synthetic microstructure (LSM, optimized for low Z elements) crystals for wavelength dispersive spectrometry (WDS). With EDS methods, boron can be identified, however, quantification is almost impossible due to the low yield of X-rays of boron. Even with WDS, the quantification of light elements is a challenge, and it largely depends on the instrument setup and the matrix of the sample and the standard (McGee 1996). Electron microprobe measurements have been performed on aluminoborate samples early in this study, however, results were not reproducible and this method was not further pursued.

Quantitative boron isotope analyses can be performed with high precision with magnetic mass spectrometers. The sample is usually thermally ionized and positive or negative boron-complex ions are measured. Standardization, sample preparation and instrumental calibration and setup are difficult and require much time (Swihart 1996). Especially during sample preparation (boron must be isolated from the sample) contamination and boron-loss are an issue. SIMS (secondary ion mass spectrometry) is a favorable method for boron quantification because it combines the relatively easy sample preparation of the electron microprobe with high-precision results of mass spectrometry. Standardization is problematic and a calibration curve from known standards is needed. Once set up, due to the high quantification precision, measurements of diffusion coefficients are possible, as well as element mapping and isotope measurements (Hervig 1996). Quadrupole mass spectrometers are less sensitive but easier to operate and may thus be used to good advantage for certain experiments (Swihart 1996). It has been shown in this study, that laser-ablation coupled with an ICP (inductively coupled plasma) quadrupole mass spectrometer allows good estimation of boron content, however not boron isotope measurements. The advantage of this method is that time-consuming and complex sample preparation could be avoided.

X-ray diffraction measurements with conventional single-crystal laboratory diffractometers

offer the possibility to locate boron in crystal structures. Correlations with (anisotropic) displacement parameters and the overall scale factor make precise quantification (site occupancy factors) difficult. Due to the low amount of information obtained from powder X-ray diffraction measurements, it is doubtful if boron sites can be identified and occupancy fractions of boron sites are not reliable.

Fourier transformed infrared, Raman and nuclear magnetic resonance (NMR) spectroscopy do not allow straightforward and precise quantification of boron content, however, both provide evidence on boron occurrence in a sample and unambiguous information about the coordination of boron can be obtained. In Raman and FTIR spectroscopy, the difference in the mass of the two B isotopes (10 rel.-%) has to be accounted for (Siebert 1966, Farmer 1974, Harris and Bertolucci 1989). In NMR experiments, ^{10}B and ^{11}B have different resonance frequencies and can therefore be measured independently. Due to different frequency and quantum spins, ^{10}B measurements are less sensitive (D. Rentsch, personal communication). In this study, all three methods were used to obtain additional structural information of the investigated compounds.

Further techniques for boron analysis include nuclear methods and parallel electron energy-loss spectroscopy (EELS). With EELS, a sample is probed with monoenergetic electrons. After interaction with the sample, electron energy distribution is analyzed. The resulting spectra provide information on elemental composition, coordination and site symmetry, valence, spin state and bonding of atoms at very high spatial resolution. The high potential of EELS can be increased in combination with transmission electron microscopy (Lawrence and Buseck 1996). Nuclear methods comprise particle-induced gamma-ray (PIGE) and particle emission (NRA), prompt-gamma neutron activation analysis (PGNAA) and fast neutron activation analysis (FNAA). All of these methods have the great advantage that the bulk sample (or depths up to 100 μm in thin sections) is analyzed. Furthermore, matrix effects are subordinate. Nuclear methods are based on nuclear reactions due to interaction of nuclei with charged particles or neutrons. They offer precise information on isotope type and concentration in a bulk sample. However, particle accelerators or nuclear reactors are required and minimum sample mass is rather large (up to ca. 1000 μg) when neutrons are used (Robertson and Dyar 1996).

3 Boron Mullite Synthesis Experiments

Synthesis experiments in this study were performed in a Nabertherm LHT04/17 furnace equipped with Superkanthal (MoSi_2) heating elements in air atmosphere. Charges were placed in lid covered platinum crucibles or in sealed platinum capsules cut from a platinum tube with 4 mm inner diameter. Solid starting materials were thoroughly ground in agate mortars and pressed as tablets before heating. Prior to further investigations, excess B_2O_3 or H_3BO_3 was washed away with deionized H_2O in samples with aluminoborate compositions. Chemical compounds used for precursor preparation are listed in Table 3.1.

Preliminary sample identification was done by powder X-ray diffraction analyses in combination with the ICDD PDF-2 2004 database. As the phases Al_5BO_9 and $\text{Al}_{18}\text{B}_4\text{O}_{33}$ cannot be distinguished by X-ray diffraction methods, the term "ABO" is used in this chapter for Al_5BO_9 and $\text{Al}_{18}\text{B}_4\text{O}_{33}$ in space group $Cmc2_1$. $\text{Al}_4\text{B}_2\text{O}_9$ in space group $C2/m$ was identified using structural information from Fischer et al. (2008b). Identification of mullite-like phases was done with LeBail refinements starting with lattice parameters $a = 7.6 \text{ \AA}$, $b = 7.5 \text{ \AA}$ and $c = 2.8 \text{ \AA}$ in space group $Pbam$.

Table 3.1: Chemical compounds used in this study.

Chemical compound, formula	Catalogue no.	Vendor
Aluminium nitrate nonahydrate 98+%, $\text{Al}(\text{NO}_3)_3 \cdot 9\text{H}_2\text{O}$	237973-100G	Sigma-Aldrich
Aluminium nitrate nonahydrate p.a., $\text{Al}(\text{NO}_3)_3 \cdot 9\text{H}_2\text{O}$	1.01063.0500	Merck
Aluminum oxide -100 mesh 99%, Al_2O_3	23,474-5	Sigma-Aldrich
Aluminium sulfate hexahydrate p.p.a., $\text{Al}_2(\text{SO}_4)_3 \cdot 16\text{H}_2\text{O}$	06421	Fluka
Borax p.a., $\text{Na}_2\text{B}_4\text{O}_5(\text{OH})_4 \cdot 10\text{H}_2\text{O}$	6308	Merck
Boric acid p.a., H_3BO_3	165	Merck
Boron oxide 97.5% min., B_2O_3	012290 500G	Alfa Aesar
Boron oxide 99.98%, B_2O_3	339075-100G	Sigma-Aldrich
Glycerol 85%, $\text{C}_3\text{H}_5(\text{OH})_3$	07-3800-01	Haenseler AG
Molybdenum(VI) oxide p.p.a., MoO_3	69850 100g	Sigma-Aldrich
Potassium carbonate p.a., K_2CO_3	1.04928.0500	Merck
Potassium sulfate p.a., $\text{K}_2(\text{SO}_4)_2$	5153	Merck
Silica gel, grade 62, 60–200 mesh, 150\AA , SiO_2	112926-00-8	Aldrich
Tetra ethyl orthosilicate (TEOS), $\text{C}_8\text{H}_{20}\text{O}_4\text{Si}$	91689-250ML	Sigma-Aldrich
Yttrium oxide 99.99%, Y_2O_3	205168-50G	Sigma-Aldrich

3.1 Al₂O₃-B₂O₃ Compounds with Mullite-Type Structure

3.1.1 Overview

Until the late 20th century, routes for the synthesis of aluminoborates with mullite-type structures (Al₅BO₉ (5Al₂O₃:B₂O₃), Al₁₈B₄O₃₃ (9Al₂O₃:2B₂O₃) and Al₄B₂O₉ (4Al₂O₃:2B₂O₃)) aimed at the production of single-crystal or powder samples for subsequent structural or crystal-chemical analyses and for the investigation of material properties. In this context, "single-crystal" is used for crystals with dimensions suitable for measurements with conventional laboratory single-crystal X-ray diffractometers (a few 100 μm or larger), whereas the term "powder" is used for loose crystals or sintered aggregates of crystals with a few μm length, which are too small to be measured with single-crystal X-ray diffractometers.

Since the 21st century, methods for large-scale synthesis of ABO and Al₄B₂O₉ as advanced materials were investigated. This includes production of μm-large whiskers, micro- and nanotubes, nanorods and nanowires with and without coatings for specialized applications (Cheng et al. 2004, Ma et al. 2002, Kim et al. 2004, Zhang et al. 2005, Li and Chang 2006, Peng et al. 2006, Zhang et al. 2006, Elssfah et al. 2007, Song et al. 2007, Wang et al. 2008, Lee et al. 2010 and more). Preparation methods for such specialized materials are not considered here.

Four different methods for single-crystal or powder synthesis of aluminoborates ABO and Al₄B₂O₉ are repeatedly reported in literature: (1) Synthesis from α-Al₂O₃ and B₂O₃ with additional excess B₂O₃ as flux; (2) Synthesis of an aluminum and a boron source (α-Al₂O₃, Al(OH)₃, Al₂(SO₄)₃,... and B₂O₃ or H₃BO₃) in a flux of different composition; (3) Solid-state reactions of α- or γ-Al₂O₃ and B₂O₃ or H₃BO₃; (4) Synthesis from amorphous precursors prepared via sol-gel routes.

Flux of different chemical composition (K₂CO₃, MoO₃, Y₂O₃, K₂SO₄, CaO)

ABO single-crystals have been synthesized by Sokolova et al. (1978) from Al₂O₃ and B₂O₃ in a K₂CO₃-MoO₃-Y₂O₃ flux with unknown composition by cooling the melt from 1150°C to 950°C.

Azizov et al. (1982) and Nekrasova and Leonyuk (2008) showed that ABO may crystallize during synthesis of (Yb,Y)Al₃(BO₃)₄ and YAl₃(BO₃)₄ from K₂MoO₃O₁₀ flux (= K₂CO₃ + 3MoO₃) as a side phase. Starting from a mixture CaO, Al₂O₃ and H₃BO₃ with johachidolite composition (CaAlB₃O₇, Kadiyski et al. 2008), Leonyuk and Shvanskiy (1998) produced ABO. The same observations were made when K₂MoO₄ flux was added.

Ihara et al. (1980) reported prismatic crystals of up to 1 mm length from a mixture of 25.0 mol-% α-Al₂O₃, 43.8 mol-% B₂O₃ and 31.2 mol-% CaO (ratio Al₂O₃:B₂O₃ = 4.5:8) by cooling the melt from 1440°C to 1250°C.

ABO whiskers of a few μm length were produced from Al(OH)₃ and H₃BO₃ in KCl flux by cooling the melt from 900°C and from Al₂(SO₄)₃ and H₃BO₃ in K₂SO₄ flux by cooling from 1100°C (Wada et al. 1991). A similar procedure was used by Gönenli and Tas (2000), who

dissolved $Al_2(SO_4)_3 \cdot 18H_2O$ and H_3BO_3 with K_2SO_4 in water. The material obtained from the dried solution was heated at 1073°C and 1150°C. In a TEM study, Carazeanu et al. (2004) determined formation temperature of ABO nanocrystals at around 900°C. The crystals were produced from $Al_2(SO_4)_3$, H_3BO_3 and K_2SO_4 with K_2CO_3 or KCl as fluxing agent. The optimum heating temperature found was 1000°C for 50% K_2SO_4 flux.

Isochemical flux (B_2O_3)

Benner and Baumann (1938) synthesized ABO crystals of up to 2 cm length (reported by Baumann and Moore 1942) by melting B_2O_3 in molten α - Al_2O_3 using an electric arc furnace.

By heating 30 wt.-% α - Al_2O_3 in 70 wt.-% molten B_2O_3 at 1100°C, Scholze (1956) was able to crystallize ABO. With the same precursor, he produced $Al_4B_2O_9$ at 1000°C. As Scholze (1956) measured optical properties of the materials, it is likely that he obtained large crystallites, however, crystal size is not mentioned.

Solid-state reaction

Dietzel and Scholze (1955) synthesized ABO crystals by heating a stoichiometric mixture of 9α - Al_2O_3 : $2B_2O_3$ in a molybdenum boat under reducing atmosphere and Ray (1992) produced ABO powder by calcining the same mixture at 1300°C. His observations showed that at temperatures lower than 700°C, no aluminoborate phase formed. Between 800°C and 1000°C, ca. 10% of the mixture reacted to $Al_4B_2O_9$ and between 1000°C and 1100°C, formation of ABO started at the expense of $Al_4B_2O_9$. After 1100°C, only ABO was observed. The temperatures are in agreement with those Rymon-Lipinski et al. (1984) determined with thermogravimetric analyses and those of the phase diagram by Gielisse and Forster (1962), which was derived by preparing samples from γ - Al_2O_3 and B_2O_3 in sealed platinum capsules between 600°C and 1650°C.

Garsche et al. (1991) obtained ABO powder as well as single-crystal samples from 9α - Al_2O_3 and $2B_2O_3$. Powder samples were produced by annealing the mixture at 1350°C for 2h. Single-crystals were obtained from the same starting material, however, heat treatment was performed at 1500°C for 7 days in sealed platinum capsules.

Sol-gel derived precursors

From a precursor made from a denitrified gel of stoichiometric amounts of $Al(NO_3)_3 \cdot 9H_2O$ and H_3BO_3 , Mazza et al. (1992) produced metastable mullite-like " Al_5BO_9 " and " $Al_4B_2O_9$ " in space group $Pbam$ at 880°C and 917°C, respectively. Further heating of the products above 900°C – 1000°C yielded $Al_4B_2O_9$ and ABO. The same compounds were also produced and investigated with powder X-ray diffraction, ^{11}B and ^{27}Al MAS NMR by MacKenzie et al. (2007). In a study on Al-B-Si compounds, both compounds were also found by Griesser et al. (2008) from a similar precursor and Fischer et al. (2008b) used the preparation method of

Mazza et al. (1992) to crystallize $\text{Al}_4\text{B}_2\text{O}_9$ from a non-stoichiometric ($\text{Al}_2\text{O}_3:2\text{B}_2\text{O}_3$) starting mixture at 950°C .

Precipitation process derived precursors

To avoid boron evaporation at higher temperatures, Duoy (2005) dissolved $\text{Al}(\text{NO}_3)_3 \cdot 9\text{H}_2\text{O}$ and H_3BO_3 in distilled H_2O . The aqueous solution was subsequently precipitated into a mixture of ammonium bicarbonate and ammonium carbamate (yielding solid ammonium borate and ammonium nitrate) before the liquid was evaporated. The resulting precursors were heated at 1000°C , when ABO and $\text{Al}_4\text{B}_2\text{O}_9$ were found and at 1100°C , ABO formed together with $\alpha\text{-Al}_2\text{O}_3$. At temperatures below 950°C , formation of transition alumina phases ($\gamma\text{-Al}_2\text{O}_3$, Chakravorty 1993, Chakraborty and Das 2003 and Gutierrez et al. 2002) is reported.

3.1.2 $\text{Al}_2\text{O}_3\text{-B}_2\text{O}_3$ Synthesis Experiments

Flux of different chemical composition (K_2CO_3 , MoO_3 , Y_2O_3 , K_2SO_4 , $\text{Na}_2\text{B}_4\text{O}_7 \cdot 10\text{H}_2\text{O}$)

Assuming that Sokolova et al. (1978) were performing synthesis experiments for preparation of an Al-B-Y-O phase from a $\text{K}_2\text{CO}_3 + 3\text{MoO}_3$ flux, the first experiment for synthesizing ABO single crystals (# 1) was performed by starting from $9\alpha\text{-Al}_2\text{O}_3$, $2\text{B}_2\text{O}_3$ and K_2CO_3 with 3MoO_3 yielding $\text{K}_2\text{Mo}_3\text{O}_{10}$ as flux. Weighed ratios and heating rates are shown in Table 3.2. Elongated prismatic ABO single-crystals of a maximum length of about 1 mm and a rather smooth surface, intergrown in radial aggregates (Figures 3.1 - 3.3) could easily be separated from the flux in boiling H_2O . The crystals were mostly twinned, as estimated from polarized light microscopy, and Al_2O_3 inclusions could be identified with electron microprobe analyses (Figure 3.4). The inclusions are the reason for excess corundum as identified with an X-ray powder diffraction pattern of ground crystals (Figure 3.5). SEM images of the crystals of this synthesis experiment are shown in Figures 3.6 and 3.7.

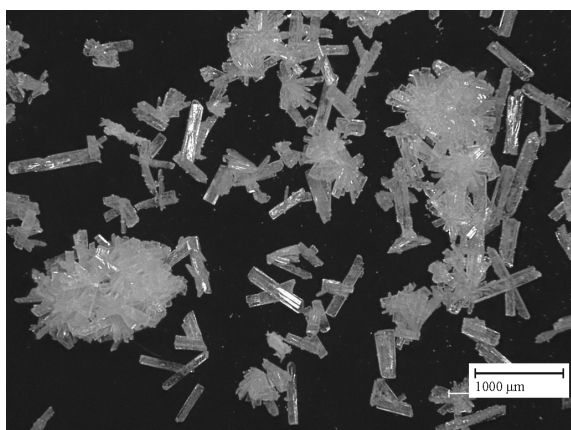


Figure 3.1: Microscope photograph of the ABO crystals and radially grown crystal aggregates produced in run #01.

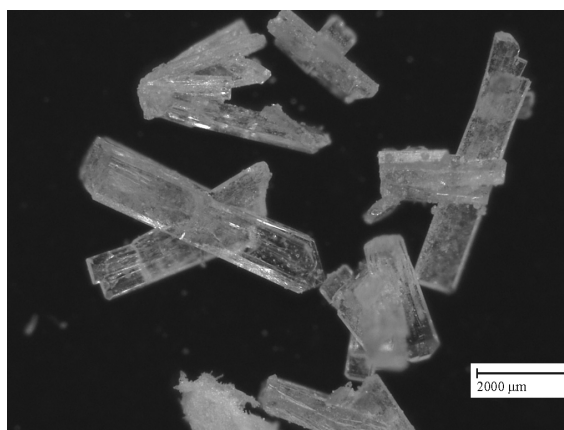


Figure 3.2: Microscope photograph of the ABO crystals from run #01 at higher magnification.

Table 3.2: List of ABO synthesis experiments performed with $\text{K}_2\text{CO}_3+3\text{MoO}_3$ flux.

#	$\alpha\text{-Al}_2\text{O}_3$ (g)	B_2O_3 (g)	A:B (mol)	(AB):Flux (wt.)	Wt. (g)	T_{\max} ($^{\circ}\text{C}$)	T_{end} ($^{\circ}\text{C}$)	∇ ($^{\circ}\text{C}/\text{h}$)	Type	Phases (XRD)
01	0.197	0.03	9:2	0.111	2.29	1100	600	10	X	1, 2
02	0.659	0.20	9:4	0.368	2.92	1100	600	10	P	1, 2
04	0.395	0.06	9:2	0.152*	3.45	1100	700	5	P	1, 2
05	0.395	0.07	9:2.2	0.225	2.61	1100	600	5	P	1, 2
06	1.977	0.30	9:2	0.083	29.66	1150	600	3	P	1, 2
07	2.372	0.36	9:2	0.111	27.47	1100	600	10	P	1, 2, 3
08	2.768	0.42	9:2	0.129	27.93	1100	600	10	P	1, 2, 3, 4
09	1.713	0.26	9:2	0.098	21.97	1100	600	10	P	1, 2, 4
10	1.858	0.282	9:2	0.086*	26.88	1100	400	10	P	2, 4, U
11	1.858	0.282	9:2	0.086	26.88	1100	400	10	P	1, 2, 4
12	0.395	0.06	9:2	0.111	4.58	1100	600	10	P	1, 2, 3, 4
13	3.295	0.50	9:2	0.460	12.04	1100	450	10	P	1, 2, U
16	0.659	0.10	9:2	0.153	5.71	1100	450	10	P	1, 2
18	1.318	0.20	9:2	0.153	11.41	1100	450	10	P	1, 2, 4, 5
19	0.659	0.14	9:2.8	0.153	6.18	1100	450	10	P	1, 4, 5
20	0.659	0.14	9:2.8	0.153	6.18	1250	1000	10	P	1, 2, 3, 4
21	0.659	0.14	9:2.8	0.153	6.18	1250	1000	10	P	1, 4
22	0.659	0.14	9:2.8	0.115	7.76	1100	600	10	P	1, 4, U
31	0.329	0.08†	5:2	0.099	4.53	1100	600	10	P	1, 4, 5
45	0.197	0.20	2:3	0.111	2.46	1100	800	5	P	1, 2, U
46	0.197	0.20	2:3	0.111	2.46	1100	750	5	P	1, 3

X = crystals, P = powder

* single-phase $\text{K}_2\text{Mo}_3\text{O}_{10}$ as flux† H_3BO_3 instead of B_2O_3

1 = ABO

2 = $\alpha\text{-Al}_2\text{O}_3$ 3 = $\text{K}_2\text{Mo}_4\text{O}_{13}$ 4 = $\text{KAl}(\text{MoO}_4)_2$ 5 = $\text{K}_2\text{Mo}_3\text{O}_{10} \cdot 3\text{H}_2\text{O}$

U = unidentified phase(s)

In another 20 runs with $\text{K}_2\text{CO}_3 + 3\text{MoO}_3$ flux, the total precursor amount and the ratio $(\text{Al}_2\text{O}_3+\text{B}_2\text{O}_3):\text{flux}$ were varied from ca. 0.46 to 0.08, up to 100 wt.-% of excess boron were added and the $\text{K}_2\text{CO}_3 + 3\text{MoO}_3$ flux was replaced by previously prepared $\text{K}_2\text{Mo}_3\text{O}_{10}$. T_{\max} was varied from 1100°C to 1250°C , T_{end} from 400°C to 1000°C and the cooling gradient from $3^{\circ}\text{C}/\text{h}$ to $10^{\circ}\text{C}/\text{h}$ (Table 3.2) but the synthesis yielding large single-crystals could not be reproduced. Samples consisted either of only small crystals of ABO powder or of sintered tablets (Figure 3.8), accompanied by excess corundum (Figure 3.10), or of large, yellowish $\text{KAl}(\text{MoO}_4)_2$ crystals (Figure 3.9) together with small ABO crystals and excess corundum (Figure 3.11). With the $\text{K}_2\text{CO}_3 + 3\text{MoO}_3$ flux method, no synthesis run yielded single-phase ABO.

Similar to Gönenli and Tas (2000) and Wada et al. (1991), a synthesis with H_3BO_3 , $\text{Al}_2(\text{SO}_4)_3 \cdot 16\text{H}_2\text{O}$ and K_2SO_4 was performed. The precursor material consisted of 7.32g of $\text{Al}_2(\text{SO}_4)_3 \cdot 16\text{H}_2\text{O}$ and 0.35g H_3BO_3 (molar ratio of $8\text{Al}_2\text{O}_3:2\text{B}_2\text{O}_3$) and 5g K_2SO_4 . The compounds were diluted in deionized H_2O which was evaporated after the solution was homogeneous. The obtained powder was subsequently heated at 1100°C and slowly cooled to 450°C at $10^{\circ}\text{C}/\text{h}$. The synthesized product consisted of ABO, $\alpha\text{-Al}_2\text{O}_3$ and at least one unidentifiable phase.

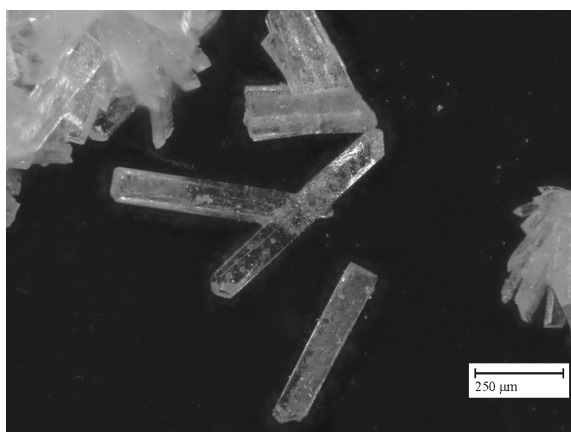


Figure 3.3: Microscope photograph of single ABO crystals from run #01. The bright spots in the crystals were identified as Al_2O_3 inclusions.

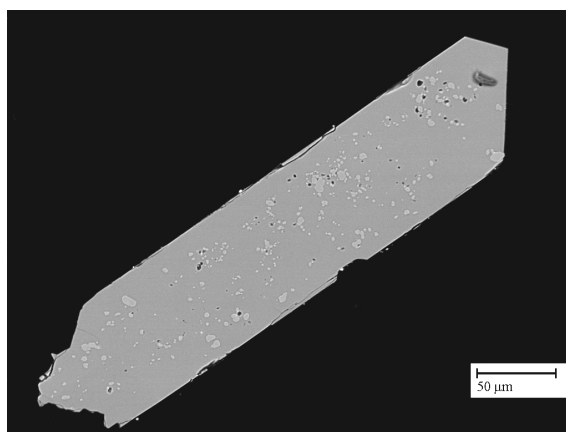


Figure 3.4: Electron microprobe photograph of an ABO crystal from run #01. The bright spots were identified as Al_2O_3 inclusions.

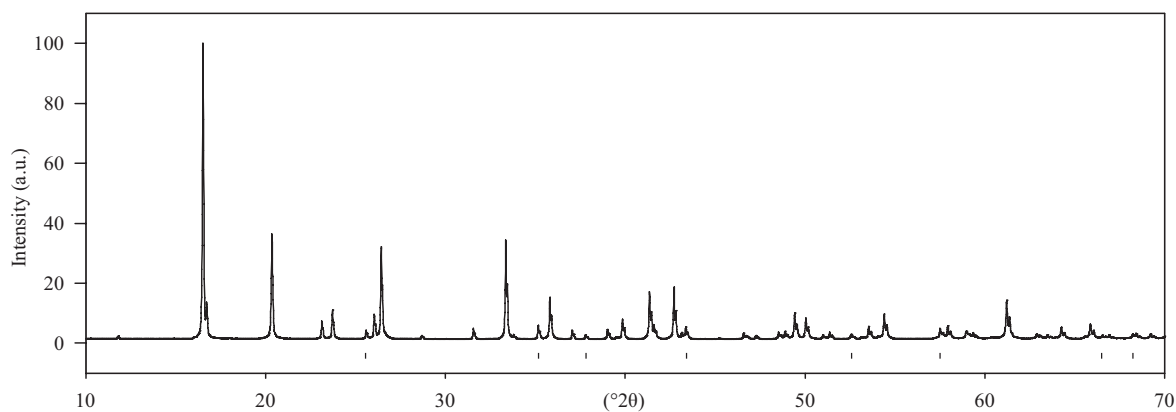


Figure 3.5: Powder XRD pattern of ground ABO crystals from run #01. *hkl*-ticks of corundum are indicated.

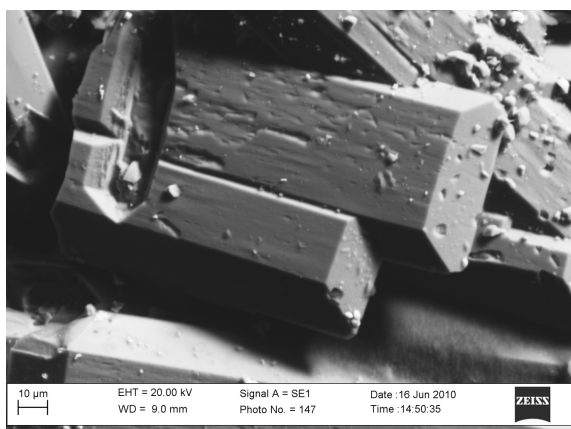


Figure 3.6: Secondary electrons SEM photograph of the ABO crystals from run #01 showing the rather smooth crystal surface.

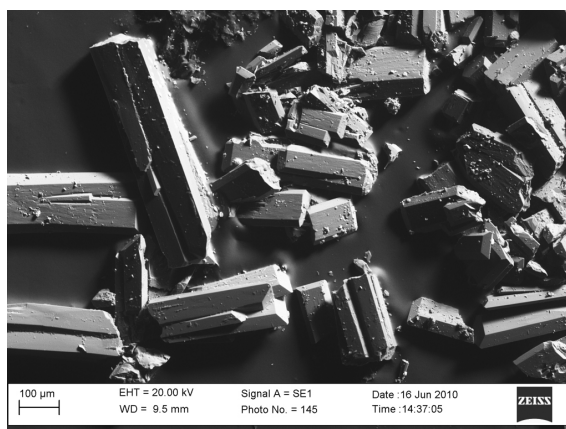


Figure 3.7: Secondary electrons SEM photograph of the ABO crystals from run #01.

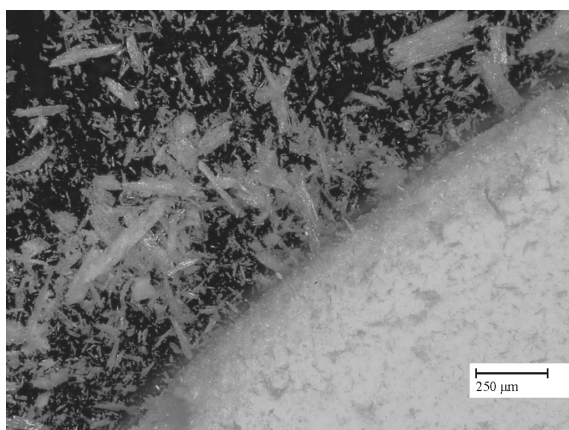


Figure 3.8: Small crystals and a piece of a sintered tablet of ABO crystals and corundum from run #05.

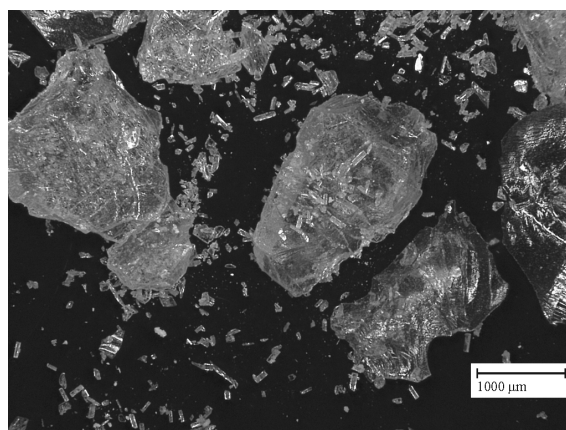


Figure 3.9: Small ABO crystals and large $\text{KAl}(\text{MoO}_4)_2$ crystals from run #09.

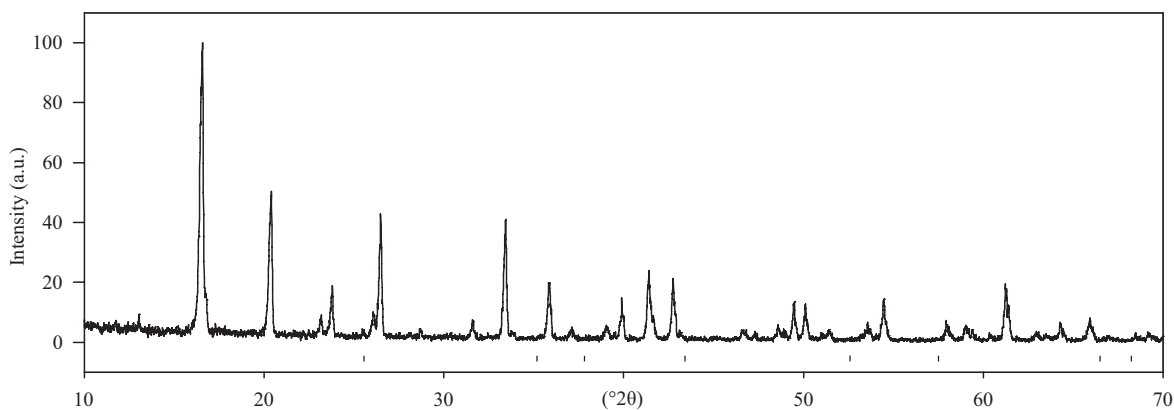


Figure 3.10: Powder XRD pattern of the ground sintered tablet of ABO crystals shown in Figure 3.8 from run #05. *hkl*-ticks of corundum are indicated.

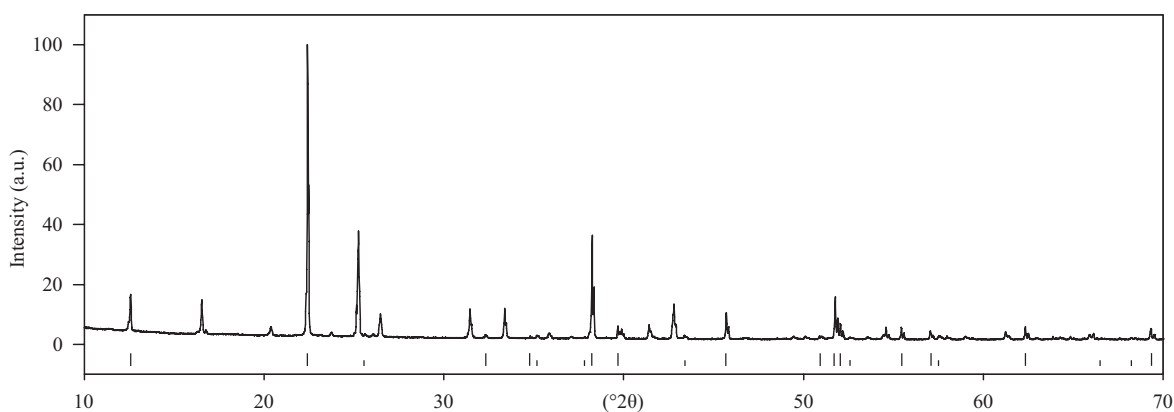


Figure 3.11: Powder XRD pattern of the large $\text{KAl}(\text{MoO}_4)_2$ crystals, ABO and corundum, shown in Figure 3.9. Short *hkl*-ticks indicate corundum peaks, long *hkl*-ticks indicate peaks assigned to $\text{KAl}(\text{MoO}_4)_2$.

Sokolova et al. (1978) used a mixture of Y_2O_3 - K_2CO_3 - MoO_3 as flux without indicating molar ratios. Nekrasova and Leonyuk (2008) and Azizov et al. (1982) showed that ABO may crystallize during synthesis of $(Yb,Y)Al_3(BO_3)_4$ from $K_2Mo_3O_{10}$ flux. Y and Er have similar ionic radii, thus, the molar amount of Er_2O_3 was replaced by Y_2O_3 in a recipe for the synthesis of $ErAl_3(BO_3)_4$ crystals in a $K_2Mo_3O_{10}$ flux (Teshima et al. 2006 and Beregi et al. 1999). The syntheses yielded ABO with $KY(MoO_4)_2$ and ABO with $KY(MoO_4)_2$ together with $K_2Mo_3O_{10}$. The presence of $K_2Mo_3O_{10}$ was apparently due to incomplete washing in H_2O and $KY(MoO_4)_2$ was also found in similar experiments by Azizov et al. (1982). After washing in hot HCl, ABO crystals with μm size remained as the only solid.

Syntheses of ABO with borax ($Na_2B_4O_7 \cdot 10H_2O$) as flux were prepared as listed in Table 3.3. In all runs, a glass remained in the platinum crucible which was soluble in warm HNO_3 . No crystals were found after dissolving the glass. However, few very thin crystals grew at the rim of the platinum crucible but they could not be removed. Scratched-off pieces of the crystalline products were identified as ABO.

Table 3.3: List of ABO syntheses performed with borax ($Na_2B_4O_7 \cdot 10H_2O$) as flux.

#	Al_2O_3 (g)	B_2O_3 (g)	A:B (mol)	(AB):Flux (wt.-%)	Wt. (g)	T_{max} (°C)	T_{end} (°C)	∇ (°C/h)	Type	Phases (XRD)
40	0.764	0.104	5:1	80:20	3.53	1100	900	3	X, G	ABO
41	1.274	0.174	5:1	60:40	3.35	1100	900	3	X, G	ABO
42	1.784	0.243	5:1	40:60	3.17	1100	900	3	X, G	ABO
43	1.019	0.139	5:1	70:30	3.45	1100	900	3	X, G	ABO
44	0.892	0.121	5:1	75:25	3.49	1050	850	2	X, G	ABO

X = crystals, G = glass

Isochemical flux (B_2O_3)

Four different synthesis routes were tested starting from α - Al_2O_3 and H_3BO_3 : (1) A pressed tablet of 0.2g Al_2O_3 and 0.8g H_3BO_3 was covered with ca. 3g H_3BO_3 in a platinum crucible. The charge was heated at 1500°C, then heated to 1550°C and held at this temperature for one hour and subsequently quenched. Yield were small crystals at the rim of the crucible. (2) A pressed tablet of 0.2g Al_2O_3 and 0.8g H_3BO_3 was fired for 2h at 1200°C. The ground ABO powder was subsequently mixed with more H_3BO_3 and pressed as tablet, which was covered with ca. 3g H_3BO_3 in a platinum crucible and heated for 1h at 1550°C and then slowly cooled to 1250°C at 15°C/h. Yield were ABO crystals (Figure 3.12 and 3.13) which could be removed from the crucible by dissolving remaining B_2O_3 in hot water. The crystals were coexisting with loose aggregates of tiny ABO crystals (Figures 3.14 and 3.15). SEM images of the crystals show that the crystals have a rather flaky surface (Figures 3.16 and 3.17). From powder X-ray diffraction patterns, the product was identified as single-phase ABO (Figure 3.18). (3) A presintered piece of 0.1g ABO was put into a platinum tube. The tube was filled with H_3BO_3 which was heated to obtain B_2O_3 , sealed and subsequently heat treated at

1500°C for 72h and then cooled to 1200°C in 72h. After the heat treatment, the presintered piece of ABO remained almost unaltered (Figure 3.19). (4) A platinum tube was filled with roughly 50:50 wt.-% Al_2O_3 and B_2O_3 . The sealed tube was heated for 72h at 1500°C and then cooled to 1250°C in 72h. After the heat treatment, the tube contained pieces of B_2O_3 in which small crystals were trapped (Figure 3.20). After dissolving B_2O_3 in hot water, few small ABO crystals remained together with corundum.

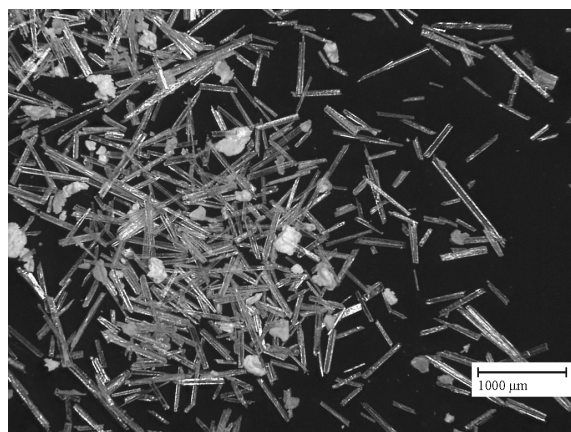


Figure 3.12: ABO crystals grown from the B_2O_3 flux (#62-2).

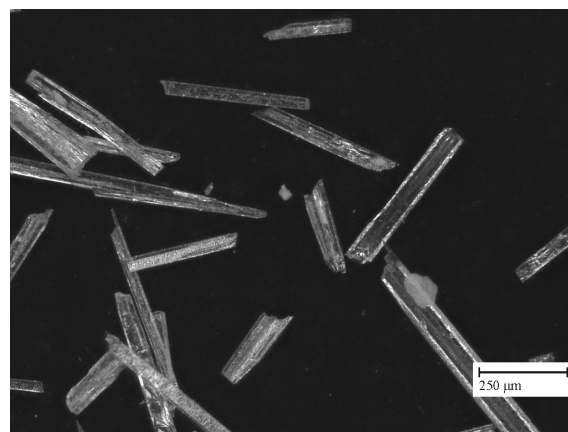


Figure 3.13: ABO crystals grown from the B_2O_3 flux (#62-2).

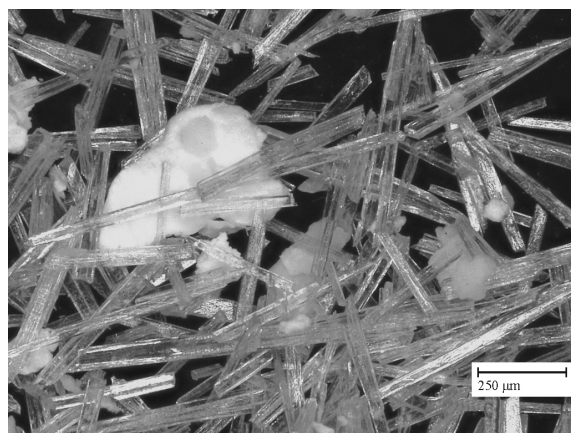


Figure 3.14: ABO crystals grown from the B_2O_3 flux coexisting with aggregates of tiny needle-like ABO crystals (#62-2).



Figure 3.15: Secondary electrons SEM picture of ABO crystals from run #62-2 coexisting with aggregates of tiny ABO crystals.

Solid-state reaction

ABO powder samples were prepared by solid-state reactions of $\alpha\text{-Al}_2\text{O}_3$ and B_2O_3 or H_3BO_3 .

Sample #24 (Table 3.4) was prepared according to Garsche et al. (1991) but one sample with a stoichiometric ratio of $\text{Al}_2\text{O}_3\text{:B}_2\text{O}_3$ of 5:1 (#24a) and another with a ratio of 9:2 (#24b). After 15 days of heating at 1500°C of 0.36g of the precursor, a sintered piece of ABO

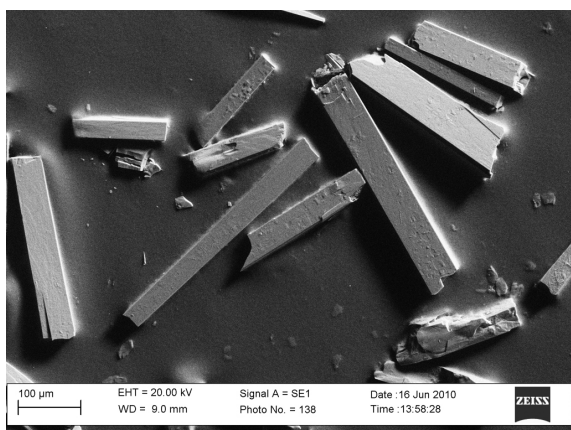


Figure 3.16: Secondary electrons SEM picture of ABO crystals from run #62-2.

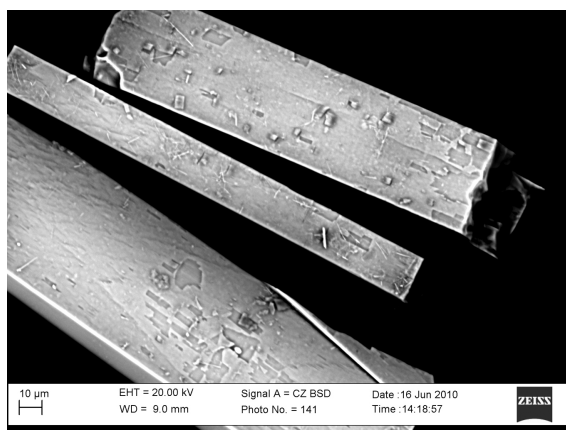


Figure 3.17: Backscattered electrons SEM picture showing the rather flaky surface of the crystals from run #62-2.

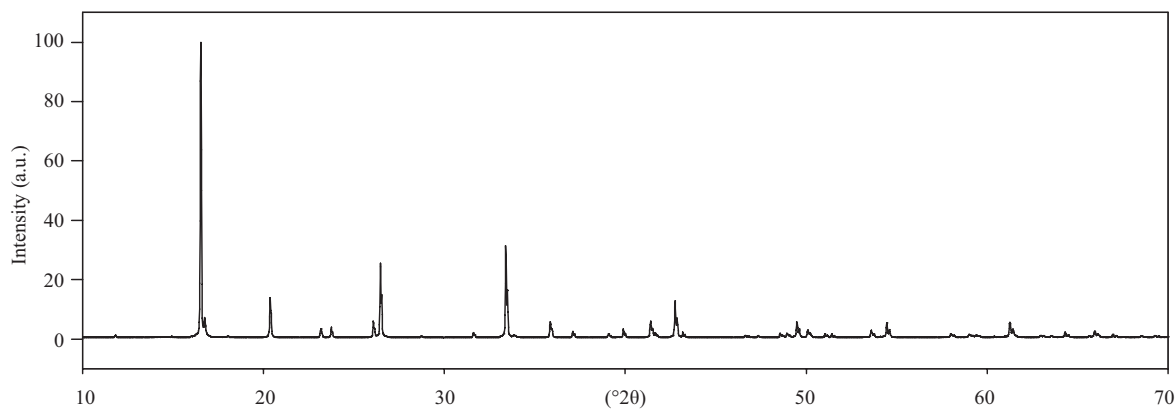


Figure 3.18: Powder XRD pattern of ground ABO crystals grown from the B_2O_3 flux (#62-2). The different relative intensities when compared to powder XRD patterns of other samples are ascribed to preferred-orientation effects due to a different sample preparation method.

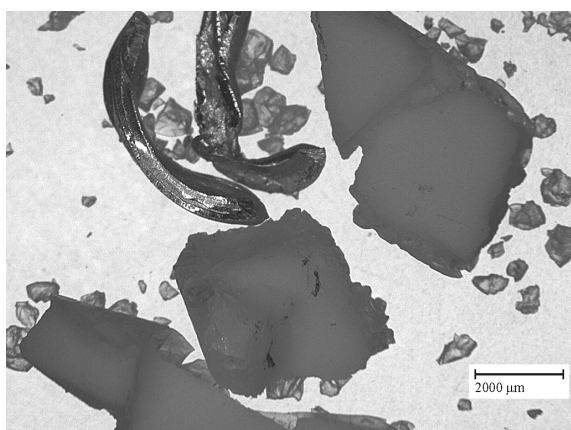


Figure 3.19: Pieces of the Pt capsule and sintered ABO after heat treatment with B_2O_3 in a sealed platinum tube (run #62-3).

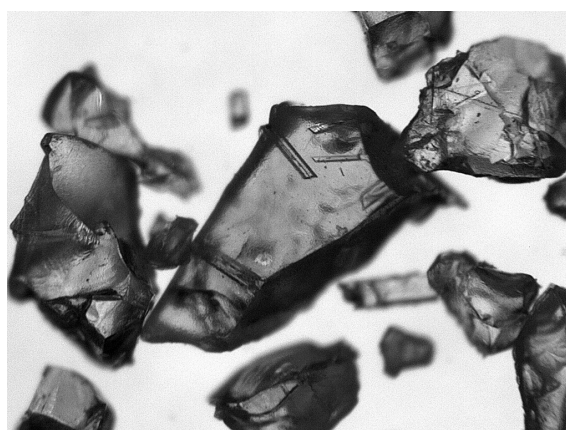


Figure 3.20: Small ABO crystals trapped in pieces of B_2O_3 (run #62-4). Length of the crystals is ca. 0.1 mm.

was found in the sealed platinum tube with the starting mixture with a 5:1 ratio, whereas the other platinum tube exploded in the furnace. Weighing the sealed capsule before and after the heat treatment indicated that it was not airtight.

Sample #38 was produced in an Anton-Paar furnace and in-situ measured with X-ray powder diffraction to monitor the solid-state reaction. Heating rate was $10^\circ\text{C}/\text{min}$ and measurements were made at 25°C and then each 100°C up to 1100°C . An additional measurement was performed at 450°C (melting point of B_2O_3). Each measurement took 20 min. After heating the sample for 2h at 1100°C , it was cooled to 25°C and measured again. A selection of the temperature dependent diffraction patterns is shown in Figure 3.21. Crystallization temperatures are in agreement with previous findings.

Table 3.4: List of solid-state reaction ABO synthesis experiments.

#	α - Al_2O_3 (g)	B_2O_3 (g)	H_3BO_3 (g)	A:B (mol)	Wt. (g)	T_{\max} ($^\circ\text{C}$)	T_{end} ($^\circ\text{C}$)	∇ ($^\circ\text{C}/\text{h}$)	Phases (XRD)
23	3.295	0.5		9:2	3.80	1200	800	100	ABO, 7% α - Al_2O_3
24a	7.322	1.0		5:1	8.32	1500	1500	-, 7d	ABO, 30% α - Al_2O_3
24b	6.590	1.0		9:2	7.59	1400	1400	-, 7d	-
28	0.2		1.1	2:9	1.3	1200	400	20	ABO
29	0.2		1.0	2:8	1.2	1200	500	7	ABO
38	0.26	0.044		8:2	0.304	1100	25	10	ABO, 30% α - Al_2O_3
50	3.66	0.50		5:1	4.16	1200	800	100	ABO, 8% α - Al_2O_3
54	1.0		1.0	1.2:1	2.0	1200	1200	-, 44h	ABO

Sol-gel derived precursors

Precursors for synthesis experiments of $Al_4B_2O_9$ were prepared according to Mazza et al. (1992) and Fischer et al. (2008b). $Al(NO_3)_3 \cdot 9H_2O$ and H_3BO_3 with 10 wt.-% of glycerol were heated to 80°C while continuously stirring with a magnetic stirrer. After homogenization, the solution was further heated to 110°C , when denitrification started. As release of NO_x gasses stopped, the foamy material was dried at 200°C , then crushed and heated at 300°C for 2h to remove remaining organics. Precursors of samples #51 and #53 (Table 3.5) were heated at 950°C and 1100°C , yielding $Al_4B_2O_9$ and ABO powder samples, respectively. The precursor of sample #52 was heated in an Anton-Paar furnace with $10^\circ\text{C}/\text{min}$ and in-situ measured with powder X-ray diffraction (Figure 3.22). Each measurement took 40 min. Results are in agreement with those of previous findings, however, when 1100°C were reached, $Al_4B_2O_9$ and ABO were coexisting for a short time ($< 2\text{h}$), which is also reported by Duoy (2005). After heating for 2h at 1100°C , the remaining $Al_4B_2O_9$ phase transformed completely to ABO.

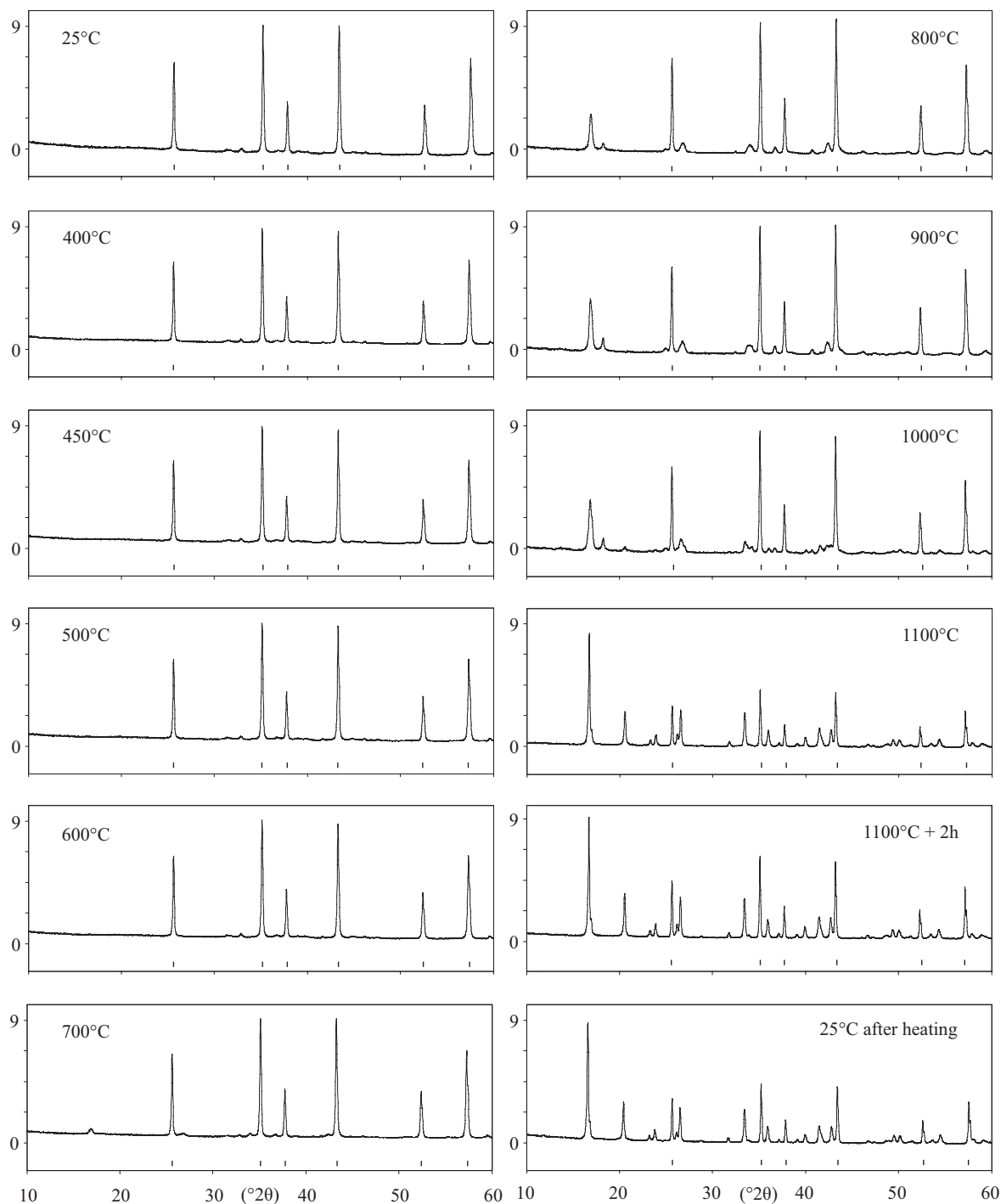


Figure 3.21: In-situ powder XRD patterns of the solid-state reaction experiment #38 starting from $8\alpha\text{-Al}_2\text{O}_3$ and $2\text{B}_2\text{O}_3$. At 25°C , only corundum can be identified (hkl -ticks). At 700°C , $\text{Al}_4\text{B}_2\text{O}_9$ starts to crystallize (confirmed by the small peak at ca. $16^\circ 2\theta$) and the phase is stable up to 1000°C . At 1100°C , $\text{Al}_4\text{B}_2\text{O}_9$ is completely transformed to ABO. After 2h at 1100° , ABO peaks have slightly smaller peak width (FWHM of the (021) reflection at ca. $16.5^\circ 2\theta$ $0.139(2)^\circ 2\theta$ instead of $0.146(2)^\circ 2\theta$), indicating increasing size of coherently scattering domains ("crystallite size"). However, this may be an effect of sample sintering. After cooling to 25°C , ABO and corundum remain as stable phases. Intensity scale is $\text{counts}\cdot 10^3$.

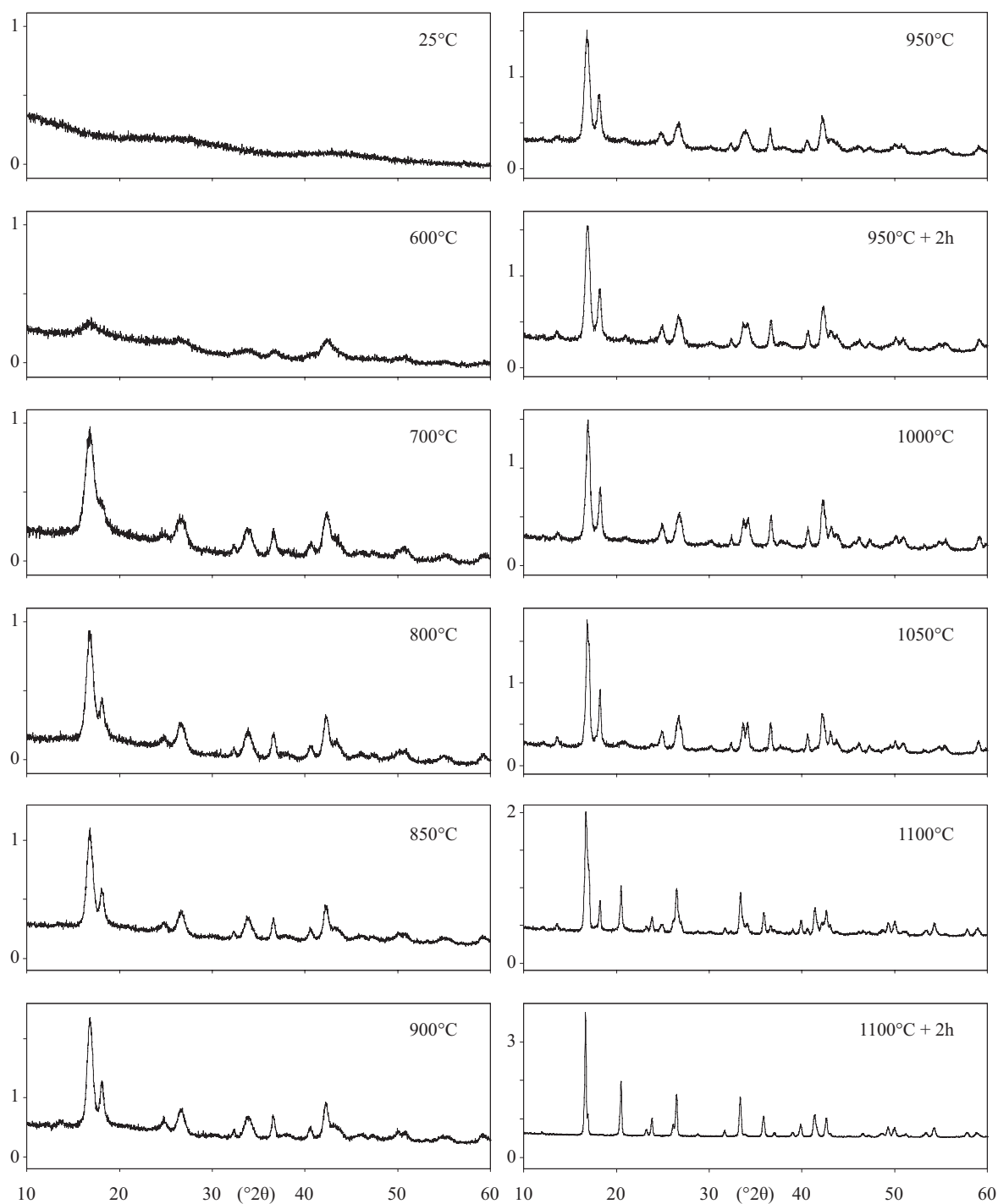


Figure 3.22: In-situ powder XRD patterns of the sol-gel precursor #52 consisting of $\text{Al}(\text{NO}_3)_3 \cdot 9\text{H}_2\text{O}$ and $2\text{H}_3\text{BO}_3$. Up to ca. 600°C , the precursor material is amorphous. At 700°C , $\text{Al}_4\text{B}_2\text{O}_9$ starts to crystallize and crystal growth continues to about 1050°C (FWHM of the $(20\bar{2})$ reflection at ca. $16.6^\circ 2\theta$ decreases from $0.74^\circ 2\theta$ at 850°C to $0.28^\circ 2\theta$ at 1050°C). At 1050°C , ABO formation starts. At 1100°C , both phases are coexisting, but after 2h at 1100°C , the $\text{Al}_4\text{B}_2\text{O}_9$ phase has completely transformed to ABO, which is the only phase present after cooling to room temperature. Intensity scale is $\text{counts} \cdot 10^3$.

Table 3.5: List of sol-gel derived precursor ABO synthesis experiments.

#	Al(NO ₃) ₃ · 9H ₂ O (g)	H ₃ BO ₃ (g)	A:B (mol)	Wt. (g)	T _{max} (°C)	T _{end} (°C)	∇ (°C/h)	Phases (XRD)
51a	9.238	0.762	2:1	10.0	950	950	0; 15h	Al ₄ B ₂ O ₉
51b	9.238	0.762	2:1	10.0	950	950	0; 10h	ABO
52	7.521	2.479	1:2	10.0	25	1100	10	Al ₄ B ₂ O ₉ , ABO, A
53a	15.042	4.958	1:2	20.0	950	950	0; 5h	Al ₄ B ₂ O ₉
53b	15.042	4.958	1:2	20.0	1100	1100	0; 5h	ABO

A = α -Al₂O₃Al₄B₂O₉ according to the structure of Fischer et al. (2008b)

3.2 Al₂O₃-B₂O₃-SiO₂ Compounds with Mullite-Type Structure

3.2.1 Overview

Three different methods for the production of compounds with mullite-type crystal structure in the system Al₂O₃-B₂O₃-SiO₂ are reported in literature: (1) Dietzel and Scholze (1955) synthesized compounds identified as "mullites" with powder X-ray diffraction from a solid-state reaction route. They used crystalline B₂O₃, α -Al₂O₃ and quartz as starting materials. The charge was heated in molybdenum boats under reducing atmosphere at temperatures between 1385°C and 1775°C. (2) From a sol-gel precursor consisting of Al(NO₃)₃ · 9H₂O, H₃BO₃ and tetra ethyl orthosilicate (TEOS, C₈H₂₀O₄Si), Griesser et al. (2008) were able to synthesize mullite-type structures. (3) Werding and Schreyer (1992) obtained a compound with an assigned stoichiometry of Al₈Si₂B₂O₁₉ at temperatures between 800°C and 830°C and pressures from 1 kbar to 4 kbar. They noticed the similarity of powder X-ray diffraction lines to those of ABO (Sokolova et al. 1978). The exact structure of the compound has not been solved yet.

3.2.2 Al₂O₃-B₂O₃-SiO₂ Synthesis Experiments

Solid-state reaction

Al₂O₃-B₂O₃-SiO₂ samples were prepared from α -Al₂O₃, previously heated silica gel and B₂O₃. In a first attempt, the stoichiometry of boralsilite Al₁₆Si₂B₆O₃₇ (sample #25) (Grew et al. 2008) and a composition of Al₂O₃:B₂O₃:SiO₂ of 8:3:4 (sample #26) were chosen. Subsequently, a hypothetical, although not charge neutral exchange of Si⁴⁺ → Al³⁺ was tested with starting mixtures representing stoichiometries of Al_{4.5}Si_{0.5}BO_{9.25} (#57), Al₄SiBO_{9.5} (#58) and Al_{3.5}Si_{1.5}BO_{9.75} (#59). Due to overlapping peaks of mullite, sillimanite, cristobalite and ABO, phase identification with powder X-ray diffraction was ambiguous and results may not be accurate. Starting material compositions and results from powder X-ray diffraction patterns are listed in Table 3.6.

Table 3.6: List of $\text{Al}_2\text{O}_3\text{-B}_2\text{O}_3\text{-SiO}_2$ solid-state reaction synthesis experiments.

#	Al_2O_3 (g)	B_2O_3 (g)	SiO_2 (g)	Theoretical stoichiometry	A:B:Si (mol)	Wt. (g)	Temp. (°C)	Time	Phases (XRD)
25	1.425	0.364	0.210	$\text{Al}_{16}\text{Si}_2\text{B}_6\text{O}_{37}$	8:3:2	2.0	1300	2h	ABO*
26	0.712	0.182	0.210	$\text{Al}_{16}\text{Si}_4\text{B}_6\text{O}_{41}$	8:3:4	1.1	1300	2h	ABO, A
57	0.714	0.192	0.090	$\text{Al}_{4.5}\text{Si}_{0.5}\text{BO}_{9.25}$	4.5:1:0.5	1.0	1200	12d	ABO, A
58	0.626	0.189	0.184	$\text{Al}_4\text{SiBO}_{9.5}$	4:1:1	1.0	1200	9d	ABO, A, C
59	0.810	0.280	0.409	$\text{Al}_{3.5}\text{Si}_{1.5}\text{BO}_{9.75}$	3.5:1.5:1	1.5	1200	4.5d	ABO, A, C

A = $\alpha\text{-Al}_2\text{O}_3$, C = cristobalite (SiO_2)

*one peak at $27.908^\circ 2\theta$ fits sillimanite

Sol-gel derived precursors

The method used by Griesser et al. (2008) was slightly modified to prepare twelve sol-gel precursors. Unlike as in Griesser et al. (2008), 5g of glycerol were added to each precursor resulting in a total weight of 23g per precursor. Glycerol forms ester complexes with boric acid at room temperature and thus prevents volatilization of H_3BO_3 at higher temperatures (Mazza et al. 1992). Furthermore, handling of the precursors is easier with glycerol. $\text{Al}(\text{NO}_3)_3 \cdot 9\text{H}_2\text{O}$, H_3BO_3 , TEOS ($\text{C}_8\text{H}_{20}\text{O}_4\text{Si}$) and glycerol were diluted with ethanol p.a. and stirred for ca. 2h at 50°C . With further heating, the solutions turned brown and at ca. 75°C , brownish NO_x gases were released. The resulting foamy gel was dried at 150°C in a furnace for 5h. After grinding the material and subsequent heat treatment at 400°C , a brownish powder was obtained. This precursor material was heat treated at 950°C and 1250°C for 5h.

Table 3.7: List of $\text{Al}_2\text{O}_3\text{-B}_2\text{O}_3\text{-SiO}_2$ sol-gel derived precursor synthesis experiments at 950°C .

#	Theoretical stoichiometry	Al_2O_3 (mol-%)	B_2O_3 (mol-%)	SiO_2 (mol-%)	Phases (XRD)
A	Al_5BO_9	83.33	16.67	0.00	Mullite-type*†
B		76.55	13.35	10.00	Mullite-type*†
C		70.00	10.00	20.00	Mullite-type*†
D	Boromullite $\text{Al}_9\text{Si}_2\text{BO}_{19}$	64.29	7.14	28.57	Mullite-type*†
E		56.57	3.35	40.00	Mullite-type*†
F	Sillimanite Al_2SiO_5	50.00	0.00	50.00	$\gamma\text{-Al}_2\text{O}_3$, Quartz
G		53.37	5.59	40.00	Mullite-type*†
H	close to $\text{Al}_8\text{Si}_2\text{B}_2\text{O}_{19}$	56.61	13.38	30.00	Mullite-type*†
I		60.00	20.00	20.00	Mullite-type*, Quartz
J	Boralsilite $\text{Al}_{16}\text{B}_6\text{Si}_2\text{O}_{37}$	61.54	23.08	15.38	Mullite-type, Quartz?
K		63.31	26.69	10.00	Mullite-type*, Quartz?
L	$\text{Al}_4\text{B}_2\text{O}_9$	66.67	33.33	0.00	$\text{Al}_4\text{B}_2\text{O}_9$ (Fischer et al. 2008b)

* from LeBail refinements starting with $a = 7.6 \text{ \AA}$, $b = 7.5 \text{ \AA}$, $c = 2.8 \text{ \AA}$ in space group $Pbam$

† very broad bump at $20^\circ 2\theta$ may fit $\gamma\text{-Al}_2\text{O}_3$

Tables 3.7 and 3.8 show a list of the precursor compositions and possible phase identification according to matching reflection positions of powder XRD data.

Samples prepared in the $\text{Al}_2\text{O}_3\text{-B}_2\text{O}_3\text{-SiO}_2$ system were not easy to identify by means of

Table 3.8: List of Al_2O_3 - B_2O_3 - SiO_2 sol-gel derived precursor synthesis experiments at 1250°C.

#	Theoretical stoichiometry	Al_2O_3 (mol-%)	B_2O_3 (mol-%)	SiO_2 (mol-%)	Phases (XRD)
A	Al_5BO_9	83.33	16.67	0.00	ABO-type ($Cmc2_1$)*, A
B		76.55	13.35	10.00	ABO-type ($Cmc2_1$)*, A
C		70.00	10.00	20.00	ABO-type ($Cmc2_1$)*, A
D	Boromullite $\text{Al}_9\text{Si}_2\text{BO}_{19}$	64.29	7.14	28.57	ABO-type ($Cmc2_1$)*, A
E		56.57	3.35	40.00	ABO-type ($Cmc2_1$)*, A
F	Sillimanite Al_2SiO_5	50.00	0.00	50.00	Mullite-type ($Pbam$)†, C, A
G		53.37	5.59	40.00	ABO-type ($Cmc2_1$)*, A
H	close to $\text{Al}_8\text{Si}_2\text{B}_2\text{O}_{19}$	56.61	13.38	30.00	ABO-type ($Cmc2_1$)*
I		60.00	20.00	20.00	ABO-type ($Cmc2_1$)*
J	Boralsilite $\text{Al}_{16}\text{B}_6\text{Si}_2\text{O}_{37}$	61.54	23.08	15.38	ABO-type ($Cmc2_1$)*
K		63.31	26.69	10.00	ABO-type ($Cmc2_1$)*
L	$\text{Al}_4\text{B}_2\text{O}_9$	66.67	33.33	0.00	ABO-type ($Cmc2_1$)*

A = α - Al_2O_3 , C = cristobalite (SiO_2)

* from LeBail refinements starting with $a = 5.67$ Å, $b = 15.01$ Å, $c = 7.68$ Å in space group $Cmc2_1$

† from LeBail refinements starting with $a = 7.6$ Å, $b = 7.5$ Å, $c = 2.8$ Å in space group $Pbam$

powder X-ray diffraction and Al, B and Si sites in mullite-type structures cannot be distinguished. Nevertheless, reasonable LeBail fits with a mullite-like unit cell ($a \approx 7.6$ Å, $b \approx 7.5$ Å, $c \approx 2.8$ Å in space group $Pbam$) were achieved in powder X-ray diffraction patterns of all 950°C samples except F and L. Sample F was almost amorphous, however, peaks may fit nanocrystalline γ - Al_2O_3 (Chakravorty 1993, Chakraborty and Das 2003, Gutierrez et al. 2002, Duoy 2005, Cividanis et al. 2010). According to Chakravorty (1993) and Chakraborty and Das (2003), this phase can also be interpreted as an Al-Si spinel phase. The powder pattern of sample L was in agreement with the structure of Fischer et al. (2008b).

All 1250°C samples except boron-free sample F could be indexed using a unit cell with similar lattice parameters as of ABO and boromullite (Buick et al. 2008) in space group $Cmc2_1$. Surprisingly, no excess SiO_2 was found, except in sample F, which was identified as a mixture of mullite, corundum and tetragonal cristobalite. The synthesis temperature of 1250°C is below the stability range of cristobalite. However, impure tetragonal has been observed at lower temperatures (Smallman and Bishop 1999).

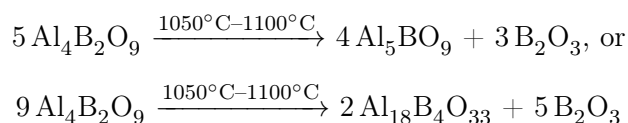
3.3 Discussion

Different types of synthesis routes yield ABO and $\text{Al}_4\text{B}_2\text{O}_9$ and the production of those materials is easy. It is, however, rather difficult to obtain single-crystals larger than ca. 100 μm . With respect to this, only two of the synthesis experiments were successful: Unreproducible run #01, yielding ABO single-crystals with a fair amount of Al_2O_3 -inclusions grown from $\text{K}_2\text{CO}_3 + 3\text{MoO}_3$ flux and run #62-2, yielding single-phase ABO crystals from presintered ABO in excess B_2O_3 as flux. It seems that T_{end} and the cooling gradient is crucial in synthesis experiments with $\text{K}_2\text{MoO}_3\text{O}_{10}$ as flux because the compound decays to several intermediate

phases (e.g. $K_2Mo_4O_{13}$, Leonyuk et al. 1980). The fact that ABO was presintered and the higher formation temperature in run #62 may be the reason that no excess corundum was found in this experiment. In any system different to Al_2O_3 - B_2O_3 - SiO_2 , products contained secondary phases, which could not be easily separated. Crystal size was very small.

All solid-state reaction experiments were successful and similar formation temperatures of $Al_4B_2O_9$ and ABO as known from literature were observed with in-situ high-temperature powder X-ray diffraction measurements. In stoichiometrically weighed precursor materials without excess boron, ABO crystallized together with excess Al_2O_3 . Obviously, lack of boron due to B_2O_3 evaporation at high temperature is the limiting factor for single-phase ABO formation from such precursors. Interestingly, experiments in sealed platinum capsules to avoid boron evaporation did not yield single-crystals suitable for XRD experiments as in Garsche et al. (1991). Nevertheless, from FWHM peak-widths of powder XRD patterns, a positive correlation of the size of coherently scattering domains ("crystallite size") and excess B_2O_3 in the starting mixture could be derived. This can have two reasons: Either, excess B_2O_3 lowers crystallization temperature of the phases, as shown by Duoy (2005) and Zhang et al. (2010), and thus larger crystallites grow, or excess B_2O_3 aids sintering of the ABO crystals. The latter argument may be supported with the observation that sintered tablets of samples produced with excess B_2O_3 were noticeably harder to grind, which is in agreement with findings of Sokolov and Gasparyan (2004).

All synthesis experiments performed with amorphous precursors obtained by the sol-gel route yielded ABO and/or $Al_4B_2O_9$. However, X-ray powder diffraction peak widths of the $Al_4B_2O_9$ phase at $1000^\circ C$ were noticeably broader than those of $Al_4B_2O_9$ produced from α - Al_2O_3 and B_2O_3 (FWHM of the $(20\bar{2})$ peak ca. $0.38^\circ 2\theta$ instead of ca. $0.28^\circ 2\theta$ at $1000^\circ C$), indicating that amorphous sol-gel precursors may not be the optimal starting materials for the production of crystalline $Al_4B_2O_9$. FWHM of ABO samples prepared by this route were comparable to those produced from solid-state reactions. This is not surprising as ABO is formed from the metastable intermediate $Al_4B_2O_9$ phase in both solid-state reaction and from sol-gel derived precursors according to the following equation:



Compared to the in-situ measured solid-state reaction synthesis experiment with Al_2O_3 and B_2O_3 as precursor, the crystallization temperature of $Al_4B_2O_9$ was slightly lower and the phase coexisted with ABO at $1100^\circ C$ for a short time ($< 2h$). This confirms the observation of Duoy (2005) that the temperature dependent stability field of $Al_4B_2O_9$ seems to be slightly extended when amorphous precursors are used.

Most samples in the system Al_2O_3 - B_2O_3 - SiO_2 yielded phases with only slightly different unit cell parameters than those of already known mullite-type phases in the systems Al_2O_3 -

B_2O_3 and $Al_2O_3-SiO_2$. From preliminary sample investigation with powder X-ray diffraction, no conclusions about Al, Si and/or B incorporation into the structures and hypothetical solid solutions can be made.

4 Crystal-Chemistry of Mullite-Type Aluminoborates $\text{Al}_{18}\text{B}_4\text{O}_{33}$ and Al_5BO_9 : A stoichiometry puzzle

Martin Fisch^{a,*}, Thomas Armbruster^a, Daniel Rentsch^b,
Eugen Libowotzky^c, Thomas Pettke^d

^a*Mineralogical Crystallography, Institute of Geological Sciences, University of Bern,
Freiestrasse 3, CH-3012 Bern, Switzerland*

^b*EMPA, Swiss Federal Laboratories for Materials Science and Research, Laboratory for
Functional Polymers, Überlandstrasse 129, CH-8600 Dübendorf, Switzerland*

^c*Institut für Mineralogie und Kristallographie, Universität Wien - Geozentrum,
Althanstrasse 14, A-1090 Wien, Austria*

^d*Rock-Water Interaction Group, Institute of Geological Sciences, University of Bern,
Baltzerstrasse 1+3, CH-3012 Bern, Switzerland*

*Corresponding author: fisch@krist.unibe.ch

Journal of Solid-State Chemistry 184 (2011) 70-80

4.1 Abstract

Orthorhombic Al_2O_3 -rich aluminoborate is an important ceramic material for which two slightly different compositions have been assumed: Al_5BO_9 ($5 Al_2O_3:B_2O_3$) and $Al_{18}B_4O_{33}$ ($9 Al_2O_3:2 B_2O_3$). The formula $Al_{18}B_4O_{33}$ ($= Al_{4.91}B_{1.09}O_9$) was derived from results of chemical analyses when crystal structure data were not yet available. Subsequent structural investigations indicated Al_5BO_9 composition. Nevertheless, $Al_{18}B_4O_{33}$ was still accepted as the correct stoichiometry assuming that additional B replaces 9% Al.

Powder samples of both compositions and ones with excess boron were prepared by solid-state reactions between α - Al_2O_3 and B_2O_3/H_3BO_3 at temperatures above $1100^\circ C$ and single-crystals were grown from flux at $1100^\circ C$ and $1550^\circ C$. Products were investigated by single-crystal and powder XRD, ^{11}B and ^{27}Al solid-state MAS-NMR, Raman and FTIR spectroscopy as well as Laser-ablation ICP-MS. No indication of the predicted 9% B \rightarrow Al substitution was found. LA ICP-MS indicated 12.36(27) wt.-% B_2O_3 corresponding to $Al_{4.97}B_{1.03}O_9$. Hence, the suggested $Al_{18}B_4O_{33}$ stoichiometry can be excluded for all synthesized samples. A very low amount of Al vacancies at a five-fold coordinated site are likely, charge balanced by an additional nearby three-fold coordinated B site. All evidence indicates that the title compound should be reported as $Al_{5-x}B_{1+x}O_9$ with $x < 0.038(6)$, which is close to Al_5BO_9 .

4.2 Introduction

Mullite used as ceramic raw material is an important and versatile compound in the system SiO_2 - Al_2O_3 . Its properties include high thermal stability, very low thermal expansion, low heat conductivity, high creep and corrosion resistance and high stiffness (Schneider and Komarneni 2005). The composition of mullite is rather variable: $Al_2(Al_{2+2x}Si_{2-2x})O_{10-x}$, $0.18 \leq x \leq 0.88$. However, the most common compositions are 3:2 mullite, $3 Al_2O_3:2 SiO_2$, $x = 0.25$ and 2:1 mullite, $2 Al_2O_3:SiO_2$, $x = 0.4$.

In the system SiO_2 - Al_2O_3 - B_2O_3 , Werding and Schreyer (1984) and Werding and Schreyer (1996) introduced the term "boron-mullite" for compounds within a compositional range between 3:2 and 2:1 mullite and two silicon-free aluminoborate members (Figure 4.1), Al_5BO_9 ($5 Al_2O_3:B_2O_3$) with a mullite-type structure (Sokolova et al. 1978) and $AlBO_3$ ($Al_2O_3:B_2O_3$) of calcite structure-type, stable under hydrothermal high-pressure conditions (Capponi et al. 1972, Vegas et al. 1977). More recently, the term mullite-type boron compound has been defined (Fischer and Schneider 2008a) for corresponding structures in the binary system Al_2O_3 - B_2O_3 whereas the name boromullite (Buick et al. 2008) is reserved for a mineral with sillimanite- and Al_5BO_9 -like modules. In addition, Al_3BO_6 (Capponi et al. 1972) with norbergite structure-type (White et al. 1965) was synthesized above 25 kbar and $800^\circ C$ and rhombohedral $Al_4B_6O_{15}$ with a microporous framework consisting of AlO_6 octahedra and BO_3 units has been produced from $AlCl_3$ and H_3BO_3 at $350^\circ C$ (Jing et al. 2004).

In the Al_2O_3 -rich part of the phase diagram, $Al_{18}B_4O_{33}$ ($9 Al_2O_3:2 B_2O_3$) is composition-

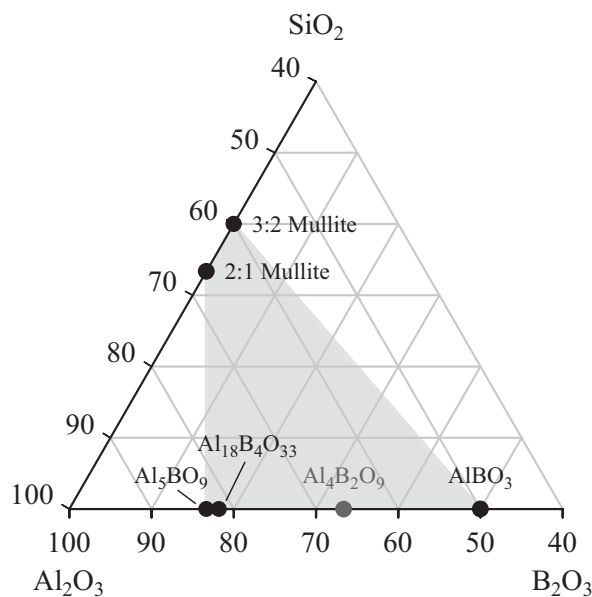


Figure 4.1: Al_2O_3 -rich part of the ternary system SiO_2 - Al_2O_3 - B_2O_3 . The boron-mullite stability field according to Werding and Schreyer (1984) and Werding and Schreyer (1996) is represented by the gray area. All units in mol-%.

ally very close to Al_5BO_9 ($5 \text{ Al}_2\text{O}_3:\text{B}_2\text{O}_3$). This material gained industrial interest because of mullite-like properties. Due to its low-cost production ($\frac{1}{10}$ to $\frac{1}{20}$ of the cost of SiC, Kim et al. 2004 and Song et al. 2007), its easy fabrication in large quantities (Zhang et al. 2006, Wang et al. 2008, Wada et al. 1991, Sokolov and Gasparyan 2004, Peng et al. 2006, Elssfah et al. 2007), its high strength (Ray 1992, Xinyong et al. 2007, Gatta et al. 2010), and its low thermal expansion and conductivity (Wada et al. 1993; 1994) the compound is used as reinforcer in metal matrix composites (Wang et al. 2008, Peng et al. 2006). Further applications include reinforcement in fire insulations for ships, construction components in nuclear reactors because of neutron absorbing capabilities, and in refractory linings due to high resistance against boron-rich glass melts (Garsche et al. 1991 and refs. therein). Recently, nanotubes have been synthesized (Ma et al. 2002, Li and Chang 2006) and aluminoborate fibers have been successfully coated by boron nitride to lower interface reactions and enhance strength between matrix and aluminoborate nanowires or whiskers (Song et al. 2007, Zhang et al. 2005, Fei et al. 2010).

Although the aluminoborate discussed above is of high importance, results of crystal-chemical investigations have remained inconsistent. This mullite-type boron compound is reported with two slightly different stoichiometries, $\text{Al}_{18}\text{B}_4\text{O}_{33} = \text{Al}_{4.91}\text{B}_{1.09}\text{O}_9 = 9 \text{ Al}_2\text{O}_3:2 \text{ B}_2\text{O}_3$ and $\text{Al}_5\text{BO}_9 = 5 \text{ Al}_2\text{O}_3:\text{B}_2\text{O}_3$ (Table 4.1), both crystallizing in the same mullite-type structure. There are no studies to date clarifying whether both similar compounds exist, probably because applications of this material were considered to be more important than its exact chemical characterization. Persistent assumption of $\text{Al}_{18}\text{B}_4\text{O}_{33}$ sto-

ichiometry may thus have complied with tradition as this compound was originally defined on early analytical data without considering the crystal structure.

Table 4.1: Theoretical composition of Al_5BO_9 and $Al_{18}B_4O_{33}$.

	$Al_2O_3:B_2O_3$	Al_2O_3 (wt.-%)	B_2O_3 (wt.-%)	Al_2O_3 (mol.-%)	B_2O_3 (mol.-%)
Al_5BO_9	5:1	87.99	12.01	83.33	16.66
$Al_{18}B_4O_{33}$	9:2	86.83	13.17	81.81	18.18

$Al_{18}B_4O_{33}$ and Al_5BO_9 contain only trivalent cations, though of different radius. Al^{3+} and B^{3+} may both occur in four-fold coordination. Therefore, both Al and B may exist as a solid solution at a tetrahedrally coordinated site of a mullite-type structure. On the other hand, Al-O distances in an AlO_4 tetrahedron are ca. 1.75 Å (Kunz and Armbruster 1990) whereas B-O distances are ca. 1.476 Å (Hawthorne et al. 1996). This bond length difference of ca. 15% seems to contradict an extensive solid solution. Furthermore, it could be expected that the degree of this substitution is temperature dependent. The aim of this study is an investigation of aluminoborate samples, produced above 1100°C by different synthesis routes with a compositional range allowing formation of $Al_{18}B_4O_{33}$ and/or Al_5BO_9 . Using single-crystal and powder X-ray diffraction, solid-state ^{11}B and ^{27}Al MAS-NMR, FTIR, Raman spectroscopy and Laser-ablation ICP-MS compositional measurements, the composition of this important compound will be clarified.

4.3 Historical Background

In the late 19th century, Mallard (1887) studied needle-like, faceted crystals with orthorhombic symmetry of supposed $3Al_2O_3:B_2O_3$ composition, synthesized by Ebelmen (1851). Until then, the only known aluminoborate was the mineral jeremejevite, $Al_6(BO_3)_5(F,OH)_3$ (Mallard 1887, Websky 1883). Benner and Baumann (1938) patented synthesis of an aluminoborate starting from molten Al_2O_3 and B_2O_3 . These acicular, orthorhombic crystals were assumed to have $3Al_2O_3:B_2O_3$ composition. Mullite-like physical properties qualified this aluminoborate as a new ceramic raw material. Cell dimensions (Table 4.2) derived from powder X-ray diffraction were presented by Baumann and Moore (1942). From the density of 2.93 g/cm³, they concluded that the correct formula of the crystals is $9Al_2O_3:2B_2O_3$ ($Al_{18}B_4O_{33}$), with a unit cell content of $Z = 1.1$. Dietzel and Scholze (1955) studied glasses in the system $SiO_2-Al_2O_3-B_2O_3$. From analyses of crystalline by-products they proposed a solid solution between 3:2 mullite and $Al_{18}B_4O_{33}$. Subsequent experiments in the system $Al_2O_3-B_2O_3$ (Scholze 1956) indicated a new mullite-type phase of $2Al_2O_3:B_2O_3$ ($Al_4B_2O_9$) composition (Mazza et al. 1992, Fischer et al. 2008b) obtained by heating Al_2O_3 in a B_2O_3 flux at 1000°C. According to the $Al_2O_3-B_2O_3$ phase diagram, $Al_4B_2O_9$ transforms to $Al_{18}B_4O_{33}$ at 1035°C (Scholze 1956, Gielisse and Forster 1962). Sokolova et al. (1978) grew aluminoborate single-crystals by cooling an $Al_2O_3-B_2O_3-Y_2O_3-K_2O-MoO_3$ melt from 1150°C to 950°C. Cell dimension and

orthorhombic symmetry were in accordance with previous findings for $\text{Al}_{18}\text{B}_4\text{O}_{33}$. However, single-crystal X-ray structure refinement yielded Al_5BO_9 composition with $Z = 4$ instead of $\text{Al}_{18}\text{B}_4\text{O}_{33}$ (Table 4.2). The structure was described with one AlO_6 octahedron, three AlO_4 tetrahedra and one planar BO_3 group. Results of unspecified chemical analyses yielded 14 wt.-% B_2O_3 (no esd's given), which is closer to $\text{Al}_{18}\text{B}_4\text{O}_{33}$ than to Al_5BO_9 (Table 4.1). Single-crystals grown in the system $\text{CaO-Al}_2\text{O}_3\text{-B}_2\text{O}_3$ were also studied by Ihara et al. (1980). Results of gravimetric analyses agreed with $\text{Al}_{18}\text{B}_4\text{O}_{33}$, $Z = 1.09$ (Table 4.2), but the structural data were in agreement with those of Sokolova et al. (1978). They concluded that two of the Al-tetrahedra specified by Sokolova et al. (1978) are more precisely characterized as five-fold coordinated $\text{Al}^{(\text{V})}$ polyhedra. The discrepancy between the crystallographically derived composition of Al_5BO_9 and the chemical composition pointing to $\text{Al}_{18}\text{B}_4\text{O}_{33}$ was explained with a disordered structure in which $\frac{1}{11} \approx 9\%$ of $\text{Al}^{(\text{IV})}$ is substituted by tetrahedrally coordinated $\text{B}^{(\text{IV})}$.

Garsche et al. (1991) produced single-crystals by fusion of Al_2O_3 and B_2O_3 in sealed platinum capsules at 1500°C . X-ray powder and single-crystal diffraction data (Table 4.2) are in agreement with findings of Sokolova et al. (1978) and Ihara et al. (1980). Without further investigations, the compound was reported as $\text{Al}_{18}\text{B}_4\text{O}_{33}$, based on the tetrahedral B substitution proposed by Ihara et al. (1980).

The Al-coordination in " $\text{Al}_{18}\text{B}_4\text{O}_{33}$ " has also been investigated by ^{27}Al MAS-NMR (Massiot et al. 1995, Gan et al. 2002, Hung et al. 2006) on samples produced according to Garsche et al. (1991). One $\text{Al}^{(\text{IV})}$, two distinct $\text{Al}^{(\text{V})}$ and one $\text{Al}^{(\text{VI})}$ site were assigned with multiplicities of 1:1:1:2 in accordance with previous crystal structure data (Sokolova et al. 1978, Garsche et al. 1991, Ihara et al. 1980).

Mazza et al. (1992) synthesized crystalline products from an amorphous precursor of H_3BO_3 and $\text{Al}(\text{NO}_3)_3 \cdot 9\text{H}_2\text{O}$ and proposed a solid solution $\text{Al}_{6-x}\text{B}_x\text{O}_9$ with $1 \leq x \leq 3$. The structures were solved using a pseudotetragonal mullite model in space group $Pbam$ (Table 4.2). FTIR spectra of a member with $x = 1$ showed no evidence of $\text{B}^{(\text{IV})}$, which was later also confirmed by ^{11}B MAS-NMR (MacKenzie et al. 2007). Mazza et al. (1992) consider Al_5BO_9 as being stable in the temperature regime between 900°C and 1000°C , leading to $\text{Al}_{18}\text{B}_4\text{O}_{33}$ with space group $Cmc2_1$ upon heating at higher temperature.

4.4 Experimental

4.4.1 Sample Preparation

Using stoichiometric mixtures and mixtures containing excess boron to exclude B_2O_3 as the limiting factor for $\text{Al}_{18}\text{B}_4\text{O}_{33}$ formation (due to boron evaporation at high temperature), starting materials were prepared in order to allow formation of $\text{Al}_{18}\text{B}_4\text{O}_{33}$ and/or Al_5BO_9 . All syntheses were performed in lid-covered platinum crucibles in air. Three different synthesis routes were followed: (1) Powder samples *b*, *c* and *e* were prepared by solid-state reactions

Table 4.2: Theoretical composition of Al_5BO_9 and $Al_{18}B_4O_{33}$.

	Baumann and al. (1942)	Dietzel and Scholze (1955)	Scholze (1956)	Sokolova et al. (1978)	Ihara et al. (1980)	Garsche et al. (1991)	Mazza et al. (1992)
<i>a</i> -axis	15.0	5.68(5)	5.6673(7)	5.682(13)	7.6942(1)	7.621	
<i>b</i> -axis	7.5	14.98(10)	15.011(2)	14.973(34)	15.0110(2)	7.621	
<i>c</i> -axis	5.67	7.68(5)	7.693(1)	7.692(17)	5.6689(1)	2.833	
Volume			654.4(2)		654.74		
Z	1.1	1.09	4	1.09	1.09	1.09	1.0
Space group	Orthorhombic	<i>Cmc2₁</i> , <i>C2cm</i> , <i>Cmcm</i>	<i>Cmc2₁</i>	<i>Cmc2₁</i>	<i>A2₁am</i>	<i>Pbam</i>	
Density (g/cm ³)	2.93	2.94(1)	2.96	2.93(1)			
Assigned formula	$Al_{18}B_4O_{33}$	$Al_{18}B_4O_{33}$	$Al_{18}B_4O_{33}$	Al_5BO_9	$Al_{18}B_4O_{33}$	$Al_{18}B_4O_{33}$	Al_5BO_9
B_2O_3 (wt.-%)	13.2	13.3	14	13.1			
Al_2O_3 (wt.-%)	86.6	86.7	86	86.9			
Stoichiometry	$Al_{18}B_4O_{33}$	$Al_{17.96}B_{4.04}O_{33}$	$Al_{17.77}B_{4.23}O_{33}$	$Al_{18.02}B_{3.98}O_{33}$			
from wt.-%	$Al_{4.91}B_{1.09}O_9$ ^a	$Al_{4.90}B_{1.10}O_9$ ^a	$Al_{4.85}B_{1.15}O_9$ ^a	$Al_{4.91}B_{1.09}O_9$ ^a			

^anormalized to 9 oxygen

of α -Al₂O₃ with B₂O₃ or H₃BO₃. The powders were thoroughly mixed, pressed to pellets and subsequently heated at 1100°C or 1200°C. (2) Powder sample *d* was produced from an amorphous precursor prepared with Al(NO₃)₃ · 9H₂O and H₃BO₃, according to Fischer et al. (2008b). The denitrified raw material was heated at 1100°C. (3) Single-crystals were grown from a mixture of 9Al₂O₃:2B₂O₃ in a K₂CO₃ + 3MoO₃ flux (borate/flux ratio ca. 1:9) by cooling the melt at 10°C/h from 1100°C to 600°C (sample *a*) and from a pressed pellet (previously heated at 1200°C) consisting of Al₂O₃:3.3H₃BO₃ in B₂O₃ flux by slow cooling (15°C/h) from 1550°C to 1250°C (sample *f*). Fluxes were dissolved in hot deionized H₂O. Prior to further investigations, samples were washed in warm deionized H₂O to eliminate any remaining H₃BO₃ or B₂O₃. Details on samples and synthesis conditions are given in Table 4.3.

Both K₂CO₃ + 3MoO₃ and H₃BO₃ flux methods yielded elongated single-crystals with different habits. Radially grown crystals from sample *a* were of elongate prismatic shape with a rather smooth surface but with Al₂O₃ inclusions. No inclusions were found in crystals from sample *f*, but they had a rather rough and flaky surface (Figure 4.2). A sample of Al₄B₂O₉ (Mazza et al. 1992, Fischer et al. 2008b) was prepared according to Fischer et al. (2008b) and used as reference compound for tetrahedrally coordinated B^(IV) in FTIR, Raman and ¹¹B MAS-NMR spectroscopy.

Table 4.3: Starting materials, synthesis conditions and analytical methods used for sample characterization.

Sample	Al ₂ O ₃ :B ₂ O ₃	Starting materials	Temperature
<i>a</i>	9:2	Al ₂ O ₃ , B ₂ O ₃ in K ₂ CO ₃ + 3MoO ₃ flux	1100°C → 600°C
<i>b</i>	9:2	Al ₂ O ₃ , B ₂ O ₃	1200°C for 10h
<i>c</i>	5:1	Al ₂ O ₃ , B ₂ O ₃	1200°C for 10h
<i>d</i>	1:2	Al(NO ₃) ₃ · 9H ₂ O, H ₃ BO ₃	1100°C for 5h
<i>e</i>	1.2:2	Al ₂ O ₃ , H ₃ BO ₃	1200°C for 44h
<i>f</i>	1:3.3	Al ₂ O ₃ , H ₃ BO ₃ in B ₂ O ₃ flux	1550°C → 1250°C

Sample	Product	Analyzed with
<i>a</i>	Single-crystals	Single-crystal and powder XRD, MAS-NMR, LA ICP-MS
<i>b</i>	Powder	Powder XRD, MAS-NMR
<i>c</i>	Powder	Powder XRD, MAS-NMR
<i>d</i>	Powder	Powder XRD, MAS-NMR
<i>e</i>	Powder	Powder XRD, MAS-NMR, Raman, FTIR
<i>f</i>	Single-crystals	Single-crystal and powder XRD, MAS-NMR, LA ICP-MS

4.4.2 X-ray Diffraction

A full intensity dataset was measured with an Enraf Nonius CAD4 diffractometer on a single-crystal of sample *a* (Table 4.4). Lattice parameters were determined from 24 reflections centered at four high-angular settings with $\pm 37.9^\circ < \theta < \pm 44.4^\circ$ in order to reduce crystal and beam alignment errors. After correcting the data for Lorentz-polarization and absorption ef-

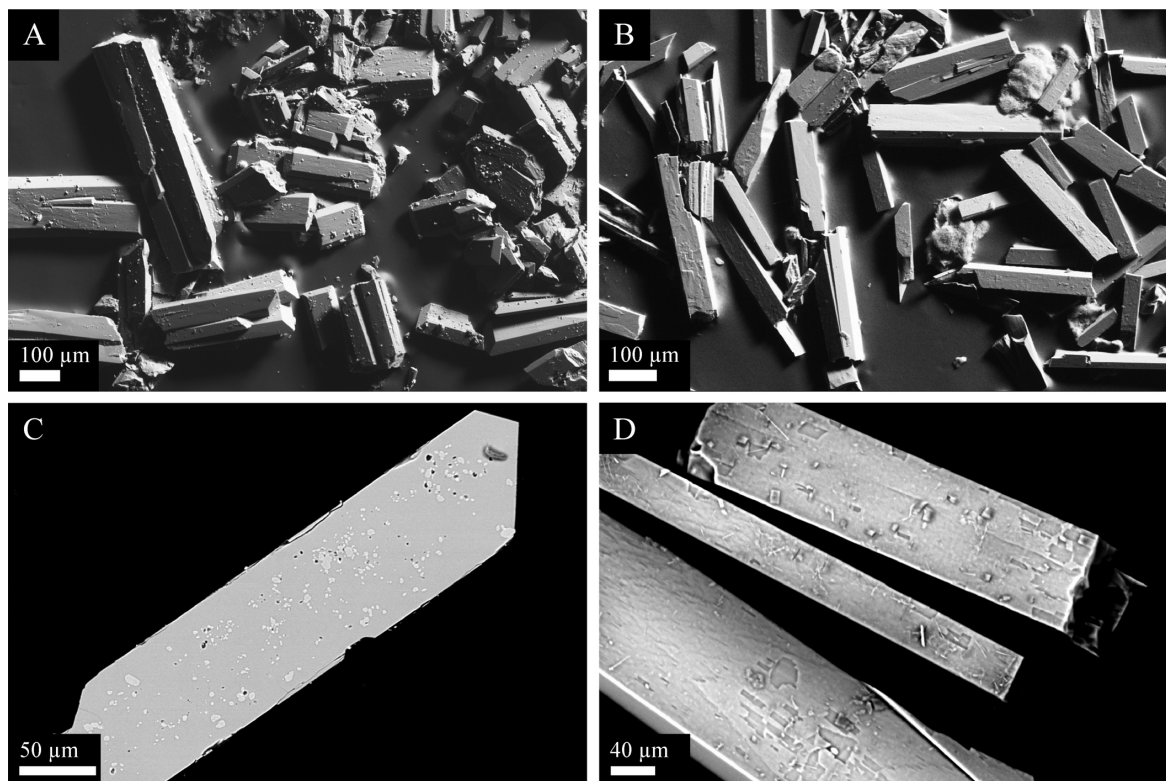


Figure 4.2: SEM image of samples *a* and *f*: (A) secondary electron (SE) picture of sample *a* showing the prismatic habit of the crystals. (B) SE picture showing the elongated prismatic crystals from sample *f*. (C) Backscattered electron (BSE) image of Al_2O_3 inclusions as bright dots in a polished crystal of sample *a*. (D) BSE image showing the rough and flaky surface of crystals from sample *f*.

fects with WinGX v. 1.80.05 software package (Farrugia 1999), the structure was solved by direct methods and refined with Bruker ShelXTL v. 6.10 (Bruker-AXS 2000) using neutral atomic scattering factors in space group $Cmc2_1$ (no. 36) with $Z = 4$. The Flack parameter (Flack 1983) of 0.43(10) indicated 1:1 merohedral twinning of the selected crystal.

Due to its significantly smaller size, a full intensity dataset of a crystal from sample *f* was collected with a Bruker Smart Apex2 CCD diffractometer (Table 4.4). Subsequently 15 reflections centered at four angular settings with $\pm 11.0^\circ < \theta < \pm 30.0^\circ$ were measured with the CAD4 for direct comparison of lattice parameters with those of sample *a*. CCD data were integrated and empirically absorption-corrected using Apex2 v. 2009-11.0 software package (Bruker-AXS 2009). The structure was refined with Bruker ShelXTL v. 6.10 (Bruker-AXS 2000) using the structural model obtained from sample *a*. A Flack parameter of 0.60(11) indicated 1:1 merohedral twinning of the crystal. Single-crystal data collection parameters are reported in Table 4.4.

XRD powder patterns were measured with a PANalytical X'Pert MPD diffractometer equipped with a Cu X-ray source (40kV/40mA) and an X'Celerator detector. Automatic divergence slits and 0.02 radian soller slits were used. Patterns were collected from 10° to

Table 4.4: Starting materials, synthesis conditions and analytical methods used for sample characterization.

	Sample <i>a</i>	Sample <i>f</i>
Measurement type	Full intensity dataset	Full intensity dataset
Diffractometer	Enraf Nonius CAD4	Bruker Smart Apex2 CCD
X-ray radiation	MoK α	MoK α
X-ray power	50 kV, 40mA	50 kV, 40 mA
Crystal size	0.2 x 0.13 x 0.05 mm ³	0.15 x 0.025 x 0.05 mm ³
Measurement time	Max. 120 s/step	60 sec/frame
Temperature (°C)	25	25
Space group	<i>Cmc</i> 2 ₁	<i>Cmc</i> 2 ₁
<i>a</i> -axis (Å)	5.6686(2)	5.6618(7) ^a
<i>b</i> -axis (Å)	15.0060(9)	14.9981(12) ^a
<i>c</i> -axis (Å)	7.6892(4)	7.6806(7) ^a
Volume (Å ³)	654.07(6)	652.21(12) ^a
<i>Z</i>	4	4
ρ (g/cm ³)	2.942	2.950
Reflections collected	4294	5915
Max. 2 θ (°)	69.93	69.94
Index range <i>h</i>	-9 ... 9	-9 ... 9
Index range <i>k</i>	-24 ... 24	-24 ... 23
Index range <i>l</i>	-12 ... 12	-12 ... 11
Resolution range (Å)	1 ... 0.6	1 ... 0.62
Unique reflections	1166	1130
Reflections > 4 σ (<i>I</i>)	1045	1088
<i>R</i> (int)	0.0510	0.0399
<i>R</i> (σ)	0.0375	0.0294
L. S. parameters	83	83
GoF	0.990	1.046
<i>R</i> 1, <i>I</i> > 4 σ (<i>I</i>)	0.0173	0.0186
<i>R</i> 1, all data	0.0273	0.0199
w <i>R</i> 2 on <i>F</i> ²	0.0295	0.0370
$\Delta\rho_{\max}$, close to	-0.21 e ⁻ ·Å ⁻³ , O1	-0.24 e ⁻ ·Å ⁻³ , Al1
$\Delta\rho_{\max}$, close to	0.24 e ⁻ ·Å ⁻³ , B1	0.24 e ⁻ ·Å ⁻³ , Al2

^alattice parameters from measurement with CAD4 diffractometer

80° 2 θ with a step size of 0.002° 2 θ /step at 100 s/step. Lattice parameters were derived from Pawley refinements to precisely extract peak maxima by treating the data independently from the structural model. Excess Al₂O₃ (if present) was quantified by Rietveld refinements. It was not possible to estimate the amount of excess B₂O₃ or H₃BO₃ prior to the final washing step due to fast hydration of B₂O₃, resulting in a poorly crystalline mix of B₂O₃ and H₃BO₃. All powder XRD data were handled with Topas-Academic v.4.1 (Coelho 2007a) using the fundamental parameter approach for peak-shape modeling.

4.4.3 Solid-State ¹¹B and ²⁷Al MAS-NMR

¹¹B and ²⁷Al MAS-NMR spectra were recorded on a Bruker Avance 400 NMR spectrometer (9.4 T) using a 2.5 mm CP/MAS probe. The ¹¹B and ²⁷Al MAS-NMR spectra were recorded

at 128.38 MHz and 104.26 MHz, respectively using the following parameters: $0.3 \mu\text{s}$ $\pi/6$ pulse widths, 25 kHz MAS rate, 3 s (0.2 s for ^{27}Al) relaxation delays, appropriate number of scans for reasonable signal to noise ratios and 77 kHz SPINAL-64 proton decoupling (Fung et al. 2000). ^{11}B and ^{27}Al chemical shifts were referenced to external samples of 1 M aqueous H_3BO_3 at 19.6 ppm (Kroeker and Stebbins 2001) and 1.1 M $\text{Al}(\text{NO}_3)_3$ solution at 0.0 ppm (Harris et al. 2001). The observed ^{27}Al NMR line shape was exactly the same when no proton decoupling was applied, whereas the ^{11}B quadrupolar powder pattern of e.g. H_3BO_3 subtly depended on the efficiency of the decoupling field (Klochko et al. 2009). Owing to the presence of boron nitride devices in the probe, a ≈ 16 kHz broad, asymmetric background signal was present in the ^{11}B NMR spectra. Before further analysis of these spectra, the background signal recorded with an empty spinner was subtracted from the spectrum of interest. Quadrupolar parameters and the relative amounts of $\text{B}^{(\text{III})}$ and/or $\text{B}^{(\text{IV})}$ atoms were determined by non-linear least-square fits of the regions of interest using the software Dmfit v. 20080716 (Massiot et al. 2002). For H_3BO_3 , the parameters $C_q = 2.51$ MHz, $\delta_{\text{iso}} = 19.7$ ppm and $\eta = 0.04$ were in good accordance with literature data (Klochko et al. 2009). For resonances originating from single components only, the parameters for amplitude, position, quadrupolar coupling constant, asymmetry parameter and the zero order base line were automatically and independently optimized by the fit routine. In the case where $\text{B}^{(\text{III})}$ and $\text{B}^{(\text{IV})}$ resonances were observed simultaneously ($\text{Al}_4\text{B}_2\text{O}_9$, Mazza et al. 1992 and Fischer et al. 2008b), the asymmetry parameter was kept constant for the trigonal $\text{B}^{(\text{III})}$ site and a Gaussian shape was chosen for tetrahedrally coordinated $\text{B}^{(\text{IV})}$ in order to compare results to those of Fischer et al. (2008b). ^{27}Al NMR parameters (δ_{iso} , C_q , η) were determined from slices of a z-filtered MQ-MAS-NMR spectrum and the 1D NMR spectra were subsequently simulated keeping the preliminary evaluated parameters C_q and η constant, while the parameters for amplitude, chemical shift and zero order base line were optimized.

4.4.4 FTIR and Raman Spectroscopy

FTIR and Raman spectra were collected for sample *e* and $\text{Al}_4\text{B}_2\text{O}_9$ as reference for tetrahedrally coordinated BO_4 . IR powder spectra were acquired from 300 cm^{-1} to 4000 cm^{-1} on a Bruker Tensor 27 FTIR spectrometer equipped with a global MIR light source, a KBr beam splitter, and a DLaTGS detector. Sample and background spectra were averaged from 100 scans at 4 cm^{-1} resolution. Two methods were used to obtain absorption spectra: (1) The finely ground sample was dispersed in KBr ($\approx 1:200$), pressed to transparent pellets, and measured in transmission mode in the usual sample compartment. (2) The undiluted sample powder was pressed on the diamond window of a Harrick MVP 2 diamond ATR accessory. Background spectra were obtained from a pure KBr pellet and from the empty ATR unit. Data handling was performed with OPUS v. 5.5 software (Bruker Optik GmbH 2005).

Powder Raman spectra were obtained from 70 cm^{-1} to 1670 cm^{-1} on a confocal edge filter-based Renishaw RM1000 micro-Raman system equipped with a 17 mW HeNe-laser (632.8 nm

excitation) and a 50 mW multimode Ar⁺-laser (488 nm and 514.5 nm excitation, each ≈ 20 mW), a 1200 lines/mm grating, using a thermo-electrically cooled CCD detector. Raman intensities were collected with a Leica DMLM microscope with a 50x/0.85 n.a. objective. Excitation at 488 nm and 10 min acquisition time yielded Raman spectra with reasonable signal to noise ratio at a resolution of 5–6 cm⁻¹. Data was processed with Grams32 software v. 4.14 (Galactic Industries Corp. 1996).

4.4.5 Laser-Ablation ICP-MS

Al₂O₃ and B₂O₃ wt.-% were measured in-situ on epoxy-embedded single-crystals from samples *a* and *f* (Table 4.3) by laser-ablation inductively-coupled-plasma mass-spectrometry (LA ICP-MS). The system consists of a pulsed 193 nm ArF Excimer laser Geolas Pro system (Lambda Physik, Germany) coupled with a Perkin Elmer ELAN DRCE quadrupole mass spectrometer. Details on the setup and optimization strategies to minimize matrix effects by setting up robust plasma conditions can be found in Pettke (2008).

Al₂O₃ inclusion-free crystal domains in sample *a* were usually smaller than 50 μm ; Hence, the beam diameter for analysis was set to 32 μm . To minimize matrix-load induced elemental fractionation (Kroslakova and Günther 2007), ablation rate tests were performed at 6 J/cm² energy density on the sample with a 10 Hz pulse rate, revealing a much higher ablation rate for NIST SRM 610 used for calibration than for the aluminoborate crystals. Calibration shots were thus made with 16 μm beam size, resulting in near-equal aerosol masses ablated per unit time. Only 10 s signals were used for quantification, to ensure a crater aspect (depth/diameter) ratio < 1. The aerosol was transported to the ICP-MS using mixed He-Ar gas. For samples *a* and *f*, a total of 11 and 12 individual spot analyses were acquired, respectively. Data quantification was done using SILLIS v. 1.2.0 (Guillong et al. 2008), employing 356 ± 7 $\mu\text{g/g}$ for B (Pearce et al. 1997) and 2.04 wt.-% Al₂O₃. Internal standardization was carried out by summing B₂O₃ and Al₂O₃ to 100 wt.-%.

4.5 Results

4.5.1 X-ray Diffraction

Single-crystal X-ray (CAD4) refined cell dimensions of sample *a* yielded $V = 654.07(6)$ \AA^3 whereas corresponding parameters (CAD4) for sample *f* were significantly smaller: $V = 652.21(12)$ \AA^3 (Table 4.4).

Three refinement strategies were followed for both crystals *a* and *f*: (1) The structures were refined with all positions fully occupied. (2) The occupancy of the Al4 tetrahedron was fixed at 9% B \rightarrow Al substitution according to the suggestion of Ihara et al. (1980), and (3) a mixed Al, B population was refined at each Al site in separate refinements. In strategy (3), intensity data were restricted to $0.6 \text{\AA} \leq \lambda/(2 \cdot \sin\theta) \leq 1 \text{\AA}$ (high-angle data) in order to reduce contributions from bonding electrons. X-ray diffraction data containing bonding

electron information are not properly modeled in standard site-occupancy refinements and lead to incorrect occupancy fractions (Armbruster et al. 1990).

After refinement in accordance with model (1), atomic displacement parameters ($U_{eq.}$) were very similar for all Al sites except for Al2. $U_{eq.}$ of Al2 was about 12% higher than the average of the remaining three.

Strategy (2) led to increased least squares agreement factors compared to (1) and most important, the atomic displacement parameter of the tetrahedrally coordinated Al4 site decreased to ca. 50% of the value refined in strategy (1).

Strategy (3) resulted in fully occupied Al-polyhedra, except for Al2. This type of population refinement has to be performed stepwise for each Al site to reduce correlations with the scale factor. Due to correlations between displacement parameters and occupancy, vacancies at the Al2 site were also refined with an isotropic displacement parameter of Al2 constrained to the one of Al3. No significant difference in vacancy concentration was observed, thus, we chose to refine all displacement parameters individually. For Al2, final occupancies were Al:B = 0.973(5):0.027(5) for sample *a* and Al:B = 0.962(6):0.038(6) for sample *f*. As an alternative approach, Al vacancies were refined at the Al2 site, resulting in 2.1(4)% vacancies for sample *a* and 3.2(4)% for sample *f*. All refinements of strategy (3) reduced the originally (according to strategy (1)) enlarged atomic displacement factor $U_{eq.}$ of Al2 to values similar to the ones of other Al sites within the same structure.

Atomic coordinates, isotropic and anisotropic displacement parameters of the vacancy model (strategy 3) for samples *a* and *f* and calculated bond valences of sample *a* are listed in Appendix A.1.

The main features of the structure (Figure 4.3) are isolated mullite-like chains of edge-sharing Al1-octahedra running parallel to the *a*-axis. Compared to mullite, the cell is doubled along [100] and [010] resulting in an additional symmetry equivalent octahedral chain at $b/2$. Proximate octahedral chains are connected by pairs of irregular edge-sharing AlO_5 polyhedra (Al2 and Al3) and, additionally, by alternating AlO_4 tetrahedra (Al4) and BO_3 triangles (B1). One side of an edge-connected AlO_5 polyhedra pair is edge-connected to octahedra and corner-linked to BO_3 triangles, whereas the other side is edge-connected to octahedra and corner-linked to tetrahedra. As a result, octahedral chains are separated along [010] by two different alternating segments within (101). One segment comprises AlO_4 and AlO_5 polyhedra (segment 1, Figure 4.3); The other consists of BO_3 and AlO_5 polyhedra (segment 2). The Al1 octahedron, the tetrahedron and the BO_3 triangle are rather regular: $\Delta(Al1-O)_{max} = 0.0553 \text{ \AA}$, $\Delta(Al4-O)_{max} = 0.0250 \text{ \AA}$ and $\Delta(B1-O)_{max} = 0.0138 \text{ \AA}$, whereas the AlO_5 polyhedra are fairly distorted with $\Delta(Al2-O)_{max} = 0.2966 \text{ \AA}$, and $\Delta(Al3-O)_{max} = 0.3692 \text{ \AA}$ (Appendix A.1). The AlO_5 polyhedra are more precisely described as AlO_{4+1} , as Al occupies the center of the four closest O ligands, which is also responsible for the increased distortion.

After preferred-orientation corrections in XRD Rietveld refinements, all patterns from samples *a-f* were matching the Al_5BO_9 structure, differing only in the amount of excess corun-

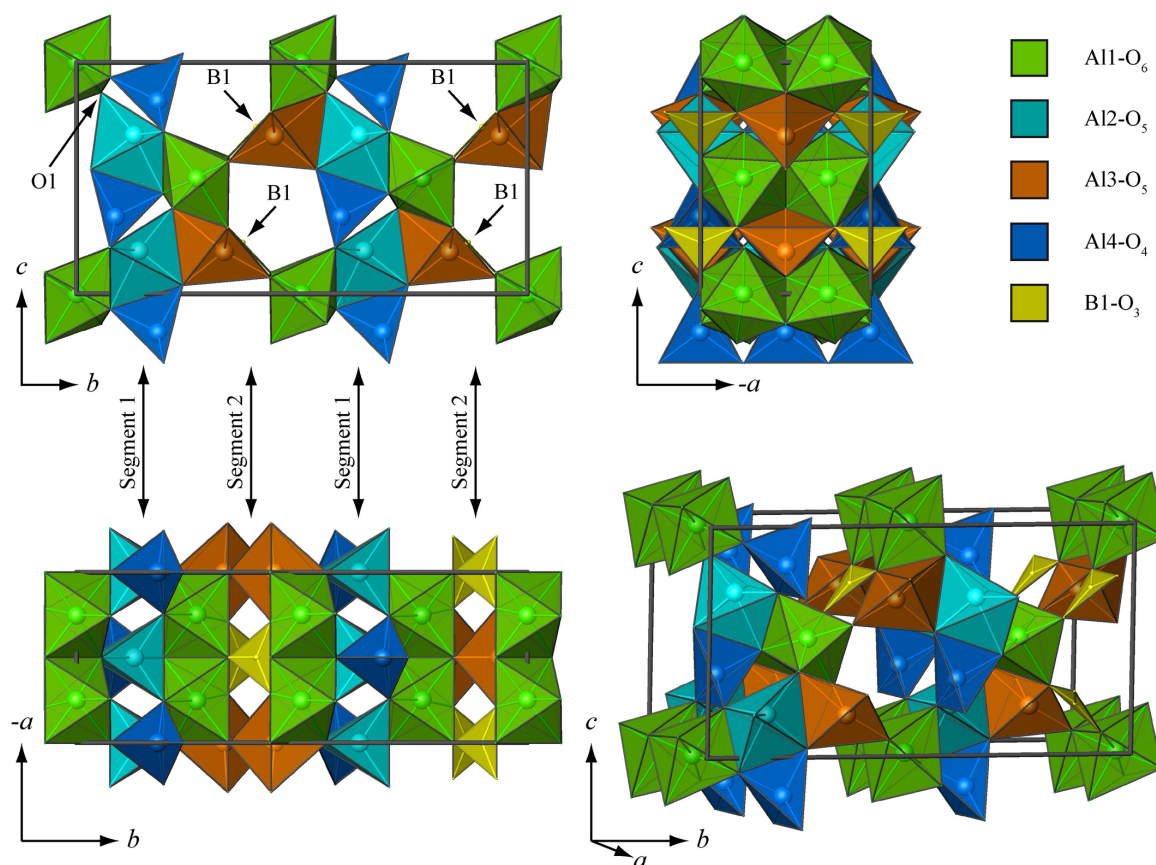


Figure 4.3: Structural drawing of an Al_5BO_9 unit cell projected along the a -axis (top left), the b -axis (top right), the c -axis (bottom left) and in an arbitrary view (bottom right). Segments dividing the mullite-like AlO_6 chains are indicated with arrows: Segment 1 consists of Al2-O_5 polyhedra and Al4-O_4 tetrahedra, whereas segment 2 contains Al3-O_5 polyhedra and B1-O_3 triangles. Note that Al2 and Al3 atoms are not in the center of the polyhedron. For better illustration of the similarity to the mullite structure, the unit cell has been shifted by 0, 0.1164, 0.5.

dum. Pawley-refinement-derived lattice parameters of all samples are shown in Table 4.5. They are the same within a maximum deviation of 6 esd's, except for the significantly smaller values of sample f , confirming our previous single-crystal results. Excess corundum was only found in samples a – c (Table 4.3) whereas no corundum was found in samples d – f , prepared with excess $\text{B}_2\text{O}_3/\text{H}_3\text{BO}_3$ in the starting mixtures (Table 4.5).

4.5.2 Solid-State ^{11}B and ^{27}Al MAS-NMR

In the ^{11}B MAS-NMR spectrum of $\text{Al}_4\text{B}_2\text{O}_9$, which was collected as a reference, signals of highly symmetric four-fold coordinated $\text{B}^{(\text{IV})}$ and second-order quadrupolar broadened planar three-fold coordinated $\text{B}^{(\text{III})}$ were observed at distinct positions (Figure 4.4). The ratio of $\approx 25:75$ determined by line shape analysis for the $\text{B}^{(\text{IV})}/\text{B}^{(\text{III})}$ sites fits reasonably to the value of $\approx 20:80$ estimated by Fischer et al. (2008b). Nevertheless, accurate quantitative results can

Table 4.5: Lattice parameters and excess Al_2O_3 content of all samples determined by powder X-ray diffraction. For better comparison, lattice parameters obtained from single-crystal XRD are given in the two bottom rows.

Sample	a (Å)	b (Å)	c (Å)	V (Å ³)	GoF	Al_2O_3 (wt.-%)
a	5.66848(4)	15.00512(12)	7.68971(5)	654.057(8)	1.04	8
b	5.66738(3)	15.00687(10)	7.69230(4)	654.225(7)	1.52	7
c	5.66789(4)	15.00604(14)	7.69157(6)	654.188(9)	1.47	8
d	5.66775(3)	15.00642(6)	7.68943(3)	654.006(5)	1.60	0
e	5.66869(2)	15.00741(7)	7.69005(3)	654.211(5)	1.47	0
f	5.66421(3)	15.00214(7)	7.68428(3)	652.974(5)	1.83	0
a^a	5.6686(2)	15.0060(9)	7.6892(4)	654.07(6)	n/a	n/a
f^a	5.6618(7)	14.9981(12)	7.6806(7)	652.21(12)	n/a	n/a

^alattice parameters from single-crystal XRD for comparison

only be evaluated including the signal intensities of spinning sidebands.

The ¹¹B MAS-NMR spectra of samples a – f showed the same shapes of resonances (Figure 4.4). Chemical shifts and quadrupolar parameters obtained by line shape analysis (Table 4.6) yielded convergent results for all synthesis routes (Table 4.3). The influence of a simulated B^(IV) signal on the expected experimental line shape of sample a is shown in Figure 4.5. For fractions as low as 2–3% of B^(IV), a distinct deviation of the quadrupolar broadened line shape of the spectra can be observed. As shown in Figure 4.4, none of the measured ¹¹B MAS-NMR spectra suggest evidence for B^(IV).

²⁷Al MAS-NMR spectra of samples a – f match each other (Figure 4.6), only the amount of excess corundum varies, depending on synthesis conditions. In the ²⁷Al 3Q-MAS-NMR spectrum of sample a (Appendix A.1) at least three distinct aluminum species were observed and from chemical shift arguments Al^(IV), Al^(V) and Al^(VI) are present. The spectrum showed the same resonances already observed by Gan et al. (2002), recorded at the same magnetic field. Since they also collected MQ-MAS data at higher frequencies, it is evident that two different Al^(V) sites are present. DOR NMR diffusion experiments (Hung et al. 2006) allowed assignment of the Al^(V) signals to Al^(V)₁ (Al2 in this study) and Al^(V)₂ (Al3 in this study). All 1D ²⁷Al MAS-NMR line shape simulations performed in our study (Figure 4.7) yielded four different Al species: Al^(IV), Al^(V)₁, Al^(V)₂ and Al^(VI) (Appendix A.1) with a ratio of ca. 1:1:1:2. The shape of the 1D ²⁷Al NMR spectra of sample d and e (lowest amounts of Al_2O_3) are both in perfect agreement with literature data (Massiot et al. 1995).

4.5.3 Raman and FTIR Spectroscopy

FTIR powder spectra are shown in Figure 4.8. Note that IR band positions from the KBr and ATR techniques are almost identical, although different intensities result in somewhat different band patterns. Moreover, compared to KBr spectra, ATR band positions are systematically shifted to slightly lower values, which is a common effect in ATR spectra (Harrick 1967). In contrast, due to different selection rules, Raman spectra appear quite different (Fig-

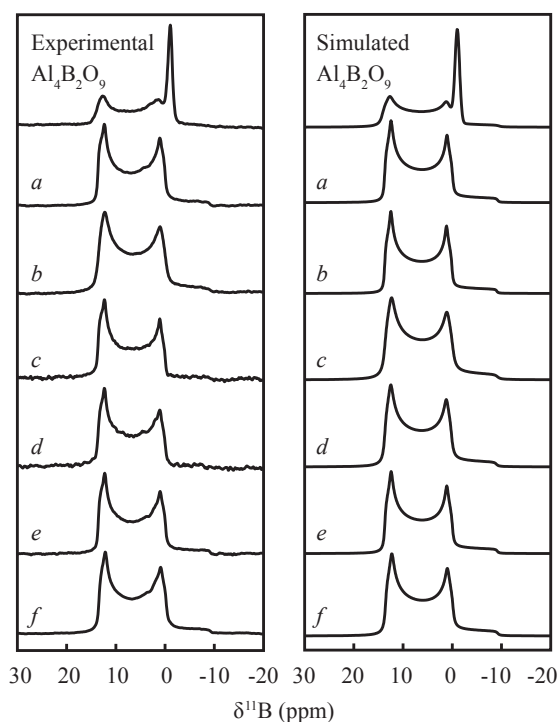


Figure 4.4: Experimental and simulated $^{11}\text{B}\{^1\text{H}\}$ MAS-NMR spectra (128.38 MHz) of reference $\text{Al}_4\text{B}_2\text{O}_9$ powder and powdered samples *a*–*f*. In the spectra of $\text{Al}_4\text{B}_2\text{O}_9$, the narrow resonance around -1 ppm is assigned to BO_4 .

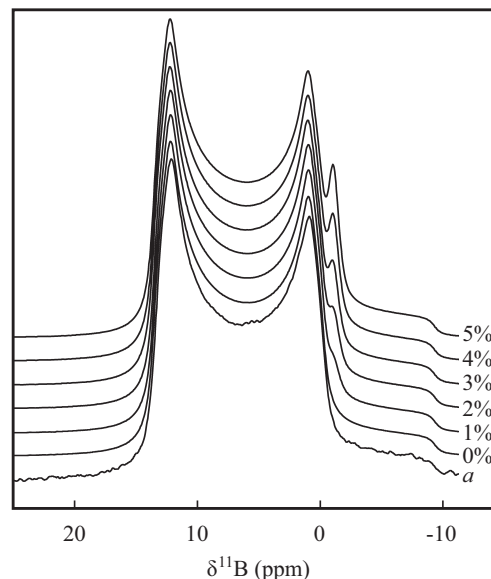


Figure 4.5: Experimental $^{11}\text{B}\{^1\text{H}\}$ MAS-NMR spectra of powdered single-crystals from sample *a* with a series of simulated spectra considering the signals of 0–5% tetrahedrally coordinated BO_4 .

Table 4.6: Chemical shifts and ^{11}B quadrupolar parameters obtained by line shape simulation.

Sample	$\delta^{11}\text{B}_{\text{iso}}$ (ppm)	C_q (MHz)	η
H_3BO_3	19.7	2.51	0.04
$\text{Al}_4\text{B}_2\text{O}_9^{\text{a}}$	17.4	2.66	0.10
<i>a</i>	16.8	2.62	0.09
<i>b</i>	16.7	2.61	0.09
<i>c</i>	16.8	2.61	0.09
<i>d</i>	16.8	2.61	0.08
<i>e</i>	16.8	2.62	0.08
<i>f</i>	16.7	2.61	0.09

^athe BO_4 site was simulated by a Gaussian shape at -1.0 ppm (line width of ≈ 140 Hz).

Ratio determined: $\text{B}^{(\text{III})}/\text{B}^{(\text{IV})} \approx 75:25$

ure 4.9). Considering the structural units of the investigated borates, the spectral regions (both IR and Raman) may be assigned to certain vibrations. The antisymmetric stretching vibrations of the BO_3 group are expected at $\approx 1450\text{ cm}^{-1}$ – 1200 cm^{-1} (predominant in IR spectra, Figure 4.8), the symmetric stretching vibration at $\approx 900\text{ cm}^{-1}$ – 1050 cm^{-1} (predominant in Raman spectra, Figure 4.9). The characteristic IR-active antisymmetric stretching bands of the BO_4 tetrahedron in the vibrational region at $\approx 950\text{ cm}^{-1}$ – 1200 cm^{-1} are only observed

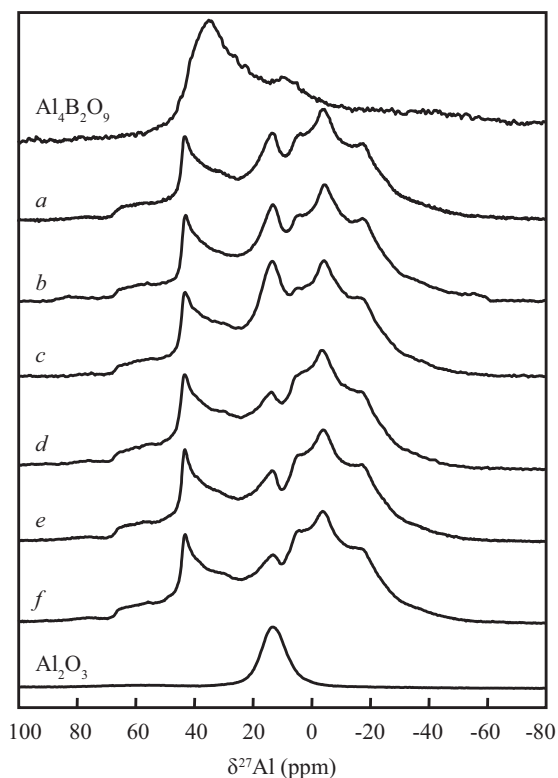


Figure 4.6: 1D ^{27}Al MAS-NMR spectra (104.26 MHz) of $Al_4B_2O_9$ (top), samples *a*–*f* and pure corundum (bottom).

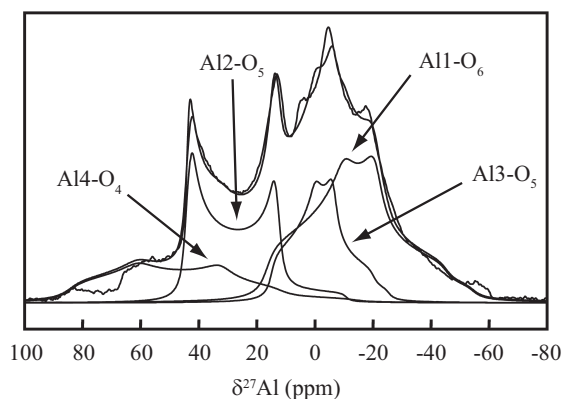


Figure 4.7: 1D ^{27}Al MAS-NMR spectrum of sample *b* with spectrum simulation using the quadrupolar parameters extracted from simulation of the ^{27}Al 3Q-MAS-NMR spectrum.

for the $Al_4B_2O_9$ reference but not in sample *e* (Figure 4.8). The strong BO_3 characteristic symmetric stretching mode of the BO_3 group occurs in Raman spectra at 1016 cm^{-1} (Figure 4.9). The Raman spectrum of the reference material $Al_4B_2O_9$ shows in addition a strong BO_4 characteristic band at $\approx 960\text{ cm}^{-1}$, which is absent in sample *e* (Figure 4.9). The bending motions of the BO_3 group and all other vibrations of the AlO_x polyhedra and lattice vibrations are contained in the complex band region between 900 cm^{-1} and 100 cm^{-1} . Because of this complexity, the latter will not be discussed.

To answer the question for boron speciation ($B^{(III)}$ and/or $B^{(IV)}$ coordination, one or more structural sites) the possible vibrations of a BO_3 group need to be considered. The ideal anion group (e.g. in solution or in a calcite-type structure) has symmetry D_{3h} resulting in four possible vibrations (Appendix A.1). Two of them, i.e. the E' species ν_3 and ν_4 , are doubly degenerate and active in both IR and Raman spectra. In contrast, ν_1 is only Raman-active and ν_2 is only IR-active. If the symmetry of the BO_3 group is lowered in a crystal structure, the degenerate E' species split into two bands, and formerly inactive vibrations may become active. In Al_5BO_9 the Wyckoff site of boron is $4a$ with site symmetry m (Appendix A.1). The effective symmetry of the BO_3 group, however, is higher, as is indicated by the very

similar bond lengths of B-O3 (1.36 Å) and 2 x B-O7 (1.38 Å) (Appendix A.1), and almost identical bond angles close to 120°, i.e. it represents a flat isosceles triangle with symmetry C_{2v} ($mm2$). Independently, if the true site symmetry or the effective symmetry are preferred, the vibrational E' modes split up and the selection rules are released.

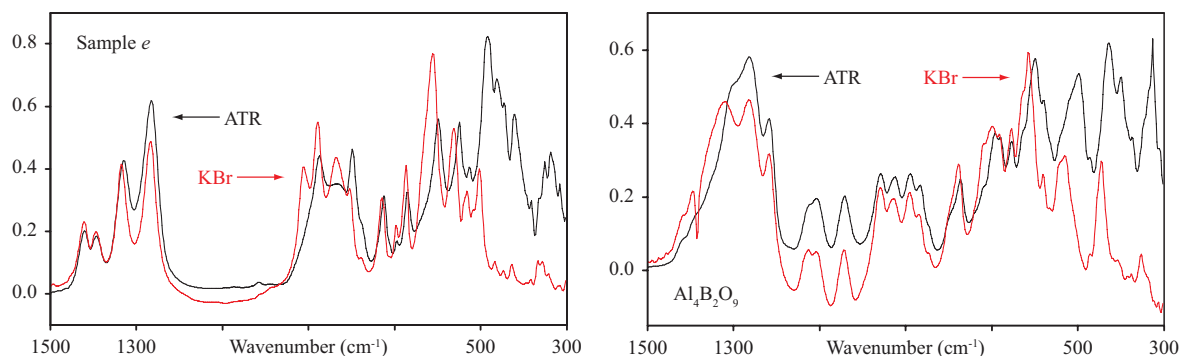


Figure 4.8: ATR and KBr pellet FTIR spectra of sample *e* (left) and $\text{Al}_4\text{B}_2\text{O}_9$ (right). The well resolved peaks between 1250 cm^{-1} and 1450 cm^{-1} (left) are assigned to the BO_3 group in sample *e*. Peaks of stretching vibrations of BO_4 in reference $\text{Al}_4\text{B}_2\text{O}_9$ (right) are between 950 cm^{-1} and 1200 cm^{-1} (right). In the spectra of sample *e*, no indication for BO_4 can be found. Intensity scale is (ATR) absorbance

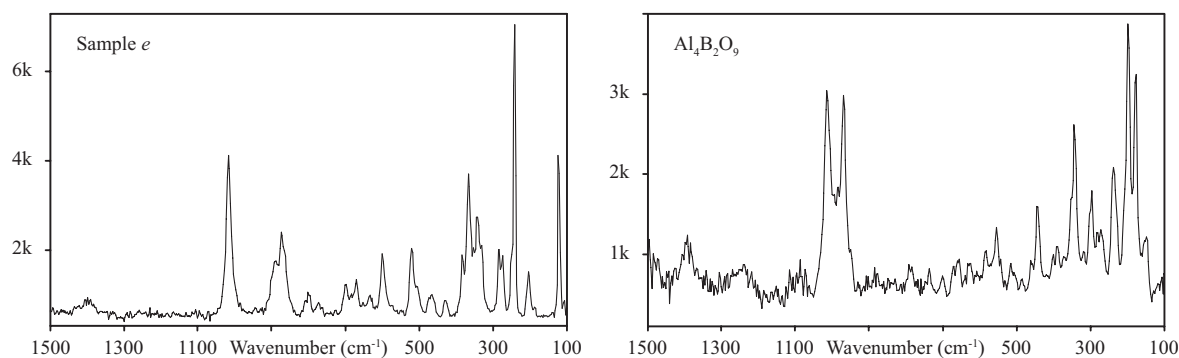


Figure 4.9: Raman spectra of sample *e* (left) and reference $\text{Al}_4\text{B}_2\text{O}_9$ (right). The single strong Raman band at 1016 cm^{-1} is assigned to the symmetric stretching mode of the BO_3 group (left), whereas the double peak in the $\text{Al}_4\text{B}_2\text{O}_9$ pattern corresponds to vibrations of BO_3 and BO_4 groups. Intensity scale is arbitrary units.

In addition to the symmetry considerations above, it is important to note that boron consists of two abundant natural isotopes ^{11}B and ^{10}B with a ratio of about 80:20 (Hannaford and Lowe 1977). This isotope ratio is also found in the common boron-bearing chemicals, such as B_2O_3 and H_3BO_3 used in the syntheses of the present study. Due to the different mass of the isotopes (10 rel.-%), the frequencies of vibrations, where motions of boron isotopes are involved (therefore not in $\nu_1!$), are different by several tens of cm^{-1} (Siebert 1966, Farmer 1974, Harris and Bertolucci 1989).

4.5.4 Laser-Ablation ICP-MS

LA ICP-MS measurement data for samples *a* and *f* are reported in Table 4.7. Compositions of the two synthetic products are identical. They are marginally higher with ≈ 12.35 wt.-% B_2O_3 than expected for pure Al_5BO_9 (12.01 wt.-% B_2O_3), but significantly lower than for $Al_{18}B_4O_{33}$ (13.17 wt.-% B_2O_3 , Table 4.1). External reproducibility of one standard deviation uncertainties on B_2O_3 are ca. 0.25 wt.-% which is of the same order as the uncertainty quoted for the B concentration of the standard reference material NIST SRM 610 used for calibration (Pearce et al. 1997).

Table 4.7: Al_2O_3 and B_2O_3 concentrations (wt.-%) from LA ICP-MS.

Spot no.	Sample <i>a</i>		Sample <i>f</i>	
	Al_2O_3	B_2O_3	Al_2O_3	B_2O_3
1	87.71	12.29	87.65	12.35
2	87.75	12.25	87.65	12.35
3	87.63	12.37	87.99	12.01
4	87.72	12.28	87.33	12.67
5	87.69	12.31	87.72	12.28
6	87.75	12.25	87.29	12.71
7	87.60	12.40	87.72	12.28
8	87.72	12.28	87.69	12.31
9	87.84	12.16	87.78	12.22
10	87.09	12.91	87.08	12.92
11	87.71	12.29	87.89	12.11
12	87.86	12.14	n/a	n/a
Average	87.66	12.33	87.62	12.38
ESD	0.20	0.20	0.27	0.27
ESD SRM610 ^a	n/a	0.25	n/a	0.25

^astandard deviation according to uncertainty of NIST SRM 610 (Pearce et al. 1997)

4.6 Discussion

The excellent agreement of cell dimensions (Table 4.5) of samples *a–e* synthesized along different routes and starting compositions suggests that they are structurally and chemically very similar differing in the amount of excess corundum. This is also confirmed by ^{11}B and ^{27}Al MAS-NMR data (Figures 4.4 and 4.6, Table 4.6). LA ICP-MS compositional data of samples *a* and *f* are equal within esd's (Table 4.7). Atomic coordinates of samples *a* and *f* (single-crystal X-ray data) are also identical. Indications for differences between sample *a* and *f* are: (1) The cell dimensions (Table 4.5), which are most sensitive due to their ability to sum up small structural differences, (2) the crystal from sample *f* had also systematically larger atomic displacement parameters than the crystal from sample *a* (ca. 20% for cation sites, corresponding to ca. 10 esd's, and ca. 10% for O sites, corresponding to 5 esd's). Both data sets were of corresponding quality but were measured on different machines. Nevertheless, we

have previously tested reference crystals to corroborate that both machines produce comparable results. Thus, the increased displacement parameters of sample *f* must be related to crystal properties, such as increased strain compared to the crystal from sample *a*. The only systematic experimental difference between samples *a–e* and sample *f*, distinct by their unit cell volumes (Table 4.5), is the higher synthesis temperature for sample *f* (at 1550°C cooled to 1250°C) whereas samples *a–e* were treated at 1200°C or below. The higher crystallization temperature and subsequent air quenching to ambient conditions could explain the suspected increased strain. But is B → Al substitution the origin of the significantly smaller unit cell volume of sample *f*? LA ICP-MS results (Table 4.7) seem to exclude this interpretation. A possible answer will be discussed below.

The "hypothetical" $\text{Al}_{18}\text{B}_4\text{O}_{33}$ (= $\text{Al}_{4.91}\text{B}_{1.09}\text{O}_9$) composition with the structure of Al_5BO_9 can only be achieved if:

- (1) 9% B substitutes for Al at the Al4 tetrahedron according to Ihara et al. (1980). B is only known in three- and four-fold coordination by O (Hawthorne et al. 1996, Leonyuk 1997). Therefore, B is not expected to occupy one of the other five- or six-fold coordinated sites within the mullite type Al_5BO_9 structure.
- (2) Minor Al vacancies at one of the other Al sites (six-coordinate Al1 or five-coordinate Al2 and Al3) may be charge balanced by a BO_4 or BO_3 polyhedron at a nearby interstitial position. In case of $\text{Al}_{18}\text{B}_4\text{O}_{33} = \text{Al}_{4.91}\text{B}_{1.09}\text{O}_9$, 9% Al vacancies may either be located (2a) at one single position, or (2b) 9% vacancies are statistically distributed throughout all Al positions in the structure.

Ad (1): Single-crystal XRD investigations on crystals from samples *a* and *f* do not show any indication for the 9% B → Al4 substitution as proposed by Ihara et al. (1980). If applying a constraint of 9% B and 91% Al to the tetrahedral Al4 site, agreement factors increase (*R*1: from 0.0198 to 0.0203 for sample *a* and 0.0212 to 0.0218 for sample *f*) and most important, the atomic displacement factor (U_{eq}) at Al4 becomes halved. This U_{eq} behavior has a straightforward explanation: If the electron density (occupancy) at a structural site is underestimated in the refinement model, the probability density cloud around the atomic site (represented by U_{eq}) contracts because integration over the observed electron density is already satisfied (according to the model) for a smaller cloud volume. Theoretically (Kunz and Armbruster 1990) the opposite should be observed: Occupational disorder leads to increased displacement parameters. Furthermore, the Al4 tetrahedron is rather undistorted with $\Delta(\text{Al4-O})_{\text{max}} = 0.0250 \text{ \AA}$ and the average bond length $\langle \text{Al4-O} \rangle_{\text{tet}} = 1.7464(12) \text{ \AA}$ is in agreement with a fully occupied AlO_4 tetrahedron (Kunz and Armbruster 1990). By assuming a mean tetrahedral bond length for BO_4 of 1.476 Å (Hawthorne et al. 1996), the average bond length of a tetrahedron occupied with 91% Al and 9% B is expected to be $\approx 1.72 \text{ \AA}$.

^{11}B MAS-NMR spectra show no evidence for tetrahedrally coordinated $\text{B}^{(\text{IV})}$ in samples *a–f*. Due to the low detection limit and the good agreement of the $\text{B}^{(\text{III})}:\text{B}^{(\text{IV})}$ ratio for

$Al_4B_2O_9$ (Fischer et al. 2008b), partially occupied tetrahedral BO_4 sites with occupancies $> 2\%$ should be clearly detectable (Figure 4.5). From FTIR spectra, 9% of $B^{(IV)}$ in tetrahedral coordination can also be excluded, because the characteristic vibrational region of the IR-active antisymmetric stretching vibrations of the BO_4 tetrahedron at $\approx 950\text{ cm}^{-1}$ – 1200 cm^{-1} (Farmer 1974) is empty (Figure 4.8). Moreover, there is only one Raman band at 1016 cm^{-1} (Figure 4.9) that can unequivocally be assigned to the symmetric stretching mode of the BO_3 group; Hence, no band is left to be assigned to ν_1 of a potential BO_4 group.

Ad (2a): Site occupancy refinements on crystals *a* and *f* provided no evidence for 9% vacancies at Al1, Al2 or Al3. In addition, all spectroscopic methods applied in this study yielded no indication of additional BO_4 or BO_3 with 9% occupancy.

The single, strong Raman band at 1016 cm^{-1} (Figure 4.9) does not suggest an additional BO_3 group occupied to 9%. Within detection limits (2–3%), IR and Raman spectra (Figures 4.8 and 4.9 and Appendix A.1) are consistent with assumption of a single BO_3 group, considering both natural B isotopes. The symmetric stretching mode ν_1 is visible only as a very weak band at 1015 cm^{-1} in IR spectra (IR active due to distortion from the ideal symmetry of the planar BO_3 group). The different B isotopes do not split this mode, as the central B atom is almost inert during this vibration. A similar position ($1017/1019\text{ cm}^{-1}$) of this ν_1 mode was observed in Raman spectra of another aluminoborate with additional REEs by Xia et al. (1999). The antisymmetric stretching mode (doubly degenerate in case of ideal planar symmetry) is split into two modes by the lower site symmetry and further doubled by the two B isotopes. The resulting four bands are clearly visible between 1250 cm^{-1} and 1450 cm^{-1} in the IR spectra, whereas only two very weak bands are observed around 1400 cm^{-1} in Raman spectra (Xia et al. 1999).

Ad (2b): The hypothesis that ca. 9% vacancies are distributed over several Al-polyhedra ($Al1^{(VI)}$, $Al2^{(V)}$, $Al3^{(V)}$, and $Al4^{(IV)}$) and for charge balance BO_3 triangles at nearby interstitial positions are occupied, can also be rejected based on the above spectroscopic arguments. Most convincing, results of LA ICP-MS measurements clearly show that the investigated crystals of samples *a* and *f* cannot have a composition of $Al_{18}B_4O_{33}$. Averaged LA ICP-MS data of 12.36 wt.-% B_2O_3 with a standard deviation of 0.25 wt.-% result in $Al_{4.99}B_{1.01}O_9 \leq Al_{4.97}B_{1.03}O_9 \leq Al_{4.95}B_{1.05}O_9$. Due to reasons mentioned above (e.g. similarity in unit cell volumes), it is very likely that these values apply for all samples.

One of the striking results of structure refinements presented in this study is the significantly large U_{eq} value for Al2 compared to all other Al sites. This observation is consistent with previous, less accurate structural data (Sokolova et al. 1978, Ihara et al. 1980, Garsche et al. 1991). Results of single-crystal structure refinements allow the interpretation of a small amount B at Al2 (2.7(5)% for sample *a* and 3.8(6)% for sample *f*). In corresponding refinements, displacement parameters for the Al2 site are no longer larger than those of the other Al sites in refinements with fully occupied cation sites (Appendix A.1). In this model B occupies the center of the tetrahedron formed by O1, 2 x O2 and O5. For samples a $^{11}B\{^1H\}$

MAS-NMR simulations of BO_4 with more than ca. 2% occupancy in addition to BO_3 can be excluded (Figure 4.5). On the other hand, the average of the four shortest Al2-O distances is ca. 1.79 Å. It seems that this type of substitution is rather unlikely, considering the large size difference due to the characteristic tetrahedral B-O bond length of 1.476 Å.

An X-ray site occupation refinement is mainly sensitive on the number of scattering electrons. Thus alternatively to partial B occupancy, 2.1(4)% and 3.2(4)% vacancies at Al2 may also be successfully modeled for samples *a* and *f*, respectively. In this case, we assume interstitial B in three-fold coordination for charge balance. The Al2 polyhedron comprises 5 oxygen ligands, of which O1 has the lowest bond valence (Appendix A.1). Therefore, a new boron position must be close to the Al2 site and close to O1. Due to the low occupancy, no distinct new boron position could be found in difference Fourier-maps of single-crystal X-ray structure refinements (2% B is equal to an electron density of $0.10e^-$). Nevertheless, we assume that the new boron position is centered within one of the three faces of the Al2 polyhedron sharing O1 as apex. A similar substitution is known from the natural mullite-type borosilicate werdingite (Niven et al. 1991), in which BO_3 groups are correspondingly disordered with Al-tetrahedra. If the interstitial boron site in Al_5BO_9 is statistically distributed among all three faces, it is below the detection limit of FTIR/Raman or single-crystal X-ray diffraction methods. Low concentrations of vacancies at Al2 with B in three-fold coordination distributed in the O1-O5-O2 (twice due to symmetry equivalent sites) and the O1-O2-O2 faces would locally distort the structure because O-O separations are much shorter in BO_3 than in the irregular AlO_5 polyhedron. Therefore, slightly different concentrations of vacancies at the Al2 position compensated by interstitial BO_3 polyhedra could explain the observed difference in cell parameters of samples *a* and *f*.

None of the Al_2O_3 -rich mullite-type aluminoborates synthesized above 1100°C had $\text{Al}_{18}\text{B}_4\text{O}_{33}$ composition. The exact stoichiometry is close to Al_5BO_9 . Values derived from single-crystal diffraction data suggest $\text{Al}_{5-x}\text{B}_{1+x}\text{O}_9$ with $0.021(6) < x < 0.038(6)$, which agrees with compositional data from LA ICP-MS yielding $x = 0.03(2)$. Considering the historical background, it is assumed that the claimed $\text{Al}_{18}\text{B}_4\text{O}_{33}$ stoichiometry is probably an artifact due to old inaccurate chemical analyses.

Acknowledgements

This study was financed by the Swiss National Science Foundation, Grant 200020-112198 "Crystal Chemistry of Minerals". We thank Ruth Maeder for lab assistance, Mariko Nagashima for the translation of Japanese articles and Evgeny Galuskin and Piotr Dzierzanowski for providing EPMA data and images and Eva Wadoski for English corrections.

Note

This text represents the contents of the article "Crystal-chemistry of mullite-type aluminoborates $Al_{18}B_4O_{33}$ and Al_5BO_9 : A stoichiometry puzzle", as published in the Journal of Solid-State Chemistry 184 (2011) 70-80. The composition of mullite $Al_2(Al_{2+2x}Si_{2-2x})O_{10-x}$, $0.2 < x < 0.5$ has been changed to $0.18 \leq x \leq 0.88$ in the introduction and in Table 4.4, "Reflections $> 2\sigma(I)$ " was changed to "Reflections $> 4\sigma(I)$ ". Some passages have been slightly modified to fit the layout of this thesis.

5 Thermal Expansion of Aluminoborates

Martin Fisch and Thomas Armbruster

*Mineralogical Crystallography, Institute of Geological Sciences, University of Bern,
Switzerland.*

E-Mail: fisch@krist.unibe.ch

Submitted to:

*Sergey Krivovichev (Ed.) Minerals as Advanced Materials II,
Springer-Verlag, Berlin*

15. October 2010

5.1 Abstract

Borates are known for low thermal expansion due to rigid behavior of BO_3 and BO_4 groups. Aluminoborates Al_5BO_9 , $\text{Al}_4\text{B}_2\text{O}_9$, grandidierite $(\text{Mg,Fe})\text{Al}_3\text{BSiO}_9$ and jeremejevite $\text{Al}_6\text{B}_5\text{O}_{15}(\text{F,OH})_3$ were investigated by temperature dependent X-ray diffraction methods. Thermal expansion of all investigated structures is mainly due to bending and stretching of M-O-M angles and unusual thermal behavior of AlO_5 and MgO_5 polyhedra. Anisotropic expansion of the studied structures is compared with data of structurally related compounds.

5.2 Introduction

Crystal structures containing triangular BO_3 and tetrahedral BO_4 units are known for low or even negative thermal expansion behavior. Filatov and Bubnova (2008) conclude that (1) BO_3 or BO_4 units behave as rigid bodies, comparable to SiO_4 tetrahedra (Hazen and Prewitt 1977, Tucker et al. 2000); (2) BO_3 and BO_4 units act as hinges, which is a reason for anisotropic thermal expansion; (3) The more cations with low bond strength a borate structure contains, the higher is its thermal expansion.

Thermal expansion of borate structures is therefore controlled by translational and vibrational motions of BO_3 and BO_4 groups combined with expansion and/or tilting of other polyhedra in the structure.

Temperature dependent behavior of two synthetic aluminoborates Al_5BO_9 (Sokolova et al. 1978, Fisch et al. 2011 and refs. therein) and $\text{Al}_4\text{B}_2\text{O}_9$ (Fischer et al. 2008b and refs. therein) and the minerals grandidierite $(\text{Mg,Fe})\text{Al}_3\text{BSiO}_9$ (Stephenson and Moore 1968) and jeremejevite $\text{Al}_6\text{B}_5\text{O}_{15}(\text{F,OH})_3$ (Golovastikov et al. 1955, Foord et al. 1981) were investigated by high-temperature X-ray diffraction (XRD) methods. Al_5BO_9 , $\text{Al}_4\text{B}_2\text{O}_9$ and grandidierite belong to the group of boron-mullites. They have mullite-type crystal structures characterized by unfolded, infinite edge-connected chains of AlO_6 octahedra and crystallize in subgroups of space group $P4/mbm$ (Fischer and Schneider 2008a). Jeremejevite crystallizes in space group $P6_3/m$ and has no structural relation to the mullite-types. The compound was included in this study because it only contains Al and B cations, as in synthetic Al_5BO_9 and $\text{Al}_4\text{B}_2\text{O}_9$. The four investigated structures contain chains of rather undistorted edge-connected AlO_6 octahedra and planar coordinated BO_3 triangles together with AlO_5 and AlO_4 (Al_5BO_9), AlO_5 , AlO_4 and BO_4 ($\text{Al}_4\text{B}_2\text{O}_9$), and AlO_5 , SiO_4 and MgO_5 (grandidierite). In jeremejevite, Al octahedra have five O and one (F,OH) ligand.

5.3 Sample Description

The Al_5BO_9 single-crystal (0.13·0.07·0.4 mm³) was obtained from a mixture of 9 Al_2O_3 :2 B_2O_3 in a $\text{K}_2\text{CO}_3 + 3 \text{MoO}_3$ melt (slowly cooled from 1373K) whereas the powder sample resulted

from a solid-state reaction of 9 Al₂O₃ with 2 B₂O₃ heated at 1473K. Al₄B₂O₉ powder was prepared according to Fischer et al. (2008b).

The grandierite fragment (0.17·0.34·0.27 mm³) was cut from a raw, bluish gemstone from Madagascar. The jeremejevite crystal (0.14·0.14·0.07 mm³) was separated from a pale light-blue sample from Erongo region, Namibia. The remaining jeremejevite material was powdered and mixed with corundum as internal standard for high-temperature powder XRD measurements. Grandierite could not be measured with powder XRD due to the small sample available. All single-crystals were squeezed into quartz glass capillaries and subsequently mounted on a goniometer head for high-temperature data collection.

5.4 X-ray Diffraction Methods

Single-crystal XRD data were collected with a Bruker Smart APEX2 CCD diffractometer (graphite monochromatized MoK α) at 298K and 873K. During high-temperature measurements, crystals were heated using a hot N₂-gas blower, calibrated to known phase transitions. Data were collected with ω - ϕ -scans and subsequently treated using Apex2 v. 2009-11.0 software package (Bruker-AXS 2009). The structural model by Fisch et al. (2011) was used for refinement of Al₅BO₉ data whereas grandierite and jeremejevite structures were solved by direct methods. Details of single-crystal XRD data treatment are given in Table 5.1. Atomic coordinates and anisotropic displacement parameters are listed in Appendix A.2.

According to Hazen and Prewitt (1977), average bond-expansion in polyhedra obeys the following rule: $\langle\alpha\rangle = 32.9 \cdot (0.75 - z/\rho) \cdot 10^{-6} \text{K}^{-1}$, where z is the cation charge and ρ the coordination number. If $z/\rho \geq 0.75$ (e.g. AlO₄, SiO₄, BO₃), $\langle\alpha\rangle$ is predicted as 0K⁻¹. Average α values were calculated from mean polyhedral bond distances $\langle d \rangle$ according to: $\langle\alpha\rangle = (\langle d_{873\text{K}} \rangle - \langle d_{298\text{K}} \rangle) / \langle d_{298\text{K}} \rangle \cdot (873\text{K} - 298\text{K})$.

Bond-lengths data were not corrected for rigid body thermal motion effects (Johnson 1970) because the differences between corrected and uncorrected data were only slightly larger than uncorrected data within standard deviations. Average bond expansion in polyhedra calculated from uncorrected data sometimes resulted in negative thermal expansion for BO₃ units, with errors almost as large as the value itself.

Negative expansion with increasing temperature for MO_x polyhedra is physically not feasible, thus, negative values are artifacts of not applied corrections for thermal rigid body librational effects and may be interpreted as zero expansion between 298K and 873K.

Powder XRD data were measured with a PANalytical X'Pert PRO MPD diffractometer (Cu radiation) equipped with an Anton-Paar HTK 1200 high-temperature goniometer attachment. Samples were measured at 298K, 323K and then in 50K steps up to 1273K (Al₅BO₉), 1323K (Al₄B₂O₉) and 1073K (jeremejevite). Diffraction patterns were measured from 10° 2 θ to 70° 2 θ at 0.008°/step with 30-90 s/step. To eliminate outliers, lattice parameters were parameterized by a 2nd order polynomial: $\text{Length}_i(T) = x_{0i} + x_{1i} \cdot T + x_{2i} \cdot T^2$. Polynomial parameters x_{0i} ,

Table 5.1: Details of crystal structure data collection and structure refinements.

Sample	Al ₅ BO ₉		Jeremejevite		Granddierite	
Temperature	298K ^a	873K	298K	873K	298K	873K
Space group	<i>Cmc</i> 2 ₁	<i>Cmc</i> 2 ₁	<i>P</i> 6 ₃ / <i>m</i>	<i>P</i> 6 ₃ / <i>m</i>	<i>Pnma</i>	<i>Pnma</i>
<i>a</i> -axis	5.6689(6) Å	5.6825(6) Å	8.5526(3) Å	8.5840(16) Å	10.9967(1) Å	11.0193(1) Å
<i>b</i> -axis	15.0045(13) Å	15.0754(16) Å	8.5526(3) Å	8.5840(16) Å	5.7634(1) Å	5.7884(1) Å
<i>c</i> -axis	7.6897(11) Å	7.7121(7) Å	8.1793(4) Å	8.2187(15) Å	10.3321(1) Å	10.3434(1) Å
Volume	654.07(13) Å ³	660.67(12) Å ³	518.13(4) Å ³	524.46(17) Å ³	653.05(3) Å ³	659.74(3) Å ³
Z	4	4	2	2	4	4
Time p. frame	10 s	30 s	40 s	40 s	10 s	20 s
Refl. coll.	4919	1277	5491	2522	10569	14415
Max. 2θ	69.91°	65.64°	69.21°	60.86°	63.20°	89.18°
Index range <i>h</i>	-8...8	-7...7	-12...11	-9...12	-15...14	-16...21
Index range <i>k</i>	-23...23	-21...20	-11...13	-11...11	-8...8	-10...10
Index range <i>l</i>	-12...12	-10...10	-12...8	-11...11	-14...15	-15...18
Unique refl.	1110	595	781	555	1105	2468
Refl. > 4σ(<i>I</i>)	1056	581	673	465	1118	2283
<i>R</i> (int)	0.0423	0.0414	0.0324	0.0270	0.0167	0.0162
<i>R</i> (σ)	0.0349	0.0529	0.0222	0.0251	0.0095	0.0110
L. S. param.	83	83	50	50	87	87
GoF	1.001	1.076	1.064	1.236	1.278	1.262
<i>R</i> 1, <i>I</i> > 4σ(<i>I</i>)	0.0195	0.0242	0.0258	0.0308	0.0182	0.0207
<i>R</i> 1, all data	0.0211	0.0247	0.0326	0.0434	0.0186	0.0230
w <i>R</i> 2 on <i>F</i> ²	0.0351	0.0557	0.0627	0.1145	0.0563	0.0636
Δ <i>P</i> _{max} , near	0.23 e ⁻ ·Å ⁻³ , B1	0.26 e ⁻ ·Å ⁻³ , A11	0.49 e ⁻ ·Å ⁻³ , O1	0.69 e ⁻ ·Å ⁻³ , O3	0.46 e ⁻ ·Å ⁻³ , O6	0.53 e ⁻ ·Å ⁻³ , O3
Δ <i>P</i> _{min} , near	-0.18 e ⁻ ·Å ⁻³ , O4	-0.26 e ⁻ ·Å ⁻³ , A11	-0.40 e ⁻ ·Å ⁻³ , A11	-0.73 e ⁻ ·Å ⁻³ , O1	-0.39 e ⁻ ·Å ⁻³ , Si1	-0.37 e ⁻ ·Å ⁻³ , Si1

^alattice parameters from measurement with CAD4 diffractometer, see text

x_{1i} and x_{2i} (i are lattice parameters a , b and c) were refined simultaneously for all diffraction patterns using Topas-Academic v. 4.1 (Coelho 2007a). Sample displacement was refined as a function of temperature due to its correlation with lattice parameters. From polynomials expressing temperature dependent lattice parameters, thermal expansion parameters $\alpha(T)$ were derived according to the formula $\alpha(T) = a(T)^{-1} \cdot \delta a(T) / \delta T$. From $\alpha(T)$, the anisotropy factor A can be obtained as follows: $A = (|\alpha_a - \alpha_b| + |\alpha_a - \alpha_c| + |\alpha_b - \alpha_c|) \cdot 10^6$ (Dreyer 1974, Schneider and Eberhard 1990). For hexagonal jermeyejvite ($\alpha_a = \alpha_b$), $A = 2|\alpha_a - \alpha_c| \cdot 10^6$.

5.5 Results and Discussion

5.5.1 Thermal Evolution of Al_5BO_9

Main feature of the Al_5BO_9 structure are mullite-type chains of edge-connected AlO_6 octahedra extending parallel to the a -axis. Adjacent AlO_6 chains are interconnected by two alternating segments parallel (010). One contains Al_2O_5 and AlO_4 polyhedra whereas the other consists of Al_3O_5 and BO_3 polyhedra, which build corner-linked chains ($-\text{BO}_3-\text{Al}_3\text{O}_5-\text{BO}_3-$) parallel b linking adjacent octahedra. Both AlO_5 polyhedra are more accurately described as AlO_{4+1} polyhedra as one Al-O bond is significantly longer than the other four. The latter segment containing the BO_3 unit is less dense than the former one, resulting in a cavity parallel to the AlO_6 chains (Figure 5.1).

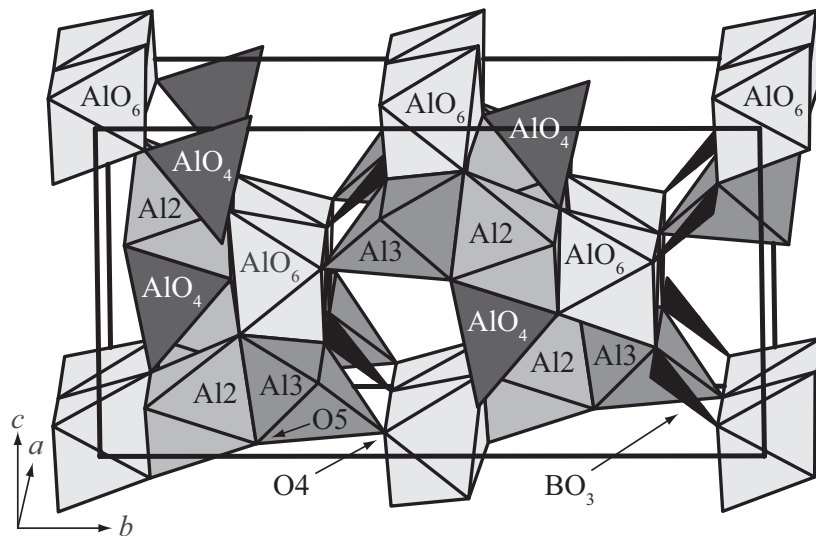


Figure 5.1: The structure of Al_5BO_9 . The distance O4-O5 (marked) shows a large increase in the investigated temperature regime indicating that the corner linkages between Al_3O_5 and BO_3 and the adjacent chain of octahedra are the weakest part of the structure.

Temperature dependent lattice parameters and $\alpha(T)$ are shown in Tables 5.2 and 5.3, respectively. Between 298K and 1273K, the b -axis expands strongly, followed by the c - and the a -axis (the latter parallel to chains of AlO_6 octahedra). The volumetric expansion is +1.56%.

In the same temperature interval, α_a increases most, followed by α_c and α_b , indicating that the shortest crystal axis (a -axis) has the steepest gradient, followed by the c -axis, whereas the longest crystal axis (b -axis) displays the lowest slope (Figure 5.2). As a result, thermal expansion of Al_5BO_9 trends to more isotropic expansion behavior with increasing temperature, which is confirmed by a decrease of A from $A_{298\text{K}} = 6.3$ to $A_{1273\text{K}} = 2.4$.

Inter-polyhedral angles remain the same within standard deviations in the investigated temperature interval, except the O5-Al3-O4 angle. This angle changes from $112.51(06)^\circ$ to $113.56(13)^\circ$, resulting in an increase of the O4-O5 distance from $2.9236(17) \text{ \AA}$ to $2.9470(36) \text{ \AA}$ (Figure 5.1). Expansion of the AlO_6 , BO_3 and Al_2O_5 polyhedra is in perfect agreement with the predicted values of Hazen and Prewitt (1977). However, for the Al_3O_5 polyhedron, $\langle \alpha \rangle = 8.9(2.5) \cdot 10^{-6} \text{K}^{-1}$ is about 180% of the expected value. In addition, the AlO_4 tetrahedron has $\langle \alpha \rangle = 4.6(2.4) \cdot 10^{-6} \text{K}^{-1}$ instead of the expected value of 0K^{-1} (Table 5.4). Thermal expansion of Al_5BO_9 is therefore controlled by expansion of the Al_3O_5 polyhedron and the AlO_4 tetrahedron.

One side of the $-\text{BO}_3\text{-Al}_3\text{O}_5\text{-BO}_3-$ chain linking two adjacent octahedral chains running parallel a is only corner-linked to AlO_6 polyhedra (Figure 5.1). As this is the only part of the structure where only corner-linkages exist, it is obvious that this joint is the weakest part of the structure, which agrees with Al_3O_5 having the largest expansion of all polyhedra in the structure (Table 5.4).

Table 5.2: Coefficients for the 2nd order polynomial $\text{length}_i(T) = x_{0i} + x_{1i} \cdot T + x_{2i} \cdot T^2$ expressing lattice parameters i as function of temperature.

Parameter	x_0	x_1	x_2
Al_5BO_9 for $298\text{K} \leq T \leq 1273\text{K}^{\text{a}}$			
$a(T)$ (\AA)	5.66407	$1.44340 \cdot 10^{-5}$	$6.02392 \cdot 10^9$
$b(T)$ (\AA)	14.98650	$9.45645 \cdot 10^{-5}$	$9.24350 \cdot 10^{10}$
$c(T)$ (\AA)	7.68450	$3.61387 \cdot 10^{-5}$	$3.71557 \cdot 10^9$
$V(T)$ (\AA^3)	652.299	$8.829 \cdot 10^{-3}$	$1.112 \cdot 10^6$
$\text{Al}_4\text{B}_2\text{O}_9$ for $298\text{K} \leq T \leq 1323\text{K}^{\text{a}}$			
$a(T)$ (\AA)	14.76128	$1.49152 \cdot 10^{-4}$	$-1.33666 \cdot 10^8$
$b(T)$ (\AA)	5.54025	$1.49592 \cdot 10^{-5}$	$4.33164 \cdot 10^9$
$c(T)$ (\AA)	15.05004	$8.43267 \cdot 10^{-5}$	$1.70444 \cdot 10^8$
$V(T)$ (\AA^3)	1230.685	$2.263 \cdot 10^{-2}$	$1.417 \cdot 10^6$
Grandidierite for $298\text{K} \leq T \leq 973\text{K}^{\text{b}}$			
$a(T)$ (\AA)	10.9548	$6.2274 \cdot 10^{-5}$	$2.4334 \cdot 10^8$
$b(T)$ (\AA)	5.7557	$2.6772 \cdot 10^{-5}$	$1.5226 \cdot 10^8$
$c(T)$ (\AA)	10.3292	$5.7471 \cdot 10^{-6}$	$1.6289 \cdot 10^8$
$V(T)$ (\AA^3)	651.29	$7.03 \cdot 10^{-3}$	$4.30 \cdot 10^6$
Jeremejevite for $298\text{K} \leq T \leq 1073\text{K}^{\text{a}}$			
$a(T)$ (\AA)	8.53719	$6.51545 \cdot 10^{-5}$	$1.05757 \cdot 10^9$
$c(T)$ (\AA)	8.16183	$6.20481 \cdot 10^{-5}$	$-6.17363 \cdot 10^{10}$
$V(T)$ (\AA^3)	515.169	$1.178 \cdot 10^{-2}$	$1.834 \cdot 10^7$

^afrom powder XRD, ^bfrom single-crystal XRD

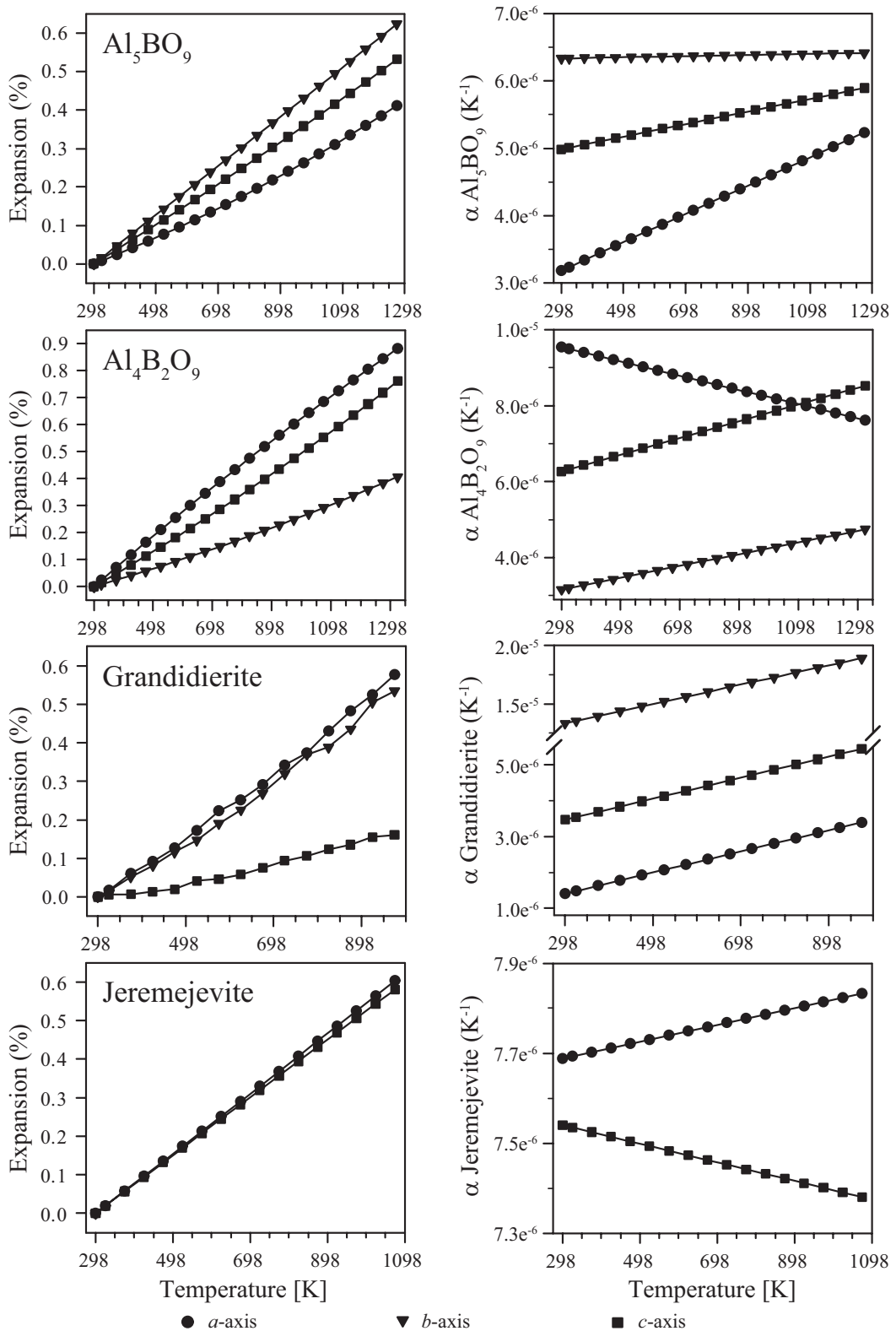


Figure 5.2: Normalized lattice parameters vs. temperature (left) and thermal expansion parameters α as a function of temperature (right).

5.5.2 Thermal Evolution of $\text{Al}_4\text{B}_2\text{O}_9$

Several ambiguous structure solutions for mullite-type $\text{Al}_4\text{B}_2\text{O}_9$ exist. The most promising one is the monoclinic model (space group $C2/m$) of Fischer et al. (2008b) based on powder XRD, ^{11}B and ^{27}Al MAS-NMR data. This structure is related to the one of boralsilite (Peacor et al. 1999) but could not be completely solved from available data.

Three types of edge-connected chains of AlO_6 octahedra extend parallel to the b -axis. The chains are linked among each other by three different polyhedral configurations. One of them is a complex arrangement of distorted AlO_5 (AlO_{4+1}), AlO_4 polyhedra and BO_3 triangles. The second type comprises AlO_{4+1} and BO_4 tetrahedra which are disordered with AlO_4 tetrahedra and BO_3 triangles due to a partially occupied oxygen site. The third type contains BO_3 and/or BO_4 units. However, its exact configuration has not been resolved yet.

Lattice parameters as function of temperature and thermal expansion coefficients $\alpha(T)$ are listed in Tables 5.2 and 5.3. The a -axis expands most, followed by the c - and the b -axis (the latter parallel to AlO_6 chains). The volumetric expansion is +2.06% and the monoclinic angle decreases from $90.8290(10)^\circ$ at 298K to $90.7808(13)^\circ$ at 1323K. α_b of the shortest crystal axis increases most (in percent), followed by α_c whereas α_a decreases, meaning that the length-change of the a -axis diminishes with increasing temperature (Figure 5.2). The overall anisotropy of expansion decreases with temperature (A decreases from $A_{298\text{K}} = 12.6$ to $A_{1323\text{K}} = 7.6$). However, from room-temperature to about 1098K ($\alpha_a = \alpha_c$), anisotropy of thermal expansion is most pronounced along the a -axis whereas at temperatures higher than 1098K, expansion is dominated along the c -axis.

Table 5.3: Coefficients for polynomials $\alpha(T) = a_0 + a_1 \cdot T$ expressing thermal expansion as a function of temperature (i corresponds to lattice parameters).

Parameter	a_0	a_1	Parameter	a_0	a_1
Al ₅ BO ₉ for 298K ≤ T ≤ 1273K			Al ₄ B ₂ O ₉ for 298K ≤ T ≤ 1323K		
$\alpha_a(T)$ (K ⁻¹)	2.55439·10 ⁻⁶	2.10359·10 ⁻⁹	$\alpha_a(T)$ (K ⁻¹)	1.00906·10 ⁻⁵	-1.87160·10 ⁻⁹
$\alpha_b(T)$ (K ⁻¹)	6.31045·10 ⁻⁶	8.21191·10 ⁻¹¹	$\alpha_b(T)$ (K ⁻¹)	2.70463·10 ⁻⁶	1.54378·10 ⁻⁹
$\alpha_c(T)$ (K ⁻¹)	4.70661·10 ⁻⁶	9.33647·10 ⁻¹⁰	$\alpha_c(T)$ (K ⁻¹)	5.61555·10 ⁻⁶	2.19838·10 ⁻⁹
$\alpha_V(T)$ (K ⁻¹)	1.357·10 ⁻⁵	3.114·10 ⁻⁹	$\alpha_V(T)$ (K ⁻¹)	1.842·10 ⁻⁵	1.870·10 ⁻⁹
Grandierite for 298K ≤ T ≤ 973K			Jeremejevite for 298K ≤ T ≤ 1073K		
$\alpha_a(T)$ (K ⁻¹)	5.3387·10 ⁻⁷	2.9700·10 ⁻⁹	$\alpha_a(T)$ (K ⁻¹)	7.63280·10 ⁻⁶	1.86261·10 ⁻¹⁰
$\alpha_b(T)$ (K ⁻¹)	1.0853·10 ⁻⁵	8.2929·10 ⁻⁹	$\alpha_c(T)$ (K ⁻¹)	7.60138·10 ⁻⁶	-2.06187·10 ⁻¹⁰
$\alpha_c(T)$ (K ⁻¹)	2.5960·10 ⁻⁶	2.9337·10 ⁻⁹	$\alpha_V(T)$ (K ⁻¹)	2.286·10 ⁻⁵	1.730·10 ⁻¹⁰
$\alpha_V(T)$ (K ⁻¹)	1.09·10 ⁻⁵	1.27·10 ⁻⁵			

5.5.3 Thermal Evolution of Grandierite (Mg,Fe^{2+}) Al_3BSiO_9

Grandierite (Mg,Fe) Al_3BSiO_9 is the Mg-rich member of the grandierite-ominelite series (Dzikowski et al. 2007, Hiroi et al. 2001) and is of particular interest because it contains both Al and (Mg,Fe) in five-fold coordination (MacKenzie and Meinhold 1997, Dzikowski

et al. 2007, Farges 2001). Structure refinement of single-crystal XRD room-temperature data indicated an almost pure Mg endmember with 97.3(3)% Mg and 2.7(3)% Fe for the selected sample.

The grandierite structure (space group $Pnma$) contains two different chains of edge-connected AlO_6 octahedra parallel to the b -axis. The $Al1O_6$ chain is rather straight whereas chains of $Al2O_6$ octahedra are strongly folded (Figure 5.3). Parallel (100), adjacent Al octahedra are directly connected by corner-linked chains of $-BO_3-AlO_5-BO_3-$ extending along b . Parallel (001), the chains of octahedra are joined by corner-linked chains of $-SiO_4-MgO_5-SiO_4-$ extending parallel b . Along b , channels between adjacent chains of octahedra are either occupied by arrangements of SiO_4 , AlO_5 and MgO_5 polyhedra, or are locally empty if BO_3 polyhedra link octahedra parallel to (100). AlO_5 and MgO_5 polyhedra are regular bipyramids.

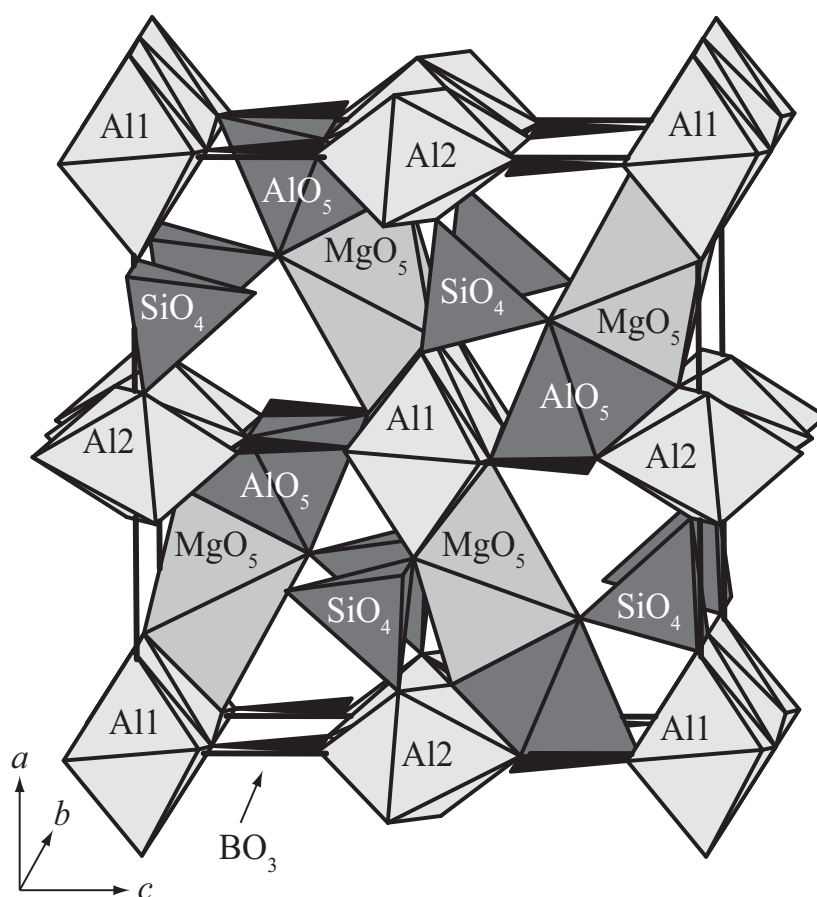


Figure 5.3: The crystal structure of grandierite in space group $Pnma$.

Polynomials expressing temperature dependence of lattice parameters and $\alpha(T)$ are shown in Tables 5.2 and 5.3. Between 298K and 973K, expansion of the a -axis is dominant, followed by the b -axis (parallel to the AlO_6 chains) and the c -axis. The volumetric expansion is +1.28%. Temperature dependence of expansion parameters is $\alpha_a > \alpha_c > \alpha_b$ (Figure 5.2). Expansion of grandierite is highly anisotropic. A increases from $A_{298K} = 23.8$ to $A_{873K} =$

31.0. This high anisotropy results from α_b being a factor of ten larger than α_a and α_c . The increase in anisotropy is therefore due to the strong expansion along the b -axis.

Polyhedral bond lengths and average thermal expansion values obtained from the single-crystal structural refinements are listed in Table 5.4. Average thermal expansion of the AlO_6 , AlO_5 and SiO_4 polyhedra are in perfect agreement with values of Hazen and Prewitt (1977), Table 5.4. Values for Al_2O_6 and BO_3 fit to predicted values within two standard deviations. The expansion of the MgO_5 polyhedron is too low ($\langle\alpha\rangle = 8.3(1.0)\cdot 10^{-6}\text{K}^{-1}$ instead of $11.5\cdot 10^{-6}\text{K}^{-1}$).

Table 5.4: Average polyhedral bond lengths at 298K and 873K, their average thermal expansion coefficient $\langle\alpha\rangle$ and expected $\langle\alpha\rangle$ values according to Hazen and Prewitt (1977).

Polyhedron	298K (Å)	873K (Å)	$\langle\alpha\rangle$ (K^{-1})
Al₅BO₉:			
AlO_6	1.9004(9)	1.909(2)	$7.7(1.8)\cdot 10^{-6}$
Al_2O_5	1.8642(11)	1.869(2)	$4.5(2.3)\cdot 10^{-6}$
Al_3O_5	1.8822(12)	1.892(3)	$8.9(2.5)\cdot 10^{-6}$
AlO_4	1.7472(11)	1.752(2)	$4.6(2.4)\cdot 10^{-6}$
BO_3	1.3769(14)	1.377(3)	$-0.7(3.8)\cdot 10^{-6}$
Grandidierite:			
AlO_6	1.8981(7)	1.9076(4)	$8.2(0.8)\cdot 10^{-6}$
Al_2O_6	1.9094(8)	1.9171(4)	$7.1(0.8)\cdot 10^{-6}$
AlO_5	1.8548(11)	1.8604(6)	$5.3(1.2)\cdot 10^{-6}$
MgO_5	2.0311(19)	2.0407(6)	$8.3(1.0)\cdot 10^{-6}$
SiO_4	1.6290(10)	1.6289(6)	$-0.2(1.2)\cdot 10^{-6}$
BO_3	1.3656(14)	1.3631(8)	$-3.2(2.0)\cdot 10^{-6}$
Jeremejevite:			
$\text{AlO}_5(\text{F},\text{OH})^a$	1.8861(8)	1.8961(16)	$9.2(2.0)\cdot 10^{-6}$
B_1O_3	1.3855(13)	1.3851(40)	$-0.5(4.4)\cdot 10^{-6}$
B_2O_3	1.3646(7)	1.3623(19)	$-2.9(2.6)\cdot 10^{-6}$
Expected values for $\langle\alpha\rangle$:			
$\langle\alpha\rangle \text{AlO}_6$:	$8.23\cdot 10^{-6}\text{K}^{-1}$	$\langle\alpha\rangle \text{MgO}_5$:	$11.5\cdot 10^{-6}\text{K}^{-1}$
$\langle\alpha\rangle \text{AlO}_5$:	$4.94\cdot 10^{-6}\text{K}^{-1}$	$\langle\alpha\rangle \text{BO}_3$:	0K^{-1}
$\langle\alpha\rangle \text{AlO}_4$:	0K^{-1}	$\langle\alpha\rangle \text{SiO}_4$:	0K^{-1}

^atreated as AlO_6

The most significant changes in inter-polyhedral angles occur at $\text{Al}_2\text{-O}_5\text{-Al}_2$ (stretching from $100.48(5)^\circ$ to $101.10(3)^\circ$) and at $\text{Al}_2\text{-O}_4\text{-Al}_2$ (bending from $94.01(5)^\circ$ to $93.40(3)^\circ$), which results from stretching of the folded chain of Al_2O_6 octahedra. Further angular changes occur at $\text{Mg-O}_2\text{-Al}_3$ ($124.32(6)^\circ$ to $124.69(3)^\circ$), $\text{Mg-O}_5\text{-Al}_2$ ($129.00(3)^\circ$ to $128.73(1)^\circ$), $\text{Si}_1\text{-O}_4\text{-Al}_2$ ($132.91(2)^\circ$ to $133.28(1)^\circ$) and at $\text{B}_1\text{-O}_7\text{-Al}_3$ ($130.82(8)^\circ$ to $131.22(5)^\circ$). Except unfolding of the Al_2O_6 chain, the largest structural changes are observed in the configuration of SiO_4 , AlO_5 and MgO_5 polyhedra within the channels along b . Expansion of this channel is limited to expansion of the AlO_6 octahedra at its corners because the channel walls are held together by non-expanding BO_3 units parallel to the (100) plane and by a face of the non-expanding SiO_4 tetrahedra parallel to the (001) plane. MgO_5 has the lowest bond strength

in the structure ($z/\rho = 0.4$) making it the most preferable buffer to compensate expansion of other polyhedra in the structure.

5.5.4 Thermal Evolution of Jeremejevite $\text{Al}_6\text{B}_5\text{O}_{15}(\text{F},\text{OH})_3$

Jeremejevite $\text{Al}_6\text{B}_5\text{O}_{15}(\text{F},\text{OH})_3$ was the first known aluminoborate mineral (Mallard 1887). The unit-cell volume of $518.13(4) \text{ \AA}^3$ (Table 5.1) indicates that our sample is close to a F-endmember of jeremejevite, which is a common composition for natural jeremejevite (Foord et al. 1981).

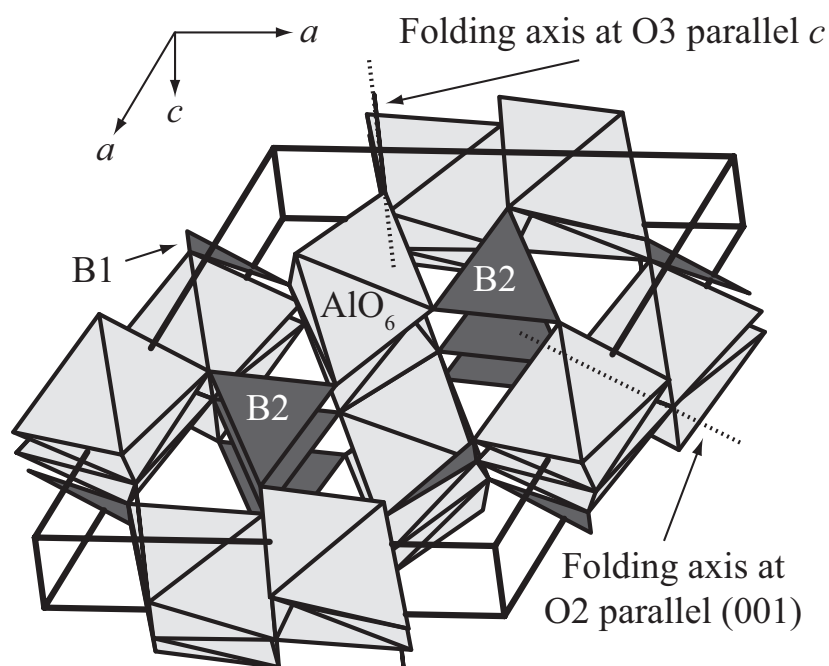


Figure 5.4: The crystal structure of jeremejevite. Dashed lines indicate axes at which M-O-M angular changes are observed. B1 and B2 indicate B1O_3 and B2O_3 triangles, respectively.

Viewed along the c -axis, the jeremejevite structure (Figure 5.4) is characterized by two types of channels. An empty hexagonal channel is located at $0, 0, c$, whereas the other is triangular and located at $\frac{2}{3}, \frac{1}{3}, c$ and $\frac{1}{3}, \frac{2}{3}, c$. The triangular channels are enclosed by chains of edge sharing AlO_5F octahedra. These chains are not straight as in mullite-type structures but consist of staggered arrangements of edge connected dimers of AlO_5F octahedra expanding along c . B1O_3 triangles (face parallel to the c -direction) support the chains along c . B2O_3 units (face parallel to the (001) plane) within the triangular channel connect adjacent octahedra apexes at the same c -height. Along c , every third octahedral apex pointing towards the center of a triangular channel consists of F instead of O and is thus not connected to a BO_3 unit.

Polynomials expressing temperature dependent lattice parameters are shown in Table 5.2 and polynomials expressing $\alpha(T)$ in Table 5.3. Between 298K and 1073K, all axes expand similarly. The volumetric expansion is +1.8%. At 298K α_a is slightly larger than α_c and

with increasing temperature α_a expands and α_c decreases slightly (Figure 5.2) resulting in an increase of the anisotropy factor A from $A_{298\text{K}} = 0.3$ to $A_{1073\text{K}} = 0.9$. Jeremejevite has the lowest A of all investigated structures. Expansion of BO_3 triangles and AlO_5F (Table 5.4) is in good agreement with the expected values of Hazen and Prewitt (1977).

In the investigated temperature regime, structural changes in jeremejevite are controlled by inter-polyhedral folding at Al1-O3-Al1 from $140.93(2)^\circ$ to $141.11(6)^\circ$ and at Al1-O2-Al1 from $124.19(2)^\circ$ to $123.86(6)^\circ$ (Al1-O2-Al1 is the angle between two connected dimers of octahedra). Angular changes are a result of AlO_6 expansion, which is attenuated by non-expanding BO_3 units connected to them. Larger expansion of AlO_5F octahedra (compared to zero expansion of BO_3 units) can only be compensated by rotation. Dimers of octahedra are rotated at the edge joining two dimers (Figure 5.4), resulting in decrease of the Al1-O2-Al1 angle. In addition, at the linking corner of two adjacent octahedral chains the Al1-O3-Al1-angle expands.

5.6 Discussion

Thermal behavior of the investigated boron-mullite compounds can be compared to those of the Al_2SiO_5 polymorphs andalusite and sillimanite and mullite ($\text{Al}_2(\text{Al}_{2+2x}\text{Si}_{2-2x})\text{O}_{10-x}$, $0.18 \leq x \leq 0.88$). All three have mullite-type structures with AlO_6 chains, interlinked by single chains of alternating Si- and Al-tetrahedra (sillimanite), double-chains of AlO_5 and SiO_4 polyhedra (andalusite) and by disordered arrangements of Al and Si in mullite (Fischer and Schneider 2005).

Winter and Ghose (1979) investigated thermal expansion of sillimanite and andalusite. In sillimanite, from 298K to 1273K, lattice parameter expansion with temperature is $b > c > a$ (c is parallel to the chains of octahedra) and A decreases from 11.3 to 10.8. The most distinctive expansion along the b -axis is due to anisotropic expansion of octahedra. Even though the mullite-type chain is held together by chains of rigid non-expanding $\text{SiO}_4/\text{AlO}_4$ tetrahedra, octahedral rotation into the channels is responsible for expansion $c > a$. The expansion of andalusite is most expressed along the a -axis, followed by the b - and c -axis (mullite-type chains parallel to c). Average expansion of AlO_6 is slightly higher than expected ($\langle \alpha \rangle = 12.6(3.2) \cdot 10^{-6} \text{K}^{-1}$ instead of $8.2 \cdot 10^{-6} \text{K}^{-1}$). Anisotropic expansion of AlO_6 units is has its strongest contribution to the a -axis whereas expansion along the c -axis is constrained by the double-chain of rigid $\text{AlO}_5/\text{SiO}_4$ polyhedra. Due to the double-chains, no open channels exist and AlO_6 rotation is limited leading to the lowest expansion along the c -axis. Andalusite shows high and increasing anisotropy of thermal expansion ($A_{298\text{K}} = 20.6$, $A_{1273\text{K}} = 21.75$).

In 3:2 mullite, cell dimensions increase in the sequence $b > c > a$ (mullite-type chains parallel to c). Anisotropy factors are rather low, $A = 6.2$ between 298K and 1173K (Schneider and Eberhard 1990) and $A = 3.8$ between 298K and 1273K (Brunauer et al. 2001b). Based on neutron powder diffraction data, structural changes in mullite with increasing temperature

are due to rotation and increasing distortion of Al-octahedra and shifts in coordinates and varying Si and Al populations between mullite-type chains (Brunauer et al. 2001a).

In all investigated structures, BO_3 units (and SiO_4 in grandidierite) behave as rigid bodies and therefore act as rigid linkages (hinges) between other polyhedra, confirming the statement of Filatov and Bubnova (2008). Between 298K and 973K, Al_5BO_9 has the lowest volumetric expansion, followed by grandidierite, $\text{Al}_4\text{B}_2\text{O}_9$ and jeremejevite.

The smallest volumetric expansion of Al_5BO_9 can be explained by its structural relation to sillimanite: Expansion of polyhedra is balanced by the empty channels parallel to the mullite-type chains. As one wall of the channel is formed by the O4-O5 edge of Al_3O_5 , the channel is rather flexible. However, in contrast to sillimanite, mullite-type chains are only close to two channels instead of four, and therefore, rotation of octahedra is limited. To explain the smallest expansion behavior along the a -axis, the relation to the andalusite structure becomes relevant: Expansion along the a -axis is limited by the chain of $-\text{BO}_3-\text{Al}_3\text{O}_5-\text{BO}_3-$ consisting of rigid BO_3 units (rigid AlO_4 and SiO_4 in andalusite) parallel to the mullite-type chains (Wada et al. 1993). Combined with limited rotation of octahedra, expansion along the a -axis (parallel to the mullite-type chains) has the strongest restrictions. For structures containing AlO_4 and AlO_6 polyhedra Hazen and Prewitt (1977) state that structural changes with increasing pressure correspond to those with decreasing temperature. Elastic behavior of Al_5BO_9 was investigated by Gatta et al. (2010) and the behavior of lattice parameters with increasing pressure (compression is highest along the b -axis, followed by the c - and a -axis) is in agreement with our results for expansion of lattice parameters with temperature.

In grandidierite, all polyhedra except MgO_5 expand as expected according to Hazen and Prewitt (1977). The MgO_5 polyhedron buffers thermal expansion due to its low bond strength ($z/\rho = 0.4$). Furthermore, slightly anisotropic expansion of the Al2-octahedra combined with unfolding of the corresponding chain is responsible for $b > c$ expansion (mullite-type chains parallel b). All polyhedra in jeremejevite behave as rigid bodies. No flexible parts in the structure can compensate expansion and the structure reacts to rising temperature with folding and tilting of polyhedral arrangements.

The observed sequence of volumetric expansion may seem to contradict the conclusion of Filatov and Bubnova (2008) stating that thermal expansion of borates decreases with the number of cations with low bond strength (according to which grandidierite should undergo the largest expansion). It has to be considered that all of the structures investigated in this study are of similar chemical composition. In other words, AlO_4 behaves not much different to SiO_4 , as do MgO_5 and AlO_5 . Expansion properties of the investigated compounds are therefore mainly controlled by structural flexibility characteristic of each individual structure, i.e. their ability to buffer expansion by soft links between polyhedra rather than by differences in bond-strengths.

6 Thermal Stability of Jeremejevite

6.1 Introduction

Investigating strain related optical properties of crystals, Foord and Cunningham (1978) noticed that natural jeremejevite ($\text{Al}_6\text{B}_5\text{O}_{15}(\text{F},\text{OH})_3$, very F-rich in nature, Foord et al. 1981) from Swakopmund, Namibia, changes from blue to an opaque white compound at 800°C .

In a study on synthesis, stability and breakdown products of the synthetic (OH)-endmember of jeremejevite, Stachowiak and Schreyer (1998) observed $\text{Al}_4\text{B}_2\text{O}_9$, $\text{Al}_6\text{B}_8\text{O}_{21}$, Al_3BO_6 (Capponi et al. 1972), AlBO_3 (Capponi et al. 1972, Bither 1973, Vegas et al. 1977) and corundum as secondary phases in hydrothermal synthesis experiments. $\text{Al}_4\text{B}_2\text{O}_9$ was also found as inclusions in (OH)-jeremejevite crystals. The type and amount of secondary phases depended on synthesis conditions (pressure, temperature). $\text{Al}_6\text{B}_8\text{O}_{21}$ was previously reported in jeremejevite synthesis experiments by Reynaud (1977). Synthetic (OH)-jeremejevite remains stable up to fluid pressures of 50 kbar with a maximum temperature of ca. 750°C at 35 kbar (Schreyer and Werding 1997). Most interesting is the conclusion of Stachowiak and Schreyer (1998) that (OH)-jeremejevite breaks down to $\text{Al}_4\text{B}_2\text{O}_9$ at ca. 625°C and 3 kbar. With increasing pressure, $\text{Al}_4\text{B}_2\text{O}_9$ is reported to decompose to Al_3BO_6 and AlBO_3 . From extrapolated data of Stachowiak and Schreyer (1998), breakdown of the synthetic (OH)-endmember of jeremejevite can be predicted at ca. 500°C and ambient pressure:



During the investigation of thermal expansion of aluminoborates (Chapter 5), temperature-dependent jeremejevite lattice parameters were refined up to 800°C , however, data were collected up to 1100°C . Above ca. 800°C jeremejevite decomposed to an aluminoborate phase.

6.2 Experimental

Two natural blueish jeremejevite samples from Erongo region Namibia were investigated with powder X-ray diffraction and FTIR spectroscopy.

One sample (jeremejevite#1, characterized in Chapter 5) was ground, mixed with corundum as internal standard and subsequently measured with high-temperature powder X-ray diffraction up to 1100°C . After cooling to room temperature, the sample was re-measured with powder XRD and Fourier transformed infrared spectroscopy. The second sample (jeremejevite#2) was heated at 925°C for one hour and then heated at 950°C for two hours in air

atmosphere, whereas another fragment of the same sample was heated at 1250°C. Both specimens turned white and were measured with powder X-ray diffraction and FTIR spectroscopy at room temperature.

Unit cell volumes of 518.13(4) Å³ (#1, Chapter 5) and 518.91(6)Å³ (#2) indicate that both jeremejevites are close to F-endmembers (Foord et al. 1981).

Powder XRD data were measured with a PANalytical X'Pert PRO MPD diffractometer (Cu radiation) equipped with an Anton-Paar HTK 1200 high-temperature goniometer attachment. Temperature-dependent data were acquired at 25°C, 50°C and then each 50°C up to 1100°C.

Diffraction patterns were collected from 10° 2θ to 70° 2θ at 0.008°/step with 40 s/step. Lattice parameters of the phases were derived from Rietveld refinements performed with Topas-Academic v. 4.1 (Coelho 2007a), using the structural models of Al₅BO₉ (Chapter 4) Al₄B₂O₉ (Fischer et al. 2008b).

Fourier transformed infrared powder spectra were collected with a Perkin Elmer Spectrum One FTIR spectrometer equipped with a Perkin Elmer universal ATR accessory (Zn-Se + diamond crystal). The beam path included a mid-infrared light source, a KBr beam splitter and a TGS detector. Sample and background spectra were averaged from 50 scans measured 550 cm⁻¹ to 1500 cm⁻¹ at 4 cm⁻¹ resolution.

6.3 Results

A selection of temperature-dependent powder XRD patterns of jeremejevite#1 is shown in Figure 6.1. Between 25°C and 800°C, the pattern of jeremejevite does not significantly change, except of minor shifts due to thermal expansion (Section 5.5.4 in Chapter chap:HiTemp). At 850°C, the powder X-ray diffraction pattern is similar to Al₄B₂O₉ (Fischer et al. 2008b). This phase retained stable up to ca. 1000°C when it transformed to a phase with an Al₅BO₉-like powder pattern (Chapter 3). Rietveld refined lattice parameters of in-situ high-temperature powder XRD experiment of jeremejevite#1 and of jeremejevite#2, measured at room temperature, are given in Table 6.1.

FTIR spectra of the jeremejevite#2 sample are shown in Figure 6.2. For comparison, spectra of Al₅BO₉ and Al₄B₂O₉ are also shown (measured with the same spectrometer with the same setup and settings).

6.4 Discussion

Unit cell dimensions of the phase measured at 950°C (jeremejevite#1) do not significantly differ from those of Al₄B₂O₉ measured at 950°C ($a = 14.9178(3)$ Å, $b = 5.56376(5)$ Å, $c = 15.1724(3)$ Å, $V = 1259.180(19)$ Å³, $\beta = 90.7864(9)^\circ$) and those of the 1050°C phase can be compared to Al₅BO₉ measured at 1000°C ($a = 5.69221(3)$ Å, $b = 15.10838(11)$ Å, $c = 7.73652(5)$ Å, $V = 665.342(8)$ Å³).

Table 6.1: Refined lattice parameters of jeremejevite in-situ measured by high-temperature powder X-ray diffraction (#1) and previously heated jeremejevite measured at room temperature (#2).

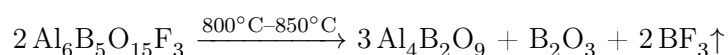
	T_M (°C)	T_H (°C)	a -axis (Å)	b -axis (Å)	c -axis (Å)	Volume (Å ³)	β (°)
#1	850	850	14.919(3)	5.5622(8)	15.143(4)	1256.5(4)	90.639(8)
#1	1050	1050	5.6832(4)	15.1077(15)	7.7285(8)	663.57(11)	
#1	25	1100	5.6626(4)	15.0060(13)	7.6855(7)	653.06(9)	
#2	25	850	14.820(8)	5.5498(17)	15.098(6)	1241.6(9)	90.938(8)
#2	25	1250	5.6651(3)	15.0147(9)	7.6891(5)	654.03(7)	

T_M = temperature during measurement, T_H maximum heating temperature of the sample

Room-temperature lattice parameters of the $\text{Al}_4\text{B}_2\text{O}_9$ and Al_5BO_9 phases obtained by heating jeremejevite#2 at 950°C and 1100°C, respectively, are in the range of literature-data of $\text{Al}_4\text{B}_2\text{O}_9$ and Al_5BO_9 . According to Fischer et al. (2008b), $\text{Al}_4\text{B}_2\text{O}_9$ lattice parameters are: $a = 14.8056(7)$ Å, $b = 5.5413(2)$ Å, $c = 15.0531(6)$ Å, $V = 1234.83$ Å³, $\beta = 90.913(2)^\circ$. Al_5BO_9 lattice parameters (Chapter 4) are $a = 5.6686(2)$ Å, $b = 15.0060(9)$ Å, $c = 7.6892(7)$ Å, $V = 654.07(6)$ Å³.

FTIR spectra of jeremejevite#2 heated at 950°C and $\text{Al}_4\text{B}_2\text{O}_9$ are very similar, however, peaks are better resolved in the $\text{Al}_4\text{B}_2\text{O}_9$ reference spectrum. The only difference in the spectra of jeremejevite#2 heated at 1250°C and Al_5BO_9 can be found at ca. 850 cm⁻¹. According to MacKenzie (2005), bands in the region of 830 cm⁻¹ to 909 cm⁻¹ are ascribed to AlO_4 -stretch vibrations.

In-situ high-temperature powder X-ray diffraction experiments indicate that natural jeremejevite decomposes at temperatures between 800°C and 850°C. Agreement of lattice parameters and corresponding FTIR spectra yield $\text{Al}_4\text{B}_2\text{O}_9$ as product. For an F endmember of jeremejevite, the reaction of $\text{Al}_4\text{B}_2\text{O}_9$ formation from jeremejevite at high temperature can be described as:



BF_3 is a volatile gas even at room temperature and will escape. At the formation conditions of $\text{Al}_4\text{B}_2\text{O}_9$ (> 850°C), B_2O_3 may either be present as melt or evaporate. A minor concentration of residual B_2O_3 may cause the differences in FTIR spectra between reference Al_5BO_9 and $\text{Al}_4\text{B}_2\text{O}_9$ compounds and those produced by decomposition of jeremejevite. Residual B_2O_3 hydrates under ambient conditions to X-ray amorphous $2 \text{H}_3\text{BO}_3$ and can therefore not be detected in diffraction patterns.

Formation of Al_5BO_9 from $\text{Al}_4\text{B}_2\text{O}_9$ at ca. 1050 °C is already known and has been extensively discussed in literature (Chapter 3, Scholze 1956, Gielisse and Forster 1962, Ray 1992, Mazza et al. 1992, Duoy 2005 and others).

The significant difference in breakdown temperature between natural (ca. 800°C–850°C) and synthetic (OH)-jeremejevite (ca. 500°C, Stachowiak and Schreyer 1998) can thus be ascribed to the chemical difference (F or OH) of the compounds.

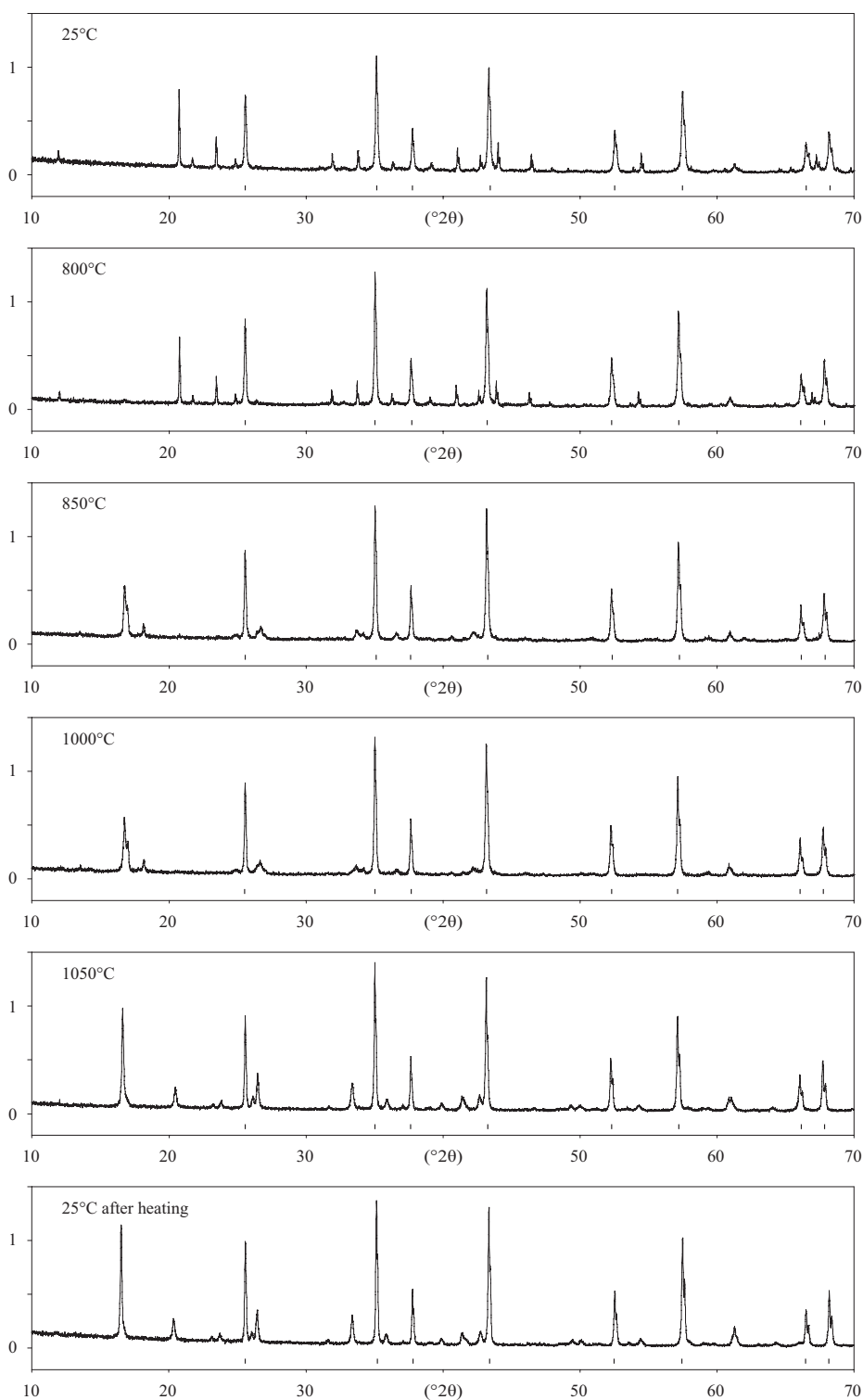


Figure 6.1: Temperature-dependent powder XRD pattern of jeremejevite mixed with ca. 70 wt.-% corundum as internal standard. The pattern measured at 25°C shows diffraction peaks of jeremejevite and corundum (hkl -ticks). At 800°C, jeremejevite is still stable. Diffraction peaks of the pattern at 850°C fit the structure of $\text{Al}_4\text{B}_2\text{O}_9$ according to Fischer et al. (2008b). Peaks of the pattern measured at 1050°C and at 25°C after heating fit the Al_5BO_9 structure. Intensity scale is counts $\cdot 10^3$.

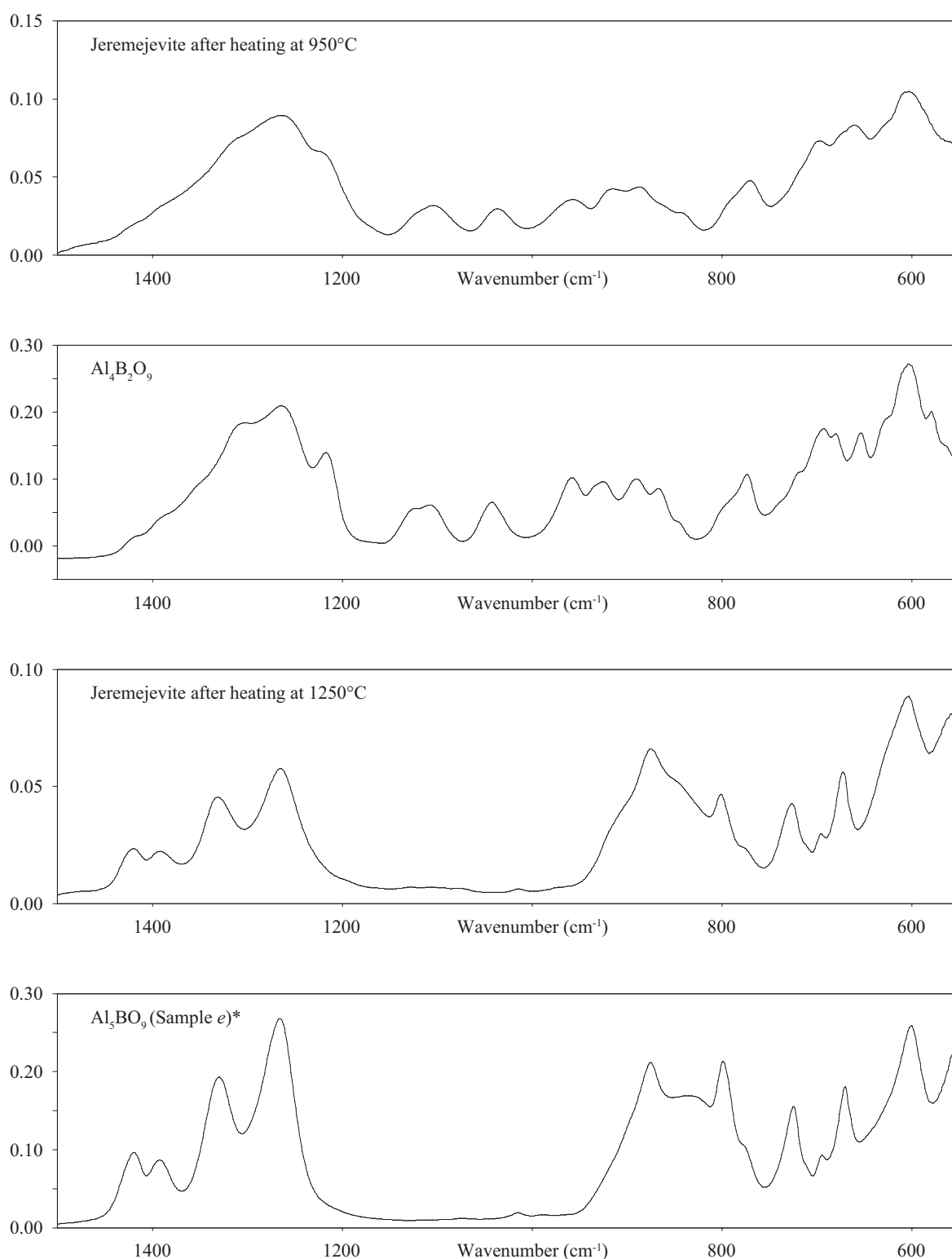


Figure 6.2: Top to bottom: FTIR spectra of jeremejevite after heating at 950°C, Al₄B₂O₉ (prepared according to Fischer et al. 2008b), jeremejevite measured after heating at 1250°C and an FTIR spectrum of Al₅BO₉ (sample *e* in Chapter 4). Peaks between 1450 cm⁻¹ and 1250 cm⁻¹ are assigned to BO₃ vibrations, whereas peaks in the region of 1200 cm⁻¹ to 950 cm⁻¹ are assigned to BO₄ stretching vibrations. Intensity scale is ATR absorbance.

7 Stability at High Pressure, Elastic Behavior and Pressure-Induced Structural Evolution of "Al₅BO₉", a Mullite-Type Ceramic Material

G. Diego Gatta^{a,*}, Nicola Rotiroti^a, Martin Fisch^b, Thomas Armbruster^b

^a*Dipartimento di Scienze della Terra, Università degli Studi di Milano, Via Botticelli 23,
20133 Milan, Italy*

^b*Institute of Geological Sciences, Mineralogical Crystallography, University of Bern,
Freiestrasse 3, 3012 Bern, Switzerland*

*Corresponding author: diego.gatta@unimi.it

Physics and Chemistry of Minerals 37 (2010) 227-236

7.1 Abstract

Elastic behavior and pressure-induced structural evolution of synthetic boron-mullite "Al₅BO₉" ($a = 5.678(2)$ Å, $b = 15.015(4)$ Å and $c = 7.700(3)$ Å, space group $Cmc2_1$, $Z = 4$) were investigated up to 7.4 GPa by in-situ single-crystal X-ray diffraction with a diamond anvil cell under hydrostatic conditions. No phase-transition or anomalous compressional behavior occurred within the investigated P -range. Fitting the P - V data with a truncated second-order (in energy) Birch-Murnaghan Equation-of-State (BM-EoS), using the data weighted by the uncertainties in P and V , we obtained: $V_0 = 656.4(3)$ Å³ and $K_{T0} = 165(7)$ GPa ($\beta_{V0} = 0.0061(3)$ GPa⁻¹). The evolution of the Eulerian finite strain vs. normalized stress (f_E - F_E plot) leads to an almost horizontal trend, showing that a truncated second-order BM-EoS is appropriate to describe the elastic behavior of "Al₅BO₉" within the investigated P -range. The weighted linear regression through the data points gives: $F_E(0) = 159(11)$ GPa. Axial compressibility coefficients yielded: $\beta_a = 1.4(2) \cdot 10^{-3}$ GPa⁻¹, $\beta_b = 3.4(4) \cdot 10^{-3}$ GPa⁻¹, and $\beta_c = 1.7(3) \cdot 10^{-3}$ GPa⁻¹ ($\beta_a:\beta_b:\beta_c = 1:2.43:1.21$). The highest compressibilities observed in this study within (100) can be ascribed to the presence of voids represented by 5-membered rings of polyhedra: Al1-Al3-Al4-Al1-Al3, which allow accommodating the effect of pressure by polyhedral tilting. Polyhedral tilting around the voids also explains the higher compressibility along [010] than along [001]. The stiffer crystallographic direction observed here might be controlled by the infinite chains of edge-sharing octahedra running along [100], which act as "pillars", making the structure less compressible along the a -axis than along the b - and c -axis. Along [100], compression can only be accommodated by deformation of the edge-sharing octahedra (and/or by compression of the Al-O bond lengths), as no polyhedral tilting can occur. In addition, a comparative elastic analysis among the mullite-type materials is carried out.

7.2 Introduction

Compounds with chemical composition belonging to the ternary system Al₂O₃-B₂O₃-SiO₂ are a class of ceramic materials investigated in particular for industrial applications. Their high-temperature stability, low-thermal expansion coupled with high creep resistance, low electric conductivity, high chemical stability and low-density are leading to an increasing number of outstanding applications of such materials: As construction and engineering ceramics, refractory linings due to their high resistance to corrosion, optically translucent ceramics for high-temperature furnace windows, fire-protecting lining in nuclear plants due to the low density and the capability of absorbing neutrons, substrates for catalytic convertors, and electronic devices (Fischer and Schneider 2005; 2008a, Li and Chang 2006, Peng et al. 2006, Tang et al. 2006, Zhang et al. 2006, Tao et al. 2007, Wei et al. 2007). Among those, mullite (Al₂(Al_{2+2x}Si_{2-2x})O_{10-x} with $\approx 0.2 < x < \approx 0.9$ and B₂O₃ = 0) (Saalfeld and Guse 1981, Angel et al. 1991, Schneider and Komarneni 2005) is doubtless of great importance. Several

studies have been devoted to the stability fields, solubility and crystal-chemistry of the compounds belonging to the ternary system $\text{Al}_2\text{O}_3\text{-B}_2\text{O}_3\text{-SiO}_2$ (Baumann and Moore 1942, Letort 1952, Dietzel and Scholze 1955, Scholze 1956, Gielisse and Forster 1962, Kim and Hummel 1962, Capponi et al. 1972, Reynaud 1977, Sokolova et al. 1978, Werding and Schreyer 1984; 1992; 1996, Rymon-Lipinski et al. 1985, Mazza et al. 1992, Peacor et al. 1999, Fischer and Schneider 2005; 2008a, Buick et al. 2008, Fischer et al. 2008b, Grew et al. 2008, Griesser et al. 2008). In their recent review paper on crystal-chemistry of borosilicates with mullite-type structures, Fischer and Schneider (2008a) described the structural relationship in the $\text{Al}_2\text{O}_3\text{-B}_2\text{O}_3\text{-SiO}_2$ compounds, showing that all boron-mullites can be derived from a hypothetical aristotype with topological symmetry $P4/mbm$, in which the main building block is represented by chains of edge-sharing MO_6 octahedra running along [001].

Thermo-elastic behavior and pressure (P) and temperature (T) structural evolution of aluminosilicates along the joint $\text{Al}_2\text{O}_3\text{-SiO}_2$ have been extensively investigated by Brillouin spectroscopy (Vaughan and Weidner 1978) and by in-situ X-ray/neutron single-crystal/powder diffraction (Brace et al. 1969, Winter and Ghose 1979, Ralph et al. 1984, Schneider and Eberhard 1990, Comodi et al. 1997, Yang et al. 1997a;b, Brunauer et al. 2001b, Friedrich et al. 2004, Burt et al. 2006, Gatta et al. 2006b). The P/T -induced main deformation mechanisms were described on the basis of in-situ HP/HT -structure refinements. For $2\text{Al}_2\text{O}_3\text{:SiO}_2$ mullite, a full description of the elastic properties (i.e. stiffness coefficients (c_{ij}), elastic compliances (s_{ij}), Young's moduli (E_{ij}), Poisson's ratios (ν_{ij}), bulk modulus (K) and shear modulus (G)) was reported by Hildmann et al. (2001) by single-crystal resonant ultrasound spectroscopy (RUS); Temperature derivatives of the elastic constants between -170°C and 1400°C were later derived by Schreuer et al. (2006) by single-crystal RUS. The elastic constants and their T -derivatives of $2.5\text{Al}_2\text{O}_3\text{:SiO}_2$ mullite have been reported by Kriven et al. (1999) and Palko et al. (2002) by Brillouin spectroscopy. In contrast, no elastic data are available for borosilicate or borosilicates.

Aim of the present study was to investigate the elastic behavior and P -induced structural evolution of a borosilicate by means of in-situ single-crystal X-ray diffraction, with a diamond anvil cell, in order to elucidate the role of boron on the elastic features of mullite-type materials. We selected the " Al_5BO_9 " compound for this first HP -experiment. Two slightly different compositions of the investigated compound are present in literature: Baumann and Moore (1942), Ihara et al. (1980) and Garsche et al. (1991) interpreted the material as $9\text{Al}_2\text{O}_3\text{:}2\text{B}_2\text{O}_3$ ($\text{Al}_{4.91}\text{B}_{1.09}\text{O}_9$, $Z = 4$, commonly cited as $\text{Al}_{18}\text{B}_4\text{O}_{33}$), whereas Sokolova et al. (1978) concluded the compound to consist of $10\text{Al}_2\text{O}_3\text{:}2\text{B}_2\text{O}_3$ (Al_5BO_9 , $Z = 4$). In $\text{Al}_{18}\text{B}_4\text{O}_{33}$, 9% of aluminum tetrahedra are substituted by four-fold coordinated boron. In Al_5BO_9 , boron is only present on a three-fold coordinated site. In this study, test single-crystal X-ray refinements with boron constraint to the three-fold coordinated site were superior to refinements with excess boron according to $\text{Al}_{4.91}\text{B}_{1.09}\text{O}_9$. For this reason, the investigated compound is here referred to as " Al_5BO_9 ".

Sokolova et al. (1978) described the structure in space group $Cmc2_1$ ($a = 5.6673(7)$ Å, $b = 15.011(2)$ Å, $c = 7.693(1)$ Å), consisting of mullite-type octahedral chains (in this set running along [100]), linked by edge-sharing AlO₅ bipyramids alternating with AlO₄ tetrahedra and BO₃ triangular units (Figure 7.1). In their classification of mullite-type materials, Fischer and Schneider (2008a) assigned this compound to the "MUL-VIII.33, $Bb2_1m$: A9B2" group, together with Al₁₈B₄O₃₃, Al₉BSi₂O₁₉ (boromullite) and Al_{16.6}Cr_{1.4}B₄O₃₃. Due to the structural homologies with mullite, the authors considered the terms "boron-mullite" and "B-mullite" as appropriate for "Al₅BO₉". Garsche et al. (1991) showed that Cr³⁺ can replace Al³⁺ at the octahedral site in Al₁₈B₄O₃₃ up to about 10 wt.-% Cr₂O₃. A further Al₅BO₉ structural model was reported by Mazza et al. (1992), with a pseudo-tetragonal unit-cell ($a \approx b \approx 7.6$ Å and $c \approx 2.8$ Å) in space group $Pbam$. This compound is supposed to be metastable and transforms to equilibrium phase upon heating Fischer and Schneider (2008a).

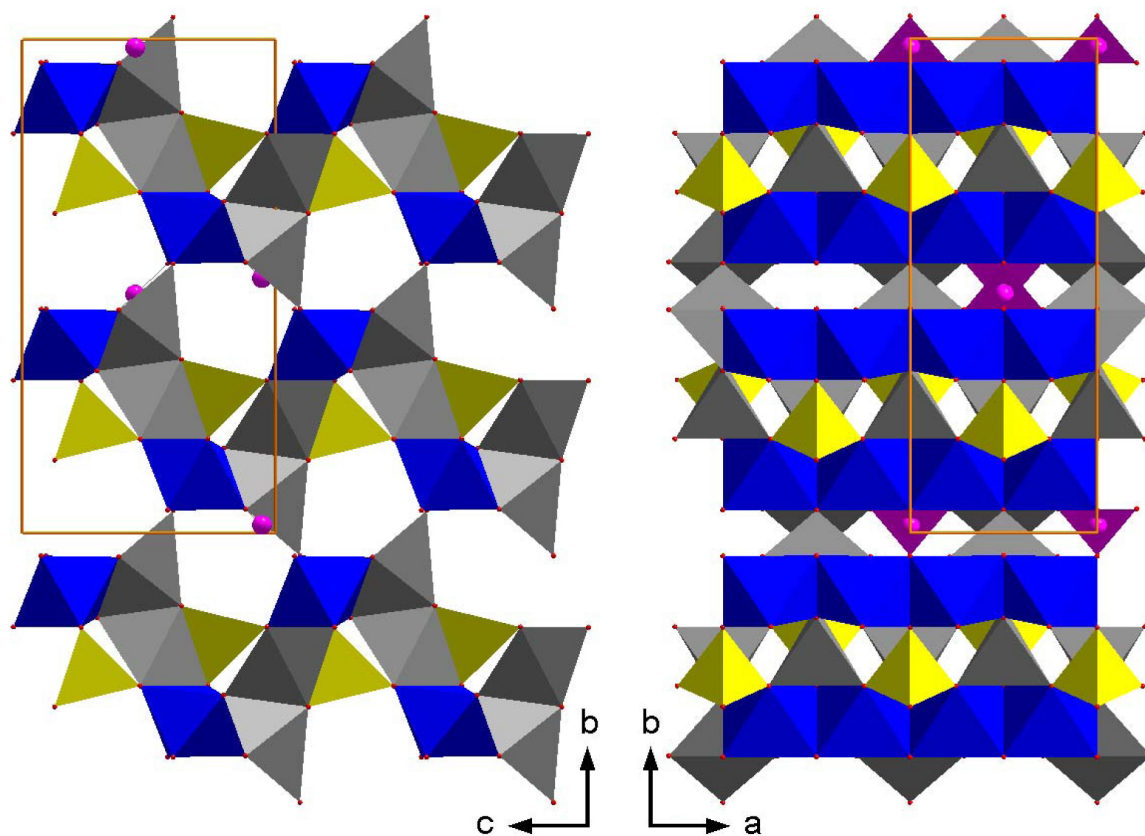


Figure 7.1: The crystal-structure of "Al₅BO₉" viewed down [100] (left) and down [001] (right) in $Cmc2_1$. Octahedra are represented in blue, distorted bipyramidal polyhedra in gray, tetrahedra in yellow and triangular BO₃ units in purple (purple spheres represent the B-sites). The edge-sharing octahedral chains running along [100] are well evident (right), as well as the distorted 5-membered rings of polyhedra forming the voids (left).

7.3 Experimental Methods

"Al₅BO₉" crystals were synthesized by slow cooling of a starting mixture in a flux consisting of 0.50 g K₂CO₃ and 1.56 g MoO₃ corresponding to 1 K₂CO₃ + 3 MoO₃ → K₂Mo₃O₁₀ + CO₂↑. The starting mixture was composed of Al₂O₃ and B₂O₃ mixed in a molar ratio of 9:2 (0.03 g B₂O₃ and 0.19 g Al₂O₃). All compounds were ground for 10 min in an agate mortar and placed in a lid-covered platinum crucible. The mixture was heated to 800°C at a gradient of 100°C/h and then further heated to 1100°C at a rate of 50°C/h. After 2h at 1100°C, the melt was slowly cooled down to 600°C at 10°C/h.

Separation of the whitish, half-transparent crystals from yellowish flux was done by soaking the melt in hot water. Yield was about 0.1 g of radially grown aggregates of needle-like crystals with a maximum size of about 0.2·0.2·0.8 mm³.

One platy crystal (180·140·60 μm³), free of defects or twinning under the transmitting polarized light microscope, was selected for X-ray diffraction experiments. Diffraction data were first collected at room conditions with an Oxford Diffraction–Xcalibur diffractometer equipped with CCD, using graphite monochromatized MoKα-radiation, operated at 50 kV and 40 mA. A combination of ω/φ scans was used in order to maximize the reciprocal space coverage and redundancy, with a scan width of 0.4° and an exposure time of 30 s/frame (Table 7.1). The distance between the crystal and the detector was 80 mm. 7265 Bragg reflections were collected in the range 2 < 2θ < 70° 2θ, of which 1302 were unique and 926 with $I > 4\sigma(I)$ (Table 7.1). The diffraction pattern was fully indexed with an orthorhombic lattice with $a = 5.678(2)$ Å, $b = 15.015(4)$ Å and $c = 7.700(3)$ Å, in agreement with the experimental findings of Sokolova et al. (1978) for Al₅BO₉. Integrated intensities were then corrected for Lorentz-polarization (Lp) and for absorption effects (by Gaussian integration based upon the shape and dimensions of the crystal), using the CrysAlis package (Oxford Diffraction Ltd. 2005). After corrections, the discrepancy factor among symmetry-related reflections (Laue class *mmm*) was $R(\text{int}) = 0.074$ (Table 7.1) and reflection conditions were consistent with space group *Cmc*2₁, as reported by Sokolova et al. (1978). The anisotropic structural refinement was then performed using the SHELX-97 software (Sheldrick 1997), starting from atomic coordinates of Sokolova et al. (1978). The refined Flack parameter (Sheldrick 1997) was 0 within 1σ(x). Neutral atomic scattering factors of B, Al and O from the International Tables for Crystallography (Wilson and Prince 1999) were used. No peak larger than +0.82/-0.61 e⁻/Å³ was present in the final difference-Fourier synthesis and the variance-covariance matrix showed no significant correlation between refined parameters. Further details pertaining to the structural refinement at ambient conditions are reported in Tables 7.1 and 7.2–7.13.

An ETH-type diamond anvil cell (DAC) (Miletich et al. 2000) was used to perform the in-situ high-pressure experiment. 250 μm thick T301 steel foil was used as gasket, which was pre-indented to a thickness of about 110 μm before drilling a 300 μm hole by spark-erosion. The crystal of "Al₅BO₉" already measured at ambient conditions was placed into the gasket hole together with a single-crystal of quartz for pressure calibration (Angel et al. 1997).

Table 7.1: Details pertaining to the data collections and refinements of "Al₅BO₉" at different pressures.

<i>P</i> (GPa)	0.0001	<i>P</i> ₀ : 0.0001 ^a	<i>P</i> ₁ : 0.15(5)	<i>P</i> ₂ : 0.91(4)	<i>P</i> ₃ : 1.99(6)	<i>P</i> ₄ : 3.32(6)	<i>P</i> ₅ : 4.78(6)	<i>P</i> ₆ : 5.83(5)	<i>P</i> ₇ : 5.99(5)	<i>P</i> ₈ : 6.45(6)
Diffractometer	Xcalibur CCD									
X-ray radiation	MoK α	MoK α	MoK α	MoK α	MoK α	MoK α	MoK α	MoK α	MoK α	MoK α
Scan type	ω/ϕ	ω/ϕ	ω/ϕ	ω/ϕ	ω/ϕ	ω/ϕ	ω/ϕ	ω/ϕ	ω/ϕ	ω/ϕ
Scan width ($^\circ$ /fr.)	0.4	0.4	0.4	0.4	0.4	0.4	0.4	0.4	0.4	0.4
Exposure (s/fr.)	30	30	30	30	30	30	30	30	30	30
Temperature (K)	298	298	298	298	298	298	298	298	298	298
Space Group	<i>Cm</i> c2 ₁	<i>Cm</i> c2 ₁	<i>Cm</i> c2 ₁	<i>Cm</i> c2 ₁	<i>Cm</i> c2 ₁	<i>Cm</i> c2 ₁	<i>Cm</i> c2 ₁	<i>Cm</i> c2 ₁	<i>Cm</i> c2 ₁	<i>Cm</i> c2 ₁
<i>a</i> -axis (Å)	5.678(2)	5.680(3)	5.677(3)	5.668(4)	5.662(4)	5.655(4)	5.648(4)	5.639(4)	5.641(2)	5.639(4)
<i>b</i> -axis (Å)	15.015(4)	15.02(60)	15.020(50)	14.990(30)	14.940(30)	14.860(30)	14.790(20)	14.760(40)	14.760(30)	14.730(30)
<i>c</i> -axis (Å)	7.700(3)	7.698(2)	7.694(4)	7.683(6)	7.669(6)	7.652(7)	7.644(7)	7.635(17)	7.626(5)	7.618(7)
Volume	656.5(4)	657(3)	656(2)	652.8(15)	648.7(15)	643.0(15)	638.5(11)	635(2)	635.0(14)	632.8(15)
<i>Z</i>	4	4	4	4	4	4	4	4	4	4
Maximum 2 θ ($^\circ$)	70.02	77.99	78.02	78.40	78.02	77.07	77.60	75.61	78.09	77.37
Measured refl.	7265	1672	1421	1570	1580	1659	1641	1613	1609	1279
Unique refl.	1302	411	503	603	585	600	555	538	534	463
Ref. > 4 σ (<i>I</i>)	926	311	350	361	357	401	402	383	385	307
<i>R</i> (int)	0.0739	0.1011	0.1007	0.1315	0.1163	0.1260	0.1131	0.1199	0.0952	0.1009
L.S. parameters	82	31	30	30	30	30	30	30	30	30
<i>R</i> ₁ , <i>I</i> > 4 σ (<i>I</i>)	0.0444	0.0753	0.0845	0.0866	0.0919	0.1098	0.1089	0.1020	0.1182	0.1187
<i>wR</i> ₂	0.0821	0.1109	0.1181	0.1270	0.1268	0.1417	0.1305	0.1313	0.1437	0.1320
Goof	1.001	1.274	1.084	1.008	1.041	1.220	1.252	1.215	1.367	1.223

^awith the crystal in the DAC without *P*-medium

$$R(\text{int}) = \frac{\sum |F_{\text{obs}}^2 - \langle F_{\text{obs}}^2 \rangle| / \sum (F_{\text{obs}}^2)}{\sum |F_{\text{calc}}| - |F_{\text{calc}}|} / \sum |F_{\text{obs}}|, \quad wR2 = \sqrt{\frac{\sum (w(F_{\text{obs}}^2 - F_{\text{calc}}^2)^2)}{\sum (w(F_{\text{obs}}^2)^2)}},$$

$$w = 1 / (\sigma^2(F_{\text{obs}}^2) + (0.02P)^2), \quad P = (\text{Max}(F_{\text{obs}}^2, 0) + 2F_{\text{calc}}^2) / 3$$

A methanol:ethanol mixture (4:1) was used as hydrostatic pressure-transmitting medium (Angel et al. 2007). Intensity data collections at 0.0001 GPa (crystal in DAC without any pressure medium, P_0), 0.15(5) (P_1), 0.91(5) (P_2), 1.99(6) (P_3), 3.32(6) (P_4), 4.78(6) (P_5), 5.83(5) (P_6), 5.99(5) (P_7) and 6.45(6) (P_8) GPa (Table 7.1) were performed adopting the same experimental set-up and data collection protocol used with the crystal in air (Table 7.1). At any given pressure, integrated intensity data were corrected for L_p and absorption effects due to the crystal and the DAC using the ABSORB 5.2 computer program (Burnham 1966, Angel 2002). No violation of reflection conditions dictated by space group $Cmc2_1$ was observed within the investigated P -range. The structure refinements were conducted using soft geometrical restraints aimed to restrain Al-O and B-O distances to those obtained at room-pressure in air, with an estimated standard deviation of ± 0.04 Å. This improved the stability of the HP-refinements, as soft restraints act as if they were additional experimental observations (Sheldrick 1997, Gatta et al. 2006a; 2008). In order to reduce the number of refined variables, isotropic displacement parameters were refined by grouping all of the Al-sites and all of the O-sites. Refined atomic positions and displacement parameters are reported in Tables 7.2–7.13. Bond distances and angles are listed in Appendix A.3. At 7.4 GPa, the gasket hole collapsed and the "Al₅BO₉" crystal was incidentally broken. Unit-cell constants measured at ambient conditions after decompression using a small fragment of the "Al₅BO₉" crystal (60·40·30 μm) recovered from the gasket hole showed that P -induced structural changes up to 7.4 GPa are completely reversible.

7.4 Elastic Behavior

The monotonic variation of "Al₅BO₉" unit-cell parameters with pressure is shown in Figure 7.2. No evidence of phase-transition or change in the compressional behavior were observed within the investigated pressure-range. The elastic behavior of "Al₅BO₉" is here described with a truncated second-order Birch-Murnaghan Equation-of-State (II-BM-EoS) (Birch 1947). This EoS is based upon the assumption that the high-pressure strain energy in a solid can be expressed as a Taylor series in the Eulerian finite strain, defined as

$$f_E = \frac{1}{2} \cdot \sqrt[3]{\left(\frac{V_0}{V}\right)^2} - 1$$

where V_0 and V represent the unit-cell volume at ambient and HP conditions, respectively. Expansion in the Eulerian strain polynomial has the following form:

$$P(f_E) = 3 \cdot K_{T0} \cdot f_E \cdot \sqrt[5]{(1 + 2 \cdot f_E)^2} \cdot \left\{ 1 + \frac{3}{2} \cdot (K' - 4) \cdot f_E + \frac{3}{2} \cdot \left[K_{T0} \cdot K'' + (K' - 4) \cdot (K' - 3) + \frac{35}{9} \right] \cdot f_E^2 + \dots \right\}$$

where K_{T0} represents the bulk modulus ($K_{T0} = -V_0(\delta P/\delta V)_{P=0} = 1/\beta V_0$, where βV_0 is the volume compressibility coefficient at ambient conditions), K' and K'' represent its pressure

derivatives ($K' = \delta K_0 / \delta P$; $K'' = \delta^2 K_0 / \delta P^2$). Fitting the P - V data with a truncated second-order (in energy) BM-EoS with the EOS-FIT 5.2 program (Angel 2001), using the data weighted by the uncertainties in P and V , we obtain: $V_0 = 656.4(3) \text{ \AA}^3$, $K_{T0} = 165(7) \text{ GPa}$ ($\beta_{V0} = 0.0061(3) \text{ GPa}^{-1}$), and $K' = 4$ (fixed). A fitting with a third-order BM-EoS leads to a strong correlation between the refined parameters (especially K_{T0} and K'), with worse fitting statistic parameters.

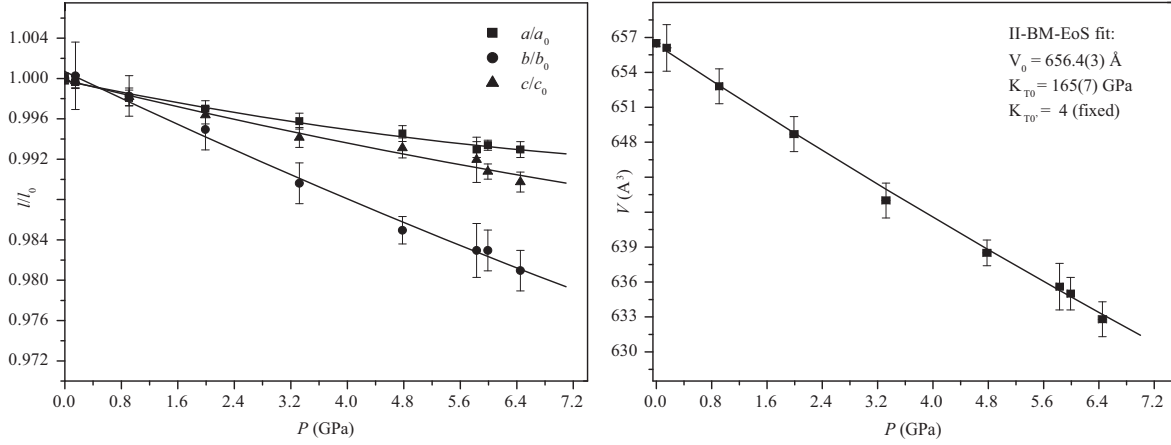


Figure 7.2: Evolution of the unit-cell parameters of "Al₅BO₉" with pressure. For the unit-cell lengths, the solid lines represent polynomial regression curves through the data points. For the unit-cell volume, the second-order Birch-Murnaghan Equation-of-State fit is shown.

The evolution of Eulerian finite strain vs. normalized stress ($F_E = P/[3f_E \sqrt{(1+2f_E)^2}]$) (Angel 2000) is shown in Figure 7.3. The weighted linear regression through the data points leads to: $F_E(0) = 159(11) \text{ GPa}$. The almost horizontal regression function confirms that the use of a truncated second-order BM-EoS is appropriate to describe the elastic behavior of "Al₅BO₉" within the P -range investigated. The value of the normalized stress extrapolated at ambient conditions ($F_E(0)$) and the bulk modulus (K_{T0}) refined on the basis of the BM-EoS are in good agreement.

The axial compressibility coefficients ($\beta_j = 1/l_{0j} \cdot (\delta l_j / \delta P)$, where l_{0j} ($j = a, b, c$) is the length of the unit-cell edges under room conditions) were calculated by weighted polynomial regressions through the data points, yielding to:

$$\begin{aligned} a/a_0 &= 1 - 0.0014(2) \cdot P + 6(3) \cdot 10^{-5} \cdot P^2 \quad (R^2 = 0.9906), \\ b/b_0 &= 1 - 0.0034(4) \cdot P + 5(6) \cdot 10^{-5} \cdot P^2 \quad (R^2 = 0.6647), \\ c/c_0 &= 1 - 0.0017(3) \cdot P + 4(5) \cdot 10^{-5} \cdot P^2 \quad (R^2 = 0.9855), \end{aligned}$$

with $\beta_a = 1.4(2) \cdot 10^{-3} \text{ GPa}^{-1}$, $\beta_b = 3.4(4) \cdot 10^{-3} \text{ GPa}^{-1}$, $\beta_c = 1.7(3) \cdot 10^{-3} \text{ GPa}^{-1}$ ($\beta_a:\beta_b:\beta_c = 1:2.43:1.21$).

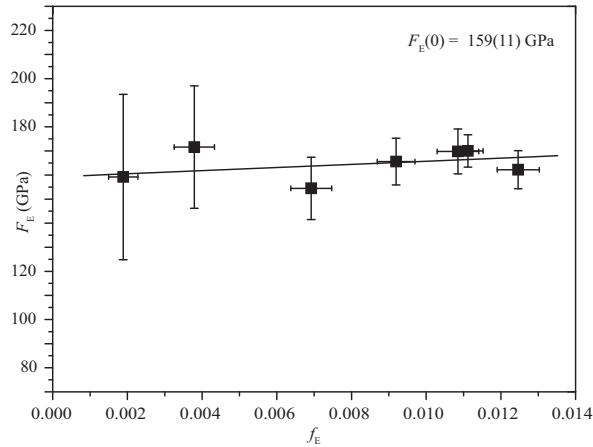


Figure 7.3: Eulerian finite (f_E) strain vs. normalized stress (F_E) plot. The weighted linear regression through the data points is shown.

7.5 Structural Evolution with Pressure

The single-crystal structural refinement of "Al₅BO₉" at room conditions confirms the structure model previously reported by Sokolova et al. (1978). Among the boroaluminosilicates, the topology of the "Al₅BO₉" structure is unique, although several structural homologies can be found with the mullite and mullite-type materials (e.g. sillimanite). In particular, the main building units are represented by edge-sharing octahedral chains linked by edge-sharing AlO₅ bipyramids alternating with AlO₄ tetrahedra, forming small cavities that host boron coordinated by three framework oxygens (BO₃ triangular units), as shown in Figure 7.1. In the structural model of Sokolova et al. (1978) used in this study (i.e. space group *Cmc*2₁ with $a \approx 5.67$ Å, $b \approx 15.01$ Å, $c \approx 7.69$ Å), octahedral chains run parallel to [100]. Atomic positions, bond-distances and angles refined in this study at room conditions agree with those previously reported (Tables 7.2–7.13). Bond-distances and angles show that octahedra, forming the [100]-chains, and the tetrahedra are not regular (octahedron: $\langle \text{Al1-O} \rangle_{\text{oct}} = 1.903$ Å and $\Delta(\text{Al1-O})_{\text{max}} = 0.116$ Å; Tetrahedron: $\langle \text{Al4-O} \rangle_{\text{tet}} = 1.753$ Å and $\Delta(\text{Al4-O})_{\text{max}} = 0.041$ Å). The two bipyramidal units are strongly distorted (i.e. $\Delta(\text{Al2-O})_{\text{max}} = 0.418$ Å and $\Delta(\text{Al3-O})_{\text{max}} = 0.516$ Å). The BO₃ triangular unit is almost regular, with $\text{B-O}_{\text{max}} = 1.382(4)$ Å and $\text{B-O}_{\text{min}} = 1.372(6)$ Å (i.e. $\Delta(\text{B-O})_{\text{max}} = 0.010$ Å).

Table 7.2: Atomic positions and isotropic displacement parameters of Al1 at different pressure.

Site	P (GPa)	x	y	z	$U_{\text{eq.}}/U_{\text{iso}}^{\text{b}}$ (\AA^2)
Al1	0.0001	0.2519(2)	0.11653(6)	0.3336(2)	0.0069(2)
8b ^c	P_0^{a}	0.2513(4)	0.1155(8)	0.3337(4)	0.0072(4)
	P_1	0.2521(3)	0.1171(6)	0.3343(4)	0.0079(4)
	P_2	0.2521(4)	0.1167(4)	0.3304(5)	0.0082(4)
	P_3	0.2513(4)	0.1164(4)	0.3326(6)	0.0086(4)
	P_4	0.2528(5)	0.1174(4)	0.3325(5)	0.0090(5)
	P_5	0.2520(5)	0.1171(4)	0.3328(6)	0.0086(4)
	P_6	0.2518(5)	0.1171(4)	0.3333(6)	0.0081(4)
	P_7	0.2524(6)	0.1172(5)	0.3325(7)	0.0084(5)
	P_8	0.2517(7)	0.1160(6)	0.3326(7)	0.0077(5)

^awith the crystal in the DAC without pressure medium^b $U_{\text{eq.}}$ from anisotropic refinements with the crystal in air (0.0001 GPa), U_{iso} for isotropic refinements^cWyckoff position**Table 7.3:** Atomic positions and isotropic displacement parameters of Al2 at different pressure.

Site	P (GPa)	x	y	z	$U_{\text{eq.}}/U_{\text{iso}}^{\text{b}}$ (\AA^2)
Al2	0.0001	0.0	0.25515(9)	0.5199(2)	0.0096(4)
4a ^c	P_0^{a}	0.0	0.2590(8)	0.5208(5)	0.0072(4)
	P_1	0.0	0.2547(6)	0.5216(6)	0.0079(4)
	P_2	0.0	0.2552(5)	0.5216(6)	0.0082(4)
	P_3	0.0	0.2561(4)	0.5198(6)	0.0086(4)
	P_4	0.0	0.2556(5)	0.5207(7)	0.0090(5)
	P_5	0.0	0.2546(5)	0.5214(7)	0.0086(4)
	P_6	0.0	0.2553(5)	0.5200(7)	0.0081(4)
	P_7	0.0	0.2554(5)	0.5210(8)	0.0084(5)
	P_8	0.0	0.2551(6)	0.5199(8)	0.0077(5)

^awith the crystal in the DAC without pressure medium^b $U_{\text{eq.}}$ from anisotropic refinements with the crystal in air (0.0001 GPa), U_{iso} for isotropic refinements^cWyckoff position**Table 7.4:** Atomic positions and isotropic displacement parameters of Al3 at different pressure.

Site	P (GPa)	x	y	z	$U_{\text{eq.}}/U_{\text{iso}}^{\text{b}}$ (\AA^2)
Al3	0.0001	0.0	0.44410(9)	0.5156(2)	0.0075(3)
4a ^c	P_0^{a}	0.0	0.4444(8)	0.5151(5)	0.0072(4)
	P_1	0.0	0.4456(6)	0.5140(5)	0.0079(4)
	P_2	0.0	0.4457(5)	0.5134(6)	0.0082(4)
	P_3	0.0	0.4457(5)	0.5152(6)	0.0086(4)
	P_4	0.0	0.4453(5)	0.5188(7)	0.0090(5)
	P_5	0.0	0.4445(5)	0.5162(8)	0.0086(4)
	P_6	0.0	0.4443(5)	0.5170(8)	0.0081(4)
	P_7	0.0	0.4458(6)	0.5189(8)	0.0084(5)
	P_8	0.0	0.4465(6)	0.5202(9)	0.0077(5)

^awith the crystal in the DAC without pressure medium^b $U_{\text{eq.}}$ from anisotropic refinements with the crystal in air (0.0001 GPa), U_{iso} for isotropic refinements^cWyckoff position

Table 7.5: Atomic positions and isotropic displacement parameters of Al4 at different pressure.

Site	P (GPa)	x	y	z	$U_{\text{eq.}}/U_{\text{iso}}^{\text{b}}$ (\AA^2)
Al4	0.0001	0.0	0.29682(9)	0.1677(2)	0.0084(4)
4a ^c	P_0^{a}	0.0	0.2966(7)	0.1676(5)	0.0072(4)
	P_1	0.0	0.2966(6)	0.1675(5)	0.0079(4)
	P_2	0.0	0.2954(5)	0.1667(6)	0.0082(4)
	P_3	0.0	0.2980(5)	0.1677(6)	0.0086(4)
	P_4	0.0	0.2965(5)	0.1677(6)	0.0090(5)
	P_5	0.0	0.2969(5)	0.1667(7)	0.0086(4)
	P_6	0.0	0.2973(5)	0.1658(7)	0.0081(4)
	P_7	0.0	0.2976(6)	0.1658(8)	0.0084(5)
	P_8	0.0	0.2979(7)	0.1677(8)	0.0077(5)

^awith the crystal in the DAC without pressure medium^b $U_{\text{eq.}}$ from anisotropic refinements with the crystal in air (0.0001 GPa), U_{iso} for isotropic refinements^cWyckoff position**Table 7.6:** Atomic positions and isotropic displacement parameters of B1 at different pressure.

Site	P (GPa)	x	y	z	$U_{\text{eq.}}/U_{\text{iso}}^{\text{b}}$ (\AA^2)
B1	0.0001	0.0	0.0164(4)	0.0542(7)	0.0112(14)
4a ^c	P_0^{a}	0.0	0.0201(17)	0.0549(13)	0.004(3)
	P_1	0.0	0.0176(15)	0.0542(13)	0.0079(4)
	P_2	0.0	0.0193(14)	0.0515(16)	0.0082(4)
	P_3	0.0	0.0209(14)	0.0482(17)	0.0086(4)
	P_4	0.0	0.0166(15)	0.0513(18)	0.0090(5)
	P_5	0.0	0.0177(15)	0.0555(19)	0.0086(4)
	P_6	0.0	0.0176(15)	0.0529(19)	0.0081(4)
	P_7	0.0	0.0186(17)	0.052(2)	0.0084(5)
	P_8	0.0	0.0173(17)	0.048(2)	0.0077(5)

^awith the crystal in the DAC without pressure medium^b $U_{\text{eq.}}$ from anisotropic refinements with the crystal in air (0.0001 GPa), U_{iso} for isotropic refinements^cWyckoff position**Table 7.7:** Atomic positions and isotropic displacement parameters of O1 at different pressure.

Site	P (GPa)	x	y	z	$U_{\text{eq.}}/U_{\text{iso}}^{\text{b}}$ (\AA^2)
O1	0.0001	0.0	0.3285(2)	0.7049(5)	0.0090(8)
4a ^c	P_0^{a}	0.0	0.3289(16)	0.700(1)	0.0082(6)
	P_1	0.0	0.3266(12)	0.7027(10)	0.0085(6)
	P_2	0.0	0.3262(10)	0.7016(11)	0.0068(7)
	P_3	0.0	0.3290(9)	0.6994(12)	0.0082(7)
	P_4	0.0	0.3265(10)	0.7008(14)	0.0083(8)
	P_5	0.0	0.3285(10)	0.7049(14)	0.0079(7)
	P_6	0.0	0.3308(10)	0.7014(14)	0.0067(7)
	P_7	0.0	0.3254(12)	0.7026(16)	0.0065(8)
	P_8	0.0	0.3238(13)	0.6990(16)	0.0036(8)

^awith the crystal in the DAC without pressure medium^b $U_{\text{eq.}}$ from anisotropic refinements with the crystal in air (0.0001 GPa), U_{iso} for isotropic refinements^cWyckoff position

Table 7.8: Atomic positions and isotropic displacement parameters of O2 at different pressure.

Site	P (GPa)	x	y	z	$U_{\text{eq.}}/U_{\text{iso}}^{\text{b}}$ (\AA^2)
O2	0.0001	0.2558(4)	0.19016(15)	0.5345(3)	0.0073(6)
8b ^c	P_0^{a}	0.2564(7)	0.1914(13)	0.5330(7)	0.0082(6)
	P_1	0.2566(8)	0.1882(10)	0.5345(7)	0.0085(6)
	P_2	0.2566(9)	0.1918(7)	0.5339(7)	0.0068(7)
	P_3	0.2567(9)	0.1908(7)	0.5335(8)	0.0082(7)
	P_4	0.2590(11)	0.1895(7)	0.5343(8)	0.0083(8)
	P_5	0.2566(10)	0.1905(7)	0.5308(9)	0.0079(7)
	P_6	0.2549(10)	0.1903(7)	0.5311(9)	0.0067(7)
	P_7	0.2582(12)	0.1891(8)	0.5337(9)	0.0065(8)
	P_8	0.2578(12)	0.1901(9)	0.5321(9)	0.0036(8)

^awith the crystal in the DAC without pressure medium^b $U_{\text{eq.}}$ from anisotropic refinements with the crystal in air (0.0001 GPa), U_{iso} for isotropic refinements^cWyckoff position**Table 7.9:** Atomic positions and isotropic displacement parameters of O3 at different pressure.

Site	P (GPa)	x	y	z	$U_{\text{eq.}}/U_{\text{iso}}^{\text{b}}$ (\AA^2)
O3	0.0001	0.0	0.4541(2)	0.9045(5)	0.0086(8)
4a ^c	P_0^{a}	0.0	0.4535(15)	0.9073(10)	0.0082(6)
	P_1	0.0	0.4534(11)	0.9060(9)	0.0085(6)
	P_2	0.0	0.454(1)	0.9086(13)	0.0068(7)
	P_3	0.0	0.4554(8)	0.9062(14)	0.0082(7)
	P_4	0.0	0.4554(9)	0.9033(15)	0.0083(8)
	P_5	0.0	0.4536(9)	0.9100(16)	0.0079(7)
	P_6	0.0	0.4550(9)	0.9101(17)	0.0067(7)
	P_7	0.0	0.4561(11)	0.9008(17)	0.0065(8)
	P_8	0.0	0.4553(12)	0.9021(18)	0.0036(8)

^awith the crystal in the DAC without pressure medium^b $U_{\text{eq.}}$ from anisotropic refinements with the crystal in air (0.0001 GPa), U_{iso} for isotropic refinements^cWyckoff position**Table 7.10:** Atomic positions and isotropic displacement parameters of O4 at different pressure.

Site	P (GPa)	x	y	z	$U_{\text{eq.}}/U_{\text{iso}}^{\text{b}}$ (\AA^2)
O4	0.0001	0.0	0.0465(2)	0.4250(5)	0.0096(8)
4a ^c	P_0^{a}	0.0	0.0434(14)	0.4261(11)	0.0082(6)
	P_1	0.0	0.0457(10)	0.4245(10)	0.0085(6)
	P_2	0.0	0.0477(8)	0.4260(13)	0.0068(7)
	P_3	0.0	0.0465(8)	0.4243(13)	0.0082(7)
	P_4	0.0	0.0468(8)	0.4194(16)	0.0083(8)
	P_5	0.0	0.0445(9)	0.4232(16)	0.0079(7)
	P_6	0.0	0.0463(8)	0.4246(16)	0.0067(7)
	P_7	0.0	0.0458(10)	0.4204(18)	0.0065(8)
	P_8	0.0	0.0480(11)	0.4180(19)	0.0036(8)

^awith the crystal in the DAC without pressure medium^b $U_{\text{eq.}}$ from anisotropic refinements with the crystal in air (0.0001 GPa), U_{iso} for isotropic refinements^cWyckoff position

Table 7.11: Atomic positions and isotropic displacement parameters of O5 at different pressure.

Site	P (GPa)	x	y	z	$U_{\text{eq.}}/U_{\text{iso}}^{\text{b}}$ (\AA^2)
O5	0.0001	0.0	0.3522(2)	0.3716(5)	0.0090(8)
4a ^c	P_0^{a}	0.0	0.348(2)	0.3721(9)	0.0082(6)
	P_1	0.0	0.3475(14)	0.3706(8)	0.0085(6)
	P_2	0.0	0.3503(11)	0.3738(10)	0.0068(7)
	P_3	0.0	0.3504(10)	0.3722(10)	0.0082(7)
	P_4	0.0	0.3516(11)	0.3692(11)	0.0083(8)
	P_5	0.0	0.3521(12)	0.3672(12)	0.0079(7)
	P_6	0.0	0.3534(12)	0.3712(12)	0.0067(7)
	P_7	0.0	0.3505(13)	0.3663(13)	0.0065(8)
	P_8	0.0	0.3530(16)	0.3698(13)	0.0036(8)

^awith the crystal in the DAC without pressure medium^b $U_{\text{eq.}}$ from anisotropic refinements with the crystal in air (0.0001 GPa), U_{iso} for isotropic refinements^cWyckoff position**Table 7.12:** Atomic positions and isotropic displacement parameters of O6 at different pressure.

Site	P (GPa)	x	y	z	$U_{\text{eq.}}/U_{\text{iso}}^{\text{b}}$ (\AA^2)
O6	0.0001	0.0	0.1911(2)	0.2671(5)	0.0076(8)
4a ^c	P_0^{a}	0.0	0.1908(17)	0.2687(10)	0.0082(6)
	P_1	0.0	0.1912(13)	0.2668(10)	0.0085(6)
	P_2	0.0	0.1933(10)	0.2667(11)	0.0068(7)
	P_3	0.0	0.1903(10)	0.2654(11)	0.0082(7)
	P_4	0.0	0.1898(11)	0.2626(13)	0.0083(8)
	P_5	0.0	0.1907(11)	0.2674(13)	0.0079(7)
	P_6	0.0	0.1904(11)	0.2658(13)	0.0067(7)
	P_7	0.0	0.1910(12)	0.2641(15)	0.0065(8)
	P_8	0.0	0.1933(13)	0.2628(16)	0.0036(8)

^awith the crystal in the DAC without pressure medium^b $U_{\text{eq.}}$ from anisotropic refinements with the crystal in air (0.0001 GPa), U_{iso} for isotropic refinements^cWyckoff position**Table 7.13:** Atomic positions and isotropic displacement parameters of O7 at different pressure.

Site	P (GPa)	x	y	z	$U_{\text{eq.}}/U_{\text{iso}}^{\text{b}}$ (\AA^2)
O7	0.0001	0.2110(5)	0.04838(16)	0.1183(3)	0.0097(6)
8b ^c	P_0^{a}	0.2113(9)	0.0540(13)	0.1187(6)	0.0082(6)
	P_1	0.2105(8)	0.050(1)	0.1193(6)	0.0085(6)
	P_2	0.2106(8)	0.0491(8)	0.1201(7)	0.0068(7)
	P_3	0.2130(8)	0.0479(7)	0.1192(9)	0.0082(7)
	P_4	0.2112(9)	0.0472(7)	0.1216(8)	0.0083(8)
	P_5	0.2124(9)	0.0494(7)	0.1172(10)	0.0079(7)
	P_6	0.2124(10)	0.0489(7)	0.1188(10)	0.0067(7)
	P_7	0.2119(10)	0.0479(8)	0.1220(9)	0.0065(8)
	P_8	0.2117(10)	0.0478(10)	0.1223(9)	0.0036(8)

^awith the crystal in the DAC without pressure medium^b $U_{\text{eq.}}$ from anisotropic refinements with the crystal in air (0.0001 GPa), U_{iso} for isotropic refinements^cWyckoff position

The refinements at HP-conditions show only minor change of the "Al₅BO₉" structure (Tables 7.2–7.13 and Appendix A.3). The variation of the polyhedral bond-distances and angles is not larger than $2(\sigma)$ within the P -range investigated. In other words, between 0.0001 and 6.5 GPa, polyhedra behave as rigid units. A corresponding behavior is also found for the BO₃-unit (Appendix A.3). Polyhedral distortions at 6.5 GPa are comparable to those observed at room-conditions (at 6.45 GPa: $\Delta(\text{Al1-O})_{\text{max}} = 0.12 \text{ \AA}$, $\Delta(\text{Al2-O})_{\text{max}} = 0.46 \text{ \AA}$, $\Delta(\text{Al3-O})_{\text{max}} = 0.56 \text{ \AA}$, $\Delta(\text{Al4-O})_{\text{max}} = 0.04 \text{ \AA}$ and $\Delta(\text{B-O})_{\text{max}} = 0.01 \text{ \AA}$). However, inter-polyhedral angles and distances vary significantly with pressure, which are interpreted as the main compressional mechanisms governing the unit-cell elastic anisotropy. In particular, if the structure is viewed down [100], voids with pentagonal shape, formed by 5-membered rings of polyhedra (i.e. Al1-Al3-Al4-Al1-Al3, Figure 7.4) occur. The decrease of the O7-O5, O7-O2 and O3-O2 distances between 0.0001 and 6.45 GPa (-5.2% , -4.6% and -2.7% , respectively) is significantly larger than the O3-O3 and O3-O5 ones (-1.6% and -1.1%) (Figures 7.4 and 7.5). The P -induced compression along O7-O5 and O7-O2 contributes more to the shortening of the b -axis, whereas the P -induced decrease of O3-O3 and O3-O2 distances controls compression along the c -axis (Figure 7.4). Shortening of the O7-O5, O7-O2, O3-O2, O3-O3 and O3-O5 distances is ascribable to polyhedral tilting, rather than an intra-polyhedral compression, as shown by the evolution of the O-O-O angles inscribed in the pentagonal distorted rings. In particular, the O2-O3-O7 angle decreases from $85.8(2)^\circ$ to $82.5(2)^\circ$ (i.e. $\Delta(\text{O2-O3-O7}) \approx 3.6^\circ$) and O7-O3-O5 from $88.2(4)^\circ$ to $87.0(3)^\circ$ (i.e. $\Delta(\text{O7-O3-O5}) \approx 1.2^\circ$), whereas the variation of O3-O5-O2, O5-O2-O3 and O3-O7-O3 are $< 1^\circ$. These P -induced mechanisms lead to a preferred compression along [010].

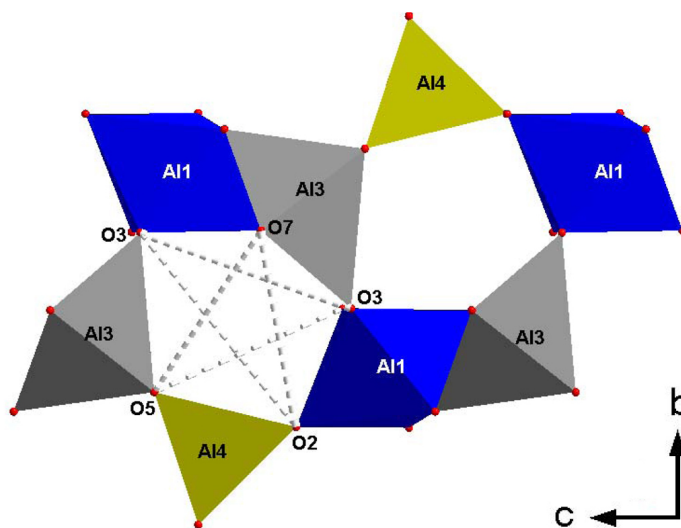


Figure 7.4: Configuration of the voids represented by 5-membered rings of polyhedra (i.e. Al1-Al3-Al4-Al1-Al3). The "diameters" of the voids (i.e. O7-O5, O7-O2, O3-O3, O3-O2 and O3-O5) are shown as dashed lines.

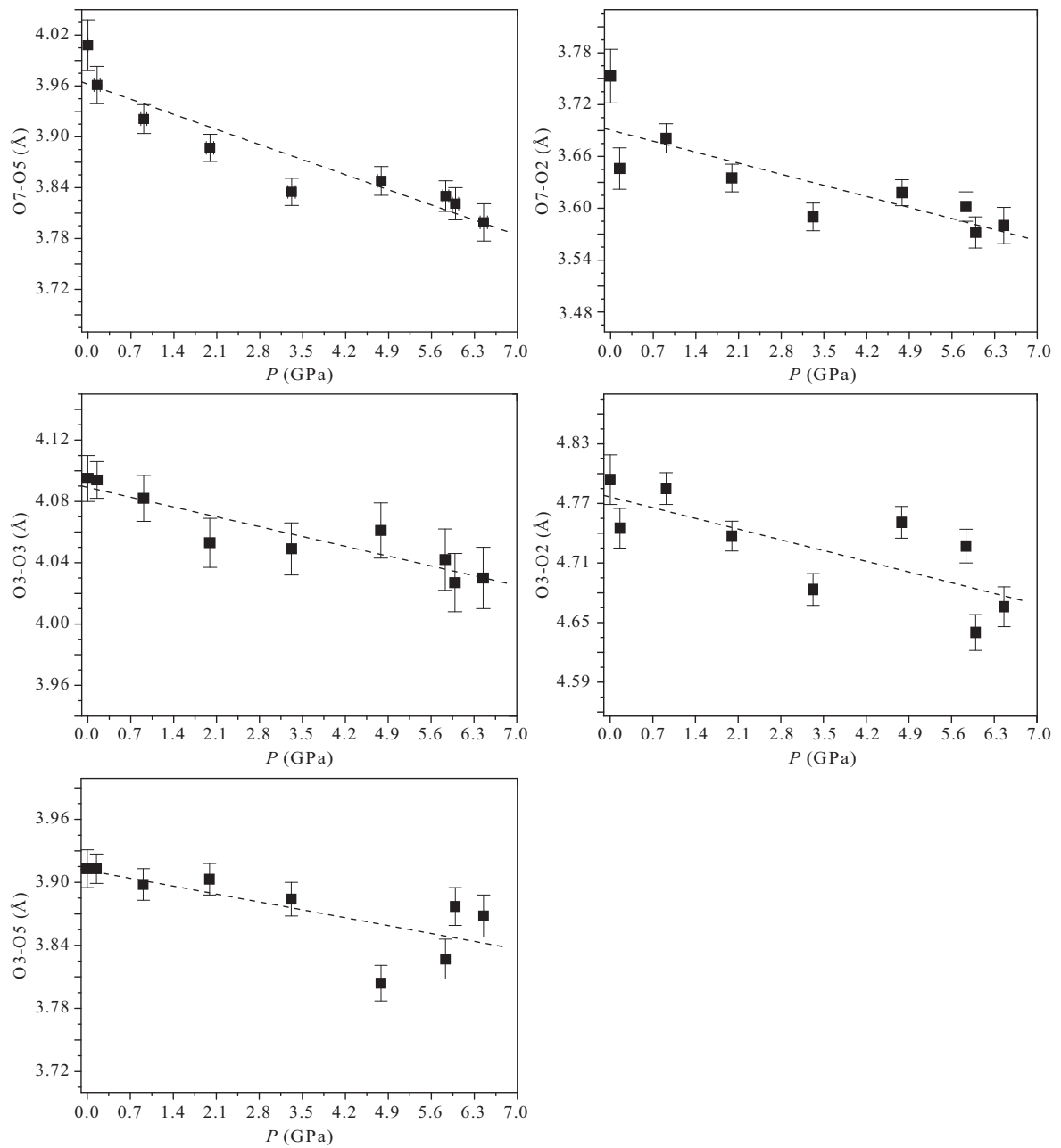


Figure 7.5: Evolution of the O7-O5, O7-O2, O3-O3, O3-O2 and O3-O5 distances (i.e. "diameters" of the voids represented by the 5-membered ring of polyhedra). Dashed lines represent the weighted linear regressions through the data points.

7.6 Discussion and Conclusions

The present in-situ high-pressure experiment shows that " Al_5BO_9 " remains crystalline at least up to 7.4 GPa, and any P -induced structural change is completely reversible. No phase-transition or anomalous elastic behavior have been observed within the P -range investigated, proving the high stability in elastic regime of this ceramic material at least up to 7.4 GPa.

The elastic analysis shows that "Al₅BO₉" is a stiff material. Its isothermal bulk modulus is similar to the one of mullite (adiabatic bulk modulus of 2:1-mullite: $K_S = 169.1$ GPa, Schreuer et al. 2006; $K_S = 2:1$ -mullite: 169.2 GPa, Hildmann et al. 2001; $K_S = 2.5:1$ -mullite: 173.6.0 GPa, Palko et al. 2002; $K_S = 2.5:1$ -mullite: 171.6 GPa, Kriven et al. 1999; Values recalculated by Schreuer et al. 2006 as average of Voigt and Reuss model) and sillimanite ($K_S = 171.4$ GPa, Vaughan and Weidner 1978; $K_{T0} = 171(1)$ GPa, Yang et al. 1997b, and $K_{T0} = 164(1)$ GPa, Burt et al. 2006). The elastic anisotropy of mullite-type materials observed in previous experiments is strikingly high (e.g. 2:1-mullite: $(s_{11} + s_{12} + s_{13}) : (s_{21} + s_{22} + s_{23}) : (s_{31} + s_{32} + s_{33}) = \beta_a : \beta_b : \beta_c = 1.40 : 1.86 : 1$, Hildmann et al. 2001; Sillimanite: $\beta_a : \beta_b : \beta_c = 1.22 : 1.63 : 1$, based on single-crystal unit-cell parameters measured between 0.0001 and 5.3 GPa by Yang et al. 1997b, and $(3K_a)^{-1} : (3K_b)^{-1} : (3K_c)^{-1} = \beta_a : \beta_b : \beta_c = 1.82 : 2.63 : 1$, based on single-crystal unit-cell parameters measured between 0.0001 and 8.5 GPa by Burt et al. 2006). All the aforementioned studies showed that mullite-type materials are stiffer along the *c*-axis than along the *a*- or *b*-axis. For a comparative elastic analysis of the mullite-type materials extended to "Al₅BO₉", we have to consider an origin shift by $\mathbf{t} = (0, 0, \frac{1}{3})$ and a transformation matrix by $\mathbf{T} = (\mathbf{b}, \mathbf{c}, \mathbf{a})$, according to Fischer and Schneider (2008a), from *Cmc2₁* setting used in this study and in Sokolova et al. (1978) to *Bb2₁m* setting. In this light, there is a full agreement between the stiffer direction found in this study (i.e. [100]) and that found in mullite-type materials previously investigated (i.e. [001]). The higher compressibilities observed in this study within (100) can be ascribed to the presence of voids, which allow accommodating the effect of pressure by polyhedral tilting. Polyhedral tilting around the aforementioned 5-membered rings (Al1-Al3-Al4-Al1-Al3) also explains the higher compressibility along [010] than along [001]. The stiffer crystallographic direction observed here might be controlled by the infinite chains of edge-sharing octahedra running along [100], which act as "pillars", making the structure less compressible along the *a*-axis than along the *b*- and *c*-axis. The reason is that along [100] compression can be accommodated only by deformation of the edge-sharing octahedra (and/or by compression of the Al-O bond lengths), as no polyhedral tilting can occur. In response to the applied pressure, any structure is expected to react first by tilting the polyhedra, then by distorting the polyhedra, and finally by decreasing the bond distances. This hierarchy is due to the fact that the first mechanism is energetically less costly than the other two (Gatta 2010).

Following the comparative analysis on the elastic behavior of mullite-type materials, we observed a similar elastic behavior between "Al₅BO₉" and mullite(s) or sillimanite along the direction of the octahedral chains, which is the less compressible direction, but a different behavior occurs in the plane perpendicular to the chains. Considering the aforementioned metrical relationship with other mullite-type materials, we expected that "Al₅BO₉" were more compressible along [001] than along [010]. However, we believe that this different elastic behavior on (100) is due to the different structural configuration on (100) in "Al₅BO₉" compared to other mullite-type materials. In particular, the presence of distorted bipyramids in

"Al₅BO₉", which act as bridging-units of the [100]-octahedral chains and are not present in mullite or sillimanite, might explain the different elastic behavior on (100).

Acknowledgments

GDG and NR thank the Italian CNR – Istituto per la Dinamica dei Processi Ambientali, Milano, for the financial support. MF and TA thank the Swiss National Science Foundation, Grant 200020-112198 "Crystal Chemistry of Minerals" for financial support. R. X. Fischer, an anonymous reviewer and the Editor Milan Rieder are thanked for their efficient revision of the manuscript.

Note

This text represents the contents of the article "Stability at high pressure, elastic behavior and pressure-induced structural evolution of "Al₅BO₉", a mullite-type ceramic material", as published in *Physics and Chemistry of Minerals* 37(4) (2010) 227-236. The unit cell volume has been added to Table 7.1 and some passages have been slightly modified to fit the layout of this thesis.

8 Solid Solution Experiments

8.1 Introduction

Since Dietzel and Scholze (1955) reported compounds with mullite-like properties consisting of B_2O_3 , SiO_2 and Al_2O_3 , solid solutions in the system Al_2O_3 - B_2O_3 - SiO_2 were assumed. The chemical variability of natural boromullite samples investigated by Buick et al. (2008) is close to compositions of synthetic samples of Dietzel and Scholze (1955) and may thus support this assumption.

$Al_{6-x}B_xO_9$ solid solutions were investigated by Mazza et al. (1992) ($1 \leq x \leq 3$) and MacKenzie et al. (2007) ($1 \leq x \leq 4$). Both reported decreasing lattice parameters with increasing x . From FTIR spectra, Mazza et al. (1992) showed that four-fold coordinated boron is incorporated into the mullite structure (for $x = 2$) and MacKenzie et al. (2007) identified BO_4 in boron-mullites with $x \geq 1.2$ by ^{11}B MAS NMR spectroscopy.

Recently, Griesser et al. (2008) investigated boron incorporation into the mullite structure in samples synthesized at 950°C and 1300°C. Starting materials were of compositions between 3:2 mullite and $Al_6B_4O_{15}$ and between 7:3 mullite and a hypothetical compound with 70:30 mol-% Al_2O_3 : B_2O_3 . Al_2O_3 ratio was kept constant and B_2O_3 and SiO_2 were varied according to a hypothetical $B \rightarrow Si$ substitution. Samples with less than 20 mol-% B_2O_3 were identified as Al-Si-B-mullites (powder XRD) and lattice parameters decreased with increasing boron content. The compositional ranges of starting materials resulting in samples identified as Al-Si-B-mullites (based on lattice parameters) are indicated with the two thick gray lines in Figure 8.1. 950°C samples with B_2O_3 contents above 15–20 mol-% were reported as $Al_4B_2O_9$ (Mazza et al. 1992) with excess SiO_2 . Samples with the same composition but heated at 1300°C were identified as $Al_{18}B_4O_{33}$ (Scholze 1956, Garsche et al. 1991) with excess SiO_2 . BO_4 incorporation in $Al_4B_2O_9$ samples was confirmed by FTIR spectroscopy.

In a recent study, Zhang et al. (2010) investigated boron doped (max. 6.14 wt.-% B_2O_3) mullites. Starting from 3:2 mullite, the Al/Si ratio was kept constant at 3/1 and the B/Al ratio was varied from 0–0.4/3 (shown with the thin gray line in Figure 8.1). Samples heated at 1000°C, are reported to consist of mullite, $Al_4B_2O_9$ (Mazza et al. 1992) and a "spinel phase". At 1400°C, $Al_{18}B_4O_{33}$ and mullite were identified with X-ray powder diffraction. With increasing B_2O_3 content, Zhang et al. (2010) report decreasing lattice parameters.

Grew et al. (2008) investigated chemical variability of compounds between $Al_8Si_2B_2O_{19}$ and $Al_{18}B_4O_{33}$ and for compositions close to boralsilite ($Al_{16}B_6Si_2O_{37}$). Results of chemical analyses of their own synthesis products and from literature indicated mullite-type boron

compounds with different composition between $\text{Al}_8\text{B}_2\text{Si}_2\text{O}_{19}$ and $\text{Al}_{16}\text{B}_6\text{Si}_2\text{O}_{37}$ and close to the ideal composition of boralsilite.

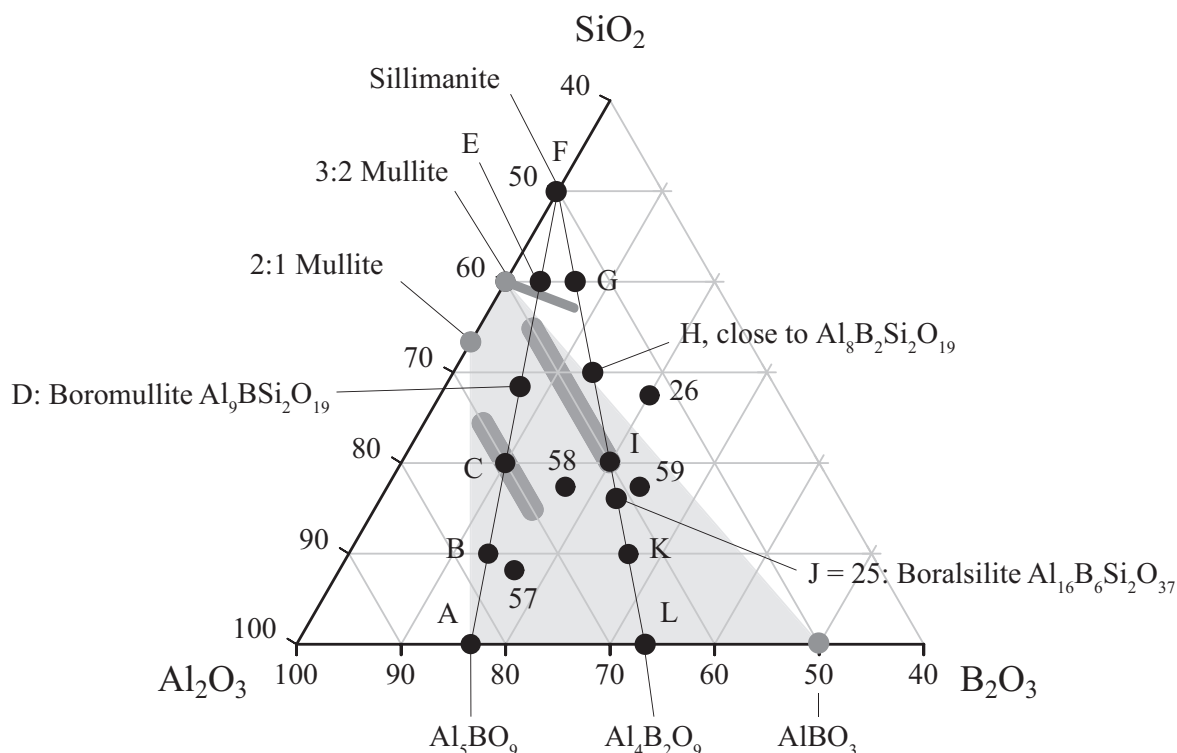


Figure 8.1: Compositions of starting materials A–L in the system Al_2O_3 - B_2O_3 - SiO_2 are indicated with black dots. The boron-mullite stability field is plotted as gray area (Werding and Schreyer 1996, compare Section 2.2 in Chapter 2). Incorporation of boron into the mullite crystal structure as investigated by Griesser et al. (2008) is indicated with the two thick gray lines. Compositions of boron-doped mullites according to Zhang et al. (2010) plot on the thin gray line.

Chemically slightly different samples of natural boromullite (Buick et al. 2008) and synthetic compounds of similar composition (Dietzel and Scholze 1955) plot on a line between Al_5BO_9 and sillimanite. Furthermore, the $\text{Al}/(\text{Si}+\text{B})$ ratio on a line from sillimanite to $\text{Al}_4\text{B}_2\text{O}_9$ (via $\text{Al}_8\text{B}_2\text{Si}_2\text{O}_{19}$ and boralsilite $\text{Al}_{16}\text{B}_6\text{Si}_2\text{O}_{37}$) is constant (Fischer and Schneider 2008a). This may be interpreted as indicator for solid solutions. Unfortunately, except of the study by Griesser et al. (2008), only very restricted areas of the boron-mullite compositional field were systematically investigated.

Hence, 12 samples with starting compositions on the two lines (Figure 8.1) were synthesized by sol-gel routes at 950°C and 1250°C . In addition, five samples with different compositions in or close to the boron-mullite stability field were prepared by a solid-state reaction route.

Boron incorporation into mullite-type crystal structures in the system Al_2O_3 - B_2O_3 - SiO_2 is most likely due to the following exchange mechanisms: B can either replace Si in SiO_4 tetrahedra or replace Al in AlO_4 tetrahedra. Further, B can be incorporated as a BO_3 unit in place of an AlO_4 or SiO_4 tetrahedron. $\text{B}^{3+} \rightarrow \text{Si}^{4+}$ substitutions are not charge neutral,

thus, oxygen vacancies will be involved. In boron-mullites ($\text{Al}_2\text{O}_3\text{-B}_2\text{O}_3$), B can be present in the mullite-type structure due to $\text{BO}_4 \rightarrow \text{AlO}_4$ and/or $\text{BO}_3 \rightarrow \text{AlO}_4$ substitutions.

Any $\text{BO}_x \rightarrow (\text{Al,Si})\text{O}_4$ substitution in a crystal structure will result in a reduction of unit cell volume due to the smaller space required by BO_3 and BO_4 units compared to $(\text{Al,Si})\text{O}_4$ tetrahedra. BO_3 were distinguished from BO_4 groups with FTIR investigations, whereas lattice parameters were derived from refined powder X-ray diffraction patterns.

Table 8.1: Composition of starting materials of samples A–L (sol-gel route) and #25, #26 and #57–59 (solid-state route).

Sample	Theoretical stoichiometry	Al_2O_3 (mol-%)	B_2O_3 (mol-%)	SiO_2 (mol-%)
A	Al_5BO_9	83.33	16.67	0.00
B		76.55	13.35	10.00
C		70.00	10.00	20.00
D	Boromullite $\text{Al}_9\text{Si}_2\text{BO}_{19}$	64.29	7.14	28.57
E		56.57	3.35	40.00
F	Sillimanite Al_2SiO_5	50.00	0.00	50.00
G		53.37	5.59	40.00
H	close to $\text{Al}_8\text{Si}_2\text{B}_2\text{O}_{19}$	56.61	13.38	30.00
I		60.00	20.00	20.00
J	Boralsilite $\text{Al}_{16}\text{B}_6\text{Si}_2\text{O}_{37}$	61.54	23.08	15.38
K		63.31	26.69	10.00
L	$\text{Al}_4\text{B}_2\text{O}_9$	66.67	33.33	0.00
25	Boralsilite $\text{Al}_{16}\text{Si}_2\text{B}_6\text{O}_{37}$	61.54	23.08	15.38
26	$\text{Al}_{16}\text{Si}_4\text{B}_6\text{O}_{41}$	53.33	20.00	26.67
57	$\text{Al}_{4.5}\text{Si}_{0.5}\text{BO}_{9.25}$	75.00	16.67	8.33
58	$\text{Al}_4\text{SiBO}_{9.5}$	66.67	16.67	16.67
59	$\text{Al}_{3.5}\text{Si}_{1.5}\text{BO}_{9.75}$	58.33	25.00	16.67

8.2 Experimental

Samples A–L were produced from sol-gel precursors consisting of aluminum nitrate nonahydrate ($\text{Al}(\text{NO}_3)_3 \cdot 9\text{H}_2\text{O}$), tetra ethyl orthosilicate ($\text{C}_8\text{H}_{20}\text{O}_4\text{Si}$) and boric acid (H_3BO_3). Each precursor was heated at 950°C and at 1250°C , respectively. Samples #25, #26 and #57–59 were produced by a solid-state reaction from corundum (Al_2O_3), dehydrated silica gel (SiO_2) and B_2O_3 at 1200°C (#25 and #26) or 1300°C (#57–59). Sample compositions are shown in Figure 8.1 and listed Table 8.1. Further details on sample preparation are given in Section 3.2.2 in Chapter 3.

After grinding, all samples were measured with a PANalytical X'pert Pro MPD powder diffractometer ($\text{CuK}\alpha$) and phases were identified with the ICDD PDF-2 2004 database. Samples A–F were measured with exactly the same conditions ($5^\circ\text{--}75^\circ$ 2θ , 40 s/step and $0.008^\circ/\text{step}$). Powder XRD pattern of all samples are shown in Figures 8.5 to 8.9.

Fourier transformed infrared powder spectra of 950°C samples A–L (Figures 8.10 and 8.11) were measured on a Perkin Elmer Spectrum One FTIR spectrometer with a Perkin

Elmer universal ATR accessory (Zn-Se + diamond crystal). The beam path included a MIR light source, a KBr beam splitter and a TGS detector. Sample and background spectra were averaged from 50 scans measured 550 cm^{-1} to 1500 cm^{-1} at 4 cm^{-1} resolution. A sample of pure corundum, and a mixture of 50:50 mol-% sillimanite were also measured on this spectrometer (Figure 8.14).

FTIR spectra of 1250°C samples A–L (Figures 8.12 and 8.13) were acquired from 300 cm^{-1} to 2000 cm^{-1} on a Bruker Tensor 27 FTIR spectrometer equipped with a globar MIR light source, a KBr beam splitter, a DLATGS detector and a Harrick MVP 2 diamond ATR accessory. Sample and background spectra were averaged from 100 scans at 4 cm^{-1} resolution. Reference spectra of Al_5BO_9 and $\text{Al}_4\text{B}_2\text{O}_9$ (Chapter 4) were measured on this spectrometer (Figure 8.14).

Spectra were interpreted based on literature data (band assignment according to Griesser et al. 2008) and by comparison to spectra of reference samples of $\text{Al}_4\text{B}_2\text{O}_9$, Al_5BO_9 , corundum and the 50:50 mol-% mixture of sillimanite and Al_5BO_9 .

8.3 Results

Lattice parameters of 950°C samples A–L were Pawley refined starting with mullite-like lattice parameters $a = 7.5 \text{ \AA}$, $b = 7.6 \text{ \AA}$, $c = 2.8 \text{ \AA}$ in space group *Pbam*. Refined lattice parameters are given in Table 8.2 and shown in Figure 8.2. Samples A–H showed a broad peak at ca. $20^\circ 2\theta$ which may fit a cubic phase with $a \approx 7.887 \text{ \AA}$ (space group *Fd $\bar{3}m$* , e.g. $\gamma\text{-Al}_2\text{O}_3$, Chakravorty 1993, Gutierrez et al. 2002, Duoy 2005 and Cividanes et al. 2010). According to Chakravorty (1993) and Chakraborty and Das (2003), a Si-Al spinel-type phase with a similar X-ray powder pattern exists. This phase may incorporate minor amounts of Si and is referred to as "spinel-type" phase here. Quartz could be identified in sample I and may be present in samples J and K. X-ray diffraction patterns of the Pawley refinements are shown in Figures 8.5 and 8.6.

Samples A–L heated at 1250°C and samples #25, #26 (1300°C) and #57–59 (1200°C) fit to ICDD PDF-2 database entries of $\text{Al}_5\text{BO}_9/\text{Al}_{18}\text{B}_4\text{O}_{33}$ and corundum (A–E and G–L). In sample F, mullite, corundum and cristobalite were identified. Cristobalite is normally not formed below 1470°C, however, impurities may lead to metastable cristobalite formation at lower temperatures (Smallman and Bishop 1999).

Choosing a suitable structural model for Rietveld refinements is tricky. Based on peak positions an Al_5BO_9 - or boromullite-like phase in space group *Cmc2₁* can also be fitted with a mullite-type phase in *Pbam*. In the latter case, a single peak at ca. $20^\circ 2\theta$ will not be fitted. A phase in *Cmc2₁* with similar lattice parameters as Al_5BO_9 has two peaks at ca. $16.5^\circ 2\theta$ and $16.7^\circ 2\theta$ ((021) and (110)). Mullite in *Pbam* has only one peak at ca. $16.4^\circ 2\theta$ (110). The occurrence of the two peaks at ca. $16.5^\circ 2\theta$ (unambiguously present in patterns of samples A–D and H–L; It may also be assumed in E and G) and the unassigned peak at ca. 20°

2 θ were taken as evidence that a boromullite-like phase in space group $Cmc2_1$ (Buick et al. 2008) but not a mullite-like phase in $Pbam$ is present. Lattice parameters of this phase are listed in Table 8.3 and plotted in Figure 8.3.

The percentage of Al_5BO_9 - and sillimanite-like modules was refined by introducing a new parameter "wt. BM". For Al_5BO_9 , wt. BM = 1, for a sillimanite-like structure (in space group $Cmc2_1$ with a doubled b -axis), wt. BM = 0, whereas 0.5 presents ideal boromullite ($Al_5BO_9:Al_4Si_2O_{10}$). From simulated powder XRD patterns of Al_5BO_9 and boromullite, refinement of the wt. BM parameter proved to be stable and reproducible. Values of the wt. BM parameter are shown in Figure 8.4 and listed in Table 8.4. Refining wt. BM vastly improved fitting of intensities, however, simultaneous refinement of atomic positions was not possible.

By applying the Rietveld method, excess phases could be quantified (Table 8.4 and Figure 8.3). Corundum quantification of sample E yielded 4.4 wt.-% more excess corundum than Al_2O_3 in the starting mixture (refining wt. BM is not the reason for this result). Thus, the presence of X-ray amorphous phases is assumed. The different intensities of the diffraction patterns (Figures 8.7 and 8.8) can also be explained with varying amount of amorphous phases.

In all B_2O_3 -containing 950°C samples (A–E, G–L), BO_3 groups are present based on IR bands between 1200 cm^{-1} and 1400 cm^{-1} . BO_4 characteristic absorptions are expected between ca. 1030 cm^{-1} and 1150 cm^{-1} . SiO_4 vibrations have IR bands in the same region, thus a distinction in samples containing both SiO_2 and B_2O_3 in the starting materials is difficult. However, BO_4 groups are apparently present in samples I–L (containing 20 or more mol-% B_2O_3), as the two IR bands at ca. 1030 cm^{-1} and 1150 cm^{-1} increase with decreasing SiO_2 content.

The region below ca. 900 cm^{-1} is mainly ascribed to AlO_4 and AlO_6 vibrations. Resolution of the spectra in this region differ significantly. Whenever the spinel-type phase is clearly identifiable in powder XRD patterns, resolution is poor (Figures 8.7 and 8.8).

BO_3 IR vibrations are also observed for in 1250°C samples A–L (except F, which does not contain B_2O_3). In samples with SiO_4 contents below ca. 40 mol-% SiO_2 , an IR band at 1015 cm^{-1} fits to the symmetric stretching mode ν_1 of a BO_3 group (discussed in Section 4.6 in Chapter 4). The spectrum of sample F (mullite, cristobalite and corundum) differs from the other spectra by a broad IR band at ca. 1040 cm^{-1} to 1200 cm^{-1} . AlO_x vibrations are generally found at lower wavenumbers (reference spectrum of corundum in Figure 8.14, and Griesser et al. 2008) and the spectrum of the Al_5BO_9 -sillimanite mixture shows a similar, but less broad IR band in the same range. Intensity of bands in the same region increases with composition towards sample F and decreases towards sample L. For the 1250°C samples, this region is ascribed to SiO_4 vibrations.

8.4 Discussion

950°C samples A–L

According to results of FTIR spectra and powder XRD data, 950°C samples can be divided into four groups:

Samples A₉₅₀–C₉₅₀. Only a mullite-like phase and a broad bump at ca. 20° 2θ can be identified from XRD patterns of samples A–C. This peak may fit quartz but as this peak is also present in the sample without SiO₂, the peak is assigned to the spinel-type phase (Chakravorty 1993, Chakraborty and Das 2003). Hence, it is not possible to make any assumption on Al₂O₃, B₂O₃ and SiO₂ distribution.

With chemical compositions towards sillimanite (sample F), lattice parameters of samples A–C increase (Table 8.2 and Figure 8.2). Starting materials of samples B and C (towards sillimanite composition) contain more SiO₂ at the expense of Al₂O₃ and B₂O₃. It is thus likely that unit cell parameters increase due to incorporation of Si into the mullite structure.

Despite increasing lattice parameters, the region of SiO₄ vibrations (around ca. 1100 cm⁻¹) is empty in FTIR spectra of samples A–C (Figure 8.10), or IR bands with low intensity cannot be identified due to poor resolution of the spectra. Bands between 1200 cm⁻¹ and 1400 cm⁻¹ indicate that boron is three-fold coordinated. The strong increase of IR absorptions below 700 cm⁻¹ may be due to the spinel-type phase, as this absorption is similar for all samples except I–L, where the spinel-type phase cannot be found in diffraction patterns.

Table 8.2: Pawley refined lattice parameters of the mullite-like phase (space group *Pbam*) of samples A–L heat treated at 950°C.

Sample	<i>a</i> -axis (Å)	<i>b</i> -axis (Å)	<i>c</i> -axis (Å)	Volume (Å ³)
A	7.551(8)	7.6655(7)	2.8395(2)	164.36(3)
B	7.563(8)	7.6657(7)	2.8430(2)	164.83(3)
C	7.568(8)	7.6658(7)	2.85095(19)	165.40(2)
D	7.523(3)	7.651(3)	2.8182(7)	162.19(9)
E	7.4961(16)	7.659(3)	2.8203(7)	161.92(8)
F	7.577(17)	7.781(17)	2.888(4)	170.3(6)
G	7.554(2)	7.610(2)	2.8292(5)	163.70(7)
H	7.5494(8)	7.6590(7)	2.82845(18)	163.54(2)
I	7.4985(8)	7.6438(6)	2.80875(17)	160.99(2)
J	7.4883(11)	7.6175(10)	2.7995(3)	159.69(3)
K	7.4978(16)	7.6243(14)	2.8002(3)	160.07(5)
L ^a	14.984(17)	5.569(4)	15.41(2)	1285(3)

^aspace group *C2/m*, monoclinic angle β = 90.98(7)° (Fischer et al. 2008b)

Samples D₉₅₀ and E₉₅₀. X-ray diffraction patterns of samples D and E show two strong broad peaks at ca. 46° 2θ and 67° 2θ. Position and intensities of those peaks are compatible with the spinel-type phase (Chakravorty 1993, Chakraborty and Das 2003). Lattice param-

eters of the mullite-type phases in samples D and E are significantly smaller than those of samples A–C. The significantly lower intensity in the diffraction patterns (Figure 8.5) may be an indicator for at least one X-ray amorphous phase (SiO_2 ?). The presence of the excess spinel-type and possibly an amorphous phase may inhibit further Si incorporation into the mullite-type phase. Thus, it is assumed that the mullite-type phase is in a non-equilibrium state at this composition and temperature.

IR absorptions in the region of 1200 cm^{-1} and 1400 cm^{-1} (BO_3) are strongly reduced in sample E, which is in agreement with the fewer amount of B_2O_3 in the starting mixture. In the spectrum of the same sample, a new peak appearing at ca. 1015 cm^{-1} may be ascribed to vibrations of SiO_4 (Griesser et al. 2008) or to ν_1 of a BO_3 group.

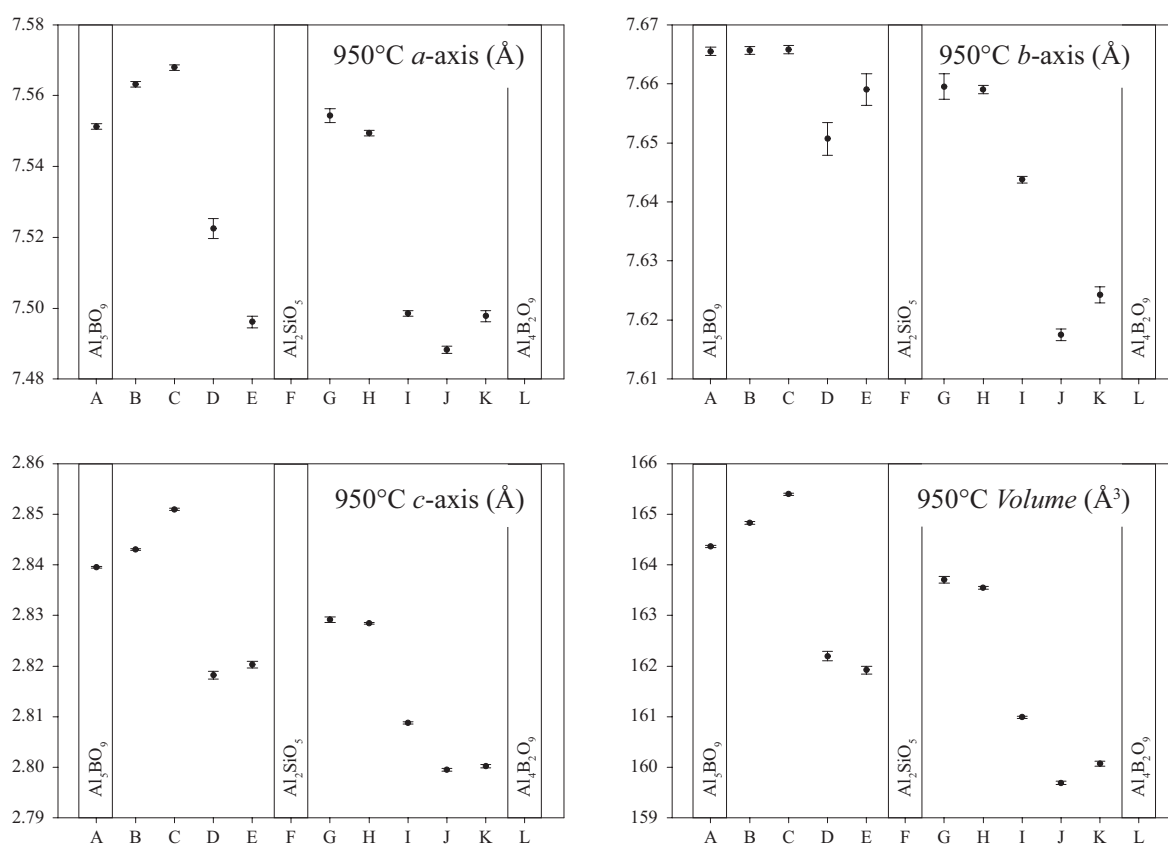


Figure 8.2: Pawley-refined lattice parameters of mullite-like phases in space group *Pbam* of samples A–E and G–K. Lattice parameters A–C increase with composition towards F, whereas they decrease with composition from G towards K. Outliers D and E may be due to non-equilibrium conditions (see text). Data from samples F and L are not shown because diffraction patterns are not compatible with a unit cell in space group *Pbam*. For samples A, F and L, starting compositions are indicated.

Samples G₉₅₀–K₉₅₀. Lattice parameters of samples G–K decrease with increasing B_2O_3 content of the starting materials (Table 8.2 and Figure 8.2). In the powder XRD pattern of sample G, the peaks at ca. $46^\circ 2\theta$ and $67^\circ 2\theta$ indicate the presence of the spinel-type phase, whereas in sample H, this phase can only be assumed due to the broad bump at ca. $20^\circ 2\theta$.

In sample I, powder XRD peaks match the structure of quartz, whereas in samples J and K, quartz can only be assumed (peak at $20.8^\circ 2\theta$).

Besides rather unresolved BO_3 IR bands, a new band appears in FTIR spectra between ca. 1075 cm^{-1} and 1150 cm^{-1} . This region is compatible with SiO_4 absorptions (Griesser et al. 2008) and has also been observed in FTIR spectra of sample F (see below). From the broad band at ca. 1050 cm^{-1} in spectra of samples I, J and K, the presence of BO_4 groups is evident. A second BO_4 band at ca. 1120 cm^{-1} interferes with SiO_4 bands (between 1093 cm^{-1} and 1131 cm^{-1} , Griesser et al. 2008) when BO_4 tetrahedra are present and thus complicates identification. However, from FTIR spectra, it may be assumed that absorptions between ca. 1030 cm^{-1} and 1150 cm^{-1} are predominantly due to SiO_4 in samples G and H, whereas they are due to BO_4 in samples J and K. BO_4 groups in samples with more than ca. 20 mol-% B_2O_3 (represented here with I, J, K and L) have also been reported by Griesser et al. (2008).

Samples F₉₅₀ and L₉₅₀. The powder XRD pattern of sample F indicates only poorly crystalline phases. Nonetheless, the spinel-type phase is present. The small broad peak at $26.6^\circ 2\theta$, fits the (101) peak of quartz, hence, quartz was included in the refinement. The FTIR spectrum of this sample mainly differs from spectra of the other samples in the region between 1200 cm^{-1} to 1400 cm^{-1} (as no boron is present) and by the broad, poorly resolved bump between 1000 cm^{-1} and ca. 1250 cm^{-1} . According to Griesser et al. (2008), no SiO_4 IR bands are present below 980 cm^{-1} . Between 980 cm^{-1} and 550 cm^{-1} , only AlO_4 and AlO_6 absorptions are present. Thus, the broad bump can be ascribed to quartz, whereas the slope below is due to the spinel-type phase.

Diffraction peaks of Sample L fit to a structure in space group $C2/m$ with lattice parameters (Table 8.2) similar to those of $\text{Al}_4\text{B}_2\text{O}_9$ according to Fischer et al. (2008b). From the FTIR spectrum (Figure 8.11), BO_4 IR bands are clearly visible and the pattern is similar to the FTIR spectrum of the reference $\text{Al}_4\text{B}_2\text{O}_9$ sample (Chapter 4), shown in Figure 8.14. The differences in the two spectra may be ascribed to the different sample preparation (more B_2O_3 in the starting material of reference $\text{Al}_4\text{B}_2\text{O}_9$ and to the different FTIR spectrometers used).

Griesser et al. (2008) reported this phase with mullite-like lattice parameters in space group $Pbam$. If the powder XRD pattern of sample L is indexed with a mullite-like phase in $Pbam$ instead of $C2/m$, not all peaks are considered. The sample found by Griesser et al. (2008) may thus have a different structure than sample L synthesized in this study.

1250°C samples A–L

From Rietveld-refined lattice parameters, the wt. BM parameter and excess corundum (Tables 8.3 and 8.4 and Figure 8.3), results of the samples heated at 1250°C can be divided in two groups (A–E and G–L) with a different trend each. In the plots, data for sample F are not included because the powder XRD pattern is not compatible with a phase in space group

$Cmc2_1$. Instead, a mullite-like phase ($Pbam$), corundum and cristobalite were found. This sample was subsequently heated at 1275°C for 100h but the ratios of mullite, cristobalite and corundum did not significantly change. The almost inert behavior of this sample is ascribed to preferential formation of corundum and cristobalite at the cost of mullite. Once cristobalite and corundum have crystallized, they react rather sluggish at 1275°C, thus indicating non-equilibrium conditions.

Trend from Al_5BO_9 (A_{1250}) to sillimanite (F_{1250}) composition. In Rietveld refinements of samples A–E, the wt. BM parameter increases with increasing composition of the starting materials towards the sillimanite composition (sample F). At the same time, no significant trend in the a and b lattice parameters and the cell volume can be identified. However, the c -axis decreases with composition towards F, which is in agreement with Buick et al. (2008). Towards E, samples consist of significant amounts of excess corundum. Rietveld quantifications of sample E indicate even more excess corundum than Al_2O_3 in the starting mixture. Not all of the material will thus be crystalline or incorporated into the $Cmc2_1$ -phase and actual composition of this phase is certainly different from the starting mixture.

Table 8.3: Rietveld refined lattice parameters of samples A–L heated at 1250°C and samples #25 and #26 (1300°C) and #57–59 (1200°C) in space group $Cmc2_1$.

Sample	a -axis (Å)	b -axis (Å)	c -axis (Å)	Volume (Å ³)
A	5.66830(11)	15.0228(4)	7.69732(17)	655.45(2)
B	5.66977(16)	15.0310(6)	7.6948(3)	655.77(3)
C	5.66943(18)	15.0316(6)	7.6929(3)	655.59(4)
D	5.6638(3)	15.0281(8)	7.6872(4)	654.30(6)
E	5.6663(3)	15.03356(7)	7.6879(6)	654.89(8)
F ^a	7.5652(3)	7.6885(3)	2.88304(9)	167.704(14)
G	5.6796(3)	15.05822(5)	7.6827(5)	657.05(7)
H	5.66500(16)	15.0240(5)	7.6892(2)	654.42(4)
I	5.66323(14)	15.0162(5)	7.6909(2)	654.03(3)
J	5.66159(16)	15.0161(6)	7.6899(3)	653.76(4)
K	5.66008(18)	15.0168(6)	7.6868(3)	653.35(4)
L	5.66843(9)	15.0107(3)	7.69057(14)	654.37(2)
25	5.6610(2)	15.0218(07)	7.6829(3)	653.90(5)
26	5.6675(2)	15.0263(07)	7.6788(4)	653.93(5)
57	5.6873(3)	15.0491(10)	7.6823(5)	657.51(7)
58	5.6880(4)	15.0471(13)	7.6851(7)	657.75(10)
59	5.6793(3)	15.0424(09)	7.6804(5)	656.13(7)

^aspace group $Pbam$

FTIR spectra of samples A–E show the typical absorptions ascribed to BO_3 units (1200 cm^{-1} and 1400 cm^{-1} , Figure 8.12). The low intensity band at 1015 cm^{-1} (most expressed in the FTIR spectrum of sample A) fits the ν_1 vibration of the BO_3 group. In similarly prepared samples of Griesser et al. (2008), no BO_4 was found. Hence, it is not likely that the the low-intensity bands appearing between 1200 cm^{-1} and 1020 cm^{-1} result from BO_4 groups. As

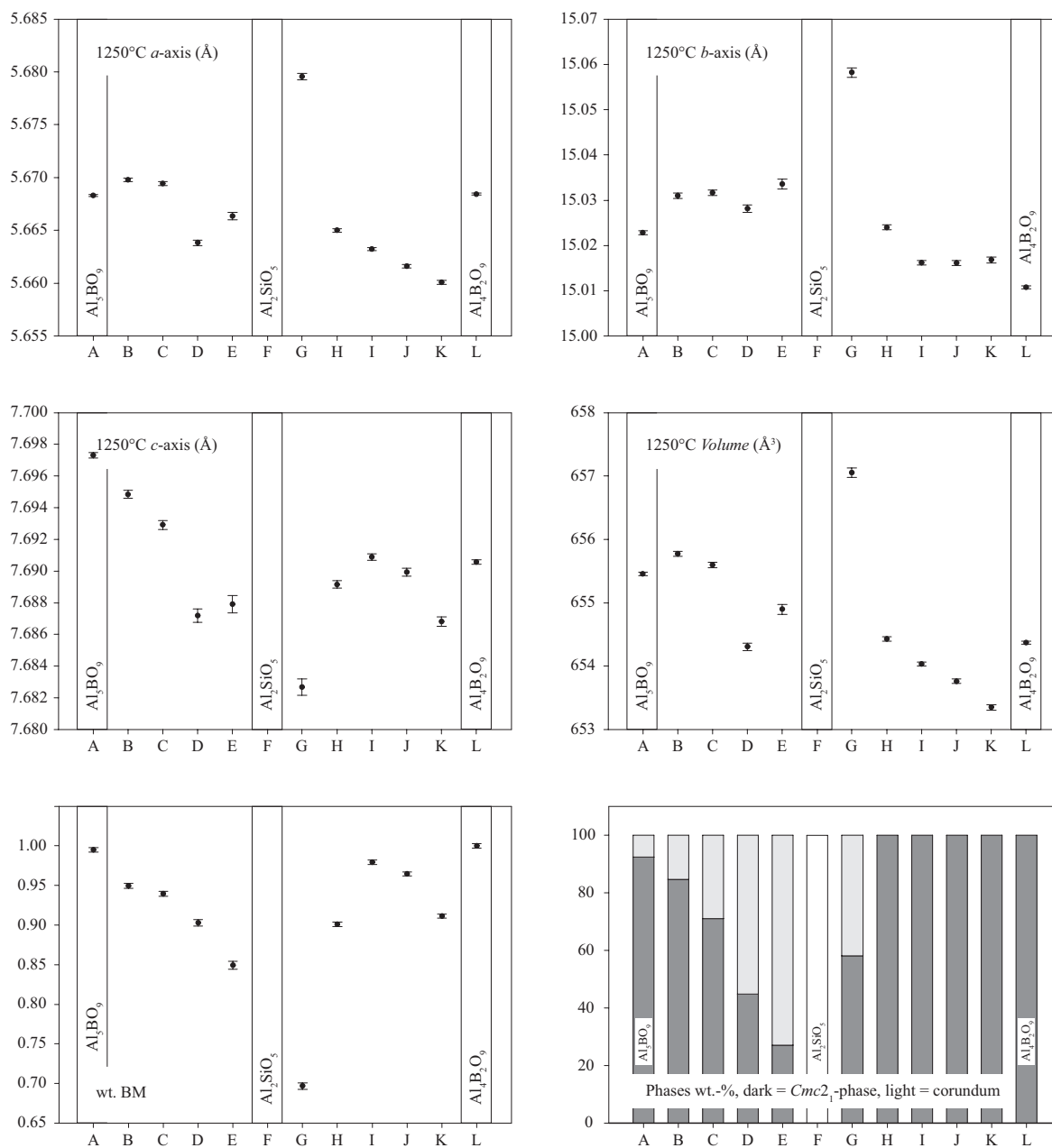


Figure 8.3: Lattice parameters from Rietveld refinements of the $Cmc2_1$ -phase (middle and top) and the wt. BM parameter (bottom left) of samples A–L. Data from sample F are not shown because lattice parameters are not compatible with a unit cell of a phase in space group $Cmc2_1$. The wt. BM factor is the weight of Al_5BO_9 and sillimanite modules in a mullite-type phase in $Cmc2_1$. A weight of 1 corresponds to Al_5BO_9 , whereas a weight of 0.5 equals boromullite. Quantification (Rietveld wt.-%) of the $Cmc2_1$ -phase and corundum is shown in the bottom right diagram. Starting material compositions of A, F and L are indicated.

mentioned before, SiO_4 bands may also occur in this region. By comparing the spectra to the one of sample F (mullite, cristobalite, corundum), and to the spectrum of the 50:50 mol-% mixture of Al_5BO_9 and sillimanite (Figure 8.14), it becomes obvious that the low-intensity

bands in this region in spectra of samples B–E are due to SiO_4 groups, although intensity does not increase with increasing SiO_2 . Below 1000 cm^{-1} , IR band positions are in agreement with the reference spectra of pure Al_5BO_9 and the sillimanite- Al_5BO_9 mixture mixture (Figure 8.14). Intensities differ significantly with increasing composition towards sample F (most expressed around ca. 550 cm^{-1} , where a high-intensity band exists in the references spectrum of corundum (Figure 8.14).

Table 8.4: Additional data from Rietveld refinements for samples A–L heated at 1250°C and samples #25, #26 and #57–59.

Sample	wt.-% $Cmc2_1$ phase	wt.-% Al_2O_3	wt. BM ^a
A	92.4(3)	7.6(3)	0.995(3)
B	84.7(4)	15.3(4)	0.950(3)
C	71.0(4)	29.0(4)	0.939(3)
D	44.8(3)	55.2(3)	0.903(4)
E	27.0(3)	73.0(3)	0.849(5)
F	n/a ^b	n/a ^b	n/a ^b
G	58.0(4)	42.0(4)	0.697(4)
H	100.0	0.0	0.901(3)
I	100.0	0.0	0.979(3)
J	100.0	0.0	0.965(3)
K	100.0	0.0	0.911(3)
L	100.0	0.0	1.000(3)
25	100.0	0.0	0.881(4)
26	98.6(4)	1.4(4)	0.780(3)
57	95.7(6)	4.3(6)	0.667(3)
58	96(2)	4(2)	0.616(4)
59	91.9(6)	n/a ^c	0.599(4)

^awt. BM = structural weight between boromullite in $Cmc2_1$ (wt. BM = 0.5) and Al_5BO_9 (wt. BM = 1)

^b68.1(4) wt.-% Mullite in $Pbam$ + 26.5(4) wt.-% corundum + 5.4(4) wt.-% cristobalite

^c2.63(6) wt.-% corundum and 5.48(6) wt.-% cristobalite

Trend from sillimanite (F_{1250}) to $\text{Al}_4\text{B}_2\text{O}_9$ (L_{1250}) composition. Considering the distribution of wt. BM, lattice parameters and missing excess corundum in samples H–L, a gap between sample G and samples H–L is obvious. FTIR spectra of sample G indicate SiO_4 vibrations (from ca. 1050 cm^{-1} to 1200 cm^{-1}), however, no distinct Si-containing phase could be found in XRD data. Probably, this $Cmc2_1$ -phase contains significantly more Si than all the others, which would make sense due to the larger lattice parameters.

In samples H–K, the amount of Al_5BO_9 -modules in the $Cmc2_1$ phase increases, combined with a decrease of the a -axis and the cell volume. These results are compatible with trends reported by Buick et al. (2008), but no clear trend is evident from evolution of the b - and c -axis. In XRD patterns (Figure 8.8), no other phase than the $Cmc2_1$ -phase could be identified.

IR bands of BO_3 groups are present in FTIR spectra of samples H–L (including the ν_1 band at 1015 cm^{-1} , Figure 8.13). SiO_4 vibrational bands (between 1200 cm^{-1} and 1020 cm^{-1} , assigned based on FTIR spectra of sample F and the 50:50 mol-% mixture of sillimanite and

Al_5BO_9) are less pronounced with lower SiO_2 content of the starting mixtures. In samples I–L, a new band appears at 1200 cm^{-1} , which could not be identified.

Previous investigations on synthesis of boron-mullites ($\text{Al}_2\text{O}_3\text{-B}_2\text{O}_3$) have shown that compounds with Al_5BO_9 compositions crystallize at temperatures above ca. 1100°C from starting materials representing $\text{Al}_4\text{B}_2\text{O}_9$. The higher amount of B_2O_3 in the starting materials can lead to larger "crystallites" in the resulting Al_5BO_9 compound. Due to a very similar FTIR spectrum of sample L and the reference spectrum of Al_5BO_9 (Figures 8.13 and 8.14), a wt. BM parameter of 1.000(3) (Table 8.4) and similar cell volume to the one of Al_5BO_9 , sample L is interpreted as compound with a composition of or close to Al_5BO_9 .

1200°C–1300°C samples #25, #26 and #57–59.

Lattice parameters and excess corundum of samples #25, #26 and #57–59 (Table 8.3 and Figure 8.4) show no trend with the compositions of the starting material (increasing sample numbers do not represent continuous change in composition of starting materials, Figure 8.1 and Table 8.1). Nonetheless, unit cell volumes of samples #25 and #26 are close to the one of Al_5BO_9 . As no SiO_2 phase can be identified in the powder patterns of those samples, Si must either be incorporated in the structure or be present as X-ray amorphous phase. In the powder XRD pattern of sample #26 (Figure 8.9), a broad bump between ca. $18^\circ\ 2\theta$ and $25^\circ\ 2\theta$ may indicate an almost X-ray amorphous phase ($\text{SiO}_2?$). The same can be observed in the difference plots of sample #57 and #58. A single weak peak at ca. $21.7^\circ\ 2\theta$ might fit cristobalite.

Due to the inconsistent behavior of lattice parameters and the wt. BM parameter, it can be assumed that the synthesis route via solid-state reaction is not suitable for the incorporation of Si into a mullite-type structure in space group $Cmc2_1$, most likely due to the sluggish reaction behavior of Al_2O_3 and the lack of a fluxing agent (e.g. B_2O_3 in sufficient quantities).

Comparison with literature data

Trends of the 950°C samples are in accordance with findings of Griesser et al. (2008), although not the same area of the boron-mullite stability field (Werdinger and Schreyer 1996) was covered with the composition of the starting materials. Decreasing lattice parameters with increasing B_2O_3 content and incorporation of four-fold coordinated boron into the structure for samples produced with more than ca. 20 mol-% B_2O_3 in the starting mixture can be confirmed. However, excess SiO_2 has not been found in samples with BO_4 in the mullite-like structure. The spinel-type phase has not been reported by Griesser et al. (2008) and it is unknown if X-ray amorphous phases were considered.

For samples A and L (both consisting solely of Al_2O_3 and B_2O_3), results of Mazza et al. (1992) and MacKenzie et al. (2007), reporting decreasing lattice parameters and BO_4 incorporation into the structure, can be confirmed (for better comparison with literature data,

indexing the powder XRD pattern of sample L with a mullite-like structure in space group *Pbam* leads to a cell volume of 157.59(7) Å³.

Combining our data with those of Griesser et al. (2008) and MacKenzie et al. (2007), may indicate that all samples synthesized at 950°C with a maximum of 20 mol-% SiO₂ and more than 20 mol-% B₂O₃ in the starting mixtures contain four-fold coordinated boron. As the chemical difference between sample composition and the composition of the starting materials is not precisely known (this study, Griesser et al. 2008 and MacKenzie et al. 2007), suggestion of a stability field for BO₄-containing mullite-type structures may not be accurate and is only mentioned as suggestion for further studies.

No studies exist in which Al₂O₃-B₂O₃-SiO₂-phases synthesized at 1250°C were investigated for variable structural incorporation of Al₅BO₉ and sillimanite-like modules. Furthermore, our data of the 1250°C samples are significantly different to those of 1300°C samples by Griesser et al. (2008), because in this study, mullite (with mullite-like lattice parameters in space group *Pbam*) was only found in sample F containing no B₂O₃ in the precursor. Unfortunately, Griesser et al. (2008) do not mention how they identified the phases reported as "mullite" and if they found unidentified peaks in their powder XRD data. Further, Griesser et al. (2008) did also not indicate which SiO₂ phase they identified in the powder XRD patterns. This is a crucial point. If a diffraction pattern of a *Cmc2*₁-phase like boromullite or Al₅BO₉ is fitted with a mullite-like unit cell in space group *Pbam*, the unassigned peaks can be misleadingly interpreted as quartz, although with slightly too large lattice parameters.

As previously mentioned for the 950°C samples, based on FTIR and powder X-ray diffraction data, it is unknown how much the composition of the synthesized mullite-type phases is represented by the composition of the starting materials. High amounts of excess corundum clearly indicate that this difference is rather large. Once corundum has crystallized from the initially amorphous precursor material, it is almost inactive and hinders further crystallization of mullite-type compounds.

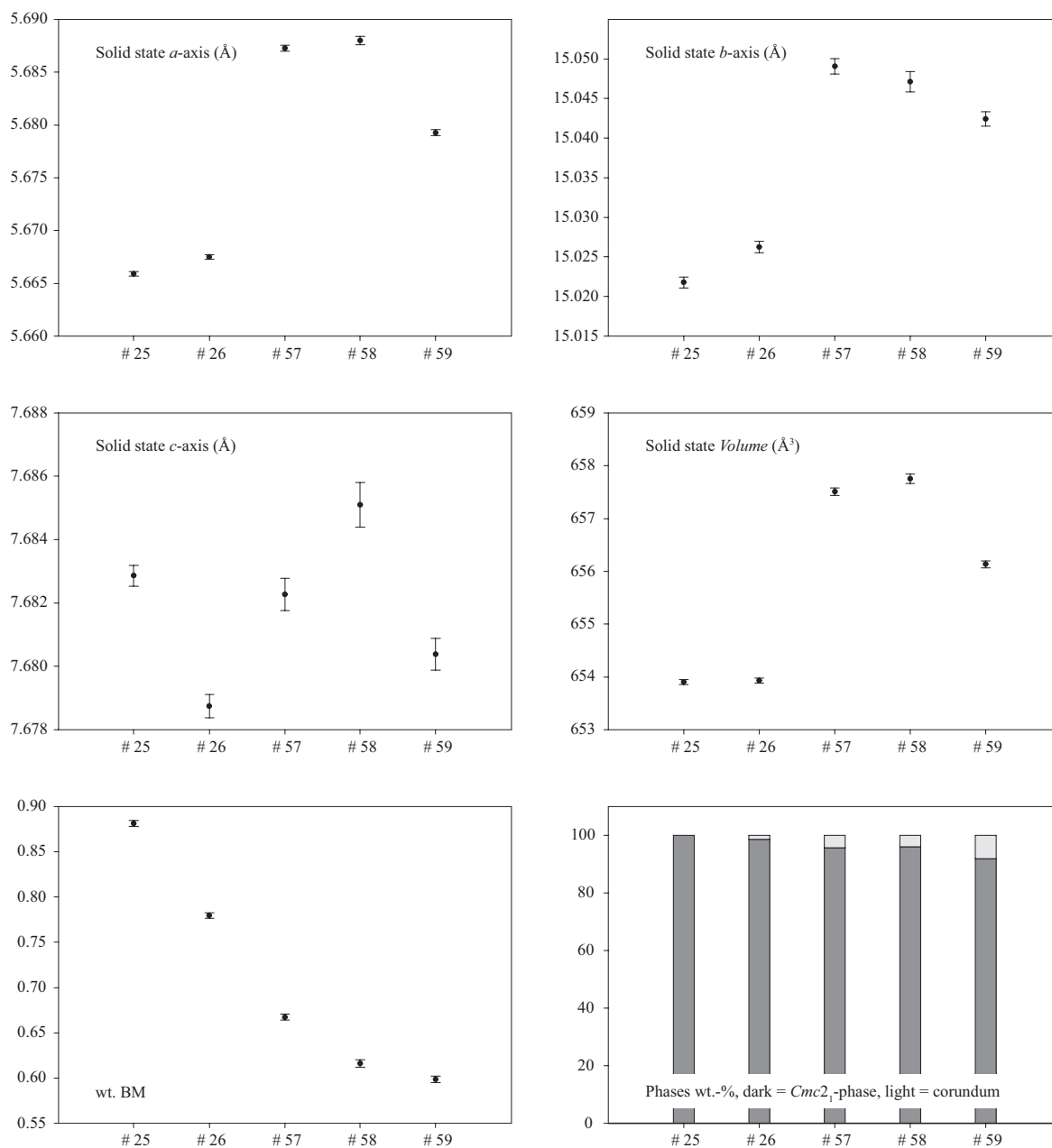


Figure 8.4: Rietveld-refinement results of samples #25, #26 and #57–59. Sample nomenclature does not represent continuous change in composition of the starting mixtures, thus, the decrease of the wt. BM parameter is not in agreement with continuous change of starting compositions. Lattice parameters of the $Cmc2_1$ -phase are shown top and middle left and right. The wt. BM factor (bottom left) is the fraction of Al_5BO_9 and sillimanite modules in this mullite-type phase. A weight of 1 corresponds to Al_5BO_9 , whereas a weight of 0.5 equals boromullite. Quantification of the $Cmc2_1$ -phase and corundum is shown in the bottom right diagram. For sample #59, the quantification the light-gray area represents summed wt.-% of corundum and cristobalite.

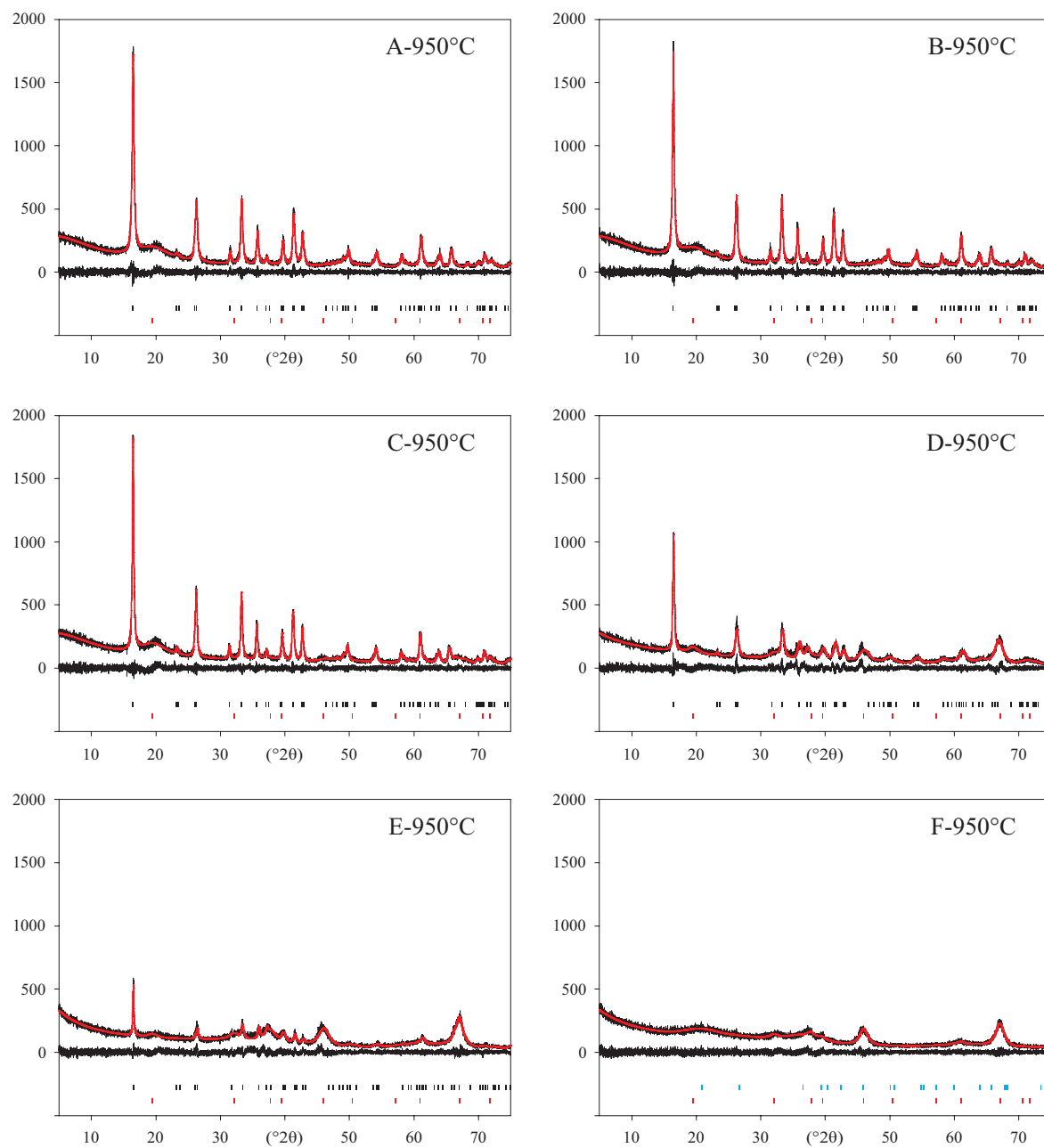


Figure 8.5: Pawley-refined XRD patterns of 950°C samples A–F. *hkl*-ticks of phases with mullite-like lattice parameters in space group *Pbam* are black, *hkl*-ticks of the cubic spinel-type phase are red, *hkl*-ticks of quartz are blue. Intensity scale is counts.

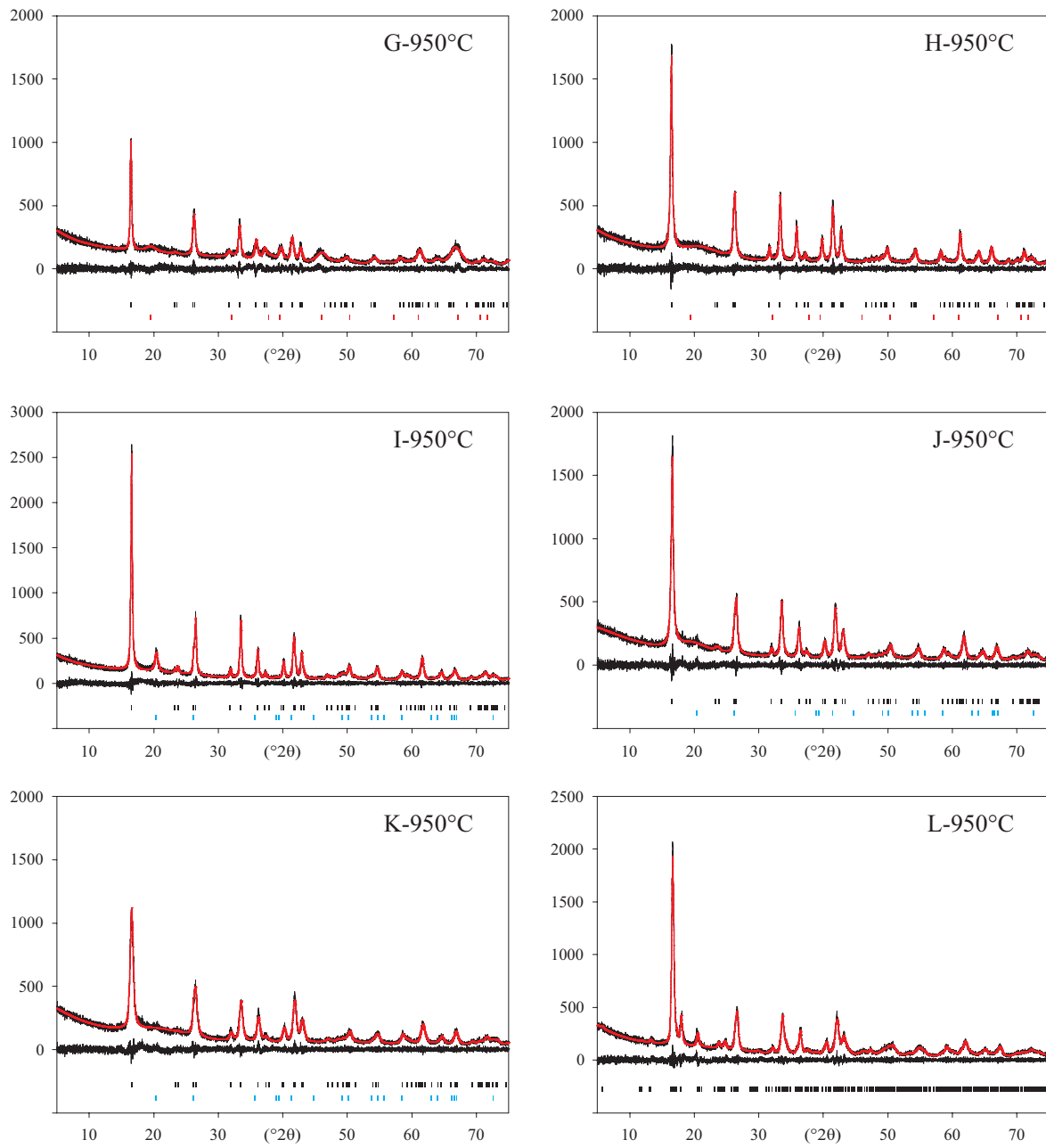


Figure 8.6: Pawley-refined XRD patterns of 950°C samples G–L. *hkl*-ticks of phases with mullite-like lattice parameters in space group *Pbam* are black, *hkl*-ticks of the cubic spinel-type phase are red, *hkl*-ticks of quartz are blue. Intensity scale is counts.

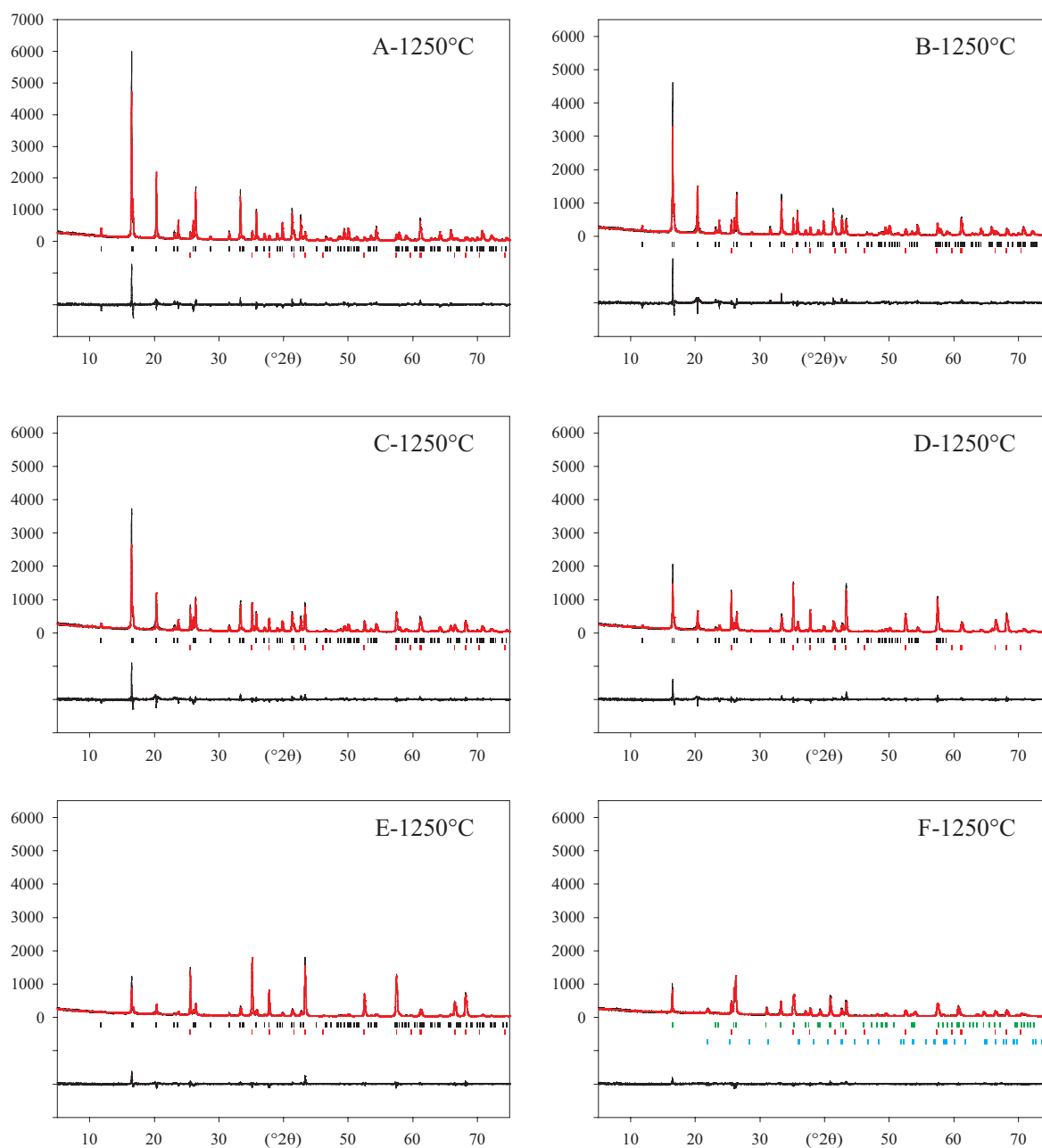


Figure 8.7: Rietveld-refined XRD patterns of 1250°C samples A–F. *hkl*-ticks of phases refined in space group $Cmc2_1$ with variable ratio of Al_5BO_9 and sillimanite modules are black. Corundum *hkl*-ticks are red, *hkl*-ticks of cristobalite are blue and *hkl*-ticks of the phase identified as mullite (sample F) in $Pbam$ are green. Intensity scale is counts.

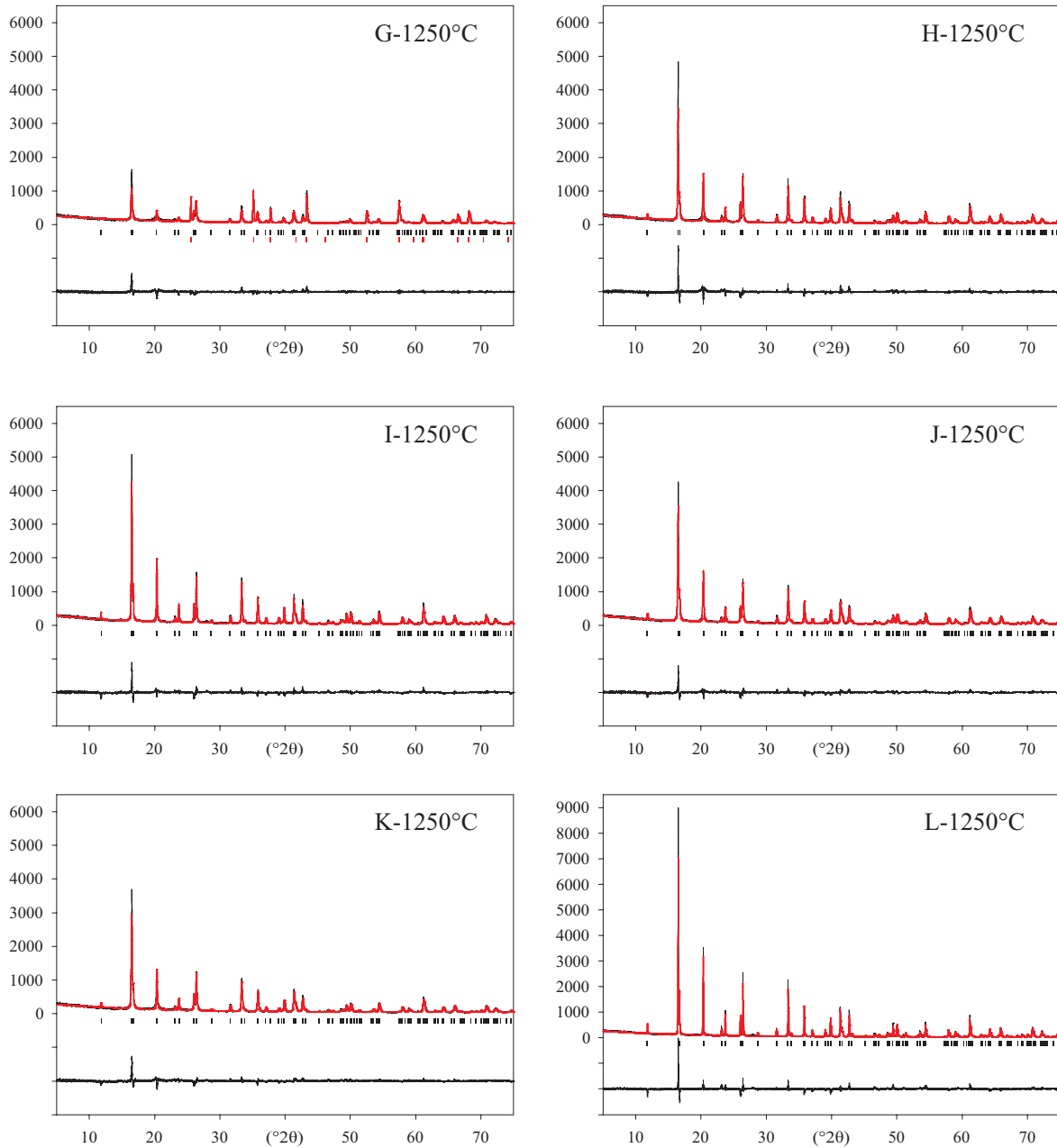


Figure 8.8: Rietveld-refined XRD patterns of 1250°C samples G–L. hkl -ticks of phases refined in space group $Cmc2_1$ with variable ratio of Al_5BO_9 and sillimanite modules are black. Corundum hkl -ticks are red. Intensity scale is counts.

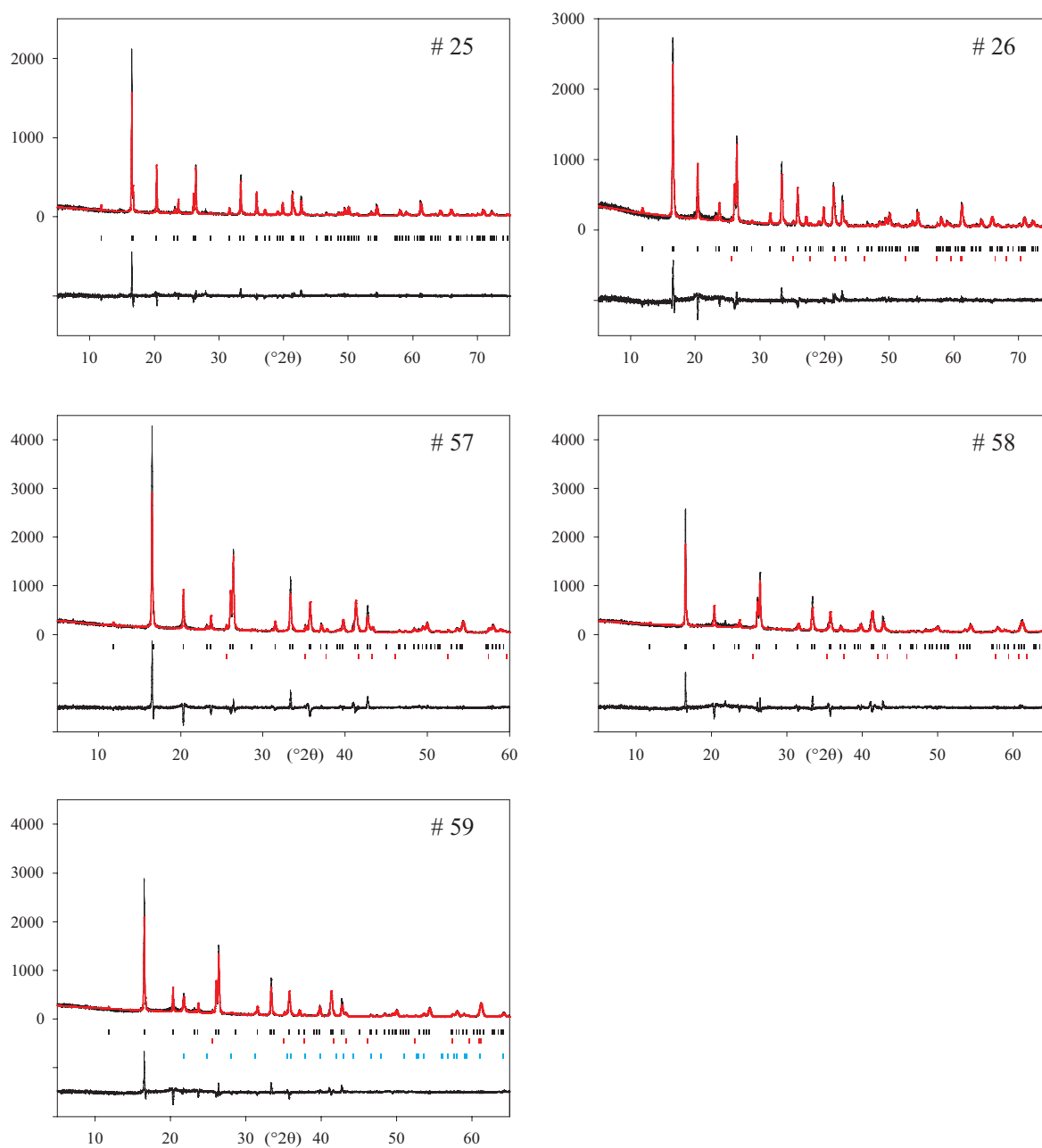


Figure 8.9: Rietveld-refined XRD patterns of samples #25, #26 and #57–59 synthesized by solid-state reactions at 1200°C or 1300°C. hkl -ticks of phases refined in space group $Cmc2_1$ with variable ratio of Al_5BO_9 and sillimanite modules are black. Corundum hkl -ticks are red, cristobalite hkl -ticks are blue. Diffraction patterns were not collected with the same conditions, thus, differing intensities are not meaningful. Intensity scale is counts.

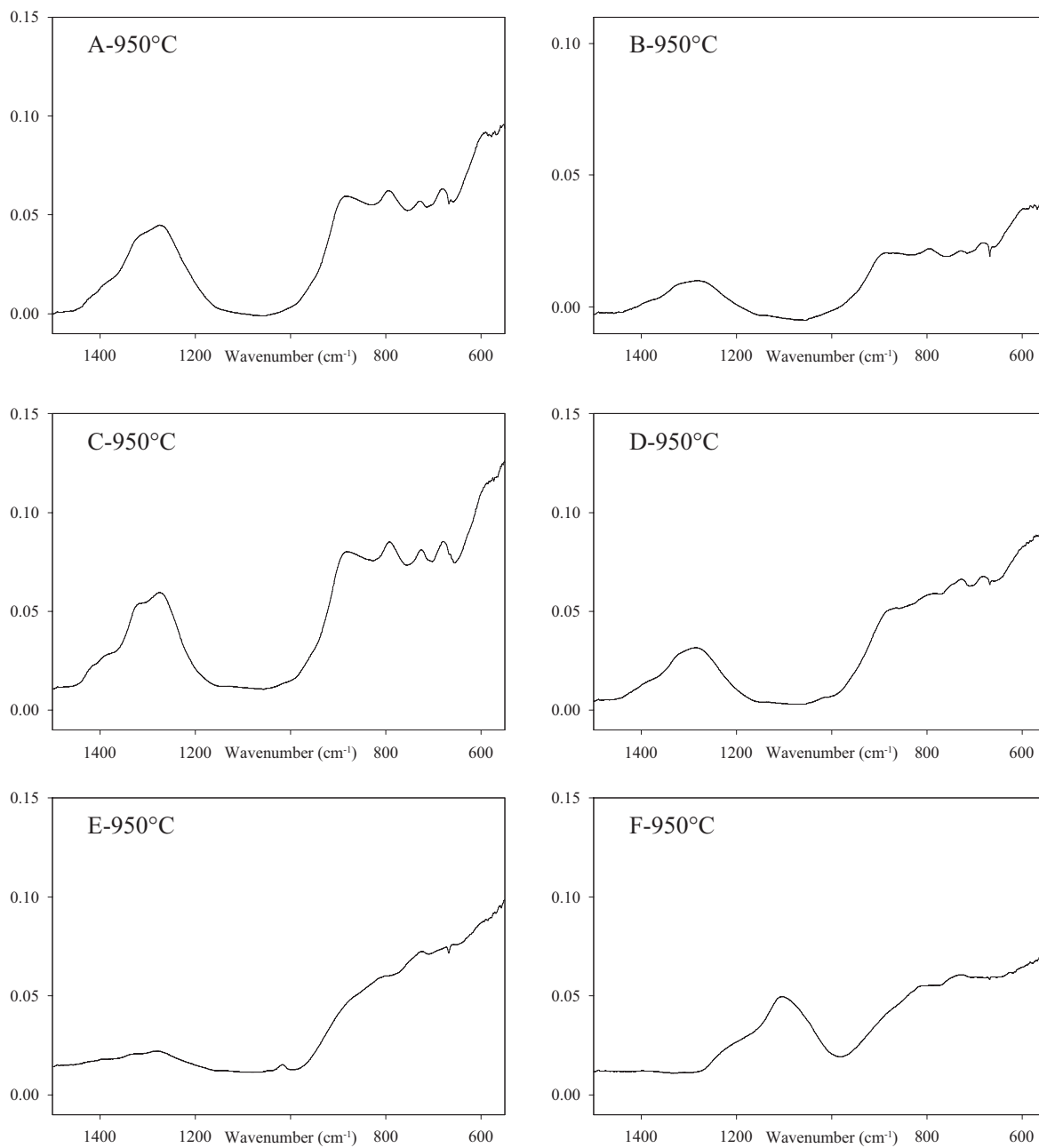


Figure 8.10: ATR-FTIR spectra of samples A–F heated at 950°C. Absorptions between 1400 cm⁻¹ and 1200 cm⁻¹ are ascribed to BO₃ vibrations, those between ca. 1200 cm⁻¹ and 1000 cm⁻¹ to SiO₄ and IR bands below ca. 900 cm⁻¹ to AlO_x groups. Intensity scale is ATR absorbance.

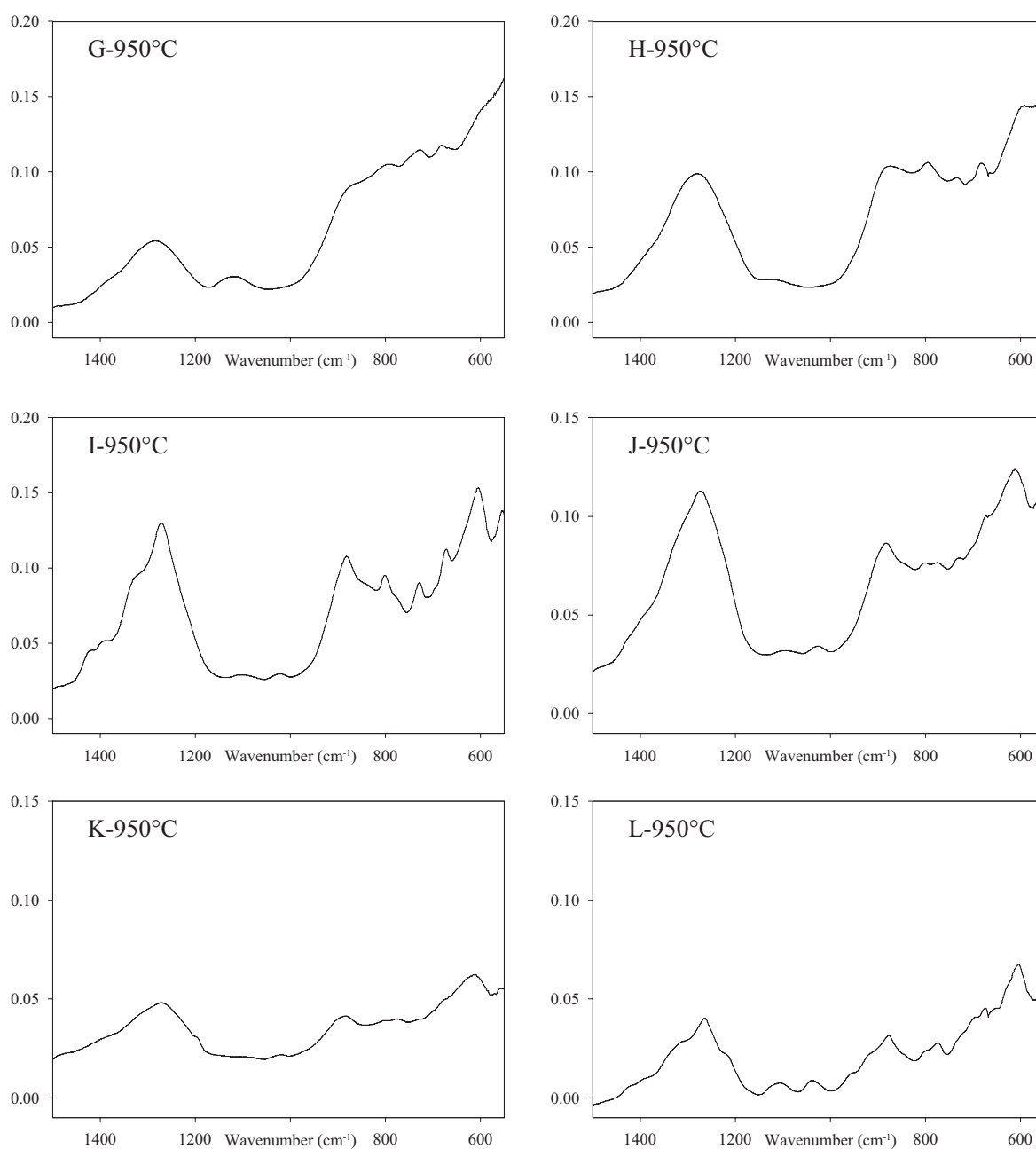


Figure 8.11: ATR-FTIR spectra of samples G–L heated at 950°C. Absorptions between 1400 cm^{-1} and 1200 cm^{-1} are ascribed to BO_3 vibrations and those below ca. 900 cm^{-1} to AlO_x groups. IR bands between 1200 cm^{-1} and 1000 cm^{-1} (assigned to SiO_4 vibrations in Figure 8.10) decrease with increasing B_2O_3 content of the starting materials. The two resolved bands observed at ca. 1050 cm^{-1} and 1130 cm^{-1} dominant in samples I–L are ascribed to BO_4 units. Intensity scale is ATR absorbance.

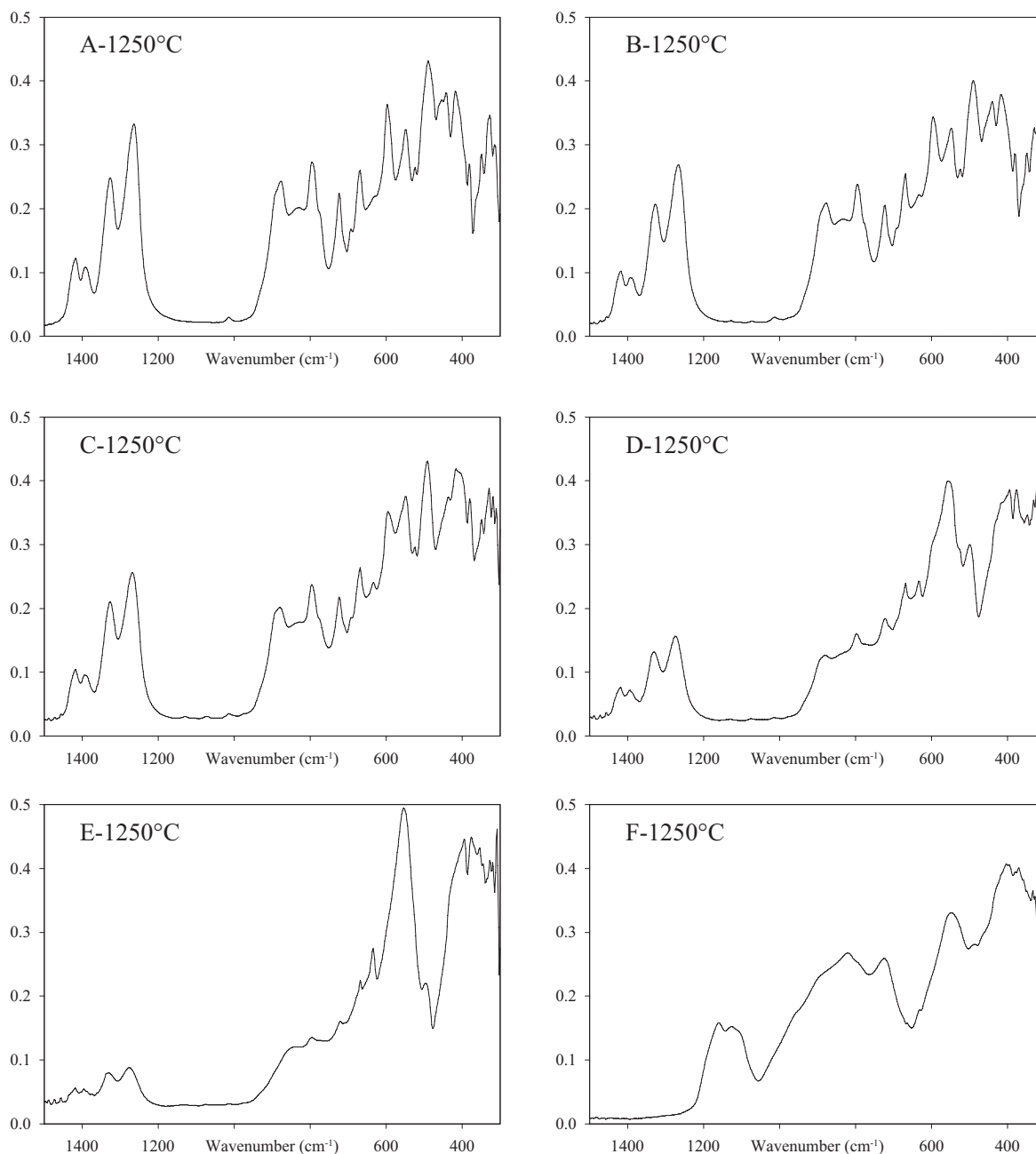


Figure 8.12: ATR-FTIR spectra of samples A–F heated at 1250°C. IR bands between 1400 cm^{-1} and 1200 cm^{-1} are ascribed to BO_3 vibrations and those between ca. 1200 cm^{-1} and 1000 cm^{-1} to SiO_4 (most expressed in sample F consisting of mullite, cristobalite and corundum). Bands below ca. 900 cm^{-1} are ascribed to AlO_x groups. The predominant broad peak at 600 cm^{-1} (samples D and E) is likely correlated with the high amount of excess corundum. Intensity scale is ATR absorbance.

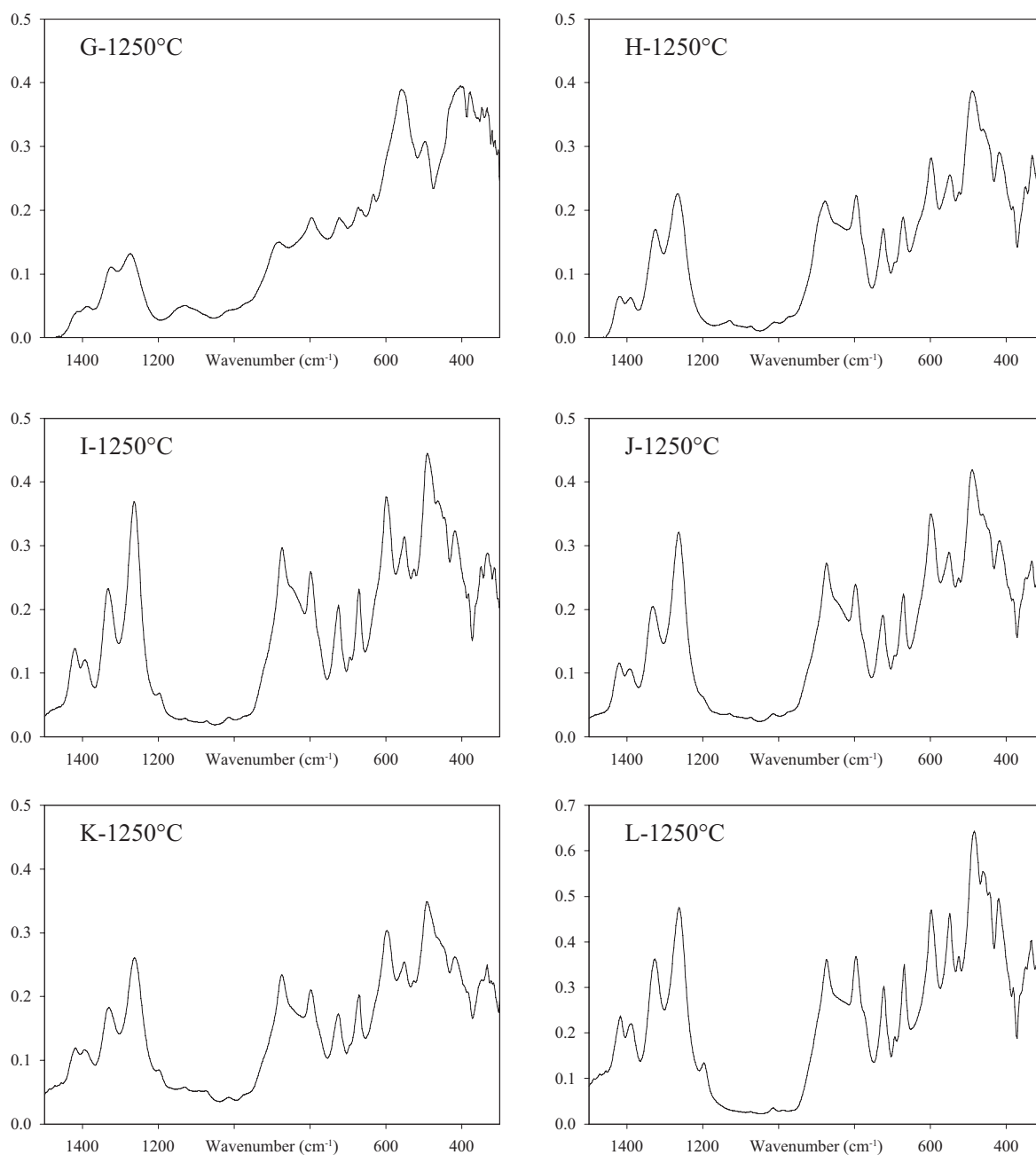


Figure 8.13: ATR-FTIR spectra of samples G–L heated at 1250°C. IR bands between 1400 cm^{-1} and 1200 cm^{-1} are ascribed to BO_3 vibrations. From a sample consisting of mullite, cristobalite and corundum, bands between ca. 1200 cm^{-1} and 1000 cm^{-1} are ascribed to SiO_4 vibrations. They are less pronounced with decreasing SiO_2 content of starting materials. Bands below ca. 900 cm^{-1} are ascribed to AlO_x groups. The predominant broad peak at 600 cm^{-1} in sample G is likely correlated with the high amount of excess corundum. A peak appearing at ca. 1200 cm^{-1} could not be identified. Intensity scale is ATR absorbance.

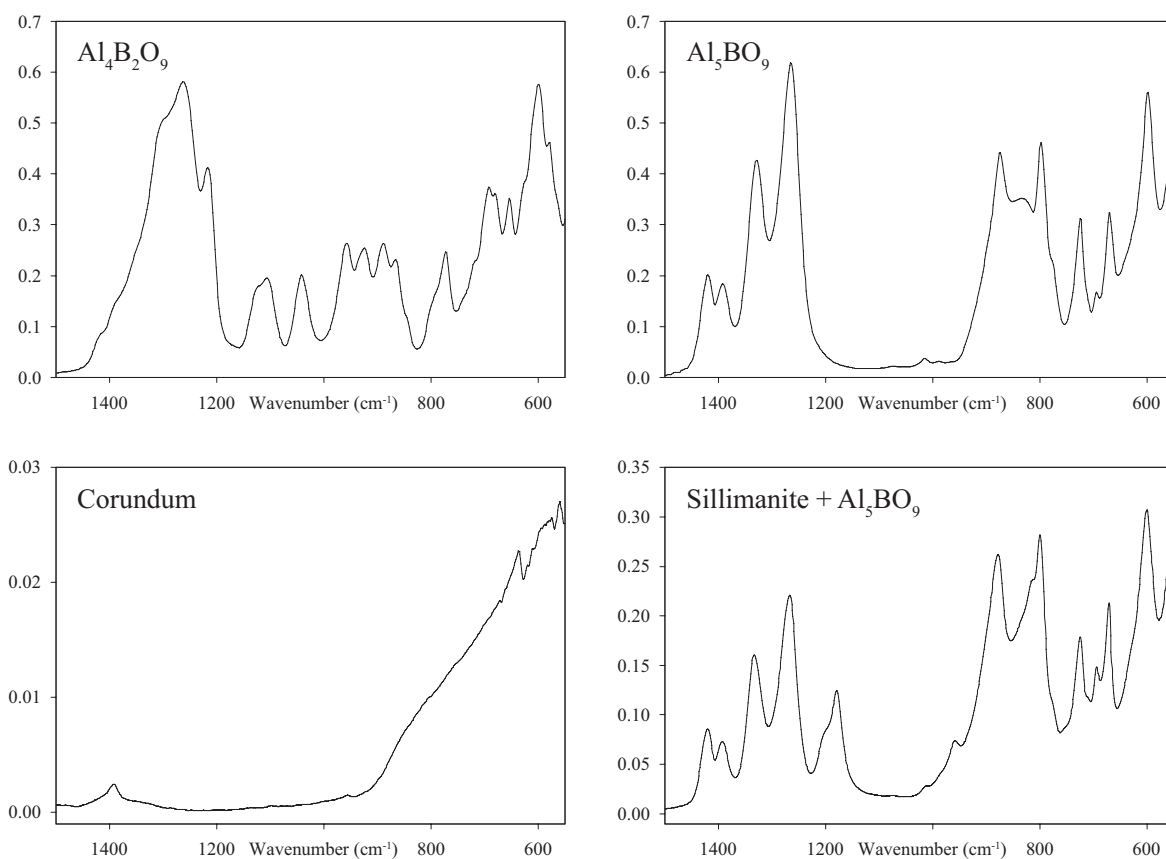


Figure 8.14: ATR-FTIR spectra of reference samples Al_5BO_9 , $\text{Al}_4\text{B}_2\text{O}_9$, corundum and a mixture of 50:50 mol-% sillimanite and Al_5BO_9 . From the spectrum of Al_4BO_9 , compared to Al_5BO_9 , the two additional IR bands at ca. 1050 cm^{-1} and 1150 cm^{-1} can be assigned to BO_4 vibrations. The spectrum of the mixture of 50:50 mol-% sillimanite and Al_5BO_9 differs mainly from the spectrum of pure Al_5BO_9 by the broad band below 1200 cm^{-1} , which can be ascribed to SiO_4 vibrations. Corundum absorptions are most expressed below ca. 900 cm^{-1} and will interfere in samples with excess corundum. Intensity scale is ATR absorbance.

References

- Åhman J., Svensson G., Grins J.: Lithium aluminum borate $\text{LiAl}_7\text{B}_4\text{O}_{17}$. *The Rigaku Journal* 51 (1997) 17–30.
- Angel R.J.: Equation of State. In *High-Temperature and High-Pressure Crystal Chemistry*, R.M. Hazen, R.T. Downs, editors, volume 41 of *Reviews in Mineralogy*, 35–59, Mineralogical Society of America, Washington, D.C. (2000).
- Angel R.J.: *EOS-FIT v. 6.0*. Crystallography Laboratory, Department of Geological Sciences, Virginia Tech, Blacksburg, VA (2001).
- Angel R.J.: *ABSORB v. 5.2*. Crystallography Laboratory, Department of Geological Sciences, Virginia Tech, Blacksburg, VA (2002).
- Angel R.J., Allan D.R., Miletich R., Finger L.W.: The use of quartz as an internal pressure standard in high-pressure crystallography. *Journal of Applied Crystallography* 30 (1997) 461–466.
- Angel R.J., Bujak M., Zhao J., Gatta G.D., Jacobsen S.D.: Effective hydrostatic limits of pressure media for high-pressure crystallographic studies. *Journal of Applied Crystallography* 40 (2007) 26–32.
- Angel R.J., McMullan R.K., Prewitt C.T.: Substructure and superstructure of mullite by neutron diffraction. *American Mineralogist* 76 (1991) 332–342.
- Angel R.J., Prewitt C.T.: Crystal structure of mullite: A re-investigation of the average structure. *American Mineralogist* 71 (1986) 1476–1482.
- Anovitz L.M., Grew E.S.: Introduction. In *Boron*, E.S. Grew, L.M. Anovitz, editors, volume 33 of *Reviews in Mineralogy*, 1–40, Mineralogical Society of America, Washington, D.C. (1996).
- Anthony J.W., Bideaux R.A., Bladh K.W., Nichols M.C.: *Handbook of Mineralogy*, volume II. Mineralogical Society of America, Washington, D.C. (2003).
- Appleman D.G., Clark J.R.: A boron-bearing potassium feldspar in volcanic ash and tuffaceous rocks from Miocene lake deposits, Samos Island, Greece. *American Mineralogist* 50 (1965) 1827–1850.
- Armbruster T., Bürgi H.B., Kunz M., Gnos E., Brönnimann S., Lienert C.: Variation of displacement parameters in structure refinements of low albite. *American Mineralogist* 75(1-2) (1990) 135–140.
- Azizov A.V., Leoniuk N.I., Rezvyi V.R., Timchenko T.I., Belov N.V.: Solubility and peculiarities of yttrium-aluminum borate crystal-growth. *Doklady Akademii Nauk SSSR* 262(6) (1982) 1384–1386.
- Balakrishnarajan M.M., Pancharatna P.D., Hoffmann R.: Structure and bonding in boron carbide: The invincibility of imperfections. *New Journal of Chemistry* 31(4) (2007) 473–485.

- Basu S., Sarin V.: Mullite Coatings. In *Mullite*, H. Schneider, S. Komarneni, editors, 349–376, Wiley-VCH, Weinheim, D (2005).
- Baudis U., Fichte R.: Boron and Boron Alloys. In *Ullmann's Encyclopedia of Industrial Chemistry, Volume A4: Benzyl Alcohol to Calcium Sulfate*, F.T. Campbell, R. Pfefferkorn, editors, 281–294, Weinheim, Deerfield Beach, FL, 5th edition (1985).
- Baumann H.N., Moore C.H.: Electric furnace boroaluminate. *Journal of the American Ceramic Society* 25(14) (1942) 391–394.
- Benner R.C., Baumann H.N.: Refractory material, US patent no. 2,118,143 (1938).
- Beregi E., Hartmann E., Malicsko L., Madarasz J.: Growth and morphology of Nd³⁺, Er³⁺ and Cr³⁺ doped YAl₃(BO₃)₄ single crystals. *Crystal Research and Technology* 34(5-6) (1999) 641–645.
- Birch F.: Finite elastic strain of cubic crystals. *Physical Review* 71(11) (1947) 809–824.
- Bither T.A.: Isotypic borates of aluminum, rhodium and thallium of calcite-type crystal structure, US patent no. 3,755,536 (1973).
- Bonatti E., Lawrence J.R., Morandi N.: Serpentinization of oceanic peridotites: Temperature dependence of mineralogy and boron content. *Earth and Planetary Science Letters* 70(1) (1984) 88–94.
- Bowen N.L., Greig J.W.: The system: Al₂O₃·B₂O₃. *Journal of the American Ceramic Society* 9(10) (1924b) 238–354.
- Bowen N.L., Greig J.W., Zies E.G.: Mullite. *American Mineralogist* 9(10) (1924a) 211–212.
- Bowen N.L., Greig J.W., Zies E.G.: Mullite, a silicate of alumina. *Washington Academy of Sciences* 14(9) (1924c) 183–191.
- Brace W.F., Scholz C.H., Lamori P.N.: Isothermal compressibility of kyanite andalusite and sillimanite from synthetic aggregates. *Journal of Geophysical Research* 74(8) (1969) 2089–2098.
- Brotherton R.J., Guibert C.R.: Boron Compounds. In *Ullmann's Encyclopedia of Industrial Chemistry, Volume A4: Benzyl Alcohol to Calcium Sulfate*, F.T. Campbell, R. Pfefferkorn, editors, 309–330, Weinheim, Deerfield Beach, FL, 5th edition (1985).
- Bruker-AXS: *ShelXTL*. Bruker AXS, Inc., Madison, WI, USA (2000).
- Bruker-AXS: *Apex2 Software v. 2009-11.0*. Bruker AXS, Inc., Madison, WI, USA (2009).
- Bruker Optik GmbH: *OPUS v. 5.5*. Bruker Optik GmbH, Ettlingen, Germany (2005).
- Brunauer G., Boysen H., Frey F., Hansen T., Kriven W.: High temperature crystal structure of 3:2 mullite from neutron diffraction data. *Zeitschrift für Kristallographie* 216 (2001a) 284–290.
- Brunauer G., Frey F., Boysen H., Schneider H.: High temperature thermal expansion of mullite: An in situ neutron diffraction study up to 1600°C. *Journal of the European Ceramic Society* 21 (2001b) 2563–2567.

- Buick I.S., Grew E.S., Armbruster T., Medenbach O., Yates M.G., Bebout G.E., Clarke G.L.: Boromullite, $\text{Al}_9\text{BSi}_2\text{O}_{19}$, a new mineral from granulite-facies metapelites, Mount Stafford, central Australia: A natural analogue of a synthetic "boron-mullite". *European Journal of Mineralogy* 20(5) (2008) 935–950.
- Burnham C.W.: Computation of absorption corrections and significance of end effect. *American Mineralogist* 51(1-2) (1966) 159–167.
- Burns P.C., Grice J.D., Hawthorne F.C.: Borate minerals I. Polyhedral clusters and fundamental building-blocks. *Canadian Mineralogist* 33 (1995) 1131–1151.
- Burt J.B., Ross N.L., Angel R.J., Koch M.: Equations of state and structures of andalusite to 9.8 GPa and sillimanite to 8.5 GPa. *American Mineralogist* 91(2-3) (2006) 319–326.
- Capponi J.J., Chenavas J., Joubert J.C.: Nouveaux borates d'aluminium et de gallium obtenus par synthèse hydrothermale à haute pression. *Bulletin de la Société Française Minéralogie et de Cristallographie* 95(3) (1972) 412–417.
- Carazeanu I., Ciupina V., Guguta C., Prodan G.: Transmission electron microscopy study on the formation of $\text{Al}_{18}\text{B}_4\text{O}_{33}$ whiskers. *Microchimica Acta* 147(3) (2004) 147–150.
- Carpenter S.B., Kistler R.B.: Boron and Borates. In *Industrial Minerals & Rocks, Commodities, Markets and Uses*, J.E. Kogel, C.T. Nikhil, J.M. Barker, S.T. Krukowski, editors, 275–284, Society for Mining, Metallurgy, and Exploration, Inc. (SMF), Littleton, CO, 7th edition (2006).
- Chakraborty A.K., Das S.: Al-Si spinel phase formation in diphasic mullite gels. *Ceramics International* 29(1) (2003) 27–33.
- Chakravorty A.K.: Intermediate Si-Al spinel phase-formation in phase-transformation of diphasic mullite gel. *Journal of Materials Science* 28(14) (1993) 3839–3844.
- Cheary R.W., Coelho A.A.: Fundamental parameters line profile fitting in laboratory diffractometers. *Journal of Research of the National Institute of Standards and Technology* 109 (2004) 1–25.
- Chen A.M., Xu S.F., Ni Z.M.: Synthesis, structure and growth mechanism of aluminum borate nanorods. *Acta Physico-Chimica Sinica* 25(12) (2009) 2570–2574.
- Cheng C., Ding X.X., Shi F.J., Cheng Y., Huang X.T., Qi S.R., Tang C.: Preparation of aluminum borate nanowires. *Journal of Crystal Growth* 263(1-4) (2004) 600–604.
- Christ C.L., Harder H.: Boron. In *Handbook of Geochemistry*, K.H. Wedepohl, editor, volume II/1, 5A1–5O3, Springer Verlag, Berlin, D (1974).
- Cividanes L.S., Campos T.M.B., Rodrigues L.A., Brunelli D.D., Thim G.P.: Review of mullite synthesis routes by sol-gel method. *Journal of Sol-Gel Science and Technology* 55 (2010) 111–125.
- Coelho A.A.: Indexing of powder diffraction patterns by iterative use of singular value decomposition. *Journal of Applied Crystallography* 36 (2003) 86–95.
- Coelho A.A.: *Topas-Academic, v. 4.1*. Coelho Software, Brisbane, Australia (2007a).

- Coelho A.A.: *Technical Reference, Topas Academic Version 4.1*. Coelho Software, Brisbane, Australia (2007b).
- Comodi P., Zanazzi P.F., Poli S., Schmidt M.W.: High-pressure behavior of kyanite: Compressibility and structural deformations. *American Mineralogist* 82(5-6) (1997) 452–459.
- Deegan F.M., Troll V.R., Deyhle A., Hansteen T.H.: Boron isotopes in feldspar: Tracing magmatic processes on Gran Canaria. *Geophysical Research Abstracts* 12 (2010) EGU General Assembly 2010.
- Deville S.C., Caron S.: Nouveau mode de production a l'état cristallisé d'un certain nombre d'espèces chimiques et minéralogiques. *Annales de chimie et de physique* 4(5) (1865) 104–118.
- Dietzel A., Scholze H.: Untersuchungen im System B_2O_3 - Al_2O_3 - SiO_2 . *Glastechnische Berichte* 28(2) (1955) 47–52.
- Dingwell D.B., Pichavant M., Holtz F.: Experimental Studies in Granitic Melts. In *Boron*, E.S. Grew, L.M. Anovitz, editors, volume 33 of *Reviews in Mineralogy*, 331–385, Mineralogical Society of America, Washington, D.C. (1996).
- Dobrzhinetskaya L., Wirth R., Yang J., Green H., Weber P., Hutcheon I.: Goldschmidt Conference Abstracts - D: Boron and Nitrogen in ultrahigh-pressure terrestrial rocks. *Geochimica et Cosmochimica Acta* 72(12) (2008) A221–A221.
- Dreyer W.: *Materialverhalten anisotroper Festkörper*. Springer, Wien, A. and New York, NY (1974).
- Duoy A.: Aluminium borates: Synthesis via a precipitation process and study of their formation by DSC analysis. *Solid State Sciences* 7(1) (2005) 117–122.
- Dzikowski T.J., Groat L.A., Grew E.S.: The geometric effects of $Fe^{V(2+)}$ for Mg^V substitution on the crystal structures of the grandidierite-ominelite series. *American Mineralogist* 92(5-6) (2007) 863–872.
- Ebelmen J.J.: Recherches sur une nouvelle méthode de cristallisation par la voie sèche, et sur ses applications à la reproduction des espèces minérales. *Comptes Rendus de l'Académie des sciences* 32 (1851) 330–333.
- Elssfah E.M., Song H.S., Tang C.C., Zhang J., Ding X.X., Qi S.R.: Synthesis of aluminum borate nanowires via a novel flux method. *Materials Chemistry and Physics* 101(2-3) (2007) 499–504.
- Fan G.H., Geng L., Lai Z.H., Wang G.S.: Preparation and properties of hybrid composite based on $(BaPbO_3+Al_{18}B_4O_{33})/6061Al$ system. *Journal of Alloys and Compounds* 482(1-2) (2009) 512–515.
- Farges F.: Crystal chemistry of iron in natural grandidierites: An X-ray absorption fine-structure spectroscopy study. *Physics and Chemistry of Minerals* 28(9) (2001) 619–629.
- Farmer V.C. (Editor): *The Infrared Spectra of Minerals*. Mineralogical Society, London, UK (1974).
- Farrugia L.J.: WinGX suite for small-molecule single-crystal crystallography. *Journal of Applied Crystallography* 32(4) (1999) 837–838.

- Fei W.D., Yue H.Y., Wang L.D.: Equicohesive temperature of the interface and matrix and its effect on the tensile plasticity of $\text{Al}_{18}\text{B}_4\text{O}_{33}$ whiskers reinforced aluminum composite at elevated temperatures. *Materials Chemistry and Physics* 119(3) (2010) 515–518.
- Feng Y.C., Geng L., Fan G.H., Li A.B., Zheng Z.Z.: The properties and microstructure of hybrid composites reinforced with WO_3 particles and $\text{Al}_{18}\text{B}_4\text{O}_{33}$ whiskers by squeeze casting. *Materials & Design* 30(9) (2009) 3632–3635.
- Filatov S.K., Bubnova R.S.: Borate crystal chemistry. *Physics and Chemistry of Glasses* 41(5) (2000) 216–224.
- Filatov S.K., Bubnova R.S.: Structural Mineralogy of Borates as Perspective Materials for Technological Applications. In *Minerals as Advanced Materials I*, S.V. Krivovichev, editor, 111–115, Springer, Berlin, D (2008).
- Fisch M., Armbruster T., Rentsch D., Libowitzky E., Pettke T.: Crystal-chemistry of mullite-type aluminoborates $\text{Al}_{18}\text{B}_4\text{O}_{33}$ and Al_5BO_9 : A stoichiometry puzzle. *Journal of Solid State Chemistry* 184(1) (2011) 70–80.
- Fischer R.X., Kahlenberg V., Voll D., MacKenzie K.J.D., Smith M.E., Schnetger B., Brumsack H.J., Schneider H.: Crystal structure of synthetic $\text{Al}_4\text{B}_2\text{O}_9$: A member of the mullite family closely related to boralsilite. *American Mineralogist* 93(5-6) (2008b) 918–927.
- Fischer R.X., Schneider H.: The Mullite-type Family of Crystal Structures. In *Mullite*, H. Schneider, S. Komarneni, editors, 1–46, Wiley-VCH, Weinheim, D (2005).
- Fischer R.X., Schneider H.: Crystal chemistry of borates and borosilicates with mullite-type structures: A review. *European Journal of Mineralogy* 20(5) (2008a) 917–933.
- Fischer R.X., Schneider H., Schmücker M.: Crystal structure of Al-rich mullite. *American Mineralogist* 79 (1994) 983–990.
- Fischer R.X., Schneider H., Voll D.: Formation of alumina rich 9:1 mullite and its transformation to low alumina mullite upon heating. *Journal of the European Ceramic Society* 16 (1996) 109–113.
- Flack H.D.: On enantiomorph-polarity estimation. *Acta Crystallographica Section A: Foundations of Crystallography* A39 (1983) 876–881.
- Foord E.E., Cunningham C.G.: Thermal transformation of anomalously biaxial dimetric crystals. *American Mineralogist* 63(1-2) (1978) 747–749.
- Foord E.E., Erd R.C., Hunt G.R.: New data for jeremejevite. *Canadian Mineralogist* 19(303-310).
- Friedrich A., Kunz M., Winkler B., Le Bihan T.: High-pressure behavior of sillimanite and kyanite: Compressibility, decomposition and indications of a new high-pressure phase. *Zeitschrift für Kristallographie* 219(6) (2004) 324–329.
- Fung B.M., Khitrin A.K., Ermolaev K.: An improved broadband decoupling sequence for liquid crystals and solids. *Journal of Magnetic Resonance* 142(1) (2000) 97–101.

- Galactic Industries Corp.: *GRAMS/32 v. 4.14*. Galactic Industries Corporation, Salem, NH, USA (1996).
- Gan Z.H., Gor'kov P., Cross T.A., Samoson A., Massiot D.: Seeking higher resolution and sensitivity for NMR of quadrupolar nuclei at ultrahigh magnetic fields. *Journal of the American Chemical Society* 124(20) (2002) 5634–5635.
- Garrett D.E.: *Borates: Handbook of Deposits, Processing, Properties, and Use*. Academic Press, San Diego, CA (1998).
- Garsche M., Tillmanns E., Almen H., Schneider H., Kupcik V.: Incorporation of chromium into aluminium borate $9\text{Al}_2\text{O}_3 \cdot 2\text{B}_2\text{O}_3$ (A9B2). *European Journal of Mineralogy* 3(5) (1991) 793–808.
- Gatta G.D.: Extreme deformation mechanisms in open-framework silicates at high-pressure: Evidence of anomalous inter-tetrahedral angles. *Microporous and Mesoporous Materials* 128(1-3) (2010) 78–84.
- Gatta G.D., Nestola F., Ballaran T.B.: Elastic behavior, phase transition, and pressure induced structural evolution of analcime. *American Mineralogist* 91(4) (2006a) 568–578.
- Gatta G.D., Nestola F., Walter J.M.: On the thermo-elastic behaviour of kyanite: a neutron powder diffraction study up to 1200°C. *Mineralogical Magazine* 70(3) (2006b) 309–317.
- Gatta G.D., Rotiroti N., Fisch M., Armbruster T.: Stability at high pressure, elastic behavior and pressure-induced structural evolution of " Al_5BO_9 ", a mullite-type ceramic material. *Physics and Chemistry of Minerals* 37(4) (2010) 227–236.
- Gatta G.D., Rotiroti N., Fisch M., Kadiyski M., Armbruster T.: Stability at high-pressure, elastic behaviour and pressure-induced structural evolution of $\text{CsAlSi}_5\text{O}_{12}$, a potential host for nuclear waste. *Physics and Chemistry of Minerals* 35(9) (2008) 521–533.
- Geng L., Guan L.N., Lu K.M.: Effects of whisker surface treatment on microstructure and properties of $\text{Al}_{18}\text{B}_4\text{O}_{33}\text{w}/6061\text{Al}$ composites. *Transactions of Nonferrous Metals Society of China* 20(3) (2010) 349–354.
- Gielisse P.J.M., Forster W.R.: The system $\text{Al}_2\text{O}_3\text{-B}_2\text{O}_3$. *Nature* 195 (1962) 69–70.
- Golovastikov N.I., Belova E.N., Belov N.V.: The crystal structure of jeremejevite. *Doklady Akademii Nauk SSSR* 104 (1955) 78–81.
- Gönenli I.E., Tas A.C.: Chemical preparation of aluminum borate whiskers. *Powder Diffraction* 15(2) (2000) 104–107.
- Grew E.S.: Borosilicates (Exclusive of Tourmaline) and Boron in Rock-Forming Minerals in Metamorphic Environments. In *Boron*, E.S. Grew, L.M. Anovitz, editors, volume 33 of *Reviews in Mineralogy*, 387–502, Mineralogical Society of America, Washington, D.C. (1996).
- Grew E.S., Bada J.L., Hazen R.M.: Borate Minerals and Origin of the RNA World. *Origins of Life and Evolution of Biospheres* (2011), available online at DOI 10.1007/s11084-010-9233-y.

- Grew E.S., Graetsch H.A., Pöter B., Yates M.G., Buick I., Bernhardt H.J., Schreyer W., Werding G., Carson C.J., Clarke G.L.: Boralsilite, $\text{Al}_{16}\text{B}_6\text{Si}_2\text{O}_{37}$, and "boron-mullite": Compositional variations and associated phases in experiment and nature. *American Mineralogist* 93(2-3) (2008) 283–299.
- Grew E.S., Hinthorne J.R.: Boron in sillimanite. *Science* 221(4610) (1983) 547–549.
- Grew E.S., McGee J.J., Yates M.G., Peacor D.R., Rouse R.C., Huijsmans J.P.P., Shearer C.K., Wiedenbeck M., Thost D.E., Su S.C.: Boralsilite ($\text{Al}_{16}\text{B}_6\text{Si}_2\text{O}_{37}$): A new mineral related to sillimanite from pegmatites in granulite-facies rocks. *American Mineralogist* 83 (1998) 638–651.
- Grice J.D., Burns P.C., Hawthorne F.C.: Borate minerals II. A hierarchy of structures based upon the borate fundamental building block. *Canadian Mineralogist* 37 (1995) 731–762.
- Griesser K.J., Beran A., Voll D., Schneider H.: Boron incorporation into mullite. *Mineralogy and Petrology* 92(3-4) (2008) 309–320.
- Guillong M., Meier D.L., Allan M.M., Heinrich C.A., Yardley B.W.D.: SILLS: A MATLAB-based program for the reduction of laser ablation ICP-MS data of homogeneous materials and inclusions. In *Laser Ablation ICP-MS in the Earth Sciences: Current Practices and Outstanding Issues*, P. Sylvester, editor, volume 40 of *Short Course Series*, 328–333, Mineralogical Association of Canada, Vancouver, BC (2008).
- Gutierrez G., Taga A., Johansson B.: Theoretical structure determination of $\gamma\text{-Al}_2\text{O}_3$. *Physical Review B (Condensed Matter and Materials Physics)* 65(1) (2002) 012101/1–4.
- Hammond C.R.: The Elements. In *Handbook of Chemistry and Physics*, R.C. Weast, editor, B4–B38, CRC Press, Cleveland, OH, 55th edition (1985).
- Hannaford P., Lowe R.M.: Determination of boron isotope ratio by atomic-absorption spectrometry. *Analytical Chemistry* 49(12) (1977) 1852–1857.
- Harrick N.J.: *Internal Reflection Spectroscopy*. Interscience Publishers / Wiley, New York, NY (1967).
- Harris D., Bertolucci M.D.: *Symmetry and Spectroscopy. An Introduction to Vibrational and Electronic Spectroscopy*. Dover, New York, NY (1989).
- Harris R.K., Becker E.D., De Menezes S.M.C., Goodfellow R., Granger P.: NMR nomenclature. Nuclear spin properties and conventions for chemical shifts - (IUPAC recommendations 2001). *Pure and Applied Chemistry* 73(11) (2001) 1795–1818.
- Hawthorne F.C., Burns P.C., Grice J.D.: The Crystal Chemistry of Boron. In *Boron*, E.S. Grew, L.M. Anovitz, editors, volume 33 of *Reviews in Mineralogy*, 41–115, Mineralogical Society of America, Washington, D.C. (1996).
- Hazen R.M., Prewitt C.T.: Effects of temperature and pressure on interatomic distances in oxygen-based minerals. *American Mineralogist* 62(3-4) (1977) 309–315.
- Henry D.J., Dutrow B.L.: Metamorphic Tourmaline and its Petrologic Applications. In *Boron*, E.S. Grew, L.M. Anovitz, editors, volume 33 of *Reviews in Mineralogy*, 503–557, Mineralogical Society of America, Washington, D.C. (1996).

- Hervig R.L.: Analyses of Geological Materials for Boron by Secondary Ion Mass Spectrometry. In *Boron*, E.S. Grew, L.M. Anovitz, editors, volume 33 of *Reviews in Mineralogy*, 789–803, Mineralogical Society of America, Washington, D.C. (1996).
- Higgins M.D., Shaw D.M.: Boron cosmochemistry interpreted from abundances in mantle xenoliths. *Nature* 308 (1984) 172–173.
- Hildmann B., Ledbetter H., Kim S., Schneider H.: Structural control of elastic constants of mullite in comparison to sillimanite. *Journal of the American Ceramic Society* 84(10) (2001) 2409–2414.
- Hiroi Y., Grew E.S., Motoyoshi Y., Peacor D.R., Rouse E.C., Matsubara S., Yokohama K., Miyawaki R., McGee J.J., Su S.C., Hokada T., Furuwaka N., Shibasaki H.: Ominelite, $(\text{Fe,Mg})\text{Al}_3\text{BSiO}_9$ (Fe^{2+} analogue of grandierite), a new mineral from porphyritic granite in Japan. *American Mineralogist* 87 (2001) 160–170.
- Hung I., Howes A.P., Anupold T., Samoson A., Massiot D., Smith M.E., Brown S.P., Dupree R.: ^{27}Al double rotation two-dimensional spin diffusion NMR: Complete unambiguous assignment of aluminium sites in $9\text{Al}_2\text{O}_3\cdot 2\text{B}_2\text{O}_3$. *Chemical Physics Letters* 432(1-3) (2006) 152–156.
- Ihara M., Imai K., Fukunaga J., Yoshida N.: Crystal structure of boroaluminate, $9\text{Al}_2\text{O}_3\cdot 2\text{B}_2\text{O}_3$. *Yogyo Kyokai Shi* 88(1014) (1980) 77–84.
- Jing J., Tao Y., Li G.B., Liao F.H., Wang Y.X., You L.P., Lin J.H.: PKU-5: An aluminoborate with novel octahedral framework topology. *Chemistry - A European Journal* 10(16) (2004) 3901–3906.
- Johnson C.K.: An Introduction to Thermal Motion Analysis. In *Crystallographic Computing*, F.R. Ahmed, editor, Munksgaard, Copenhagen, DK (1970).
- Kadiyski M., Armbruster T., Gunther D., Reusser E., Peretti A.: Johachidolite, $\text{CaAl}[\text{B}_3\text{O}_7]$, a mineralogical and structural peculiarity. *European Journal of Mineralogy* 20(5) (2008) 965–973.
- Kaduk J.A., Satek L.C., McKenna S.T.: Crystal structures of metal aluminum borates. *The Rigaku Journal* 16(2) (1999) 17–30.
- Kakihana H., Kotaka M., Satoh S., Nomura M., Okamoto M.: Fundamental studies on ion-exchange separation of boron isotopes. *Bulletin of the Chemical Society of Japan* 50(1) (1977) 158–163.
- Kerr R., Needham J., Wood N.: *Science and Civilization in China*, volume 5. Cambridge University Press, Cambridge, UK (2004).
- Kim K.H., Hummel F.A.: Studies in lithium oxide systems - XII, $\text{Li}_2\text{O}\cdot\text{B}_2\text{O}_3\cdot\text{Al}_2\text{O}_3$. *Journal of the American Ceramic Society* 45(10) (1962) 487–489.
- Kim S.W., Lee S.G., Kim J.K., Kwon J.Y., Park H.C., Park S.S.: Synthesis of aluminum borate whiskers via flux method with and without microwaves. *Journal of Materials Science* 39(4) (2004) 1445–1447.
- Kistler R.B., Helvacı C.: Boron and Borates. In *Industrial Minerals & Rocks, Commodities, Markets and Uses*, D.D. Carr, editor, 171–186, Society for Mining, Metallurgy, and Exploration, Inc. (SMF), Littleton, CO, 6th edition (2006).

- Klochko K., Cody G.D., Tossell J.A., Dera P., Kaufman A.J.: Re-evaluating boron speciation in biogenic calcite and aragonite using ^{11}B MAS NMR. *Geochimica et Cosmochimica Acta* 73(7) (2009) 1890–1900.
- Komarneni S., Schneider H., Okada K.: Mullite Synthesis and Processing. In *Mullite*, H. Schneider, S. Komarneni, editors, 251–286, Wiley-VCH, Weinheim, D (2005).
- Kriven W.M., Palko J.W., Sinogeikin S., Bass J.D., Sayir A., Brunauer G., Boysen H., Frey F., Schneider J.: High temperature single crystal properties of mullite. *Journal of the European Ceramic Society* 19(13-14) (1999) 2529–2541.
- Kroeker S., Stebbins J.F.: Three-coordinated ^{11}B boron chemical shifts in borates. *Inorganic Chemistry* 40(24) (2001) 6239–6246.
- Kroslakova I., Günther D.: Elemental fractionation in laser ablation-inductively coupled plasma-mass spectrometry: Evidence for mass load induced matrix effects in the icp during ablation of a silicate glass. *Journal of Analytical Atomic Spectrometry* 22(1) (2007) 51–62.
- Kunz M., Armbruster T.: Difference displacement parameters in alkali feldspars: Effects of (Si,Al) order-disorder. *American Mineralogist* 75(1-2) (1990) 141–149.
- Lawrence A.J., Buseck P.R.: Parallel Electron Energy-Loss Spectroscopy of Boron in Minerals. In *Boron*, E.S. Grew, L.M. Anovitz, editors, volume 33 of *Reviews in Mineralogy*, 821–843, Mineralogical Society of America, Washington, D.C. (1996).
- Lee H.K., Zerbetto S., Colombo P., Pantano C.G.: Glass-ceramics and composites containing aluminum borate whiskers. *Ceramics International* 36 (2010) 1589–1596.
- Leeman W.P., Sisson V.B.: Boron Isotope Geochemistry: Implications for Earth Processes. In *Boron*, E.S. Grew, L.M. Anovitz, editors, volume 33 of *Reviews in Mineralogy*, 789–803, Mineralogical Society of America, Washington, D.C. (1996).
- Lehmann H.A., Teske K.: Über einige neue Borate des Aluminiums. *Zeitschrift für anorganische und allgemeine Chemie* 400 (1973) 169–175.
- Leonyuk N.I.: Structural aspects in crystal growth of anhydrous borates. *Journal of Crystal Growth* 174(1-4) (1997) 301–307.
- Leonyuk N.I., Pashkova A.V., Gokhman L.Z.: Volatility of potassium trimolybdate melt and solubility of yttrium-aluminium borate in it. *Journal of Crystal Growth* 49(1) (1980) 141–144.
- Leonyuk N.I., Shvanskiy E.P.: X-ray powder diffraction study of solids in the $\text{CaO-Al}_2\text{O}_3\text{-B}_2\text{O}_3$ system. *Materials Science Forum: EPDIC 5, Pts 1 and 2* 278-2 (1998) 589–593.
- Letort Y.: Contribution à l'étude de la synthèse de la mullite. *Transactions of the International Ceramic Congress* 19–32.
- Li Y., Chang R.P.H.: Synthesis and characterization of aluminum borate ($\text{Al}_{18}\text{B}_4\text{O}_{33}$, $\text{Al}_4\text{B}_2\text{O}_9$) nanowires and nanotubes. *Materials Chemistry and Physics* 97(1) (2006) 23–30.

- Liu G., Ren W.C., Sun Y.L., Hu J.: Damping behavior of Bi₂O₃-coated Al₁₈B₄O₃₃ whisker-reinforced pure Al composite. *Materials Science and Engineering A: Structural Materials: Properties, Microstructure and Processing* 527(20) (2010a) 5136–5142.
- Liu G., Sun Y., Hu J., Zhou K.: Damping capacity of Bi₂O₃-coated Al₁₈B₄O₃₃ whisker reinforced Al matrix composites. *Acta Metallurgica Sinica* 46(8) (2010b) 979–983.
- London D., Morgan G.B., Wolf M.B.: Boron in Granitic Rocks and their Contact Aureoles. In *Boron*, E.S. Grew, L.M. Anovitz, editors, volume 33 of *Reviews in Mineralogy*, 299–330, Mineralogical Society of America, Washington, D.C. (1996).
- Ma R.Z., Bando Y., Sato T., Tang C.C., Xu F.F.: Single-crystal Al₁₈B₄O₃₃ microtubes. *Journal of the American Chemical Society* 124(36) (2002) 10668–10669.
- MacKenzie K.J.D.: Spectroscopy of Mullite and Compounds with Mullite-related Structures. In *Mullite*, H. Schneider, S. Komarneni, editors, 189–215, Wiley-VCH, Weinheim, D (2005).
- MacKenzie K.J.D., Meinhold R.H.: MAS NMR study of pentacoordinated magnesium in grandidierite. *American Mineralogist* 82(5-6) (1997) 479–482.
- MacKenzie K.J.D., Smith M.E., Kemp T.F., Voll D.: Crystalline aluminium borates with the mullite structure: A ¹¹B and ²⁷Al solid-state NMR study. *Applied Magnetic Resonance* 32(4) (2007) 647–662.
- Mallard E.: Sur diverses substances cristallisées qu’Ebelmen avait préparées et non decrites. *Bulletin de la Société Française Minéralogie et de Cristallographie* 105 (1887) 1260–1265.
- Marcos M.T., Rehren T., Freestone C.: Mullite and the mystery of Hessian wares. *Nature* 444 (2006) 437–438.
- Massiot D., Fayon F., Capron M., King I., Le Calve S., Alonso B., Durand J.O., Bujoli B., Gan Z.H., Hoatson G.: Modelling one- and two-dimensional solid-state NMR spectra. *Magnetic Resonance in Chemistry* 40(1) (2002) 70–76.
- Massiot D., Muller D., Hubert T., Schneider M., Kentgens A.P.M., Cote B., Coutures J.P., Gessner W.: Double-rotation and magic-angle-spinning nuclear-magnetic-resonance study of ²⁷Al: Reexamination of the aluminum borate 9Al₂O₃·2B₂O₃. *Solid State Nuclear Magnetic Resonance* 5(2) (1995) 175–180.
- Mazza D., Ronchetti S., Delmastro A., Tribaudino M., Kockelmann W.: Silica-free mullite structures in the Al₂O₃-B₂O₃-P₂O₅ ternary system. *Chemistry of Materials* 13 (2001) 103–108.
- Mazza D., Vallino M., Busca G.: Mullite-type structures in the systems Al₂O₃-Me₂O₃ (Me = Na,K) and Al₂O₃-B₂O₃. *Journal of the American Ceramic Society* 75(7) (1992) 1929–1934.
- McCusker L.B., Von Dreele R.B., Cox D.E., Louër D., Scardi P.: Indexing of powder diffraction patterns by iterative use of singular value decomposition. *Journal of Applied Crystallography* 32 (1999) 36–50.

- McGee J.J.: Electron Probe Microanalysis of Geological Materials for Boron. In *Boron*, E.S. Grew, L.M. Anovitz, editors, volume 33 of *Reviews in Mineralogy*, 771–788, Mineralogical Society of America, Washington, D.C. (1996).
- MIL-HDBK-17-5: *Composite Materials Handbook, Volume 5: Ceramic Matrix Composites*. Department of Defense, USA (2002).
- Miletich R., Allan D.R., Kuhs W.F.: High-pressure single-crystal techniques. *High-Temperature and High-Pressure Crystal Chemistry* 41 (2000) 445–519.
- Moore J.M., Waters D.J., Niven M.L.: Werdingite, a new borosilicate mineral from the granulite facies of the western Namaqualand metamorphic complex, South-Africa. *American Mineralogist* 75 (1990) 415–420.
- Nekrasova L.V., Leonyuk N.I.: YbAl₃(BO₃)₄ and YAl₃(BO₃)₄ crystallization from K₂Mo₃O₁₀-based high-temperature solutions: Phase relationships and solubility diagrams. *Journal of Crystal Growth* 311(1) (2008) 7–9.
- Nelmes R.J., Loveday J.S., Allan D.R., Besson J.M., Hamel G., Grima P., Hull S.: Neutron- and X-ray-diffraction measurements of the bulk modulus of boron. *Physical Review B (Condensed Matter and Materials Physics)* 47(13) (1993) 7668–7673.
- Niven M.L., Waters D.J., Moore J.M.: The crystal-structure of werdingite, (Mg,Fe)₂Al₁₂(Al,Fe)₂Si₄(B,Al)₄O₃₇, and its relationship to sillimanite, mullite, and grandierite. *American Mineralogist* 76(1-2) (1991) 246–256.
- Oganov A.R.: Phase Diagram and novel High-Pressure Phase. In *Boron Rich Solids: Sensors, Ultra High Temperature Ceramics, Thermoelectrics, Armor*, N. Orlovskaya, M. Lugovy, editors, NATO Science for Peace and Security Series - B: Physics and Biophysics, 207–227, Springer, Dordrecht, NL (2010).
- Oganov A.R., Chen J., Gatti C., Ma Y., Ma Y., Glass C.W., Liu Z., Yu T., Kurakevych O.O., Solozhenko V.L.: Ionic high-pressure form of elemental boron. *Nature* 457 (2009) 863–867.
- Okada K., Schneider H.: Applications of Mullite Ceramics. In *Mullite*, H. Schneider, S. Komarneni, editors, 327–348, Wiley-VCH, Weinheim, D (2005).
- Oxford Diffraction Ltd.: *Xcalibur CCD System and CrysAlis Software system, v. 1.170*. Oxford Diffraction Ltd., Tubney Woods, Abingdon, Oxfordshire, UK (2005).
- Palko J.W., Sayir A., Sinogeikin S.V., Kriven W.M., Bass J.D.: Complete elastic tensor for mullite (similar to 2.5Al₂O₃·SiO₂) to high temperatures measured from textured fibers. *Journal of the American Ceramic Society* 85(8) (2002) 2005–2012.
- Palmer M.R., Swihart G.H.: Boron Isotope Geochemistry: An Overview. In *Boron*, E.S. Grew, L.M. Anovitz, editors, volume 33 of *Reviews in Mineralogy*, 709–744, Mineralogical Society of America, Washington, D.C. (1996).
- Park H., Barbier J., Hammond R.P.: Crystal structure and polymorphism of PbAlBO₄. *Chemistry of Materials* 5 (2003) 565–571.

- Peacor D.R., Rouse R.C., Grew E.S.: Crystal structure of boralsilite and its relation to a family of boroaluminosilicates, sillimanite, and andalusite. *American Mineralogist* 84(7-8) (1999) 1152–1161.
- Pearce N.J.G., Perkins W.T., Westgate J.A., Gorton M.P., Jackson S.E., Neal C.R., Chenery S.P.: A compilation of new and published major and trace element data for NIST SRM 610 and NIST SRM 612 glass reference materials. *Geostandards Newsletter: The Journal of Geostandards and Geoanalysis* 21(1) (1997) 115–144.
- Peng L.M., Li X.K., Li H., Wang J.H., Gong M.: Synthesis and microstructural characterization of aluminum borate whiskers. *Ceramics International* 32(4) (2006) 365–368.
- Pettke T.: Analytical protocols for element concentration and isotope ratio measurements in fluid inclusions by LA-(MC)-ICP-MS. In *Laser Ablation ICP-MS in the Earth Sciences: Current Practices and Outstanding Issues*, P. Sylvester, editor, volume 40 of *Short Course Series*, 189–218, Mineralogical Association of Canada, Vancouver, BC (2008).
- Plachinda P.A., Belokoneva E.L.: Synthesis and crystal structure of commensurate polymorph of $Ln_4AlCu_2B_9O_{23}$ ($Ln=Lu, Ho$) and refinement of $Cu_2Al_6B_4O_{17}$. *Zeitschrift für anorganische und allgemeine Chemie* 634 (2008) 1965–1970.
- Rahman S., Freimann S.: The Real Structure of Mullite. In *Mullite*, H. Schneider, S. Komarneni, editors, 46–70, Wiley-VCH, Weinheim, D (2005).
- Ralph R.L., Finger L.W., Hazen R.M., Ghose S.: Compressibility and crystal-structure of andalusite at high-pressure. *American Mineralogist* 69(5-6) (1984) 513–519.
- Ray S.P.: Preparation and characterization of aluminum borate. *Journal of the American Ceramic Society* 75(9) (1992) 2605–2609.
- Reynaud C.: Synthèse, analyse thermique et micrographie de nouveaux borates d'aluminium. *Bulletin de la Société Française Minéralogie et de Cristallographie* 100(3) (1977) 28–32.
- Robertson J.D., Dyar M.D.: Nuclear Methods for Analysis of Boron in Minerals. In *Boron*, E.S. Grew, L.M. Anovitz, editors, volume 33 of *Reviews in Mineralogy*, 805–820, Mineralogical Society of America, Washington, D.C. (1996).
- Rogers F.R.: Glass compositions, US patent no. 2,693,423 (1950).
- Rymon-Lipinski T., Hennicke H.W., Lingenberg W.: Die Reaktion von Al_2O_3 mit B_2O_3 bei hohen Temperaturen. *Keramische Zeitschrift* 36(11) (1984) 601–606.
- Rymon-Lipinski T., Hennicke H.W., Lingenberg W.: Die Zersetzung von $9Al_2O_3 \cdot 2B_2O_3$ bei hohen Temperaturen. *Keramische Zeitschrift* 365(37) (1985) 450–453.
- Saalfeld H., Guse W.: Structure refinement of 3:2-mullite ($3Al_2O_3 \cdot 2SiO_2$). *Neues Jahrbuch für Mineralogie - Monatshefte* 4 (1981) 145–150.
- Schneider H.: Mullit. In *Technische Keramik*, W. Kollenberg, editor, 226–230, Vulkan-Verlag GmbH, Essen, D (2004).

-
- Schneider H.: General introduction. In *Mullite*, H. Schneider, S. Komarneni, editors, XV–XIX, Wiley-VCH, Weinheim, D (2005a).
- Schneider H.: Mullite Matrix Composites. In *Mullite*, H. Schneider, S. Komarneni, editors, 397–467, Wiley-VCH, Weinheim, D (2005b).
- Schneider H., Eberhard E.: Thermal expansion of mullite. *Journal of the American Ceramic Society* 73 (1990) 2073–2076.
- Schneider H., Komarneni S.: *Mullite*. Wiley-VCH, Weinheim, D (2005).
- Schneider H., Schreuer J., Hildmann B.: Structures and properties of mullite – A review. *Journal of the European Ceramic Society* 28 (2008) 329–344.
- Scholz H.: Über Aluminiumborate. *Zeitschrift für anorganische und allgemeine Chemie* 284(4-6) (1956) 272–277.
- Schreuer J., Hildmann B., Schneider H.: Elastic properties of mullite single crystals up to 1400°C. *Journal of the American Ceramic Society* 89(5) (2006) 1624–1631.
- Schreyer W., Werding G.: High-pressure behaviour of selected boron minerals and the question of boron distribution between fluids and rocks. *Lithos* 41 (1997) 251–266.
- Schwetz K.A.: Boron Carbide, Boron Nitride, and Metal Borides. In *Ullmann's Encyclopedia of Industrial Chemistry, Volume A4: Benzyl Alcohol to Calcium Sulfate*, F.T. Campbell, R. Pfeifferkorn, editors, 295–308, Weinheim, Deerfield Beach, FL, 5th edition (1985).
- Sheldrick G.M.: *SHELX-97. Programs for crystal structure determination and refinement*. University of Göttingen, D (1997).
- Shepherd E.S., Rankin G.A., Wright F.E.: The binary systems of alumina with silica, lime and magnesia. *American Journal of Science* 28(166) (1909) 293–333.
- Siebert H.: *Anwendungen der Schwingungsspektroskopie in der anorganischen Chemie*. Springer, Berlin, D (1966).
- Smallman R.E., Bishop R.J.: *Modern Physical Metallurgy & Materials Engineering*. Butterworth-Heinemann, Oxford, UK, 6th edition (1999).
- Smith G.I., Medrano M.J.: Continental Borate Deposits of Cenozoic Age. In *Boron*, E.S. Grew, L.M. Anovitz, editors, volume 33 of *Reviews in Mineralogy*, 263–298, Mineralogical Society of America, Washington, D.C. (1996).
- Smith R.A.: Boric Oxide, Boric Acide, and Borates. In *Ullmann's Encyclopedia of Industrial Chemistry, Volume A4: Benzyl Alcohol to Calcium Sulfate*, F.T. Campbell, R. Pfeifferkorn, editors, 263–280, Weinheim, Deerfield Beach, FL, 5th edition (1985).
- Smith R.A.: Basic geology and geochemistry of borates. *American Ceramic Society Bulletin* 81(8) (2002) 61–64.

- Sokolov V.A., Gasparyan M.A.: Synthesis and properties of fusion-cast refractories in the $\text{Al}_2\text{O}_3\text{-B}_2\text{O}_3$ system. *Refractories and Industrial Ceramics* 45(3) (2004) 177–180.
- Sokolova E.V., Azizov A.V., Simonov M.A., Leoniuk N.I., Belov N.V.: Crystal-structure of synthetic ortho-3-borate, $\text{Al}_5(\text{BO}_3)\text{O}_6$. *Doklady Akademii Nauk SSSR* 243(3) (1978) 655–658.
- Song H.S., Zhang J., Lin J., Liu S.J., Luo J.J., Huang Y., Elssfah E.M., Elsanousi A., Ding X.X., Gao J.M., Tang C.C.: Coating aluminum borate ($\text{Al}_{18}\text{B}_4\text{O}_{33}$) nanowire webs with BN. *Journal of Physical Chemistry C* 111(3) (2007) 1136–1139.
- Stachowiak A., Schreyer W.: Synthesis, stability and breakdown products of the hydroxyl end member of jeremejevite in the system $\text{Al}_2\text{O}_3\text{-B}_2\text{O}_3\text{-H}_2\text{O}$. *European Journal of Mineralogy* 10 (1998) 875–888.
- Stamatakis M.G.: Crystal structure of reedmergnerite, a boron albite, and its relation to feldspar crystal chemistry. *American Mineralogist* 74 (1989) 230–235.
- Stephenson D.A., Moore P.B.: The crystal structure of grandidierite, $(\text{Mg,Fe})\text{Al}_3\text{SiBO}_9$. *Acta Crystallographica Section B: Structural Science* B24 (1968) 1518–1522.
- Stinton W.G., Evans J.E.: Parametric rietveld refinement. *Journal of Applied Crystallography* 40 (2007) 87–95.
- Swihart G.H.: Instrumental Techniques for Boron Isotope Analysis. In *Boron*, E.S. Grew, L.M. Anovitz, editors, volume 33 of *Reviews in Mineralogy*, 789–803, Mineralogical Society of America, Washington, D.C. (1996).
- Tang C.C., Elssfah E.M., Zhang J., Chen D.F.: Morphology- and composition-controlled synthesis of aluminium borate nanowires without catalysts. *Nanotechnology* 17(9) (2006) 2362–2367.
- Tao X.Y., Wang X.N., Li X.D.: Nanomechanical characterization of one-step, combustion-synthesized $\text{Al}_4\text{B}_2\text{O}_9$ and $\text{Al}_{18}\text{B}_4\text{O}_{33}$ nanowires. *Nano Letters* 7 (2007) 3172–3176.
- Teshima K., Kikuchi Y., Suzuki T., Oishi S.: Growth of $\text{ErAl}_3(\text{BO}_3)_4$ single crystals from a $\text{K}_2\text{Mo}_3\text{O}_{10}$ flux. *Crystal Growth & Design* 6(8) (2006) 1766–1768.
- Toby B.H.: R-factors in Rietveld analysis: How good is good enough? *Powder Diffraction* 21 (2006) 67–70.
- Travitzky N.A.: Mechanical properties and microstructure of mullite whisker-reinforced magnesium aluminosilicate glass with cordierite composition. *Journal of Materials Science Letters* 17 (1998) 1609–1611.
- Tröger W.E.: *Optische Bestimmung der gesteinsbildenden Minerale*. E. Schweizerbart'sche Verlagsbuchhandlung, Stuttgart, D, 5th edition (1971).
- Tucker M.G., Dove M.T., Keen D.A.: Direct measurement of the thermal expansion of the Si-O bond by neutron total scattering. *Journal of Physics: Condensed Matter* 12(425-430) (2000) 71–75.
- Vaughan M.T., Weidner D.J.: Relationship of elasticity and crystal-structure in andalusite and sillimanite. *Physics and Chemistry of Minerals* 3(2) (1978) 133–144.

- Vegas A., Cano F.H., Garciablanco S.: Refinement of aluminum orthoborate. *Acta Crystallographica Section B: Structural Science* 33(Nov) (1977) 3607–3609.
- Vils F., Pelletier L., Kalt A., Münthener O., Ludwig T.: The lithium, boron and beryllium content of serpentinized peridotites from ODP Leg 209 (sites 1272A and 1274A): Implications for lithium and boron budgets of oceanic lithosphere. *Geochimica et Cosmochimica Acta* 72 (2008) 5475–5504.
- Vlasse M., Naslain R., Kasper J.S., Ploog K.: Crystal-structure of tetragonal boron related to α -AlB₁₂. *Journal of Solid State Chemistry* 28(3) (1979) 289–301.
- Wada H., Sakane K., Kitamura T., Hata H., Kambara H.: Synthesis of aluminum borate whiskers in potassium-sulphate flux. *Journal of Materials Science Letters* 10(18) (1991) 1076–1077.
- Wada H., Sakane K., Kitamura T., Kayahara Y., Kawahara A., Sasaki N.: Thermal conductivity of aluminum borate. *Journal of the Ceramic Society of Japan* 102(8) (1994) 695–701.
- Wada H., Sakane K., Kitamura T., Sunai M., Sasaki N.: Thermal-expansion of aluminum borate. *Journal of Materials Science Letters* 12(22) (1993) 1735–1737.
- Wang J., Ning G.L., Yang X.F., Gan Z.H., Liu H.Y., Lin Y.: Large-scale synthesis of Al₄B₂O₉/Al₁₈B₄O₃₃ whiskers via a novel method. *Materials Letters* 62(8-9) (2008) 1208–1211.
- Watanabe T.: Continental Borate Deposits of Cenozoic Age. In *Geochemistry of Boron*, C.T. Walker, editor, volume 23 of *Benchmark Papers in Geology*, 388–400, Dowden, Hutchinson & Ross, Inc., Stroudsburg, PA (1975).
- Websky M.: Über Jeremejewit und Eichwaldit vom Berge Soktuj in Daurien. *Sitzungsberichte der Königlich Preussischen Akademie der Wissenschaften zu Berlin* 2 (1883) 671–675.
- Wei S.Y., Zhang J., Elsanousi A., Lin J., Shi F.J., Liu S.J., Ding X.X., Gao J.M., Qi S.R., Tang C.C.: From Al₄B₂O₉ nanorods to AlOOH (boehmite) hierarchical nanoarchitectures. *Nanotechnology* 18(25) (2007) 255605.
- Werding G., Schreyer W.: Alkali-free tourmaline in the system MgO-Al₂O₃-B₂O₃-SiO₂-H₂O. *Geochimica et Cosmochimica Acta* 48(6) (1984) 1331–1344.
- Werding G., Schreyer W.: Synthesis and stability of werdingite, a new phase in the system MgO-Al₂O₃-B₂O₃-SiO₂ (MABS), and another new phase in the ABS-system. *European Journal of Mineralogy* 4(1) (1992) 193–207.
- Werding G., Schreyer W.: Experimental Studies on Borosilicates and Selected Borates. In *Boron*, E.S. Grew, L.M. Anovitz, editors, volume 33 of *Reviews in Mineralogy*, 117–163, Mineralogical Society of America, Washington, D.C. (1996).
- White J.G., Miller A., Nielsen R.E.: Fe₃BO₆ a borate isostructural with mineral norbergite. *Acta Crystallographica* 19 (1965) 1060–1061.
- Widom M., Mihalkovič M.: Symmetry-broken crystal structure of elemental boron at low temperature. *Physical Review B (Condensed Matter and Materials Physics)* 77(6) (2008) 64113–1–64113–8.

- Will G., Kiefer B.: Electron deformation density in rhombohedral α -boron. *Zeitschrift für anorganische und allgemeine Chemie* 627 (2001) 2100–2104.
- Wilson A.J.C., Prince E.: *Internal Tables for X-ray Crystallography, Volume C: Mathematical, Physical and Chemical Tables*. Kluwer, Dordrecht, NL, 2nd edition (1999).
- Wilson E.B.J., Decius J.C., Cross P.C.: *Molecular Vibrations. The Theory of Infrared and Raman Vibrational Spectra*. Dover, New York, NY (1980).
- Winter J.K., Ghose S.: Thermal expansion and high-temperature crystal chemistry of the Al_2SiO_5 polymorphs. *American Mineralogist* 64 (1979) 573–586.
- Xia H.R., Li L.X., Wang J.Y., Yu W.T., Yang P.: Raman scattering investigation in $\text{Pr}_x\text{Y}_{1-x}\text{Al}_3(\text{BO}_3)_4$ single crystals. *Journal of Raman Spectroscopy* 30 (1999) 557–561.
- Xinyong T., Xinnan W., Xiaodong L.: Nanomechanical characterization of one-step combustion-synthesized $\text{Al}_4\text{B}_2\text{O}_9$ and $\text{Al}_{18}\text{B}_4\text{O}_{33}$ nanowires. *Nano Letters* 3172–6.
- Yang H., Hazen R.M., Finger L.W., Prewitt C.T., Downs R.T.: Compressibility and crystal structure of sillimanite, Al_2SiO_5 , at high pressure. *Physics and Chemistry of Minerals* 25(1) (1997b) 39–47.
- Yang H.X., Downs R.T., Finger L.W., Hazen R.M., Prewitt C.T.: Compressibility and crystal structure of kyanite, Al_2SiO_5 , at high pressure. *American Mineralogist* 82(5–6) (1997a) 467–474.
- Yang T., Ju J., Li G., Liao F., Zou X., Deng F., Chen L., Wang Y., Lin J.: Square-pyramidal/triangular framework oxide: Synthesis and structure of PKU-6. *Inorganic Chemistry* 46(12) (2007) 4772–4774.
- Yue H.Y., Yu Z.M., Guo E.J., Wang L.P., Sun F.L.: Tensile properties and fracture mechanisms of ZnO and ZnAl_2O_4 -coated $\text{Al}_{18}\text{B}_4\text{O}_{33}$ whisker reinforced aluminum composites. *Materials Characterization* 61(5) (2010) 542–547.
- Zhang G., Fu Z., Wang Y., Wang H., Wang W., Zhang J., Lee S.W., Niihara K.: Boron-doped mullite derived from single-phase gels. *Journal of the European Ceramic Society* 30 (2010) 2435–2441.
- Zhang J., Huang Y., Lin J., Ding X.X., Huang Z.X., Qi S.R., Tang C.C.: From $\text{Al}_4\text{B}_2\text{O}_9$ nanowires to BN-coated $\text{Al}_{18}\text{B}_4\text{O}_{33}$ nanowires. *Journal of Physical Chemistry B* 109(27) (2005) 13060–13062.
- Zhang J., Lin J., Song H.S., Elssfah E.M., Liu S.J., Luo J.J., Ding X.X., Tang C., Qi S.R.: Bulk-quantity fast production of $\text{Al}_4\text{B}_2\text{O}_9/\text{Al}_{18}\text{B}_4\text{O}_{33}$ single-crystal nanorods by a novel technique. *Materials Letters* 60(27) (2006) 3292–3295.
- Zhou J., Su D.G., Luo J.M., Zhong M.F.: Synthesis of aluminum borate nanorods by a low-heating-temperature solid-state precursor method. *Materials Research Bulletin* 44(1) (2009) 224–226.

A.1 Supplementary Data for Chapter 4

Single-crystal XRD data of sample *a* refined with fully occupied positions according to refinement strategy 1

Table A1.1: Details for single-crystal X-ray diffraction data collection and crystal structure refinement of sample *a* without resolution restriction and fully occupied positions (refinement strategy 1).

Diffractometer: Enraf Nonius CAD4			
X-ray radiation	MoK α (0.71073 Å)	Reflections rejected	92
X-ray power	50 kV, 40 mA	Reflections used	5636
Crystal size	0.2 · 0.13 · 0.05 mm ³	Max. 2 θ	69.93°
Measurement time	Max. 120 sec/step	Index range <i>h</i>	-9 ... 9
Absorption corr.	ψ scans	Index range <i>k</i>	-24 ... 24
Resolution	No restriction	Index range <i>l</i>	-12 ... 12
Sample name	<i>a</i> (ABO-01-2009, # 01)	Unique reflections	1552
Temperature	298K	Reflections > 4 $\sigma(I)$	1423
Space group	<i>Cmc</i> 2 ₁	<i>R</i> (int)	0.0373
<i>a</i> -axis	5.6682(2) Å	<i>R</i> (σ)	0.0265
<i>b</i> -axis	15.0060(9) Å	Refined parameters	82
<i>c</i> -axis	7.6892(4) Å	GoF	1.183
Volume	654.07(6) Å ³	<i>R</i> 1, <i>I</i> > 4 $\sigma(I)$	0.0200
<i>Z</i>	4	<i>R</i> 1, all data	0.0263
Density ρ	2.942 g/cm ³	w <i>R</i> 2 on <i>F</i> ²	0.0510
Absorption coeff. μ	0.88 mm ⁻¹	$\Delta\rho_{\max}$	0.54 e ⁻ ·Å ⁻³ near Al2
Reflections collected	5728	$\Delta\rho_{\min}$	-0.29 e ⁻ ·Å ⁻³ near Al1

Table A1.2: Atomic positions and isotropic displacement parameters of single-crystal XRD data from sample *a* without resolution restriction and fully occupied positions (refinement strategy 1).

Site	<i>x</i>	<i>y</i>	<i>z</i>	Occ.	W. S. ^a	<i>U</i> _{eq.} (Å ²)
Al1	0.24814(7)	0.38355(3)	0.0	1.0	8b	0.00412(7)
Al2	0.0	0.25529(4)	0.68662(10)	1.0	4a	0.00550(10)
Al3	0.0	0.44414(4)	0.68202(11)	1.0	4a	0.00484(10)
Al4	0.0	0.29692(4)	0.33410(11)	1.0	4a	0.00449(10)
B1	0.5	0.51575(13)	0.2216(3)	1.0	4a	0.0051(3)
O1	0.0	0.32926(9)	0.87072(19)	1.0	4a	0.0068(2)
O2	0.24304(16)	0.30970(7)	0.20133(15)	1.0	8b	0.00671(17)
O3	0.5	0.45357(9)	0.09233(19)	1.0	4a	0.0059(2)
O4	0.0	0.54594(9)	0.57205(19)	1.0	4a	0.0061(2)
O5	0.0	0.35189(9)	0.53795(18)	1.0	4a	0.0074(2)
O6	0.0	0.19136(9)	0.4349(2)	1.0	4a	0.0050(2)
O7	0.28876(17)	0.45168(7)	0.78556(14)	1.0	8b	0.00681(16)

^aWyckoff site: 4a with multiplicity = 1, 8b with multiplicity = 2

Table A1.3: Anisotropic displacement parameters from single-crystal XRD data of sample *a* without resolution restriction and fully occupied positions (refinement strategy 1).

Site	U_{11} (Å ²)	U_{22} (Å ²)	U_{33} (Å ²)	U_{23} (Å ²)	U_{13} (Å ²)	U_{12} (Å ²)
A11	0.00319(13)	0.00474(14)	0.00442(13)	0.00044(14)	-0.00007(11)	0.00022(11)
A12	0.0050(2)	0.0048(2)	0.0067(2)	-0.0001(2)	0.0	0.0
A13	0.0039(2)	0.0042(2)	0.0064(2)	-0.0005(2)	0.0	0.0
A14	0.0043(2)	0.0052(2)	0.0039(2)	0.00042(18)	0.0	0.0
B1	0.0047(7)	0.0058(8)	0.0050(8)	0.0003(6)	0.0	0.0
O1	0.0044(5)	0.0083(5)	0.0075(5)	-0.0037(5)	0.0	0.0
O2	0.0056(4)	0.0078(4)	0.0068(4)	0.0022(3)	0.0013(3)	0.0011(3)
O3	0.0050(5)	0.0057(5)	0.0068(5)	-0.0023(4)	0.0	0.0
O4	0.0038(5)	0.0053(5)	0.0091(6)	0.0028(5)	0.0	0.0
O5	0.0110(6)	0.0054(5)	0.0058(5)	-0.0008(4)	0.0	0.0
O6	0.0045(5)	0.0037(5)	0.0069(5)	0.0006(4)	0.0	0.0
O7	0.0049(3)	0.0085(4)	0.0071(4)	0.0035(3)	-0.0007(3)	-0.0008(3)

Table A1.4: Individual and mean polyhedral bond lengths of the refined structure from sample *a* without resolution restriction and fully occupied positions (refinement strategy 1).

Center	Ligand	Distance (Å)	Center	Ligand	Distance (Å)
A11	O4	1.8453(9)	A12	O2 (x2)	1.7566(9)
A11	O6	1.8849(9)	A12	O1	1.7989(14)
A11	O2	1.9041(11)	A12	O5	1.8460(15)
A11	O1	1.9054(10)	A12	O6	2.1603(16)
A11	O3	1.9095(10)		<A12-O>	1.8637(13)
A11	O7	1.9538(10)			
	<A11-O>	1.9005(10)	A13	O4	1.7460(14)
			A13	O5	1.7730(14)
A14	O2 (x2)	1.7254(10)	A13	O7 (x2)	1.8237(10)
A14	O6	1.7633(14)	A13	O1	2.2531(16)
A14	O5	1.7713(15)		<A13-O>	1.8839(13)
	<A14-O>	1.7466(12)			
B1	O3	1.363(2)			
B1	O7 (x2)	1.3837(14)			
	<B1-O>	1.3699(18)			

Single-crystal XRD data of sample *f* refined with fully occupied positions according to refinement strategy 1

Table A1.5: Details for single-crystal X-ray diffraction data collection and crystal structure refinement of sample *f* without resolution restriction and fully occupied positions (refinement strategy 1).

Diffractometer: Bruker Smart APEX 2			
X-ray radiation	MoK α (0.71073 Å)	Reflections rejected	170
X-ray power	50 kV, 40 mA	Reflections used	9250
Crystal size	0.15 · 0.025 · 0.05 mm ³	Max. 2 θ	73.38°
Measurement time	60 s/frame	Index range <i>h</i>	-9 ... 9
Absorption corr.	Empirical ψ scans	Index range <i>k</i>	-24 ... 25
Resolution	No restriction	Index range <i>l</i>	-12 ... 11
Sample name	<i>f</i> (ABO-62, # 62-2)	Unique reflections	1618
Temperature	298K	Reflections > 4 $\sigma(I)$	1565
Space group	<i>Cmc</i> 2 ₁	<i>R</i> (int)	0.0258
<i>a</i> -axis*	5.6618(7) Å	<i>R</i> (σ)	0.0194
<i>b</i> -axis*	14.9981(12) Å	Refined parameters	82
<i>c</i> -axis*	7.6806(7) Å	GoF	1.152
<i>Volume</i> *	652.21(12) Å ³	<i>R</i> 1, <i>I</i> > 4 $\sigma(I)$	0.0228
<i>Z</i>	4	<i>R</i> 1, all data	0.0239
Density ρ	2.250 g/cm ³	w <i>R</i> 2 on <i>F</i> ²	0.0605
Absorption coeff. μ	0.88 mm ⁻¹	$\Delta\rho_{\max}$	0.50 e ⁻ ·Å ⁻³ near Al3
Reflections collected	9420	$\Delta\rho_{\min}$	-0.43 e ⁻ ·Å ⁻³ near Al2

*lattice parameters from CAD4 (15 centered reflections with $\pm 11^\circ < \theta < \pm 30^\circ$)

Table A1.6: Atomic positions and isotropic displacement parameters of single-crystal XRD data from sample *f* without resolution restriction and fully occupied positions (refinement strategy 1).

Site	<i>x</i>	<i>y</i>	<i>z</i>	Occ.	W. S. ^a	<i>U</i> _{eq.} (Å ²)
Al1	0.24812(6)	0.38351(3)	0.0	1.0	8b	0.00532(8)
Al2	0.0	0.25533(4)	0.68638(11)	1.0	4a	0.00695(10)
Al3	0.0	0.44415(4)	0.68164(11)	1.0	4a	0.00614(10)
Al4	0.0	0.29686(4)	0.33409(12)	1.0	4a	0.00626(10)
B1	0.5	0.51544(13)	0.2215(3)	1.0	4a	0.0064(3)
O1	0.0	0.32905(9)	0.8706(2)	1.0	4a	0.0073(2)
O2	0.24297(16)	0.30960(7)	0.20111(17)	1.0	8b	0.00836(18)
O3	0.5	0.45349(9)	0.0927(2)	1.0	4a	0.0067(2)
O4	0.0	0.54592(9)	0.5721(2)	1.0	4a	0.0074(2)
O5	0.0	0.35200(9)	0.5380(2)	1.0	4a	0.0087(2)
O6	0.0	0.19128(9)	0.4350(2)	1.0	4a	0.0066(2)
O7	0.28883(18)	0.45169(7)	0.78536(15)	1.0	8b	0.00778(17)

^aWyckoff site: 4a with multiplicity = 1, 8b with multiplicity = 2

Table A1.7: Anisotropic displacement parameters from single-crystal XRD data of sample *f* without resolution restriction and fully occupied positions (refinement strategy 1).

Site	U_{11} (Å ²)	U_{22} (Å ²)	U_{33} (Å ²)	U_{23} (Å ²)	U_{13} (Å ²)	U_{12} (Å ²)
A11	0.00412(14)	0.00617(14)	0.00569(15)	0.00001(15)	-0.00016(11)	0.00032(11)
A12	0.0061(2)	0.0064(2)	0.0084(2)	0.0(2)	0.0	0.0
A13	0.0049(2)	0.0058(2)	0.0077(2)	-0.0001(2)	0.0	0.0
A14	0.0060(2)	0.0071(2)	0.0057(2)	0.00013(19)	0.0	0.0
B1	0.0061(7)	0.0073(8)	0.0057(8)	-0.0004(6)	0.0	0.0
O1	0.0047(5)	0.0089(5)	0.0083(6)	-0.0036(5)	0.0	0.0
O2	0.0075(4)	0.0090(4)	0.0086(4)	0.0020(3)	0.0014(3)	0.0006(3)
O3	0.0058(5)	0.0062(5)	0.0080(6)	-0.0023(4)	0.0	0.0
O4	0.0052(5)	0.0060(5)	0.0109(6)	0.0027(5)	0.0	0.0
O5	0.0113(6)	0.0072(5)	0.0076(6)	-0.0009(4)	0.0	0.0
O6	0.0051(5)	0.0058(5)	0.0088(6)	0.0012(4)	0.0	0.0
O7	0.0048(3)	0.0102(4)	0.0083(4)	0.0038(3)	-0.0002(3)	-0.0009(3)

Table A1.8: Individual and mean polyhedral bond lengths of the refined structure from sample *f* without resolution restriction and fully occupied positions (refinement strategy 1).

Center	Ligand	Distance (Å)	Center	Ligand	Distance (Å)
A11	O4	1.8441(9)	A12	O2 (x2)	1.7547(10)
A11	O6	1.8818(9)	A12	O1	1.7958(14)
A11	O2	1.9015(12)	A12	O5	1.8443(15)
A11	O1	1.9047(10)	A12	O6	2.1566(16)
A11	O3	1.9087(10)		<A12-O>	1.8776(14)
A11	O7	1.9536(11)			
	<A11-O>	1.8991(9)	A13	O4	1.7428(14)
			A13	O5	1.7685(15)
A14	O2 (x2)	1.7240(11)	A13	O7 (x2)	1.8225(10)
A14	O6	1.7629(14)	A13	O1	2.2555(16)
A14	O5	1.7709(16)		<A13-O>	1.8824(13)
	<A14-O>	1.7526(14)			
B1	O3	1.357(2)			
B1	O7 (x2)	1.3832(14)			
	<B1-O>	1.3657(19)			

Single-crystal XRD data of sample *a* refined with fully occupied positions and resolution restriction

Table A1.9: Details for single-crystal X-ray diffraction data collection and crystal structure refinement of sample *a* with resolution restriction ($0.6 \text{ \AA} \leq \lambda/(2 \cdot \sin\theta) \leq 1 \text{ \AA}$) and fully occupied positions.

Diffractometer: Enraf Nonius CAD4			
X-ray radiation	MoK α (0.71073 \AA)	Reflections rejected	1434
X-ray power	50 kV, 40 mA	Reflections used	4294
Crystal size	0.2 · 0.13 · 0.05 mm ³	Max. 2 θ	69.93°
Measurement time	Max. 120 sec/step	Index range <i>h</i>	-9 ... 9
Absorption corr.	ψ scans	Index range <i>k</i>	-24 ... 24
Resolution	1 \AA ... 0.6 \AA	Index range <i>l</i>	-12 ... 12
Sample name	<i>a</i> (ABO-01-2009, # 01)	Unique reflections	1166
Temperature	298K	Reflections > 4 $\sigma(I)$	1045
Space group	<i>Cmc2</i> ₁	<i>R</i> (int)	0.0510
<i>a</i> -axis	5.6682(2) \AA	<i>R</i> (σ)	0.0375
<i>b</i> -axis	15.0060(9) \AA	Refined parameters	82
<i>c</i> -axis	7.6892(4) \AA	GoF	0.993
Volume	654.07(6) \AA^3	<i>R</i> 1, <i>I</i> > 4 $\sigma(I)$	0.0174
<i>Z</i>	4	<i>R</i> 1, all data	0.0274
Density ρ	2.942 g/cm ³	w <i>R</i> 2 on <i>F</i> ²	0.0296
Absorption coeff. μ	0.88 mm ⁻¹	$\Delta\rho_{\max}$	0.24 e ⁻ · \AA^{-3} near B1
Reflections collected	5728	$\Delta\rho_{\min}$	-0.21 e ⁻ · \AA^{-3} near O1

Table A1.10: Atomic positions and isotropic displacement parameters of single-crystal XRD data from sample *a* with resolution restriction ($0.6 \text{ \AA} \leq \lambda/(2 \cdot \sin\theta) \leq 1 \text{ \AA}$) and fully occupied positions.

Site	<i>x</i>	<i>y</i>	<i>z</i>	Occ.	W. S. ^a	<i>U</i> _{eq.} (\AA^2)
A11	0.24818(6)	0.383521(18)	0.0	1.0	8b	0.00388(6)
A12	0.0	0.25538(3)	0.68663(7)	1.0	4a	0.00513(8)
A13	0.0	0.44420(3)	0.68198(9)	1.0	4a	0.00450(8)
A14	0.0	0.29699(3)	0.33427(9)	1.0	4a	0.00408(8)
B1	0.5	0.51566(10)	0.22105(19)	1.0	4a	0.0049(2)
O1	0.0	0.32947(8)	0.87054(15)	1.0	4a	0.00647(16)
O2	0.24291(12)	0.30983(5)	0.20164(11)	1.0	8b	0.00663(12)
O3	0.5	0.45338(8)	0.09228(14)	1.0	4a	0.00542(16)
O4	0.0	0.54602(7)	0.57211(14)	1.0	4a	0.00587(16)
O5	0.0	0.35181(7)	0.53798(14)	1.0	4a	0.00741(17)
O6	0.0	0.19126(7)	0.43504(16)	1.0	4a	0.00507(16)
O7	0.28862(14)	0.45174(5)	0.78567(11)	1.0	8b	0.00670(12)

^aWyckoff site: 4a with multiplicity = 1, 8b with multiplicity = 2

Table A1.11: Anisotropic displacement parameters from single-crystal XRD data of sample *a* with resolution restriction ($0.6 \text{ \AA} \leq \lambda/(2 \cdot \sin\theta) \leq 1 \text{ \AA}$) and fully occupied positions.

Site	U_{11} (\AA^2)	U_{22} (\AA^2)	U_{33} (\AA^2)	U_{23} (\AA^2)	U_{13} (\AA^2)	U_{12} (\AA^2)
A11	0.00300(9)	0.00439(10)	0.00424(9)	0.00053(10)	-0.00006(8)	0.00021(8)
A12	0.00457(16)	0.00455(15)	0.00626(16)	-0.00024(14)	0.0	0.0
A13	0.00354(16)	0.00386(14)	0.00610(16)	-0.00050(14)	0.0	0.0
A14	0.00414(15)	0.00470(16)	0.00341(15)	0.00027(12)	0.0	0.0
B1	0.0038(5)	0.0060(5)	0.0048(5)	-0.0007(4)	0.0	0.0
O1	0.0040(3)	0.0085(4)	0.0069(4)	-0.0035(3)	0.0	0.0
O2	0.0055(3)	0.0079(3)	0.0065(3)	0.0021(2)	0.0011(2)	0.00132(19)
O3	0.0045(4)	0.0058(4)	0.0060(4)	-0.0025(3)	0.0	0.0
O4	0.0035(3)	0.0056(4)	0.0085(4)	0.0026(3)	0.0	0.0
O5	0.0113(4)	0.0053(4)	0.0055(4)	-0.0007(3)	0.0	0.0
O6	0.0040(4)	0.0037(4)	0.0074(4)	0.0013(3)	0.0	0.0
O7	0.0045(3)	0.0084(3)	0.0071(2)	0.0035(2)	-0.00067(19)	-0.0010(2)

Table A1.12: Individual and mean polyhedral bond lengths of the refined structure from sample *a* with resolution restriction ($0.6 \text{ \AA} \leq \lambda/(2 \cdot \sin\theta) \leq 1 \text{ \AA}$) and fully occupied positions.

Center	Ligand	Distance (\AA)	Center	Ligand	Distance (\AA)
A11	O4	1.8452(7)	A12	O2 (x2)	1.7593(7)
A11	O6	1.8832(7)	A12	O1	1.7989(11)
A11	O2	1.9046(8)	A12	O5	1.8440(12)
A11	O1	1.9048(8)	A12	O6	2.1606(13)
A11	O3	1.9079(8)		<A12-O>	1.8644(10)
A11	O7	1.9535(8)			
	<A11-O>	1.8999(8)	A13	O4	1.7459(12)
			A13	O5	1.7743(11)
A14	O2 (x2)	1.7243(8)	A13	O7 (x2)	1.8235(8)
A14	O6	1.7658(11)	A13	O1	2.2507(13)
A14	O5	1.7692(12)		<A13-O>	1.8836(10)
	<A14-O>	1.7459(10)			
B1	O3	1.3615(17)			
B1	O7 (x2)	1.3864(10)			
	<B1-O>	1.3968(15)			

Single-crystal XRD data of sample *f* refined with fully occupied positions and resolution restriction

Table A1.13: Details for single-crystal X-ray diffraction data collection and crystal structure refinement of sample *f* with resolution restriction ($0.62 \text{ \AA} \leq \lambda/(2 \cdot \sin\theta) \leq 1 \text{ \AA}$) and fully occupied positions.

Diffractometer: Bruker Smart APEX 2			
X-ray radiation	MoK α (0.71073 \AA)	Reflections rejected	3505
X-ray power	50 kV, 40 mA	Reflections used	5915
Crystal size	0.15 · 0.025 · 0.05 mm ³	Max. 2θ	69.94°
Measurement time	60 s/frame	Index range <i>h</i>	-9 ... 9
Absorption corr.	Empirical ψ scans	Index range <i>k</i>	-24 ... 23
Resolution	1 \AA ... 0.62 \AA	Index range <i>l</i>	-12 ... 11
Sample name	<i>f</i> (ABO-62, # 62-2)	Unique reflections	1130
Temperature	298K	Reflections > $4\sigma(I)$	1088
Space group	<i>Cmc</i> 2 ₁	<i>R</i> (int)	0.0399
<i>a</i> -axis*	5.6618(7) \AA	<i>R</i> (σ)	0.0294
<i>b</i> -axis*	14.9981(12) \AA	Refined parameters	82
<i>c</i> -axis*	7.6806(7) \AA	GoF	1.043
<i>Volume</i> *	652.21(12) \AA^3	<i>R</i> 1, <i>I</i> > $4\sigma(I)$	0.0187
<i>Z</i>	4	<i>R</i> 1, all data	0.0201
Density ρ	2.250 g/cm ³	w <i>R</i> 2 on <i>F</i> ²	0.0375
Absorption coeff. μ	0.88 mm ⁻¹	$\Delta\rho_{\max}$	0.25 e ⁻ · \AA^{-3} near Al2
Reflections collected	9420	$\Delta\rho_{\min}$	-0.25 e ⁻ · \AA^{-3} near Al1

*lattice parameters from CAD4 (15 centered reflections with $\pm 11^\circ < \theta < \pm 30^\circ$)

Table A1.14: Atomic positions and isotropic displacement parameters of single-crystal XRD data from sample *f* with resolution restriction ($0.62 \text{ \AA} \leq \lambda/(2 \cdot \sin\theta) \leq 1 \text{ \AA}$) and fully occupied positions.

Site	<i>x</i>	<i>y</i>	<i>z</i>	Occ.	W. S. ^a	<i>U</i> _{eq.} (\AA^2)
Al1	0.24810(6)	0.38347(2)	0.0	1.0	8b	0.00474(8)
Al2	0.0	0.25544(3)	0.68639(8)	1.0	4a	0.00620(10)
Al3	0.0	0.44419(3)	0.68167(9)	1.0	4a	0.00543(10)
Al4	0.0	0.29688(3)	0.33416(9)	1.0	4a	0.00559(10)
B1	0.5	0.51556(10)	0.2212(2)	1.0	4a	0.0057(2)
O1	0.0	0.32932(8)	0.87043(16)	1.0	4a	0.00683(18)
O2	0.24280(13)	0.30975(6)	0.20137(13)	1.0	8b	0.00796(15)
O3	0.5	0.45336(8)	0.09288(16)	1.0	4a	0.00615(19)
O4	0.0	0.54600(8)	0.57220(17)	1.0	4a	0.00703(19)
O5	0.0	0.35172(8)	0.53799(16)	1.0	4a	0.0084(2)
O6	0.0	0.19123(7)	0.43511(17)	1.0	4a	0.00595(18)
O7	0.28870(15)	0.45178(6)	0.78534(12)	1.0	8b	0.00727(14)

^aWyckoff site: 4a with multiplicity = 1, 8b with multiplicity = 2

Table A1.15: Anisotropic displacement parameters from single-crystal XRD data of sample *f* with resolution restriction ($0.62 \text{ \AA} \leq \lambda/(2 \cdot \sin\theta) \leq 1 \text{ \AA}$) and fully occupied positions.

Site	U_{11} (\AA^2)	U_{22} (\AA^2)	U_{33} (\AA^2)	U_{23} (\AA^2)	U_{13} (\AA^2)	U_{12} (\AA^2)
A11	0.00358(12)	0.00544(12)	0.00522(12)	-0.00004(12)	-0.00014(8)	0.00037(8)
A12	0.00540(17)	0.00570(17)	0.00750(18)	-0.00008(15)	0.0	0.0
A13	0.00404(17)	0.00507(16)	0.00717(18)	-0.00011(15)	0.0	0.0
A14	0.00565(17)	0.00607(18)	0.00506(17)	0.00014(14)	0.0	0.0
B1	0.0048(5)	0.0069(6)	0.0054(6)	-0.0012(4)	0.0	0.0
O1	0.0039(4)	0.0093(4)	0.0074(4)	-0.0034(3)	0.0	0.0
O2	0.0072(3)	0.0086(3)	0.0080(3)	0.0019(2)	0.0015(2)	0.0007(2)
O3	0.0048(4)	0.0065(4)	0.0071(4)	-0.0024(3)	0.0	0.0
O4	0.0046(4)	0.0064(4)	0.0101(5)	0.0025(3)	0.0	0.0
O5	0.0115(5)	0.0072(4)	0.0064(4)	-0.0015(3)	0.0	0.0
O6	0.0039(4)	0.0056(4)	0.0083(4)	0.0015(3)	0.0	0.0
O7	0.0040(3)	0.0097(3)	0.0081(3)	0.0039(2)	0.0005(2)	-0.0012(2)

Table A1.16: Individual and mean polyhedral bond lengths of the refined structure from sample *f* with resolution restriction ($0.62 \text{ \AA} \leq \lambda/(2 \cdot \sin\theta) \leq 1 \text{ \AA}$) and fully occupied positions.

Center	Ligand	Distance (\AA)	Center	Ligand	Distance (\AA)
A11	O4	1.8438(8)	A12	O2 (x2)	1.7578(8)
A11	O6	1.8808(8)	A12	O1	1.7961(12)
A11	O2	1.9014(9)	A12	O5	1.8396(13)
A11	O1	1.9034(8)	A12	O6	2.1569(13)
A11	O3	1.9084(8)		<A12-O>	1.8616(11)
A11	O7	1.9547(9)			
	<A11-O>	1.8988(8)	A13	O4	1.7431(12)
			A13	O5	1.7725(12)
A14	O2 (x2)	1.7226(9)	A13	O7 (x2)	1.8217(9)
A14	O6	1.7642(12)	A13	O1	2.2517(13)
A14	O5	1.7684(13)		<A13-O>	1.8821(11)
	<A14-O>	1.7445(11)			
B1	O3	1.3570(19)			
B1	O7 (x2)	1.3834(11)			
	<B1-O>	1.3746(14)			

Single-crystal XRD data of sample *a* refined with 91% Al and 9% B at the Al4 site according to refinement strategy 2

Table A1.17: Details for single-crystal X-ray diffraction data collection and crystal structure refinement of sample *a* without resolution restriction and a fixed ratio of 91% Al and 9% B at the Al4 site (refinement strategy 2).

Diffractometer: Enraf Nonius CAD4			
X-ray radiation	MoK α (0.71073 Å)	Reflections rejected	92
X-ray power	50 kV, 40 mA	Reflections used	5636
Crystal size	0.2 · 0.13 · 0.05 mm ³	Max. 2 θ	69.93°
Measurement time	Max. 120 sec/step	Index range <i>h</i>	-9 ... 9
Absorption corr.	ψ scans	Index range <i>k</i>	-24 ... 24
Resolution	No restriction	Index range <i>l</i>	-12 ... 12
Sample name	<i>a</i> (ABO-01-2009, # 01)	Unique reflections	1552
Temperature	298K	Reflections > 4 $\sigma(I)$	1423
Space group	<i>Cmc</i> 2 ₁	<i>R</i> (int)	0.0373
<i>a</i> -axis	5.6682(2) Å	<i>R</i> (σ)	0.0265
<i>b</i> -axis	15.0060(9) Å	Refined parameters	82
<i>c</i> -axis	7.6892(4) Å	GoF	1.239
Volume	654.07(6) Å ³	<i>R</i> 1, <i>I</i> > 4 $\sigma(I)$	0.0205
<i>Z</i>	4	<i>R</i> 1, all data	0.0268
Density ρ	2.942 g/cm ³	w <i>R</i> 2 on <i>F</i> ²	0.0533
Absorption coeff. μ	0.88 mm ⁻¹	$\Delta\rho_{\max}$	0.54 e ⁻ ·Å ⁻³ near O1
Reflections collected	5728	$\Delta\rho_{\min}$	-0.35 e ⁻ ·Å ⁻³ near Al2

Table A1.18: Atomic positions and isotropic displacement parameters of single-crystal XRD data from sample *a* without resolution restriction and fully occupied positions (refinement strategy 2).

Site	<i>x</i>	<i>y</i>	<i>z</i>	Occ.	W. S. ^a	<i>U</i> _{eq.} (Å ²)
Al1	0.24813(7)	0.38355(3)	0.0	1.0	8b	0.00459(7)
Al2	0.0	0.25534(4)	0.68658(10)	1.0	4a	0.00600(10)
Al3	0.0	0.44419(4)	0.68193(11)	1.0	4a	0.00527(10)
Al4	0.0	0.29693(4)	0.33414(12)	0.91	4a	0.00254(10)
B ^b	0.0	0.29693(4)	0.33414(12)	0.09	4a	0.00254(10)
B1	0.5	0.51579(14)	0.2211(3)	1.0	4a	0.0056(3)
O1	0.0	0.32913(10)	0.8708(2)	1.0	4a	0.0073(2)
O2	0.24309(16)	0.30963(7)	0.20124(16)	1.0	8b	0.00708(18)
O3	0.5	0.45347(10)	0.0923(2)	1.0	4a	0.0063(2)
O4	0.0	0.54587(9)	0.5717(2)	1.0	4a	0.0066(2)
O5	0.0	0.35173(9)	0.53787(19)	1.0	4a	0.0081(3)
O6	0.0	0.19132(9)	0.4350(2)	1.0	4a	0.0056(2)
O7	0.28860(18)	0.45167(7)	0.78561(15)	1.0	8b	0.00734(17)

^aWyckoff site: 4a with multiplicity = 1, 8b with multiplicity = 2; ^bat Al4 site

Table A1.19: Anisotropic displacement parameters from single-crystal XRD data of sample *a* without resolution restriction and a fixed ratio of 91% Al and 9% B at the Al4 site (refinement strategy 2).

Site	U_{11} (Å ²)	U_{22} (Å ²)	U_{33} (Å ²)	U_{23} (Å ²)	U_{13} (Å ²)	U_{12} (Å ²)
Al1	0.00365(13)	0.00519(14)	0.00492(13)	0.00045(16)	-0.00002(12)	0.00008(12)
Al2	0.0053(2)	0.0055(2)	0.0072(2)	-0.0001(2)	0.0	0.0
Al3	0.0043(2)	0.0047(2)	0.0068(2)	-0.0005(2)	0.0	0.0
Al4	0.0025(2)	0.0032(2)	0.0019(2)	0.00039(19)	0.0	0.0
B ^a	0.0025(2)	0.0032(2)	0.0019(2)	0.00039(19)	0.0	0.0
B1	0.0053(8)	0.0065(8)	0.0048(8)	0.0004(6)	0.0	0.0
O1	0.0040(5)	0.0094(6)	0.0085(6)	-0.0036(5)	0.0	0.0
O2	0.0061(4)	0.0079(4)	0.0072(4)	0.0022(3)	0.0013(3)	0.0011(3)
O3	0.0058(5)	0.0063(6)	0.0069(6)	-0.0026(5)	0.0	0.0
O4	0.0043(5)	0.0058(6)	0.0098(6)	0.0025(5)	0.0	0.0
O5	0.0115(6)	0.0057(6)	0.0070(6)	-0.0006(4)	0.0	0.0
O6	0.0052(5)	0.0042(5)	0.0074(6)	0.0008(4)	0.0	0.0
O7	0.0055(4)	0.0089(4)	0.0076(4)	0.0036(3)	-0.0009(3)	-0.0008(3)

^aat Al4 site

Table A1.20: Individual and mean polyhedral bond lengths of the refined structure from sample *a* without resolution restriction and a fixed ratio of 91% Al and 9% B at the Al4 site (refinement strategy 2).

Center	Ligand	Distance (Å)	Center	Ligand	Distance (Å)
Al1	O4	1.8451(9)	Al2	O2 (x2)	1.7562(10)
Al1	O6	1.8843(9)	Al2	O1	1.7978(14)
Al1	O2	1.9041(11)	Al2	O5	1.8437(15)
Al1	O1	1.9058(10)	Al2	O6	2.1599(17)
Al1	O3	1.9087(10)		<Al2-O>	1.8628(13)
Al1	O7	1.9532(11)			
	<Al1-O>	1.9002(10)	Al3	O4	1.7453(15)
			Al3	O5	1.7753(15)
Al4	O2 (x2)	1.7261(10)	Al3	O7 (x2)	1.8233(10)
Al4	O6	1.7643(15)	Al3	O1	2.2560(17)
Al4	O5	1.7693(16)		<Al3-O>	1.8846(13)
	<Al4-O>	1.7465(13)			
B1	O3	1.362(2)			
B1	O7 (x2)	1.3858(14)			
	<B1-O>	1.3779(16)			

Single-crystal XRD data of sample *f* refined with 91% Al and 9% B at the Al4 site according to refinement strategy 2

Table A1.21: Details for single-crystal X-ray diffraction data collection and crystal structure refinement of sample *f* without resolution restriction and a fixed ratio of 91% Al and 9% B at the Al4 site (refinement strategy 2).

Diffractometer: Bruker Smart APEX 2			
X-ray radiation	MoK α (0.71073 Å)	Reflections rejected	170
X-ray power	50 kV, 40 mA	Reflections used	9250
Crystal size	0.15 · 0.025 · 0.05 mm ³	Max. 2 θ	73.38°
Measurement time	60 s/frame	Index range <i>h</i>	-9 ... 9
Absorption corr.	Empirical ψ scans	Index range <i>k</i>	-24 ... 25
Resolution	No restriction	Index range <i>l</i>	-12 ... 11
Sample name	<i>f</i> (ABO-62, # 62-2)	Unique reflections	1618
Temperature	298K	Reflections > 4 $\sigma(I)$	1565
Space group	<i>Cmc</i> 2 ₁	<i>R</i> (int)	0.0258
<i>a</i> -axis*	5.6618(7) Å	<i>R</i> (σ)	0.0194
<i>b</i> -axis*	14.9981(12) Å	Refined parameters	82
<i>c</i> -axis*	7.6806(7) Å	GoF	1.186
<i>Volume</i> *	652.21(12) Å ³	<i>R</i> 1, <i>I</i> > 4 $\sigma(I)$	0.0234
<i>Z</i>	4	<i>R</i> 1, all data	0.0245
Density ρ	2.250 g/cm ³	w <i>R</i> 2 on <i>F</i> ²	0.0629
Absorption coeff. μ	0.88 mm ⁻¹	$\Delta\rho_{\max}$	0.47 e ⁻ ·Å ⁻³ near Al3
Reflections collected	9420	$\Delta\rho_{\min}$	-0.49 e ⁻ ·Å ⁻³ near Al2

*lattice parameters from CAD4 (15 centered reflections with $\pm 11^\circ < \theta < \pm 30^\circ$)

Table A1.22: Atomic positions and isotropic displacement parameters of single-crystal XRD data from sample *f* without resolution restriction and a fixed ratio of 91% Al and 9% B at the Al4 site (refinement strategy 2).

Site	<i>x</i>	<i>y</i>	<i>z</i>	Occ.	W. S. ^a	<i>U</i> _{eq.} (Å ²)
Al1	0.24810(7)	0.38350(3)	0.0	1.0	8b	0.00578(8)
Al2	0.0	0.25539(4)	0.68638(11)	1.0	4a	0.00748(11)
Al3	0.0	0.44418(4)	0.68161(12)	1.0	4a	0.00659(11)
Al4	0.0	0.29687(4)	0.33412(12)	0.91	4a	0.00435(11)
B ^b	0.0	0.29687(4)	0.33412(12)	0.09	4a	0.00435(11)
B1	0.5	0.51543(13)	0.2212(3)	1.0	4a	0.0069(3)
O1	0.0	0.32895(9)	0.8708(2)	1.0	4a	0.0077(2)
O2	0.24297(17)	0.30945(7)	0.20104(18)	1.0	8b	0.00867(19)
O3	0.5	0.45346(9)	0.0927(2)	1.0	4a	0.0073(2)
O4	0.0	0.54593(9)	0.5718(2)	1.0	4a	0.0079(2)
O5	0.0	0.35185(9)	0.5379(2)	1.0	4a	0.0093(3)
O6	0.0	0.19127(9)	0.4350(2)	1.0	4a	0.0071(2)
O7	0.28874(18)	0.45165(7)	0.78539(16)	1.0	8b	0.00828(18)

^aWyckoff site: 4a with multiplicity = 1, 8b with multiplicity = 2; ^bat Al4 site

Table A1.23: Anisotropic displacement parameters from single-crystal XRD data of sample *f* without resolution restriction and a fixed ratio of 91% Al and 9% B at the Al4 site (refinement strategy 2).

Site	U_{11} (Å ²)	U_{22} (Å ²)	U_{33} (Å ²)	U_{23} (Å ²)	U_{13} (Å ²)	U_{12} (Å ²)
Al1	0.00456(15)	0.00660(15)	0.00618(15)	0.00001(15)	-0.00011(12)	0.00030(11)
Al2	0.0064(2)	0.0071(2)	0.0089(2)	0.0(2)	0.0	0.0
Al3	0.0054(2)	0.0063(2)	0.0081(2)	-0.0001(2)	0.0	0.0
Al4	0.0043(2)	0.0049(2)	0.0038(2)	0.0002(2)	0.0	0.0
B ^a	0.0043(2)	0.0049(2)	0.0038(2)	0.0002(2)	0.0	0.0
B1	0.0063(7)	0.0081(8)	0.0061(8)	-0.0002(6)	0.0	0.0
O1	0.0046(5)	0.0095(6)	0.0090(6)	-0.0037(5)	0.0	0.0
O2	0.0081(4)	0.0091(4)	0.0088(4)	0.0018(3)	0.0015(3)	0.0006(3)
O3	0.0064(5)	0.0068(5)	0.0087(6)	-0.0022(5)	0.0	0.0
O4	0.0058(5)	0.0065(6)	0.0112(6)	0.0027(5)	0.0	0.0
O5	0.0119(6)	0.0076(6)	0.0083(6)	-0.0007(5)	0.0	0.0
O6	0.0055(5)	0.0065(5)	0.0092(6)	0.0010(5)	0.0	0.0
O7	0.0053(4)	0.0107(4)	0.0088(4)	0.0040(3)	-0.0004(3)	-0.0009(3)

^aat Al4 site

Table A1.24: Individual and mean polyhedral bond lengths of the refined structure from sample *f* without resolution restriction and a fixed ratio of 91% Al and 9% B at the Al4 site (refinement strategy 2).

Center	Ligand	Distance (Å)	Center	Ligand	Distance (Å)
Al1	O4	1.8433(9)	Al2	O2 (x2)	1.7539(10)
Al1	O6	1.8817(9)	Al2	O1	1.7954(15)
Al1	O2	1.9023(12)	Al2	O5	1.8422(16)
Al1	O1	1.9045(10)	Al2	O6	2.1570(17)
Al1	O3	1.9085(10)		<Al2-O>	1.8605(14)
Al1	O7	1.9531(11)			
	<Al1-O>	1.9057(10)	Al3	O4	1.7434(15)
			Al3	O5	1.7710(15)
Al4	O2 (x2)	1.7242(11)	Al3	O7 (x2)	1.8222(11)
Al4	O6	1.7631(15)	Al3	O1	2.2579(16)
Al4	O5	1.7689(17)		<Al3-O>	1.8833(14)
	<Al4-O>	1.7451(14)			
B1	O3	1.356(3)			
B1	O7 (x2)	1.3846(14)			
	<B1-O>	1.375(2)			

Single-crystal XRD data of sample *a* refined with 91% Al and 9% B at the Al4 site and resolution restriction

Table A1.25: Details for single-crystal X-ray diffraction data collection and crystal structure refinement of sample *a* with resolution restriction ($0.6 \text{ \AA} \leq \lambda/(2 \cdot \sin\theta) \leq 1 \text{ \AA}$) and a fixed ratio of 91% Al and 9% B at the Al4 site.

Diffractometer: Enraf Nonius CAD4			
X-ray radiation	MoK α (0.71073 \AA)	Reflections rejected	1434
X-ray power	50 kV, 40 mA	Reflections used	4294
Crystal size	0.2 · 0.13 · 0.05 mm ³	Max. 2 θ	69.93°
Measurement time	Max. 120 sec/step	Index range <i>h</i>	-9 ... 9
Absorption corr.	ψ scans	Index range <i>k</i>	-24 ... 24
Resolution	1 \AA ... 0.6 \AA	Index range <i>l</i>	-12 ... 12
Sample name	<i>a</i> (ABO-01-2009, # 01)	Unique reflections	1166
Temperature	298K	Reflections > 4 $\sigma(I)$	1045
Space group	<i>Cmc</i> 2 ₁	<i>R</i> (int)	0.0510
<i>a</i> -axis	5.6682(2) \AA	<i>R</i> (σ)	0.0375
<i>b</i> -axis	15.0060(9) \AA	Refined parameters	82
<i>c</i> -axis	7.6892(4) \AA	GoF	0.822
Volume	654.07(6) \AA^3	<i>R</i> 1, <i>I</i> > 4 $\sigma(I)$	0.0810
<i>Z</i>	4	<i>R</i> 1, all data	0.0279
Density ρ	2.942 g/cm ³	w <i>R</i> 2 on <i>F</i> ²	0.0385
Absorption coeff. μ	0.88 mm ⁻¹	$\Delta\rho_{\max}$	0.27 e ⁻ · \AA^{-3} near B1
Reflections collected	5728	$\Delta\rho_{\min}$	-0.19 e ⁻ · \AA^{-3} near O6

Table A1.26: Atomic positions and isotropic displacement parameters of single-crystal XRD data from sample *a* with resolution restriction ($0.6 \text{ \AA} \leq \lambda/(2 \cdot \sin\theta) \leq 1 \text{ \AA}$) and a fixed ratio of 91% Al and 9% B at the Al4 site.

Site	<i>x</i>	<i>y</i>	<i>z</i>	Occ.	W. S. ^a	<i>U</i> _{eq.} (\AA^2)
Al1	0.24815(6)	0.38353(2)	0.0	1.0	8b	0.00423(8)
Al2	0.0	0.25538(3)	0.68661(8)	1.0	4a	0.00541(9)
Al3	0.0	0.44417(3)	0.68198(10)	1.0	4a	0.00487(9)
Al4	0.0	0.29700(3)	0.33424(10)	0.91	4a	0.00254(10)
B ^b	0.0	0.29700(3)	0.33424(10)	0.09	4a	0.00254(10)
B1	0.5	0.51573(11)	0.2210(2)	1.0	4a	0.0053(2)
O1	0.0	0.32949(9)	0.87047(17)	1.0	4a	0.00683(19)
O2	0.24289(14)	0.30987(6)	0.20158(12)	1.0	8b	0.00692(14)
O3	0.5	0.45335(9)	0.09233(16)	1.0	4a	0.00574(19)
O4	0.0	0.54595(8)	0.57201(17)	1.0	4a	0.00624(19)
O5	0.0	0.35171(8)	0.53810(17)	1.0	4a	0.0077(2)
O6	0.0	0.19119(8)	0.43512(19)	1.0	4a	0.00533(18)
O7	0.28858(15)	0.45171(6)	0.78567(12)	1.0	8b	0.00699(14)

^aWyckoff site: 4a with multiplicity = 1, 8b with multiplicity = 2; ^bat Al4 site

Table A1.27: Anisotropic displacement parameters from single-crystal XRD data of sample *a* with resolution restriction ($0.6 \text{ \AA} \leq \lambda/(2 \cdot \sin\theta) \leq 1 \text{ \AA}$) and a fixed ratio of 91% Al and 9% B at the Al4 site.

Site	U_{11} (\AA^2)	U_{22} (\AA^2)	U_{33} (\AA^2)	U_{23} (\AA^2)	U_{13} (\AA^2)	U_{12} (\AA^2)
Al1	0.00342(11)	0.00473(12)	0.00454(11)	0.00051(12)	-0.00006(9)	0.00019(9)
Al2	0.00477(18)	0.00491(17)	0.00654(18)	-0.00022(16)	0.0	0.0
Al3	0.00385(17)	0.00416(16)	0.00660(18)	-0.00057(16)	0.0	0.0
Al4	0.00276(16)	0.00310(18)	0.00178(17)	0.00024(14)	0.0	0.0
B ^a	0.00276(16)	0.00310(18)	0.00178(17)	0.00024(14)	0.0	0.0
B1	0.0043(5)	0.0061(6)	0.0054(6)	-0.0003(4)	0.0	0.0
O1	0.0045(4)	0.0088(4)	0.0072(4)	-0.0032(4)	0.0	0.0
O2	0.0055(3)	0.0081(3)	0.0071(3)	0.0022(2)	0.0012(2)	0.0014(2)
O3	0.0051(4)	0.0061(4)	0.0060(4)	-0.0026(3)	0.0	0.0
O4	0.0037(4)	0.0060(4)	0.0090(5)	0.0027(4)	0.0	0.0
O5	0.0118(5)	0.0053(4)	0.0060(4)	-0.0010(3)	0.0	0.0
O6	0.0042(4)	0.0040(4)	0.0078(4)	0.0013(3)	0.0	0.0
O7	0.0047(3)	0.0087(3)	0.0076(3)	0.0035(2)	-0.0008(2)	-0.0009(2)

^aat Al4 site

Table A1.28: Individual and mean polyhedral bond lengths of the refined structure from sample *a* with resolution restriction ($0.6 \text{ \AA} \leq \lambda/(2 \cdot \sin\theta) \leq 1 \text{ \AA}$) and a fixed ratio of 91% Al and 9% B at the Al4 site.

Center	Ligand	Distance (\AA)	Center	Ligand	Distance (\AA)
Al1	O4	1.8453(8)	Al2	O2 (x2)	1.7596(8)
Al1	O6	1.8827(8)	Al2	O1	1.7987(12)
Al1	O2	1.9040(9)	Al2	O5	1.8422(14)
Al1	O1	1.9048(9)	Al2	O6	2.1604(14)
Al1	O3	1.9079(9)		<Al2-O>	1.8641(11)
Al1	O7	1.9532(9)			
	<Al1-O>	1.8997(9)	Al3	O4	1.7458(13)
			Al3	O5	1.7745(13)
Al4	O2 (x2)	1.7244(9)	Al3	O7 (x2)	1.8233(9)
Al4	O6	1.7671(12)	Al3	O1	2.2499(14)
Al4	O5	1.7695(14)		<Al3-O>	1.8834(14)
	<Al4-O>	1.7464(11)			
B1	O3	1.3621(19)			
B1	O7 (x2)	1.3864(11)			
	<B1-O>	1.3783(14)			

Single-crystal XRD data of sample *f* refined with 91% Al and 9% B at the Al4 site and resolution restriction

Table A1.29: Details for single-crystal X-ray diffraction data collection and crystal structure refinement of sample *f* with resolution restriction ($0.62 \text{ \AA} \leq \lambda/(2 \cdot \sin\theta) \leq 1 \text{ \AA}$) and a fixed ratio of 91% Al and 9% B at the Al4 site.

Diffractometer: Bruker Smart APEX 2			
X-ray radiation	MoK α (0.71073 \AA)	Reflections rejected	3505
X-ray power	50 kV, 40 mA	Reflections used	5915
Crystal size	0.15 · 0.025 · 0.05 mm ³	Max. 2 θ	69.94°
Measurement time	60 s/frame	Index range <i>h</i>	-9 ... 9
Absorption corr.	Empirical ψ scans	Index range <i>k</i>	-24 ... 23
Resolution	1 \AA ... 0.62 \AA	Index range <i>l</i>	-12 ... 11
Sample name	<i>f</i> (ABO-62, # 62-2)	Unique reflections	1130
Temperature	298K	Reflections > 4 σ (<i>I</i>)	1088
Space group	<i>Cmc</i> 2 ₁	<i>R</i> (int)	0.0399
<i>a</i> -axis*	5.6618(7) \AA	<i>R</i> (σ)	0.0294
<i>b</i> -axis*	14.9981(12) \AA	Refined parameters	82
<i>c</i> -axis*	7.6806(7) \AA	GoF	0.815
<i>Volume</i> *	652.21(12) \AA^3	<i>R</i> 1, <i>I</i> > 4 σ (<i>I</i>)	0.0192
<i>Z</i>	4	<i>R</i> 1, all data	0.0205
Density ρ	2.250 g/cm ³	w <i>R</i> 2 on <i>F</i> ²	0.0463
Absorption coeff. μ	0.88 mm ⁻¹	$\Delta\rho_{\max}$	0.25 e ⁻ · \AA^{-3} near Al2
Reflections collected	9420	$\Delta\rho_{\min}$	-0.25 e ⁻ · \AA^{-3} near Al1

*lattice parameters from CAD4 (15 centered reflections with $\pm 11^\circ < \theta < \pm 30^\circ$)

Table A1.30: Atomic positions and isotropic displacement parameters of single-crystal XRD data from sample *f* with resolution restriction ($0.62 \text{ \AA} \leq \lambda/(2 \cdot \sin\theta) \leq 1 \text{ \AA}$) and a fixed ratio of 91% Al and 9% B at the Al4 site.

Site	<i>x</i>	<i>y</i>	<i>z</i>	Occ.	W. S. ^a	<i>U</i> _{eq.} (\AA^2)
Al1	0.24809(6)	0.38347(2)	0.0	1.0	8b	0.00516(10)
Al2	0.0	0.25544(3)	0.68638(9)	1.0	4a	0.00654(11)
Al3	0.0	0.44419(3)	0.68166(10)	1.0	4a	0.00585(11)
Al4	0.0	0.29690(3)	0.33413(10)	0.91	4a	0.00404(11)
B ^b	0.0	0.29690(3)	0.33413(10)	0.09	4a	0.00404(11)
B1	0.5	0.51562(11)	0.2212(2)	1.0	4a	0.0062(3)
O1	0.0	0.32925(8)	0.87053(18)	1.0	4a	0.0072(2)
O2	0.24286(14)	0.30974(6)	0.20135(14)	1.0	8b	0.00822(16)
O3	0.5	0.45338(8)	0.09282(17)	1.0	4a	0.0066(2)
O4	0.0	0.54594(8)	0.57215(19)	1.0	4a	0.0074(2)
O5	0.0	0.35170(8)	0.53801(18)	1.0	4a	0.0088(2)
O6	0.0	0.19118(8)	0.43510(19)	1.0	4a	0.00643(19)
O7	0.28852(16)	0.45173(6)	0.78528(13)	1.0	8b	0.00763(15)

^aWyckoff site: 4a with multiplicity = 1, 8b with multiplicity = 2; ^bat Al4 site

Table A1.31: Anisotropic displacement parameters from single-crystal XRD data of sample *f* with resolution restriction ($0.62 \text{ \AA} \leq \lambda/(2 \cdot \sin\theta) \leq 1 \text{ \AA}$) and a fixed ratio of 91% Al and 9% B at the Al4 site.

Site	U_{11} (\AA^2)	U_{22} (\AA^2)	U_{33} (\AA^2)	U_{23} (\AA^2)	U_{13} (\AA^2)	U_{12} (\AA^2)
Al1	0.00408(13)	0.00584(13)	0.00555(14)	-0.00008(12)	-0.00011(9)	0.00038(8)
Al2	0.00567(19)	0.00616(18)	0.0078(2)	-0.00016(16)	0.0	0.0
Al3	0.00460(19)	0.00544(18)	0.0075(2)	-0.00017(16)	0.0	0.0
Al4	0.00417(18)	0.00451(19)	0.00343(18)	0.00008(15)	0.0	0.0
B ^a	0.00417(18)	0.00451(19)	0.00343(18)	0.00008(15)	0.0	0.0
B1	0.0054(6)	0.0072(6)	0.0061(6)	-0.0012(4)	0.0	0.0
O1	0.0042(4)	0.0097(5)	0.0077(5)	-0.0032(4)	0.0	0.0
O2	0.0075(3)	0.0089(3)	0.0082(3)	0.0020(2)	0.0014(2)	0.0007(2)
O3	0.0051(4)	0.0070(4)	0.0077(5)	-0.0025(4)	0.0	0.0
O4	0.0048(4)	0.0069(5)	0.0103(5)	0.0025(4)	0.0	0.0
O5	0.0118(5)	0.0078(4)	0.0068(5)	-0.0015(4)	0.0	0.0
O6	0.0044(4)	0.0060(4)	0.0089(5)	0.0014(4)	0.0	0.0
O7	0.0043(3)	0.0099(3)	0.0087(3)	0.0041(3)	-0.0005(2)	-0.0012(2)

^aat Al4 site

Table A1.32: Individual and mean polyhedral bond lengths of the refined structure from sample *f* with resolution restriction ($0.62 \text{ \AA} \leq \lambda/(2 \cdot \sin\theta) \leq 1 \text{ \AA}$) and a fixed ratio of 91% Al and 9% B at the Al4 site.

Center	Ligand	Distance (\AA)	Center	Ligand	Distance (\AA)
Al1	O4	1.8442(8)	Al2	O2(x2)	1.7573(9)
Al1	O6	1.8805(8)	Al2	O1	1.7961(13)
Al1	O2	1.9014(10)	Al2	O5	1.8394(15)
Al1	O1	1.9034(9)	Al2	O6	2.1572(15)
Al1	O3	1.9083(9)		<Al2-O>	1.8615(12)
Al1	O7	1.9546(10)			
	<Al1-O>	1.8987(9)	Al3	O4	1.7424(13)
			Al3	O5	1.7724(13)
Al4	O2(x2)	1.7228(10)	Al3	O7(x2)	1.8206(9)
Al4	O6	1.7650(13)	Al3	O1	2.2531(14)
Al4	O5	1.7686(14)		<Al3-O>	1.8818(12)
	<Al4-O>	1.7448(12)			
B1	O3	1.358(2)			
B1	O7(x2)	1.3841(12)			
	<B1-O>	1.3754(15)			

Single-crystal XRD data of sample *a* refined with vacancies at the Al2 site and resolution restriction according to refinement strategy 3

Table A1.33: Details for single-crystal X-ray diffraction data collection and crystal structure refinement of sample *a* with resolution restriction ($0.6 \text{ \AA} \leq \lambda/(2 \cdot \sin\theta) \leq 1 \text{ \AA}$) and Al2 vacancies (refinement strategy 3).

Diffractometer: Enraf Nonius CAD4			
X-ray radiation	MoK α (0.71073 \AA)	Reflections rejected	1434
X-ray power	50 kV, 40 mA	Reflections used	4294
Crystal size	0.2 · 0.13 · 0.05 mm ³	Max. 2θ	69.93°
Measurement time	Max. 120 sec/step	Index range <i>h</i>	-9 ... 9
Absorption corr.	ψ scans	Index range <i>k</i>	-24 ... 24
Resolution	1 \AA ... 0.6 \AA	Index range <i>l</i>	-12 ... 12
Sample name	<i>a</i> (ABO-01-2009, # 01)	Unique reflections	1166
Temperature	298K	Reflections > 4 σ (<i>I</i>)	1045
Space group	<i>Cmc</i> 2 ₁	<i>R</i> (int)	0.0510
<i>a</i> -axis	5.6682(2) \AA	<i>R</i> (σ)	0.0375
<i>b</i> -axis	15.0060(9) \AA	Refined parameters	83
<i>c</i> -axis	7.6892(4) \AA	GoF	0.990
<i>Volume</i>	654.07(6) \AA^3	<i>R</i> 1, <i>I</i> > 4 σ (<i>I</i>)	0.0173
<i>Z</i>	4	<i>R</i> 1, all data	0.0273
Density ρ	2.942 g/cm ³	w <i>R</i> 2 on <i>F</i> ²	0.0295
Absorption coeff. μ	0.88 mm ⁻¹	$\Delta\rho_{\max}$	0.54 e ⁻ · \AA^{-3} near Al2
Reflections collected	5728	$\Delta\rho_{\min}$	-0.29 e ⁻ · \AA^{-3} near Al1

Table A1.34: Atomic positions and isotropic displacement parameters of single-crystal XRD data from sample *a* with resolution restriction ($0.6 \text{ \AA} \leq \lambda/(2 \cdot \sin\theta) \leq 1 \text{ \AA}$) and Al2 vacancies (refinement strategy 3).

Site	<i>x</i>	<i>y</i>	<i>z</i>	Occ.	W. S. ^a	<i>U</i> _{eq.} (\AA^2)
Al1	0.24819(6)	0.383523(18)	0.0	1.0	8b	0.00397(7)
Al2	0.0	0.25538(3)	0.68660(7)	0.979(4)	4a	0.0046(2)
Al3	0.0	0.44420(3)	0.68197(9)	1.0	4a	0.00462(9)
Al4	0.0	0.29699(3)	0.33426(9)	1.0	4a	0.00419(9)
B1	0.5	0.51567(10)	0.22105(19)	1.0	4a	0.0050(2)
O1	0.0	0.32949(8)	0.87053(15)	1.0	4a	0.00659(17)
O2	0.24288(12)	0.30984(5)	0.20162(11)	1.0	8b	0.00672(13)
O3	0.5	0.45337(8)	0.09229(14)	1.0	4a	0.00551(17)
O4	0.0	0.54602(7)	0.57211(14)	1.0	4a	0.00596(16)
O5	0.0	0.35183(7)	0.53796(14)	1.0	4a	0.00750(18)
O6	0.0	0.19126(7)	0.43506(16)	1.0	4a	0.00516(17)
O7	0.28862(14)	0.45173(5)	0.78568(11)	1.0	8b	0.00678(12)

^aWyckoff site: 4a with multiplicity = 1, 8b with multiplicity = 2

Table A1.35: Anisotropic displacement parameters from single-crystal XRD data of sample *a* with resolution restriction ($0.6 \text{ \AA} \leq \lambda/(2 \cdot \sin\theta) \leq 1 \text{ \AA}$) and Al2 vacancies (refinement strategy 3).

Site	U_{11} (\AA^2)	U_{22} (\AA^2)	U_{33} (\AA^2)	U_{23} (\AA^2)	U_{13} (\AA^2)	U_{12} (\AA^2)
Al1	0.00308(10)	0.00447(11)	0.00435(10)	0.00051(10)	-0.00005(8)	0.00022(8)
Al2	0.0040(3)	0.0040(3)	0.0057(3)	-0.00022(14)	0.0	0.0
Al3	0.00365(16)	0.00397(15)	0.00623(16)	-0.00050(14)	0.0	0.0
Al4	0.00422(15)	0.00485(17)	0.00350(15)	0.00026(12)	0.0	0.0
B1	0.0040(5)	0.0060(5)	0.0050(5)	-0.0007(4)	0.0	0.0
O1	0.0042(3)	0.0087(4)	0.0069(4)	-0.0035(3)	0.0	0.0
O2	0.0055(3)	0.0080(3)	0.0066(3)	0.0021(2)	0.0010(2)	0.00133(19)
O3	0.0046(4)	0.0059(4)	0.0061(4)	-0.0025(3)	0.0	0.0
O4	0.0036(3)	0.0058(4)	0.0085(4)	0.0027(3)	0.0	0.0
O5	0.0114(4)	0.0054(4)	0.0056(4)	-0.0007(3)	0.0	0.0
O6	0.0041(4)	0.0038(4)	0.0076(4)	0.0013(3)	0.0	0.0
O7	0.0046(3)	0.0085(3)	0.0072(2)	0.0035(2)	-0.00066(19)	-0.0010(2)

Table A1.36: Individual and mean polyhedral bond lengths of the refined structure from sample *a* with resolution restriction ($0.6 \text{ \AA} \leq \lambda/(2 \cdot \sin\theta) \leq 1 \text{ \AA}$) and Al2 vacancies (refinement strategy 3).

Center	Ligand	Distance (\AA)	Center	Ligand	Distance (\AA)
Al1	O4	1.8451(7)	Al2	O2 (x2)	1.7594(7)
Al1	O6	1.8832(7)	Al2	O1	1.7991(11)
Al1	O2	1.9044(8)	Al2	O5	1.8441(12)
Al1	O1	1.9047(8)	Al2	O6	2.1603(13)
Al1	O3	1.9078(8)		<Al2-O>	1.8645(10)
Al1	O7	1.9534(8)			
	<Al1-O>	1.8998(8)	Al3	O4	1.7459(12)
			Al3	O5	1.7741(11)
Al4	O2 (x2)	1.7242(8)	Al3	O7 (x2)	1.8236(8)
Al4	O6	1.7658(11)	Al3	O1	2.2506(13)
Al4	O5	1.7693(12)		<Al3-O>	1.8836(10)
	<Al4-O>	1.7459(10)			
B1	O3	1.3616(17)			
B1	O7 (x2)	1.3864(10)			
	<B1-O>	1.3782(12)			

Table A1.37: M-O-M angles of the refined structure from sample *a* with resolution restriction ($0.6 \text{ \AA} \leq \lambda/(2 \cdot \sin\theta) \leq 1 \text{ \AA}$) and Al2 vacancies (refinement strategy 3).

Sites	Angle (°)	Sites	Angle (°)
Al1-O1-Al1 (x2)	95.23(5)	Al3-O5-Al2	103.08(5)
Al1-O1-Al3	90.64(4)	Al4-O5-Al2	100.58(6)
Al2-O1-Al1 (x2)	132.38(2)	Al4-O5-Al3	156.33(7)
Al2-O1-Al3	88.07(4)	Al1-O6-Al1	98.58(5)
Al2-O2-Al1	104.86(4)	Al1-O6-Al2 (x2)	91.60(4)
Al4-O2-Al1	123.99(4)	Al4-O6-Al1 (x2)	130.68(3)
Al4-O2-Al2	129.65(4)	Al4-O6-Al2	89.59(5)
Al1-O3-Al1	96.87(5)	Al3-O7-Al1	103.37(4)
B1-O3-Al1 (x2)	130.36(3)	B1-O7-Al1	126.06(7)
Al1-O4-Al1	99.37(5)	B1-O7-Al3	129.83(7)
Al3-O4-Al1 (x2)	130.31(3)		

Table A1.38: O-M-O angles of the refined structure from sample *a* with resolution restriction ($0.6 \text{ \AA} \leq \lambda/(2 \cdot \sin\theta) \leq 1 \text{ \AA}$) and Al2 vacancies (refinement strategy 3).

Sites	Angle (°)	Sites	Angle (°)
O1-Al1-O3	168.80(5)	O2-Al2-O2	111.87(5)
O1-Al1-O7	82.46(4)	O2-Al2-O5 (x2)	118.51(3)
O2-Al1-O1	99.59(4)	O2-Al2-O6 (x2)	79.11(3)
O2-Al1-O3	91.61(4)	O5-Al2-O6	78.15(5)
O2-Al1-O7	173.12(4)	O4-Al3-O1	168.83(5)
O3-Al1-O7	86.45(4)	O4-Al3-O5	112.44(5)
O4-Al1-O1	80.66(3)	O4-Al3-O7 (x2)	99.05(3)
O4-Al1-O2	94.36(4)	O5-Al3-O1	78.73(5)
O4-Al1-O3	98.28(4)	O5-Al3-O7 (x2)	108.75(3)
O4-Al1-O6	177.57(6)	O7-Al3-O1 (x2)	76.45(3)
O4-Al1-O7	92.45(4)	O7-Al3-O7	127.58(6)
O6-Al1-O1	99.65(4)	O2-Al4-O2	105.98(5)
O6-Al1-O2	83.21(4)	O2-Al4-O5 (x2)	118.14(3)
O6-Al1-O3	81.89(4)	O2-Al4-O6 (x2)	111.11(3)
O6-Al1-O7	89.98(5)	O6-Al4-O5	91.68(5)
O1-Al2-O5	90.12(6)	O3-B1-O7 (x2)	120.19(6)
O1-Al2-O6	168.27(5)	O7-B1-O7	119.60(11)
O2-Al2-O1 (x2)	106.99(3)		

Single-crystal XRD data of sample *f* refined with vacancies at the Al2 site and resolution restriction according to refinement strategy 3

Table A1.39: Details for single-crystal X-ray diffraction data collection and crystal structure refinement of sample *f* with resolution restriction ($0.62 \text{ \AA} \leq \lambda/(2 \cdot \sin\theta) \leq 1 \text{ \AA}$) and Al2 vacancies (refinement strategy 3).

Diffractometer: Bruker Smart APEX 2			
X-ray radiation	MoK α (0.71073 \AA)	Reflections rejected	3505
X-ray power	50 kV, 40 mA	Reflections used	5915
Crystal size	0.15 · 0.025 · 0.05 mm ³	Max. 2 θ	69.94°
Measurement time	60 s/frame	Index range <i>h</i>	-9 ... 9
Absorption corr.	Empirical ψ scans	Index range <i>k</i>	-24 ... 23
Resolution	1 \AA ... 0.62 \AA	Index range <i>l</i>	-12 ... 11
Sample name	<i>f</i> (ABO-62, # 62-2)	Unique reflections	1130
Temperature	298K	Reflections > 4 σ (<i>I</i>)	1088
Space group	<i>Cmc</i> 2 ₁	<i>R</i> (int)	0.0399
<i>a</i> -axis*	5.6618(7) \AA	<i>R</i> (σ)	0.0294
<i>b</i> -axis*	14.9981(12) \AA	Refined parameters	83
<i>c</i> -axis*	7.6806(7) \AA	GoF	1.046
<i>Volume</i> *	652.21(12) \AA^3	<i>R</i> 1, <i>I</i> > 4 σ (<i>I</i>)	0.0186
<i>Z</i>	4	<i>R</i> 1, all data	0.0199
Density ρ	2.250 g/cm ³	w <i>R</i> 2 on <i>F</i> ²	0.0370
Absorption coeff. μ	0.88 mm ⁻¹	$\Delta\rho_{\max}$	0.24 e ⁻ · \AA^{-3} near Al2
Reflections collected	9420	$\Delta\rho_{\min}$	-0.24 e ⁻ · \AA^{-3} near Al1

*lattice parameters from CAD4 (15 centered reflections with $\pm 11^\circ < \theta < \pm 30^\circ$)

Table A1.40: Atomic positions and isotropic displacement parameters of single-crystal XRD data from sample *f* with resolution restriction ($0.62 \text{ \AA} \leq \lambda/(2 \cdot \sin\theta) \leq 1 \text{ \AA}$) and Al2 vacancies (refinement strategy 3).

Site	<i>x</i>	<i>y</i>	<i>z</i>	Occ.	W. S. ^a	<i>U</i> _{eq.} (\AA^2)
Al1	0.24810(6)	0.38347(2)	0.0	1.0	8b	0.00489(9)
Al2	0.0	0.25544(3)	0.68636(8)	0.968(4)	4a	0.0053(3)
Al3	0.0	0.44420(3)	0.68166(9)	1.0	4a	0.00558(11)
Al4	0.0	0.29688(3)	0.33415(9)	1.0	4a	0.00576(11)
B1	0.5	0.51556(10)	0.2212(2)	1.0	4a	0.0059(2)
O1	0.0	0.32935(8)	0.87041(16)	1.0	4a	0.00700(19)
O2	0.24275(13)	0.30977(6)	0.20136(13)	1.0	8b	0.00810(15)
O3	0.5	0.45335(8)	0.09289(16)	1.0	4a	0.00630(19)
O4	0.0	0.54600(8)	0.57221(17)	1.0	4a	0.00718(19)
O5	0.0	0.35174(8)	0.53797(16)	1.0	4a	0.0085(2)
O6	0.0	0.19125(7)	0.43511(17)	1.0	4a	0.00608(18)
O7	0.28868(15)	0.45178(6)	0.78535(12)	1.0	8b	0.00741(15)

^aWyckoff site: 4a with multiplicity = 1, 8b with multiplicity = 2

Table A1.41: Anisotropic displacement parameters from single-crystal XRD data of sample *f* with resolution restriction ($0.62 \text{ \AA} \leq \lambda/(2 \cdot \sin\theta) \leq 1 \text{ \AA}$) and Al2 vacancies (refinement strategy 3).

Site	U_{11} (\AA^2)	U_{22} (\AA^2)	U_{33} (\AA^2)	U_{23} (\AA^2)	U_{13} (\AA^2)	U_{12} (\AA^2)
Al1	0.00371(12)	0.00555(12)	0.00540(13)	-0.00006(11)	-0.00013(8)	0.00037(8)
Al2	0.0046(3)	0.0048(3)	0.0066(3)	-0.00006(15)	0.0	0.0
Al3	0.00419(18)	0.00520(17)	0.00735(19)	-0.00011(15)	0.0	0.0
Al4	0.00577(17)	0.00629(19)	0.00522(17)	0.00013(14)	0.0	0.0
B1	0.0050(5)	0.0069(6)	0.0057(6)	-0.0012(4)	0.0	0.0
O1	0.0040(4)	0.0096(4)	0.0074(4)	-0.0034(3)	0.0	0.0
O2	0.0074(3)	0.0088(3)	0.0081(3)	0.0019(2)	0.0014(2)	0.0007(2)
O3	0.0049(4)	0.0066(4)	0.0073(4)	-0.0023(3)	0.0	0.0
O4	0.0048(4)	0.0067(4)	0.0100(5)	0.0025(3)	0.0	0.0
O5	0.0116(5)	0.0073(4)	0.0065(4)	-0.0015(3)	0.0	0.0
O6	0.0041(4)	0.0057(4)	0.0085(4)	0.0015(3)	0.0	0.0
O7	0.0042(3)	0.0099(3)	0.0082(3)	0.0038(2)	-0.0005(2)	-0.0012(2)

Table A1.42: Individual and mean polyhedral bond lengths of the refined structure from sample *f* with resolution restriction ($0.62 \text{ \AA} \leq \lambda/(2 \cdot \sin\theta) \leq 1 \text{ \AA}$) and Al2 vacancies (refinement strategy 3).

Center	Ligand	Distance (\AA)	Center	Ligand	Distance (\AA)
Al1	O4	1.8439(8)	Al2	O2 (x2)	1.7581(8)
Al1	O6	1.8810(8)	Al2	O1	1.7964(12)
Al1	O2	1.9012(9)	Al2	O5	1.8398(13)
Al1	O1	1.9034(8)	Al2	O6	2.1566(13)
Al1	O3	1.9082(8)		<Al2-O>	1.8617(11)
Al1	O7	1.9546(9)			
	<Al1-O>	1.8987(8)	Al3	O4	1.7429(12)
			Al3	O5	1.7723(12)
Al4	O2 (x2)	1.7224(9)	Al3	O7 (x2)	1.8217(9)
Al4	O6	1.7639(12)	Al3	O1	2.2514(13)
Al4	O5	1.7685(13)		<Al3-O>	1.8820(11)
	<Al4-O>	1.7443(11)			
B1	O3	1.3570(18)			
B1	O7 (x2)	1.3836(11)			
	<B1-O>	1.3747(14)			

Table A1.43: M-O-M angles of the refined structure from sample *f* with resolution restriction ($0.62 \text{ \AA} \leq \lambda/(2 \cdot \sin\theta) \leq 1 \text{ \AA}$) and Al2 vacancies (refinement strategy 3).

Sites	Angle (°)	Sites	Angle (°)
Al1-O1-Al1 (x2)	95.13(5)	Al3-O5-Al2	103.21(6)
Al1-O1-Al3	90.60(5)	Al4-O5-Al2	100.56(6)
Al2-O1-Al1 (x2)	132.43(3)	Al4-O5-Al3	156.24(8)
Al2-O1-Al3	88.01(5)	Al1-O6-Al1	98.61(5)
Al2-O2-Al1	104.89(4)	Al1-O6-Al2 (x2)	91.65(5)
Al4-O2-Al1	124.03(5)	Al4-O6-Al1 (x2)	130.66(3)
Al4-O2-Al2	129.60(5)	Al4-O6-Al2	89.56(5)
Al1-O3-Al1	96.73(5)	Al3-O7-Al1	103.33(4)
B1-O3-Al1 (x2)	130.47(3)	B1-O7-Al1	126.00(7)
Al1-O4-Al1	99.25(5)	B1-O7-Al3	129.95(7)
Al3-O4-Al1 (x2)	130.37(3)		

Table A1.44: O-M-O angles of the refined structure from sample *f* with resolution restriction ($0.62 \text{ \AA} \leq \lambda/(2 \cdot \sin\theta) \leq 1 \text{ \AA}$) and Al2 vacancies (refinement strategy 3).

Sites	Angle (°)	Sites	Angle (°)
O1-Al1-O3	168.91(5)	O2-Al2-O2	111.87(6)
O1-Al1-O7	82.49(5)	O2-Al2-O5 (x2)	118.51(3)
O2-Al1-O1	99.53(5)	O2-Al2-O6 (x2)	79.06(4)
O2-Al1-O3	91.55(5)	O5-Al2-O6	78.24(5)
O2-Al1-O7	173.10(4)	O4-Al3-O1	168.75(6)
O3-Al1-O7	86.54(5)	O4-Al3-O5	112.65(6)
O4-Al1-O1	80.78(4)	O4-Al3-O7 (x2)	98.98(3)
O4-Al1-O2	94.40(5)	O5-Al3-O1	78.60(5)
O4-Al1-O3	98.15(4)	O5-Al3-O7 (x2)	108.73(3)
O4-Al1-O6	177.58(7)	O7-Al3-O1 (x2)	76.48(3)
O4-Al1-O7	92.44(5)	O7-Al3-O7	127.59(6)
O6-Al1-O1	99.61(4)	O2-Al4-O2	105.87(6)
O6-Al1-O2	83.18(5)	O2-Al4-O5 (x2)	118.16(4)
O6-Al1-O3	81.93(4)	O2-Al4-O6 (x2)	111.17(4)
O6-Al1-O7	89.98(5)	O6-Al4-O5	91.64(6)
O1-Al2-O5	90.18(6)	O3-B1-O7 (x2)	120.14(6)
O1-Al2-O6	168.41(5)	O7-B1-O7	119.70(12)
O2-Al2-O1 (x2)	106.96(4)		

Bond valences of sample a

Table A1.45: Bond valences calculated according to the structure refinement of sample *a* according to refinement strategy 1.

Site	O1	O2	O3	O4	O5	O6	O7	Σ_{Cation}
Al1	0.462 ^a	0.464	0.457 ^a	0.544 ^a		0.489 ^a	0.406	2.822
Al2	0.617	0.691 ^b			0.543	0.232		2.774
Al3	0.181			0.711	0.661		0.577 ^b	2.707
Al4		0.752 ^b			0.664	0.679		2.847
B1			1.021				0.966 ^b	2.953
Σ_{Anion}	1.722	1.907	1.935	1.799	1.868	1.889	1.949	

^abonds to two cations, ^bbonds to two anions

FTIR correlation table

Table A1.46: Correlation table of vibrational species of ideal and distorted borate groups, modified after Wilson et al. (1980).

Vibrations of the (BO ₃) ³⁻ group	Ideal symmetry <i>D3h</i> (-62 <i>m</i>)	Effective symmetry ^a <i>C2v</i> (<i>mm2</i>)	Site symmetry ^b <i>Cs</i> (<i>m</i>)
ν_1 , symmetrical stretching	<i>A</i> ₁ '	<i>A</i> ₁	<i>A</i> '
ν_3 , antisymmetrical stretching	<i>E</i> '	<i>A</i> ₁ + <i>B</i> ₂	<i>A</i> ' + <i>A</i> ''
ν_2 , out-of-plane bending	<i>A</i> ₂ ''	<i>B</i> ₁	<i>A</i> '
ν_4 , within-plane bending	<i>E</i> '	<i>A</i> ₁ + <i>B</i> ₂	<i>A</i> ' + <i>A</i> ''

^aaccording to the real bond lengths B-O3 (1.36 Å) and 2 x B-O7 (1.38 Å) and bond angles of 120° the borate group has the shape of an isosceles triangle, ^bWyckoff site symmetry 4a of the B and O3 atoms

²⁷Al MAS NMR parameters and ²⁷Al 3Q-MAS NMR spectra

Table A1.47: Chemical shifts and quadrupolar parameters obtained by line shape analysis of the ²⁷Al 3Q-MAS NMR spectrum of sample *a*.

Site	Species ^a	$\delta^{27}\text{Al}_{\text{iso}}$ (ppm)	C_q (MHz)	η
Al1	Al ^(VI)	11.9	5.91	0.39
Al2	Al ^(V) ₁	56.0	6.65	0.11
Al3	Al ^(V) ₂	48.6	7.78	0.71
Al4	Al ^(IV)	75.2	9.18	0.41

^anomenclature in agreement with Gan et al. (2002) and Hung et al. (2006)

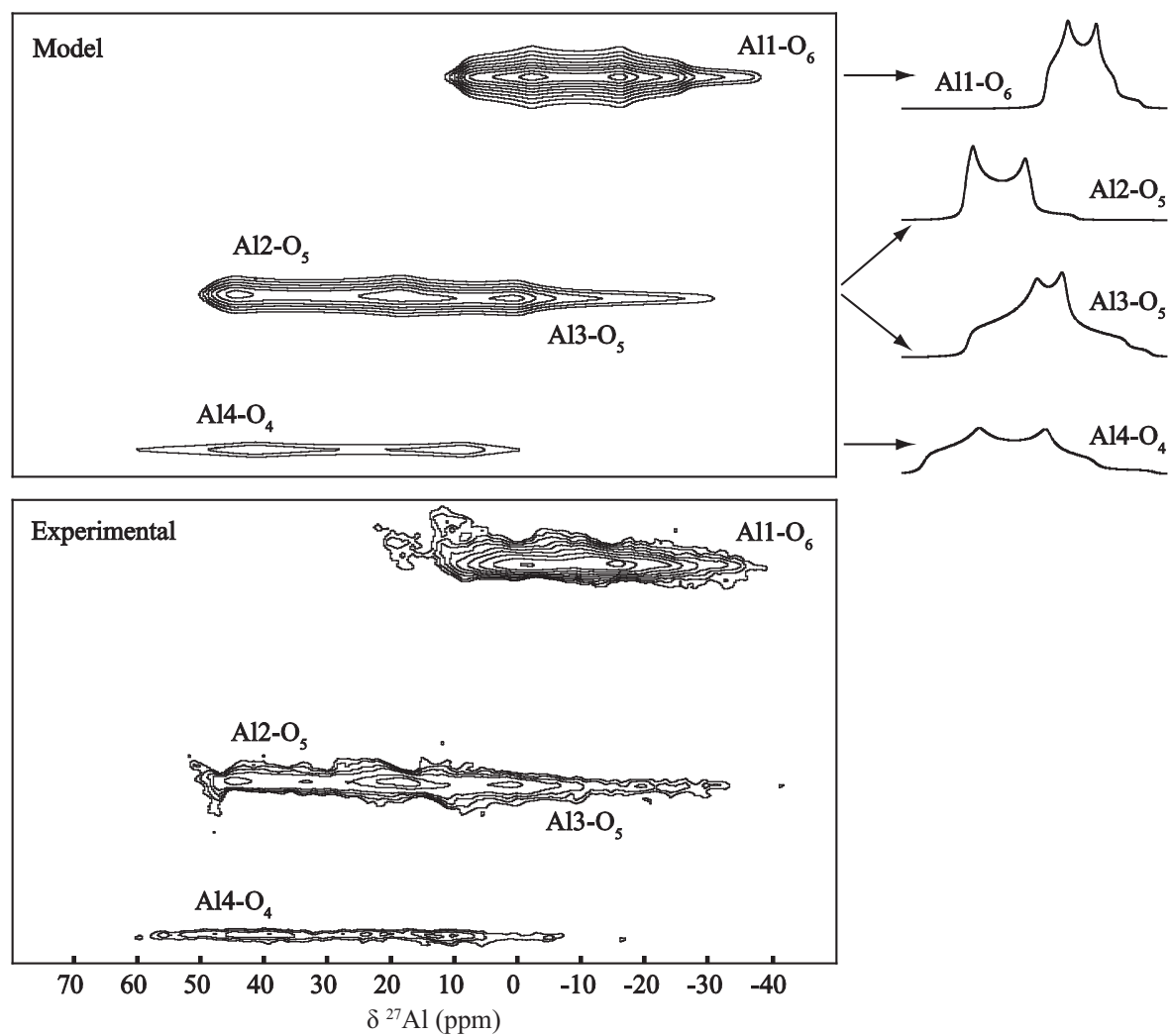


Figure A1.1: Experimental and modeled ^{27}Al 3Q-MAS NMR spectra of sample *a*. The chemical shifts and the quadrupolar parameters of the four aluminum species were evaluated by fitting the 2D NMR spectrum using the program Dmfit (Massiot et al. 2002). The simulated 1D slices of the four species are shown at the right margin of the 2D plot.

A.2 Supplementary Data for Chapter 5

Supplementary data for Al₅BO₉**Table A2.1:** Details for single-crystal X-ray diffraction data collection and crystal structure refinement of Al₅BO₉.

Diffractometer: Bruker Smart APEX 2, MoK α (0.71073 Å), 50 kV, 40 mA		
Crystal size	0.13 · 0.07 · 0.4 mm ³	
Detector distance	59.5 mm	
Rotation axis	ϕ, ω	
Collection mode	Automated hemisphere	
Frame size	512 · 512 pixel	
Absorption corr.	Empirical ψ correction	
Resolution	1 Å ... 0.62 Å	
Sample name	ABO-01-CAP	
Temperature	298K ^a	873K
Space group	<i>Cmc2</i> ₁	<i>Cmc2</i> ₁
<i>a</i> -axis	5.6689(6) Å	5.6825(6) Å
<i>b</i> -axis	15.0045(13) Å	15.0754(16) Å
<i>c</i> -axis	7.6897(13) Å	7.7121 Å
Volume	654.07(13) Å ³	660.67 Å ³
<i>Z</i>	4	4
Density ρ	2.942 g/cm ³	2.913 g/cm ³
Absorption coeff. μ	0.88 mm ⁻¹	0.87 mm ⁻¹
Time per frame	10 s	30 s
Reflections collected	8857	3199
Reflections rejected	3938	1922
Reflections used	4919	1277
Max. 2θ	69.91°	64.64°
Index range <i>h</i>	-8 ... 8	-7 ... 7
Index range <i>k</i>	-23 ... 23	-21 ... 20
Index range <i>l</i>	-12 ... 12	-10 ... 10
Unique reflections	1110	595
Reflections > 4 $\sigma(I)$	1118	581
<i>R</i> (int)	0.0423	0.0414
<i>R</i> (σ)	0.0349	0.0529
Refined parameters	83	83
GoF	1.001	1.076
<i>R</i> 1, <i>I</i> > 4 $\sigma(I)$	0.0195	0.0242
<i>R</i> 1, all data	0.0211	0.0247
w <i>R</i> 2 on <i>F</i> ²	0.0351	0.0557
$\Delta\rho_{\max}$	0.23 e ⁻ ·Å ⁻³ , near B1	0.26 e ⁻ ·Å ⁻³ , near Al1
$\Delta\rho_{\min}$	-0.18 e ⁻ ·Å ⁻³ , near O4	-0.26 e ⁻ ·Å ⁻³ , near Al1

^alattice parameters from CAD4

Table A2.2: Atomic positions and isotropic displacement parameters of Al₅BO₉.

Site	<i>T</i> (K)	<i>x</i>	<i>y</i>	<i>z</i>	<i>U</i> _{eq.} (Å ²)
Al1	298	0.24807(7)	0.38356(2)	0.0	0.00437(10)
	873	0.24823(11)	0.38348(5)	0.0	0.0104(3)
Al2	298 _a	0.0	0.25537(3)	0.68676(8)	0.0052(3)
	873 _b	0.0	0.25535(6)	0.68865(16)	0.0114(6)
Al3	298	0.0	0.44416(3)	0.68216(9)	0.00515(11)
	873	0.0	0.44438(6)	0.68045(19)	0.0110(3)
Al4	298	0.0	0.29692(3)	0.33421(9)	0.00471(11)
	873	0.0	0.29686(6)	0.33490(17)	0.0102(3)
B1	298	0.5	0.51545(11)	0.2209(2)	0.0057(3)
	873	0.5	0.5158(2)	0.2203(4)	0.0102(6)
O1	298	0.0	0.32948(8)	0.87041(16)	0.0071(2)
	873	0.0	0.32915(18)	0.8714(3)	0.0146(5)
O2	298	0.24297(15)	0.30993(6)	0.20155(12)	0.00698(16)
	873	0.2432(3)	0.30959(15)	0.2026(3)	0.0156(4)
O3	298	0.5	0.45351(8)	0.09240(15)	0.0056(2)
	873	0.5	0.45346(18)	0.0929(3)	0.0137(5)
O4	298	0.0	0.54584(8)	0.57239(16)	0.0065(2)
	873	0.0	0.54610(17)	0.5721(4)	0.0156(5)
O5	298	0.0	0.35176(8)	0.53855(16)	0.0078(2)
	873	0.0	0.35135(16)	0.5391(3)	0.0179(5)
O6	298	0.0	0.19121(8)	0.43486(17)	0.0057(2)
	873	0.0	0.19109(15)	0.4356(3)	0.0123(4)
O7	298	0.28875(17)	0.45168(6)	0.78551(12)	0.00705(15)
	873	0.2893(4)	0.45132(13)	0.7836(2)	0.0159(4)

^aoccupancy: 0.983(10) ^boccupancy: 0.99(2)**Table A2.3:** Anisotropic displacement parameters of Al₅BO at 298K.

Site	<i>U</i> ₁₁ (Å ²)	<i>U</i> ₂₂ (Å ²)	<i>U</i> ₃₃ (Å ²)	<i>U</i> ₂₃ (Å ²)	<i>U</i> ₁₃ (Å ²)	<i>U</i> ₁₂ (Å ²)
Al1	0.00320(14)	0.00509(13)	0.00482(13)	0.00049(12)	0.00012(9)	0.00026(9)
Al2	0.0045(3)	0.0050(3)	0.0060(3)	0.00001(15)	0.0	0.0
Al3	0.0042(2)	0.00460(17)	0.00663(18)	−0.00047(15)	0.0	0.0
Al4	0.0046(2)	0.00523(19)	0.00428(17)	0.00034(14)	0.0	0.0
B1	0.0048(6)	0.0061(6)	0.0063(6)	−0.0005(4)	0.0	0.0
O1	0.0052(5)	0.0089(4)	0.0073(4)	−0.0037(4)	0.0	0.0
O2	0.0058(4)	0.0087(3)	0.0065(3)	0.0022(2)	0.0012(2)	0.0012(2)
O3	0.0040(5)	0.0066(5)	0.0062(4)	−0.0027(3)	0.0	0.0
O4	0.0048(5)	0.0054(5)	0.0094(4)	0.0023(3)	0.0	0.0
O5	0.0107(5)	0.0066(4)	0.0059(4)	−0.0009(3)	0.0	0.0
O6	0.0046(5)	0.0054(4)	0.0070(4)	0.0011(3)	0.0	0.0
O7	0.0051(3)	0.0090(3)	0.0071(3)	0.0033(2)	−0.0006(2)	−0.0004(3)

Table A2.4: Anisotropic displacement parameters of Al₅BO at 873K.

Site	U_{11} (Å ²)	U_{22} (Å ²)	U_{33} (Å ²)	U_{23} (Å ²)	U_{13} (Å ²)	U_{12} (Å ²)
Al1	0.0073(4)	0.0145(4)	0.0094(3)	0.0006(3)	-0.00054(14)	0.00090(15)
Al2	0.0090(7)	0.0130(7)	0.0120(7)	-0.0003(3)	0.0	0.0
Al3	0.0086(5)	0.0124(5)	0.0119(4)	-0.0004(3)	0.0	0.0
Al4	0.0084(4)	0.0155(5)	0.0067(4)	0.0013(3)	0.0	0.0
B1	0.0034(14)	0.0160(15)	0.0113(12)	-0.0034(9)	0.0	0.0
O1	0.0077(10)	0.0232(11)	0.0130(11)	-0.0083(8)	0.0	0.0
O2	0.0105(8)	0.0223(9)	0.0139(7)	0.0065(5)	0.0048(4)	0.0031(4)
O3	0.0088(11)	0.0197(13)	0.0125(9)	-0.0066(9)	0.0	0.0
O4	0.0107(11)	0.0161(11)	0.0199(10)	0.0089(9)	0.0	0.0
O5	0.0266(14)	0.0167(11)	0.0103(9)	-0.0015(8)	0.0	0.0
O6	0.0090(10)	0.0135(9)	0.0143(9)	0.0027(7)	0.0	0.0
O7	0.0089(7)	0.0242(9)	0.0147(6)	0.0089(6)	0.0006(5)	-0.0026(5)

Table A2.5: Polyhedral bond lengths of Al₅BO₉.

Center	Ligand	d _{298K} (Å)	d _{873K} (Å)	α (K ⁻¹)	esd α (K ⁻¹)
Al1	O1	1.9050(9)	1.9091(17)	3.743E-06	1.756E-06
	O2	1.9035(9)	1.919(2)	1.416E-05	2.087E-06
	O3	1.9095(9)	1.9165(17)	6.375E-06	1.752E-06
	O4	1.8464(8)	1.8511(16)	4.333E-06	1.685E-06
	O6	1.8839(8)	1.8861(16)	2.031E-06	1.651E-06
	O7	1.9541(9)	1.9710(18)	1.504E-05	1.791E-06
	<Al1-O>	1.9004(9)	1.909(2)	7.672E-06	1.787E-06
Al2	O1	1.7974(12)	1.795(2)	-2.129E-06	2.510E-06
	O2	1.7596(9)	1.7603(19)	6.919E-07	1.467E-06
	O2	1.7596(9)	1.7603(19)	6.919E-07	2.078E-06
	O5	1.8413(14)	1.851(3)	8.878E-06	2.957E-06
	O6	2.1632(14)	2.179(3)	1.262E-05	2.304E-06
	<Al2 ^(V) -O>	1.8642(11)	1.869(2)	4.534E-06	2.268E-06
Al3	O1	2.2486(14)	2.277(3)	2.204E-05	2.421E-06
	O4	1.7436(13)	1.746(3)	2.593E-06	2.899E-06
	O5	1.7725(13)	1.776(3)	3.827E-06	2.852E-06
	O7	1.8231(10)	1.830(2)	6.201E-06	2.133E-06
	O7	1.8231(10)	1.830(2)	6.201E-06	2.133E-06
	<Al3 ^(V) -O>	1.8822(12)	1.892(3)	8.870E-06	2.479E-06
Al4	O2	1.7250(9)	1.7287(17)	3.730E-06	1.939E-06
	O3	1.7250(9)	1.7287(17)	3.730E-06	1.939E-06
	O5	1.7737(13)	1.776(3)	2.255E-06	2.938E-06
	O6	1.7650(13)	1.774(2)	8.474E-06	2.689E-06
	<Al4-O>	1.7472(11)	1.752(2)	4.554E-06	2.382E-06
B1	O3	1.3567(19)	1.360(4)	3.846E-06	5.446E-06
	O7	1.3870(12)	1.385(2)	-2.884E-06	3.142E-06
	O7	1.3870(12)	1.385(2)	-2.884E-06	3.142E-06
	<B1-O>	1.3769(14)	1.377(3)	-6.736E-07	3.898E-06

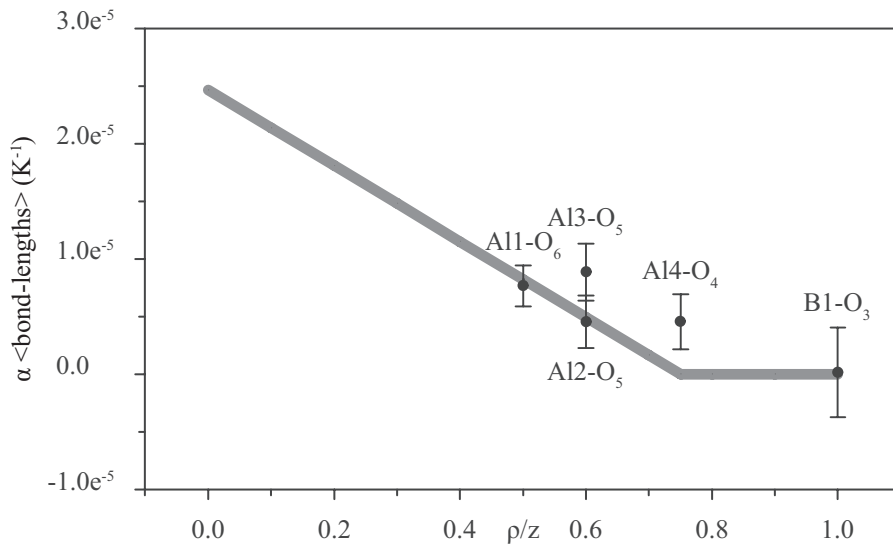


Figure A2.1: Expansion parameters α calculated from averaged polyhedral bond length of Al_5BO_9 . Expected values according to Hazen and Prewitt (1977) plot on the gray line.

Table A2.6: M-O-M angles of the refined structure of Al_5BO_9 at 298K.

Sites	Angle ($^\circ$)	Sites	Angle ($^\circ$)
Al1-O1-Al1	95.15(6)	Al3-O5-Al2	103.22(6)
Al1-O1-Al3 (x2)	90.62(5)	Al3-O5-Al4	156.18(8)
Al2-O1-Al1 (x2)	132.42(3)	Al4-O5-Al2	100.60(6)
Al2-O1-Al3	88.14(5)	Al1-O6-Al1	98.60(6)
Al2-O2-Al1	104.95(4)	Al1-O6-Al2 (x2)	91.54(5)
Al4-O2-Al1	124.01(5)	Al4-O6-Al1 (x2)	130.67(3)
Al4-O2-Al2	129.52(5)	Al4-O6-Al2	89.58(6)
Al1-O3-Al1	96.82(6)	Al3-O7-Al1	103.27(5)
B1-O3-Al1 (x2)	130.36(3)	B1-O7-Al1	126.16(8)
Al1-O4-Al1	99.20(6)	B1-O7-Al3	129.88(8)
Al3-O4-Al1 (x2)	130.39(3)		

Table A2.7: M-O-M angles of the refined structure of Al_5BO_9 at 873K.

Sites	Angle ($^\circ$)	Sites	Angle ($^\circ$)
Al1-O1-Al1	95.27(11)	Al3-O5-Al2	103.58(12)
Al1-O1-Al3 (x2)	90.50(10)	Al3-O5-Al4	155.41(16)
Al2-O1-Al1 (x2)	132.35(5)	Al4-O5-Al2	101.01(13)
Al2-O1-Al3	88.01(10)	Al1-O6-Al1	98.67(11)
Al2-O2-Al1	105.12(8)	Al1-O6-Al2 (x2)	91.66(9)
Al4-O2-Al1	123.83(10)	Al4-O6-Al1 (x2)	130.63(5)
Al4-O2-Al2	129.57(12)	Al4-O6-Al2	89.57(11)
Al1-O3-Al1	96.58(11)	Al3-O7-Al1	103.42(10)
B1-O3-Al1 (x2)	130.58(6)	B1-O7-Al1	125.94(16)
Al1-O4-Al1	99.29(11)	B1-O7-Al3	130.08(14)
Al3-O4-Al1 (x2)	130.35(6)		

Table A2.8: O-M-O angles of the refined structure of Al_5BO_9 at 298K.

Sites	Angle (°)	Sites	Angle (°)
O1-Al1-O3	168.78(5)	O2-Al2-O2	111.80(6)
O1-Al1-O7	82.44(5)	O2-Al2-O5 (x2)	118.52(3)
O2-Al1-O1	99.64(5)	O2-Al2-O6 (x2)	79.05(3)
O2-Al1-O3	91.57(5)	O5-Al2-O6	78.19(5)
O2-Al1-O7	173.04(5)	O4-Al3-O1	168.88(6)
O3-Al1-O7	86.46(5)	O4-Al3-O5	112.51(6)
O4-Al1-O1	80.79(4)	O4-Al3-O7 (x2)	99.02(4)
O4-Al1-O2	94.35(5)	O5-Al3-O1	78.61(5)
O4-Al1-O3	98.17(4)	O5-Al3-O7 (x2)	108.66(3)
O4-Al1-O6	177.60(7)	O7-Al3-O1 (x2)	76.51(3)
O4-Al1-O7	92.54(5)	O7-Al3-O7	127.76(6)
O6-Al1-O1	99.61(4)	O2-Al4-O2	105.96(6)
O6-Al1-O2	83.25(5)	O2-Al4-O5 (x2)	118.12(4)
O6-Al1-O3	81.91(5)	O2-Al4-O6 (x2)	111.16(4)
O6-Al1-O7	89.86(5)	O6-Al4-O5	91.63(6)
O1-Al2-O5	90.02(6)	O3-B1-O7 (x2)	120.29(7)
O1-Al2-O6	168.21(6)	O7-B1-O7	119.40(13)
O2-Al2-O1 (x2)	107.08(4)		

Table A2.9: O-M-O angles of the refined structure of Al_5BO_9 at 873K.

Sites	Angle (°)	Sites	Angle (°)
O1-Al1-O3	169.09(12)	O2-Al2-O2	111.96(15)
O1-Al1-O7	82.55(11)	O2-Al2-O5 (x2)	118.23(8)
O2-Al1-O1	99.39(11)	O2-Al2-O6 (x2)	78.90(7)
O2-Al1-O3	91.51(10)	O5-Al2-O6	77.84(11)
O2-Al1-O7	172.84(9)	O4-Al3-O1	168.29(13)
O3-Al1-O7	86.68(10)	O4-Al3-O5	113.56(13)
O4-Al1-O1	80.75(8)	O4-Al3-O7 (x2)	99.08(7)
O4-Al1-O2	94.41(11)	O5-Al3-O1	78.15(10)
O4-Al1-O3	98.09(9)	O5-Al3-O7 (x2)	108.19(7)
O4-Al1-O6	177.50(14)	O7-Al3-O1 (x2)	76.26(6)
O4-Al1-O7	92.70(11)	O7-Al3-O7	127.96(13)
O6-Al1-O1	99.66(9)	O2-Al4-O2	106.18(14)
O6-Al1-O2	83.09(9)	O2-Al4-O5 (x2)	118.16(8)
O6-Al1-O3	81.97(8)	O2-Al4-O6 (x2)	110.99(9)
O6-Al1-O7	89.79(11)	O6-Al4-O5	91.58(12)
O1-Al2-O5	90.27(13)	O3-B1-O7 (x2)	120.16(13)
O1-Al2-O6	168.11(12)	O7-B1-O7	119.7(3)
O2-Al2-O1 (x2)	107.26(8)		

Table A2.10: Temperature dependent lattice parameters and agreement factors from powder XRD refinements of Al_5BO_9 .

T (K)	a -axis (\AA)	b -axis (\AA)	c -axis (\AA)	$Volume$ (\AA^3)	R_{wp}	GoF
298	5.66891(4)	15.01477(12)	7.69560(5)	655.029(9)	7.51	1.14
323	5.66936(4)	15.01715(11)	7.69656(5)	655.267(8)	7.54	1.14
373	5.67029(3)	15.02191(9)	7.69849(4)	655.747(7)	7.54	1.14
423	5.67125(3)	15.02667(7)	7.70045(3)	656.233(6)	7.59	1.15
473	5.67225(2)	15.03144(6)	7.70242(3)	656.724(5)	7.57	1.14
523	5.67327(2)	15.03621(6)	7.70442(3)	657.221(4)	7.50	1.13
573	5.67432(2)	15.04099(6)	7.70643(2)	657.724(4)	7.56	1.14
623	5.67540(2)	15.04578(6)	7.70846(2)	658.231(4)	7.63	1.15
673	5.67651(2)	15.05056(6)	7.71050(3)	658.745(4)	7.63	1.15
723	5.67766(2)	15.05536(6)	7.71257(3)	659.264(4)	7.64	1.15
773	5.67883(2)	15.06015(6)	7.71466(3)	659.788(4)	7.63	1.15
823	5.68003(2)	15.06496(6)	7.71676(3)	660.319(4)	7.71	1.16
873	5.68126(2)	15.06976(6)	7.71888(3)	660.854(4)	7.73	1.16
923	5.68253(2)	15.07457(6)	7.72102(3)	661.396(4)	7.69	1.15
973	5.68382(2)	15.07939(6)	7.72318(2)	661.942(4)	7.68	1.15
1023	5.68514(2)	15.08421(5)	7.72536(2)	662.495(4)	7.66	1.15
1073	5.68649(2)	15.08904(6)	7.72755(3)	663.053(4)	7.63	1.14
1123	5.68788(2)	15.09387(6)	7.72977(3)	663.617(5)	7.73	1.15
1173	5.68929(2)	15.09870(7)	7.73200(4)	664.186(6)	7.70	1.15
1223	5.69073(3)	15.10354(9)	7.73425(4)	664.761(7)	7.68	1.14
1273	5.69221(3)	15.10838(11)	7.73652(5)	665.342(8)	7.87	1.17

Table A2.11: Temperature dependent thermal expansion parameters α of Al_5BO_9 . AF is the anisotropy factor.

T (K)	$\alpha_{a\text{-axis}}$ (K^{-1})	$\alpha_{b\text{-axis}}$ (K^{-1})	$\alpha_{c\text{-axis}}$ (K^{-1})	α_{Volume} (K^{-1})	AF
298	3.17949E-06	6.33479E-06	4.98378E-06	1.44906E-05	6.31
323	3.23237E-06	6.33687E-06	5.00730E-06	1.45702E-05	6.21
373	3.33807E-06	6.34101E-06	5.05430E-06	1.47291E-05	6.01
423	3.44372E-06	6.34515E-06	5.10127E-06	1.48876E-05	5.80
473	3.54932E-06	6.34929E-06	5.14820E-06	1.50458E-05	5.60
523	3.65486E-06	6.35342E-06	5.19510E-06	1.52036E-05	5.40
573	3.76035E-06	6.35755E-06	5.24195E-06	1.53611E-05	5.19
623	3.86577E-06	6.36167E-06	5.28878E-06	1.55182E-05	4.99
673	3.97113E-06	6.36579E-06	5.33556E-06	1.56749E-05	4.79
723	4.07643E-06	6.36990E-06	5.38231E-06	1.58312E-05	4.59
773	4.18167E-06	6.37401E-06	5.42901E-06	1.59872E-05	4.38
823	4.28684E-06	6.37811E-06	5.47568E-06	1.61427E-05	4.18
873	4.39194E-06	6.38221E-06	5.52231E-06	1.62979E-05	3.98
923	4.49697E-06	6.38631E-06	5.56891E-06	1.64527E-05	3.78
973	4.60193E-06	6.39040E-06	5.61546E-06	1.66071E-05	3.58
1023	4.70682E-06	6.39448E-06	5.66197E-06	1.67611E-05	3.38
1073	4.81164E-06	6.39857E-06	5.70844E-06	1.69147E-05	3.17
1123	4.91637E-06	6.40264E-06	5.75488E-06	1.70679E-05	2.97
1173	5.02103E-06	6.40671E-06	5.80127E-06	1.72207E-05	2.77
1223	5.12562E-06	6.41078E-06	5.84762E-06	1.73731E-05	2.57
1273	5.23012E-06	6.41484E-06	5.89393E-06	1.75251E-05	2.37

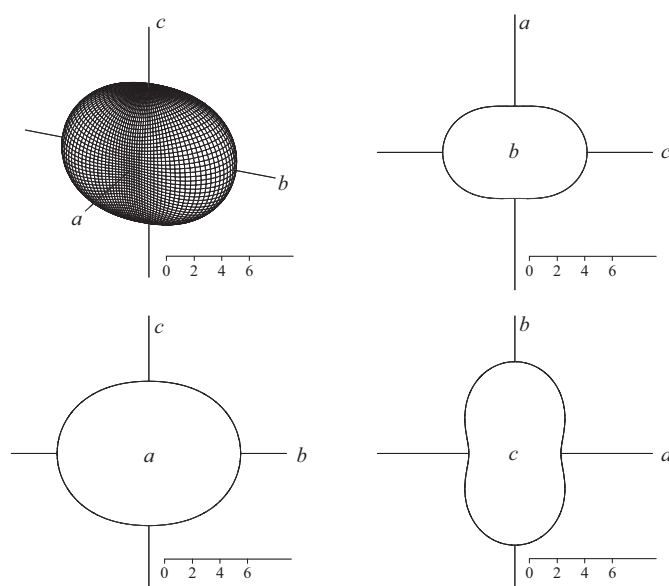


Figure A2.2: Representation surface of thermal expansion tensor components of Al_5BO_9 at 298K. Top left: Arbitrary view, top right: Cross-section in (010), bottom left: Cross-section in (100) and bottom right: Cross-section in (001). a , b and c are directions parallel to unit cell axes, scale bar unit is $10^{-6} \cdot \text{K}^{-1}$.

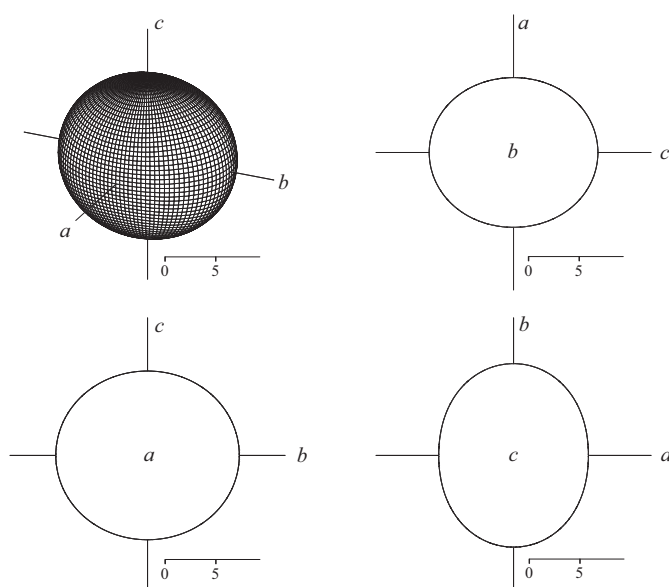


Figure A2.3: Representation surface of thermal expansion tensor components of Al_5BO_9 at 1273K. Top left: Arbitrary view, top right: Cross-section in (010), bottom left: Cross-section in (100) and bottom right: Cross-section in (001). a , b and c are directions parallel to unit cell axes, scale bar unit is $10^{-6} \cdot \text{K}^{-1}$.

Supplementary data for $\text{Al}_4\text{B}_2\text{O}_9$

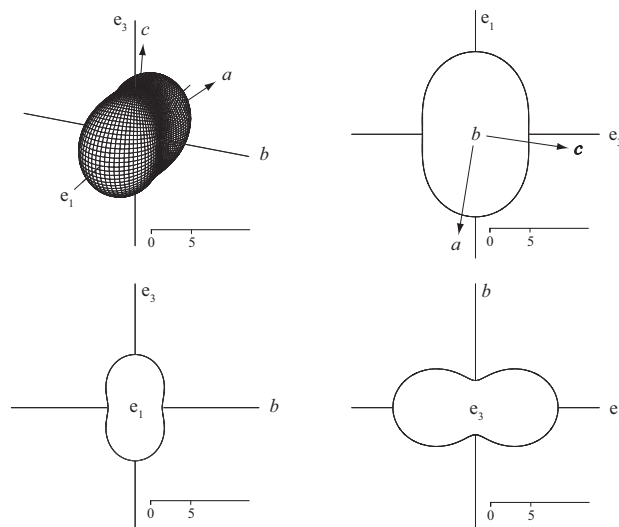


Figure A2.4: Representation surface of thermal expansion tensor components of $\text{Al}_4\text{B}_2\text{O}_9$ at 298K after principal axis transformation. e_1 , e_2 and e_3 are eigenvectors of the unit cell axes, the b -axis is parallel to e_2 . Top left: Arbitrary view, top right: Cross-section of the e_1 - e_3 -plane, bottom left: Cross-section of the b - e_3 -plane and bottom right: Cross section of the b - e_1 -plane. a - and c -axes are plotted approximately. Scale bar unit is $10^{-6}\cdot\text{K}^{-1}$.

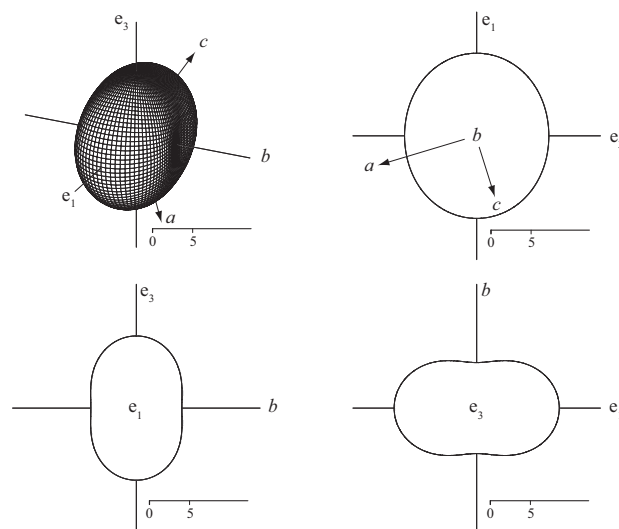


Figure A2.5: Representation surface of thermal expansion tensor components of $\text{Al}_4\text{B}_2\text{O}_9$ at 1323K after principal axis transformation. e_1 , e_2 and e_3 are eigenvectors of the unit cell axes, the b -axis is parallel to e_2 . Top left: Arbitrary view, top right: Cross-section of the e_1 - e_3 -plane, bottom left: Cross-section of the b - e_3 -plane and bottom right: Cross section of the b - e_1 -plane. a - and c -axes are plotted approximately. Scale bar unit is $10^{-6}\cdot\text{K}^{-1}$.

Plots were made with WinTensor v. 1.2 by Werner Kaminsky, Dept. of Chemistry, University of Washington.

Table A2.12: Temperature dependent lattice parameters and agreement factors from powder XRD refinements of $\text{Al}_4\text{B}_2\text{O}_9$.

T (K)	a -axis (Å)	b -axis (Å)	c -axis (Å)	Volume (Å ³)	β (°)	R_{wp}	GoF
298	14.8045(3)	5.54509(8)	15.07669(19)	90.8290(10)	1237.55(2)	9.50	1.24
323	14.8081(2)	5.54553(7)	15.07906(18)	90.8276(9)	1238.14(2)	9.78	1.27
373	14.8151(2)	5.54643(6)	15.08387(17)	90.8247(8)	1239.32(2)	9.83	1.27
423	14.8220(2)	5.54735(6)	15.08876(17)	90.8219(7)	1240.512(18)	9.88	1.28
473	14.82884(18)	5.54829(6)	15.09374(16)	90.8191(6)	1241.707(17)	10.02	1.30
523	14.83563(17)	5.54926(5)	15.09881(16)	90.8164(6)	1242.909(16)	9.94	1.28
573	14.84235(16)	5.55024(5)	15.10396(16)	90.8138(5)	1244.118(16)	10.07	1.30
623	14.84901(16)	5.55125(5)	15.10919(15)	90.8112(5)	1245.334(17)	9.98	1.28
673	14.85560(16)	5.55228(5)	15.11452(15)	90.8086(5)	1246.558(16)	10.03	1.29
723	14.86213(16)	5.55333(5)	15.11992(15)	90.8062(5)	1247.788(16)	10.10	1.30
773	14.86859(16)	5.5544(5)	15.12541(15)	90.8037(5)	1249.025(17)	10.05	1.29
823	14.87498(17)	5.55549(4)	15.13099(16)	90.8014(5)	1250.270(16)	10.28	1.32
873	14.8813(18)	5.55661(4)	15.13665(16)	90.7991(6)	1251.521(16)	10.02	1.28
923	14.88756(19)	5.55774(4)	15.14240(17)	90.7968(6)	1252.780(16)	10.12	1.29
973	14.8936(2)	5.55890(4)	15.14823(18)	90.7946(6)	1254.045(16)	10.19	1.30
1023	14.8999(2)	5.56008(4)	15.1542(2)	90.7925(7)	1255.318(16)	10.13	1.29
1073	14.9059(3)	5.56129(4)	15.1602(2)	90.7904(7)	1256.598(16)	10.03	1.28
1123	14.9119(3)	5.56251(5)	15.1662(3)	90.7884(8)	1257.886(17)	10.02	1.27
1173	14.9178(3)	5.56376(5)	15.1724(3)	90.7864(9)	1259.180(19)	10.27	1.30
1223	14.9237(4)	5.56502(6)	15.1787(3)	90.7845(10)	1260.48(2)	10.23	1.30
1273	14.92950(4)	5.56631(7)	15.1850(4)	90.7826(12)	1261.79(3)	10.12	1.28
1323	14.9352(5)	5.56762(8)	15.1914(4)	90.7808(13)	1263.11(3)	10.04	1.27

Table A2.13: Temperature dependent thermal expansion parameters α of $\text{Al}_4\text{B}_2\text{O}_9$. AF is the anisotropy factor.

T (K)	$\alpha_{a\text{-axis}}$ (K ⁻¹)	$\alpha_{b\text{-axis}}$ (K ⁻¹)	$\alpha_{c\text{-axis}}$ (K ⁻¹)	α_{Volume} (K ⁻¹)	AF
298	9.53666E-06	3.16331E-06	6.26697E-06	1.89688E-05	12.75
323	9.48925E-06	3.20212E-06	6.32250E-06	1.90170E-05	12.57
373	9.39455E-06	3.27969E-06	6.43348E-06	1.91132E-05	12.23
423	9.29998E-06	3.35724E-06	6.54435E-06	1.92091E-05	11.89
473	9.20554E-06	3.43474E-06	6.65512E-06	1.93048E-05	11.54
523	9.11123E-06	3.51220E-06	6.76577E-06	1.94001E-05	11.20
573	9.01704E-06	3.58962E-06	6.87631E-06	1.94951E-05	10.85
623	8.92298E-06	3.66700E-06	6.98674E-06	1.95898E-05	10.51
673	8.82905E-06	3.74433E-06	7.09705E-06	1.96843E-05	10.17
723	8.73523E-06	3.82163E-06	7.20724E-06	1.97784E-05	9.83
773	8.64154E-06	3.89887E-06	7.31731E-06	1.98723E-05	9.49
823	8.54797E-06	3.97608E-06	7.42725E-06	1.99658E-05	9.14
873	8.45451E-06	4.05323E-06	7.53708E-06	2.00591E-05	8.80
923	8.36118E-06	4.13034E-06	7.64678E-06	2.01520E-05	8.46
973	8.26795E-06	4.20741E-06	7.75635E-06	2.02446E-05	8.12
1023	8.17485E-06	4.28442E-06	7.86580E-06	2.03370E-05	7.78
1073	8.08185E-06	4.36138E-06	7.97511E-06	2.04290E-05	7.44
1123	7.98897E-06	4.43829E-06	8.08429E-06	2.05208E-05	7.29
1173	7.89620E-06	4.51516E-06	8.19334E-06	2.06122E-05	7.36
1223	7.80353E-06	4.59196E-06	8.30226E-06	2.07033E-05	7.42
1273	7.71097E-06	4.66872E-06	8.41103E-06	2.07941E-05	7.48
1323	7.61852E-06	4.74542E-06	8.51967E-06	2.08847E-05	7.55

Supplementary data for grandidierite

Table A2.14: Details for single-crystal X-ray diffraction data collection and crystal structure refinement of grandidierite.

Diffractometer: Bruker Smart APEX 2, MoK α (0.71073 Å), 50 kV, 40 mA		
Crystal size	0.17 · 0.34 · 0.27 mm ³	
Detector distance	59.5 mm	
Rotation axis	ϕ, ω	
Collection mode	Automated hemisphere	
Frame size	512 · 512 pixel	
Absorption corr.	Empirical ψ correction	
Resolution	No restriction	
Sample name	Grandidierite	
Temperature	298K	873K
Space group	<i>Pnma</i>	<i>Pnma</i>
<i>a</i> -axis	10.9967(1) Å	11.0193(1) Å
<i>b</i> -axis	5.7634(1) Å	5.7884(1) Å
<i>c</i> -axis	10.3321(1) Å	10.3434(1) Å
Volume	653.05(3) Å ³	659.74(3) Å ³
<i>Z</i>	4	4
Density ρ	2.947 g/cm ³	2.917 g/cm ³
Absorption coeff. μ	1.00 mm ⁻¹	0.99 mm ⁻¹
Time per frame	10 s	20 s
Reflections collected	11250	15049
Reflections rejected	681	634
Reflections used	10569	14415
Max. 2θ	63.20°	89.18°
Index range <i>h</i>	-15 ... 14	-16 ... 21
Index range <i>k</i>	-8 ... 8	-10 ... 10
Index range <i>l</i>	-14 ... 15	-15 ... 18
Unique reflections	1105	2468
Reflections > $4\sigma(I)$	1118	2283
<i>R</i> (int)	0.0167	0.0162
<i>R</i> (σ)	0.0095	0.0110
Refined parameters	87	87
GoF	1.278	1.262
<i>R</i> 1, <i>I</i> > $4\sigma(I)$	0.0182	0.0207
<i>R</i> 1, all data	0.0186	0.0230
w <i>R</i> 2 on <i>F</i> ²	0.0563	0.0636
$\Delta\rho_{\max}$	0.46 e ⁻ ·Å ⁻³ , near O6	0.53 e ⁻ ·Å ⁻³ , near O3
$\Delta\rho_{\min}$	-0.39 e ⁻ ·Å ⁻³ , near Si1	-0.37 e ⁻ ·Å ⁻³ , near Si1

Table A2.15: Atomic positions and isotropic displacement parameters of grandidierite.

Site	T (K)	x	y	z	$U_{eq.}$ (\AA^2)
Al1	298	0.0	0.0	0.0	0.00552(12)
	873	0.0	0.0	0.0	0.01061(5)
Al2	298	0.0	0.0	0.5	0.00582(12)
	873	0.0	0.0	0.5	0.01194(6)
Al3	298	0.44790(4)	0.25	0.22632(4)	0.00531(12)
	873	0.44836(2)	0.25	0.22639(2)	0.01087(5)
Si1	298	0.26328(4)	0.25	0.43360(4)	0.00556(11)
	873	0.26376(2)	0.25	0.43284(2)	0.01029(5)
Mg1	298 ^a	0.21907(5)	0.25	0.09193(5)	0.00713(19)
	873 ^b	0.21984(3)	0.25	0.09065(3)	0.01554(10)
O1	298	0.28803(10)	0.25	0.27516(10)	0.0084(2)
	873	0.28891(6)	0.25	0.27480(6)	0.01763(12)
O2	298	0.52252(10)	0.25	0.38146(10)	0.0062(2)
	873	0.52276(6)	0.25	0.38136(6)	0.01139(9)
O3	298	0.00338(9)	0.25	-0.12097(11)	0.0072(2)
	873	0.00383(6)	0.25	-0.12137(7)	0.01455(11)
O4	298	0.11999(10)	0.25	0.47382(11)	0.0075(2)
	873	0.12076(5)	0.25	0.47120(8)	0.01589(11)
O5	298	0.10016(10)	-0.25	0.54648(10)	0.0061(2)
	873	0.09928(5)	-0.25	0.54548(6)	0.01147(9)
O6	298	0.32917(7)	0.02270(14)	0.49260(7)	0.00760(17)
	873	0.32896(4)	0.02350(8)	0.49222(5)	0.01606(9)
O7	298	0.50112(7)	-0.04508(15)	0.18058(8)	0.00808(16)
	873	0.49932(5)	-0.04632(9)	0.18077(5)	0.01725(9)
B1	298	-0.00037(13)	0.25	-0.25127(16)	0.0067(3)
	873	0.00112(8)	0.25	-0.25123(9)	0.01210(14)

^aoccupancy: 0.973(3) Mg, 0.030(3) Fe; ^boccupancy: 0.9651(19) Mg, 0.0349(19) Fe

Table A2.16: Anisotropic displacement parameters of grandidierite at 298K.

Site	U_{11} (\AA^2)	U_{22} (\AA^2)	U_{33} (\AA^2)	U_{23} (\AA^2)	U_{13} (\AA^2)	U_{12} (\AA^2)
Al1	0.0059(2)	0.0048(2)	0.0058(2)	-0.00025(14)	0.00015(13)	-0.00004(14)
Al2	0.0074(2)	0.0052(2)	0.0049(2)	0.00019(14)	-0.00001(13)	0.00055(14)
Al3	0.0060(2)	0.0052(2)	0.0047(2)	0.0	-0.00027(14)	0.0
Si1	0.00512(18)	0.00545(18)	0.00609(19)	0.0	0.00028(13)	0.0
Mg1 ^a	0.0068(3)	0.0065(3)	0.0082(3)	0.0	-0.00134(17)	0.0
O1	0.0069(5)	0.0121(5)	0.0064(5)	0.0	0.0008(4)	0.0
O2	0.0074(4)	0.0053(4)	0.0058(4)	0.0	-0.0004(4)	0.0
O3	0.0104(5)	0.0056(5)	0.0057(5)	0.0	-0.0001(3)	0.0
O4	0.0054(5)	0.0066(5)	0.0105(5)	0.0	0.0013(4)	0.0
O5	0.0064(4)	0.0056(4)	0.0064(4)	0.0	-0.0003(3)	0.0
O6	0.0064(4)	0.0065(3)	0.0099(4)	0.0018(3)	0.0000(2)	0.0004(3)
O7	0.0128(4)	0.0058(3)	0.0057(3)	0.0003(3)	0.0002(2)	0.0009(2)
B1	0.0063(7)	0.0068(7)	0.0069(7)	0.0	0.0002(5)	0.0

^aoccupancy: 0.973(3) Mg, 0.030(3)

Table A2.17: Anisotropic displacement parameters of grandierite at 873K.

Site	U_{11} (Å ²)	U_{22} (Å ²)	U_{33} (Å ²)	U_{23} (Å ²)	U_{13} (Å ²)	U_{12} (Å ²)
Al1	0.01149(10)	0.00909(11)	0.01127(12)	-0.00059(8)	0.00021(6)	-0.00010(6)
Al2	0.01653(11)	0.01002(12)	0.00926(11)	0.00067(8)	-0.00063(7)	0.00203(7)
Al3	0.01320(10)	0.01055(11)	0.00886(10)	0.0	-0.00076(7)	0.0
Si1	0.00890(8)	0.01062(10)	0.01134(10)	0.0	0.00026(6)	0.0
Mg1 ^a	0.01417(14)	0.01446(16)	0.01799(17)	0.0	-0.00357(9)	0.0
O1	0.0138(2)	0.0280(4)	0.0111(2)	0.0	0.00057(18)	0.0
O2	0.0143(2)	0.0105(2)	0.0094(2)	0.0	-0.00135(16)	0.0
O3	0.0241(3)	0.0114(3)	0.0082(2)	0.0	-0.00007(17)	0.0
O4	0.00985(19)	0.0145(3)	0.0233(3)	0.0	0.00305(18)	0.0
O5	0.01085(18)	0.0110(2)	0.0126(2)	0.0	-0.00069(15)	0.0
O6	0.01218(15)	0.01259(18)	0.0234(2)	0.00506(15)	-0.00041(13)	0.00099(12)
O7	0.0325(3)	0.00941(18)	0.00987(17)	0.00119(14)	0.00038(14)	0.00229(14)
B1	0.0180(3)	0.0096(3)	0.0087(3)	0.0	0.0003(2)	0.0

^aoccupancy: 0.9651(19) Mg, 0.0349(19) Fe

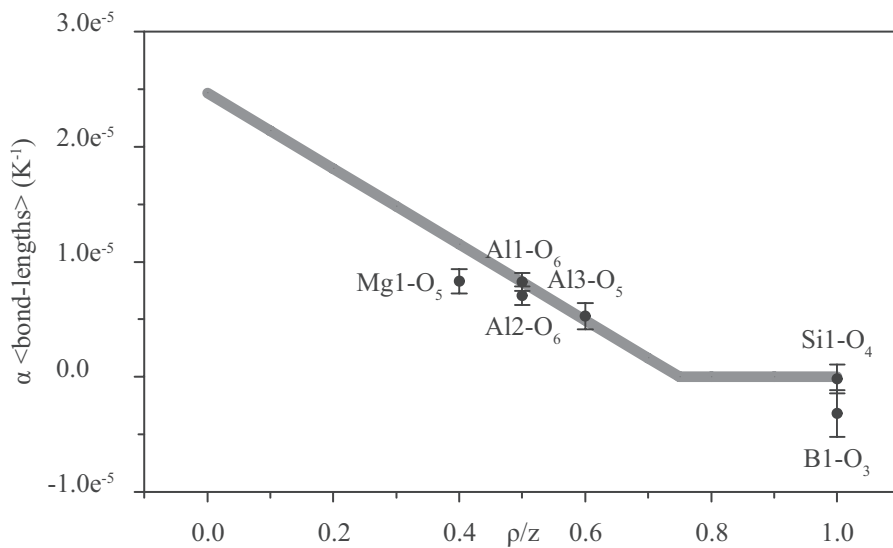


Figure A2.6: Expansion parameters α calculated from averaged polyhedral bond length of grandierite. Expected values according to Hazen and Prewitt (1977) plot on the gray line.

Table A2.18: Polyhedral bond lengths of grandidierite.

Center	Ligand	d _{298K} (Å)	d _{873K} (Å)	α (K ⁻¹)	esd α (K ⁻¹)
Al1	O2	1.9071(7)	1.9139(4)	6.201E-06	7.352E-07
	O2	1.9071(7)	1.9139(4)	6.201E-06	7.352E-07
	O3	1.9078(7)	1.9162(4)	7.657E-06	7.350E-07
	O3	1.9078(7)	1.9192(4)	7.657E-06	7.350E-07
	O6	1.8795(8)	1.8913(5)	1.092E-05	8.730E-07
	O6	1.8795(8)	1.8913(5)	1.092E-05	8.730E-07
	<Al1-O>	1.8981(7)	1.9076(4)	8.246E-06	7.804E-07
Al2	O4	1.9699(7)	1.9883(4)	1.624E-05	7.118E-07
	O4	1.9699(7)	1.9883(4)	1.624E-05	7.118E-07
	O5	1.8743(7)	1.8741(4)	-1.856E-07	7.481E-07
	O5	1.8743(7)	1.8741(4)	-1.856E-07	7.481E-07
	O7	1.8838(8)	1.8889(5)	4.708E-06	8.710E-07
	O7	1.8839(9)	1.8889(5)	4.616E-06	9.504E-07
	<Al2-O>	1.9094(8)	1.9171(4)	7.059E-06	7.890E-07
Al3	O1	1.8244(12)	1.8270(7)	2.478E-06	1.324E-06
	O2	1.7998(12)	1.8004(7)	5.798E-07	1.342E-06
	O5	1.9314(11)	1.9435(7)	1.090E-05	1.174E-06
	O7	1.8591(9)	1.8655(5)	5.987E-06	9.631E-07
	O7	1.8591(9)	1.8655(5)	5.987E-06	9.631E-07
		<Al3-O>	1.8548(11)	1.8604(6)	5.270E-06
Mg1	O1	2.0386(12) ^a	2.0512(7) ^b	1.075E-05	1.185E-06
	O2	2.1792(12) ^a	2.1908(7) ^b	9.257E-06	1.109E-06
	O5	2.0373(12) ^a	2.0472(7) ^b	8.451E-06	1.186E-06
	O6	1.9503(8) ^a	1.9575(5) ^b	6.420E-06	8.413E-07
	O6	1.9503(8) ^a	1.9575(5) ^b	6.420E-06	8.413E-07
		<Mg1-O>	2.0311(19) ^a	2.0407(6) ^b	8.305E-06
Si1	O1	1.6593(12)	1.6580(7)	-1.363E-06	1.456E-06
	O4	1.6255(12)	1.6250(6)	-5.350E-07	1.435E-06
	O6	1.6155(8)	1.6162(5)	7.536E-07	1.016E-06
	O6	1.6158(8)	1.6162(5)	4.305E-07	1.015E-06
		<Si1-O>	1.6290(10)	1.6289(6)	-1.868E-07
B1	O3	1.3469(19)	1.3436(11)	-4.261E-06	2.835E-06
	O7	1.3750(11)	1.3729(7)	-2.656E-06	1.649E-06
	O7	1.3750(11)	1.3729(7)	-2.656E-06	1.649E-06
		<B1-O>	1.3656(14)	1.3631(8)	-3.184E-06

^aoccupancy: 0.973(3) Mg, 0.030(3) Fe;^boccupancy: 0.9651(19) Mg, 0.0349(19) Fe

Table A2.19: M-O-M angles of the refined structure of grandidierite at 298K.

Sites	Angle (°)	Sites	Angle (°)
Al3-O1-Mg1	95.72(5)	Al2-O5-Al2	100.48(5)
Si1-O1-Al3	115.47(6)	Al2-O5-Al3(x2)	94.97(4)
Si1-O1-Mg1	148.81(7)	Al2-O5-Mg1(x4)	129.00(3)
Al1-O2-Al1	98.14(5)	Al3-O5-Mg1(x2)	92.51(5)
Al1-O2-Mg1(x4)	92.71(4)	Mg1-O5-Mg1	0.0
Al3-O2-Al1(x2)	120.87(4)	Al1-O6-Mg1(x2)	101.12(4)
Al3-O2-Mg1(x2)	124.32(6)	Mg1-O6-Mg1	0.00(3)
Mg1-O2-Mg1	0.00(3)	Si1-O6-Al1	121.18(5)
Al1-O3-Al1	98.10(5)	Si1-O6-Mg1(x2)	136.94(5)
B1-O3-Al1(x2)	130.86(3)	Al3-O7-Al2	97.10(4)
Al2-O4-Al2	94.01(5)	B1-O7-Al2	128.72(8)
Si1-O4-Al2(x2)	132.91(2)	B1-O7-Al3	130.82(8)

Table A2.20: M-O-M angles of the refined structure of grandidierite at 873K.

Sites	Angle (°)	Sites	Angle (°)
Al3-O1-Mg1	95.87(3)	Al2-O5-Al2	101.10(3)
Si1-O1-Al3	115.53(4)	Al2-O5-Al3(x2)	94.82(2)
Si1-O1-Mg1	148.60(4)	Al2-O5-Mg1(x4)	128.729(14)
Al1-O2-Al1	98.24(3)	Al3-O5-Mg1(x2)	92.48(3)
Al1-O2-Mg1(x4)	92.59(2)	Mg1-O5-Mg1	0.000(19)
Al3-O2-Al1(x2)	120.74(2)	Al1-O6-Mg1(x2)	101.15(2)
Al3-O2-Mg1(x2)	124.69(3)	Mg1-O6-Mg1	0.000(19)
Mg1-O2-Mg1	0.000(18)	Si1-O6-Al1	121.16(3)
Al1-O3-Al1	98.09(3)	Si1-O6-Mg1(x2)	137.02(3)
B1-O3-Al1(x2)	130.880(16)	Al3-O7-Al2	96.95(2)
Al2-O4-Al2	93.40(3)	B1-O7-Al2	128.98(5)
Si1-O4-Al2(x2)	133.279(13)	B1-O7-Al3	131.22(5)

Table A2.21: O-M-O angles of the refined structure of grandidierite at 298K.

Sites	Angle (°)	Sites	Angle (°)
O2-A11-O2	180.0	O1-Al3-O7(x2)	111.84(3)
O2-A11-O3(x2)	81.23(4)	O2-Al3-O1	100.99(5)
O2-A11-O3(x2)	98.77(4)	O2-Al3-O5	168.79(5)
O3-A11-O3	180.0	O2-Al3-O7(x2)	94.80(3)
O6-A11-O2(x2)	92.89(4)	O7-Al3-O5(x2)	80.86(3)
O6-A11-O2(x2)	87.11(4)	O7-Al3-O7	132.35(5)
O6-A11-O3(x2)	89.63(4)	O3-B1-O7(x2)	120.80(7)
O6-A11-O3(x2)	90.38(4)	O7-B1-O7	118.39(14)
O6-A11-O6	180.0	O1-Mg1-O2	104.51(5)
O4-A12-O4	180.00(5)	O5-Mg1-O1	81.55(5)
O5-A12-O4(x2)	101.89(4)	O5-Mg1-O2	173.94(5)
O5-A12-O4(x2)	78.11(4)	O6-Mg1-O1(x2)	126.11(3)
O5-A12-O5	180.00(1)	O6-Mg1-O2(x2)	78.31(3)
O5-A12-O7(x2)	98.28(4)	O6-Mg1-O5(x2)	98.21(3)
O5-A12-O7(x2)	81.72(4)	O6-Mg1-O6	107.39(5)
O7-A12-O4(x2)	87.74(4)	O4-Si1-O1	114.23(6)
O7-A12-O4(x2)	92.26(4)	O6-Si1-O1(x2)	107.40(4)
O7-A12-O7	180.00(5)	O6-Si1-O4(x2)	109.63(4)
O1-Al3-O5	90.22(5)	O6-Si1-O6	108.36(6)

Table A2.22: O-M-O angles of the refined structure of grandidierite at 873K.

Sites	Angle (°)	Sites	Angle (°)
O2-A11-O2	180.0	O1-Al3-O7(x2)	111.028(18)
O2-A11-O3(x2)	81.15(2)	O2-Al3-O1	101.18(3)
O2-A11-O3(x2)	98.85(2)	O2-Al3-O5	168.58(3)
O3-A11-O3	180.0	O2-Al3-O7(x2)	95.05(2)
O6-A11-O2(x2)	92.81(2)	O7-Al3-O5(x2)	80.663(19)
O6-A11-O2(x2)	87.19(2)	O7-Al3-O7	133.69(4)
O6-A11-O3(x2)	89.74(3)	O3-B1-O7(x2)	120.82(4)
O6-A11-O3(x2)	90.26(3)	O7-B1-O7	118.36(8)
O6-A11-O6	180.0	O1-Mg1-O2	104.18(3)
O4-A12-O4	180.0	O5-Mg1-O1	81.41(3)
O5-A12-O4(x2)	102.06(2)	O5-Mg1-O2	174.40(3)
O5-A12-O4(x2)	77.94(2)	O6-Mg1-O1(x2)	125.795(17)
O5-A12-O5	180.0	O6-Mg1-O2(x2)	78.257(19)
O5-A12-O7(x2)	98.12(2)	O6-Mg1-O5(x2)	98.55(2)
O5-A12-O7(x2)	81.88(2)	O6-Mg1-O6	107.95(3)
O7-A12-O4(x2)	87.57(3)	O4-Si1-O1	113.75(4)
O7-A12-O4(x2)	92.43(3)	O6-Si1-O1(x2)	107.48(2)
O7-A12-O7	180.0	O6-Si1-O4(x2)	109.77(2)
O1-Al3-O5	90.24(3)	O6-Si1-O6	108.43(4)

Table A2.23: Temperature dependent lattice parameters from single-crystal unit cell refinements of grandidierite.

T (K)	a -axis (Å)	b -axis (Å)	c -axis (Å)	Volume (Å ³)
298	10.9753(6)	5.7650(4)	10.3327(6)	653.78(5)
323	10.9772(6)	5.7659(3)	10.3333(6)	654.03(5)
373	10.9820(6)	5.7680(4)	10.3334(6)	654.57(5)
423	10.9854(6)	5.7697(3)	10.3341(6)	655.00(5)
473	10.9892(6)	5.7717(3)	10.3348(5)	655.50(5)
523	10.9942(7)	5.7735(4)	10.3370(6)	656.14(5)
573	10.9998(6)	5.7760(3)	10.3375(6)	656.79(5)
623	11.0029(6)	5.7780(3)	10.3387(6)	657.28(5)
673	11.0072(6)	5.7805(3)	10.3405(5)	657.94(5)
723	11.0128(7)	5.7834(4)	10.3424(6)	658.72(6)
773	11.0163(7)	5.7863(4)	10.3437(6)	659.34(6)
823	11.0225(6)	5.7874(3)	10.3455(6)	659.96(6)
873	11.0283(6)	5.7901(4)	10.3467(6)	660.69(6)
923	11.0329(7)	5.7941(4)	10.3488(6)	661.55(6)
973	11.0386(7)	5.7958(4)	10.3493(6)	662.12(6)

Table A2.24: Temperature dependent thermal expansion parameters α of grandidierite. AF is the anisotropy factor.

T (K)	$\alpha_{a\text{-axis}}$ (K ⁻¹)	$\alpha_{b\text{-axis}}$ (K ⁻¹)	$\alpha_{c\text{-axis}}$ (K ⁻¹)	α_{Volume} (K ⁻¹)	AF
298	1.40815E-06	1.33177E-05	3.46936E-06	1.46746E-05	23.82
323	1.48210E-06	1.35266E-05	3.54291E-06	1.49979E-05	24.09
373	1.62989E-06	1.39442E-05	3.68996E-06	1.56432E-05	24.63
423	1.77756E-06	1.43612E-05	3.83696E-06	1.62870E-05	25.17
473	1.92510E-06	1.47778E-05	3.98389E-06	1.69293E-05	25.71
523	2.07251E-06	1.51939E-05	4.13077E-06	1.75699E-05	26.24
573	2.21977E-06	1.56094E-05	4.27759E-06	1.82088E-05	26.78
623	2.36689E-06	1.60245E-05	4.42433E-06	1.88459E-05	27.32
673	2.51385E-06	1.64390E-05	4.57100E-06	1.94812E-05	27.85
723	2.66067E-06	1.68530E-05	4.71760E-06	2.01147E-05	28.38
773	2.80732E-06	1.72664E-05	4.86412E-06	2.07462E-05	28.92
823	2.95381E-06	1.76792E-05	5.01055E-06	2.13757E-05	29.45
873	3.10013E-06	1.80914E-05	5.15691E-06	2.20032E-05	29.98
923	3.24628E-06	1.85029E-05	5.30317E-06	2.26287E-05	30.51
973	3.39225E-06	1.89139E-05	5.44934E-06	2.32519E-05	31.04

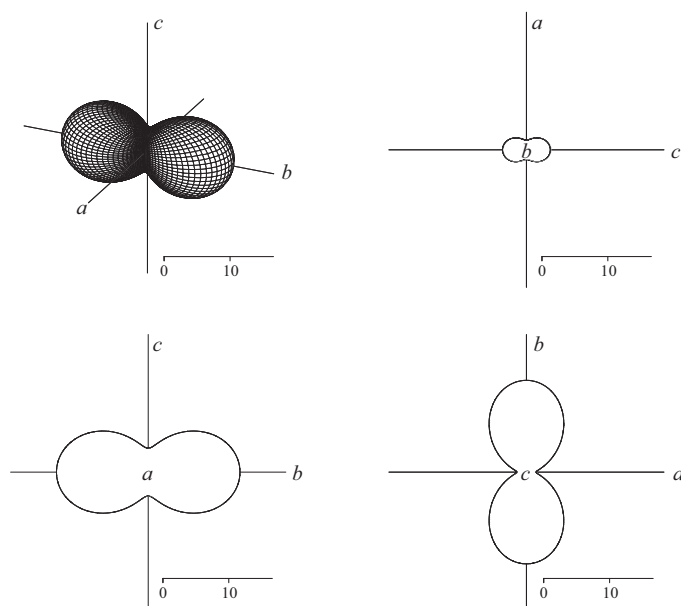


Figure A2.7: Representation surface of thermal expansion tensor components of grandierite at 298K. Top left: Arbitrary view, top right: Cross-section in (010), bottom left: Cross-section in (100) and bottom right: Cross section in (001). a , b and c are directions parallel to unit cell axes, scale bar unit is $10^{-6} \cdot \text{K}^{-1}$.

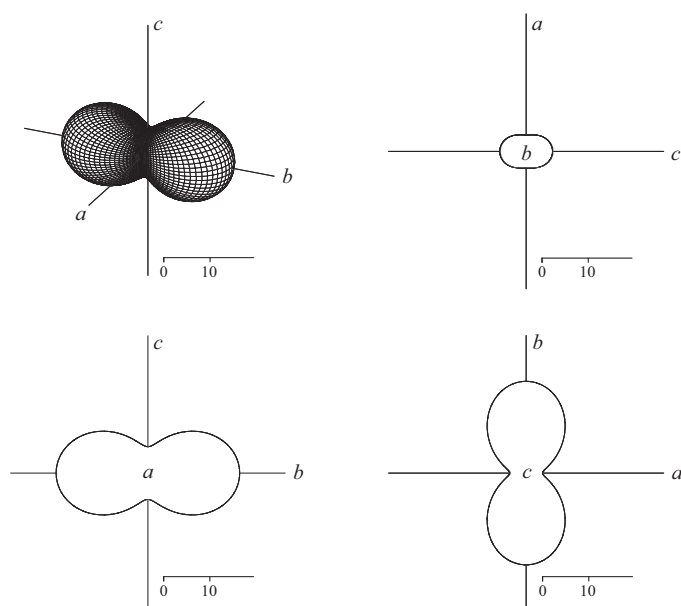


Figure A2.8: Representation surface of thermal expansion tensor components of grandierite at 973K. Top left: Arbitrary view, top right: Cross-section in (010), bottom left: Cross-section in (100) and bottom right: Cross section in (001). a , b and c are directions parallel to unit cell axes, scale bar unit is $10^{-6} \cdot \text{K}^{-1}$.

Plots were made with WinTensor v. 1.2 by Werner Kaminsky, Dept. of Chemistry, University of Washington.

Supplementary data for jeremejevite

Table A2.25: Details for single-crystal X-ray diffraction data collection and crystal structure refinement of jeremejevite.

Diffractometer: Bruker Smart APEX 2, MoK α (0.71073 Å), 50 kV, 40 mA		
Crystal size	0.14 · 0.14 · 0.07 mm ³	
Detector distance	49.5 mm	
Rotation axis	ϕ, ω	
Collection mode	Automated hemisphere	
Frame size	512 · 512 pixel	
Absorption corr.	Empirical ψ correction	
Resolution	No restriction	
Sample name	Jeremejevite	
Temperature	298K	873K
Space group	$P6_3/m$	$P6_3/m$
<i>a</i> -axis	8.5526(3) Å	8.5840(16) Å
<i>c</i> -axis	8.1793(4) Å	8.2187(15) Å
<i>Volume</i>	518.13(4) Å ³	524.46(17) Å ³
<i>Z</i>	2	2
Density ρ	3.288 g/cm ³	3.288 g/cm ³
Absorption coeff. μ	0.79 mm ⁻¹	0.78 mm ⁻¹
Time per frame	40 s	40 s
Reflections collected	5498	4806
Reflections rejected	7	2284
Reflections used	5491	2522
Max. 2θ	69.21°	60.86°
Index range <i>h</i>	-12 ... 11	-16 ... 21
Index range <i>k</i>	-11 ... 13	-11 ... 11
Index range <i>l</i>	-12 ... 8	-11 ... 11
Unique reflections	781	555
Reflections $> 4\sigma(I)$	673	465
<i>R</i> (int)	0.0324	0.0270
<i>R</i> (σ)	0.0222	0.0251
Refined parameters	50	50
GoF	1.064	1.236
<i>R</i> 1, <i>I</i> $> 4\sigma(I)$	0.0258	0.0308
<i>R</i> 1, all data	0.0326	0.0434
w <i>R</i> 2 on <i>F</i> ²	0.0627	0.1145
$\Delta\rho_{\max}$	0.49 e ⁻ ·Å ⁻³ , near O1	0.69 e ⁻ ·Å ⁻³ , near O3
$\Delta\rho_{\min}$	-0.40 e ⁻ ·Å ⁻³ , near Al1	-0.73 e ⁻ ·Å ⁻³ , near O1

Table A2.26: Atomic positions and isotropic displacement parameters of jeremejevite.

Site	T (K)	x	y	z	$U_{eq.}$ (\AA^2)
Al1	298	0.33719(4)	0.35252(4)	0.57536(4)	0.00522(11)
	873	0.33696(10)	0.35223(11)	0.57509(9)	0.0120(3)
F1	298	0.38689(11)	0.49995(11)	0.75	0.00745(18)
	873	0.3868(3)	0.4994(3)	0.75	0.0178(5)
B1	298	0.2335(2)	0.0023(2)	0.75	0.0060(3)
	873	0.2320(6)	0.0031(6)	0.75	0.0121(7)
B2	298	0.6667	0.3333	0.5545(2)	0.0058(3)
	873	0.6667	0.3333	0.5539(6)	0.0120(9)
O1	298	0.30281(13)	0.18634(13)	0.75	0.0063(2)
	873	0.3020(4)	0.1854(4)	0.75	0.0136(5)
O2	298	0.58909(10)	0.43927(10)	0.55453(9)	0.00632(16)
	873	0.5890(3)	0.4383(3)	0.5538(2)	0.0141(4)
O3	298	0.08819(9)	0.28503(10)	0.60141(9)	0.00630(16)
	873	0.0874(3)	0.2845(3)	0.6018(2)	0.0138(4)

Table A2.27: Anisotropic displacement parameters of jeremejevite at 298K.

Site	U_{11} (\AA^2)	U_{22} (\AA^2)	U_{33} (\AA^2)	U_{23} (\AA^2)	U_{13} (\AA^2)	U_{12} (\AA^2)
Al1	0.00537(15)	0.00532(15)	0.00505(17)	-0.00002(10)	0.00006(10)	0.00273(11)
F1	0.0096(4)	0.0066(4)	0.0054(4)	0.0	0.0	0.0035(3)
B1	0.0054(6)	0.0061(6)	0.0065(6)	0.0	0.0	0.0029(5)
B2	0.0063(4)	0.0063(4)	0.0048(8)	0.0	0.0	0.0031(2)
O1	0.0077(4)	0.0057(4)	0.0059(4)	0.0	0.0	0.0037(3)
O2	0.0058(3)	0.0057(3)	0.0074(3)	0.0006(2)	0.0004(3)	0.0029(2)
O3	0.0057(3)	0.0084(3)	0.0051(3)	0.0006(2)	0.0006(2)	0.0038(3)

Table A2.28: Anisotropic displacement parameters of jeremejevite at 873K.

Site	U_{11} (\AA^2)	U_{22} (\AA^2)	U_{33} (\AA^2)	U_{23} (\AA^2)	U_{13} (\AA^2)	U_{12} (\AA^2)
Al1	0.0124(4)	0.0128(4)	0.0110(4)	0.0003(3)	0.0004(3)	0.0065(3)
F1	0.0241(13)	0.0157(11)	0.0132(10)	0.0	0.0	0.0097(10)
B1	0.0133(18)	0.0130(18)	0.0106(15)	0.0	0.0	0.0071(15)
B2	0.0118(13)	0.0118(13)	0.0124(19)	0.0	0.0	0.0059(7)
O1	0.0185(14)	0.0113(12)	0.0131(11)	0.0	0.0	0.0089(11)
O2	0.0134(9)	0.0132(9)	0.0171(8)	0.0023(7)	0.0010(7)	0.0076(7)
O3	0.0121(9)	0.0185(10)	0.0106(7)	0.0017(7)	0.0014(6)	0.0076(8)

Table A2.29: Polyhedral bond lengths of jeremejevite.

Center	Ligand	d_{298K} (Å)	d_{873K} (Å)	α (K ⁻¹)	esd α (K ⁻¹)
A11	O1	1.9310(7)	1.9438(20)	1.153E-05	1.908E-06
	O2	1.8907(8)	1.9021(20)	8.955E-06	2.053E-06
	O2	1.9033(8)	1.9131(21)	1.049E-05	1.981E-06
	O3	1.9196(8)	1.9312(21)	1.051E-05	2.036E-06
	O3-6	1.8623(8)	1.8683(20)	5.603E-06	2.012E-06
	F1	1.8097(6)	1.8182(20)	8.169E-06	1.849E-06
	<A11-O>	1.8861(8)	1.8961(16)	9.236E-06	1.972E-06
B1	O1	1.3767(18)	1.3673(48)	-1.187E-05	6.476E-06
	O3	1.3899(10)	1.3940(26)	5.130E-06	3.486E-06
	O3	1.3899(10)	1.3940(26)	5.130E-06	3.486E-06
	<B1-O>	1.3855(13)	1.3851(40)	-5.021E-07	4.476E-06
B2	O2	1.3646(7)	1.3622(19)	-2.931E-06	2.581E-06
	O2	1.3646(7)	1.3623(19)	-2.931E-06	2.581E-06
	O2	1.3646(7)	1.3623(19)	-2.931E-06	2.581E-06
	<B2-O>	1.3646(7)	1.3623(19)	-2.931E-06	2.581E-06

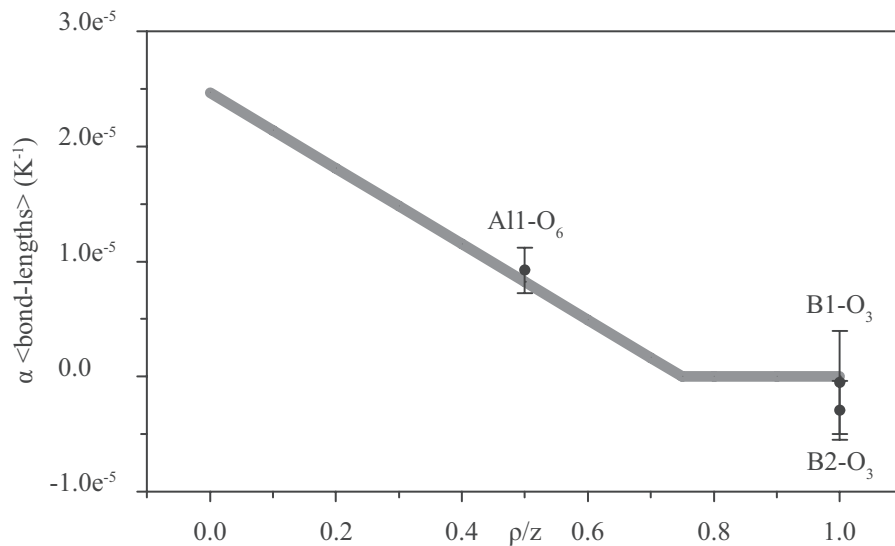


Figure A2.9: Expansion parameters α calculated from averaged polyhedral bond length of jeremejevite. Expected values according to Hazen and Prewitt (1977) plot on the gray line.

Table A2.30: M-O-M angles of the refined structure of jeremejevite at 298K.

Sites	Angle (°)	Sites	Angle (°)
Al1-F1-Al1	104.24(5)	B2-O2-Al1	124.93(5)
Al1-O1-Al1	95.41(5)	Al1-O3-Al1	115.51(4)
B1-O1-Al1 (x2)	131.41(3)	B1-O3-Al1	120.38(7)
Al1-O2-Al1	101.35(3)	B1-O3-Al1	123.16(7)
B2-O2-Al1	125.55(8)		

Table A2.31: M-O-M angles of the refined structure of jeremejevite at 873K.

Sites	Angle (°)	Sites	Angle (°)
A11-F1-A11	104.49(13)	B2-O2-A11	125.27(13)
A11-O1-A11	95.39(12)	A11-O3-A11	115.14(9)
B1-O1-A11 (x2)	131.37(8)	B1-O3-A11	120.9(2)
A11-O2-A11	101.21(9)	B1-O3-A11	123.14(19)
B2-O2-A11	125.65(19)		

Table A2.32: O-M-O angles of the refined structure of jeremejevite at 298K.

Sites	Angle (°)	Sites	Angle (°)
F1-A11-O1	79.94(3)	O2-A11-O3	175.23(4)
F1-A11-O2	86.32(3)	O3-A11-O1	98.87(3)
F1-A11-O2	88.47(4)	O3-A11-O1	87.64(4)
F1-A11-O3	178.81(4)	O3-A11-O2	94.87(3)
F1-A11-O3	87.74(4)	O3-A11-O2	91.66(3)
O2-A11-O1	164.85(4)	O3-A11-O3	92.18(4)
O2-A11-O1	94.55(4)	O1-B1-O3 (x2)	119.01(6)
O2-A11-O2	78.65(4)	O3-B1-O3	121.95(12)
O2-A11-O3	98.22(3)	O2-B2-O2 (x3)	120.0

Table A2.33: O-M-O angles of the refined structure of jeremejevite at 873K.

Sites	Angle (°)	Sites	Angle (°)
F1-A11-O1	79.83(9)	O2-A11-O3	175.42(10)
F1-A11-O2	86.10(9)	O3-A11-O1	99.03(9)
F1-A11-O2	88.64(10)	O3-A11-O1	87.40(10)
F1-A11-O3	178.86(10)	O3-A11-O2	95.03(9)
F1-A11-O3	87.66(10)	O3-A11-O2	91.55(9)
O2-A11-O1	164.63(10)	O3-A11-O3	92.21(11)
O2-A11-O1	94.60(10)	O1-B1-O3 (x2)	119.13(17)
O2-A11-O2	78.79(9)	O3-B1-O3	121.7(3)
O2-A11-O3	98.27(9)	O2-B2-O2 (x3)	120.002(1)

Table A2.34: Temperature dependent lattice parameters and agreement factors from powder XRD refinements of jeremejevite.

T (K)	a -axis (Å)	c -axis (Å)	Volume (Å ³)	R_{wp}	GoF
298	8.55670(4)	8.18027(7)	518.694(6)	13.13	1.16
323	8.55835(4)	8.18181(7)	518.991(6)	12.93	1.13
373	8.56164(4)	8.18489(6)	519.587(6)	13.05	1.14
423	8.56494(4)	8.18797(6)	520.183(6)	13.23	1.15
473	8.56825(3)	8.19105(6)	520.780(5)	13.03	1.13
523	8.57156(3)	8.19412(5)	521.377(5)	13.31	1.15
573	8.57487(3)	8.19719(5)	521.976(5)	13.36	1.15
623	8.57819(3)	8.20025(5)	522.576(5)	13.30	1.14
673	8.58152(3)	8.20331(5)	523.177(5)	13.46	1.15
723	8.58485(3)	8.20637(5)	523.778(5)	13.40	1.15
773	8.58819(3)	8.20943(5)	524.381(5)	13.27	1.13
823	8.59153(4)	8.21248(5)	524.984(5)	13.16	1.12
873	8.59488(4)	8.21553(6)	525.589(6)	13.35	1.14
923	8.59823(4)	8.21858(7)	526.194(6)	13.29	1.13
973	8.60159(5)	8.22162(8)	526.800(7)	13.38	1.14
1023	8.60495(5)	8.22467(9)	527.407(8)	13.74	1.17
1073	8.60832(6)	8.22770(10)	528.015(9)	13.55	1.15

Table A2.35: Temperature dependent thermal expansion parameters α of jeremejevite. AF is the anisotropy factor.

T (K)	$\alpha_{a\text{-axis}}$ (K ⁻¹)	$\alpha_{c\text{-axis}}$ (K ⁻¹)	α_{Volume} (K ⁻¹)	AF
298	7.68811E-06	7.54012E-06	2.29131E-05	0.30
323	7.69281E-06	7.53492E-06	2.29177E-05	0.32
373	7.70220E-06	7.52454E-06	2.29267E-05	0.36
423	7.71158E-06	7.51418E-06	2.29357E-05	0.39
473	7.72095E-06	7.50382E-06	2.29447E-05	0.43
523	7.73030E-06	7.49347E-06	2.29535E-05	0.47
573	7.73965E-06	7.48313E-06	2.29623E-05	0.51
623	7.74898E-06	7.47281E-06	2.29711E-05	0.55
673	7.75830E-06	7.46249E-06	2.29798E-05	0.59
723	7.76761E-06	7.45219E-06	2.29884E-05	0.63
773	7.77690E-06	7.44189E-06	2.29970E-05	0.67
823	7.78619E-06	7.43161E-06	2.30055E-05	0.71
873	7.79546E-06	7.42134E-06	2.30139E-05	0.75
923	7.80472E-06	7.41107E-06	2.30223E-05	0.79
973	7.81397E-06	7.40082E-06	2.30306E-05	0.83
1023	7.82321E-06	7.39058E-06	2.30389E-05	0.87
1073	7.83243E-06	7.38034E-06	2.30471E-05	0.90

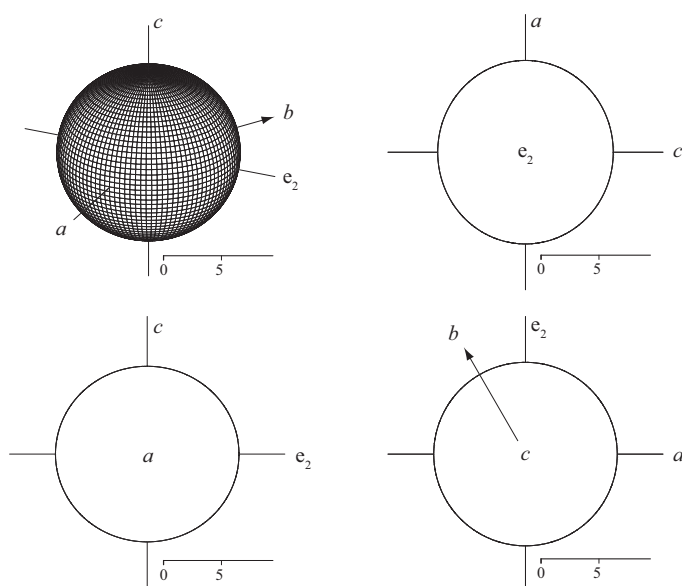


Figure A2.10: Representation surface of thermal expansion tensor components of jeremejevite at 298K. Eigenvector e_1 is parallel a , e_3 is parallel c , the angle between the a -axis and the b -axis is 120° . Top left: Arbitrary view, top right: Cross-section of the a - c -plane, bottom left: Cross-section of the e_2 - c -plane and bottom right: Cross section of the e_2 - a -plane. a , b and c are directions parallel to unit cell axes, scale bar unit is $10^{-6} \cdot \text{K}^{-1}$.

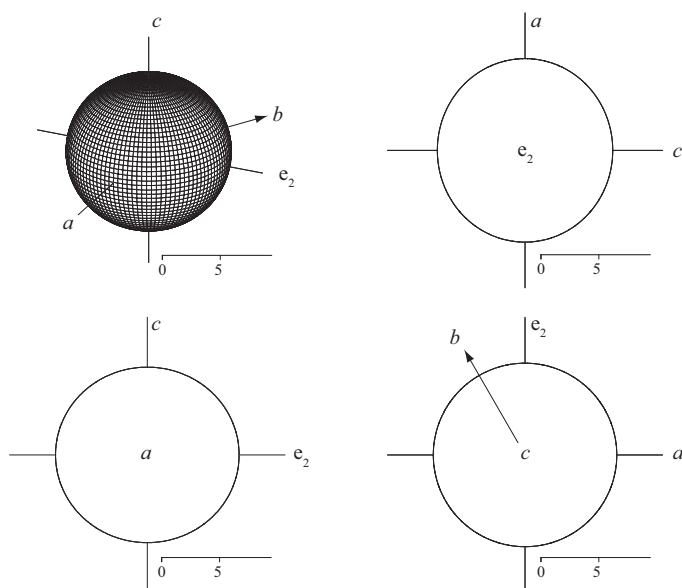


Figure A2.11: Representation surface of thermal expansion tensor components of jeremejevite at 1073K. Eigenvector e_1 is parallel a , e_3 is parallel c , the angle between the a -axis and the b -axis is 120° . Top left: Arbitrary view, top right: Cross-section of the a - c -plane, bottom left: Cross-section of the e_2 - c -plane and bottom right: Cross section of the e_2 - a -plane. a , b and c are directions parallel to unit cell axes, scale bar unit is $10^{-6} \cdot \text{K}^{-1}$.

A.3 Supplementary Data for Chapter 7

Table A3.1: Bond distances at $P0$ (0.001 GPa), crystal in air.

Center	Ligand	Distance (Å)	Center	Ligand	Distance (Å)
A11	O1	1.910(3)	A12	O1	1.801(4)
A11	O2	1.902(3)	A12	O2 (x2)	1.753(2)
A11	O3	1.846(2)	A12	O5	1.851(4)
A11	O4	1.910(2)	A12	O6	2.171(4)
A11	O6	1.887(2)		<A12-O>	1.866(3)
A11	O7	1.962(3)			
	<A11-O>	1.903(3)	A13	O1	2.267(4)
			A13	O3	1.752(4)
A14	O2 (x2)	1.736(3)	A13	O5	1.770(4)
A14	O5	1.777(4)	A13	O7 (x2)	1.825(3)
A14	O6	1.762(3)		<A13-O>	1.888(4)
	<A14-O>	1.753(3)			
B1	O4	1.372(7)			
B1	O7 (x2)	1.382(4)			
	<A15-O>	1.379(5)			

Table A3.2: Bond distances at $P0$ (0.001 GPa), crystal in DAC.

Center	Ligand	Distance (Å)	Center	Ligand	Distance (Å)
A11	O1	1.937(13)	A12	O1	1.734(18)
A11	O2	1.912(15)	A12	O2 (x2)	1.778(14)
A11	O3	1.841(15)	A12	O5	1.76(3)
A11	O4	1.928(14)	A12	O6	2.194(15)
A11	O6	1.889(17)		<A12-O>	1.849(18)
A11	O7	1.909(12)			
	<A11-O>	1.903(14)	A13	O1	2.24(2)
			A13	O3	1.74(2)
A14	O2 (x2)	1.738(6)	A13	O5	1.82(3)
A14	O5	1.753(16)	A13	O7 (x2)	1.824(5)
A14	O6	1.77(3)		<A13-O>	1.890(14)
	<A14-O>	1.750(15)			
B1	O4	1.38(3)			
B1	O7 (x2)	1.393(13)			
	<B1-O>	1.389(19)			

Table A3.3: Bond distances at *P1* (0.15(5) GPa).

Center	Ligand	Distance (Å)	Center	Ligand	Distance (Å)
A11	O1	1.929(10)	A12	O1	1.763(14)
A11	O2	1.875(11)	A12	O2 (x2)	1.769(11)
A11	O3	1.846(11)	A12	O5	1.815(19)
A11	O4	1.918(11)	A12	O6	2.180(13)
A11	O6	1.886(13)		<A12-O>	1.860(14)
A11	O7	1.951(10)			
	<A11-O>	1.900(11)	A13	O1	2.303(17)
			A13	O3	1.730(18)
A14	O2 (x2)	1.735(6)	A13	O5	1.841(19)
A14	O5	1.740(12)	A13	O7 (x2)	1.834(5)
A14	O6	1.76(2)		<A13-O>	1.908(14)
	<A14-O>	1.743(11)			
B1	O4	1.38(2)			
B1	O7 (x2)	1.384(11)			
	<B1-O>	1.383(14)			

Table A3.4: Bond distances at *P2* (0.91(4) GPa).

Center	Ligand	Distance (Å)	Center	Ligand	Distance (Å)
A11	O1	1.920(9)	A12	O1	1.745(13)
A11	O2	1.927(9)	A12	O2 (x2)	1.740(8)
A11	O3	1.86(1)		Al2O5	1.823(15)
A11	O4	1.911(9)	A12	O6	2.167(11)
A11	O6	1.897(10)		<A12-O>	1.843(11)
A11	O7	1.922(9)			
	<A11-O>	1.906(9)	A13	O1	2.302(15)
			A13	O3	1.706(16)
A14	O2 (x2)	1.727(6)	A13	O5	1.788(16)
A14	O5	1.791(12)	A13	O7 (x2)	1.835(5)
A14	O6	1.712(16)		<A13-O>	1.893(11)
	<A14-O>	1.739(10)			
B1	O4	1.39(2)			
B1	O7 (x2)	1.379(10)			
	<B1-O>	1.383(14)			

Table A3.5: Bond distances at *P*3 (1.99(6) GPa).

Center	Ligand	Distance (Å)	Center	Ligand	Distance (Å)
A11	O1	1.921(9)	A12	O1	1.756(12)
A11	O2	1.90(1)	A12	O2 (x2)	1.754(8)
A11	O3	1.858(9)	A12	O5	1.807(14)
A11	O4	1.900(9)	A12	O6	2.185(11)
A11	O6	1.873(10)		<A12-O>	1.851(11)
A11	O7	1.942(10)			
	<A11-O>	1.899(10)	A13	O1	2.244(14)
			A13	O3	1.698(14)
A14	O2 (x2)	1.728(6)	A13	O5	1.797(15)
A14	O5	1.753(11)	A13	O7 (x2)	1.813(6)
A14	O6	1.775(16)		<A13-O>	1.873(11)
	<A14-O>	1.746(10)			
B1	O4	1.38(2)			
B1	O7 (x2)	1.383(10)			
	<B1-O>	1.38(17)			

Table A3.6: Bond distances at *P*4 (3.32(6) GPa).

Center	Ligand	Distance (Å)	Center	Ligand	Distance (Å)
A11	O1	1.914(9)	A12	O1	1.735(14)
A11	O2	1.880(9)	A12	O2 (x2)	1.767(9)
A11	O3	1.849(10)	A12	O5	1.838(15)
A11	O4	1.894(9)	A12	O6	2.204(13)
A11	O6	1.867(11)		<A12-O>	1.862(12)
A11	O7	1.936(9)			
	<A11-O>	1.890(10)	A13	O1	2.249(15)
			A13	O3	1.720(15)
A14	O2 (x2)	1.715(7)	A13	O5	1.803(15)
A14	O5	1.746(12)	A13	O7 (x2)	1.816(6)
A14	O6	1.744(17)		<A13-O>	1.881(12)
	<A14-O>	1.730(11)			
B1	O4	1.38(2)			
B1	O7 (x2)	1.387(11)			
	<B1-O>	1.38(14)			

Table A3.7: Bond distances at *P*5 (4.78(6) GPa).

Center	Ligand	Distance (Å)	Center	Ligand	Distance (Å)
A11	O1	1.888(9)	A12	O1	1.778(14)
A11	O2	1.863(10)	A12	O2 (x2)	1.733(8)
A11	O3	1.845(10)	A12	O5	1.862(16)
A11	O4	1.912(10)	A12	O6	2.159(13)
A11	O6	1.860(11)		<A12-O>	1.853(12)
A11	O7	1.941(10)			
	<A11-O>	1.885(10)	A13	O1	2.241(15)
			A13	O3	1.712(15)
A14	O2 (x2)	1.733(7)	A13	O5	1.779(16)
A14	O5	1.737(13)	A13	O7 (x2)	1.801(6)
A14	O6	1.749(17)		<A13-O>	1.867(12)
	<A14-O>	1.738(11)			
B1	O4	1.37(2)			
B1	O7 (x2)	1.372(11)			
	<B1-O>	1.37(12)			

Table A3.8: Bond distances at *P*6 (5.83(5) GPa).

Center	Ligand	Distance (Å)	Center	Ligand	Distance (Å)
A11	O1	1.888(9)	A12	O1	1.778(14)
A11	O2	1.857(10)	A12	O2 (x2)	1.730(9)
A11	O3	1.853(10)	A12	O5	1.840(17)
A11	O4	1.896(9)	A12	O6	2.164(13)
A11	O6	1.858(11)		<A12-O>	1.848(12)
A11	O7	1.935(10)			
	A11-O>	1.881(10)	A13	O1	2.188(15)
			A13	O3	1.696(15)
A14	O2 (x2)	1.732(7)	A13	O5	1.743(17)
A14	O5	1.773(13)	A13	O7 (x2)	1.801(7)
A14	O6	1.753(17)		<A13-O>	1.846(12)
	<A14-O>	1.748(11)			
B1	O4	1.36(2)			
B1	O7 (x2)	1.379(11)			
	<B1-O>	1.373(14)			

Table A3.9: Bond distances at *P7* (5.99(5) GPa).

Center	Ligand	Distance (Å)	Center	Ligand	Distance (Å)
A11	O1	1.910(11)	A12	O1	1.728(16)
A11	O2	1.866(11)	A12	O2 (x2)	1.757(10)
A11	O3	1.842(12)	A12	O5	1.834(18)
A11	O4	1.894(11)	A12	O6	2.178(14)
A11	O6	1.867(12)		<A12-O>	1.851(14)
A11	O7	1.917(11)			
	<A11-O>	1.883(11)	A13	O1	2.263(18)
			A13	O3	1.705(18)
A14	O2 (x2)	1.707(8)	A13	O5	1.826(18)
A14	O5	1.717(14)	A13	O7 (x2)	1.808(7)
A14	O6	1.743(19)		<A13-O>	1.882(14)
	<A14-O>	1.719(12)			
B1	O4	1.38(3)			
B1	O7 (x2)	1.379(12)			
	<B1-O>	1.379(18)			

Table A3.10: Bond distances at *P8* (6.45(6) GPa).

Center	Ligand	Distance (Å)	Center	Ligand	Distance (Å)
A11	O1	1.945(12)	A12	O1	1.699(17)
A11	O2	1.871(12)	A12	O2 (x2)	1.743(11)
A11	O3	1.829(13)	A12	O5	1.84(2)
A11	O4	1.855(12)	A12	O6	2.160(15)
A11	O6	1.896(14)		<A12-O>	1.837(15)
A11	O7	1.904(12)			
	<A11-O>	1.883(13)	A13	O1	2.263(19)
			A13	O3	1.703(19)
A14	O2 (x2)	1.722(8)	A13	O5	1.79(2)
A14	O5	1.740(16)	A13	O7 (x2)	1.804(7)
A14	O6	1.70(2)		<A13-O>	1.873(15)
	<A14-O>	1.721(13)			
B1	O4	1.38(3)			
B1	O7 (x2)	1.395(13)			
	<B1-O>	1.390(19)			

Table A3.11: M-O-M angles at $P0$ (0.001 GPa), crystal in air.

Sites	Angle ($^{\circ}$)	Sites	Angle ($^{\circ}$)
A11-O1-A11	95.05(5)	A13-O5-A12	103.13(16)
A11-O1-A13 (x2)	90.16(3)	A13-O5-A14	156.69(23)
A12-O1-A11 (x2)	132.44(4)	A14-O5-A12	100.18(20)
A12-O1-A13	87.69(13)	A11-O6-A12 (x2)	91.12(4)
A12-O2-A11	105.17(12)	A11-O6-A11	98.56(5)
A14-O2-A11	123.75(13)	A14-O6-A11 (x2)	130.71(3)
A14-O2-A12	129.56(14)	A14-O6-A12	89.45(17)
A11-O3-A11	99.49(5)	A13-O7-A11	103.15(12)
A13-O3-A11 (x2)	130.23(3)	B1-O7-A11	125.85(16)
A11-O4-A11	97.01(5)	B1-O7-A13	130.26(19)
B1-O4-A11 (x2)	130.27(3)		

Table A3.12: O-M-O angles at $P0$ (0.001 GPa), crystal in air.

Sites	Angle ($^{\circ}$)	Sites	Angle ($^{\circ}$)
O1-A11-O4	169.00(7)	O2-A12-O5 (x2)	118.53(7)
O1-A11-O7	82.78(10)	O2-A12-O6 (x2)	79.10(8)
O2-A11-O1	99.34(10)	O2-A12-O2	111.86(10)
O2-A11-O4	91.66(9)	O5-A12-O6	78.21(16)
O2-A11-O7	172.76(12)	O3-A13-O1	169.21(16)
O3-A11-O1	80.73(4)	O3-A13-O5	111.98(16)
O3-A11-O2	94.85(9)	O3-A13-O7 (x2)	99.07(8)
O3-A11-O4	98.41(5)	O5-A13-O1	78.81(14)
O3-A11-O6	178.21(7)	O5-A13-O7 (x2)	108.64(8)
O3-A11-O7	92.33(10)	O7-A13-O1 (x2)	76.63(7)
O4-A11-O7	86.31(10)	O7-A13-O7	128.09(13)
O6-A11-O1	99.31(5)	O2-A14-O5 (x2)	118.00(8)
O6-A11-O2	83.37(9)	O2-A14-O6 (x2)	110.98(8)
O6-A11-O4	81.90(4)	O2-A14-O2	106.04(11)
O6-A11-O7	89.45(9)	O6-A14-O5	92.17(17)
O1-A12-O5	90.37(16)	O4-B1-O7 (x2)	119.89(10)
O1-A12-O6	168.58(17)	O7-B1-O7	120.22(17)
O2-A12-O1 (x2)	106.84(8)		

Table A3.13: M-O-M angles at *P*0 (0.001 GPa), crystal in DAC.

Sites	Angle (°)	Sites	Angle (°)
A11-O1-A11	93.65(11)	A12-O5-A13	102.18(153)
A11-O1-A13 (x2)	90.21(14)	A14-O5-A12	104.45(42)
A12-O1-A11 (x2)	133.15(10)	A14-O5-A13	153.37(59)
A12-O1-A13	87.91(101)	A11-O6-A11	98.19(11)
A12-O2-A11	106.61(33)	A11-O6-A12 (x2)	92.59(11)
A14-O2-A11	123.53(31)	A14-O6-A11 (x2)	130.87(15)
A14-O2-A12	128.64(25)	A14-O6-A12	88.27(40)
A11-O3-A11	100.20(11)	A13-O7-A11	105.41(25)
A13-O3-A11 (x2)	129.90(14)	B1-O7-A11	125.80(35)
A11-O4-A11	95.54(11)	B1-O7-A13	128.70(34)
B1-O4-A11 (x2)	130.95(12)		

Table A3.14: O-M-O angles at *P*0 (0.001 GPa), crystal in DAC.

Sites	Angle (°)	Sites	Angle (°)
O2-A11-O1	99.11(19)	O2-A12-O6 (x2)	77.3(2)
O2-A11-O4	92.87(23)	O2-A12-O2	110.00(19)
O3-A11-O1	81.18(18)	O5-A12-O2 (x2)	117.92(25)
O3-A11-O2	94.42(24)	O5-A12-O6	77.25(45)
O3-A11-O4	97.95(10)	O3-A13-O1	169.05(63)
O3-A11-O6	176.73(18)	O3-A13-O5	114.34(113)
O3-A11-O7	94.92(21)	O3-A13-O7 (x2)	101.33(25)
O4-A11-O1	168.02(16)	O5-A13-O1	76.61(60)
O6-A11-O1	98.75(10)	O5-A13-O7 (x2)	105.97(21)
O6-A11-O2	82.35(19)	O7-A13-O1 (x2)	74.5(2)
O6-A11-O4	82.79(23)	O7-A13-O7	128.11(23)
O6-A11-O7	88.29(25)	O2-A14-O5 (x2)	119.32(18)
O7-A11-O1	80.49(31)	O2-A14-O6 (x2)	110.82(26)
O7-A11-O2	170.47(33)	O2-A14-O2	105.52(19)
O7-A11-O4	87.70(22)	O5-A14-O6	90.03(66)
O1-A12-O2 (x2)	107.69(22)	O4-B1-O7 (x2)	120.49(25)
O1-A12-O5	93.30(48)	O7-B1-O7	118.97(30)
O1-A12-O6	170.55(46)		

Table A3.15: M-O-M angles at *P1* (0.15(5) GPa).

Sites	Angle (°)	Sites	Angle (°)
A11-O1-A11	93.70(9)	A12-O5-A13	103.36(108)
A11-O1-A13 (x2)	89.47(14)	A14-O5-A12	103.74(38)
A12-O1-A11 (x2)	133.11(10)	A14-O5-A13	152.90(53)
A12-O1-A13	88.69(77)	A11-O6-A12 (x2)	90.6(1)
A12-O2-A11	105.33(34)	A11-O6-A11	98.73(9)
A14-O2-A11	124.79(32)	A14-O6-A11 (x2)	130.63(12)
A14-O2-A12	127.94(28)	A14-O6-A12	89.82(41)
A11-O3-A11	99.38(9)	A13-O7-A11	104.33(24)
A13-O3-A11 (x2)	130.30(12)	B1-O7-A11	126.36(34)
A11-O4-A11	96.50(9)	B1-O7-A13	128.8(3)
B1-O4-A11 (x2)	130.36(10)		

Table A3.16: O-M-O angles at *P1* (0.15(5) GPa).

Sites	Angle (°)	Sites	Angle (°)
O1-A11-O7	82.52(20)	O2-A12-O5 (x2)	118.01(25)
O2-A11-O1	99.88(20)	O2-A12-O6 (x2)	78.66(20)
O2-A11-O4	91.80(22)	O2-A12-O2	110.86(22)
O2-A11-O6	84.28(21)	O5-A12-O6	76.13(42)
O2-A11-O7	172.97(33)	O3-A13-O1	169.63(57)
O3-A11-O1	81.49(18)	O3-A13-O5	114.46(87)
O3-A11-O2	94.06(23)	O3-A13-O7 (x2)	100.41(24)
O3-A11-O4	98.05(8)	O5-A13-O1	75.91(52)
O3-A11-O6	178.34(13)	O7-A13-O1 (x2)	75.49(19)
O3-A11-O7	92.83(19)	O7-A13-O5 (x2)	107.08(20)
O4-A11-O1	168.32(13)	O7-A13-O7	127.37(20)
O4-A11-O7	85.85(19)	O2-A14-O5 (x2)	118.17(18)
O6-A11-O1	98.65(8)	O2-A14-O6 (x2)	112.02(26)
O6-A11-O4	82.15(22)	O2-A14-O2	105.62(22)
O6-A11-O7	88.83(21)	O5-A14-O6	90.31(60)
O1-A12-O2 (x2)	107.55(23)	O4-B1-O7 (x2)	120.30(24)
O1-A12-O5	92.03(46)	O7-B1-O7	119.40(27)
O1-A12-O6	168.17(48)		

Table A3.17: M-O-M angles at $P2$ (0.91(4) GPa).

Sites	Angle ($^{\circ}$)	Sites	Angle ($^{\circ}$)
A11-O1-A11	94.08(11)	A13-O5-A12	104.59(88)
A11-O1-A13 (x2)	88.67(15)	A13-O5-A14	154.22(63)
A12-O1-A11 (x2)	132.87(12)	A14-O5-A12	101.19(45)
A12-O1-A13	88.67(65)	A11-O6-A12 (x2)	91.49(12)
A12-O2-A11	105.31(34)	A11-O6-A11	97.72(11)
A14-O2-A11	123.71(33)	A14-O6-A11 (x2)	131.04(13)
A14-O2-A12	129.74(31)	A14-O6-A12	91.31(44)
A11-O3-A11	98.15(11)	A13-O7-A11	104.11(27)
A13-O3-A11 (x2)	130.91(14)	B1-O7-A11	126.73(37)
A11-O4-A11	96.80(11)	B1-O7-A13	128.07(30)
B1-O4-A11 (x2)	131.05(12)		

Table A3.18: O-M-O angles at $P2$ (0.91(4) GPa).

Sites	Angle ($^{\circ}$)	Sites	Angle ($^{\circ}$)
O1-A11-O2	98.52(22)	O2-A12-O5 (x2)	117.46(24)
O1-A11-O7	83.76(22)	O2-A12-O6 (x2)	79.35(20)
O3-A11-O1	82.39(19)	O2-A12-O2	113.42(24)
O3-A11-O2	93.49(26)	O5-A12-O6	76.81(44)
O3-A11-O4	97.61(10)	O3-A13-O1	169.26(63)
O3-A11-O6	175.75(17)	O3-A13-O5	114.96(81)
O3-A11-O7	93.65(21)	O3-A13-O7 (x2)	99.99(25)
O4-A11-O1	170.66(17)	O5-A13-O1	75.78(54)
O4-A11-O2	90.82(27)	O5-A13-O7 (x2)	107.58(22)
O4-A11-O7	86.92(21)	O7-A13-O1 (x2)	75.67(21)
O6-A11-O1	98.54(10)	O7-A13-O7	126.68(20)
O6-A11-O2	82.28(23)	O2-A14-O5 (x2)	118.28(19)
O6-A11-O4	82.16(21)	O2-A14-O2	106.07(24)
O6-A11-O7	90.58(24)	O6-A14-O2 (x2)	111.37(24)
O7-A11-O2	172.74(36)	O6-A14-O5	90.69(60)
O1-A12-O5	90.96(51)	O7-B1-O4 (x2)	119.89(27)
O1-A12-O6	167.77(50)	O7-B1-O7	119.88(27)
O2-A12-O1 (x2)	106.86(22)		

Table A3.19: M-O-M angles at *P3* (1.99(6) GPa).

Sites	Angle (°)	Sites	Angle (°)
A11-O1-A11	94.26(12)	A13-O5-A12	103.61(80)
A11-O1-A13 (x2)	90.28(16)	A14-O5-A12	102.25(45)
A12-O1-A11 (x2)	132.87(13)	A14-O5-A13	154.13(63)
A12-O1-A13	89.32(60)	A11-O6-A11	98.85(11)
A12-O2-A11	105.28(36)	A11-O6-A12 (x2)	91.12(15)
A14-O2-A11	123.54(36)	A14-O6-A11 (x2)	130.57(14)
A14-O2-A12	129.99(32)	A14-O6-A12	88.23(42)
A11-O3-A11	98.56(11)	A13-O7-A11	104.05(31)
A13-O3-A11 (x2)	130.70(14)	B1-O7-A11	125.63(40)
A11-O4-A11	96.99(11)	B1-O7-A13	128.59(30)
B1-O4-A11 (x2)	130.83(13)		

Table A3.20: O-M-O angles at *P3* (1.99(6) GPa).

Sites	Angle (°)	Sites	Angle (°)
O1-A11-O7	81.81(32)	O2-A12-O5 (x2)	118.11(26)
O2-A11-O1	99.84(24)	O2-A12-O6 (x2)	78.65(22)
O2-A11-O4	91.92(25)	O2-A12-O2	111.95(24)
O2-A11-O7	173.34(42)	O5-A12-O6	77.96(42)
O3-A11-O1	81.44(21)	O3-A13-O1	170.48(61)
O3-A11-O2	94.54(26)	O3-A13-O5	112.90(73)
O3-A11-O4	97.92(10)	O3-A13-O7 (x2)	99.83(27)
O3-A11-O6	178.22(17)	O5-A13-O1	76.62(52)
O3-A11-O7	92.09(21)	O5-A13-O7 (x2)	108.08(25)
O4-A11-O1	168.24(17)	O7-A13-O1 (x2)	76.35(25)
O4-A11-O7	86.48(22)	O7-A13-O7	127.39(20)
O6-A11-O1	99.22(11)	O2-A14-O5 (x2)	119.32(21)
O6-A11-O2	83.71(23)	O2-A14-O6 (x2)	109.83(27)
O6-A11-O4	81.78(22)	O2-A14-O2	105.76(25)
O6-A11-O7	89.65(24)	O5-A14-O6	91.56(60)
O1-A12-O5	90.45(51)	O7-B1-O4 (x2)	118.83(30)
O1-A12-O6	168.41(50)	O7-B1-O7	121.34(27)
O2-A12-O1 (x2)	107.34(24)		

Table A3.21: M-O-M angles at *P*4 (3.32(6) GPa).

Sites	Angle (°)	Sites	Angle (°)
A11-O1-A11	93.81(14)	A13-O5-A12	101.48(85)
A11-O1-A13 (x2)	89.09(15)	A14-O5-A12	101.13(49)
A12-O1-A11 (x2)	133.05(12)	A14-O5-A13	157.39(69)
A12-O1-A13	89.13(67)	A11-O6-A11	99.91(14)
A12-O2-A11	104.66(39)	A11-O6-A12 (x2)	89.94(13)
A14-O2-A11	124.94(38)	A14-O6-A11 (x2)	130.02(15)
A14-O2-A12	128.78(38)	A14-O6-A12	88.27(48)
A11-O3-A11	98.25(14)	A13-O7-A11	102.63(31)
A13-O3-A11 (x2)	130.74(15)	B1-O7-A11	127.21(41)
A11-O4-A11	98.03(14)	B1-O7-A13	128.80(34)
B1-O4-A11 (x2)	129.40(13)		

Table A3.22: O-M-O angles at *P*4 (3.32(6) GPa).

Sites	Angle (°)	Sites	Angle (°)
O1-A11-O7	83.37(25)	O2-A12-O2	112.01(29)
O2-A11-O1	99.82(26)	O2-A12-O5 (x2)	117.95(26)
O2-A11-O4	92.37(29)	O2-A12-O6 (x2)	78.82(22)
O2-A11-O7	173.80(39)	O5-A12-O6	77.24(48)
O3-A11-O1	81.77(19)	O3-A13-O1	172.65(66)
O3-A11-O2	94.51(30)	O3-A13-O5	109.66(76)
O3-A11-O4	98.26(13)	O3-A13-O7 (x2)	99.78(26)
O3-A11-O6	179.16(21)	O5-A13-O1	77.69(58)
O3-A11-O7	91.20(23)	O5-A13-O7 (x2)	108.81(23)
O4-A11-O1	167.77(20)	O7-A13-O1 (x2)	77.29(24)
O4-A11-O7	84.40(23)	O7-A13-O7	128.12(23)
O6-A11-O1	99.05(13)	O2-A14-O5 (x2)	117.95(21)
O6-A11-O2	85.48(27)	O2-A14-O6 (x2)	110.98(27)
O6-A11-O4	80.90(21)	O2-A14-O2	105.21(29)
O6-A11-O7	88.78(26)	O6-A14-O5	93.36(67)
O1-A12-O2 (x2)	106.91(24)	O4-B1-O7 (x2)	120.49(29)
O1-A12-O5	91.70(57)	O7-B1-O7	118.94(30)
O1-A12-O6	168.94(58)		

Table A3.23: M-O-M angles at *P*5 (4.78(6) GPa).

Sites	Angle (°)	Sites	Angle (°)
A11-O1-A11	95.78(14)	A13-O5-A12	100.93(92)
A11-O1-A13 (x2)	90.40(16)	A14-O5-A12	101.22(53)
A12-O1-A11 (x2)	132.09(14)	A14-O5-A13	157.85(76)
A12-O1-A13	87.87(65)	A11-O6-A12 (x2)	90.83(15)
A12-O2-A11	105.87(40)	A11-O6-A11	99.83(14)
A14-O2-A11	124.11(40)	A14-O6-A11 (x2)	130.07(15)
A14-O2-A12	129.00(35)	A14-O6-A12	90.15(50)
A11-O3-A11	98.79(14)	A13-O7-A11	103.54(35)
A13-O3-A11 (x2)	130.59(15)	B1-O7-A11	124.68(45)
A11-O4-A11	96.21(14)	B1-O7-A13	131.20(35)
B1-O4-A11 (x2)	130.18(14)		

Table A3.24: O-M-O angles at *P*5 (4.78(6) GPa).

Sites	Angle (°)	Sites	Angle (°)
O1-A11-O4	168.12(20)	O2-A12-O5 (x2)	116.73(28)
O1-A11-O7	82.28(31)	O2-A12-O6 (x2)	78.34(25)
O2-A11-O1	99.32(27)	O2-A12-O2	113.47(27)
O2-A11-O4	92.52(28)	O5-A12-O6	76.69(49)
O2-A11-O7	172.73(45)	O3-A13-O1	168.25(68)
O3-A11-O1	81.02(21)	O3-A13-O5	111.88(81)
O3-A11-O2	93.43(30)	O3-A13-O7 (x2)	99.16(29)
O3-A11-O4	97.54(13)	O5-A13-O1	79.86(60)
O3-A11-O6	176.87(21)	O5-A13-O7 (x2)	108.24(26)
O3-A11-O7	93.82(24)	O7-A13-O1 (x2)	76.26(27)
O4-A11-O7	86.07(24)	O7-A13-O7	128.86(23)
O6-A11-O1	100.32(13)	O2-A14-O5 (x2)	118.59(23)
O6-A11-O2	83.57(26)	O2-A14-O6 (x2)	111.12(28)
O6-A11-O4	81.73(22)	O2-A14-O2	104.97(27)
O6-A11-O7	89.17(26)	O5-A14-O6	91.94(69)
O1-A12-O5	91.34(58)	O4-B1-O7 (x2)	118.97(33)
O1-A12-O6	168.03(58)	O7-B1-O7	122.0(3)
O2-A12-O1 (x2)	107.67(26)		

Table A3.25: M-O-M angles at *P*6 (5.83(5) GPa).

Sites	Angle (°)	Sites	Angle (°)
A11-O1-A11	95.69(14)	A13-O5-A12	102.20(94)
A11-O1-A13 (x2)	91.80(16)	A13-O5-A14	157.52(76)
A12-O1-A11 (x2)	132.14(14)	A14-O5-A12	100.28(53)
A12-O1-A13	88.78(67)	A11-O6-A12 (x2)	90.52(15)
A12-O2-A11	105.96(40)	A11-O6-A11	99.67(14)
A12-O2-A14	129.29(35)	A14-O6-A11 (x2)	130.16(15)
A14-O2-A11	123.49(41)	A14-O6-A12	89.55(50)
A11-O3-A11	98.07(14)	A13-O7-A11	103.46(36)
A13-O3-A11 (x2)	130.96(15)	B1-O7-A11	125.65(47)
A11-O4-A11	97.00(14)	B1-O7-A13	130.04(38)
B1-O4-A11 (x2)	130.33(15)		

Table A3.26: O-M-O angles at *P*6 (5.83(5) GPa).

Sites	Angle (°)	Sites	Angle (°)
O1-A11-O4	167.39(21)	O2-A12-O5 (x2)	117.81(28)
O1-A11-O7	81.12(42)	O2-A12-O6 (x2)	78.38(25)
O2-A11-O1	100.94(27)	O2-A12-O2	112.35(27)
O2-A11-O4	91.65(30)	O5-A12-O6	78.15(50)
O2-A11-O6	83.91(26)	O3-A13-O1	168.73(70)
O2-A11-O7	172.75(46)	O3-A13-O5	111.55(83)
O3-A11-O1	80.96(21)	O3-A13-O7 (x2)	99.14(29)
O3-A11-O2	94.0(3)	O5-A13-O1	79.73(62)
O3-A11-O4	97.63(13)	O5-A13-O7 (x2)	108.57(27)
O3-A11-O6	177.66(21)	O7-A13-O1 (x2)	76.41(27)
O3-A11-O7	93.20(26)	O7-A13-O7	128.42(25)
O4-A11-O7	86.47(26)	O2-A14-O5 (x2)	118.40(23)
O6-A11-O1	100.45(13)	O2-A14-O6 (x2)	110.71(28)
O6-A11-O4	81.41(23)	O2-A14-O2	105.84(27)
O6-A11-O7	88.88(27)	O6-A14-O5	92.01(69)
O1-A12-O5	89.30(59)	O4-B1-O7 (x2)	119.69(34)
O1-A12-O6	167.45(59)	O7-B1-O7	120.61(33)
O2-A12-O1 (x2)	108.03(27)		

Table A3.27: M-O-M angles at *P7* (5.99(5) GPa).

Sites	Angle (°)	Sites	Angle (°)
A11-O1-A11	93.95(17)	A13-O5-A12	100.35(98)
A11-O1-A13 (x2)	88.44(19)	A14-O5-A12	102.99(59)
A12-O1-A11 (x2)	132.90(16)	A14-O5-A13	156.65(81)
A12-O1-A13	88.48(78)	A11-O6-A12 (x2)	90.19(17)
A12-O2-A11	104.88(44)	A11-O6-A11	99.39(16)
A14-O2-A11	124.38(43)	A14-O6-A11 (x2)	130.31(18)
A14-O2-A12	129.10(41)	A14-O6-A12	89.59(56)
A11-O3-A11	98.63(17)	A13-O7-A11	103.27(34)
A13-O3-A11 (x2)	130.40(18)	B1-O7-A11	126.50(46)
A11-O4-A11	97.48(17)	B1-O7-A13	128.84(38)
B1-O4-A11 (x2)	129.76(17)		

Table A3.28: O-M-O angles at *P7* (5.99(5) GPa).

Sites	Angle (°)	Sites	Angle (°)
O1-A11-O7	83.66(27)	O2-A12-O5 (x2)	117.50(29)
O2-A11-O1	99.28(31)	O2-A12-O6 (x2)	78.84(25)
O2-A11-O4	92.21(33)	O2-A12-O2	111.95(32)
O2-A11-O6	84.91(30)	O5-A12-O6	75.84(53)
O2-A11-O7	173.77(48)	O3-A13-O1	173.63(77)
O3-A11-O1	81.53(26)	O3-A13-O5	108.52(89)
O3-A11-O2	95.06(34)	O3-A13-O7 (x2)	100.72(28)
O3-A11-O4	98.23(16)	O5-A13-O1	77.85(67)
O3-A11-O6	179.61(25)	O7-A13-O1 (x2)	76.77(27)
O3-A11-O7	90.79(27)	O7-A13-O5 (x2)	108.47(26)
O4-A11-O1	168.48(25)	O7-A13-O7	128.05(25)
O4-A11-O7	84.83(28)	O2-A14-O5 (x2)	118.25(24)
O6-A11-O1	98.85(16)	O2-A14-O6 (x2)	110.96(30)
O6-A11-O4	81.39(27)	O2-A14-O2	106.08(32)
O6-A11-O7	89.22(30)	O5-A14-O6	91.58(78)
O1-A12-O2 (x2)	106.79(27)	O7-B1-O4 (x2)	119.79(32)
O1-A12-O5	93.32(66)	O7-B1-O7	120.22(33)
O1-A12-O6	169.16(67)		

Table A3.29: M-O-M angles at *P*8 (6.45(6) GPa).

Sites	Angle (°)	Sites	Angle (°)
A11-O1-A11	92.10(19)	A13-O5-A12	101.83(121)
A11-O1-A13 (x2)	87.18(21)	A14-O5-A12	100.62(59)
A12-O1-A11 (x2)	133.78(17)	A14-O5-A13	157.55(84)
A12-O1-A13	89.56(87)	A11-O6-A12 (x2)	89.93(17)
A12-O2-A11	105.17(46)	A11-O6-A11	96.96(19)
A14-O2-A11	124.18(44)	A14-O6-A11 (x2)	131.52(21)
A14-O2-A12	129.58(42)	A14-O6-A12	90.26(61)
A11-O3-A11	99.94(19)	A13-O7-A11	103.38(35)
A13-O3-A11 (x2)	129.84(21)	B1-O7-A11	127.76(47)
A11-O4-A11	99.84(19)	B1-O7-A13	127.66(38)
B1-O4-A11 (x2)	128.89(19)		

Table A3.30: O-M-O angles at *P*8 (6.45(6) GPa).

Sites	Angle (°)	Sites	Angle (°)
O2-A11-O1	98.38(32)	O2-A12-O5 (x2)	117.61(31)
O2-A11-O6	83.76(32)	O2-A12-O6 (x2)	79.45(25)
O2-A11-O7	173.22(49)	O2-A12-O2	113.01(32)
O3-A11-O1	82.08(27)	O5-A12-O6	76.52(57)
O3-A11-O2	94.92(37)	O3-A13-O1	174.88(82)
O3-A11-O4	100.03(19)	O3-A13-O5	108.36(98)
O3-A11-O6	178.13(29)	O3-A13-O7 (x2)	100.85(31)
O3-A11-O7	91.79(29)	O5-A13-O1	76.76(74)
O4-A11-O1	168.68(28)	O5-A13-O7 (x2)	108.15(27)
O4-A11-O2	92.53(36)	O7-A13-O1 (x2)	77.16(28)
O4-A11-O6	81.36(30)	O7-A13-O7	128.61(25)
O4-A11-O7	85.39(29)	O2-A14-O5 (x2)	118.88(24)
O6-A11-O1	96.80(18)	O2-A14-O2	105.00(32)
O6-A11-O7	89.55(34)	O6-A14-O2 (x2)	110.38(32)
O7-A11-O1	83.43(31)	O6-A14-O5	92.61(87)
O1-A12-O2 (x2)	106.52(28)	O4-B1-O7 (x2)	121.02(33)
O1-A12-O5	91.85(69)	O7-B1-O7	117.62(33)
O1-A12-O6	168.36(69)		

B Powder X-ray Diffraction Tips & Tricks

*Appendix B is a reprint of a Manual for using the
PANalytical X'Pert Pro MPD Powder Diffractometer
at the Institute of Geological Sciences, University of Bern*

B.1 Configuring a Measurement Program for the X'Pert Pro Diffractometer

Most used programs are Absolute Scan, which contains information for a simple Theta-2-Theta scan, General Batch, which can contain several batched absolute scans combined with diffractometer settings and Non-ambient Program (a special batch for the HTK 1200 furnace).

Absolute Scan (Theta-2-Theta Scan Program)

To create a new absolute scan, choose 'New' from the 'File' menu in X'Pert DataCollector software. When asked for the measurement type, choose 'Absolute Scan'.

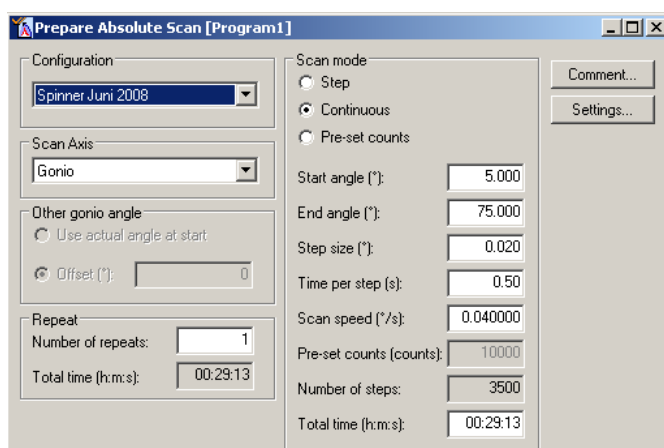


Fig. B1.1: Absolute scan program window.

In the scan program window (Figure B1.1), select a configuration: 'Spinner' for normal usage, 'HTK' for high-temperature measurements or 'Bracket'.

The scan axis is always 'Gonio' and scan mode is 'Continuous'. At this time, no diffractometer setup is defined and the measurement program will not work correctly!

Click 'Settings...'. A new window opens (Figure B1.2) where the diffractometer setup can be entered. At the moment, all settings are 'actual', which means that they are undefined.

Click through all items in the tree list and change all values highlighted in red from 'actual' to the setting as in Figure B1.2. Values can be changed in the field highlighted green. This field is different for each item in the tree list. Items highlighted in red must be defined exactly as shown in Figure B1.2, items highlighted in yellow depend on the setup. Choosing the right setup is described in the part 'Configuring the X'Pert Pro MPD Diffractometer'. Do not enter any offsets!

Blue values are sent to the diffractometer by the DataCollector software and the hardware is automatically adjusted. Black values are for information purposes only. They are written

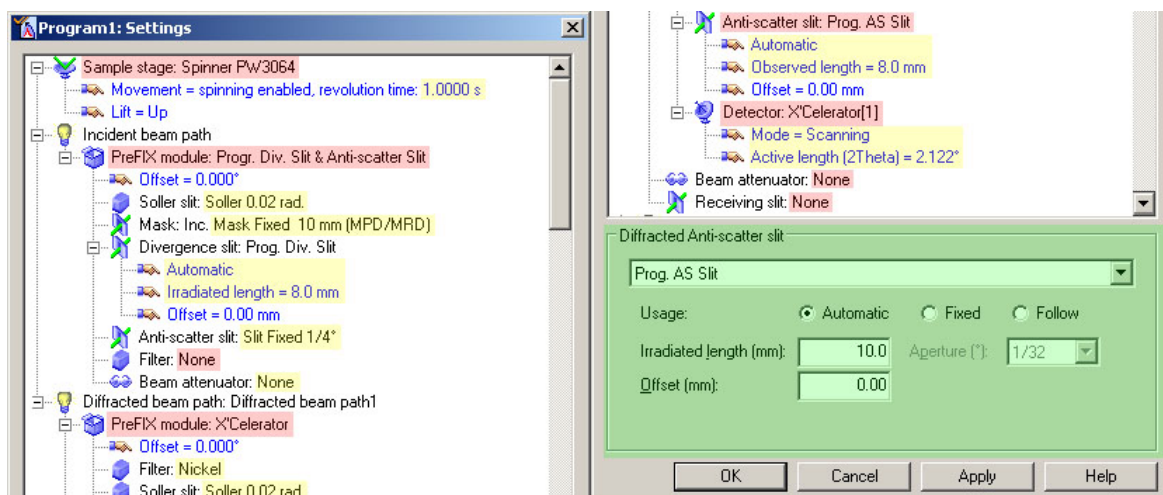


Fig. B1.2: Measurement program settings.

to the .xrxml file but the hardware configuration must be manually changed and verified by the user. When finished, click 'Apply' and then 'OK'. The step size has now changed in the 'Absolute Scan Program' window.

2-Theta start and end angle. The required scan range depends on the purpose of the measurement. For phase identification, 10° to 55° 2-Theta is usually enough because most PDF entries do not contain high-angle data. Make sure the scan range covers all strong peaks. For lattice parameter refinements, make sure that peaks with low hkl values are covered by the scan range. For crystal structure analysis, the more the better but high-angle data is essential.

Step size. The X'Cellerator detector allows step sizes of 0.033xx, 0.016xx, 0.008xx, 0.004xx and 0.002xx $^\circ$ /step. For phase identification and phase quantification by the Rietveld method, a step size of 0.016xx $^\circ$ /step is usually small enough. For crystal structure refinements and determination of precise lattice parameters, a smaller step size is recommended.

Time per step. Longer step times result in higher intensities and better counting statistics. For phase identification, there is no need to acquire data with very high intensities. As long as the peaks separate well from the noise, they can be identified. For phase quantification, a maximum intensity of 1'500 to 2'000 counts is usually good enough. For structural analyses, ca. 10'000 counts is a good start because there will still be peaks at high angles.

Repeat. A scan program can be repeated by entering a value in the 'Number of repeats' field. The .xrxml measurement file then contains more than one measurement which can be

summed or averaged in HighScore Plus. This is useful to reduce noise.



Fig. B1.3: Do not check 'Available to all users'!

When saving the program, enter a program name and a description of the program (optional). **Be sure to uncheck the option 'Available to all users'** (Figure B1.3).

General Batch (to set the generator to stand-by after measurement)

Use this program type to set up a batch of different measurement files, ambient settings or generator settings. The general batch is especially useful to set the generator to stand-by after the measurement.

Select 'New' from the 'File' menu and chose 'General Batch' from the program type pull-down menu.

In the 'General Batch' window (Figure B1.4), add one or more previously defined scan programs by clicking 'Insert Measurement Program...', if needed, add timer settings or batch settings. Batch settings can be different temperature (when using the HTK furnace) or generator settings. In a general batch the shutter is not closed between individual measurements. This can result in radiation damage on the sample surface. The following picture shows a batch that sets the generator to stand-by after completion of a single measurement:

- Item number 1 is the measurement program (added by clicking 'Insert Measurement Program...'),
- Item number 2 is a general batch setting to set the generator to 30 kV, 10 mA.

Non-Ambient Program (for high-temperature measurements)

The 'Non-ambient program' (Figure B1.5) is tailored for high-temperature measurements. It is set up the same way as the general batch but together with the diffraction patterns, an .xrdml file containing measured temperature and temperature set-points is saved.

When performing high-temperature measurements, it is recommended to insert a timer setting before a measurement is started to allow temperature equilibration in the furnace (see the example in Figure B1.5). It is not recommended to use the maximum heating rate. Try ca

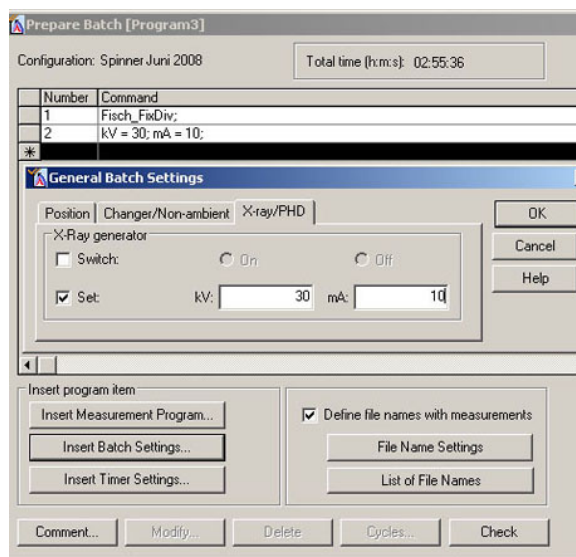


Fig. B1.4: General batch program.

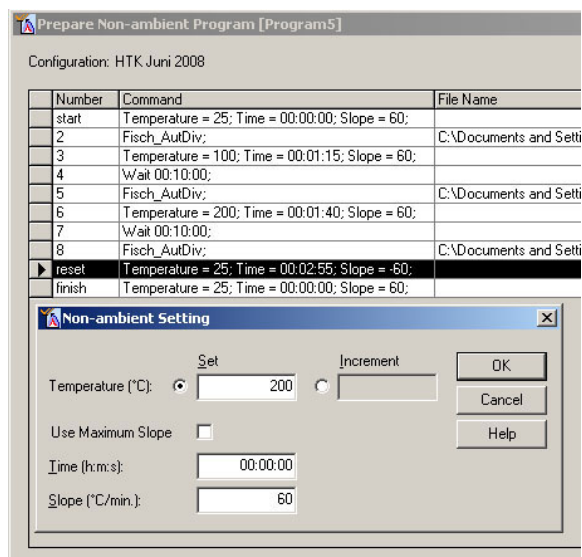


Fig. B1.5: Non-ambient program.

10°C/min.

In a non-ambient program the shutter is not closed between individual measurements. This can result in radiation damage on the sample surface.

Running a Measurement Program

After connecting to the diffractometer ('Instrument' menu → 'Connect'), choosing the required configuration and setting the generator to 40kV, 40mA, select 'Program...' from the 'Measure' menu and choose a previously defined program. Before the program starts, program name and comments are displayed and the file name and file path can be entered (Figure B1.6).

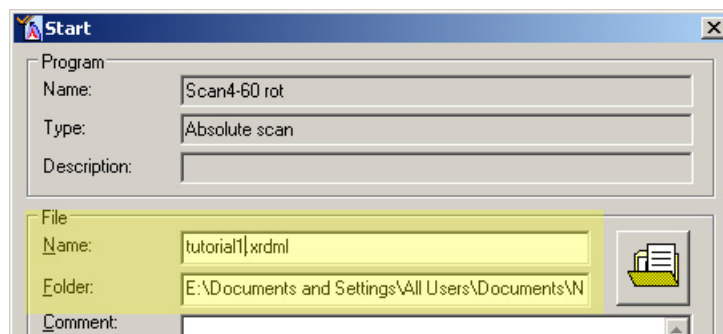


Fig. B1.6: Starting the measurement.

B.2 Configuring the X'Pert Pro MPD Diffractometer

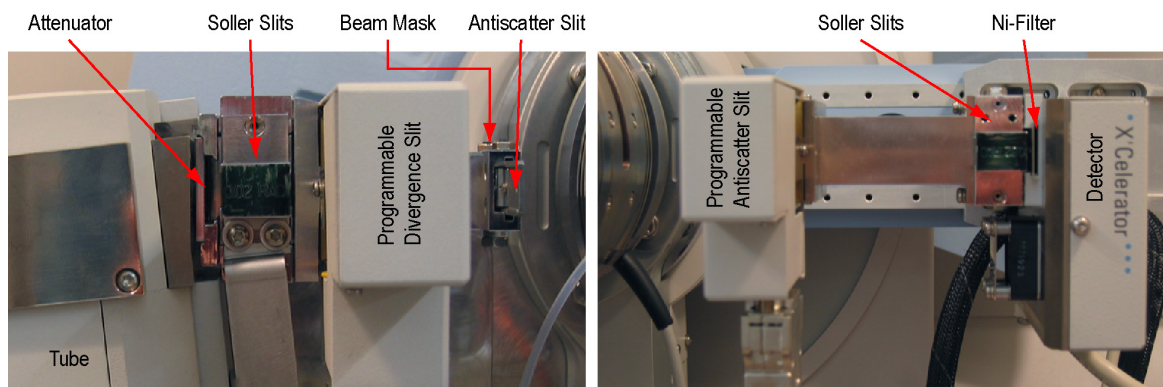


Fig. B1.7: Primary and secondary beam path Prefix modules.

Primary Beam Path Options

Attenuation foils. Cu attenuation foils of 0.1mm and 0.2mm thickness are available (Figure B1.8). They are inserted directly after the X-ray tube in the primary beam path (Figure B1.7) and used for alignment purposes only.

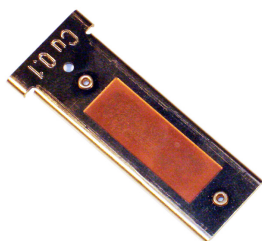


Fig. B1.8: Cu attenuator foil.

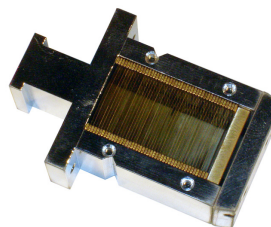


Fig. B1.9: Soller slits.

Soller Slits. Soller slits of 0.02 rad. and 0.04 rad. opening (Figure B1.9) can be inserted in the primary and secondary beam path (Figure B1.7). Use the same soller slit size in the primary and diffracted beam path. Smaller soller slits reduce axial divergence resulting in lower peak asymmetry at low 2-Theta angles (Figure B1.10), however, intensity is vastly reduced. Whenever possible, use the 0.02 rad. soller slits.

Handle them with care. Do not touch the lamellae!

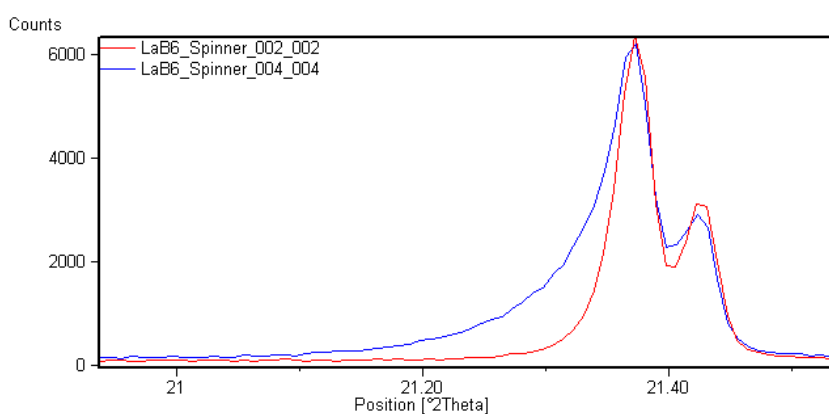


Fig. B1.10: Scans with 0.04 rad. (blue) and 0.02 rad. soller slits (red). Intensities are normalized.

Programmable divergence slit. The divergence slit in the primary beam path (Figure B1.7) reduces the equatorial divergence of the primary beam (in the plane perpendicular to the sample, parallel to the primary beam).

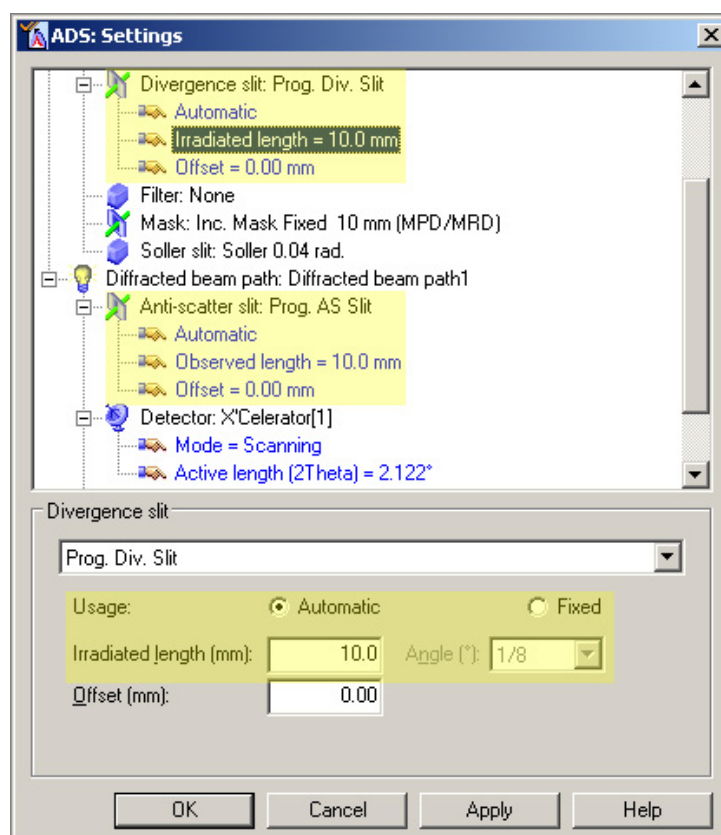


Fig. B1.11: Options for fixed or automatic divergence slits.

In the measurement program settings, check the options marked yellow in Figure B1.11 and be sure that the same setting is applied to both the programmable divergence slit in the incident beam path and the programmable antiscatter slit in the diffracted beam path. The programmable antiscatter slit in the diffracted beam path can also be set to 'follow'.

Fixed slit mode: The divergence of the incident beam is constant over the 2-Theta range (Figure B1.12). This agrees with the assumption of a constant sample volume: At low angles, a large sample area but low depth is irradiated. At high angles, a small area but large sample depth is irradiated. Large divergence slits can result in primary beam overspill at low 2-Theta angles!

Constant irradiated length mode: The slit size varies with 2-Theta and the irradiated sample surface is kept constant. This results in higher intensities, better s/n ratio at high 2-Theta and is a favorable option for fast data collection, e.g. phase identification. Usually, a length of 10 mm to 20 mm is appropriate. However, the assumption of constant volume is no longer valid, relative intensities are not correct and resolution is a bit lower (Figure B1.13). For matching intensities with PDF files, the pattern must be intensity-corrected to a fixed divergence of 0.5° . This is done in HighScore Plus in the 'Treatment' menu → 'Corrections' → 'Convert Divergence Slit'.

Samples prepared on silicon plates: As the sample is usually very thin, constant volume is not guaranteed. Samples prepared on silicon plates must be measured with automatic slits. Do not set the irradiated length larger than the physical length of the sample.

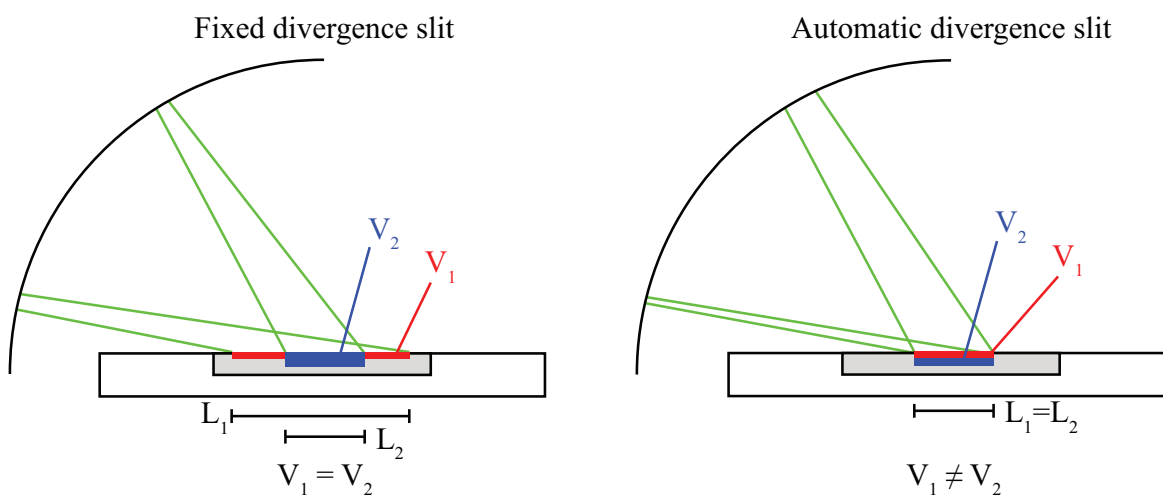


Fig. B1.12: Difference in sample volume when measuring with fixed or automatic divergence slits.

Choosing the right slits...

When using automatic divergence slits with constant irradiated area, the illuminated length should not be set larger than the sample length.

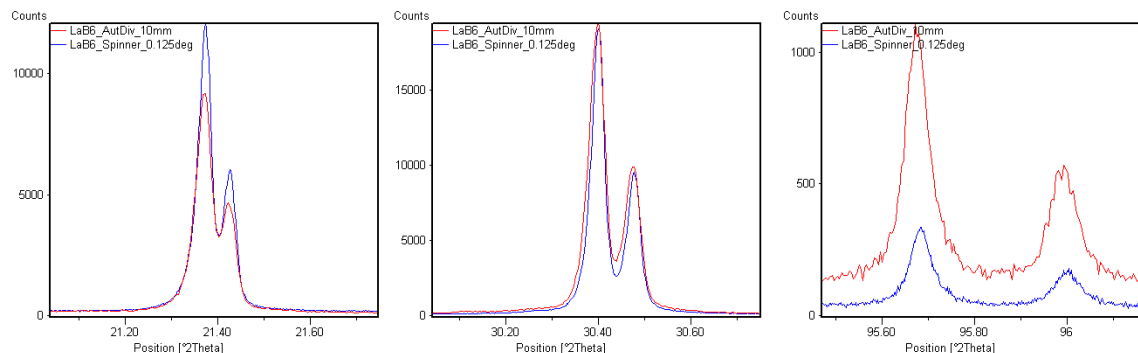


Fig. B1.13: The same pattern was measured with a fixed divergence slit of $1/8^\circ$ (blue) and a constant irradiated area of 10 mm (red). Intensities were normalized to the peak at 30.4° 2-Theta. Note different relative intensities and the lower resolution at low angles.

When using fixed divergence slits, use the table below to determine correct slit size. Irradiated sample length with fixed slits can be calculated according to Equation B.1 and most often used slit sizes and irradiated lengths at the sample position are listed in Table B1.1. Selecting the correct slit size depends on the starting 2-Theta angle of the measurement and the sample size. For a 25 mm sample, the lowest starting angle with a $1/4^\circ$ divergence slit is 5° 2-Theta. Select the slit as large as possible, larger slits result in higher intensities.

$$\text{Irradiated length (mm)} = R_{\text{Goniometer}} \text{ (mm)} \cdot \frac{\text{DivSlit}(\text{°}) \cdot \frac{\pi}{180}}{\sin\theta(\text{°})} \quad (\text{B.1})$$

Table B1.1: 2-Theta dependent irradiated length in mm at sample position with slit size.

2-Theta (°)	$1/16^\circ$	$1/8^\circ$	$1/4^\circ$	$1/2^\circ$	1°	2°
1	30.0	60.0	120.0	240.0	480.0	960.0
2	15.0	30.0	60.0	120.0	240.0	480.0
3	10.0	20.0	40.0	80.0	160.0	320.0
4	7.5	15.0	30.0	60.0	120.0	240.0
5	6.0	12.0	24.0	48.0	96.0	192.1
6	5.0	10.0	20.0	40.0	80.0	160.1
7	4.3	8.6	17.2	34.3	68.6	137.2
8	3.8	7.5	15.0	30.0	60.0	120.1
9	3.3	6.7	13.3	26.7	53.4	106.8
10	3.0	6.0	12.0	24.0	48.1	96.1
11	2.7	5.5	10.9	21.9	43.7	87.4
12	2.5	5.0	10.0	20.0	40.1	80.1

Beam mask. The beam mask (Figure B1.14) limits the axial beam width (parallel to the sample surface on the goniometer axis) on the sample. They are inserted in the primary beam path after the divergence slit (Figure B1.7). Masks with a beam width of ca. 5 mm, 10 mm, 15 mm and 20 mm at the sample position are available. The 10 mm mask suits most requirements.



Fig. B1.14: Beam masks.



Fig. B1.15: Fixed antiscatter slits.

Antiscatter slit. The antiscatter slit (Figure B1.15) reduces scattering of the incident X-ray beam (Figure B1.7). When measuring with a fixed divergence slit, the size of the antiscatter should be double the size of the divergence slit. If automatic divergence slits are used, remove it or make sure that the antiscatter slit is not smaller than the maximum opening of the automatic divergence slit: With an irradiated length of 10 mm, the 2° fixed antiscatter slit can be used for measurements up to 60° 2-Theta, with 8 mm irradiated length it can be used up to 80° 2-Theta (Table B1.2). Select the smallest slit possible. For measurements with automatic divergence slits starting at angles below 4° 2-Theta, a fixed antiscatter slit must be inserted!

Table B1.2: Max. 2-Theta angle with constant irradiated length and fixed antiscatter slits.

Irradiated Length	5 mm	7.5 mm	10 mm	12.5 mm	15 mm	17.5 mm	20 mm
4° Slit (6 mm)	180°	180°	180°	110°	85°	70°	60°
2° Slit (3 mm)	180°	85°	60°	48°	40°	35°	30°

Diffracted Beam Path Options

Programmable antiscatter slit. The programmable antiscatter slit in the diffracted beam path (Figure B1.7) reduces air and sample scattering that does not contribute to Bragg reflections. In order to make sure that the detector observes all of the irradiated sample, this slit has to be set to the same setting as the programmable divergence slit. Set it to the same irradiated length as the divergence slit, to the same fixed divergence or set it to 'follow' in the measurement program settings.

Soller slits. Diffracted beam path soller slits (Figure B1.7) serve the same purpose as in the incident beam path and should have the same size.

Filter. The nickel filter is inserted before the detector (Figure B1.7) to cut off $K\beta$ radiation. Do not remove it.

X'Celerator detector. The X'Celerator detector (Figure B1.7) is a linear position sensitive multiple strip (LPSD) solid state detector. It consists of 127 channels, which work like an array of 127 individual point detectors. For normal measurements it should be set to 'Scanning' mode with an active area of 2.122° . Reducing the active area may decrease tangential aberration (because the detector is not only sensitive at a single point on the goniometer radius but at an area that is tangential to the goniometer circle). Since each strip of the detector works similar to a single point detector, the height of each strip (0.07 mm) is comparable to the detector slit in conventional point detectors.

B.3 Theory on Rietveld Refinements

General Remarks on Data Quality

- Data quality is crucial! Read McCusker et al. (1999) and Toby (2006),
- Use the 0.02 rad. soller slits in any case,
- Acquire data with good s/n ratio,
- Acquire data with a max. count rate of the strongest peak of ca. 10'000 counts,
- Careful sample preparation is crucial (backloaded sample holders),
- Samples prepared on silicon plates must be measured with automatic divergence slits,
- For quantification, the 2-Theta range must cover all strong peaks,
- For precise lattice parameter determination, measure all peaks with low *hkl* indices,
- For structure refinements, measure at least up to 80° 2-Theta and use single-phase samples.

How a Rietveld Refinement Works

A calculated pattern of one or more phases is fitted to the measured one. Each phase is linear scaled by the scale factor. Parameters influencing peak positions (lattice parameters and space group) and relative peak intensities (atomic content of the unit cell and preferred orientation correction) are refined until the fit is satisfying. Thus, all phases present in the sample and their crystal structure must be known.

Crystal structure information is usually available from .cif files (Crystallographical Information File). Most important sections of a LaB6.cif file are described below (Table B1.3).

Calculated reflection positions depend on:

- Wavelength λ (for Cu X-radiation $\lambda = 1.540598 \text{ \AA}$),
- Specimen displacement (mm) and zero shift ($^{\circ}$ 2-Theta),
- Lattice parameters a, b, c (\AA) and α, β, γ ($^{\circ}$),
- Crystal system and space group.

The position of a reflection is calculated from Bragg's law (Equation B.2) and the line-spacing equation of the corresponding crystal-system (Equation B.3 for the cubic crystal system). Resulting values for LaB₆ with $\lambda = 1.54 \text{ \AA}$ are shown in Table B1.4.

$$\sin \theta = \frac{\lambda}{2 \cdot d} \quad (\text{B.2})$$

Table B1.3: LaB6.cif file information relevant for Rietveld refinements.

_cell_length_a	4.157	This part of the .cif file describes the unit cell lengths and angles, formula units per unit cell ($Z = 1$ means one La and six B atoms per unit cell) and the space group setting.
_cell_length_b	4.157	
_cell_length_c	4.157	
_cell_angle_alpha	90.0	
_cell_angle_alpha	90.0	
_cell_angle_alpha	90.0	
_symmetry_space_group_name_H-M	Pm-3m	Peak positions are calculated from this information.
_symmetry_Int_Tables_number	221	
_cell_formula_units_Z	1	
_atom_site_label		Atom label (name), atom type, site multiplicity and Wyckoff site (the latter two are also defined by the space group symbol above), fractional coordinates, x , y and z , isotropic displacement parameters B or U and the site occupancy (from 0 to 1) are defined.
_atom_site_type_symbol		
_atom_symmetry_multiplicity		
_atom_site_Wyckoff_symbol		
_atom_site_fract_x		
_atom_site_fract_y		
_atom_site_fract_z		
_atom_site_B_iso_or_equiv		
_atom_site_occupancy		
La1 La0+ 1 a 0.0 0.0 0.0 0.0052 1.0		
B1 B0+ 6 f 0.1975 0.5 0.5 0.0041 1.0		Peak intensities are calculated from this information.

$$\frac{1}{d^2} = \frac{h^2 + k^2 + l^2}{a^2} \quad (\text{B.3})$$

Table B1.4: Peak positions of LaB₆.

h	k	l	d-spacing (Å)	2-Theta (°)
1	0	0	4.157	21.380
1	1	0	2.937	30.407
1	1	1	2.399	37.463
2	1	0	1.858	48.978
2	1	1	1.696	54.009
2	2	0	1.469	63.238

Specimen displacement and zero shift cannot be refined together. Refining specimen displacement also accounts to some extent to sample transparency (for materials with low mass absorption coefficient) and should therefore be preferred.

Calculated reflection intensities depend on:

- Atom types,

- Atom coordinates (x, y, z between 0 and 1),
- Atomic displacement parameters B or U (usually a positive number < 3),
- Preferred orientation correction (value around 1, hkl direction must be known!).

Intensity of a reflection is calculated from the atomic content of the unit cell (structure factor F from atomic types and positions) and thermal vibration of atoms (displacement parameter B or U , with $B = 8 \cdot \pi \cdot U^2$). If displacement parameters are missing in the .cif file, use 0.5 as start value. Equation B.4 describes intensity of a reflection in a powder diffractometer. Sample dependent parameters are the scale factor S , the structure factor F (atomic content of the unit cell), the atomic displacement parameter B and intensity corrections p (e.g. preferred orientation).

$$I \sim |F|^2 \cdot S \cdot p \cdot \left(\frac{1 + \cos^2 2\theta}{\sin^2 \theta \cdot \cos \theta} \right) \cdot e^{-2 \cdot \left(\frac{\sin \theta}{\lambda} \right)^2 \cdot B} \quad (\text{B.4})$$

Peak shape. The shape of measured diffraction peaks is a convolution of peak shapes resulting from the diffractometer setup and microstructural properties of the phase like size of coherently scattering domains ('crystallite size' and microstrain). Calculated peaks are usually modeled with a pseudo Voigt function (linear combination of Gauss and Lorentz functions) with additional corrections for asymmetry and microstructural effects. The broader a peak, the smaller the 'crystallites' in the corresponding sample. In conventional powder diffractometers, peak width at half maximum (FWHM) is a function of Theta and is described by the Caglioti function (Equation B.5).

$$\text{FWHM}_k^2 = U \cdot \tan^2 \theta_k + V \cdot \tan \theta_k + W \quad (\text{B.5})$$

The setup dependent peak shape and peak width of the diffractometer is determined by measuring a standard with (theoretically) infinite size of coherently scattering domains and no microstrain, such as NIST SRM 660a LaB₆.

Profile Shape Function Parameters in PANalytical HighScore Plus

The following parameters are valid for the X'Pert Pro MPD diffractometer when using a 10 mm beam mask, 0.02 rad. soller slits and the detector set to a sensitive area of 2.122°.

Intensities of data collected with constant irradiated sample length must be converted. In HighScore Plus, go to 'Treatment' → 'Corrections' → 'Convert Divergence Slit'.

After adding phases, double click 'Global Parameters' in the 'Lists Pane' (Figure B1.16) to open the 'Object Inspector' (Figure B1.17). In the 'Refinement' submenu (Figure B1.17), choose 'Pseudo Voigt 3(JFC Asymmetry)' and enter 20 in the 'Profile Base Width' field. In the 'Lists Pane', enter the values shown in Figure B1.16 in the 'Profile Parameters' submenu for each phase as start values. Calculated peaks will be too narrow because microstructural effects are not considered.

Name	Refine	Value
Global Parameters		
LaB6	<input checked="" type="checkbox"/>	
Profile Parameters		
U	<input type="checkbox"/>	0.001363
V	<input type="checkbox"/>	0.001565
W	<input type="checkbox"/>	0.000238
Anisotropic Broadening	<input type="checkbox"/>	0.000000
Asymmetry (Finger, Cox, Jephcoat) S/L	<input type="checkbox"/>	0.015000
Asymmetry (Finger, Cox, Jephcoat) D/L	<input type="checkbox"/>	0.015000
Peak Shape 1	<input type="checkbox"/>	0.699679
Peak Shape 2	<input type="checkbox"/>	-0.000891
Peak Shape 3	<input type="checkbox"/>	0.000029

Fig. B1.16: Profile parameters in Lists Pane.

Selected object: Global Parameters	
Background	
Agreement Indices	
General Properties	
Refinement	
Weighting Scheme	Against Iobs
Use summed March/Dollase Function	<input type="checkbox"/>
Recycle HKL's (Le-Bail Fit only)	<input checked="" type="checkbox"/>
Profile Function	Pseudo Voigt 3(FJC Asymm)
Profile Base Width	20.00000
Intensity Limit	0.00000
Max. No. of Least-Squares Cycles	20
EPS (stop if all shifts < EPS*esd)	0.50000
Job Type	X-rays
Least Squares Type	Newton-Raphson

Fig. B1.17: Object Inspector options.

Manual Refinement Steps

Use steps 1, 2, 3 and 4 for quantitative phase analysis and steps 1, 2, 4, 5 and 6 for structural analysis. Check all values for their physical meaning (e.g. a specimen displacement of 0.5 mm or negative displacement parameters are physically not feasible!). A sample refinement of LaB₆ is shown in Figure B1.18.

1. Refine specimen displacement (global parameters) and the scale factor for each phase,
2. Refine lattice parameters of each phase. Take care when refining lattice parameters with low intensities,
3. Refine B overall for each phase,
4. Refine profile parameters in the following sequence: U (if data $> 90^\circ$ 2-Theta, otherwise leave fixed!), V , W , Peak Shape 1, Peak Shape 2 for each phase. If the refinement is unstable, refine only V and W . Verify the values, especially for phases with low intensities. Instead of refining the values manually, the size-strain batch in HighScore Plus can be used. Set the refinement mode to 'Automatic' and choose 'size-strain' from the menu next to the refinement button. This batch also refines other parameters in the following order: Specimen displacement, scale, U , V , W , lattice parameters, shape 1 and shape 2,
5. Refine atomic positions. Never refine special positions (e.g. 0 , $\frac{1}{4}$, $\frac{1}{3}$, $\frac{1}{2}$, ...),

- Refine individual B 's of the atoms. Constraining B 's of atoms (e.g. one parameter for each atom type) can help if the refinement is unstable.

Name	Refine	Value	Deviation
Global Parameters			
Zero Shift [$^{\circ}2\theta$]	<input type="checkbox"/>	0.000000	0.000000
Specimen Displacement [mm]	<input checked="" type="checkbox"/> 1	-0.045239	0.000083
Wavelength [Å]	<input type="checkbox"/>	1.540598	0.000000
LaB6			
Scale factor	<input checked="" type="checkbox"/> 1	0.008972	0.000012
Preferred Orientation	<input type="checkbox"/>	1.000000	0.000000
B overall	<input type="checkbox"/>	0.000000	0.000000
Extinction	<input type="checkbox"/>	0.000000	0.000000
Flat Plate Absorption Correction	<input type="checkbox"/>	0.000000	0.000000
Porosity	<input type="checkbox"/>	0.000000	0.000000
Roughness	<input type="checkbox"/>	0.000000	0.000000
Unit Cell			
a [Å]	<input checked="" type="checkbox"/> 2	4.156921	0.000003
b [Å]	<input checked="" type="checkbox"/>	4.156921	0.000003
c [Å]	<input checked="" type="checkbox"/>	4.156921	0.000003
alpha [$^{\circ}$]	<input type="checkbox"/>	90.000000	0.000000
beta [$^{\circ}$]	<input type="checkbox"/>	90.000000	0.000000
gamma [$^{\circ}$]	<input type="checkbox"/>	90.000000	0.000000
Atomic coordinates			
La1			
X	<input type="checkbox"/>	0.000000	0.000000
Y	<input type="checkbox"/>	0.000000	0.000000
Z	<input type="checkbox"/>	0.000000	0.000000
B isotropic	<input checked="" type="checkbox"/> 6	0.018844	0.004861
Occupancy	<input type="checkbox"/>	1.000000	0.000000
B1			
X	<input checked="" type="checkbox"/> 5	0.199256	0.000357
Y	<input type="checkbox"/>	0.500000	0.000000
Z	<input type="checkbox"/>	0.500000	0.000000
B isotropic	<input checked="" type="checkbox"/> 6	0.000000	0.029987
Occupancy	<input type="checkbox"/>	1.000000	0.000000
Profile Parameters			
U	<input checked="" type="checkbox"/> 4.1	0.001547	0.000051
V	<input checked="" type="checkbox"/> 4.2	0.001206	0.000050
W	<input checked="" type="checkbox"/> 4.3	0.000350	0.000012
Anisotropic Broadening	<input type="checkbox"/>	0.000000	0.000000
Asymmetry (Finger,Cox,Jeph...)	<input type="checkbox"/>	0.015000	0.000000
Asymmetry (Finger,Cox,Jeph...)	<input type="checkbox"/>	0.015000	0.000000
Peak Shape 1	<input checked="" type="checkbox"/> 4.4	0.737512	0.007034
Peak Shape 2	<input checked="" type="checkbox"/> 4.5	-0.000815	0.000108
Peak Shape 3	<input type="checkbox"/>	0.000029	0.000000

Fig. B1.18: Refined parameters are numbered according to the refinement sequence above. Step 3 was not performed because displacement parameters were refined individually for each atom.

Agreement Factors (R -Values)

Agreement factors or R -values provide information about the quality of the fit of the calculated pattern to the measured one. They are only meaningful if all phases are included in the refinement. However, the most important way to determine the quality of a Rietveld fit is by viewing the observed and calculated patterns graphically (difference plot) and to ensure that the model is chemically plausible (McCusker et al. 1999 and Toby 2006).

R_{wp} The weighted-profile R -factor (Equation B.6) is an indicator for the fit quality. Misfits at low intensities are weighted higher than misfits at peak tops. R_{wp} is influenced by the background, therefore, a refinement with a high background and poor counting statistics can result in good R_{wp} values even if the overall refinement is of low quality. Good values for R_{wp} are around 10%.

R_{exp} The expected R -factor (Equation B.7) reflects data quality (counting statistics). It indicates the lowest possible R_{wp} when using available data with the current refinement model.

χ^2 For a perfect refinement, the goodness of fit parameter χ^2 (Equation B.8) approaches

1. If data are over collected (i.e. high-intensity data where errors are dominated by the structural model and not the data), R_{exp} is very small, resulting in a large χ^2 . If data have been collected too quickly, R_{exp} will be large and χ^2 can be less than 1.

R_B The Bragg R -factor (Equation B.9) is not used in the refinement process, however, it can be used to monitor the improvement of the model. The better the model, the lower R -Bragg.

$$R_{\text{wp}} = \sqrt{\frac{\sum_i w_i (y_{i,\text{obs}} - y_{i,\text{calc}})^2}{\sum_i w_i (y_{i,\text{obs}})^2}} \quad (\text{B.6})$$

$$R_{\text{exp}} = \sqrt{\frac{N - P}{\sum_i w_i (y_{i,\text{obs}})^2}} \quad (\text{B.7})$$

$$\chi^2 = \frac{R_{\text{wp}}}{R_{\text{exp}}} \quad (\text{B.8})$$

$$R_B = \sum_{hkl} \frac{|I_{hkl,\text{obs}} - I_{hkl,\text{calc}}|}{\sum_{hkl} |I_{hkl,\text{obs}}|} \quad (\text{B.9})$$

Where $y_{i,\text{obs}}$ is observed intensity at step i ; $y_{i,\text{calc}}$ is calculated intensity at step i ; w_i is a weighting factor; N is number of data points; P is number of refined parameters and I_{hkl} is intensity of a Bragg reflection.

B.4 High-Temperature Measurements Using the Anton-Paar HTK 1200 Furnace

Mounting the Anton-Paar HTK 1200 Furnace

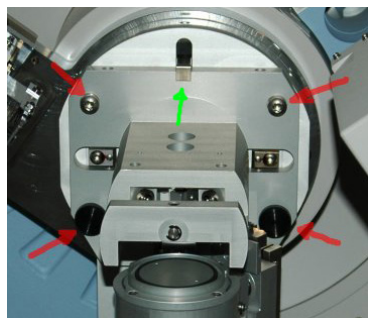


Fig. B1.19: Spinner unmount.



Fig. B1.20: Insert the screws.

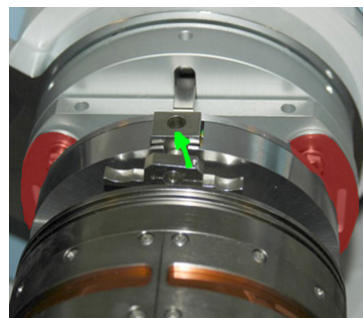


Fig. B1.21: Attach the HTK.

Unmount the sample spinner by loosening the four black screws (red arrows, Figure B1.19). The spinner is still held by the latch at the top (green arrow, B1.19). Hold the spinner with one hand and lift the latch. Pull the spinner away towards you.

Insert the four hex-head bolts with washers and let them stick out ca. 1.5 cm (marked red, Figure B1.20).

With one hand, attach the HTK onto the goniometer while simultaneously lifting the latch. As soon as the latch has snapped in place, the HTK is fixed. Add the metal plates (marked red, Figure B1.21) between the HTK stage and the hex-head screws and tighten them carefully.



Fig. B1.22: Micrometer.



Fig. B1.23: Sample cup.

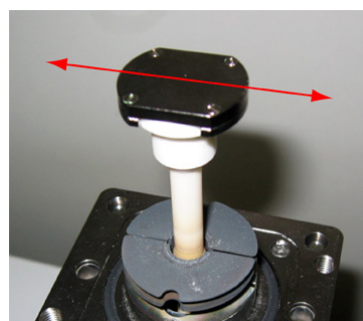


Fig. B1.24: Alignment slit.

Mount the micrometer on top of the motorized stage of the HTK (green arrow, Figure B1.22) and tighten it using the butterfly nut.

Screw a sample cup onto the HTK spinner (Figure B1.23). Tighten gently!

Attach the alignment slit onto the sample cup. The two slit openings must be perpendicular to the goniometer axis and face the X-ray tube and the detector (arrows, Figure B1.24).

Slide the spinner into the HTK by making sure the guidance is aligned (Figure B1.25). Tighten all four knurled screws gently by hand. **Do not switch on the sample spinner!**

Slide in the 0.1 mm Cu attenuator foil in the primary beam path (Figure B1.26). **Do not continue without the attenuator foil!** Open the cooling-water tap (Figure B1.27) and check for leaking water. Switch on the heater (gray switch on HTK controller at the lower left of diffractometer).

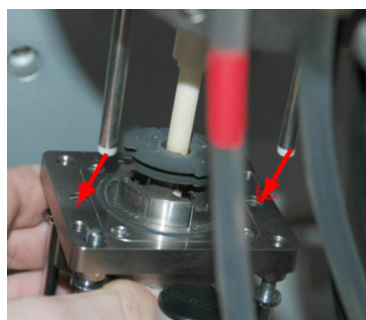


Fig. B1.25: Insert the spinner.



Fig. B1.26: Insert attenuator.



Fig. B1.27: Water tap.

Start the X'Pert DataCollector software. Before connecting to the instrument, go to the 'Tools' menu and select 'Exchange Sample Stage'. Change the sample stage to 'Anton Paar HTK-1200 Oven' and click 'Apply'. Confirm all messages and connect to the diffractometer.

Adjusting the Height and Rotation of the High-Temperature Furnace

Adjusting HTK rotation. This is an essential step. With the Cu attenuator foil inserted, set the generator to 40 kV, 30 mA. In the same panel where generator settings are set (Instrument Settings Tab), apply the settings (and change/check them if necessary) as listed in Table B1.5.

Table B1.5: Instrument settings for aligning the HTK rotation.

Instrument settings	Incident beam optics	Diffracted beam optics
Generator: 40 kV, 30 mA	Fixed DivSlit = $1/16^\circ$	Fixed Antiscatter = 4°
Temperature: 25°C	Antiscatter Slit = none	Soller Slits = 0.02 rad.
Positions: All 0°	Soller Slits = 0.02 rad.	Detector = receiving slit
	Mask = 10 mm	

Choose 'Manual Scan' from the 'Measure' menu and perform a manual scan of type 'Omega Scan' with a step size of $0.02^\circ/\text{step}$, a scan range of 2° Omega and a counting time of 0.25

sec/step. This moves the X-ray tube from -1° to $+1^\circ$ Omega (angle between the horizontal and the X-ray source) by keeping the detector at Omega + 180° .

When the scan has finished, immediately close the shutter by clicking on the arrow (four icons to the left of the stop icon) in the DataCollector toolbar. The resulting curve shows an intensity distribution of the primary beam passing through the alignment slit. The curve looks similar to Figure B1.28 with the maximum intensity most likely not at 0° Omega because the HTK is rotated.

Right-click into the measured peak and select 'Peak Parameters' from the popup menu. The appearing window shows peak information and the peak position (Figure B1.29).

In the 'Peak Parameters' window, press the 'Move To' button. The goniometer will move to that position, keeping the detector at Omega + 180° . Note the new position and the offset in the Instrument Settings Tab on the left side of DataCollector. This position will be the new zero position for the high-temperature measurement.

In the 'User Settings' menu, select 'Fine Calibration Offsets'. Press 'Set New = 0'. In the Instrument Settings Tab, new Omega and 2-Theta positions and the offset will now be zero.

Repeat the manual Omega scan. The peak position should now be close to 0° Omega. If this is not the case, reset the fine calibration offsets and start again.

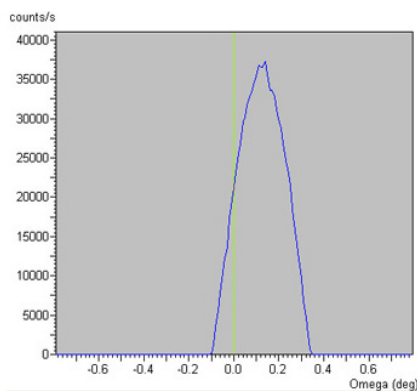


Fig. B1.28: Omega scan.

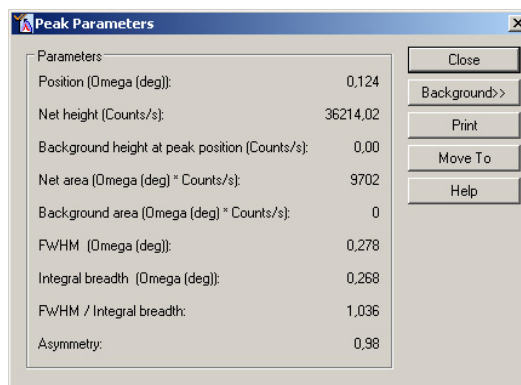


Fig. B1.29: Peak parameters window.

Ajdusting HTK height. Switch the micrometer on. Apply settings (and change/check them if necessary) as listed in Table B1.6.

Start a manual scan of '2-Theta' type with a step size of $0.016xx^\circ$ /step, a scan range of 1° 2-Theta and a counting time of 2 s/step. This keeps the X-ray tube at 0° Omega and moves the detector from -0.5° to $+0.5^\circ$ 2-Theta (angle between horizontal and the detector). Close the shutter immediately! If the resulting peak maximum is close to 0° 2-Theta, height

Table B1.6: Instrument settings for aligning the HTK height.

Instrument settings	Incident beam optics	Diffracted beam optics
Generator: 40 kV, 30 mA	Fixed DivSlit = $1/8^\circ$	Fixed Antiscatter = $1/8^\circ$
Temperature: 25° C	Antiscatter Slit = none	Soller Slits = 0.02 rad.
Positions: All 0°	Soller Slits = 0.02 rad.	Detector = scanning mode
	Mask = 10 mm	

is almost properly aligned. Right-click the peak and select 'Peak Parameters'. Write down intensity and position. If the peak maximum is at negative 2-Theta angles, the height is too low and vice versa.

Set the motor speed of the alignment stage to a low setting (black remote control on the right side of the diffractometer) and move the HTK 0.02 mm up. Perform the same scan again, close the shutter. Write down the intensity of the peak. If intensity is higher, go further upwards to find the maximum intensity. If intensity is lower, go back to 0 mm, then to -0.02 mm and repeat this step. When you have found the maximum intensity, the HTK is correctly aligned.

Always insert the beam attenuator when aligning to avoid detector damage!

Never start a measurement with the micrometer attached. The X-ray tube and detector will hit the micrometer!

Remove the 0.1 mm Cu Attenuator before you start measuring.

When finished, reset all fine calibration offsets and change the sample stage back to spinner in DataCollector.

If you are lost... Coarse alignment when the HTK is completely misaligned. Be sure what you do and clear all fine calibration offsets before starting this procedure!

With the 0.1 mm Cu attenuator foil inserted and no sample spinner in the furnace, move Omega and 2-Theta to 0° . Set the same settings as in Table B1.5 and start a manual '2-Theta' scan with a scan range of 2° 2-Theta and 1 s/step to measure the intensity distribution of the primary beam (Figure B1.30). Select 'Peak Mode'. The primary beam center must be located at 0° . Print out this measurement. Mount an empty sample holder and perform the same manual scan again. Adjust the height of the HTK until the negative 2-Theta part of the primary beam is obscured by the sample cup (i.e. from -0.25° to 0° in Figure B1.31). The maximum of the measured peak should be located in the middle between 0° 2-Theta and the right flank of the primary beam measured before (compare with the printout). The left flank of the peak should be close to 0° (Figure B1.31). Lowering the furnace will move the peak to lower angles, raising it will move the peak to higher angles. When an intensity distribution

as in Figure B1.31 is reached, continue with adjusting HTK rotation.

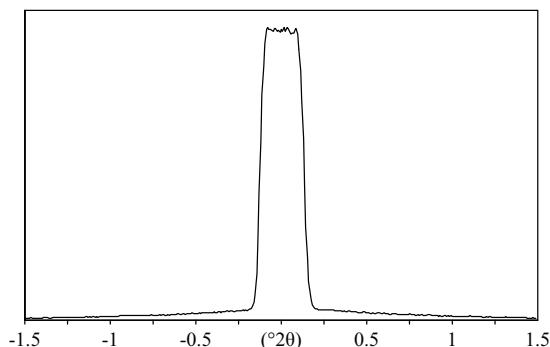


Fig. B1.30: Primary beam distribution.

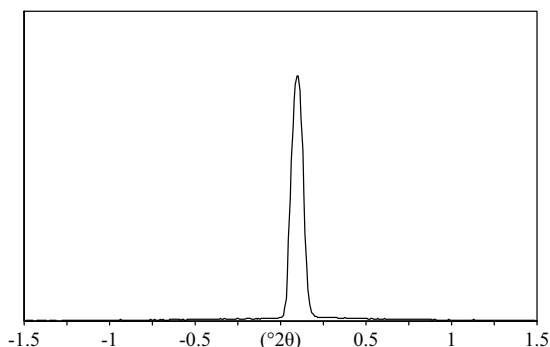


Fig. B1.31: Sample cup at correct height.

After the Measurement: Correct Diffraction Patterns for Height-Displacement

Due to thermal expansion of the HTK sample spinner, the sample moves out of the goniometer focus at high temperature. Peak positions will be shifted. To correct this, open the .xrdml file(s) in HighScore Plus Plus and select 'Correct Sample Displacement' from the 'Corrections' submenu in the 'Treatments' menu. Enter the negative value from Table B1.7. Note: HighScore Plus Plus appends data points with zero intensity at the end of the pattern, which must be clipped. For Rietveld refinements, it is also possible to use uncorrected patterns, however, height displacement starting values should be used according to Table B1.7.

Table B1.7: Height displacement due to expansion of the HTK 1200 sample spinner (mm, °C).

Temp.	Displ.	Temp.	Displ.	Temp.	Displ.	Temp.	Displ.
25	0.000	325	0.098	625	0.220	925	0.360
50	0.010	350	0.105	650	0.230	950	0.370
75	0.020	375	0.113	675	0.240	975	0.380
100	0.030	400	0.120	700	0.250	1000	0.390
125	0.038	425	0.133	725	0.263	1025	0.405
150	0.045	450	0.145	750	0.275	1050	0.420
175	0.053	475	0.158	775	0.288	1075	0.435
200	0.060	500	0.170	800	0.300	1100	0.450
225	0.068	525	0.180	825	0.313	1125	0.465
250	0.075	550	0.190	850	0.325	1150	0.480
275	0.083	575	0.200	875	0.338	1175	0.495
300	0.090	600	0.210	900	0.350	1200	0.510

B.5 Rietveld Refinements with Topas Academic v. 4.1

Using Topas Academic with jEdit

Topas Academic (Coelho 2007a) is operated with input text files containing specific keywords. The files are updated after each refinement. In order to easily access all keywords, a macro creating color-coded Topas input files for the java based text editor jEdit (www.jedit.org) is available (Figure B1.32). The macro was written by John S. O. Evans and can be obtained at the Topas Academic webpage of the University of Durham, UK at www.dur.ac.uk/john.evans/topas_academic/topas_main.htm. When both jEdit and Topas Academic programs are running, an input file edited in jEdit can be sent to Topas Academic by pressing the button marked red in Figure B1.32. All keywords can be accessed from the tree in the left side of the jEdit window (highlighted green in Figure B1.32).

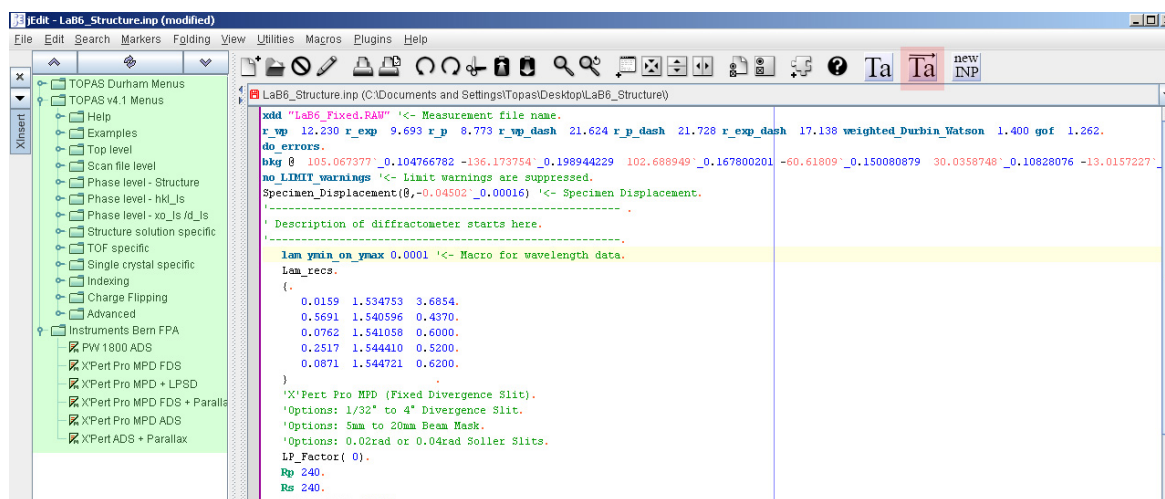


Fig. B1.32: Using jEdit with Topas Academic. The red button sends the input file to Topas. From the area highlighted in green, keywords can be inserted to the input file by simply clicking them.

Peak Shape Modeling in Topas Academic

Topas allows peak shape modeling by using the Fundamental Parameter Approach (Cheary and Coelho 2004) in which peak profiles are simulated depending on the diffractometer setup instead of being determined from a standard material (usually NIST SRM 660a LaB_6) and approximated using profile functions such as pseudo Voigt, split pseudo Voigt etc. Setting up a description of a laboratory diffractometer (PANalytical X'pert Pro MPD) for the fundamental parameter approach is shown in the commented example below:

```
lam ymin_on_ymax 0.0001
Lam_recs
{ 0.0159 1.534753 3.6854
  0.5691 1.540596 0.4370
  0.0762 1.541058 0.6000
  0.2517 1.544410 0.5200
  0.0871 1.544721 0.6200 } 'the first seven lines describe the wavelengths
LP_Factor(0) 'monochromator angle (°)
Rp 240 'primary beam radius (mm)
Rs 240 'diffracted beam radius (mm)
Slit_Width(0.07) 'receiving slit width (0.07 mm for X'Celerator detector)
Divergence(0.125) 'divergence slit (°)
axial_conv
filament_length 12 'length of X-ray tube filament (mm)
sample_length 10 'irradiated sample length parallel to the goniometer axis in (mm)
receiving_slit_length 15 'length of receiving slit parallel to the goniometer axis (mm)
primary_soller_angle 2.55 'opening of primary soller slits (°)
secondary_soller_angle 2.55 'opening of diffracted beam soller slits (°)
```

If the sample is measured with constant irradiated length instead of a fixed divergence slit, replace 'Divergence(0.125)' with the two keywords below:

```
Variable_Divergence_Shape(10) ' irradiated sample length (mm)
Variable_Divergence_Intensity
```

Creating an Input File for Topas Academic in jEdit

When creating an input file in jEdit for Topas Academic some important points have to be considered:

- Wavelength profiles are entered by clicking 'Emission profile(s)' from the 'Scan file level' branch. For laboratory diffractometers without primary beam monochromator, select 'CuKa5_Berger.lam'. Use 'CuKa4_Holzer.lam' if the instrument is equipped with a diffracted beam monochromator.
- The diffractometer description for the fundamental parameter approach can be inserted by selecting the corresponding diffractometer from the 'Instruments FPA Bern' menu. Check if you are using the correct configuration!
- The simplest way to add a structure is by clicking 'Insert CIFs in INP format' from the 'Phase level - Structure' menu. Do not forget to add the scale factor ('scale') and 'CS_L', 'CS_G', 'Strain_L' and 'Strain_G' keywords to allow for peak broadening due to microstructural effects.
- Refining parameters in Topas is done by adding an @ sign in front of them. Basically, any character combination can be used as parameter name and this is the only way to refine more than one parameter simultaneously. With: x @ 0.1234 y @

0.1234 z @ 0.1234, each coordinate is refined individually. By replacing the @ symbol with any character combination (in this example 'refinetogether'), coordinates are refined together: x refinetogether 0.1234 y refinetogether 0.1234 z refinetogether 0.1234. If you do not want a parameter to be refined, simply remove the @ sign or write an ! before the parameter name: !refinetogether is not refined. Special positions must be input as fraction followed by a semicolon: do not enter x 0.33 or y 0.66 but x = 1/3; and y = 2/3;, respectively. Note the = sign and the semicolon. Ignoring this can lead to very wrong results!

- Lattice parameters can be defined in two ways: For each crystal system, a macro is available (in the 'Lattice parameters' menu in jEdit). For example, the 'Hexagonal (@ 5.123, @ 6.321)' macro implies that $a = b = 5.123 \text{ \AA}$, $c = 6.321 \text{ \AA}$, $\alpha = \beta = 90^\circ$ and $\gamma = 120^\circ$. If you do not want to use the macro, you can add lattice parameters by writing a, b, c, al, be, ga followed by @ and the value on a new line each. The hexagonal macro above is then replaced with: a @ 5.123, b = Get(a);, c @ 6.321, al 90, be 90, ga 120. For equivalent lattice parameters it is mandatory to use the =Get(); function or at least the same parameter name.
- When the input file is updated, values and standard deviations are displayed as follows: 4.15 ` _0.01. The number before the ` sign is the refined value. The number after the _ sign is the estimated standard deviation (esd) of the value.

Example Topas Input Files

The following input files and corresponding patterns are from real refinements. However, they are printed here for demonstration purposes only and do not claim to be accurate as some parts have been deleted for reasons of clarity, some numbers have been shortened and esd values deleted.

LeBail Refinement of LaB₆. An input file of a LeBail refinement of LaB₆ is listed below and a final refinement plot is shown in (Figure B1.33). In contrast to the Rietveld method, structure factors are not calculated from the structure but are set to an equal value at the beginning of the refinement. During the refinement, those values are used as start values to calculate 'observed intensities', which are then again used as new 'calculated intensities' and so on. The LeBail refinement can be used to determine structurally independent parameters (e.g. lattice parameters, peak shape, microstructural effects), and to extract intensities which can then be used for structure solution. In a LeBail refinement, intensities do not contribute to the correlation matrix.

```
xdd "LaB6_Fixed.XY"
x_calculation_step 0.01
r_wp 11.083 r_exp 9.693 r_p 7.801 r_wp_dash 19.685 r_p_dash 19.821
r_exp_dash 17.216 weighted_Durbin_Watson 1.724 gof 1.143
do_errors
bkg @ 109.216959 ... .. 9.0985598
no_LIMIT_warnings
Specimen_Displacement(@, -0.04025)
```

This section contains the measurement file name (xdd LaB6_Fixed.XY), agreement factors, refined Chebyshev background parameters (two shown), the command to calculate errors (do_errors), a command to not display limit warnings (no_LIMIT_warnings) and refined specimen displacement in mm. Because the diffraction pattern is input as an .xy file, the step size has to be defined using the keyword x_calculation_step.

```
lam ymin_on_ymax 0.0001
Lam_recs
{ 0.0159 1.534753 3.6854
  0.5691 1.540596 0.4370
  0.0762 1.541058 0.6000
  0.2517 1.544410 0.5200
  0.0871 1.544721 0.6200 }
LP_Factor(0)
Rp 240
Rs 240
Slit_Width(0.07)
Divergence(0.125)
axial_conv
filament_length 12
sample_length 10
receiving_slit_length 15
primary_soller_angle 2.55
secondary_soller_angle 2.55
```

This part contains information to describe diffractometer settings and the wavelength for the fundamental parameter approach. The sample was measured with a fixed divergence slit with an opening of 0.125°.

```
hkl_Is
leball 1
phase_name LaB6
Cubic(@ 4.15712`_0.00000)
LVol_FWHM_CS_G_L(1, 2388.65106, 0.89, 3171.56454, csgc, 9765.63203, cs1c, 4143.99750)
e0_from_Strain(0.00097, sgcl, 0.00010, slc1, 0.00390)
volume 71.8416653
space_group "Pm-3m"
load hkl_m_d_th2 I
{ 0 0 1 6 4.15711 21.35683 11.2092731
  ... not all shown }
```

The 'hkl_Is' and 'leball 1' keywords indicate that structural information for a LeBail refinement follows. Required information are the lattice parameters ('Cubic' macro where $a = b = c$ and angles = 90°) and space group. The 'LVol_FWHM_CS_G_L' macro calculates the size of coherently scattering domains ('crystallite size'), whereas the macro 'e0_from_Strain' calculates $\epsilon_0 = \Delta d/d$. As LaB₆ should have infinite crystallite size and no microstrain, the

pattern does not significantly change when no microstructural model is applied. The 'volume' keyword calculates the unit cell volume, 'space_group' indicates the space group. The 'load hkl_m_d_th2 I' keyword is added automatically in the first refinement step and includes all reflections according to the space group and lattice parameters with their *hkl*, multiplicity, d-spacing, 2-Theta values and intensities. In a LeBail refinement, no intensity errors are calculated.

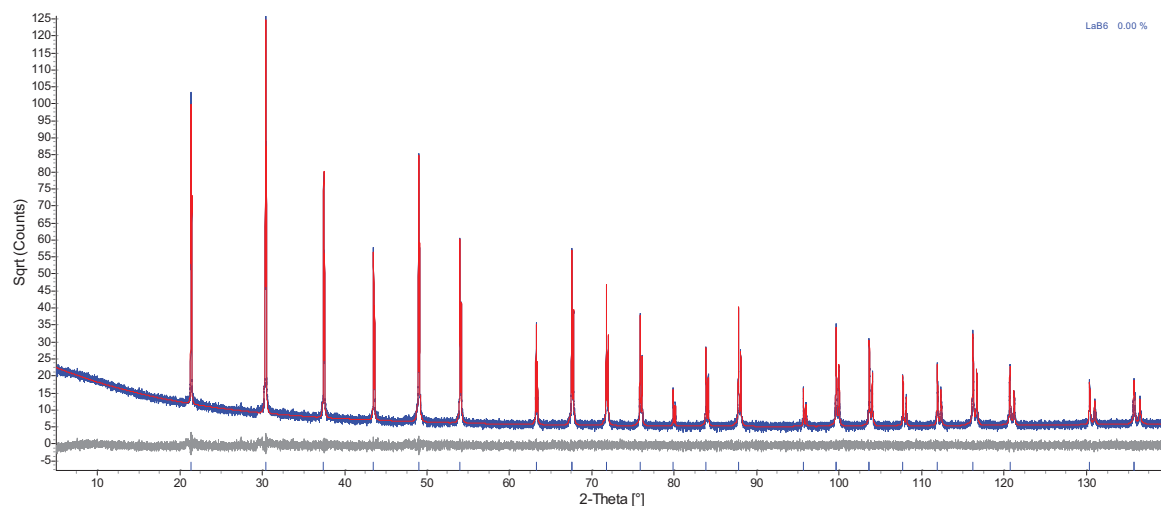


Fig. B1.33: Final refinement plot of the LeBail refinement of LaB_6 . The blue curve is the measured data, the red curve is the calculated pattern and the gray plot is the difference between observed and calculated data. *hkl* ticks of LaB_6 are shown in blue. The quantitative result is zero because no structural information is provided.

Pawley Refinement of LaB_6 . In a Pawley refinement, structure factors are not calculated from the structure but are refined as independent parameters for each reflection. They contribute to the correlation matrix. As a LeBail refinement, it can be used to determine structurally independent parameters and to extract intensities which can then be used for structure solution. In contrast to a LeBail refinement, correlation of the individual intensities can be used as additional information for structure solution. The input file is shown below and the final refinement plots are shown in Figure B1.34.

```
xdd "LaB6_Fixed.raw"
r_wp 10.966 r_exp 9.690 r_p 7.591 r_wp_dash 19.476 r_p_dash 19.284
r_exp_dash 17.208 weighted_Durbin_Watson 1.741 gof 1.132
do_errors
bkg @ 109.178088 ... .. 0.928684605
no_LIMIT_warnings
Specimen_Displacement (@, -0.04115)
```

This section contains the measurement file name (xdd LaB6_Fixed.raw), agreement factors, refined Chebyshev background parameters (two shown), the command to calculate errors (do_errors), a command to not display limit warnings (no_LIMIT_warnings) and refined specimen displacement in mm.

```
lam ymin_on_ymax 0.0001
Lam_recs
{ 0.0159 1.534753 3.6854
  0.5691 1.540596 0.4370
  0.0762 1.541058 0.6000
  0.2517 1.544410 0.5200
  0.0871 1.544721 0.6200 }
LP_Factor(0)
Rp 240
Rs 240
Slit_Width(0.07)
Divergence(0.125)
axial_conv
filament_length 12
sample_length 10
receiving_slit_length 15
primary_soller_angle 2.55
secondary_soller_angle 2.55
```

This part contains information to describe diffractometer settings and the wavelength for the fundamental parameter approach. The sample was measured with a fixed divergence slit with an opening of 0.125° .

```
hkl_Is
phase_name LaB6
Cubic(@ 4.15713`_0.00000)
LVol_FWHM_CS_G_L(1, 642.87869, 0.89, 696.16852, csgc, 962.01337, cs1c, 2435.82068)
e0_from_Strain(0.00022, sgcl, 0.00010, slcl, 0.00086)
volume 71.8421992`_0.000166559246
space_group "Pm-3m"
load hkl_m_d_th2 I
{ 0 0 1 6 4.15714 21.35670 @ 11.2568643`_0.0345796072
  0 1 1 12 2.93954 30.38313 @ 37.2642101`_0.0896171236
  ... not all shown }
```

The 'hkl_Is' keyword indicates that structural information for a Pawley refinement follows. Required information are the lattice parameters ('Cubic' macro where $a = b = c$ and angles = 90°) and space group. The 'LVol_FWHM_CS_G_L' macro calculates the size of coherently scattering domains ('crystallite size'), whereas the macro 'e0_from_Strain' calculates $\epsilon_0 = \Delta d/d$. As LaB_6 should have infinite crystallite size and no microstrain, the pattern does not significantly change when no microstructural model is applied. The 'volume' keyword calculates the unit cell volume, 'space_group' indicates the space group. The 'load hkl_m_d_th2 I' keyword is added automatically in the first refinement step and includes all reflections according to the space group and lattice parameters with their hkl , multiplicity, d-spacing, 2-Theta values and intensities with esd.

Rietveld Refinement of LaB_6 . In a Rietveld refinement, peak intensities (structure factors) are calculated from the structural content (atoms) of the unit cell. With this method, the unit cell weight is known and quantitative phase analysis of crystalline powder mixtures is possible. The input file is shown below and the final refinement plot is shown in Figure B1.35.

```
xdd "LaB6_Fixed.RAW"
r_wp 12.230 r_exp 9.693 r_p 8.773 r_wp_dash 21.624 r_p_dash 21.728
```

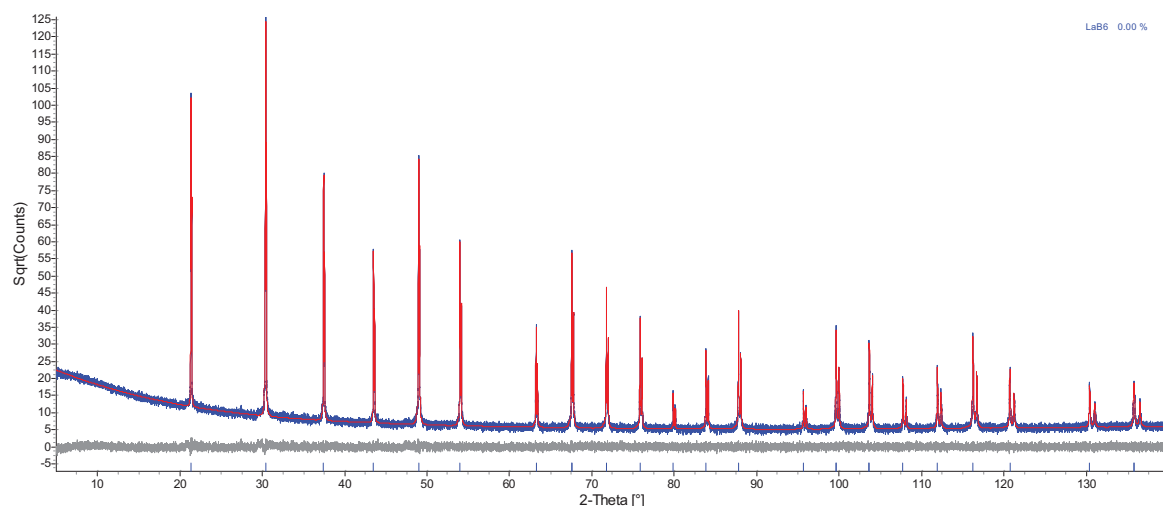


Fig. B1.34: Final refinement plot of the Pawley refinement of LaB_6 . The blue curve is the measured data, the red curve is the calculated pattern and the gray plot is the difference between observed and calculated data. hkl ticks of LaB_6 are shown in blue. The quantitative result is zero because no structural information is provided.

```
r_exp_dash 17.138 weighted_Durbin_Watson 1.400 gof 1.262
do_errors
bkg @ 105.067377 ... .. -13.0157227
no_LIMIT_warnings
Specimen_Displacement(@, -0.04502)
```

This section contains the measurement file name (xdd LaB6_Fixed.raw), agreement factors, refined Chebyshev background parameters (two shown), the command to calculate errors (do_errors), a command to not display limit warnings (no_LIMIT_warnings) and refined specimen displacement in mm.

```
lam ymin_on_ymax 0.0001
Lam_recs
{ 0.0159 1.534753 3.6854
  0.5691 1.540596 0.4370
  0.0762 1.541058 0.6000
  0.2517 1.544410 0.5200
  0.0871 1.544721 0.6200 }
LP_Factor(0)
Rp 240
Rs 240
Slit_Width(0.07)
Divergence(0.125)
axial_conv
filament_length 12
sample_length 10
receiving_slit_length 15
primary_soller_angle 2.55
secondary_soller_angle 2.55
```

This part contains information to describe diffractometer settings and the wavelength for the fundamental parameter approach. The sample was measured with a fixed divergence slit with an opening of 0.125° .

```
str
phase_name LaB6
Cubic(@ 4.15700`_0.00001)
LVol_FWHM_CS_G_L(1, 892.44090, 0.89, 1048.48902, csgc, 1768.25873, cs1c, 2201.61914)
e0_from_Strain(0.00005, sgc1, 0.00010, slc1, 0.00012)
MVW(203.778, 71.8356248`_0.000299689962, 100.000`_0.000)
volume 71.8356248`_0.000299689962
space_group "Pm-3m"
scale @ 0.00133340363
site La1 x 0.0 y 0.0 z 0.0 occ La 1.0 beq @ 0.1444`_0.0068
site B1 x @ 0.19968`_0.00048 y 0.5 z 0.5 occ B 1.0 beq @ 0.0145`_0.0413
```

The 'str' keyword indicates that a structural description of a crystallographic unit cell follows. The 'LVol_FWHM_CS_G_L' macro calculates the size of coherently scattering domains ('crystallite size'), whereas the macro 'e0_from_Strain' calculates $\epsilon_0 = \Delta d/d$. As LaB_6 is the NIST standard reference material 660a used for line profile calibration of a diffractometer. The pattern does not significantly change when no microstructural model is applied! Lattice parameters are defined by using a macro ('Cubic' macro where $a = b = c$ and angles = 90°). The 'volume' keyword outputs the unit cell volume, 'space_group' indicates the space group. The 'MVW' macro outputs unit cell mass, volume and weight percentage of the phase. The scale factor is used for linear scaling of the calculated pattern. It is also used for the calculation of the phase amount in quantitative analyses. The next two lines contain atomic site information. The site name follows the keyword 'site'. Next, x , y and z coordinates are given. The 'occ' keyword is followed by the atom type and its occupancy fraction. 'beq' is the keyword for isotropic displacement parameters.

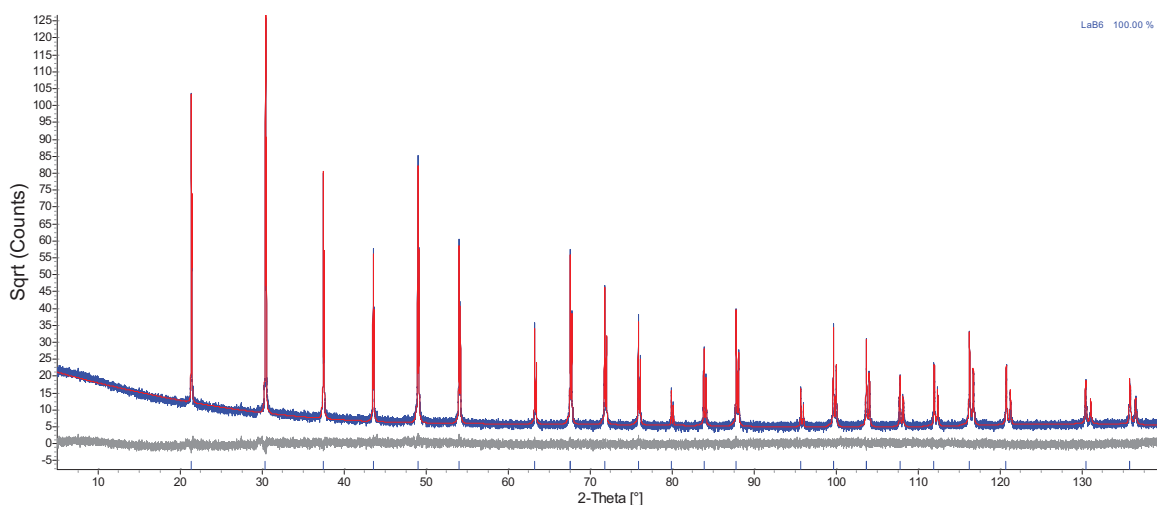


Fig. B1.35: Final refinement plot of the Rietveld refinement of LaB_6 . The blue curve is the measured data, the red curve is the calculated pattern and the gray plot is the difference between observed and calculated data. hkl ticks of LaB_6 are shown in blue. The quantitative result top right is Rietveld wt.-%, which is 100% because only one phase is present.

Indexing of LaB_6 . The following example demonstrates how to index a powder pattern. For obtaining good results, the pattern must have a reasonable s/n ratio and peaks must be well resolved. It is best to use single phase samples. Lattice parameters found by indexing

can then be used with Pawley and LeBail refinements, as well as for phase identification and structure solution.

1. Open Topas Academic and load the powder pattern (previously converted to Bruker .raw format). Go to 'File' menu and select 'Load Scan Files'.
2. Once the pattern is loaded, select 'Search Peaks' from the 'View' menu. Change peak width and noise threshold values until all peaks are found. You should see a screen as in Figure B1.36.
3. Open the tree view in the 'Parameter Window', select the list with the peak positions. Right-click and select copy all/selection (Figure B1.37).

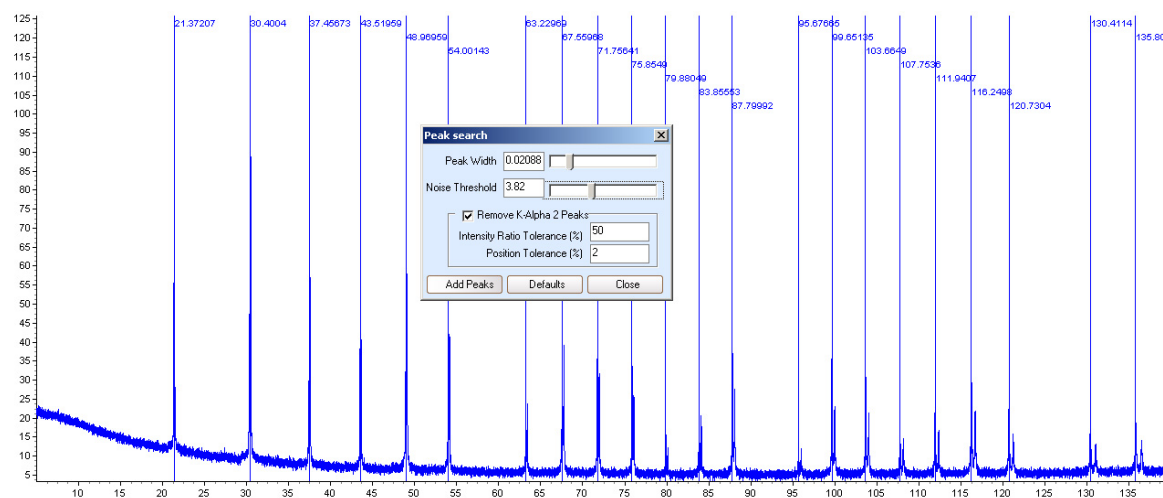


Fig. B1.36: Topas screen after peak search. The blue lines indicate identified peaks, 2-Theta angles are written next to the lines.

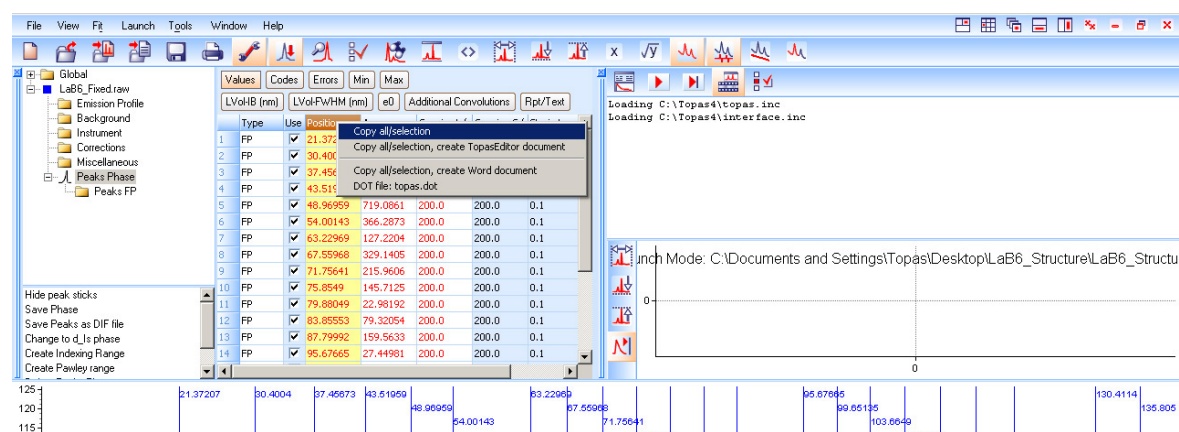


Fig. B1.37: Copy all peak positions from the 'Parameter Window'.

4. Open jEdit and create a new input file for Topas containing the measurement file name, diffractometer setup, wavelength information and background (see below). Add the keyword 'xo_Is', followed by the 'CS_L', 'CS_G',

'Strain_L' and 'Strain_G' keywords in order to allow peak broadening. Next, paste the peak list copied in step 3. Refine all positions by adding an @ sign in front of each peak position. Add @ 1 after each peak. This value is the intensity, which will also be refined. Send the file to Topas and run. After refining peak positions and intensities, you should get a screen as in Figure B1.38.

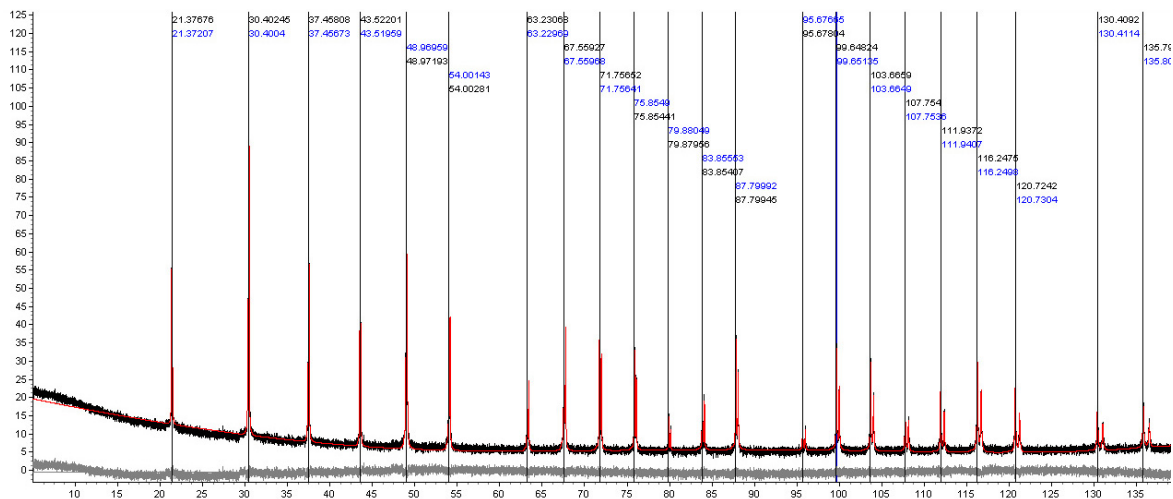


Fig. B1.38: The red curve is the pattern calculated from refined background, peak positions and peak intensities. Peak positions written in blue are positions from peak search, those in black after the refinement.

```
xdd LaB6_Fixed.raw
lam ymin_on_ymax 0.0001
Lam_recs
{ 0.0159 1.534753 3.6854
  0.5691 1.540596 0.4370
  0.0762 1.541058 0.6000
  0.2517 1.544410 0.5200
  0.0871 1.544721 0.6200 }
LP_Factor(0)
Rp 240
Rs 240
Slit_Width(0.07)
Divergence (0.125)
axial_conv
filament_length 12
sample_length 10
receiving_slit_length 15
primary_soller_angle 2.55
secondary_soller_angle 2.55
bkg @ 0 0 0 0 0
xo_Is
CS_L(@, 300)
CS_G(@, 300)
Strain_L(@, 0.05)
Strain_G(@, 0.05)
load xo I {
@ 21.3767632 @ 1
@ 30.4024544 @ 1
```

```
... not all shown }
```

- Go back to jEdit and copy the list of refined peak positions and peak intensities from the updated file to the clipboard. Create a new input file with the keywords 'seed', 'index_lam 1.540596', 'index_zero_error' and keywords for each crystal system that should be included in the indexing process. As we know that LaB_6 is a cubic phase, we only include the cubic crystal systems with the 'Cubic_F', 'Cubic_I', 'Cubic_P' keywords. Add 'load index_th2 index_I' and paste the reflection positions and intensities copied from the old file. Make sure they are no longer refined by removing the @ sign. Compare with the input shown below, send to Topas and run.

```
seed
index_lam 1.540596
index_zero_error
Cubic_F
Cubic_I
Cubic_P
load index_th2 index_I
{ 21.3767632 11.1481021
  30.4024544 37.0553548
... not all shown }
```

- When indexing has finished, go back to jEdit and open the new .ndx file (see below, only the first few lines are shown). Each row of the file contains a solution from the indexing process with line number, space group, status, number of unidentified reflections, cell volume, figure of merit, zero shift and lattice parameters (Coelho 2003). The first found solution with the highest figure of merit is already the correct one despite the obviously incorrect space group. This is because in powder diffraction, several space groups can not be distinguished and space group $P23$ has the same hkl conditions as space group $Pm\bar{3}m$, which is the correct space group of LaB_6 (consult section 12.6 of the Topas Technical Reference). Select the contents of the .ndx file and copy all to the clipboard.

```
' Indexing method - Alan Coelho (2003), J. Appl. Cryst. 36, 86-95
' Time: 0.578 seconds
' Sg Status UNI Vol Gof Zero Lps...
Indexing_Solutions_With_Zero_Error_2 {
0) P23 2 0 71.854 2074.62 0.0203 4.1573 4.1573 4.1573 90.000 90.000 90.000 '== 22
1) F-43c 2 0 574.830 1675.65 0.0203 8.3147 8.3147 8.3147 90.000 90.000 90.000 '== 22
... not all shown
```

- Go back to Topas and select 'Load INP File' from the 'File' menu. Load the input file used for indexing and select it in the 'Parameter Window'. At the bottom of the 'Parameter Window', select 'Paste INP to Node/Selections' to paste all indexing solutions from the .ndx file. On the right side of the parameter window, click the 'Solutions' button to get a graphical display of cell volume vs. figure of merit (Figure B1.39).

Quantification of known phases in a crystalline sample. The following input file shows a quantification of two known phases CaF and $\text{Na}_2\text{Al}_2\text{Ca}_3\text{F}_{14}$ in a crystalline sample. The keyword 'weight_percent' outputs weight-% of each phase, normalized to 100%. Due to absorption of the $\text{Na}_2\text{Al}_2\text{Ca}_3\text{F}_{14}$ phase, peaks are slightly asymmetric. This is corrected using a special keyword. Quantitative results are 99.468(5) wt.-% $\text{Na}_2\text{Al}_2\text{Ca}_3\text{F}_{14}$ and 0.532(5) wt.-% CaF . The final refinement plot is shown in Figure B1.40.

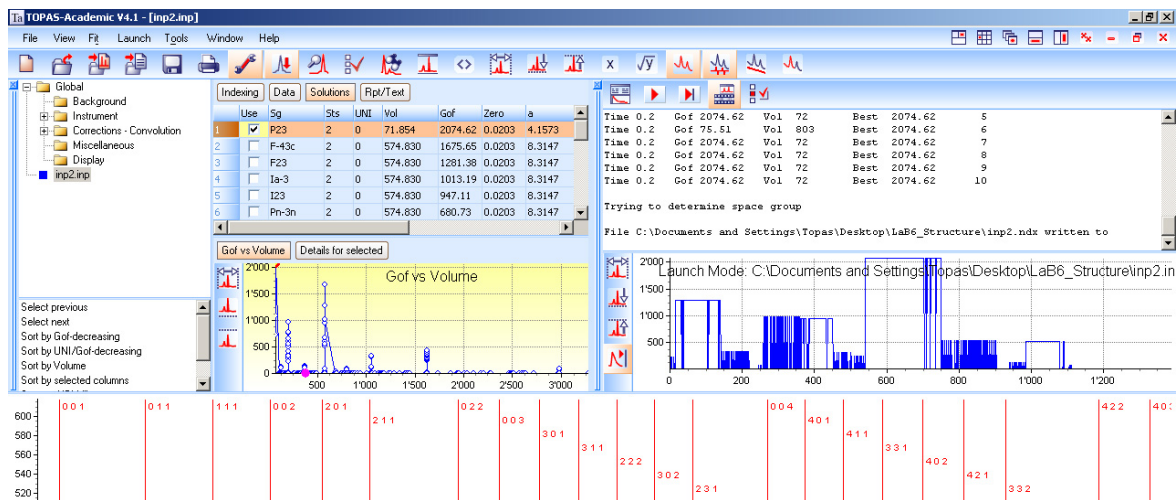


Fig. B1.39: Display of indexing solutions. Red lines are peaks belonging to the selected space group.

```
xdd "NAC.RAW"
r_wp 6.071 r_exp 3.920 r_p 4.577 r_wp_dash 10.995 r_p_dash 10.971
r_exp_dash 7.099 weighted_Durbin_Watson 0.895 gof 1.549
do_errors
bkg @ 426.075391 ... -2.45058623
no_LIMIT_warnings
Specimen_Displacement(@, -0.07846)
```

This section contains the measurement file name (xdd NAC.raw), agreement factors, refined Chebyshev background parameters (two shown), the command to calculate errors (do_errors), a command to not display limit warnings (no_LIMIT_warnings) and refined specimen displacement in mm.

```
lam ymin_on_ymax 0.0001
Lam_recs
{ 0.0159 1.534753 3.6854
  0.5691 1.540596 0.4370
  0.0762 1.541058 0.6000
  0.2517 1.544410 0.5200
  0.0871 1.544721 0.6200 }
LP_Factor(0)
Rp 240
Rs 240
Slit_Width(0.07)
Variable_Divergence_Shape(10)
Variable_Divergence_Intensity
axial_conv
filament_length 12
sample_length 10
receiving_slit_length 15
primary_soller_angle 2.55
secondary_soller_angle 2.55
```

This part contains information to describe diffractometer settings and the wavelength for the fundamental parameter approach. The sample was measured with an automatic divergence slit irradiating 10 mm of the sample surface. The

keyword 'Variable_Divergence_Intensity' corrects measured intensities.

```
str
phase_name NAC
Cubic(@ 10.25089`_0.00000)
LVol_FWHM_CS_G_L(1, 445.03952, 0.89, 491.92040, csgc, 710.14683, cs1c, 1474.39087)
e0_from_Strain(0.00004, sgc1, 0.00010, slc1, 0.00010)
MVW(1944.625, 1077.17204`_0.00133777644, 99.468`_0.005)
weight_percent 99.468`_0.005
space_group "I213"
scale @ 0.000721118589
site Ca1 x 0.46618 y 0.00000 z =1/4; occ Ca 1.0 beq 0.5771
site Al1 x 0.24754 y 0.24754 z 0.24754 occ Al 1.0 beq 0.5170
site Na1 x 0.08492 y 0.08492 z 0.08492 occ Na 1.0 beq 1.9929
site F1 x 0.13817 y 0.30571 z 0.12093 occ F 1.0 beq 0.7395
site F2 x 0.36357 y 0.36250 z 0.18886 occ F 1.0 beq 1.0556
site F3 x 0.46098 y 0.46098 z 0.46098 occ F 1.0 beq 0.4369
Absorption_With_Sample_Thickness_mm_Shape_Intensity(@, 69.10407, @, 3.11216)
```

This part contains structural information of the $\text{Na}_2\text{Al}_2\text{Ca}_3\text{F}_{14}$ phase. The 'LVol_FWHM_CS_G_L' macro calculates the size of coherently scattering domains ('crystallite size'), whereas the macro 'e0_from_Strain' calculates $\epsilon_0 = \Delta d/d$. The 'MVW' macro outputs unit cell mass, volume and wt.-% (also output by the 'weight_percent' keyword). Then follow space group, scale factor and atomic coordinates, occupancies and isotropic B_{eq} . The last macro corrects peak asymmetry due to sample absorption.

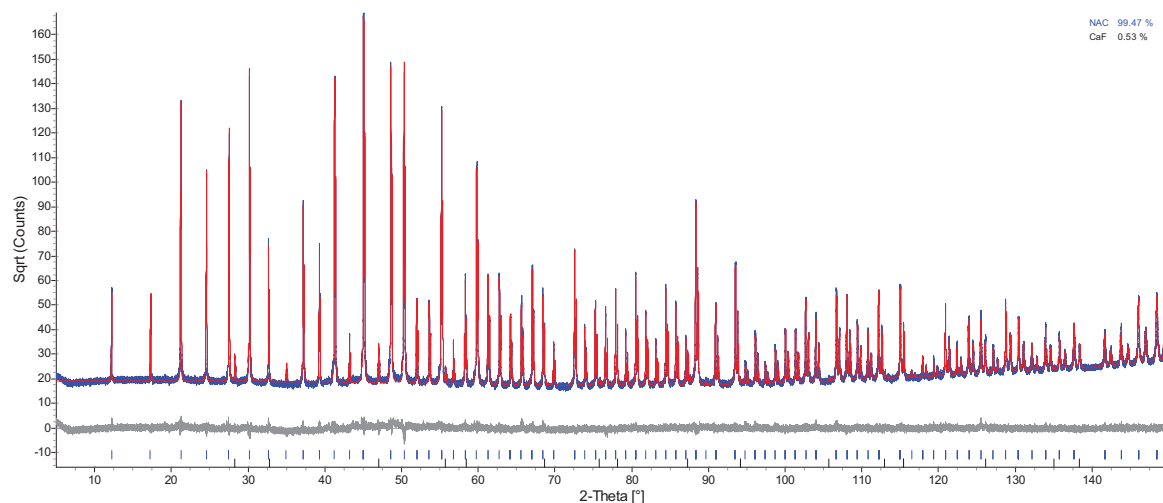


Fig. B1.40: Final refinement plot of the phase quantification. The blue curve is the measured data, the red curve is the calculated pattern and the gray plot is the difference between observed and calculated data. *hkl* ticks of $\text{Na}_2\text{Al}_2\text{Ca}_3\text{F}_{14}$ (blue) and CaF (black) are shown. The quantitative results top right are Rietveld wt.-%.

```
str
phase_name CaF
Cubic(@ 5.46555`_0.00003)
LVol_FWHM_CS_G_L(1, 445.03952, 0.89, 491.92040, csgc, 710.14683, cs1c, 1474.39087)
e0_from_Strain(0.00004, sgc1, 0.00010, slc1, 0.00010)
```

```
MVW(312.300, 163.268453`_0.00229605502, 0.532`_0.005)
weight_percent 0.532`_0.005
space_group "Fm-3m"
scale @ 0.000158590228
site Ca1 x 0.00 y 0.00 z 0.00 occ Ca 1.0 beq 0.5
site F1 x 0.25 y 0.25 z 0.25 occ F 1.0 beq 0.5
```

This part contains structural information of the CaF phase. The 'LVol_FWHM_CS_G_L' macro calculates the size of coherently scattering domains ('crystallite size'), whereas the macro 'e0_from_Strain' calculates $\epsilon_0 = \Delta d/d$. The 'MVW' macro outputs unit cell mass, volume and wt.-% (also output by the 'weight_percent' keyword). Then follow space group, scale factor and atomic coordinates, occupancies and isotropic B_{eq} . Due to the low amount of the CaF phase, B_{eq} of CaF can not be refined.

Quantification of amorphous content. The following input file describes how to quantify amorphous content. The sample was prepared from a mixture of 1g quartz (supposed as unknown), 0.5g silicon (supposed as admixed internal standard) and 0.5g glass (supposed as unknown amorphous phase). It is very important that the spiked phase has similar density and absorption properties as the other phases in the sample. The example shown below does not work when e.g. LiF is used as spike phase!

A simple quantification of quartz and silicon is performed and the Rietveld wt.-% are returned. However, they represent 100% of the crystalline phases of the mixture but not 100% of the total mixture. Ideally, Rietveld results should be 66.6% wt.-% quartz and 33.3 wt.-% silicon. It is known that 25 wt.-% silicon were added, therefore, 33.3 wt.-% silicon (from Rietveld refinements) represent 25 wt.-% of the total mixture. Normalization of the 33.3 wt.-% silicon to the 25 wt.-% silicon as admixed internal standard results in a corrected wt.-percentage of 50 wt.-% quartz for the measured 66.6 wt.-% quartz (from Rietveld). The difference to 100% represents the amorphous content of the sample: 100 wt.-% total – 25 wt.-% silicon – 50 wt.-% quartz = 25 wt.-% amorphous content (glass). This is done using the keyword 'spiked_phase_measured_weight_percent 25' in the structure description of the phase used as internal standard and 'corrected_weight_percent' in all other structures. The amorphous phase fraction can be output with 'weight_percent_amorphous'. The final refinement plot is shown in Figure B1.41.

```
xdd "Mixture.raw"
r_wp 10.747 r_exp 7.651 r_p 8.215 r_wp_dash 18.996 r_p_dash 19.772 r_exp_dash 13.523
weighted_Durbin_Watson 1.150 gof 1.405
do_errors
bkg @ 134.411527 ... .. -7.08022216
no_LIMIT_warnings
Specimen_Displacement(@, -0.03148)
```

This section contains the measurement file name (xdd Mixture.raw), agreement factors, ten refined Chebyshev background parameters (two shown), the command to calculate errors (do_errors), a command to not display limit warnings (no_LIMIT_warnings) and refined specimen displacement in mm.

```

lam ymin_on_ymax 0.0001
Lam_recs
{ 0.0159 1.534753 3.6854
  0.5691 1.540596 0.4370
  0.0762 1.541058 0.6000
  0.2517 1.544410 0.5200
  0.0871 1.544721 0.6200 }
LP_Factor( 0)
Rp 240
Rs 240
Slit_Width(0.07)
Divergence (0.125)
axial_conv
filament_length 12
sample_length 10
receiving_slit_length 15
primary_soller_angle 2.55
secondary_soller_angle 2.55

```

This part contains information to describe diffractometer settings and the wavelength for the fundamental parameter approach. This sample was measured with a fixed divergence slit with 0.125° opening.

```

str
phase_name "Silicon"
Cubic(@ 5.43258)
MVW (224.683, 160.331254`_0.0021742123, 31.532`_0.082)
scale @ 0.00111033118
space_group "Fd-3m:2"
LVol_FWHM_CS_G_L(1, 383.35715, 0.89, 534.46669, csgc1, 10000.00000, cslc1, 601.91460)
e0_from_Strain(0.02212, sgc1, 0.00010, slc1, 0.08849)
site Si1 x 0.125 y 0.125 z 0.125 occ Si 1.0 beq 0.85
phase_MAC 63.9439604
Phase_LAC_1_on_cm(148.79935)
Phase_Density_g_on_cm3(2.32703)
weight_percent 31.532`_0.082
spiked_phase_measured_weight_percent 25
corrected_weight_percent 25`_0

```

Structural information of the spiked silicon phase. The 'MVW' macro calculates unit cell mass, volume and weight-%, followed by the scale factor and space group (2nd setting of space group $Fd\bar{3}m!$). The 'LVol_FWHM_CS_G_L' macro calculates the size of coherently scattering domains ('crystallite size'), whereas the macro 'e0_from_Strain' calculates $\epsilon_0 = \Delta d/d$. Next follow atomic coordinates, occupancies and isotropic B_{eq} . The 'phase_MAC' keyword calculates the phase mass absorption coefficient, 'Phase_LAC_1_on_cm' calculates the linear absorption coefficient, 'Phase_Density_g_on_cm3' calculates the phase density. 'Weight_percent' calculates Rietveld wt-%. The 'spiked_phase_measured_weight_percent' corrects this value. The 'corrected_weight_percent' corrects Rietveld wt-% with known spiked wt-%.

```

str
phase_name "Quartz"
a @ 4.91496`_0.00003
b = Get(a);
c @ 5.40662`_0.00004
al 90

```

```

be 90
ga 120
MVW(180.252, 113.108808`_0.00145825088, 68.468`_0.082)
scale @ 0.00425994962
space_group "P3221"
LVol_FWHM_CS_G_L(1, 398.51387, 0.89, 401.71678, csgc2, 486.52138, cslc2, 3352.67231)
e0_from_Strain(0.01835, sgc2, 0.04814, slc2, 0.04032)
site Si1 x 0.46832 y 0.0 z =2/3; occ Si 1.0 beq 0.82
site O1 x 0.41353 y 0.27029 z 0.78974 occ O 1.0 beq 1.35
phase_MAC 36.0110617
Phase_LAC_1_on_cm(95.29491)
Phase_Density_g_on_cm3(2.64627)
weight_percent 68.468`_0.082
corrected_weight_percent 54.2851069`_0.0647018326
    
```

This part is the same as above but with structural information for quartz. 'Weight_percent' calculates Rietveld wt.-%, which are corrected by the spike above. Corrected wt.-% are output with the 'corrected_weight_percent' keyword.

```
weight_percent_amorphous 20.7148931`_0.205195603
```

Weight_percent_amorphous is the difference of 100% – sum of corrected wt.-%.

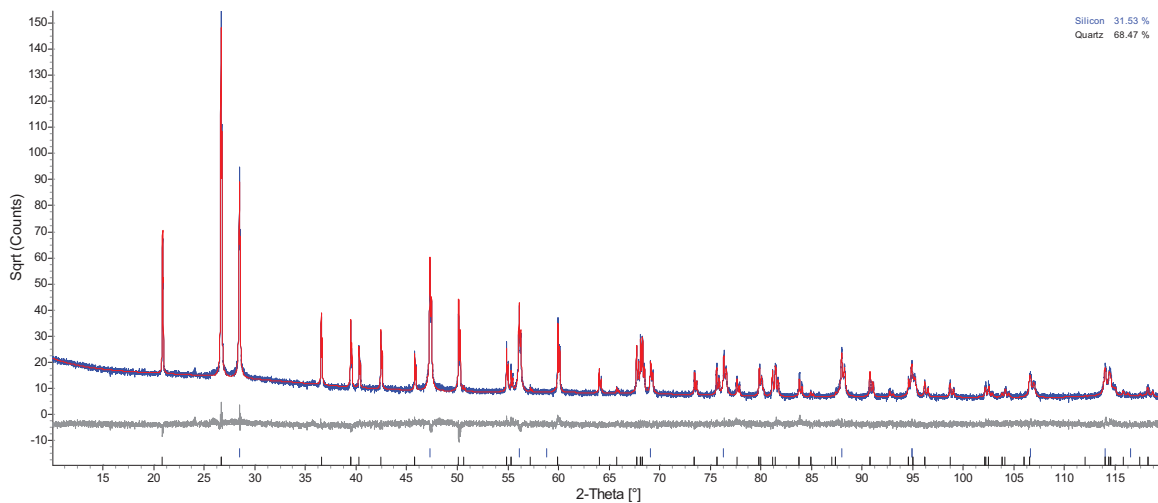


Fig. B1.41: Final refinement plot of the amorphous content quantification. *hkl* ticks of silicon (blue) and quartz (black) are shown. The blue curve is the measured data, the red curve is the calculated pattern and the gray plot is the difference between observed and calculated data. Note the very slight background bump between 20° and 35° 2-Theta which may result from the added glass phase. The quantitative results top right are Rietveld wt.-% without the spike correction.

Refinement of temperature-dependent diffraction patterns

Multipattern refinement in Topas with uncorrected diffraction patterns and no height correction. Several measurements of Al_2O_3 were performed at different temperatures in order to refine temperature-dependent lattice parameters and crystal structure of corundum. Each pattern is refined independently of the others. Measured patterns were not corrected for height displacement, thus specimen displacement must follow the values from the table describing sample holder expansion of the Anton-Paar HTK 1200 furnace (Table B1.8). This method is the easiest to use when refining temperature-dependent diffraction patterns. However, no physical model expressing temperature-dependence of lattice parameters is considered. Further, when using diffraction patterns that are not corrected for height displacements, the refinement can be unstable because of unappropriate start values of specimen displacement towards higher temperatures.

Table B1.8: Sample height displacement of the HTK 1200 ($^{\circ}\text{C}$, mm).

Temp.	Displ.	Temp.	Displ.	Temp.	Displ.	Temp.	Displ.
100	0.030	400	0.120	700	0.250	1000	0.390
200	0.060	500	0.170	800	0.300	1100	0.450
300	0.090	600	0.210	900	0.350	1200	0.510

```
r_exp 11.810 r_exp_dash 20.004 r_wp 15.268
r_wp_dash 25.862 r_p 11.450 r_p_dash 23.840
weighted_Durbin_Watson 17.399 gof 1.293
do_errors
no_LIMIT_warnings
```

This section contains agreement factors, the keyword to calculate errors (`do_errors`) and a keyword to not display limit warnings (`no_LIMIT_warnings`).

```
macro diffractometer
{ lam ymin_on_ymax 0.0001
  Lam_recs
  { 0.0159 1.534753 3.6854
    0.5691 1.540596 0.4370
    0.0762 1.541058 0.6000
    0.2517 1.544410 0.5200
    0.0871 1.544721 0.6200 }
  LP_Factor(0)
  Rp 240
  Rs 240
  Slit_Width(0.07)
  Divergence (0.25)
  axial_conv
  filament_length 12
  sample_length 10
  receiving_slit_length 15
```

```
primary_soller_angle 2.55
secondary_soller_angle 2.55
start_X 10
finish_X 140 }
```

The diffractometer setup and wavelengths for the fundamental parameter approach are defined. Instead of repeating this part in each temperature-dependent refinement below, it is defined as a macro named 'diffractometer' which is inserted below.

```
xdd Al2O3_0025.raw
diffractometer
bkg @ 46.7328227 ... .. 0.863553211
```

This part contains the datafile name (xdd Al2O3_0025.raw). The diffractometer setup is input using the macro 'diffractometer' defined above. Next, the Chebyshev background parameters are refined (two shown).

```
str
phase_name Al2O3_T0025
r_bragg 3.30189325
Trigonal(a_al2o3_T25 4.76021, c_al2o3_T25 12.99550)
cell_volume v_al2o3_T25 255.021094
Specimen_Displacement (displ_T25, 0.02462)
scale @ 0.000522534473
space_group "R-3c"
site Al1 x 0 y 0 z @ 0.35223 occ Al 1.0 beq biso_T25 0.1058
site O1 x @ 0.69378 y 0 z = 1/4; occ O 1.0 beq biso_T25 0.1058
LVol_FWHM_CS_G_L(1, 77.26262, 0.89, 85.51810, csgc_T25, 123.83196, cs1c_T25, 253.89150)
e0_from_Strain( 0.02571, sgc_T25, 0.00034, slc_T25, 0.10287)
```

This part contains all structural information of the Al₂O₃ phase for the 25°C refinement. Note that parameters of interest are given a parameter name which is different for each temperature. Both displacement parameters are refined together using the parameter name biso_T25. The last two lines are macros for peak broadening due to microstructural effects.

```
out "Al2O3_LPs_Output.TXT" append
Out_String("\n Name a-axis esd c-axis esd volume esd Rwp GoF Height esd")
Out_String("\n =====")
Out(=Get(phase_name), " \n ?%s?")
Out(a_al2o3_T25, " %11.5f", " %11.5f")
Out(c_al2o3_T25, " %11.5f", " %11.5f")
Out(v_al2o3_T25, " %11.3f", " %11.3f")
Out(Get(r_wp), " %11.2f")
Out(Get(gof), " %11.2f")
Out(displ_T25, "%11.3f", " %11.3f")
```

An output file is generated (Al2O3_LPs_Output.TXT) and values of some of the parameters above are written to the file. Out(a_al2o3_T25, " %11.5f", " %11.5f") means that the value of the parameter a_al2o3_T25 is written to the file as floating number with five digits, as is the value of the esd. The first two lines are a file header.

Similar inputs for the 100°C to 1200°C patterns follow here. Temperature dependent parameters have to be changed to the corresponding temperature in each refinement section (e.g. a_al2o3_T25 becomes a_al2o3_T100 in the 100°C refinement. Below, the last refinement (1200°C) is shown.

```

xdd Al2O3_1200.raw
diffractometer
bkg @ 45.1037186 ... .. 0.563962219

str
phase_name Al2O3_T1200
r_bragg 3.9436839
Trigonal(a_al2o3_T1200 4.80746, c_al2o3_T1200 13.13868)
cell_volume v_al2o3_T1200 262.974101
Specimen_Displacement (displ_T1200, -0.54138)
scale @ 0.000642774818
space_group "R-3c"
site Al1 x 0          y 0 z @ 0.35223 occ Al 1.0 beq biso_T1200 0.9284
site O1  x @ 0.69378 y 0 z = 1/4;   occ O 1.0 beq biso_T1200 0.9284
LVol_FWHM_CS_G_L(1, 77.91640, 0.89, 91.39145, csgc_T1200, 153.4010, cs1c_T1200, 193.4558)
e0_from_Strain( 0.02323, sgc_T1200, 0.07527, slc_T1200, 0.03029)

out "Al2O3_LPs_Output.TXT" append
Out(=Get(phase_name), " \n ?%s?")
Out(a_al2o3_T1200, " %11.5f", " %11.5f")
Out(c_al2o3_T1200, " %11.5f", " %11.5f")
Out(v_al2o3_T1200, " %11.3f", " %11.3f")
Out(Get(r_wp), " %11.2f")
Out(Get(gof), " %11.2f")
Out(displ_T1200, "%11.3f", " %11.3f")

```

Multipattern refinement in Topas with uncorrected input files and known height correction. Instead of using a specimen displacement of zero as start value for each temperature-dependent refinement, patterns can be corrected with the known height displacement as listed in the Anton-Paar table (Table B1.8). The same input file as above is shown with the known displacements implemented. At each temperature, specimen displacement is calculated as: $\text{displacement}_{\text{total}} = \text{displacement}_{\text{refined}} - \text{known value from the table}$. With this method, appropriate starting values for specimen displacement are already provided at the beginning of the refinement.

```

r_wp 15.268 r_exp 11.810 r_p 11.450
r_wp_dash 25.862 r_p_dash 23.840 r_exp_dash 20.004
weighted_Durbin_Watson 17.399 gof 1.293
do_errors
no_LIMIT_warnings

```

This section contains agreement factors, the keyword to calculate errors (`do_errors`) and a keyword to not display limit warnings (`no_LIMIT_warnings`).

```

macro diffractometer
{ lam ymin_on_ymax 0.0001
  Lam_recs
  { 0.0159 1.534753 3.6854
    0.5691 1.540596 0.4370
  }
}

```

```
0.0762 1.541058 0.6000
0.2517 1.544410 0.5200
0.0871 1.544721 0.6200 }
LP_Factor(0)
Rp 240
Rs 240
Slit_Width(0.07)
Divergence (0.25)
axial_conv
filament_length 12
sample_length 10
receiving_slit_length 15
primary_soller_angle 2.55
secondary_soller_angle 2.55
start_X 10
finish_X 140 }
```

The diffractometer setup and wavelengths for the fundamental parameter approach are defined. Instead of repeating this part for each temperature-dependent refinement below, it is defined as a macro named 'diffractometer' which is then inserted below.

```
xdd Al2O3_0025.raw
diffractometer
bkg @ 46.7328227 ... .. 0.863553211
```

This part contains the datafile name (xdd Al2O3_0025.raw), then the diffractometer setup is input using the macro 'diffractometer' defined above. Next, the Chebyshev background parameters are refined (two shown).

```
str
phase_name Al2O3_T0025
r_bragg 3.30189325
Trigonal(a_al2o3_T25 4.76021, c_al2o3_T25 12.99550)
cell_volume v_al2o3_T25 255.021094
prm height_error_T25 0.02462
Specimen_Displacement (displ_T25, =height_error_T25 - 0.0;: 0.02462)
scale @ 0.000522534473
space_group "R-3c"
site Al1 x 0 y 0 z @ 0.35223 occ Al 1.0 beq biso_T25 0.1058
site O1 x @ 0.69378 y 0 z = 1/4; occ O 1.0 beq biso_T25 0.1058
LVol_FWHM_CS_G_L(1, 77.26262, 0.89, 85.51810, csgc_T25, 123.83196, cs1c_T25, 253.89150)
e0_from_Strain( 0.02571, sgc_T25, 0.00034, slc_T25, 0.10287')
```

This part contains all structural information of the Al₂O₃ phase for the 25°C refinement. Note that parameters of interest are given a parameter name which is different for each temperature. Both displacement parameters are refined together using the parameter name biso_T25. The last two lines are macros for peak broadening due to microstructural effects. A new parameter 'height_error_T25' is defined. The actual specimen displacement is then displ_T25 = height_error_T25 - 0.0. Nothing is subtracted because the sample holder expansion at 25°C is expected to be zero. If the Anton-Paar table (Table B1.8) is exact, the value of height_error_Txy should be the same at each temperature.

```
out "Al2O3_LPs_Output.TXT" append
Out_String("\n Name a-axis esd c-axis esd volume esd Rwp GoF Ht_uncorr esd Ht_corr esd")
```

```

Out_String("\n =====")
Out(=Get(phase_name), " \n ?%s?")
Out(a_al2o3_T25, " %11.5f", " %11.5f")
Out(c_al2o3_T25, " %11.5f", " %11.5f")
Out(v_al2o3_T25, " %11.3f", " %11.3f")
Out(Get(r_wp), " %11.2f")
Out(Get(gof), " %11.2f")
Out(displ_T25, "%11.3f", " %11.3f")
Out(height_error_T25, "%11.3f", " %11.3f")

```

An output file is generated (Al2O3_LPs_Output.TXT) and values of some of the parameters above are written to the file. Out(a_al2o3_T25, " %11.5f", " %11.5f") means that the value of the parameter a_al2o3_T25 is written to the file as floating number with five digits, as is the value of the esd. The first two lines are a file header.

Similar inputs for the 100°C to 1200°C patterns follow here. Temperature dependent parameters have to be changed to the corresponding temperature in each refinement section (e.g. a_al2o3_T25 becomes a_al2o3_T100 in the 100°C refinement. Below, the last refinement (1200°C) is shown.

```

xdd Al2O3_1200.raw
diffractometer
bkg @ 46.7552041 ... .. 1.06807956

str
phase_name Al2O3_T1200
r_bragg 3.9436839
Trigonal(a_al2o3_T1200 4.80746, c_al2o3_T1200 13.13868)
cell_volume v_al2o3_T1200 262.974101
prm height_error_T1200 -0.03132
Specimen_Displacement (displ_T1200, =height_error_T1200 - 0.51;: -0.54132)
scale @ 0.000642774818
space_group "R-3c"
site Al1 x 0          y 0 z @ 0.35223 occ Al 1.0 beq biso_T1200 0.9284
site O1 x @ 0.69378 y 0 z = 1/4;   occ O 1.0 beq biso_T1200 0.9284
LVol_FWHM_CS_G_L(1, 77.91640, 0.89, 91.39145, csgc_T1200, 153.4010, cs1c_T1200, 193.4558)
e0_from_Strain( 0.02323`, sgc_T1200, 0.07527, slc_T1200, 0.03029)

out "Al2O3_LPs_Output.TXT" append
Out(=Get(phase_name), " \n ?%s?")
Out(a_al2o3_T1200, " %11.5f", " %11.5f")
Out(c_al2o3_T1200, " %11.5f", " %11.5f")
Out(v_al2o3_T1200, " %11.3f", " %11.3f")
Out(Get(r_wp), " %11.2f")
Out(Get(gof), " %11.2f")
Out(displ_T1200, "%11.3f", " %11.3f")
Out(height_error_T1200, "%11.3f", " %11.3f")

```

Specimen displacement used to correct the pattern here is $\text{displ_T1200} = \text{height_error_T1200} - 0.51$. The value of 0.51 mm is the height displacement as listed in the Anton-Paar table (Table B1.8). The value of the 'height_error_T1200' parameter is the difference between actual specimen displacement and the value listed in the table. If the Anton-Paar table is exact, the value of height_error_Txy should be the same at each temperature. Note that height_error_T25 is 0.02462 whereas height_error_T1200 is -0.03132.

Parameterized refinement of temperature-dependent diffraction patterns. The idea of the parameterization shown here is based on Stinton and Evans (2007).

Traditionally, refining temperature-dependent parameters is done by refining all parameters at each temperature individually, as shown with the two examples above. However, with this method, no physical model is considered, i.e. it is not taken in account that temperature-dependency of e.g. lattice parameters is in fact a function of temperature. This can be expressed with a mathematical function.

Instead of refining each pattern individually, it is possible to refine them simultaneously and express parameters of interest (lattice parameters, specimen displacement) as a temperature-dependent function (Figure B1.42). This eliminates outliers (which are common when treating high-temperature data individually) and it drastically reduces the number of refined parameters: Refining lattice parameters of an orthorhombic phase (a , b , c), corundum as internal standard (a , c) and specimen displacement for 21 diffraction patterns (25°C, 50°C and then each 50°C up to 1000°C) results in a total of 126 refined parameters. If lattice parameters and specimen displacement are expressed as functions of temperature, the only variable in a pattern is temperature, which is supposed to be known. Polynomial coefficients are the same for each temperature and can therefore be refined simultaneously over all measurements. This method results in a total of 18 parameters for 21 diffraction patterns. Further, the physical property implicating that lattice parameter evolution is temperature-dependent is now considered in the refinement. Prior to setting up the refinement, verify if the chosen function is accurate!

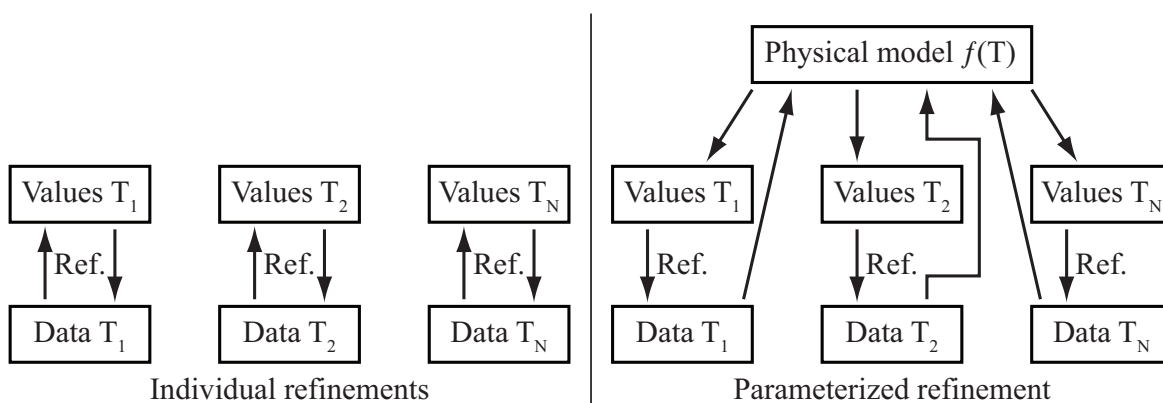


Fig. B1.42: Parameterized refinements allow consideration of a physical model (e.g. lattice parameter evolution as a function of temperature, expressed by a second order polynomial).

Results can be monitored from refined lattice parameters of an internal standard in the sample (in this case corundum) and by comparing specimen displacement values to those in the Anton-Paar table (Table B1.8).

A drawback of this method is error propagation (i.e. errors become larger at the beginning and

the end of the temperature range) when using the traditional method of error determination from a correlation matrix. This can be overcome by using the bootstrap method implemented in Topas: A series of refinements is performed, each with a fraction of observed data modified to obtain a new bootstrap sample (equals one cycle). After a given number of cycles, standard deviations of the refined values become the bootstrap errors (Coelho 2007b).

In the sample file shown below, the physical model expressing lattice parameters a and c of corundum and a , b and c of Al_5BO_9 and specimen displacement (h) as a function of temperature have been defined as shown in Equations B.10 to B.15.

$$a_{\text{al2o3}}(T) = a0_{\text{al2o3}} + ax1_{\text{al2o3}} \cdot T + ax2_{\text{al2o3}} \cdot T^2 \quad (\text{B.10})$$

$$c_{\text{al2o3}}(T) = c0_{\text{al2o3}} + cx1_{\text{al2o3}} \cdot T + cx2_{\text{al2o3}} \cdot T^2 \quad (\text{B.11})$$

$$a_{\text{al5bo9}}(T) = a0_{\text{al5bo9}} + ax1_{\text{al5bo9}} \cdot T + ax2_{\text{al5bo9}} \cdot T^2 \quad (\text{B.12})$$

$$b_{\text{al5bo9}}(T) = b0_{\text{al5bo9}} + bx1_{\text{al5bo9}} \cdot T + bx2_{\text{al5bo9}} \cdot T^2 \quad (\text{B.13})$$

$$c_{\text{al5bo9}}(T) = c0_{\text{al5bo9}} + cx1_{\text{al5bo9}} \cdot T + cx2_{\text{al5bo9}} \cdot T^2 \quad (\text{B.14})$$

$$h(T) = \text{height}_0 + \text{height}_{x1} \cdot T + \text{height}_{x2} \cdot T^2 \quad (\text{B.15})$$

At each temperature, lattice parameters and sample displacement are expressed with Equations B.10 to B.15. The only value that is changed each pattern is temperature T as a fixed parameter. The final refinement plot is shown in Figure B1.43.

```
r_exp 6.714 r_exp_dash 10.117 r_wp 7.912
r_wp_dash 11.923 r_p 6.013 r_p_dash 10.736
weighted_Durbin_Watson 37.137 gof 1.178
bootstrap_errors 200
no_LIMIT_warnings
```

This section contains agreement factors, the command to calculate bootstrap errors with 200 cycles (`bootstrap_errors 200`) and a command to not display limit warnings (`no_LIMIT_warnings`).

```
macro diffractometer
{ lam ymin_on_ymax 0.0001
  Lam_recs
  { 0.0159 1.534753 3.6854
    0.5691 1.540596 0.4370
    0.0762 1.541058 0.6000
    0.2517 1.544410 0.5200
    0.0871 1.544721 0.6200 }
  LP_Factor(0)
  Rp 240
  Rs 240
  Slit_Width(0.07)
```

```
Divergence (0.125)
axial_conv
filament_length 12
sample_length 10
receiving_slit_length 15
primary_soller_angle 2.55
secondary_soller_angle 2.55
start_X 10
finish_X 75.3 }
```

The diffractometer setup and the used wavelengths for the fundamental parameter approach are defined. Instead of repeating this part for each temperature-dependent refinement below, it is written as a macro named 'diffractometer' which is then inserted below.

```
'-----
'Al2O3 lattice parameter polynomial coefficients.
'a-axis(T) = a0_al2o3 + ax1_al2o3 *T + ax2_al2o3 *T^2.
'-----
prm a0_al2o3      4.75792`_0.00021
prm ax1_al2o3 4590.88876`_84.77322 ' * 100'000'000 too large!
prm ax2_al2o3   -0.48723`_0.07161  ' * 100'000'000 too large!
prm c0_al2o3     13.01946`_0.00067
prm cx1_al2o3 4318.12403`_294.20815 ' * 100'000'000 too large!
prm cx2_al2o3    5.21644`_0.27224  ' * 100'000'000 too large!
'-----
'Al5BO9 lattice parameter polynomial coefficients.
'a-axis(T) = a0_al5bo9 + ax1_al5bo9 *T + ax2_al5bo9 *T^2.
'-----
prm a0_al5bo9     5.66852`_0.00005
prm ax1_al5bo9 1754.40050`_25.82802 ' * 100'000'000 too large!
prm ax2_al5bo9    0.61439`_0.02564  ' * 100'000'000 too large!
prm b0_al5bo9     1  5.01305`_0.00020
prm bx1_al5bo9 9300.74475`_62.96127 ' * 100'000'000 too large!
prm bx2_al5bo9    0.22990`_0.05751  ' * 100'000'000 too large!
prm c0_al5bo9     7.69477`_0.00006
prm cx1_al5bo9 3804.41837`_27.77816 ' * 100'000'000 too large!
prm cx2_al5bo9    0.36876`_0.02333  ' * 100'000'000 too large!
'-----
'Height displacement polynomial coefficients.
'h(T) = height_0 + height_x1 *T +height_x2 *T^2.
'-----
prm height_0    0.01420`_0.00035 ' * 10'000 too large!
prm height_x1 -3.07394`_0.01445 ' * 10'000 too large!
prm height_x2 -0.00144`_0.00001 ' * 10'000 too large!
```

This section contains the second order polynomial coefficients expressing Al_5BO_9 and corundum lattice parameters and specimen displacement of the heating chamber as a function of temperature. Because Topas can handle but does not output very small numbers, coefficients were divided by a factor, which means that the numbers above are 100'000'000 times and 10'000 times too large, respectively.

```
xdd 0025.raw
diffractometer
prm !T25 = 25;
bkg @ 132.785828`_0.41725691 ... .. 2.99189097`_0.25181182
```

This part contains the data file name (xdd 0025.raw), information about the diffractometer setup is input using the macro 'diffractometer' defined above. A fixed parameter T25 defines temperature with a value of 25. Chebyshev background parameters are refined (two shown).

```

hkl_Is
leball 1
phase_name Al2O3_T25
prm !a_al2o3_T25 = a0_al2o3 + ax1_al2o3/10^8 (T25) + ax2_al2o3/10^8 (T25)^2;
prm !c_al2o3_T25 = c0_al2o3 + cx1_al2o3/10^8 (T25) + cx2_al2o3/10^8 (T25)^2;
Trigonal(=a_al2o3_T25;: 4.75906`_0.00019, =c_al2o3_T25;: 13.02057`_0.00060)
prm height_T25 = height_0 + height_x1/10000 (T25) + height_x2/10000 (T25)^2;
Specimen_Displacement (!displ_T25, =height_T25;: 0.00643`_0.00032)
CS_L(@, 10000.00000`_3176.77964)
CS_G(@, 172.58488`_21.82458)
Strain_L(@, 0.12754`_0.01169)
Strain_G(@, 0.00010`_0.03040)
space_group "R-3c"
load hkl_m_d_th2 I
{ 0 1 2 6 3.48231 25.55942 0.620856079
  ... not all shown }

```

A LeBail refinement (hkl_Is and leball 1 keywords) of corundum is set up. Lattice parameters a_al2o3_T25 and c_al2o3_T25 are calculated from the polynomials. Calculated lattice parameters are then used to describe the corundum unit cell (line starting with 'Trigonal...'). The values are only input but not refined, as corundum lattice parameters are fixed parameters. The only refinable parameters are polynomial coefficients listed further above! Specimen displacement is calculated from the polynomial and the fixed value height_T25 is used as specimen displacement for this temperature. As above, polynomial parameters are the only refineable parameters.

```

hkl_Is
leball 1
phase_name Al5BO9_T25
prm !a_al5bo9_T25 = a0_al5bo9 + ax1_al5bo9/100000000 (T25) + ax2_al5bo9/100000000 (T25)^2;
prm !b_al5bo9_T25 = b0_al5bo9 + bx1_al5bo9/100000000 (T25) + bx2_al5bo9/100000000 (T25)^2;
prm !c_al5bo9_T25 = c0_al5bo9 + cx1_al5bo9/100000000 (T25) + cx2_al5bo9/100000000 (T25)^2;
a =a_al5bo9_T25;: 5.66896`_0.00004
b =b_al5bo9_T25;: 15.01537`_0.00020
c =c_al5bo9_T25;: 7.69572`_0.00006
cell_volume v_al5bo9_T25 655.071844`_0.0108051685
Specimen_Displacement (!displ_T25, =height_T25;: 0.00643`_0.00032)
CS_L(@, 547.78105`_41.65186)
CS_G(@, 352.93544`_992.96429)
Strain_L(@, 0.11538`_0.00807)
Strain_G(@, 0.11127`_0.00777)
space_group "Cmc21"
load hkl_m_d_th2 I
{ 0 2 0 2 7.50768 11.77797 0.0931799498
  ... not all shown }

```

Parameterization of Al₅BO₉ lattice parameters is identical to the one above, however, specimen displacement for this phase is not calculated again but the value is taken from the corundum part.

```
out "results.txt" append
```

```
Out_String("\n Temp. Al2O3_a Al2O3_c Rwp GoF Height Al5BO9_a Al5BO9_b Al5BO9_c Al5BO9_v")
Out_String("\n =====")
Out(T25, " \n %11.1f")
Out(a_al2o3_T25, " %11.5f", " %11.5f")
Out(c_al2o3_T25, " %11.5f", " %11.5f")
Out(Get(r_wp), " %11.2f")
Out(Get(gof), " %11.2f")
Out(displ_T25, "%11.5f", " %11.5f")
Out(a_al5bo9_T25, "%11.5f", " %11.5f")
Out(b_al5bo9_T25, "%11.5f", " %11.5f")
Out(c_al5bo9_T25, "%11.5f", " %11.5f")
Out(v_al5bo9_T25, "%11.3f", " %11.3f")
```

An output file is saved (results.txt) and values of all parameters defined above are written to the file. Out(a_al2o3_T25, " %11.5f", " %11.5f") means that the value of the parameter a_al2o3_T25 is written to the file as floating number with five digits. When using the bootstrap error model, esds are not written to the output file. The first two lines define the file header.

Similar inputs for the 100°C to 1200°C patterns follow here. Temperature dependent parameters have to be changed to the corresponding temperature in each refinement section (e.g. a_al2o3_T25 becomes a_al2o3_T100 in the 100°C refinement and prm !T25 = 25; becomes prm !T100 = 100; in the 100°C refinement). Below, the last refinement (1000°C) is shown.

```
xdd 1000.raw
diffractometer
prm !T1000 = 1000;
bkg @ 114.453609`_0.360956049 ... .. 4.42960845`_0.26267103

hkl_Is
leball 1
phase_name Al2O3_T1000
prm !a_al2o3_T1000 = a0_al2o3 + ax1_al2o3/10^8 (T1000) + ax2_al2o3/10^8 (T1000)^2;
prm !c_al2o3_T1000 = c0_al2o3 + cx1_al2o3/10^8 (T1000) + cx2_al2o3/10^8 (T1000)^2;
Trigonal(=a_al2o3_T1000;: 4.79895`_0.00018, =c_al2o3_T1000;: 13.11481`_0.00100)
prm height_T1000 = height_0 + height_x1/10000 (T1000) + height_x2/10000 (T1000)^2;
Specimen_Displacement (!displ_T1000, =height_T1000;: -0.43681`_0.00040)
CS_L(@, 980.06673`_2824.56239)
CS_G(@, 378.67059`_2320.60807)
Strain_L(@, 0.06310`_0.02097)
Strain_G(@, 0.00010`_0.03512)
space_group "R-3c"
load hkl_m_d_th2 I
{ 0 1 2 6 3.51036 25.35179 0.590999731
  ... not all shown }

hkl_Is
leball 1
phase_name Al5BO9_T1000
prm !a_al5bo9_T1000 = a0_al5bo9 + ax1_al5bo9/10^8 (T1000) + ax2_al5bo9/10^8 (T1000)^2;
prm !b_al5bo9_T1000 = b0_al5bo9 + bx1_al5bo9/10^8 (T1000) + bx2_al5bo9/10^8 (T1000)^2;
prm !c_al5bo9_T1000 = c0_al5bo9 + cx1_al5bo9/10^8 (T1000) + cx2_al5bo9/10^8 (T1000)^2;
a =a_al5bo9_T1000;: 5.69221`_0.00004
b =b_al5bo9_T1000;: 15.10835`_0.00023
c =c_al5bo9_T1000;: 7.73650`_0.00008
cell_volume v_al5bo9_T1000 665.337929`_0.0183982884
```

```

Specimen_Displacement (!displ_T1000, =height_T1000;: -0.43681`_0.00040)
CS_L(@, 600.33718`_34.78527)
CS_G(@, 348.56574`_23.46300)
Strain_L(@, 0.11324`_0.00464)
Strain_G(@, 0.02702`_0.01518)
space_group "Cmc21"
load hkl_m_d_th2 I
{ 0 2 0 2 7.55417 11.70523 0.106817448
  ... not all shown }

```

```

out "results.txt" append
Out(T1000, " \n %11.1f")
Out(a_al2o3_T1000, " %11.5f", " %11.5f")
Out(c_al2o3_T1000, " %11.5f", " %11.5f")
Out(Get(r_wp), " %11.2f")
Out(Get(gof), " %11.2f")
Out(height_T1000, "%11.5f", " %11.5f")
Out(a_al5bo9_T1000, "%11.5f", " %11.5f")
Out(b_al5bo9_T1000, "%11.5f", " %11.5f")
Out(c_al5bo9_T1000, "%11.5f", " %11.5f")
Out(v_al5bo9_T1000, "%11.3f", " %11.3f")

```

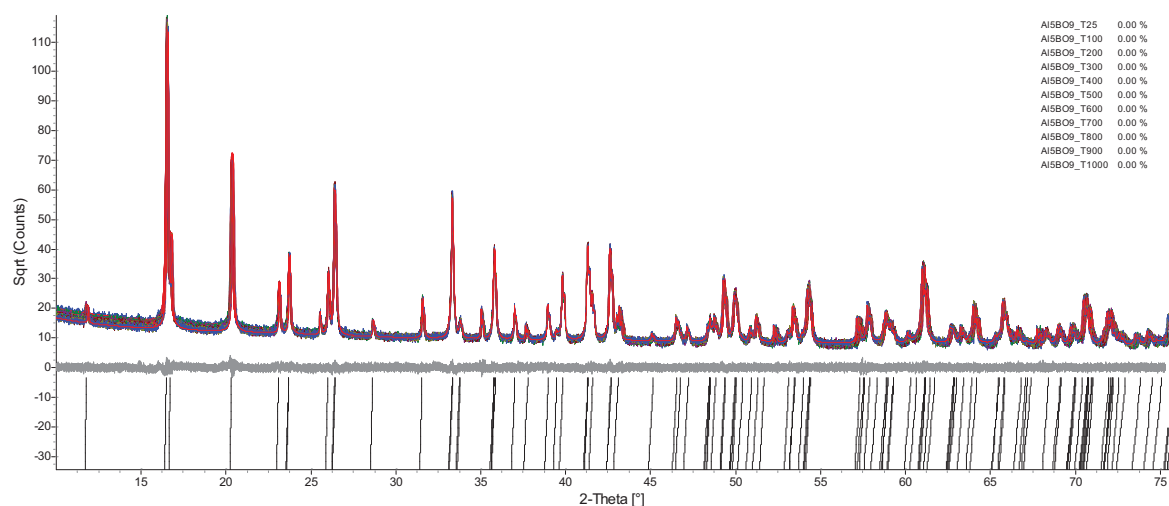


Fig. B1.43: Final refinement plot of the parameterized high-temperature refinement of Al_5BO_9 . *hkl* ticks of Al_5BO_9 from 25°C to 1000°C (top to bottom) are shown in black.

C Acknowledgments

The last chapter of this thesis is dedicated to all those who helped, encouraged and supported me during the development of my dissertation.

First and foremost, I would like to express my gratitude to Thomas Armbruster. I am thankful for the constructive discussions, his patience, and for always having a sympathetic ear for my ideas as well as my questions. He allowed me to follow my own interests but guided me back on track when I lost focus. I learned a lot from his experience and I feel honored of having obtained three academic titles under his supervision. The time of working together was a pleasure.

I am grateful to Eugen Libowitzky, Daniel Rentsch, Thomas Pettke and Diego Gatta for being interested in my research and answering my countless questions. Collaborating with them has offered me the possibility to gain insight into new methods and provided an essential basis for this thesis. Further thanks are due to Nicola Döbelin for letting me participate in his projects.

A big thank you goes to everyone of the Mineralogical Crystallography Group and the Group of Chemical Crystallography: Vladimir Malogajski for taking care of the diffractometers and constructing the mosque heater; Jürg Hauser for always taking care of party-essentials and for computer support; Mariko Nagashima for the translation of Japanese articles and for always remembering the Japanese tea; Milen Kadiyski for the good times we had abroad; To my office colleague Eva Wadoski for English-improvements and to Biljana Lazic for organizing the Praktikum. They along with Anna Malsy, Petra Simoncic and Piero Macchi helped in various aspects but especially during coffee-break crossword puzzles (and no, I won't miss that! I guess...).

The synthesis-related part of this work would have been difficult without the know-how of Ruth Maeder. Her support in the laboratory was very valuable and we had good times during lab-work and while looking for new and cleaning old platinum wares.

I thank Urs Eggenberger for his confidence and letting the powder X-ray diffraction lab become my playground. I owe him a lot for the "holidays" in Rivera, which were a welcome change from daily routine, and for the vast amount of the Institute's best coffee.

I have been knowing some of the Institute's members for nearly ten years. I thank them and especially Christoph Wanner and the Tonlabor-Crew Johannes Reinhard, Sam Gilgen and Nicolas Greber for the times we spent during our studies, on field trips, and for mutual encouragement and friendship.

Last but not least I wish to thank my family and friends for their continuous support.

D Publications

Peer Reviewed Publications

- Charles A. Geiger, Evgeny Alekseev, Biljana Lazic, Martin Fisch, Thomas Armbruster, Ramona Langner, Michael Fechtelkord, Namjun Kin, Thomas Pettke, Werner Weppner: Crystal Chemistry and Stability of "Li₇La₃Zr₂O₁₂" Garnet: A Fast Lithium-Ion Conductor.
Inorganic Chemistry 50 (2011) 1089–1097.
- Martin Fisch, Thomas Armbruster, Daniel Rentsch, Eugen Libowitzky, Thomas Pettke: Crystal-chemistry of mullite-type aluminoborates Al₁₈B₄O₃₃ and Al₅BO₉: A stoichiometry puzzle.
Journal of Solid-State Chemistry 184 (2011) 70–80.
- Eva Wadoski, Thomas Armbruster, Biljana Lazic, Martin Fisch: Dehydration of the natural zeolite goosecreekite CaAl₂Si₆O₁₆·5H₂O upon stepwise heating: A single-crystal and powder X-ray study.
American Mineralogist, accepted 2011.
- Martin Fisch, Thomas Armbruster: Thermal Expansion of Aluminoborates.
In: Sergey Krivovichev (ed.) *Minerals as Advanced Materials II*, Springer-Verlag Berlin, submitted 2010.
- Nicola Döbelin, Tobias J. Brunner, Wendelin J. Stark, Martin Fisch, Egle Conforto, Marc Bohner: Thermal treatment of flame-synthesized amorphous tricalcium phosphate nanoparticles.
Journal of the American Ceramic Society 93(10) (2010) 3455–3463.
- Martin Fisch, Thomas Armbruster, Eugen Libowitzky: Microporous CsAlSi₅O₁₂ at non-ambient conditions: Partial Na exchange at 100°C.
Proceedings of the 3rd International Symposium on Advanced micro- and mesoporous materials 2009, accepted 2010.
- G. Diego Gatta, Nicola Rotiroti, Martin Fisch, Thomas Armbruster: Stability at high pressure, elastic behavior and pressure-induced structural evolution of "Al₅BO₉", a mullite-type ceramic material.
Physics and Chemistry of Minerals 37(4) (2010) 227–236.

- Nicola Döbelin, Tobias J. Brunner, Wendelin J. Stark, Manuel Eggimann, Martin Fisch, Marc Bohner:
Phase evolution of thermally treated amorphous tricalcium phosphate nanoparticles.
Key Engineering Materials Volumes 396-398 (2009) 595–598.
- Giuseppina Balassone, Angela Mormone, Manuela Rossi, Alessandro Bernardi, Martin Fisch, Thomas Armbruster, Anna Kathrin Malsy, Alfons Berger:
Crystal chemical and structural characterization of an Mg-rich osumilite from Vesuvius volcano.
European Journal of Mineralogy 20(5) (2008) 713–720.
- G. Diego Gatta, Nicola Rotiroti, Martin Fisch, Milen Kadiyski, Thomas Armbruster:
Stability at high-pressure, elastic behaviour and pressure-induced structural evolution of $\text{CsAlSi}_5\text{O}_{12}$, a potential host for nuclear waste.
Physics and Chemistry of Minerals 35(9) (2008) 521–533.
- Martin Fisch, Thomas Armbruster, Boris Kolesov:
Temperature-dependent structural study of microporous $\text{CsAlSi}_5\text{O}_{12}$.
Journal of Solid-State Chemistry 181 (2008) 423–431.

Conference Contributions (Poster Presentations)

- Nicola Döbelin, Marc Bohner, Martin Fisch, Urs Eggenberger:
A Novel XRD Sample Preparation Technique Simulating Physiological Conditions.
23rd European Conference on Biomaterials 2010, Tampere, Finland.
- Martin Fisch, Thomas Armbruster, Daniel Rentsch, Eugen Libowitzky, Thomas Pettke:
Mullite-type Al_5BO_9 and $\text{Al}_{18}\text{B}_4\text{O}_{33}$: A crystal-chemical puzzle?
20th Meeting of the International Mineralogical Association 2010, Budapest, Hungary.
- Eva Wadoski, Thomas Armbruster, Biljana Lazic, Martin Fisch:
Stepwise dehydration of Goosecreekite: A structural study.
20th Meeting of the International Mineralogical Association 2010, Budapest, Hungary.
- Nicola Döbelin, Marc Bohner, Martin Fisch, Urs Eggenberger:
XRD analysis of brushite cement samples under simulated physiological conditions.
Swiss Society for Biomaterials 2010, Dübendorf, Switzerland.
- Martin Fisch, Thomas Armbruster:
Microporous $\text{CsAlSi}_5\text{O}_{12}$ at non-ambient conditions.
3rd International Symposium on Advanced micro- and mesoporous materials 2009, Varna, Bulgaria.

Erklärung

gemäss Art. 28 Abs. 2 RSL 05

Name/Vorname: Fisch Martin

Matrikelnummer: 01-123-827

Studiengang: Doktorat Phil.-nat. (Erdwissenschaften)

Bachelor Master Dissertation

Titel der Arbeit: Crystal Chemistry of Boron-Bearing Mullite-Type Compounds

Leiter der Arbeit: Prof. Dr. Thomas Armbruster

Ich erkläre hiermit, dass ich diese Arbeit selbständig verfasst und keine anderen als die angegebenen Quellen benutzt habe. Alle Stellen, die wörtlich oder sinngemäss aus Quellen entnommen wurden, habe ich als solche gekennzeichnet. Mir ist bekannt, dass andernfalls der Senat gemäss Artikel 36 Absatz 1 Buchstabe o des Gesetzes vom 5. September 1996 über die Universität zum Entzug des auf Grund dieser Arbeit verliehenen Titels berechtigt ist.

3012 Bern, 8. März 2011

Martin Fisch

F Curriculum Vitae

Personal Details

Name: Fisch
First name: Martin A.
Date of birth: 29. August 1979
Place of birth: Egnach TG
Citizenship: Swiss

Education

1987–1990: Primary School, Bremgarten BE
1990–1994: Secondary School, Bremgarten BE
1994–2001: Grammar School, Freies Gymnasium Bern
05/2001: Matura Typus C (Natural Sciences)
07/2001–10/2001: Military service as Medic/Truck Driver (Soldier), Monte Ceneri (TI)
10/2001–07/2003: Studies of Physics, University of Bern
10/2003–08/2007: Studies of Earth Sciences, University of Bern
08/2005: Bachelor in Earth Sciences, University of Bern
Thesis: *CH-Asbest*
Supervisor: Prof. Dr. T. Armbruster
08/2007: Master of Science in Earth Sciences, University of Bern
Specialization: Major in Earth Materials
Thesis: *Synthesis and Temperature Dependent Structure Characterization of Microporous CsAlSi₅O₁₂*
Supervisor: Prof. Dr. T. Armbruster
10/2007–04/2011: Doctorate in Mineralogical Crystallography at the Institute of Geological Sciences, University of Bern
Thesis: *Crystal Chemistry of Boron-Bearing Mullites*
Supervisor: Prof. T. Armbruster

